Contribution to CFD Modeling of Lignite Oxy-fuel Combustion with Special Focus on Radiation Properties

Von der Fakultät für Maschinenbau, Elektrotechnik und Wirtschaftsingenieurwesen der Brandenburgischen Technischen Universität Cottbus zur Erlangung des akademischen Grades eines Doktor-Ingenieurs genehmigte Dissertation

vorgelegt von

Tanin Kangwanpongpan, M.Sc.

Geboren am 26.06.1979 in Bangkok, Thailand

Vorsitzender: Prof. Dr. rer. pol. Felix Müsgens

Gutachter: Prof. Dr.-Ing. Hans Joachim Krautz

Gutachter: Prof. Dr.-Ing. Fabian Mauß

Tag der mündlichen Prüfung: 25. Februar 2013

Acknowledgements

I would like to thank my advisor, Prof. Dr.-Ing. Hans Joachim Krautz, for the enthusiastic support for making it possible for me to conduct this work, and for encouraging my creative tendencies in the research. A special thank is extended to Dr.-Ing. Matthias Klatt for his advice and assistant during my research work.

I wish to thank my reviewer, Prof. Dr.-Ing. Fabian Mauß, for devoting time to this thesis and I would also like to thank Prof. Dr. rer. pol. Felix Müsgens for being the head of the committee for my dissertation examination board.

My thanks also go to my colleagues at the Chair of Power Plant Technology, Brandenburg University of Technology in Cottbus (BTU Cottbus): Michael Nimtz, Alexander Lisk, Kristin Schierack, Stefanie Rosplesch and all of my colleagues for assistance throughout my doctoral studies. Thank you all for your cooperation, technical assistance and helpful discussion.

I also want to gratefully acknowledge my friends: Rodrigo Corrêa da Silva, Dr.-Ing. Matthias Schreiber and Dr.-Ing. Teklay Weldeabzgi Asegehegn, for the help and friendship during our study together. Special thanks to my friend: Rodrigo Corrêa da Silva for collaborative research works and excellent efforts as co-author in many research articles throughout my doctoral studies. I would also like to thank Dr.-Ing. Matthias Schreiber for our friendship and for supporting private matters, making my life easier to stay in Cottbus. Thanks to all Thai friends in Cottbus for all the great times that we have shared.

I would like to acknowledge the great support from colleagues at Thermal Science and Energy Research Group (GESTE), the Federal University of Rio Grande do Sul (UFRGS): Prof. Dr. Francis H.R. França, Prof. Dr. Paulo Smith Schneider, Fabiano Cassol, Rogério Brittes, Leonardo Dorigon, Marcelo Galarça, André Maurente and Anderson Mossi for useful discussion in spectral radiation modeling and for the use of supercomputer to generate spectral radiation data from HITEMP 2010 database.

I would like to acknowledge financial support from the International Graduate School at BTU Cottbus, GeoEn II and Innoprofile research projects from the Federal Ministry of Education (BMBF) research program and DAAD-PROBRAL project for support during the collaborative research in Brazil.

Last but definitely not least, I would like to present my thesis to my family and my parents. I am most indebted to them for their continuous confidence and encouragement. I want to thank my wife Naraporn. She has encouraged me and helped me with her love, patience, encouragement and understanding throughout my studies.

Tanin Kangwanpongpan Cottbus, March 2013

Abstract

Coal consumption shares approximately 1/3 of a total global primary energy consumption, therefore this will mainly impact to global warming situation in the 21th century. For this reason, the natural resource such as coal should be processed in the most efficient way. Today, we have several combustion technologies to serve this purpose and oxy-fuel combustion is one of efficient method. In oxy-fuel technology, carbon dioxide (CO_2) will be captured in the liquid form for storaging into the ocean or injecting into the rock-sediment underground.

CFD is an effective tool to analyse and approximate combustion gas species, temperature and heat transfer properties in oxy-fuel furnace. However, an insight into mathematical models for oxy-coal combustion is still restricted from many unknowns such as devolatilization rate, reaction mechanism of volatile reaction, turbulent gaseous combustion of volatile product, char heterogeneous reaction, radiation properties of gaseous mixture and heat transfer inside combustion chamber and through furnace's wall. Therefore, this dissertation aims to study mathematical modeling of lignite combustion under oxy-fuel conditions and also create new correlations for weighted sum of gray gases (WSGG) model for predictions of radiation properties of oxy-coal gas mixture.

Heat transfer drastically changes due to an increasing proportion of H_2O and CO_2 in these oxy-fuel conditions and the degree of changes depends on the amount of both mentioned gases because both gases have higher thermal heat capacity than N_2 in air-fired combustion and also are a good emitter and absorber of radiation. Hence, the second big part of this thesis also dedicates to the contents of creating the new correlations for WSGG model for modeling of radiation properties of oxy-fuel mixtures under various molar fraction ratios (MR) of H_2O to CO_2 ranging from the conditions of dry flue gas recirculation (MR = 0.125) to wet flue gas recirculation (MR = 1). The total emissivity of new correlations at various molar ratios of H_2O to CO_2 is fitted to total emissivity determined by line-by-line (LBL) calculations from an up to date HITEMP 2010 database. One-dimensional infinite parallel plates problem is used to evaluate accuracy of radiative source term and heat flux predictions from the new correlations validating with the results from the LBL calculations. These new oxy-fuel correlations are further included in numerical investigation in oxy-fuel furnaces.

The mathematical models are investigated using numerical CFD software (ANSYS FLUENT 12.0) to provide predictions of aerodynamics, thermo-chemical and heat transfer quantities. The predictions were validated with experimental measurements of temperature, hemi-spherical incident intensity and species concentrations (O_2, CO_2, H_2O) from a 0.4 MW_{th} oxy-fuel furnace at BTU Cottbus. However, because the lack of measurements of velocity profile in the furnace, additional laboratory oxy-fuel case is necessary to investigate influence of choices of turbulent models. Therefore, additional experimental results and operating conditions from a 100 kW_{th} oxy-fuel furnace from publication are selected in order to investigate influence of each mathematical sub-model to the predictions of velocity, temperature and oxygen concentration, which is useful for further applying to a bigger scaled 0.4 MW_{th} oxy-fuel furnace. Because many sub-models are involved in the studies of lignite oxy-fuel combustion, contents of toxic gas (NO_x and SO_x) emission and soot formation are out of the scope of this thesis. However, particle emissivity is modeled using the knowledge of soot radiation.

Results for the new oxy-fuel radiation correlations and for two CFD numerical cases were described. There are composed of one dimensional infinite plate problem for radiation modeling of gas properties, 100 kW_{th} oxy-fuel simulations for investigating sub-models and pilot-scale 0.4 MW_{th} oxy-fuel simulations. For one dimensional infinite plate problem, the relative errors of the radiative source and of the radiative heat fluxes from the new correlations were evaluated by comparison with the benchmark LBL integration (HITEMP 2010 database). For all cases, the new oxy-fuel correlations provided the best agreement in comparison to the LBL integration of the HITEMP 2010 database and the relative errors in the predictions of the radiative quantities for all investigated cases were within 30 % for the radiative heat flux and 15 % for the radiative source terms.

The numerical results from laboratory scale (100 kW_{th}) provided a set of appropriate sub-models for oxy-fuel simulations and eliminated unnecessary employing higher order or more complex mathematical sub-models for simulations. The models included in the testing cases were char reactions models, its pore mod-

els, kinetic rates and effects for not accounting char reaction with CO_2 and H_2O, results using different oxy-fuel correlations for gas emissivity including the new oxy-fuel correlations from this thesis, turbulent models, and effects of including modified oxy-fuel reversible CO-CO_2 reactions or more steps of global reaction mechanisms in turbulent gaseous combustion models. From numerical investigations, it can be concluded that using kinetic diffusion limited rated (KD) or intrinsic model for char reactions caused in more deviations from experiments than other char reaction's model close to burner zone. Implementing global kinetic rate model for char reaction (macro kinetics) resulted in the most accurate predictions in overall when comparing predictions of temperatures, O_2 molar concentrations and velocity profiles. Slightly differences were investigated when including char-CO_2 and char-H_2O reactions for both KD and intrinsic model, implying the benefit of excluding these two heterogeneous reactions to calculation time. Using different radiation correlations did not influenced previously mentioned quantities but only the radiative source terms along centerline were different. Results from using different turbulent models were comperable and the standard k-ε model was still a good compromise between accuracy and computational effort. It was found that modified reversible CO-CO_2 oxy-fuel reaction improved numerical predictions only in the case of using global 2-step reaction mechanisms. In another word, modified oxy-fuel CO-CO_2 reaction was not required in the case of using global 3-step reaction mechanisms for turbulent gaseous combustion.

Results of developed CFD model from laboratory scale oxy-fuel furnace were used as basis for numerical predictions of pilot-scale 0.4 MW_{th} oxy-fuel furnace. The predictions were compared with measurements for temperatures, hemi-spherical radiation intensity, O_2, CO and CO_2 molar concentrations at various locations in the furnace. From mesh dependency test, computational mesh of 1 million was sufficient for the problem and numerical results have the slightly deviated trends when further increasing cells. In overall, numerical predictions had good agreements with experiments and showed similar trends for temperature, gas concentrations and also radiation quantity. However, oxy-fuel flame aerodynamics is so complicated that can cause in sharply changes in temperature and gas concentrations near the flame's core at short radial distance close to burner and the capability of the developed CFD model still provided deviated values from experiments, especially in this region. Finally, outcome of studies in this thesis and successful CFD model can be used for the purpose of design and predictions for temperature, gas concentrations of combustion gases and heat flux in oxy-fuel lignite-fired furnace.

Keyword: CFD, Oxy-fuel combustion, Radiation modeling, Lignite

Kurzfassung

Kohle besitzt einen Anteil von circa einem Drittel am weltweiten Primärenergieverbrauch und hat daher einen großen Einfluss auf die globale Erderwärmung im 21. Jahrhundert. Aus diesem Grund sollte eine natürliche Ressource wie die Kohle auf höchst effektive Weise genutzt werden. Zu diesem Zweck sind mehrere moderne Technologien verfügbar. Bei der hier betrachteten Oxyfuel-Technologie wird das Kohlenstoffdioxid (CO_2) im Verbrennungsprozess angereichert und gesammelt, um später beispielsweise in flüssiger Form zur Lagerung in Ozeanen oder zur Injektion in unterirdische Gesteinssedimente genutzt zu werden.

Zur Analyse und Abschätzung der Verbrennungsgaszusammensetzung, Temperatur und Wärmeübertragungseigenschaften in Oxyfuel-Feuerungen stellt CFD ist ein effektives Werkzeug dar. Dennoch ist der Zugang zu den mathematischen Modellen der Oxyfuel-Verbrennung auf zahlreiche Unbekannte wie Entgasungsrate, Reaktionsmechanismus der Flüchtigen, turbulente Gasverbrennung der Flüchtigen, heterogene Reaktion des Koks, Strahlungseigenschaften des Gasgemischs und Wärmeübertragung in der Brennkammer und durch die Feuerraumwände weiterhin eingeschränkt. Daher zielt diese Dissertation darauf ab, die mathematische Modellierung der Braunkohleverbrennung unter Oxyfuel-Bedingungen zu untersuchen und ebenfalls neue Korrelationen für das Weighted Sum of Gray Gases (WSGG) Modell zur Vorhersage der Strahlungseigenschaften der Oxyfuel-Gasmischung aufzustellen.

Unter Oxyfuel-Bedingungen verändert sich die Wärmeübertragung aufgrund der erhöhten Konzentration von H_2O und CO_2 drastisch. Die Stärke der Veränderung ist von der Konzentration dieser Gase abhängig, da beide eine höhere Wärmekapazität als N_2 besitzen und ebenfalls gute Strahlungsemittierer und -absorber sind. Daher befasst sich der zweite große Abschnitt dieser Arbeit mit der Erstellung einer neuen Korrelation für das WSGG Modell zur Beschreibung der Strahlungseigenschaften von Oxyfuel-Gasgemischen mit verschiedenen molaren Verhältnissen (MR) von H_2O zu O_2, die von trockener Rauchgasrezirkulation (MR = 0,125) bis zur feuchten Rauchgasrezirkulation (MR = 1) reichen. Mit den neuen Korrelationen wird der Gesamtemissionsgrad für verschiedene molare Verhältnisse von H_2O zu O_2 durch zeilenweise (LBL) Berechnungen aus einer aktuellen HITEMP 2010 Datenbank angepasst. Das eindimensionale Problem der „unendlich großen, parallelen Platten“ wird zur Evaluierung der Strahlungsquellterm- und Wärmestromvorhersagen durch die neue Korrelation angewendet. Schließlich werden die neuen Korrelationen zur numerischen Untersuchung von Oxyfuel-Feuerungen verwendet.

Die mathematischen Modelle werden mithilfe von numerischer CFD Software (ANSYS FLUENT 12.0) untersucht, um Vorhersagen zur Aerodynamik, thermo-chemischer und Wärmeübertragungseigenschaften bereitzustellen. Die Vorhersagen werden durch experimentelle Messungen von Temperatur, einfallender hemisphärischer Strahlungsintensität und Gaszusammensetzung (O_2, CO_2, H_2O) an einer 0,4 MW_{th} Oxyfuel-Feuerung an der Brandenburgischen Technischen Universität Cottbus validiert. Aufgrund der mit dieser Anlage nicht messbaren Geschwindigkeitsprofile in der Feuerung ist eine weitere Laboranlage notwendig, um den Einfluss der Turbulenzmodelle zu untersuchen. Daher werden zusätzliche experimentelle Ergebnisse und Betriebsbedingungen einer 100 kW_{th} Oxyfuel-Feuerung aus der Literatur genutzt, um den Einfluss von jedem mathematischen Submodell zur Vorhersage von Geschwindigkeit, Temperatur und Sauerstoffkonzentration zu untersuchen. Da viele Submodelle in der Studie der Oxyfuel-Verbrennung von Braunkohle involviert sind, wird die Emission toxischer Gase (NO_x und SO_x) und die Rußbildung in dieser Arbeit nicht behandelt. Dennoch wird der Partikelemissionsgrad unter Kenntnis der Rußstrahlung modelliert.

Weiterhin werden die Ergebnisse der neuen Korrelationen für die Oxyfuel-Verbrennung und zwei weitere Fälle beschrieben. Diese bestehen aus dem Problem der „unendlich großen, parallelen Platten“ für die Modellierung der Strahlungseigenschaften des Gases, die 100 kW_{th} Oxyfuel-Simulationen zur Untersuchung der Submodelle und die 0,4 MW_{th} Pilotanlagen Oxyfuel-Simulationen. Für das Problem der „unendlich großen, parallelen Platten“ wurden die relativen Fehler der Strahlungsquelle und der Strahlungswärmeströme von den neuen Korrelationen mittels Vergleich mit dem Benchmark (HITEMP 2010 Datenbank) evaluiert. In allen Fällen zeigten die neuen Oxyfuel-Korrelationen beste Übereinstimmung im Vergleich zur LBL Integration der HITEMP 2010 Datenbank. Die relativen Fehler für die Vorhersagen der Strahlungseigenschaften lagen für alle untersuchten Fälle innerhalb von 30 % für den Strahlungswärmestrom und innerhalb von 15 % für die Strahlungsquellterme.

Die numerischen Ergebnisse der 100 kW_{th} Laboranlage führten zu einem Set von passenden Submodellen für die Oxyfuel-Simulationen und eliminierten unnötige, komplexe Submodelle für die Simulationen. Die in den Testfällen eingeschlossenen Modelle waren Koksabbrandmodelle, Porenmodelle, kinetische Parameter, Effekte zur Nichtbeachtung von Koksreaktionen mit CO_2 und H_2O, Ergebnisse unter Anwendung verschiedener Oxyfuel-Korrelationen zur Gasemission inklusive den neuen Korrelationen aus dieser Arbeit, Turbulenzmodelle und Ef-

fekte bei der Anwendung modifizierter, reversibler CO-CO_2 Reaktionen oder mehrstufige Reaktionsmechanismen in den turbulenten Gasverbrennungsmodellen. Aus den numerischen Untersuchungen kann geschlussfolgert werden, dass die Anwendung des Kinetic Diffusion Limited Rated (KD) oder Intrinsic Modell für die Koksreaktionen in Brennernähe höhere Abweichungen von den Experimenten verursacht als andere Koksabbrandmodelle. Mit der Implementierung des Global Kinetic Rate Modells für die Koksreaktion (Makrokinetik) konnte die besten generellen Vorhersagen für die Temperaturen, O_2-Konzentrationen und Geschwindigkeitsprofile erzielt werden. Geringe Abweichungen wurden beobachtet als die Koks-CO_2 und Koks-H_2O Reaktionen für sowohl das KD als auch das Intrinsic Modell angewendet wurden, was den Vorteil der Nichtbetrachtung dieser beiden heterogenen Reaktionen zur Rechenzeit aufzeigt. Die Anwendung verschiedener Strahlungskorrelationen beeinflussten die bereits genannten Eigenschaften nicht, lediglich die Strahlungsquellterme entlang der Hauptachse waren unterschiedlich. Die Ergebnisse von der Verwendung verschiedener Turbulenzmodelle waren vergleichbar und das Standard k-ε Modell stellte einen guten Kompromiss zwischen Genauigkeit und Rechenaufwand dar. Es wurde festgestellt, dass die modifizierte reversible CO-CO_2 Oxyfuel-Reaktion die numerischen Vorhersagen nur im Falle des zweistufigen, globalen Reaktionsmechanismus verbesserten. Die modifizierte reversible CO-CO_2 Oxyfuel-Reaktion ist in anderen Worten nicht notwendig, wenn dreistufige, globale Reaktionsmechanismen für die turbulente Gasverbrennung angewendet werden.

Die Ergebnisse des entwickelten CFD-Modells für die Laboranlage zur Oxyfuel-Verbrennung wurde als Basis für die numerischen Untersuchungen der 0,4 MW_{th} Pilotanlage genutzt. Die Vorhersagen wurden mit Messungen der Temperaturen, hemisphärischen Strahlungsintensität, O_2-, CO- und CO_2- Konzentrationen an verschiedenen Positionen in der Feuerung verglichen. Gitterabhängigkeitstests zeigten, dass ein Gitter mit 1 Million Zellen für das Problem ausreichend ist und die Trends sich nur geringfügig ändern, wenn die Zellenanzahl erhöht wird. Insgesamt zeigten die numerischen Vorhersagen gute Übereinstimmungen mit den Experimenten und vergleichbare Trends für Temperatur, Gaskonzentrationen und Strahlungsgrößen. Dennoch ist die Aerodynamik einer Oxyfuel-Flamme so kompliziert, dass es in der Nähe des Flammenkerns in geringem radialem Abstand zum Brenner zu abrupten Veränderungen der Temperatur und Gaskonzentrationen kommen kann. Insbesondere in dieser Region zeigte das entwickelte CFD-Modell seine Abweichungen. Zusammenfassend kann nachgewiesen werden, dass das CFD-Modell zur Auslegung und Vorhersage von Temperatur, Gaskonzentrationen und Wärmeströmen in braunkohlegefeuerten Oxyfuel geeignet ist.

Schlagwörter: CFD, Oxyfuel-Verbrennung, Strahlungsmodellierung, Braunkohle

Table of contents

1 Introduction

1.1 Coal shared CO_2 emission and carbon capture technologies

Primary energy demand:

From the policies scenario from Internal Energy Agency (IEA) in 2010, global energy demand for coal climbs from 26% in 2006 to 29% in 2030 and most of the demand for coal comes from the power-generation sector [WEO10]. In the new policies scenario from IEA called the golden age of gas scenario (GAS) in 2011 [WEO11], the share of energy mix of natural gas increases from 21% to 25% between 2008 and 2035 pushing the share of coal into decline from 27% to 22% by 2035. Global primary energy demand is projected to rise by 35% from 2008 to 2035. Primary energy demand grows more quickly in non-OECD countries increasing by almost 65% from 2008 to 2035.

Coal shared CO_2 emission:

According to the new Copenhagen protocol [COP15-09], global CO_2 emission is rising from power generation due to an increasing world demand for electricity. For energy-related CO_2 emissions in 2009, 43% of CO_2 emissions from fuel combustion were produced from coal, 37% from oil and 20% from gas [CO_2Emiss-IEA11]. CO_2 emissions from coal dropped around 1% between 2008 and 2009 and equal to 12.5 Gt CO_2 in 2009. By energy sectors, CO_2 emissions from the generation of electricity and heat declined by 1.7% from 2008 to 2009. CO_2 emissions are increased due to the reduction in nuclear and renewable energy, adding 220 Mt CO_2 and 100 Mt CO_2 respectively in 2035 [WEO11]. According to the Intergovernmental Panel on Climate Change's (IPCC) [IPCC07], different scenarios are analyzed and world temperature is expected to rise between 1.8-4 °C in the coming century due to global warming, which is very likely due to human-induced greenhouse gas (GHG) concentrations in the atmosphere. From the CO_2 emission and global temperature rising trends, reducing GHG emissions is viewed as a solution to global warming and CO_2 capture and storage (CCS) is the key factor to mitigate climate change. Many CCS research projects and international cooperation were launched since 2002 [Pires11, Praetorius09, Ashworth10] including international level: Carbon Sequestration Leadership Forum (CSLF) and IEA Clean Coal Center, European level: CO_2STORE, CO2NET, ENCAP, CO2GeoNet, ZEP, ACCSEPT, CO2SINK and national level in Germany Australia and USA: GEOTECHNOLOGIEN, COORETEC (Germany), CO2CRC, CSIRO, CCSD, ZeroGen (Australia), DOE/NETL, FutureGen (USA).

Reviews on carbon dioxide capture and storage (CCS):

Many aspects were reviewed to show a feasibility of integrating CCS in existing power generation's sectors such as policy for CCS deployments [Vergragt11, Praetorius09, Stechow11, LiuH11, Torvanger11, Pollak11, Román11, Alphen10], Emission Trading System (ETS) [Rogge10-11], technology roadmap [RoadmapIEA09,11, Nagl-11], technology scenario [ETP-IEA10, Blesl-10, Schreiber10, McJeon11, Viebahn12, ChungTS11, Praetorius09, Odenberger10, ETP-IEA08], public acceptance [Upham11, Shackley09] and risk analysis [Ha-Duong11, Stigson12]. The technical aspects of various carbon dioxide capture technologies (CCT) are plant efficiency, new equipments and nat-

ural resources required for retrofitting purpose, operational parameters of CCS plants, emissions of toxic and greenhouse gases (NO_x, SO_x, CO_2), operations needed for CO_2 compression, transport and sequestration. The commercial aspects of CCS technology deployments [Lohwasser11, Tzimas10, Choi12, Akimoto10, Eskeland12] are capital cost for new CCS power plants, additional cost for retrofit, CO_2 avoidance costs and cost of electricity (COE) with CCS.

Technological-economical evaluation for carbon capture technologies (CCT):

Three potential technologies for CO_2 capture, called carbon dioxide capture technologies (CCT) , are pre-combustion, post-combustion and oxy-fuel combustion capture [Ghoniem11, Pires11, SinghB11, Olajire10, Gibbins08, MIT07, Wall07, Damen06, Steeneveldt06, CostCO_2-IEA06, IPCC05]. Currently, it is unclear which potential carbon capture technology (pre-, post-, oxy-fuel combustion), previously explained, is the most feasible technology for large-scale operation. Criteria for assessment of CCT are, for instance, net(overall) plant efficiency, net electricity production (MW_e), capital cost, cost of electricity (COE), CO_2 capture efficiency (%), CO_2 emission rate (g CO_2/kWh) and cost of CO_2 avoidance [CostCO2-IEA11, EcoGlobalCCS11, Kuramochi12, Moullec12, Strube11, Hammond11, Olajire10, Hadjipaschalis09, Gibbins08, Rubin07, Davison07, Wall07, MIT07, CostCO_2-IEA06, Damen06, Steeneveldt06,]. Additional factors effecting the calculation in each criterion are power plant types [Huang12, MIT07] (subcritical, supercritical or advanced supercritical pulverized coal fired plants), CO_2 separation technologies for post-combustion [WangM11] (adsorption, physical absorption (Selexol), chemical absorption with MEA (monoethanolamine), cryogenics separation, membrane absorption, membrane-based separation) and loan interest rate in the year of evaluation. For a better overview of techno-economic assessments, some parameters are compared for three main technologies focusing only on coal fired power plants reviewed by International Energy Agency (IEA) and Global CCS Institute, Australia [CostCO2-IEA11, EcoGlobalCCS11]. Based on the plant capacity of around 550 MW_e (Net) and CO_2 capture efficiency about 90 %, maximum net electrical efficiency was equal to 33.2 % for post-combustion capture in ultra supercritical pulverized coal fired plants (USC-PC) reported by IEA, while equal to 33.1 % for pre-combustion with IGCC power plants reported by Global CCS Institute. Both organizations reported that by employing oxy-fuel technology, cost of electricity (COE) was minimized and equal to 7.3 Euro cent/kWh reported by IEA and 8.1 Euro cent/kWh (Levelised cost of electricity, LCOE, account for variable and fixed operating and maintenance costs) reported by Global CCS Institute. IEA reported minimum CO_2 avoidance cost for pre-combustion capture (30.9 Euro/t_{CO2}), in contrast to reports from CCS Institute, in which USC-PC oxy-fuel plant resulted in minimized CO_2 avoidance cost (32 Euro/t_{CO2})among three technological options.

Carbon capture technologies (CCT):

Concepts of the three technologies were presented in a flow diagram in Fig. 1.1. Pre- and post-combustion are first briefly explained and oxy-fuel combustion is further described in details. In this thesis, list of figures, tables, nomenclatures are appended in Appendix H, I and J, respectively.

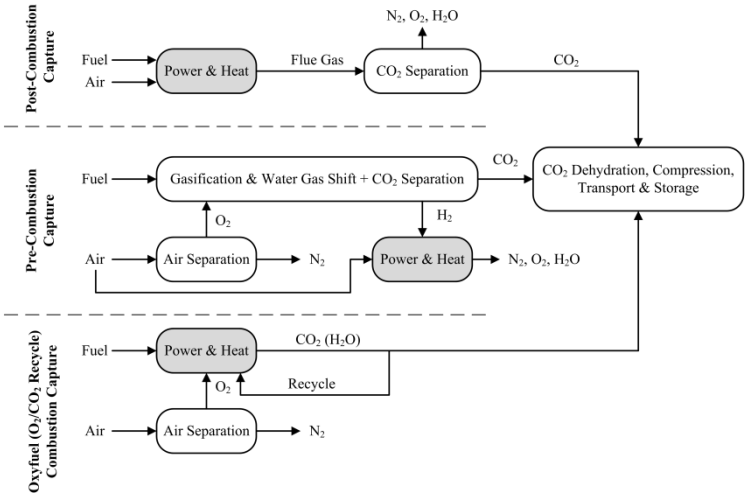

Figure 1.1: Principles of three potential CO_2 capture technologies, adapted from [Gibbins08].

In pre-combustion capture systems [Scholes10], fuel is reformed by oxygen and/or steam to finally form a mixture of H_2 and CO_2. Fossil fuels are first gasified with sub-stoichiometric amounts of oxygen at elevated pressures (approximately 30–70 atm) to give synthesis gas mixture of CO and H_2. Then, Additional steam is added and the mixture is passed through a series of catalyst beds for the water–gas shift reaction ($CO+H_2O \leftrightarrow CO_2+H_2$). After that, the CO_2 can be separated from H_2 by absorption, adsorption or membranes and the pure H_2 is combusted with air in the power plant. An advantage of this technology is the higher CO_2 concentration and pressure achieved in the output stream and the CO_2 can be compressed at above-atmospheric pressure, and later transported to storage sites. For this reason, the energy required for CO_2 capture and compression in pre-combustion capture may be half order of those required in post-combustion capture. Thus, the equipment to separate CO_2 from the flue gas stream can be smaller resulting in lower overall energy penalties. The main disadvantage of pre-combustion capture is the high capital costs of investment [Olajire10]. The most common pre-combustion CO_2 capture technology based on coal is termed integrated gasification combined cycle (IGCC) [Steeneveldt06].

In post-combustion capture [WangM11], flue gas contains CO_2 with low concentration about 4-14 % (by volume). The most economically CO_2 separation and capture process is the absorption using an amine as the absorbent (wet scrubbing with aqueous amine solutions). The CO_2 is removed from the flue gas product by a aqueous amine solvent at low temperature (50 °C) before final stage of the process and can then be further used, for example, in enhanced oil recovery (EOR), urea production and in the food and beverage industry. The rich solvent is the regenerated by adding heat in the desorption column, producing a highly pure stream of CO_2, which is, after drying sent to the compression system. Disadvantage of the post-combustion is that low CO_2 concentrations in flue gas require powerful chemical solvents and various stages of absorption/desorption, thus the process consumes high energy amounts (steam from low-pressure turbine) to regenerate the solvents. Adsorption, gas-separation membranes and cryogenic distillation can also be applied for the post-combustion capture.

1.2 Oxy-fuel combustion

Oxy-fuel combustion: *Concepts and reviews*:

Oxy-fuel combustion is one of the promising technologies for capturing CO_2 from power plants and also possibility for CO_2 transportation and storage in a depleted oil and gas well or saline-aquifer. The concept of oxy-fuel combustion is to remove N_2 from combustion process and burn fuel with a mixture composed of O_2 and recycled flue gas, producing flue gas mainly consists of CO_2, H_2O and a small amount of other combustion products. After further purification, CO_2 is compressed and transported to storage sites and sequestration at the sites [Anheden05]. The oxy-fuel research is still limited to pilot-scaled projects [OCC2-11] and combustion in oxy-fuel conditions must be further investigated for a scale-up plant. Current demonstrations of oxy-fuel projects around the world are reviewed in Appendix A (Table A.1) including start-up time for commissioning arranging by chronological order. Examples of new projects are Callide A (Australia, start-up 2012), Jamestown (USA, start-up 2013), Holland (USA, start-up 2014), Daqing (China, start-up 2015), Compostilla OXY-CFB-300 (Spain, start-up 2015), Black Hills Power (USA, start-up 2016), FutureGen 2.0 (USA, start-up 2015) and Youngdong (South Korea, start-up 2016).

Oxy-fuel combustion for carbon dioxide capture and storage (CCS) has been reviewed in literature [ChenL12, Toftegaard10, Scheffknecht11, Wall07, 09, Buhre05] covering technical (operational) aspects, combustion fundamentals and economic studies. Technical aspects for operation of oxy-fuel plants include air separation unit (ASU), burner operation, recycled ratios and position of flue gas recirculation (FGR), oxygen addition to inlet streams, flue gas cleaning equipment (desulphurization, De-NO_x and particulate removal), CO_2 purification/compression unit and plant efficiency. Oxy-fuel combustion fundamentals were also reviewed, for example, heat and mass transfer (convection and radiation), oxy-fuel flame stabilization, coal devolatilization, ignition of coal particles, char burnout, kinetics and structure of devolatilized char (morphology). In addition, economic aspects such as CO_2 avoidance cost and capital cost for installing additional equipments for oxy-fuel plants were also published [Andersson06, Kakaras07a-07c, Zanganeh07] including process evaluation of oxy-fuel combustion [Castillo11, Haryanto11, ZhouWei10]. Technical aspects are first reviewed in this chapter. Combustion fundamentals and CFD simulations and sub-models are further reviewed in chapter 2.

Oxy-fuel combustion (technical aspects): *oxy-fuel process*

A schematic diagram for coal-fired oxy-fuel process is presented in Figure 1.2. From the diagram, almost pure O_2 is prepared by separating N_2 from air using air separation unit (ASU). After O_2 production by ASU, O_2 is mixed with secondary flue gas recirculation (secondary FGR), composed mainly of CO_2 and some amount of NO_x, SO_x or Ash (depending on different configurations for secondary FGR, presented by dash lines in Fig. 1.2) before injection into the inlet streams at the burner. Primary flue gas recirculation (primary FGR), which contains dried CO_2 stream (waste water is removed by condenser), is re-heated by a pre-heater before used for driving coal particles to mix with oxidizer streams at the burner.

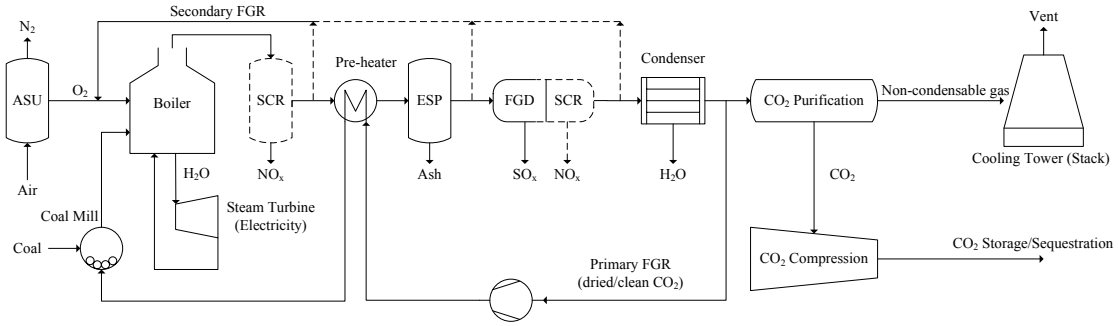

Figure 1.2: Schematic diagram for coal-fired oxy-fuel process revised based on the work in [ChenL12, Hu12, Scheffknecht11, Yan11, Tofteegard10, Wall07, Hadjipaschalis09, Buhre05]. ASU: air separation unit, SCR: selective catalytic reduction reactor, ESP: electrostatic precipitator, FGD: flue gas desulphurization, FGR: flue gas recirculation. (dashed lines = possible configurations for secondary FGR).

The primary flue gas is purified by ESP, SCR and FGD to remove fly ash, NO_x and SO_x, respectively. Non-condensable gases including other pollutants are then removed and CO_2 is finally compressed to supercritical pressures (pipeline transport) or liquified (ship transport) prior to transport and subsequent storage. The oxy-fuel process, boiler configurations and measurements in pilot-scale 0.4 MW_{th} oxy-fuel test facility at BTU Cottbus utilized lignite as fuel are explained in details in chapter 5.

Oxy-fuel combustion (technical aspects): *air separation unit (ASU)*

Almost pure O_2 for the combustion is produced from the air separation unit (ASU). At the current state of technology and plant size, cryogenic distillation is the most economically process for air separation [Burdyny10, Allam09, Darde09, Anheden05, SinghD03]. However, the cryogenic distillation requires a high energy penalty causing in a reduction of the overall plant efficiency of about 7-9 % points [Tofteegaard10]. The maximum reduction of plant efficiency was found to be even 15 % for 865 MW plant capacity [Anderson06]. To solve this problem, alternative technologies are being introduced and ion transport membranes (ITMs) is the potential option [Mancini11a, 11b].

For current oxy-fuel plant's capacity, the first large-scale oxy-fuel coal combustion demonstration plants of around 200–300 MWe are scheduled to be on stream from 2015 and the building of the first generation of commercial oxy-fuel coal plants of around 500–600 MW_e is expected to start between 2015 and 2020 to meet increasing CO_2 reduction targets in Europe and around the world [Wall11a, ChenL12]. In order to match the combustion air pressure in a conventionally-fired boiler, the amount of required O_2 is large, for instance a 500 MW_e power plant will consume around 10,000 tons per day of O_2 [Higginbotham11]. To evaluate possible O_2 production capacities for actual scale oxy-fuel power plants, Air Products has developed conceptual designs for a scalable ASU [Higginbotham11], covering the approximate ranges of O_2 production shown in Table 1.1. For machinery options in Table 1.1, centrifugal air compressors are generally lower cost than axial compressors and are now available for air flows corresponding to up to around 5000

tons per day of O_2. In contrast, axial compressors are available up to about 8000 tons per day of O_2, and have been used for many years in the steel industry as blast furnace blowers. For ASU process cycle, Air Products proposed the use of a triple column cycle to minimize the parasitic power consumption of the air separation unit for oxy-fuel power generation [Dillon05], while others suggested alternative approaches [Darde09, Beysel09, Tranier09]. Higginbotham et al. [Higginbotham11] also investigated different ASU process cycles at ISO conditions based on 5400 tons per day of O_2 production for 95 % purity and 1.1 bar pressure.

Table 1.1: Conceptual designs for a scalable plant size proposed by Air Products, adapted from [Higginbotham11].

O_2 production (tons/day)	Machinery options	Approximate power consumption (MW)
3000-4000	Centrifugal 1 or 2 train or axial 1 train	22-33
4000-5500	Centrifugal 1 or 2 train or axial 1 train	30-45
5500-7000	Centrifugal 2 train or axial 1 train	41-58
7000-10000	Centrifugal or axial 2 train	53-82

Oxy-fuel combustion (technical aspects): *configurations of flue gas re-circulation (FGR)*

Different configurations of flue gas recirculation were reported in literature [Nakayama92, Toftegaard10]. In general, there are two main configurations called wet and dry recirculation. For wet recirculation, flue gas is recycled before water cooler and condenser while after for dry recycle. This recycling system was sometime called hot and cold flue gas recirculation [Gampe06]. The pre-heater (economizer) can be installed before or after ESP which is used for re-heating flue gas before recycled back to combustion chamber to reduce energy consumption for the whole oxy-fuel process. The various configurations for oxy-fuel process are presented by Nakayama et al. [Nakayama92] illustrated in Fig. 1.3(a) for dry and Fig. 1.3(b) for wet recycle.

The configurations suggested by this author [Nakayama92] still do not include process units for removal of NO_x and SO_2. The NO_x and SO_2 removal unit must be included in the practical boiler in power plant to remove toxic gas depending on environmental regulation for each country.

Oxy-fuel combustion (technical aspects): *flue gas recycle ratio*

In oxy-fuel combustion, O_2 is mixed with recycled flue gas and used for combustion of the fuel to control oxy-fuel flame temperature and obtain a boiler heat transfer profile similar to that of air-firing in the case of retrofit. A flue gas recycle ratio of 60-80 % is required for this purpose [Toftegaard10]. In general, similar adiabatic combustion temperatures to case of conventional air-firing can be obtained at a flue gas recycle ratio of 69% as suggested by Smart et al. [Smart09,10a] when burning Russian coal. In addition, similar heat transfer flux for oxy-fuel combustion to air-firing can be achieved with flue gas recycle ratios between 72% and 74%. However, the results may change depending on coal type and also on temperature of recycled flue gas.

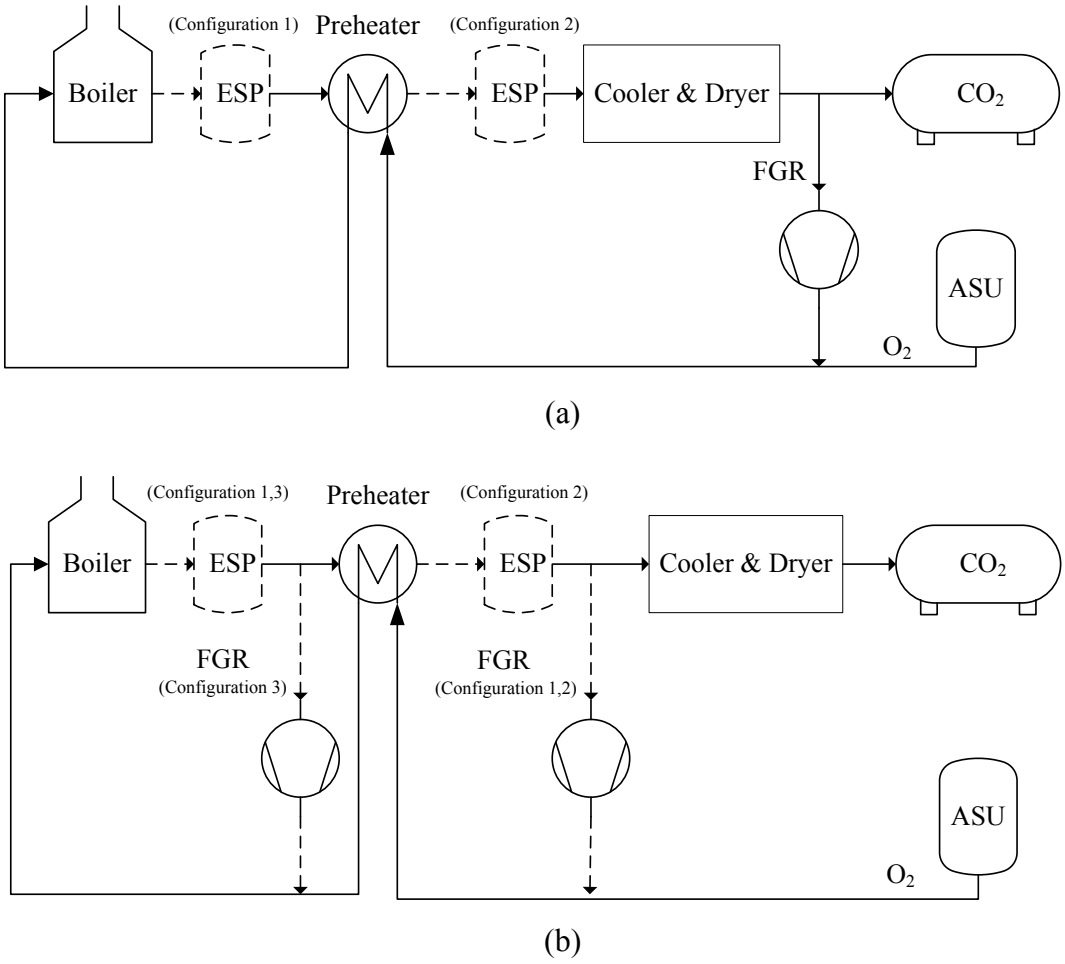

Figure 1.3: Various configurations for: (a) dry flue gas recirculation (b) wet flue gas recirculation, adapted from [Nakayama92].

It was found that the recycle ratios for hard coal (South African) rise from 65.8 % to 68.6 % when the temperature of recycled flue gas is increasing from 100 °C to 400 °C [Scheffknecht11]. The higher flue gas recycle ratio was found for dried Lusatian lignite, in which the recycle ratio increases from 67.7 % at flue gas temperature of 200 °C to 71.7 % at 400 °C. Higher flue gas recycle ratio was required for dried lignite compared to hard coal due to a significantly lower furnace exit temperature, which is influenced by ash properties of lignite. This finding is in agreement with Kather et al. [Kather06], who found that the temperature of the recycled flue gas should be between 200 and 350 °C to support the operation of an ESP and flue gas fan.

Oxy-fuel combustion (technical aspects): *Pollutants formation and flue gas cleaning*

It should be emphasized that pollutants formation (NO_x, SO_x), particulates (ash), trace elements, soot formation in oxy-fuel combustion are out of the scope of this thesis, nevertheless, pollutants formation are still briefly discussed here due to increasing number of oxy-fuel researches in this area.

In the CO_2 capture process, flue gas must be cleaned before CO_2 purification and compression. NO_x, SO_x, and particulate are removed by selective catalytic reduction (SCR) and flue gas desulphurization (FGD), consequently. Flue gas cleaning challenges for coal-fired oxy-fuel combustion with CCS was published recently by Wall et al. [Wall11b] covering aspects such as compositions of CO_2 stream and significant impact of sulfur corrosion in furnace water wall and pipeline for CO_2 transportation. In Europe, emission limits are defined as concentration limits (mg/ Nm^3 flue gas). In USA, alternative standards of unit based on emission per unit energy produced (mg/MJ electricity) encourages emission reduction by efficiency improvements and is not affected by the efficiency of the power plant. If emission per unit energy produced is employed, the emission must be reduced by around 20% per unit of energy supplied to reach same emission per unit of energy produced in an oxy-fuel power plant as in a corresponding air-fired unit [Normann09].

Experiments on NO_x and SO_x, emissions from oxy-coal combustion are investigated in many laboratories and pilot scale research facilities as reviewed by Chen et al. [ChenL12]. The research groups in the review are CANMET, University of Leeds, RWTH Aachen, IVD Stuttgart, Chalmers University of Technology, Ishikawajima-Harima Heavy Industries (IHI) and others. It is interesting that almost all experimental investigations were based on emission per unit thermal energy (mg/MJ) because of the reason previously explained. From all mentioned researches, NO_x emissions were found to be lower in oxy-coal combustion than in air-coal combustion and NO tends to increase with addition of O_2 in oxidant streams. Pronounced reductions in NO emissions were observed in case of recycling flue gas [ChenL12].

NO_x emissions in oxy-coal combustion were about 1/3 of that in air (around 70 % NO_x reduction) [ChenL12, Normann09, Wall09a, Wall07]. In oxy-fuel plants, NO_x can be reduced by either adjusting combustion parameters for burning fuel or capturing NO_x in the flue gas downstream after combustion process. The first techniques are fuel staging (reburning), oxidant-staging, low-NO_x burner and flue gas recirculation. The second techniques are selective catalytic reduction (SCR), selective non-catalytic reduction (SNCR), absorption in water, co-storage with CO_2 and distillation [Normann09]. Fundamentals of nitrogen chemistry and factors effecting NO_x formation in oxy-fuel combustion were reviewed by Normann et al. [Normann09]. For the nitrogen chemistry, NO is formed through three pathways: thermal NO, prompt NO from N_2, and oxidation of fuel-bound nitrogen. The formation of thermal NO is described by the extended Zeldovich mechanism. The mechanisms of NO formation and reduction are presented in Fig. 1.4 [Normann09, Glarborg03].

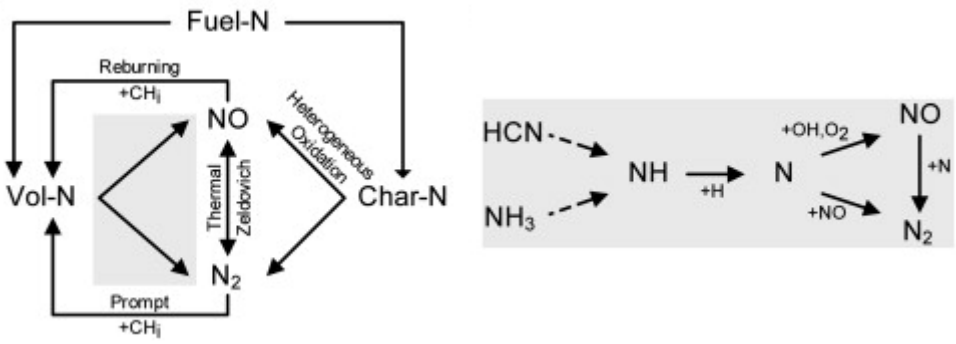

Figure 1.4: Mechanisms of NO formation and reduction and reaction-path diagram, adopted from [Normann09, Glarborg03].

Stanger and Wall [Stanger11] reviewed impacts of sulfur on oxy-coal combustion such as water wall and pipeline corrosion, ash deposition, slagging and fouling, SO_3 formation, CO_2 recovery for compression, pipeline corrosion and CO_2 quality for transport and storage. SO_2 concentration from oxy-fuel combustion is higher than that from air combustion due to flue gas recirculation [Croiset00-01], however, when using unit of mg/MJ, the oxy-fuel firing produced less SO_2 than the air firing [Stanger11]. SO_3 concentration is approximately three times higher in oxy-fuel combustion than in air combustion [Wall09]. SO_3/SO_2 conversions are comparable for oxy-fuel and air fired conditions. The effect of sulfur containing species can cause a risk for corrosion throughout the plant and transport pipelines resulting in the need for desulphurization of the recycled flue gas for oxy-fuel combustion [Buhre05]. One of desulfurization techniques against sulfur corrosion is to inject limestone ($CaCO_3$) or other calcium derivatives into the furnace. In air fired conditions, the limestone ($CaCO_3$) decomposes to produce CaO, which further reacts with SO_3 to form $CaSO_4$. It has been suggested that the higher SO_2 levels in oxy-fuel firing act to enhance the desulfurization efficiency of limestone by inhibiting $CaSO_4$ decomposition, and by the physical increase of residence time in the furnace [LiuH01]. The direct desulfurization reaction ($CaCO_3+SO_2+½O_2 \rightarrow CaSO_4+CO_2$) takes place in oxy-fuel atmospheres as suggested by Liu et al. [LiuH00], in contrast to the indirect desulfurization reaction ($CaCO_3 \rightarrow CaO+CO_2$, $CaO+SO_2+½O_2 \rightarrow CaSO_4$).

Oxy-fuel combustion (technical aspects): *CO_2 purification*

After flue gas cleaning and condensation to remove pollutants, particulate (ash), trace elements and water, the flue gas is mainly composed of 70-95% CO_2 depending on O_2 purity from ASU and air ingress into boiler and ESP [Buhre05, Davison07, SinghD03]. The CO_2 stream must be dried, purified and compressed for the purpose of transportation and sequestration. At the delivery point, pressure and temperature of CO_2 should be 80-200 bar and 0-50 °C, respectively [Toftegaard10]; nevertheless, the CO_2 supercritical state is preferable (higher than 31.1 °C and 100-110 bar) as shown in Fig. 1.5.

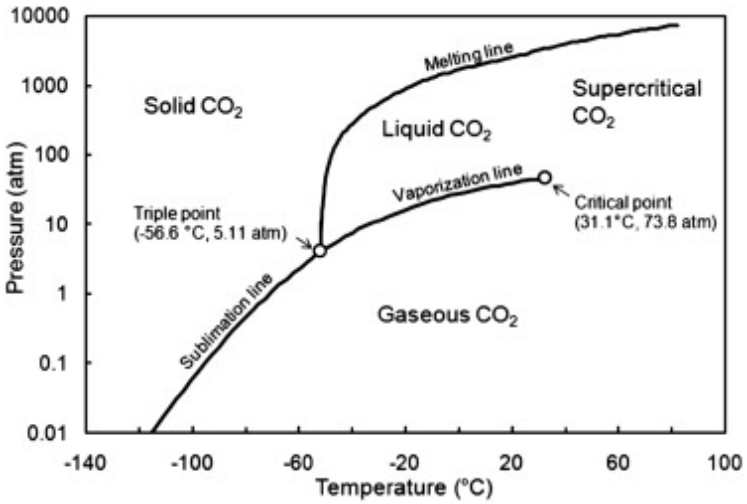

Figure 1.5: CO_2 phase diagram, adopted from [Toftegaard10].

Because non-condensable gases, such as O_2, N_2 and Ar, may result in cavitation and corrosion damage in the pipeline for transportation, these gases should be purged by multi-stage compression and liquefaction in CO_2 purification unit to separate inert gases out of the CO_2. After non-condensable gases are separated, CO_2 compression is required before transportation. This CO_2 compression step has a high energy penalty to the power plant, decreasing overall electrical efficiency about 2-3% points [Kanniche10, Wall07, Varagani05, Beér07, Dillon04,05]. The amount of non-condensable gases will be higher if air leaks into oxy-fuel plants during operation. The amount of air ingress was generally found in oxy-fuel operation and hard to be avoided. The amount of air leaking was approximately 3% of the flue gas mass flow for a new build oxy-fuel plant [Wall07, SinghD03, Dillon05], while rising up to 16% for old retrofitted oxy-fuel boiler [Anheden05]. The effect of air ingress into oxy-fuel plants will increase the costs of CO_2 purification. The CO_2 purification can be done by a flash or a distillation unit [Strömberg09, Aspelund07, Allam92]. The concepts of flash and distillation are to utilize the differences in boiling point for different gas species in order to separate them. The distillation process consumes less energy, while producing higher CO_2 purity [Aspelund07]. Typically, CO_2 capture efficiency of about 90% in oxy-fuel power plants were reported [Pehnt09, Dillon05, SinghD03].

Emerging technologies for oxy-fuel:

Some emerging technologies were suggested as new designs or integration into existing power plants. These are flameless oxidation (also called FLOX, HiTAC or MILD combustion) [Heil11, Werle10, Schaffel09, Stadler09, Krishnamurthy09], hybrid technologies with IGCC (oxy-fuel IGCC) [Romano10], hybrid technologies with post combustion capture (ECO-Scrub) [Doukelis09, Huang12], membrane technologies [Burdyny10, Hashim11, Castillo11], oxygen transport membrane (OTM) [Rosen11, Stadler11], ion transport membrane (ITM) [Mancini11a,11b, Kneer10], pressurized oxy-fuel combustion [Hong09,10] and completely new designs for oxy-fuel power plant (green-field power plant) [Kakaras07c].

1.3 Lusatian lignite and classification of coal rank

Coal is the most abundant fossil fuel existing in the world so far with a potential total reserve of approximately 1000 billion tones. The world coal consumption and production increases from around 3300 Million tones oil equivalent (Mtoe) in 2009 [WEO10] to 3500 Mtoe in 2010 [BP-review11]. Classification of coal is necessary for further utilizing in power plant because heating value of coal and impact to efficiency of plant and amount of emission are different based on chemical properties of coal. Coal could be generally classified into four main categories [Hendrickson75] as

Lignite, the lowest rank of coal, was formed from peat, which was compacted and altered. Its color has become brown to black and it is composed of recognizable woody materials imbedded in pulverized (macerated) and partially decomposed vegetable matter. Lignite displays jointing, banding, a high moisture content, and a low heating value when compared with higher coals

Sub-bituminous coal is difficult to distinguish from bituminous and is dull, black colored, shows little woody materials, is banded, and has developed bedding planes. The coal usually splits parallel to the bedding. Although it does not contain moisture, it is still of relatively low heating value.

Bituminous coal is dense, compacted, banded, brittle, and displays columnar cleavage and a dark black color. It is more resistant to disintegration in air than are sub-bituminous and lignite coals. Its moisture content is low, volatile matter content is variable from high to medium, and its heating value is high. Several varieties of bituminous coal are recognizable.

Anthracite is a highly metamorphosed coal, is jet black in color, is hard and brittle, breaks with a conchoidal fracture, and displays a high luster. Its moisture content is low and its carbon content is high.

The ASTM (American Society of Testing Materials) standard D 388 [ASTM04] could be used for classification based on fixed carbon and heating value. Table 1.2 shows general classification of coals rank.

Lusatian lignite is the abundant fuel sources, especially in the area of Brandenburg State, Germany. Therefore this coal type is used as resource for experiments under researches at the Chair of Power Plant Technology at BTU Cottbus for decade [Tappe09a-d, Kaß09, Griebe01, Owczarek00]. Although the same Lusatian lignite is used for research, coal properties differ for each experiment. The coal properties of Lusatian lignite utilized as fuel in thermo-gravimetric analysis (TGA) by Tappe [Tappe09a] denoted as TBK1 (pre-dried lignite type 1, high moisture) and TBK2 (pre-dried lignite, high ash) to determine kinetic parameters for mathematical models of char oxidation (char-O_2 reaction). For, the coal type $TBK_{0.4MWth}$ is injected into furnace for an experiment in a 0.4 MW_{th} oxy-fuel furnace in this thesis. The proximate and ultimate analysis for all coal utilized at BTU Cottbus are listed in Table 1.3.

Table 1.2: Classification of coal rank calculated on mineral-matter-free basis, adapted from [Smoot85].

Coal type	Fixed carbon (% by mass)	Volatile matter (% by mass)	Moisture (% by mass)	Heating value (MJ/kg)
Lignite	30	30	40	8.4
Sub-bituminous	35->40	40	20->30	9.5->13.8
Bituminous	42->76	40->20	20->5	13.8->15.9
Semi-anthracite	85	10	5	15.9
Anthracite	>90	<5	<3	15

Table 1.3: Proximate analysis and ultimate analysis for Lusatian lignite.

	Coal type		
	TBK1 % by mass	TBK2 % by mass	$TBK_{0.4MWth}$ % by mass
Proximate analysis:			
Fixed carbon	33.24	29.97	37.60
Volatiles	45.64	52.08	45.80
Ash	5.5	12.87	5.85
Moisture	15.62	5.08	10.75
High Heating Value (HHV), MJ/kg	-	-	22.35
Low Heating Value (LHV), MJ/kg	20.54	23.36	21.19
Ultimate analysis:			
C	52.89	55.37	57.04
H	5.48	6.42	4.29
O	19.33	16.18	20.71
N	0.55	0.49	0.65
S	0.63	3.59	0.71
Ash	5.5	12.87	5.85
Moisture	15.62	5.08	10.75

1.4 Objective of the thesis

The objective of this thesis is the numerical investigation from CFD model for the prediction of lignite combustion in oxy-fuel conditions. The values investigated are aerodynamics (velocity, kinetic energy and eddy dissipation), thermo-chemical (temperature and species concentrations) and radiation quantities (emittance, absorption coefficients, radiative source term, radiative heat flux and hemi-spherical incident intensity). Another main focus is to determine and evaluate of new correlations for the weighted-sum-of-gray-gases model to predict the radiative transfer in gases under oxy-fuel conditions. The new correlations were validated by comparing the radiative source term with line-by-line calculations from HITEMP 2010 database for a one-dimensional slab system. Other aspects such as pressurized oxy-fuel combustion, pollutants emissions (NO_x, SO_x, trace elements), corrosion, ash formation/deposition, soot formation and co-firing with biomass were out of the scope of this thesis. Particle emissivity is modeled applying the knowledge of soot radiation.

1.5 Thesis outline

Coal shared CO_2 emission, review of carbon capture technologies (CCT), demonstrations of oxy-fuel projects and oxy-fuel process for carbon-dioxide capture are presented in chapter 1. Mathematical models for lignite oxy-fuel combustion are reviewed in chapter 2 and related equation formulations and fundamental aspects are described in detail in chapter 3 in order to create suitable mathematical models for predictions of aerodynamics quantity (velocity profile), thermo-chemical quantities such as temperature and species concentrations (O_2, CO, CO_2, H_2O) and heat transfer quantities such as total emissivity, total absorption coefficients, radiative source term inside oxy-fuel furnace, incident hemispherical radiation intensity and radiative heat transfer at furnace's wall. The modeling of radiation properties for gaseous mixture in oxy-fuel conditions is presented in chapter 4 and the descriptions of investigated numerical CFD cases are explained in chapter 5. Results for the new oxy-fuel radiation correlations and for two CFD numerical cases are described in chapter 6. Finally, conclusions and recommendations for the future research are commented in chapter 7.

2 Literature Review

Comprehensively descriptions of heat and mass transfer (convection and radiation), flame stabilization and coal/char ignitions (burnout) in oxy-fuel conditions have been reviewed by Toftegaard et al. [Toftegaard10] and Chen et al. [ChenL12], which were not again explained here because the focus of this thesis is to study mathematical modeling. Other aspects such as pressurized oxy-fuel combustion, pollutants emissions (NO_x, SO_x, trace elements), corrosion, ash formation/deposition, soot formation and co-firing with biomass were out of the scope of this thesis hence not reviewed in this chapter. Wall et al. [Wall73, Andersson08a, Andersson07] presented that soot alone can contribute to 90% of the radiation at visible wavelengths and to 60% of the total wavelength-integrated radiation. For this reason, particle emissivity is assumed to be dominated by soot radiation in this thesis.

Mathematical modeling of coal combustion was studied for decades as reported by Niksa [NiksaS96] through an IEA Coal Research collaborative project from International Energy Agency (IEA). Full-scale coal combustor simulations in the review used the experimental data from furnace with total heat capacity ranged from 35-660 MWth. Firing configurations were tangential, opposed-wall, front-wall and roof-firing. From the review, the standard k-ε was applied for turbulent flow field and eddy dissipation model for turbulent gaseous reaction. Nowadays, the review is already obsolete when many new mathematical models for all sub-models in coal combustion were already much more improved in the field of coal combustion modeling [William00, 02]. Recent reviews by Eaton et al. [Eaton99], Knaus et al. [Knaus01], Versteeg et al. [Versteeg07] provided useful details of sub-model formulations for coal combustions, however, some sub-models including its correlations needed to be modified for oxy-fuel conditions, or either new sub-models should be introduced [ChenL12, Edge11a, Scheffknecht11]. The mathematical sub-models for coal combustion modeling in the reviews were turbulence, coal devolatilization, char heterogeneous reaction, gas phase reactions (reduced reaction mechanisms and turbulence-chemistry interaction), radiative properties of gas mixture, particle radiation, soot radiation and pollutant models (SO_x, NO_x).

Computational fluid dynamics (CFD) has been an efficient tool for oxy-fuel combustion researches for many years including other combustion applications (Appendix B) to provide predictions of temperature, heat transfer, and chemical species from combustion process inside furnaces. However, many sub-models in CFD require revision to account oxy-fuel environments, especially radiation modeling, which is by far different from air-fired conditions [ChenL12, Edge11a, Scheffknecht11, Toftegaard10, Wall09a, Wall07, Buhre05]. Comprehensive reviews for oxy-fuel CFD models were published by Chen et al. [ChenL12] and Edge et al. [Edge11a]. The reviews also emphasized focuses of research needs on heterogeneous char reactions (char burnout), homogeneous gas reactions (reaction mechanisms and turbulent gaseous reactions), radiation modeling of gas mixture and turbulent models. Therefore, these sub-models are also included in present studies using numerical model from laboratory scale oxy-coal burner (chapter 5). A summary of CFD models for oxy-fuel combustion are listed in Appendix B.

2.1 Governing equations for fluid and particle phase

For governing equations to describe gaseous and particulate phases, Eaton et al. [Eaton99] overviewed three main separated flow approaches, Eulerian-Eulerian, Eulerrian-Lagrangian and probabilistic methods. In the contents of coal combustion modeling, gaseous phase can be modeled by Eulerian formulations but particulate phases by Lagrangian formulation (Euler-Lagrange formulation) as presented by Smoot et al. [Smoot79, 85]. In the Euler-Lagrange formulation, the interactions between phases are exchanged by source terms of mass, momentum and energy equations. The well known technique, called the particle-source-in-cell (PSI-CELL) method, to account for particle-fluid motion had been developed by Crowe [Crowe77] and applied for fluid-particle flow for many years, especially for coal combustion applications. Knaus et al. [Knaus01] compared two approaches for the modeling of a 550 MW_e pulverized coal-fired boiler and concluded that the Eulerian-Lagrangian approach yielded a significant improvements for the predictions of O_2, CO and CO_2 species. Furthermore, it is clear from the reviews of oxy-fuel CFD simulation (Appendix B) that almost all simulations were performed with Euler-Lagrange formulation.

Force interaction between fluid and particles is determined by drag law of particle motion. The coal particles can be assumed as spherical or non-spherical shape; however, the first method is more suitable for coal combustion modeling due to its simplicity. Correlations for drag coefficients for Reynolds numbers from less than 0.1 to 50000 were proposed by Morsi et al. [Morsi72]. Size of coal particles can be randomly modeled using the Rosin-Rammler distribution [Bailey83].

In the fluid-particle motion, particle dispersion due to effect of turbulence in the fluid flow to particles can be described by either the particle cloud model [Baxter93] or stochastic tracking such as the discrete random walk model (DRW) [Gosman83]. In the particle cloud model, the concentration of particles about the mean velocity is described by a Gaussian probability density function whose variance is dependent of the degree of particle dispersion from turbulent fluctuations. In the stochastic tracking approach the turbulent dispersion of particles is estimated by integrating the trajectory equations for individual particles along path trajectory of particles. In this stochastic tracking approach, the motions of particles are determined from mean fluid phase velocity and fluctuating components based on the classical paper by Tayler [Taylor21] as reviewed in Durbin et al. [Durbin11] and Pope [Pope00]. The fluctuating components of velocity can be modeled by the discrete random walk model (DRW) [Gosman83], in which the value of fluctuating velocities are piecewise constant functions of time and maintaining constant over an interval of characteristic lifetime of eddies.

2.2 Turbulent models

Turbulence modeling has been reviewed in many standard books in CFD modeling by Versteeg et al. [Versteeg07], Chung [Chung02], Blazek [Blazek05], Tannehill et al. [Tannehill97] and in turbulent flows by Pope [Pope00] and Wilcox [Wilcox93]. The flow is defined as turbulence above a specific Reynolds number, named critical Reynolds number depending on flow types (free jet or wall flows) [Pope00, Tennekes72]. In transi-

tion regime, flow changes from laminar flow to turbulent flow. In the turbulent regime, velocity and flow properties vary randomly and fluctuating component was introduced. Pulverized coal flame is defined as turbulent diffusion flame [Smoot85], especially swirling jet flame at burner inside furnace [Beer72]; hence, it is classified as turbulent flow. Turbulent quantities such as kinetic energy and its dissipation also have highly influence on the reaction rate of gaseous combustion after volatile matter released in the coal combustion process.

A direct solution of the time-dependent conservation equations for turbulent flows, such as direct numerical simulation (DNS) requires the most efficient computer capacity and is currently not practical for numerical predictions of complex flows in combustion problem. To remedy this problem, approximated models were suggested such as Reynolds-averaged Navier-Stokes (RANS) equations and Large eddy simulation (LES) [Versteeg07]. The LES uses a spatial filtering operation to separate the larger and smaller eddies instead of time-averaging and introducing sub-grid-scale stresses (SGS). The LES model is not included here due to its requirement in substantial computing resources, which is not available for a present studies. The RANS equations are the most convenient for fast computation to provide reasonably accurate flow solution especially for numerical computation of combustion flows, which is considered for modeling in this thesis.

In RANS equations, Navier-Stokes equations are solved by time averaging concept. The concept of Reynolds averaging and Favre (mass) averaging were introduced reviewed by Blazek [Blazek05]. Time averaging was grouped in the Reynolds averaging concept. In both concepts, flow quantity is decomposed into two components, the mean and the fluctuating value. Density can be varied in the Favre averaging (compressible flows) but not in the Reynolds averaging concept (incompressible flows). The most convenient method is to use Reynolds averaging for density and pressure, and Favre averaging for velocity, temperature, internal energy, enthalpy. By employing these averaging concepts, Reynolds-stress tensor can be approximated by eddy viscosity using *Boussinesq hypothesis*. Equation closures to calculate the Reynolds stresses were classified by their complexity, staring from zero, one, two and Reynolds stress model [Versteeg07].

In the zero equation models, the Reynolds stresses is estimated using eddy viscosity. The eddy viscosity is approximated by empirical relation of Prandtl mixing length [Versteeg07, Chung02, Pope00, Tannehill97, Smoot85]. Different mixing lengths are applied depending on flow types, for example, mixing layer, jet, wake, boundary layer and pipe (channel) flow. Spalart-Allmaras one-equation model was described by Versteeg et al. [Versteeg07], Blazek [Blazek05] and Wilcox [Wilcox93]. The Spalart-Allmaras model has only one transport equation for kinematic viscosity. The relation between kinematic viscosity and eddy viscosity depending on the wall-damping function, which is increasing from zero at the wall surface to one in the free flow with high Reynolds numbers.

Well known two-equation closure models are the standard k-ε model [Launder74], the standard k-ω model [Wilcox93] and their variation of equations such as the RNG k-ε [Yakhot86], Realized k-ε [Shih95] and SST k-ω model [Menter94]. The standard k-ε model and k-ω model were comprehensively derived and explained by Veesteeg et al. [Versteeg07], Pope [Pope00] and Blazek [Blazek05]. The concept of the k-ε model is to solve two-transport equations for turbulent kinetic energy and turbulent dissipation rate based on the assumption of fully turbulent flow. Launder and Spalding [Launder74] pro-

posed the standard k-ε model including its model constants and demonstrated the model by reference to validation with different kinds of turbulent flow. For several decades, it has become the most widely employed two-equation eddy viscosity model because of its robustness of convergence and economic cost of computation. The RNG k-ε model was developed by Yakhot and Orszag [Yakhot86] using the dynamic renormalization group (RNG) method for hydrodynamic turbulence. The model introduced the strain-dependent correction term for the equation of turbulent dissipation, which can improve the performance from the standard k-ε model [Versteeg07, Pope00]. Unlike the standard k-ε model, the RNG k-ε model accounts also for the low-Reynolds number effect and enhance accuracy in backward-facing step and swirling flow. The Realized k-ε model developed by Shih et al. [Shih95] consists of a new model dissipation rate equation and a new realizable eddy viscosity formulation. The transport equation of turbulent dissipation is solved using the mean-square vorticity fluctuation at large turbulent Reynolds number. The model was validated with many benchmark flows such as rotating homogeneous shear flows, boundary-free shear flows, channel and flat boundary layer flows with and without pressure gradients and backward-facing step flows. The results showed the significant improvement over the standard k-ε model. The k-ω model, developed by Wilcox [Wilcox93], is based on sovling two transport equations for turbulent kinetic energy and specific dissipation rate (ratio of turbulent dissipation rate to turbulent kinetic energy). For boundary-layer flows, the k-ω model is superior both in the calculation of viscosity in the near-wall region, and its accounting for the effects of streamwise pressure gradients [Pope00]. Later, Menter [Menter94] merged the k-ω model of Wilcox with the standard k-ε model and introduced the shear-stress transport (SST) k-ω model. The new SST k-ω model improved accuracy from the standard models for both near-wall and free-stream flows using *the blending function*. The blending function is zero close to wall (leading to the k-ω model), whereas is unity in the free-stream flows away from wall surface (leading to the standard k-ε model) [Versteeg07, Blazek05, Pope00].

The Reynolds stress (RSM) model, second-order closure, or second-moment closure model, is the most complex RANS turbulent model reviewed by Launder et al. [Launder75], Versteeg et al. [Versteeg07], Tannehill et al. [Tannehill97] and Pope [Pope00]. It is formulated by neglecting the isotropic eddy-viscosity hypothesis and solving transport equations for Reynold stresses and turbulent dissipation rate. Seven and five additional transport equations are required for 3D geometry and 2D geometry, respectively. There are two approaches for solving transport equation. The first approach, called the *differential Reynolds-stress model* (DSM), calculates all unknown in the partial differential equations (PDE) directly [Launder75, Rotta51a-b]. The second approach avoids solving full PDE for all Reynolds stresses and applies additional assumption to simplify the problem, called the *algebraic Reynolds stress model* (ASM) [Demuren84], however the ASM is not valid for wide range of application as the standard k-ε model [Versteeg07]. The computational cost for the DSM is higher than the ASM.

The turbulent diffusion term in the RSM model can be determined using the gradient-diffusion model by Daly [Daly70]; nevertheless, resulting in computational instability. To remedy this problem, the formulation equation by Lien [Lien94] is proposed instead. The pressure-strain terms can be modeled by different approach, for example, linear pressure-strain [Gibson78, Fu87, Launder89], low-Re modification of linear pressure-strain [Laun-

der89], quadratic pressure-strain [Speziale91] and Low-Re stress-omega model [Wilcox98].

In the reviews of oxy-coal CFD simulation in Appendix B, the standard k-ε model was employed for most of researches, following by the RNG k-ε, the Realized k-ε, the LES and the RSM model. The RNG k-ε model was applied in oxy-coal simulation (as in Al-Abbas et al. [Al-Abbas11]) because of successfully applying for prediction of swirling flow in tangential pulverized coal-fired furnace published previously by Fan et al. [Fan01] and improving performance for swirling flow [ANSYS12]. At present, the best two-equation model for applying to oxy-coal simulation is still uncertain for oxy-fuel conditions. Jovanovic et al. [Jovanovic12] performed oxy-coal simulation of the drop tube reactor (DTR) applying the standard k-ε, the standard k-ω, the RNG k-ε and SST k-ω model and concluded that all results were similar. The review of oxy-coal simulation by Edge et al. [Edge11a] addressed a limitation of all two-equation models including the RSM model due to uncertainty of predictions using the empirical or semi-empirical transport equation and suggested the LES model, which can better predict complicated flow patterns near burner zone of oxy-coal flames. Unfortunately, the computer resources (work stations) at BTU Cottbus are not suitable for this purpose.

Because none of oxy-fuel researches investigated all two equation models and accuracy of flow fields-predictions are not expected to depend on conditions of gas mixture (air or oxy-firing), additional reviews are further provided from the application of air-fired swirl burners. Some researchers compared the results of applying different two-equation models to numerical simulation of swirling burner.

Aroussi et al. [Aroussi00] and Kucukgokoglan et al. [Kucukgokoglan01] investigated numerical simulation for a swirling single burner and concluded that the Realized k-ε is better than the standard k-ε and RNG k-ε model in term of accuracy and economy of computation. Benelli et al. [Benelli07] presented axial velocity profiles applying the standard k-ε, RNG k-ε, Realized k-ε and SST k-ω model in gas turbine combustor and found that the SST k-ω model is the most suitable. Stockwell et al. [Stockwell01] applied the standard k-ε, RNG k-ε model and RSM for the prediction in the non-premixed combustion in a regenerative furnace with 4 horizontal burners. The results showed the RSM improved accuracy slightly and the standard k-ε is still the best choice. Tabet-Helal et al. [Tabet-Helal06] studied turbulence modeling in hydrogen-air non-premixed flames using the standard k-ε model and RSM and concluded that the RSM provided slightly different results for velocity, mixture fraction and temperature along centerline and radial directions. The RSM was slightly superior to the standard k-ε in the near-flames regions but less accurate in downstream locations. The finding of results by Tabet-Halal et al. was in agreement with numerical studies by Gran et al. [GranIR96], who compared predictions of syngas fuel-diffusion flames and by Tsao et al. [Tsao99], who studied velocity profiles in a gas turbine combustor, using the standard k-ε model and RSM. Weber et al. [Weber90] found the same results that computation by standard k-ε failed and overpredicted turbulent viscosity in the burner quarl, in comparison with the RSM and ASM. Pfeiler et al. [Pfeiler10] compared mixture fractions and temperatures by the Realized k-ε model and RSM in a non-premixed methane flames (Sandia Flame D). A better agreement of the RSM than the standard k-ε model with measurements was not observed.

Saario et al. [Saario05] performed simulation for heavy fuel oil laboratory furnace with swirling burner installed and found that the RSM improved the predictions of gas concentrations (O_2, and CO_2) at locations close to burner. Tian et al. [Tian09] predicted velocity profiles, temperatures and species concentration (O_2 and CO_2) for non-swirl coal flame using the standard k-ε, modified k-ε, RNG k-ε, standard k-ω (Wilcox), k-ω (Menter), and SST k-ω models and concluded that all model provided good predictions and no models were superior to others. Orfanoudakis et al. [Orfanoudakis07] investigated high swirling flow in multi-fuel burner and found that predictions of velocity profile by the RNG k-ε model were in good agreement to measurements even at high swirl number, in contrast to the standard k-ε model, which tend to underestimate the axial velocity component. Hsiao et al. [Hsiao03] studied the results applying five turbulent models, the standard k-ε, Realized k-ε, RNG k-ε, standard k-ω model and the RSM to a swirl cup combustor and compared numerical results with LDV measurements. The RNG and k-ω model showed deficiency in the central recirculation zone, while the Realized k-ε model and RSM poorly predicted velocity profiles in the downstream region. The author finally found that the results by standard k-ε model matched very well with measurements following by the Realized k-ε model. Liebetruth et al. [Liebetruth01] compared temperature profiles for the predictions of wood dust combustion in cyclone burners with swirl burner (RWE Power) using the standard k-ε, RNG k-ε model and the RSM and observed that the RNG k-ε model was found to be the best model for the application. Görres et al. [Görres95] applied finite element computations for a strongly swirling pulverized coal burner and found small improvements for the predictions of velocity profiles using the ASM comparing to the standard k-ε model.

From the reviews, it is clear that the conclusions for best turbulent models were varied depending on flow types and combustion application. Therefore, in order to decide suitable RANS models for numerical oxy-coal predictions, all two-equation models and the RSM model are applied for numerical investigated cases of laboratory 100 kW_{th} oxy-coal furnace as later explained in chapter 5 and the turbulent model for the oxy-coal simulation in a pilot-scale 0.4 MW_{th} oxy-coal furnace is selected based on the comparison of previous results.

2.3 Coal devolatilization

After coal particles are exposed to heat by radiation and convection, the process of devolatilizattion begins. The term of pyrolysis often used in literature has slightly different meaning, refers to the devolatilization process in an inert atmosphere as explained by Smith [SmithKL94]. To describe complete devolatilization process in the simulation problem is unpractical. For this reason, approaches for modeling devolatilization behavior are proposed. Models for coal devolatilization were reviewed by Anthony and Howard [Anthony76], Smoot et al. [Smoot85], Smoot et al. [Smoot93] and Smith et al. [SmithKL94]. The models in the reviews were composed of constant rate [Baum71], single-step [Bazoich70], two competing rate [Kobayashi77, Ubhayakar77], Functional group (FG) [Gavalas81a-b] or network models. In the constant rate model [Baum71], volatiles are released at constant rate, which is determined empirically from experiments. Badzioich [Badzioch70] assumed that the devolatilization was a first-order reaction and

the rate of reaction was proportional to the amount of residual volatile matter contents. Kobayashi et al. [Kobayashi77] and Ubhayakar et al. [Ubhayakar77] determined and published the kinetic rates for two competing rate models for lignite and bituminous coal in the first paper and bituminous coal in the second one. In this model, the rapid devolatilization was modeled by two simultaneously competing first-order reactions at low and high temperatures. Gavalas et al [Gavalas81a-b] introduced a chemical model for devolatilization based on 14 functional group. The network model is the most accurate and also complicated, comparing to other models. The network models included the functional group-depolymerization, vaporization, and cross-linking (FG-DVC) model [Solomon88], the FLASHCHAIN model [Niksa91], and the chemical percolation devolatilization (CPD) model [Grant89, Fletcher92]. The FG-DVC model [Solomon88] consists of the FG mode, which considers specific functional group to decompose to form light gas and the DVC model, which describes the depolymerization of the macromolecular network (bridge breaking, cross-linking and tar formation). The FLASHCHAIN model [Niksa91] was based on the chemical kinetics and macromolecular configuration of the distributed-energy chain model (DISCHAIN), distributed-energy array model (DISARAY) and the flash distillation analogy developed in FLASHTWO. Coal is modeled as a distribution of linear chains composed of aromatic clusters, interconnected by labile bridges and refractory char links, with peripheral groups on the ends of the fragments. The CPD model [Grant89, Fletcher92] used chemical structural parameters to describe coal structure, and percolation statistics to describe the generation of tar precursors based on the number of cleaved labile bridges in an infinite coal lattice. Percolation statistics are used to provide mathematical expressions in a closed form to account for lattice statistics.

The single-step rate, the two competing rate, the FG-DVC and the CPD model were used in oxy-coal numerical CFD models as presented in Appendix B. In the absence of experiments, the rates of devolatilization were usually determined using data from literatures for a specific coal type or modeled as network models. Jovanovic et al. [Jovanovic12] compared numerical predictions and experimental results of ignition position for Russian coal for various O_2/N_2 and O_2/CO_2 atmospheres and concluded that the CPD and the FG give more accurate results in comparison with standard devolatilisation models such as single rate and two competing rates. Due to the superior performance of the CPD model, it is selected for modeling oxy-coal combustion in this thesis. To apply the CPD model, data from solid-state ^{13}C NMR analysis of coal are required. Unfortunately, the solid-state ^{13}C NMR spectroscopy is the expensive measurements and not available for some coal types. Therefore, correlation for the CPD model was developed by Genetti et al. [Genetti99a, 99b] based on ultimate and proximate analysis from 30 coals with different ranks.

2.4 Char heterogeneous reaction

Reviews and models:

Comprehensive knowledge of char heterogeneous reactions were presented by Smoot and Pratt [Smoot79], Smoot and Smith [Smoot85], Smoot [Smoot93], Smith et al. [SmithKL94], Walker et al. [Walker59] and Laurendeau [Laurendeau78]. From the re-

views, Smoot and Smith [Smoot85] explained that rates of char reaction differ greatly at a given temperature for different reactants, generally in the order of C(s)-O_2 >> C(s)-H_2O > C(s)-CO_2 >> C(s)-H_2. For this reason, the contribution by hydrogasification (C(s)-H_2) is quite small in char reactions and can be negligible [Smoot79].

Models for char heterogeneous reactions were reviewed by Walker et al. [Walker59], Field et al. [Field67], Laurendeau [Laurendeau78], Levenspiel [Levenspiel99], Turns [Turns00] and for char oxidation by Smith [SmithIW82], Williams et al. [Williams00-02] and Hurt et al. [Hurt01], Mitchell et al. [Mitchell07], Ma et al. [MaL09], Murphy et al. [Murphy10]. The models for char reactions were created by the true nature of char oxidation and the combustion regimes in the *three zones concept*. The concept of three char reaction regimes (*three zones concept*) was explained well by Walker et al. and also presented later in the standard books of coal combustion [Smoot85, SmithKL94]. It is suggested that the variation of reaction rate with temperature for char oxidation can be divided into three main zones. The zone I, II and III are related to the chemical limited control, chemical-pore diffusion control and external bulk gas diffusion control, respectively. The reaction orders of Arrhenius rate equation in zone I, II and III reduce from true order, approximately half of true order and zero order. The activation energies in zone I to zone III follow the same trends as the reaction order.

In general, the char reaction models can be divided into two broad categories such as macroscopic or microscopic models reviewed by Laurendeau [Laurendeau78]. The macroscopic models are usually applied due to its simplicity and less computational cost in a complex problem such as numerical simulation of coal combustion. The macroscopic models can be classified again into *progressive-conversion model* (PCM) and *shrinking-core model* (SCM) as described by Levenspiel [Levenspiel99]. The equation formulations depend on the assumptions of how gas surrounding particle reacts and/or diffuses through external film layer of char particles and internal pores. In the PCM, it is assumed that reactant gas enters and reacts throughout char particle and particle diameter is constant while the particle density is decreasing (zone I, kinetic control). In contrast, the SCM assumes that the reaction occurs at external surface of char particle and the diameter of non-reacted core of char particle is decreasing while char density is constant (zone III, diffusion control). Equation formulations for zone II are derived by combining the PCM and SCM model, which means that both diameter and density are varied.

In practical combustion problem, char reaction models for numerical predictions are either power-law or Langmuir-Hinshelwood (LH) rate expression (Langmuir adsorption isotherm) [Satterfield91, Smoot79]. The power-law rate expression has a simple form of equation depending on kinetic rate (pre-exponential factor and activation energy), concentration of reactants and its exponent (reaction order). The reaction order must be set as constant in the power-law rate model but can be varied in the Langmuir-Hinshelwood type. Choice of applied equation expressions depends on the circumstances of practical combustion problem. Other than the power-law and LH models, Hurt et al. [Hurt98] also developed char burnout kinetic (CBK) model and its modification (extended CBK [Niksa03], CBK8 [Sun00]) for the prediction of char conversion. Because most of kinetic parameters for oxy-fuel experiments nowadays are obtained for the power-law rate equation, only the power-law rate expression was used in numerical studied as explained in details in chapter 3 for mathematical formulations.

Examples of the power-law rate expressions considered in this thesis are global char reaction model (Arrhenius rate expression) [Levenspiel99, Satterfield91], general model for char reaction (sometimes called kinetic-diffusion limited rate (KD) [Field67,69] or Baum and Street's model [Baum71] in literatures) and intrinsic char reaction model [SmithIW82]. Recently, Murphy [Murphy10] and Ma [MaL09] suggested that overall particle burning rate was influenced by both external and internal burning of particle and the total reaction rate should be represented as the sum of external and internal burning rate. However, only formulations using Arrhenius expression or by Field et al. and Smith were investigated in this thesis.

The global char reaction model is described by the Arrhenius expression, empirical correlation with power functions of reactant concentrations and adjustable exponents-constants. In the global model, the rate of reaction is assumed to be formulated by Arrhenius's equation and the reaction rate depends on the particle temperature. In the Arrhenius diagram, the reaction rate is plotted against the inverse ratio of particle temperature and combustion zone as explained in the three zones concepts can be obviously investigated from specific type of experiment. The well known experiments to determine reaction rate are thermo-gravimetric analysis (TGA) and drop tube furnace (DTF) or drop tube reactor (DTR).

Field et al. [Field67,69] investigated reaction rate of low-rank coal char between 1200 – 2000 K and developed the general model to account for both diffusion and chemical reaction rate. The model was defined as kinetic-diffusion limited rate (KD) model in a number of literatures. The KD model was original based on the reaction order of one but modified later in order to account for other possible reaction orders, similar to equation formulations explained by Smith [SmithIW82].

Smith [SmithIW82] proposed the intrinsic model by combining the knowledge of bulk gas diffusion, pore diffusion and char reactivity as reviewed by Walker et al. [Walker59], Laurendeau [Laurendeau78] and Satterfield [Satterfield91]. For the intrinsic model, the char reactivity depends on intrinsic rate of chemical reaction in the internal surface of the particle and gas diffusion through internal pores of particle. The overall diffusion rate is determined by bulk diffusion and Knudsen diffusion as presented by Mitchell et al. [Mitchell07] and Satterfield [Satterfield91]. The equation for Knudsen diffusion was also published by Wheeler [Wheeler51]. To apply the intrinsic model, additional parameters are required such as the effectiveness factor, Thiele modulus, porosity, mean pore radius (pore size), specific internal surface area of char particle and apparent density. The effectiveness factor is the function of Thiele modulus. The specific internal surface area can be estimated by pore models or measured in experiments.

Intrinsic model: *effectiveness factor*

For the relation between the effectiveness factor and Thiele modulus for intrinsic kinetic rate model, three equation-formulations were published by Dutta and Wen [Dutta77], Sun and Hurt [Sun00] and Liu and Niksa [LiuG04]. The first two equation relations were developed for the power-law rate expression, but the last relation from Liu and Niksa was derived from the Langmuir-Hinshelwood rate expression. The relation for effectiveness factor by Sun and Hurt [Sun00] was applied for CFD simulation of coal fired boiler in air-firing [Pallarés07] and oxy-firing [Leiser11]. The relation by Dutta and Wen [Dutta77]

was presented in the review of coal combustion modeling by Laurendaeu [Laurendaeu78]. Recently, the relation by Liu and Niksa [LiuG04] was analysed for utilizing in oxy-fuel CFD simulation of a 1 MW_{th} combustion test facility (CTF) by Gharebaghi [Gharebaghi11b] in a pilot scale furnace (E.On's furnace). All relations are evaluated and discussed in the mathematical modeling in chapter 3.

Intrinsic model: *specific internal surface area (pore models)*

During char reactivity, the specific internal surface area of particle can varies with burnout. It can be estimated by *random pore models* (RPM) [Gavalas80, Bhatia80, Simons82, Charpenay92] as reviewed by Smith [SmithKL94]. The RPM was first developed from the *isolated pore models* by Thiele [Thiele39] and extended further by Wheeler [Wheeler51]. The isolated pore models assumed that all pores is treated as cylindrical shape with identical size extending through the particles. The RPM was first proposed by Gavalas [Gavalas80] and Bhatia et al. [Bhatia80]. It is applicable for any arbitrary pore-size distribution depending on some measure parameters. Gavalas [Gavalas80] used random capillary pore model to describe pore structure and expressed the internal surface area as functions of local char conversion (burnout). The extension of the RPM using the pore tree model was developed by Simons [Simons82]. In this model, the pores inside the interior of the particle reach the exterior by branching from successively larger pores like a tree. Later, Charpenay et al. [Charpenay92] presented the RPM for low-rank coal chars using a simple volumetric model neglecting the structure parameter as presented in the Gavalas's model. The RPM by Charpenay et al. is expected to provide a good estimation when the Lusatian lignite in this thesis can be categorized as a low-rank coal. Nevertheless, Only the RPM by Simons et al. [Simons82] and Charpenay et al. [Charpenay92] were implemented into numerical models to investigate the effect of using the pore models to predicted results of oxy-coal combustion, in which the specific internal surface area at any stage of burning was calculated from initial internal surface area, the fractional burnout and initial porosity. In the absence of measuring initial surface area, it can be estimated using relation to fixed carbon content of parent coals correlated by William et al. [Williams02] for both CO_2-BET and N_2-BET surface area.

Intrinsic model: *specific internal surface area (measurement)*

The specific internal surface area can also be measured directly in laboratory using *adsorption measurements* with Brunauer-Emmett-Teller (BET) method [SmithKL94, Satterfield91]. Either CO_2 or N_2 adsoption are conducted in the BET measurements for specific internal surface area and the measured area are called CO_2-BET or N_2-BET surface area in literatures. In oxy-fuel conditions, Borrego and Alvarez [Borrego07a] determined specific internal surface area of bituminous coal char for both air-fired (N_2 as bulk gas) and oxy-fuel conditions (CO_2 as bulk gas) with O_2 concentrations varying from 0-21 %. Two coal chars used in the measurements are high volatile and low volatile bituminous coal char. Coal chars were prepared in a drop tube reactor at 1300 °C and different O_2 concentrations (0-21 %) in O_2/N_2 and O_2/CO_2 atmospheres. Two coals were ground and sieved to 36-75 µm before char preparation. The N_2 surface area was measured by the BET method, however CO_2-surface area was obtained by adsorption isotherms using Dubinin-Radushkevich (DR) equation. The CO_2-DR surface area in oxy-fuel conditions for high volatile char was higher than for low volatile char (250 m^2/g and 125 m^2/g, respectively). The N_2-BET surface area was quite low (70 m^2/g) without using oxygen (0 % of O_2) but

increasing sharply to 200 m^2/g for high volatile char when rising O_2 concentration from 5 to 10 %.

The specific internal surface area for lignite-char in oxy-fuel conditions was recently reported [Al-Makhadmeh09]. For the measurements of internal surface area, two types of total internal surface areas measured nowadays are N_2 surface area (N_2-BET) and CO_2 surface area (CO_2-BET). The CO_2 surface areas are larger than CO_2 surface area around 2-3 times for char particles and 20-200 times larger for coal particles. This effect is even stronger for a lower rank coal such as lignite [SmithKL94] at low temperature. This is because CO_2 can penetrate and diffuse into the micro-pores better than N_2 at low temperature.

Intrinsic model: *porosity (measurements and estimation)*

In general, the porosity can be calculated from the true and apparent density as originally presented by Wheeler [Wheeler51] and reviewed later by Smith et al. [SmithKL94], Smoot et al. [Smoot85] and Smith [SmithIW82]. Definitions of apparent density and true density and also the method to measure these values are clearly explained in the Handbook of Coal Analysis [Speight05] and by Smith [SmithKL94]. The *apparent density* of coal is determined by immersing a weighted sample of coal in a specific liquid and measuring the displaced liquid (pycnometer method). The true density of coal is determined by helium displacement which often called *helium density* in literatures. Helium gas is applied due to an ability to penetrate all the pores of char sample without chemical reaction. Recently, Al-Makhadmeh [Al-Makhadmeh09] summarized char porosity based on three types of char structure measured by scanning electron microscopy (SEM) [Bailey90, Benfell00] which can be Cenosphere (Large internal hole at the core), Crassisphere (Scattering internal holes) or Inertoid (dense) and reported that Lusatian char was classified in both first and second group and is highly porous. Therefore, total porosity of Lusatian char in this thesis can be averaged from values between these two groups (50%-80%).

Intrinsic model: *mean pore radius (measurements and estimation)*

The mean pore radius can be estimated by porosity, specific surface area at current stage of burnout, tortuosity and apparent density as described Wheeler [Wheeler51] and applied in coal combustion problem by Smith [SmithIW82]. The mean pore radius for Lusatian lignite-char in oxy-fuel conditions was measured at elevated temperatures between 700 and 1150 °C by Al-Makhadmeh [Al-Makhadmeh09] using N_2-BET and CO_2-BET surface area methods.

Intrinsic model: *burning modes*

Density and diameters can vary during char conversion (burn-off or burnout) which is sometimes called *burning modes* in literatures. Changes in particle diameter and density of coal-char are dependent of the fractional of burnout (burn-off) as originally presented in the experiments using size-graded pulverized fuels (anthracite, petroleum-coke, swelling bituminous coal char) between 1200-2270 K by Smith [SmithIW71a]. The equation formulations were further published by Waters et al., Mitchell and Essenhigh [Waters88, Mitchell89, Essenhigh89] and later applied by Essenhigh [Essenhigh94], Smith [SmithIW82] and Mitchell [Mitchell07]. The parameters for burn-off for pulverized

brown coal char were also discussed by Young et al. [Young89] and Hamor et al. [Hamor73]. The selection of theses parameters are explained in details in chapter 3 for mathematical modeling.

Kinetic rates for global models:

Kinetic rates for the global model (Arrhenius expression), the general models (kinetic diffusion limited rate, KD) and the intrinsic model for char reactions (char-O_2, char-CO_2 and char-H_2O) were comprehensively reviewed by Laurendeau [Larendeau78]. The kinetic rates for various coal ranks were presented such as graphite, activated carbon, petroleum coke, anthracite, semi-anthracite, lignite char, coconut char, bituminous char, subbituminous char and lignite char; nevertheless, none of them were determined in the presence of O_2 in rich CO_2 atmospheres (oxy-fuel conditions). When the focus of this thesis is to formulate numerical models for oxy-fuel conditions, the kinetic rates of such conditions must be further reviewed. Available kinetic rates in oxy-fuel conditions, regardless of model's formulation, were individually applied for each char heterogeneous reaction (char-O_2, char-CO_2 and char-H_2O) in investigated CFD models. In the absence of kinetic rates for specific heterogeneous reaction, the existed kinetic rates from air-fired conditions were applied based on the reviews of CFD oxy-coal modeling up to date (Appendix B). In addition to the review by Laurendeau, kinetic rates for coal-char gasification with CO_2 were reviewed by Irfan et al. [Irfan11].

Most of experiments were performed to determine the kinetic rates of char oxidation (char-O_2) for the global models (Arrhenius expression). The rates were obtained using either well known experiments such as thermo-gravimetric analysis (TGA) and drop tube furnace (DTF) or other type of experiments, for example, entrained flow reactor (EFR), Flat-flame EFR, Laminar optical EFR, Laminar-flow DTF, high-pressure TGA and circulating chamber. The coals in the experiments were from high-rank coals to low-rank coals. Recently, Geier et al. [Geier12, Geier10] modified and extended a traditional single-film char oxidation model to include also heterogeneous reactions of char with CO_2 and H_2O using SKIPPY (Surface Kinetics in Porous Particles) code [Haynes99] for the purpose of improving CFD predictions of oxy-fuel combustion of pulverized coal char particles. The CO_2/CO production ratio was also incorporated into char oxidation model implied that partially CO_2 and CO were produced depending on partial pressure of O_2 and particle surface temperature. The reaction order and temperature exponent was assumed as unity in the model.

Although many kinetic rates for lignite in oxy-fuel conditions were reported, the final goal of this thesis is to investigate the numerical models using laboratory scale experiments and apply the numerical models for a pilot scale 0.4 MW_{th} oxy-fuel furnace utilizing Lusatian lignite as fuel. For this reason, experiments to determine kinetic rates for char oxidation by TGA and circulating chamber (ALVA20) performed by Tappe et al. [Tappe09a, 09b, 09d] were of interest for implementation into numerical models. The pre-exponential factor and activation energy were determined for oxy-fuel conditions covering from 5-60 % of O_2 in CO_2 atmospheres using the TGA by Tappe et al. [Tappe09a]. The reaction order of approximately 0.6 were found at lower testing temperature and gradually decreased to around 0.2. This was in agreements with previous researches that the reaction order of char oxidation was not constant depending on testing temperatures [Karlström11, Hurt01, Hurt05].

For char reactions with CO_2 and H_2O, kinetic rates for the global model by Mayers [Mayers34a, 34b] were often applied to the predictions of oxy-coal combustion as presented in Appendix B. These values were also published in the standard book of coal combustion by Smoot et al. [Smoot79]. In the absence of experiments for char-CO_2 and char-H_2O reactions, these kinetic rates by Mayers were applied to the global model and the general model for char reaction (KD) in this thesis.

Kinetic rates for intrinsic models:

At present, the intrinsic kinetic rates for char reactions in oxy-fuel conditions are not well studied. Most of numerical predictions by CFD models were still performed using existed kinetic rates for char oxidation in air-fired conditions by Smith [SmithIW82]. This must be based on the assumption that the rates by Smith are applicable for oxy-coal predictions and result in numerical predictions with acceptable accuracy, when validated with measurements from experiments. Smith [SmithIW82, Smith78] reviewed intrinsic kinetic rates for char oxidation of coal-char with different ranks from semi-anthracite to lignite-char and published summary of pre-exponential factor, activation energy and apparent order of reaction. The rates from brown coal char were also presented by Smith et al. [SmithIW74] and Hamor et al. [Hamor73], which were acquired by experiments of entrained reactor at testing temperatures from 630 to 1812 K by Smith et al. [SmithIW74] and from 630 to 2200 K by Hamor et al. [Hamor73], respectively. The apparent reaction order was equal to zero above 900 K observed by [SmithIW74] but different number of 0.5 was investigated by Hamor et al. [Hamor73]. Recently, Leiser [Leiser11] modified intrinsic kinetic rates for char reactions (char-O_2, char-CO_2 and char-H_2O) derived by Roberts [Roberts00] fitting to experimental data in oxy-fuel conditions.

Other than the global, the general (KD) and the intrinsic model, kinetic rates for char reactions in oxy-fuel conditions using the CBK [Gharebaghi11b, LiuG04] and the LH [Hecht11] models were also developed. The reaction rates for char reactions by different researches are evaluated and compared in chapter 3.

2.5 Volatile reaction

Turbulent gaseous combustion and hypotheses of combustion time-scale:

In combusting flows, the interaction between the chemistry and the turbulence is greatly complicated and the chemical reactions take place on the microscopic scale. The local turbulence controls the time that each of the reactants and products are associated when reactions proceed. Since the effect of chemistry-turbulence interactions changes for various types of chemical reactions and combustion applications, two hypothetical time-scales have been proposed [Smoot85], the reaction time-scale, $time_{react}$, and turbulent mixing time-scale, $time_{turb}$. The reaction time-scale, $time_{react}$, is the typical time required for the species of interest to react completely to equilibrium, whereas the turbulent mixing time-scale, $time_{turb}$, is the time required for large-scale turbulent eddies to break up and reduce to the small-scale where molecular interactions can occur. Three hypotheses for turbulent gaseous combustion are briefly explained here [Smoot85, Eaton99].

In the first hypothesis, the reaction time-scale is much greater than the turbulent time-scale ($time_{react} >> time_{turb}$). In this case, the turbulent mixing time-scale ($time_{turb}$) is assumed to be very fast in comparison to the reaction time-scale ($time_{react}$), implying that the reactions are very slow compared to changes in the local turbulence and the reactants are assumed to be pre-mixed. Then, the turbulent mixing can be ignored [Eaton99] and the mean reaction rate is equal to the reaction rate calculated from the mean variables of gas temperature and density of reactants (fuel and oxidizer). Although this hypothesis has been used for decades, it was found to be valid only for limited cases.

For the second hypothesis, in the other hand, the reaction time-scale is much smaller than the turbulent time-scale ($time_{react} << time_{turb}$). In this type of diffusion flame, the reaction rates are fast compared to turbulent mixing rate and the turbulent mixing is the rate limiting process. The chemical rate is fast enough to be considered as local instantaneous equilibrium. The mixture fraction is defined to indicate the degree of mixing. The statistics of local turbulent fluctuations are used and the model for probability density function (PDF) of the mixture fraction was introduced. This flame type is categorized into the non-premixed diffusion flame, in which the fuel and oxidizer are separately injected at the burner. An insight into this hypothesis was reported in the standard books by Libby, Fox and Pope [Libby94, Fox03, Pope00] and in a number of publications by Pope [PopeCornellU].

In the third hypothesis, the turbulent mixing time-scale (t_{turb}) is the same order as chemical reaction time-scale (t_{react}) and both time-scales are accounted for simultaneously ($time_{react} \cong time_{turb}$). The models based on this hypothesis are called *chemical equilibrium* or *mixed-is-burne*d approach in literatures. Spalding [Spalding71] proposed the Eddy Break-up (EBU) model, which determines local reaction rate by the rate of break-up of turbulent eddies. Later, Magnussen and Hjertager [Magnussen77] further improved the eddy break-up model and introduced the eddy dissipation model (EDM) that determined the rate of reaction by the mean concentration of reactants, turbulent kinetic energy and the rate of dissipation of turbulent eddies. The total reaction rate is calculated from the minimum of local combustion rate of reactants (fuel and oxidizer) and products. Two empirical constants were required (for reactants and products) for specific flame in combustion problem [YangW05,06, Lupant07]. For the EDM, combustion occurs whenever turbulent is present, especially for non-premixed flames. However, disadvantage of the EDM is that the reactants burn immediately when entering computational domain at burner. Therefore, the finite-rated eddy dissipation (FRED) model was proposed [Eaton99, ANSYS12] to remedy this problem. The FRED model accounts also for the Arrhenius rate equation for chemical reaction and the total reaction rate is determined from the minimum of the rate of dissipation of eddies for reactants and products and the chemical reaction rate (Arrhenius rate).

Magnussen B.F. [Magnussen81] developed a generalized model for chemical reaction in turbulent flow called the Eddy Dissipation Concept (EDC) from the eddy break-up (EBU) model from Spalding [Spalding71] and the EDM from Magnussen and Hjertager [Magnussen77]. In the EDC model, the total space is subdivided into a reaction space, called the *fine structures* and non-reaction space. The reactions occur where the dissipation of turbulence energy takes place at molecular scale within the fine structures. The model was derived using a detailed description of the dissipative process in the flow and can be applied for both premixed and non-premixed flames. The mean reaction rate for

gas specie depends on the kinetic energy, its dissipation and kinematic viscosity. In the past, the EDC model was successfully applied in combustion simulations utilizing natural gas [Brink99, BrinkPhD98] and pulverized coal [Knaus01, Förtsch98, Magel96a, 96b, 95] and recently researches in oxy-fuel simulations (Appendix B).

From the reviews of oxy-fuel CFD simulation in Appendix B, most numerical CFD models were performed by applying chemical equilibrium approach (EBU, EDM, FRED and EDC model), and just few works by mixture fraction approach (PDF model). Both approaches are valid for modeling of diffusion flames [Smoot85], when the turbulent mixing time scale is on the same order or much longer than the reaction time scales ($time_{react} \leq time_{turb}$) [Eaton99]. Because few publications studied the comparison of modeling approaches for turbulent gaseous combustion in oxy-fuel atmospheres [Goanta08, Brink00a], the best model for predictions in such atmospheres can still not be justified. Goanta et al. [Goanta08] investigated controlled staging non-stoichiometric oxy-burl natural gas burner and compared predictions of flame temperature distribution using the EDM and the PDF Laminar Flamelets model and reported the unexpected longer flame by the PDF Laminar Flamelets model, despite the high swirl number of 0.8. Brink et al. [Brink00a] modeled turbulence-chemistry interaction in oxy-natural gas flame using the EDC and the presumed PDF model and concluded that the EDC model provided better estimation of velocity, temperature and specie concentration (CO, CO_2, H_2), even the same computationally expensive calculations. The high numerical effort for the presumed PDF model was also observed, which was caused by integrating tabulated data into calculations. Andersen et al. [Andersen09] recommended the EDC model for the modeling of oxy-fuel flame instead of the EDM due to limitations of modeling multi-step reaction mechanism published by Brink et al. [Brink00b].

Comparisons of different approaches for turbulent gaseous combustion were also reported for other combustion application such as flameless oxidation (HiTAC [YangW05,06], MILD [Vascellari12, Dally10], FLOX [Lupant07]), steam cracking furnace [Stefanidis06], pulverized coal-fired boiler [Magel95]. Yang et al. [YangW05,06] found that the HiTAC flame predictions with the EBU model were more realistic than the PDF model. Vascellari et al. [Vascellari12] suggested that the EDC model with detailed kinetic mechanisms resulted in better predictions of temperatures and char burnout than the EDM for MILD combustion. Slightly improvements of predictions were observed for O_2 and CO_2 concentrations, but not for CO concentrations. Dally et al. [Dally10] found slightly better velocity prediction by the EDC model than the FRED models in MILD combustion furnace. The overestimation of temperature of diffusion flames in flameless oxidation (FLOX) burner can be reduced with the FRED model, comparing to applying the PDF model and the EDM. Magel et al. [Magel95] applied the EBU and the EDC models for the predictions of swirling flame burner and full scaled pulverized coal-fired boiler and reported significant improvements of velocity, temperature and species concentration (O_2 and CO) when using the EDC model. Even many researchers published the successful simulations by the EDC models, but nearly all of them were either applied for flameless oxidation or pulverized coal flame in air-fired conditions.

Although the EDC model provided significantly improvements of predictions, this conclusion is still valid for either natural gas flame in oxy-fuel conditions or pulverized coal-fired burner in air-fired conditions [Magel95]. Vascellari et al. [Vascellari09] and Liu et al. [LiuJ12] observed longer ignition delays and oxy-fuel flame instability outside burner

quarl when applying the EDC model for predictions in IFRF furnace no.1 [Woycenko95]. It was also emphasized by Liu et al. that only oxy-fuel flame predicted by the FRED model resulted in shorter ignition delays and stable flame inside the quarl.

From the reviews of oxy-fuel CFD simulation and comparisons, the chemical equilibrium approach (eddy dissipation-type model) is expected to be a good approach for oxy-fuel predictions, except the EDC model according to the previously mentioned observation by Vascellari et al. [Vascellari09] and Liu et al. [LiuJ12]. Therefore the eddy dissipation-type models such as the EDM and FRED model are applied for investigated cases of laboratory scaled furnace in chapter 5 and the best choice is discussed in chapter 6 before using for numerical predictions in a bigger scaled 0.4 MW_{th} furnace.

Simplification of reaction mechanisms:

In pulverized coal flame, the oxidation of hydrocarbon fuels is complex and the chemical reaction is a chain reaction composed of a number of irreversible and reversible reactions [Glassman08, Kuo05, Turn00, Warnatz06]. To account all reactions into calculation is sometimes inconvenient and also insignificant in some cases of combustion problem. A good approach is to do sensitivity analysis for all reactions in order to determine number of reactions required for a specific reaction problem of interest. Another approach is to validate global reaction mechanisms and optimize kinetic parameters to fit to results of combustion products and temperatures from either experiments from combustion flame or detailed kinetic mechanisms. The detailed mechanisms can be calculated using external source code such as GRI-Mech 3.0 (325 elementary chemical reactions, 53 species) [GRI-Mech3.0] or CHEMKIN [CHEMKIN, Kee80,89, Lutz90, Kee96]. The global reaction mechanisms are more convenient and hence considered in this thesis in order to have high reduction of computational time and to simplify the detailed reaction mechanisms.

In the past, Westbrook and Dryer [Westbrook81] presented the state of the art to develop global reaction mechanisms validated with experiments utilizing a number of fuels. Later, global reaction mechanisms for hydrocarbon proposed for combustion studies were global 1-step [Westbrook81], 2-step by Dryer and Glassman [Dryer73], 3-step by Hautman et al. [Hautman81] and 4-step mechanisms by Jones and Linstedt [Jones88]. Dryer and Glassman investigated methane oxidation using turbulent flow reactor, while Hautman et al. and Jones and Linstedt modeled global reaction mechanisms from many aliphatic hydrocarbons including alkane hydrocarbons and butane.

For the global 1-step mechanism [Westbrook81], the products of hydrocarbon combustion were assumed to be composed of CO_2 and H_2O. The kinetic parameters were obtained from validation with detailed kinetic mechanisms from laminar flame model (HCL code [Lund78]). It was presented by [Westbrook81] that the global 1-step mechanism overpredicted the total heat of reaction and the adiabatic flame temperature due to this assumption. This was because typical hydrocarbons burn in a sequential manner and CO and H_2 exist in combustion products with CO_2 and H_2O. Therefore, Dryer and Glassman [Dryer73] later introduced global 2-step reaction mechanisms for methane oxidation in a turbulent flow reactor.

In the global 2-step reaction mechanisms [Dryer73], hydrocarbon (or volatile matter in coal combustion modeling) oxidizes to CO and H_2O, and then, CO further oxidizes again

to CO_2. The kinetic parameters were obtained from experiments of methane oxidation in turbulent flow reactor. Alternative reaction rate expression was proposed by Westbrook [Westbrook81], which presented also the concentration exponents of 0.2 and 1.3 for fuel and oxidizer, respectively (equal to 0.7 and 0.8 by Dryer and Glassman).

The global 2-step mechanisms were successfully applied to the modeling predictions of pulverized coal flame in a 2.4 MW_{th} swirling burner by Peters et al. [Peters97]. Modeling approach from this work assumed that volatile matter (VM) oxidizes to CO, CO_2, H_2O and N_2 (CO as only intermediate specie). The products of CO and CO_2 species were defined by the fraction of volatile-matter-bound carbon (molar fraction of O/molar fraction of C in volatile matter) that reacts directly to CO_2. The volatile-matter-bound carbon equal to zero implies that the volatile matter is fully burn to CO. The value of 0.226 was found by Peters et at. to provide the best results of numerical predictions for the swirling pulverized coal burner.

The global 3-step mechanisms [Hautman81] were developed by combining overall and elementary kinetics in the quasi-global kinetic mechanism presented by Edelman and Fortune [Edelman69]. The mechanisms contain hydrocarbon oxidation to form the products of light hydrocarbon, CO and H_2 which are subsequently oxidized to CO_2 and H_2O. Brink [BrinkPhD98, Brink99] modified the global 3-step mechanism similar to the simplified mechanism proposed by Abdalla [Abdalla83] applied for perfectly stirred reactor (PSR) calculations. In the modified irreversible 3-step mechanisms, the CO oxidation is described by the rate expression proposed by Howard [Howard73]. The H_2 oxidation is assumed to be infinitely fast in the fuel lean case, while the amount of H_2 and H_2O are calculated from the equilibrium composition in the water-shift reaction. Rückert [Rückert03] presented alternative reaction rate for irreversible CO and H_2 oxidation applied to numerical simulation of 200 MW_e bituminous coal-fired furnace, which later used in oxy-coal CFD simulations for 100 kW_{th} lignite-fired furnace [Toporov08a, Kangwanpongpan12].

Jones and Linstedt [Jones88] presented the global 4-step mechanisms containing two competing heavy hydrocarbon breakdown reactions, reversible H_2 oxidation and one water-shift reaction ($CO + H_2O \leftrightarrow CO_2 + H_2$). The mechanisms were proposed due to the fact that most existing reaction mechanisms (global 1-step and all quasi-global 2-3 step mechanisms) incorrectly predicted H_2 and CO production in flames. The global 4-step mechanisms were validated by experiments of methane and propane diffusion flames. Other than the standard global 4-step mechanisms, two modified global 4-step mechanisms were also presented for MILD (Moderate and Intensive Low oxygen Dilution) combustion of natural gas furnace by Kim et al. [KimPJ08]. The first modification was to replace water-shift reaction and reversible H_2 oxidation by irreversible CO oxidation and irreversible H_2 oxidation. In the second modification, only kinetic rates for reversible H_2 oxidation changed using parameters from Marinov et al. [Marinov96].

The kinetic rate expressions for global reaction mechanisms in oxy-fuel conditions were proposed by Andersen et al. [Andersen09] for 2-step and 4-step mechanisms, Toporov et al. [Toporov08a] for irreversible 3 step mechanisms and Frassoldati et al. [Frassoldati09] for modified 4-step mechanisms optimized by nonlinear regression fitted to the detailed kinetic mechanism for laminar counter-flow diffusion flames fed with methane and pure oxygen. Modified global 3-step mechanisms were also proposed [Kangwanpongpan12]

by replacing reversible CO-CO_2 reactions [Andersen09] to CO oxidation in the irreversible 3 step mechanism. As basis from the modified global 4-step mechanisms by Kim et al., Yin et al. [Yin11] applied modified global 4-step mechanisms to oxy-fuel simulation of natural gas fired furnace by replacing reversible H_2 oxidation by irreversible H_2 oxidation using kinetic rates from Marinov et al. [Marinov96].

The global 2 and 3-step mechanisms are applied for numerical investigations of 100 kW_{th} laboratory-scale furnace (explained in chapter 5) because of its robustness in numerical convergence and successful oxy-fuel CFD modeling [Andersen09, Galletti10-11, Yin11, Kangwanpongpan10-12, Toporov08a] (Appendix B). The global 3-step mechanisms also showed good agreements of numerical predictions to experimental measurements in 100 kW_{th} oxy-coal furnace, as published in previous oxy-coal CFD simulations [Toporov08a, Kangwanpongpan10-12]. In addition, the global 2-step mechanisms were preformed for testing effect of reaction schemes.

2.6 Radiation modeling

Solution algorithms:

Viskanta [Viskanta87, 08] reviewed solution algorithms for radiative transfer equations (RTE) and radiative properties for combustion gases. The approaches for solution of multidimensional geometries were grouped into four broad categories, composed of directional averaging approximations (2, 4-flux, multi-flux and discrete ordinates), differential approximations (moment, spherical harmonics, P_N), energy balance methods (zone, Monte Carlo, finite volume, finite element, boundary element) and hybrid methods (discrete transfer, ray tracing, radiation element). It was concluded that only the differential methods such as P_1-approximation, discrete ordinate method (DOM), discrete transfer method (DTM) and finite volume method (FVM) are compatible with CFD procedures for solving the transport equations in complex geometries and can be applied for band calculations for radiative properties of combustion gases and do not require excessive computational capacity. Comparison of results from the DOM, DTM and FVM models in three dimensional furnace were presented by Knaus et al. [Knaus97], Carvalho et al. [Carvalho98], and Coelho et al. [Coelho98]. From all approached for solution algorithms of RTE mention previously, both the P1-approximation and the DOM can account for exchange of radiation between gas and particles including scattering effects of radiation (absorbing-emitting-scattering media). The P1 model is suitable for optical thickness higher than one in contrast to the DOM model which is valid for all ranges of optical thicknesses. The P1 model requires less computational effort and also has less accuracy than the DOM model. To account for the particle radiation and scattering effects in the calculations, numerical simulations for coal combustion were usually performed by the DOM models, including CFD simulations for oxy-fuel combustion (Appendix B). In addition to solution for the RTE, new correlations for radiation properties of gases in oxy-fuel conditions are required, which can be modeled using non-gray gases formulation in the DOM model. From above reasons, the DOM model is considered to be applied for all numerical models in this thesis (chapter 5, investigated models). The DOM model was originally proposed by Chandrasekhar [Chandrasekhar60] and later had been applied by

Fiveland et al. [Fiveland84-88] and Truelove et al. [Truelove87, 88] for radiative heat transfer problems.

Models for radiation properties of gas:

In combustion systems, CO_2, H_2O, CO and other gases are emitted during combustion process and these gases (CO_2 and H_2O) are strong absorbers and emitters of radiant energy. Band models for radiative properties of gases were reviewed by Viskanta [Viskanta87, 08], Modest [Modest03] and Lalleman et al. [Lalleman96]. The line-by-line (LBL) model is the most accurate approaches to determine spectral properties of combustion gases using spectroscopic database called HITRAN and HITEMP database developed from extensively experimental data worldwide [Rothman87-09, Rothman95,10]. In order to reduce computational efforts for complicated combustion simulations, approximated band models are required. The band models can be classified into four main groups ordering by complexity [Modest03], which are narrow band (SNB) model, wide band (WB) models and global models.

The well-known SNB models are The *Elsasser* and the *statistical models* [Tien69, Goody52]. The Elsasser model assumes that the spectral lines are equally spaced and all have the same intensity and half-width, while the statistical model assumes that the location of the spectral lines is randomly distributed. Although the SNB model has high accuracy of spectral line formulation, it is also computationally intensive and not appropriated for complicated combustion simulation. The simple WB model called *box model* [Penner59], where the spectral band is estimated by a rectangular box-shape calculated from the effective band width and height. Edwards [Edwards76] developed the exponential wide band (EWB) model from the knowledge of quantum mechanics that the line strength decreases exponentially in the band wings distant from band center. The concept of the EWB model stems from the experimental investigations that radiation absorption of gases located in the near infrared regions (1-20 μm). The average error of the EWB model is around 20% but maximum errors around 50-80%. Correlations for EWB were also presented for H_2O, CO_2, CO, CH_4, NO and SO_2 and line strengths were constructed by three band shapes (upper limited, lower limited and symmetric band).

For the global models, total emittances and absorptances for specific gas are calculated by correlations fitting to benchmarks. The benchmarks for the global models can be either LBL calculations from HITRAN (or HITEMP) database, Hottel's charts [Hottel67, McAdams54-ch.4], or more precise models such as SNB and EWB models. Examples of the global models are the weighted-sum-of-gray-gases (WSGG) model [Hottel67, Modest91], Leckner's model [Leckner72], full-spectrum k-distribution (FSK) model [Modest02] and spectral-line-based weighted-sum-of-gray-gases (SLW) model [Denison93-95]. Among these global models, the WSGG model is the most simplified expression for the predictions of total radiative properties of gases in combustion problems for several decades. In the WSGG model, the total emittance of gas is calculated by a sufficient number of gray gases using polynomial correlations for weighing factors and absorption coefficients. According to its simplicity, fast computation and acceptable precision for combustion problem, the WSGG model is selected for numerical studies and the new correlations were generated for oxy-fuel conditions in this thesis (chapter 4). However, applications of other models in oxy-fuel conditions were also published either in one dimen-

sional planar enclosure or three dimensional furnaces using the SNB model [ChuH11], FSK model [Porter10], EWB model [Erfurth09a] and Leckner's model [Andersson07].

Oxy-fuel correlations for total emittance in the WSGG model:

Radiation properties of combustion gases in oxy-fuel combustion are considerably different from those found in air-fired conditions due to the higher amount of carbon dioxide and water. Thus, the widely employed radiation correlations for the weighted-sum-of-gray-gases (WSGG) model proposed by Smith et al. [SmithTF82], are no longer applicable. To provide a good prediction of oxy-fuel combustion, new data and correlations are needed. Recently, there have been some attempts to model radiation properties of gases under oxy-fuel conditions. Johansson et al. [Johansson11] proposed weighted-sum-of-gray-gases (WSGG) correlations with the use of four gray gases from fitting of emittance data that was calculated by statistical narrow band (SNB) model with EM2C database. The study accounted for molar ratios (MR) of H_2O to CO_2 from 0.125 to 2, and pressure path-lengths between 0.01 and 60 bar-m in the temperature range of 500 to 2500 K. However, EM2C database [Scutaru94, Riviere95] is based on an outdated HITRAN 1992 database combining with H2O line near 2700 cm^{-1} and additional spectral hot lines. Therefore those WSGG correlations probably lack accuracy in combustion conditions, in which hot lines are important above 1000 K [Rothman10]. Yin et al. [Yin10] proposed new parameters for WSGG model with four gray gases derived from fitting emittance data calculated by exponential wide band (EWB) model [Edward76] at atmospheric pressure, with temperatures between 500 and 3000 K, and path-lengths from 0.001 to 60 m. Predictions of radiative source term applying this new coefficients for a 0.8 MW oxy-natural gas furnace and 609 MW tangential fired utility boiler were compared with the predictions calculated with correlations proposed by Smith et al [SmithTF82] for air-fired conditions. Rehfeldt et al. [Rehfeldt11] determined new parameters for the WSGG model using four gray gases based on the fitting of emittance data computed from EWB model in the temperature range of 600 to 2400 K, and molar ratio of H_2O to CO_2 ranging from 0.056 to 2.167, in which the remaining 5% of gas was non-radiating species (N_2 or O_2). Wall radiative heat fluxes calculated from the correlations were compared with EWB model for a rectangular furnace using a CFD tool. However, the study lacked all details of the determined parameters. Krishnamoorthy et al. [Krishnamoorthy10a] developed new WSGG model with five gray gases based on least square fit of total emittance correlations that are available in Perry's Chemical Engineers Handbook [Hottel07] for the molar ratio H_2O/CO_2 of 0.5, 1.0, 2.0 and 3.0, and at temperatures of 1000, 1500 and 2000 K. No correlation was presented in that work. Radiative source terms calculated using the correlations were compared with results from SNB model in a three dimensional enclosure having a non-uniform gas temperature profile in air-fired conditions in a mixture of 5% CO_2, 15% H_2O and 80% N_2. Khare [Khare08a] fitted correlations for WSGG model with total emittances calculated from EWB model. However, no details of the correlations were published. Although the parameters of the WSGG models can be easily implemented for predictions of radiation properties of gases in computer codes, only the correlations presented in Johansson et al. and in Yin et al. were published [Johansson10,11, Yin10].

Benchmarks for total emittance (line-by-line calculations):

In order to generate an accurate set of correlations for the WSGG model, total emittances calculated by LBL calculations with HITRAN or HITEMP database are required. Chu et

al. [ChuH11] compared wall heat fluxes and radiative source terms calculated by SNB model and line-by-line (LBL) approach, in which HITRAN 2004, HITRAN 2008, HITEMP 1995 and HITEMP 2010 database were used as database for LBL calculations. The author concluded that HITEMP 2010 database should be used as the benchmark for validation of other spectral radiation models. Becher et al. [Becher11-partA] compared the spectral transmittance of H_2O and CO_2 generated by HITRAN 2004, 2008 and HITEMP 1995, 2010 database with experiments. Transmittances of 1.8, 2.7 and 6.3 μm H_2O-bands at temperatures of 800, 1000 and 1400 °C and of 2.7 and 4.3 μm CO_2-bands at temperatures of 727, 1100 and 1500 °C at various concentrations were used as benchmarks for evaluation of deviation from experiments. The authors concluded that HITEMP 2010 database provided the smallest deviations from experimental measurements. HITEMP 2010 contains 111 million transitions for H_2O with a spectral coverage of 0-30,000 cm^{-1}, and of 11 million for CO_2 with a spectral coverage of 258-9648 cm-1 [Rothman10].

Regression analysis for determining correlations:

One of the well-known methods for fitting correlations for the WSGG model was non-linear regression analysis. the procedure of fitting correlations for WSGG model to EWB model using non-linear regression analysis were presented by Smith et al. [SmithTF82], using Fletcher-Powell technique for multivariable unconstrained non-linear problem, and by Rehfeldt et al. [Rehfeldt11], applying the Nelder-Mead method (downhill simplex method). Galarça et al. [Galarça08] employed a non-linear multiple regression analysis and the Levenberg-Marquardt (LM) algorithm to fit the absorption coefficients and weighting factors to tabulated values of total emittance calculated by the Monte Carlo-Absorption-line blackbody distribution function (MC-ALBDF). Four gray gases were used by Rehfeldt et al. and three gray gases by Smith et al. and Galarça et al.. Polynomials of order three were used for the temperature dependent polynomial coefficients of total emittance presented in Smith et al. and Galarça et al.. In the present study, the LM algorithm and non-linear multiple regression analysis was applied to obtain correlations due to its efficiency and stability of convergence.

Particle-radiation (particle emissivity and scattering factor):

Barcena et al. [Barcena07] reviewed particle emissivity in coal-fired burners and also determined the particle emissivity calculated based on measured parameters from IR sensor. The author proposed the definition of effective emissivity based on the ratio of emitted radiance from an optically thick mixture of gas and particles to blackbody radiance at the same temperature, which has the value of around 0.8 at the gas temperature of 1600 K. The particle emissivities are gradually decreased with an increasing of gas temperatures surrounding particles The author also suggested that no general equation for the approximation of particle emissivity in coal flames. Chui et al. [Chui93] proposed the model for particle emissivity, varying with fraction of burnout from around 1.0 for unburned carbon to 0.6 for fry ash. This is in an agreement with previous approximated model by Baum et al. [Baum71], determining particle emissivity from the volatiles content and burnout fraction of residual carbon. Backreedy et al. [Backreedy06] applied the value of particle emissivity of 0.85 for slag at wall and 0.9 for the combusting char. Lou et al. [Lou07] investigated radiative properties of coal particles (emissivity and scattering factor) inside different layers of full-scale pulverized coal-fired boiler (full and partial loaded

operations) using image processing method. The scattering factors vary from 0.3 to 0.75 depending on loads of operation and location of measurements at elevated level. More heat input into furnace increased radiative scattering of the particles. For heat input between 175 and 300 MW_{th}, the particle scattering factors were calculated by image processing method based on measurements and have values approximately 0.5-0.6 m^{-1}at elevation after the last burners (layer 2 for boiler A and layer 3 for boiler B). Therefore, the particle scattering factor can be assumed to be around 0.6 m^{-1} in the absence of experimental results.

In general, the particle absorption and scattering are dependent of size parameter, index of refraction and clearance to wavelength ratio between particles [Modest03]. Scattering effect can be ignored if particle volume fraction is less than 0.006 (small particles concentrations) or clearance to wavelength ratio is higher than 0.5 (large distance between particles). The Reyleigh theory for scattering of particle is valid for small particles (size parameter << 1) and the Mie scattering theory for large particles (size parameter >>1). Johansson et al. [Johansson11b] and Andersson et al. [Andersson11a] modeled particle extinction coefficient instead of particle emissivity, applying the knowledge of radiation properties of particle cloud explained by Modest [Modest03]. However, no details of the total projected area of the particles per unit volume are presented, which are fitted to total intensity measured in experiments.

Particle-radiation (soot radiation):

Wall and Stewart [Wall73] investigated soot radiation in a 20 MW brown coal-fired furnace and found that soot alone can contribute to 90% of the radiation at visible wavelengths and to 60% of the total wavelength-integrated radiation. Therefore, particle emissivity can be assumed to be mainly influenced by soot radiation without scattering effect in oxy-fuel flames as presented by Andersson et al. [Andersson08a], and later by Andersson et al. [Andersson11a]. In the experiments from propane-fired oxy-fuel flames by Andersson et al. [Andersson08b], increasing $\%O_2$ in the feeding gas mixture from 21% to 27% resulted in higher overprediction of radiation incident (intensity) on the furnace wall by approximately 20%, measured by IFRF narrow angle radiometer [Radoux98]. Furthermore, the images of the oxy-fuel flames showed the yellow/orange luminous flame for the 27% O_2-flame, comparing to blue/violet (close to transparent) for the 21% O_2-flame. This implied that the soot volume fraction is drastically reduced when reducing $\%O_2$ from 27% to 21%. Therefore, the contribution of soot radiation to radiation calculation is significant in case of retrofitted oxy-fuel furnace, when the $\%O_2$ is around 28-36%.

Modest [Modest03] explained that soot absorption coefficient can be modeled based on the assumption of non-scattering small size particle (Rayleigh's theory). The absorption coefficient is equal to extinction coefficient, depending on refractive index, soot volume fraction and wavelength of combustion gases. To simplify radiative heat transfer calculation, the total soot radiation for all optical wavelengths in consideration is calculated using the average value of Planck-mean and Rosseland-mean absorption coefficient (also extinction coefficient) presented by Felske et al. [Felske77]. The total absorption coefficient of soot particle is dependent of refractive index, volume fraction of soot, gas temperature and second Planck function constant. Soot volume fractions for turbulent oxy-fuel flames (Ethylene as fuel) in O_2 of 24%, 29% and 36% in bulk CO_2 were measured at various heights, investigated by Voigt [Voigt-MSc07]. The soot volume fractions near to

flame center have values between 10^{-6} and 1.8×10^{-6} for 24% O_2-flame and $4 \times 10^{-7} - 1.2 \times 10^{-6}$ for 29% O_2-flame. Modeling soot radiation using approach by Felske et al. [Felske77] was also presented by Krishnamoorthy et al. [Krishnamoorthy10b] in the pool fired simulation. To calculate suitable refractive index, the wavelength of interest is required. Felske et al. [Felske73] emphasized that infrared band of CO_2 and H_2O in combustion gases at above wavelength of 15 μm can be negligible, and suggested to consider important overlapping gas bands of 2.7 μm.

Empirical constants for soot absorption coefficients can be determined by index of refraction. Modest reviewed possible correlations of refraction index for modeling of soot absorption coefficients evaluated from experiments utilizing polystyrene and Plexiglas soot [Lee80], amorphous carbon [Stull60], pyrographite at 300 K [Howarth66] and propane soot [Dalzell69, Chang90, Felske84].

Recently, Andersson et al. [Andersson11a] proposed two approaches for the modeling of particle radiation. The particle radiation can be modeled as non-scattering soot radiation (soot absorption coefficient) assuming very small particle size or as particle emissivity for propane oxy-fuel flame, as scattering soot radiation [Andersson11a] for lignite oxy-fuel flame and as bigger size particle (particle emissivity) where Mie scattering theory is applied as explained by Modest [Modest03] for lignite oxy-fuel flame [Andersson11a , Johansson11b]. The influences of including soot radiation on the CFD calculations of propane oxy-fuel flames applying both the gray and non-gray approaches for propane oxy-fuel flame using the WSGG model are also presented by Hjärtstam et al. [Hjärtstam12] and Andersson et al. [Andersson11b].

2.7 Numerical method and solution algorithms

Numerical methods and solution algorithms for CFD models were comprehensively reviewed and explained in many standard CFD books by Versteeg et al. [Versteeg07], Blazek [Blazek05], Chung [Chung02], Ferziger et al. [Ferziger02], Lomax et al. [Lomax99], Tannehill et al. [Tannehill97], Anderson [Anderson95] and Patankar [Patankar80]. In order to solve the set of governing equations, many methods and aspects are involved such as time-dependency (steady- or unsteady-state flows), compressibility of gas density, segregated or coupled solution algorithms for velocity and pressure in continuity and momentum equations, discretization schemes, pressure-velocity coupling and solution of discretized equations. The discretization schemes depend also on the assumptions of compressibility of density. All aspects are discussed in details as following.

Flows can be steady-state (time independent) or unsteady-state (time dependent). If the steady-state flow is considered, the differential terms with time can be omitted from the solution procedures. Density is assumed as constant for incompressible flows and varied for compressible flows. Density is determined from the continuity equation for compressible flows but maintaining as constant for incompressible flows. Pressure is calculated using the equation of state for compressible flow but by pressure correction equation in continuity and momentum equations. The incompressible flows occur at low-speed regime, classified by a Mach number of around less than 0.3 such as combustion flows in conventional furnace and swirl burner; hence, suitable for combustion flows in this thesis

when the variation of fluid density is small and can be negligible. Therefore the discretization scheme based on the constant density is applied (incompressible flows) for oxy-fuel combustion in this thesis (sometime called pressure-based solution algorithms in literatures).

Discretization schemes:

Discretization schemes were reviewed by different authors in the CFD book [Versteeg07, Blazek05, Chung02, Ferziger02, Lomax99, Tannehill97, Anderson95, Patankar80]. The discretization schemes for the continuity and momentum equations (incompressible flows) were necessary to from the set of differential equations from the integral formulations because the governing equations are solved by numerical methods. The schemes were derivative from different methods depending on how to determine physical quantities of flows in control volume. Examples of the schemes are finite volume method, finite element method, central-difference scheme, upwind-difference (UPWIND) scheme [Courant52], Power-Law scheme [Patankar80], Quadratic Upwind Interpolation for Convective Kinematics (QUICK) scheme [Leonard90] and Monotone Upstream-Centered Schemes for Conservation Laws (MUCSL) [Van Leer79] and hybrid scheme [Versteeg07]. The upwind schemes can be grouped into four categories [Blazek05], which are flux-vector splitting, flux-difference splitting, total variation diminishing (TVD) [Harten83] and fluctuation-splitting schemes. The most popular approach for combustion CFD simulations is the UPWIND schemes due to its numerical stability and fast computation. The second-order UPWIND scheme was also proposed by Barth et al. [Barth89]. The UPWIND scheme is often applied for combustion modeling because of its simplicity, numerical stability and fast numerical convergence. When compromising between accuracy and computational time, the second order UPWIND scheme was a good option as seen in some oxy-fuel CFD simulations (Appendix B).

Because complexity of mathematical sub-models and computational grid in coal combustion simulations result in high computational cost, some strategic procedure can remedy and enhance stability of numerical convergence [ANSYS12]. In general combustion simulations, it is recommended to first converge non-reacting flow simulations (often called cold flows) using the most simplified turbulent model (standard k-ε) and the first order UPWIND scheme for continuity, momentum, energy equations, kinetic energy and its dissipation (turbulence) [Vuthaluru06]. After converging the non-reacting flow simulations (solutions of the first order UPWIND scheme), coal particles can be feed into furnace and reacting flow simulations begin. When solutions for reacting flows are achieved, the accuracy of predictions can be enhanced by switching to the higher order scheme such as the second order UPWIND for continuity, momentum equations and gas species. Finally, the radiation model can be included in computations and the last converged solutions can be obtained. During computations, numerical instability can be controlled by numerical relaxation parameters.

Pressure-velocity coupling:

For incompressible flows, the density is constant and coupling between pressure and velocity introduces a constraint in the solution of the flow fields. For incompressible flows, the density is constant and not linked to the pressure as compressible flows. The coupling between pressure and velocity introduces a constraint in the solution of the flow fields.

Algorithms for pressure-velocity coupling were reviewed by Versteeg et al. [Versteeg07], Chung [Chung02] and Patankar [Patankar80], which are the Semi-Implicit Method for Pressure-Linked Equations (SIMPLE) [Patankar72,73], the SIMPLE Revised (SIMPLER) [Patankar80], the SIMPLE-Consistent (SIMPLEC) [Van Doormal84] and the Pressure Implicit with Splitting of Operators (PISO) [Issa86] algorithm. All algorithms are developed using the concept of *staggered grid* for velocity component [Harlow65] explained well by Patankar et al. [Patankar80] and later in the standard CFD book by Versteeg et al. [Versteeg07]. In the staggered grid method, the physical quantities such as pressure, density and temperature are determined at nodes, but velocity components are calculated on staggered grids center surrounding the cell faces. The *pressure correction* is required for the SIMPLE algorithm to approximate pressure at nodes, but not for the SIMPLER algorithm. The SIMPLEC algorithm modified the SIMPLE algorithms by manipulating velocity correction equation. The PISO algorithm was first proposed to solve unsteady-state flows, but later successfully adapted for steady-state problem.

For computational costs, the SIMPLER algorithm requires less number of iterations for convergence than the SIMPLE but has more computational effort for individual iteration. This is because the SIMPLER uses the pressure correction only for the calculation of velocity, while the pressure equation is solved correctly in a separate procedure. The SIMPLEC algorithm can improve convergence only for a strong coupling between pressure and velocity. The PISO is superior to other methods only when the physical quantities (scalar variables) are strongly linked to velocities. Even Van Doormaal et al. [Van Doormaal84] suggested that the SIMPLEC algorithm is better than either the SIMPLER or SIMPLE algorithm, the conclusion was not still not ascertained for all applications [Versteeg07]. Because no clearly advantages of applying more advanced models (the SIMPLER, SIMPLEC and PISO) to oxy-fuel combustion, which is the focus of this thesis, the SIMPLE algorithm is applied for all numerical investigations due to its robustness and stability of convergence.

Solution algorithms:

There are two main solution approaches for discretized equations, *direct* and *iterative approaches* as described by Versteeg [Versteeg07]. The direct approach solves transport equations using the tri-diagonal matrix algorithm (TDMA) [Thomas49]. The TDMA algorithm requires less memory storage than iterative algorithms because additional non-zero coefficients are needed to store in computer memory, causing in large number of iterations to achieve convergence. However, if the iterative algorithm is applied with the *multi-grid technique*, computational time can be reduced extensively. The TDMA algorithm showed an undesirable instability of computations especially when the high-order discretization scheme was applied such as the QUICK scheme [Versteeg07].

Two efficient *point-iterative approaches* are *Jacobi* and *Gauss-Seidel* methods. Both approaches are slightly different in how to substitute previously iterative-step values into the set of equation matrix. After arranging equations, the Jacobi iterative method substitute all independent variables form the value of last-step iteration, while the Gauss-Seidel method substitute independent variables for each equation using update value at the current iterative step. This results in faster convergence for the Gauss-Seidel method [Versteeg07, Ralston78]. The *relaxation method* can improve the rate of convergence for both iterative methods by multiplication equations with the relaxation parameters and calculating the

residual of convergence. The parameters to control relaxation of equations are sometimes called the *under-relaxation factor* (URF) in commercial CFD code [ANSYS12]. The relaxation methods to improve the calculation of solutions for ordinary differential equations are also explained by Versteeg et al. [Versteeg07], Ferziger et al. [Ferziger02] and Lomax et al. [Lomax99].

Other schemes were also comprehensively described, for example, the Alternating Direction Implicit (ADI) scheme [Blazek05, Ferziger02, Chung02, Lomax99], the implicit Lower-Upper Symmetric Gauss-Seidel (LU-SGS) scheme [Blazek05], Conjugate Gradient Method and Biconjugate Gradients [Ferziger02].

Multigrid technique for acceleration of computation:

When refining computational mesh in the control volume, the convergence rate of iterative methods reduces rapidly. To remedy the problem, the multi-grid techniques are proposed [Versteeg07]. There are also other computing techniques to increase the rate of convergence for large-scale geometry such as the domain decomposition method (DDM) and the parallel processing as reviewed by Chung [Chung02]. The multi-grid methods were pioneered by Brandt [Brandt72] and later explained in details by Wesseling [Wesseling92]. Nowadays, the multi-grid acceleration of the Gauss-Seidel point-iterative method has become the most selected algorithm for many CFD commercial codes. Two types of multi-grid techniques are the algebraic multi-grid (AMG) [Hutchinson86] and Full-approximation storage (FAS) methods [Brandt79]. The AMG method does not require a re-discretization of numerical meshes, therefore is more attractive for unstructured meshes. The FAS method is better when solving non-linear problems. In CFD codes, the linear system of equations is efficiently solved by an implicit point iterative Gauss-Seidel method in conjunction with the AMG methods for acceleration of computation.

Pressure interpolation scheme:

Pressures at the faces of computational cells are interpolated by interpolation schemes, for example, linear, second-order, the body-force-weighted or pressure staggering option (PRESTO) schemes. Each pressure interpolation scheme has its own advantage for different flow types [ANSYS12]. The most basic scheme is the linear scheme, determining pressure from adjacent cells. The second-order scheme is more accurate than the linear scheme but causing in numerical divergence for problem with high change in pressure gradients such as flow with particle phase as in coal combustion or multiphase flow. The body-force-weight is beneficial for flow with buoyancy force. Finally, the PRESTO scheme is superior for high swirling numbers, high-speed rotating flow and flow with discrete (particle) phase, which is valid for coal combustion modeling. The concept of the PRESTO scheme is similar to the staggered grid scheme explained by Patankar [Patankar80].

3 Mathematical Modeling of Lignite Oxy-fuel Combustion

3.1 Governing equations

The relationship between the Lagrangian and Eulerian form of the governing equation is provided by the Reynolds transport theorem. Consider the mass element (Lagrangian approach) which is passing through a control volume (Eulerian approach). The Reynolds transport theorem can be written as:

$$\frac{dm\beta_f}{dx} = \frac{d}{dt}\int_{CV} \rho\beta_f d\forall + \int_{CS} \rho\beta_f u_i dA_{\boldsymbol{i}} \tag{3.1}$$

Defining β_f as some intensive property of the fluid per unit mass, where m is the mass of fluid element, ρ is the mass density, u_i is the velocity with respect to the control surface, and differential area vector, $dA_{\boldsymbol{i}}$, is normal outward from the control surface.

3.1.1 Continuity equation

Gas-phase continuity equation: By applying the Reynolds transport theorem for continuity of species k, and set β_f as the mass fraction MF_k of species k, then become the gas-phase continuity equation.

$$\sum_k \left[\frac{\partial \rho_k}{\partial t} + \frac{\partial(\rho_k u_{g,i})}{\partial x_i}\right] = 0 \tag{3.2}$$

or for gas mixture

$$\frac{\partial \rho_g}{\partial t} + \frac{\partial(\rho_g u_{g,i})}{\partial x_i} = 0 \tag{3.3}$$

The subscripts i an j are the index of velocity components in each direction. The ρ_k the mass density of species k, the ρ_g is the mass density of the gas mixture and $u_{k,i}$ is the mass-averaged velocity of specie k in the velocity direction i, which is written in the form.

$$u_{g,i} = \sum_k MF_k u_{k,i} \tag{3.4}$$

while MF_k is the mass fraction of species k

$$MF_k = \frac{\rho_k}{\rho_g} \tag{3.5}$$

Gas-phase continuity in gas-particle mixture: By applying the Reynolds transport theorem together with Gauss' theorem for conservation of gaseous mass, the gas-phase continuity equation for the gas-particle mixture can be written in the form.

$$\frac{\partial \acute{\rho}_g}{\partial t} + \frac{\partial (\acute{\rho}_g u_{g,i})}{\partial x_i} = R_p \tag{3.6}$$

where $\acute{\rho}_g$ is the mass of the gas per unit volume of gas-particle mixture (the bulk gas density), $u_{g,i}$is the mass-averaged gas velocity [Smoot79] and R_p is the rate of total mass of gas added per unit volume of mixture due to particle mass transfer.

Particle (discrete) phase continuity: Analogous to the continuity equation for gas phase, the particle phase continuity equation can be written in the form.

$$\frac{\partial \acute{\rho}_p}{\partial t} + \frac{\partial (\acute{\rho}_p u_{p,i})}{\partial x_i} = -R_p \tag{3.7}$$

where $\acute{\rho}_p$ is the bulk density of the particle phase. $u_{p,i}$ is the mass averaged particle velocity.

Overall Continuity of gas-particle mixture: With summation of two equations above yields:

$$\frac{\partial (\acute{\rho}_g + \acute{\rho}_p)}{\partial t} + \frac{\partial (\acute{\rho}_g u_{g,i} + \acute{\rho}_p u_{p,i})}{\partial x_i} = 0 \tag{3.8}$$

3.1.2 Momentum equation

Gas-phase momentum: By applying the Reynolds transport theorem to the momentum change of fluid element, then become the momentum equation for a mixture of gaseous species.

$$\frac{\partial (\rho_g u_{g,i})}{\partial t} + \frac{\partial (\rho u_{g,i} u_{g,j})}{\partial x_j} = -\frac{\partial p_i}{\partial x_i} + \frac{\partial \tau_{ij}}{\partial x_j} + \rho_g BD_i \tag{3.9}$$

The subscripts *i* an *j* are the index of velocity components in each direction. The p_i is the pressure stress tensor and τ_{ij} is the shear stress tensor and BD_i is the body force per unit mass of species *i*.

Gas-phase momentum in gas-particle mixture: By applying the Reynolds transport theorem for the momentum of gaseous phase together with divergence theorem. Assuming a spherical particle and a uniform momentum flux over the particle surface, the gas-phase momentum equation for the gas-particle mixture can be written in the form.

$$\frac{\partial (\acute{\rho}_g u_{g,i})}{\partial t} + \frac{\partial (\acute{\rho}_g u_{g,i} u_{g,j})}{\partial x_j} = -\frac{\partial p_i}{\partial x_i} + \frac{\partial (1-VF)\tau_{stn,ij}}{\partial x_j} + \frac{\partial (VF)\tau_{ij}}{\partial x_j} - f_{p,i} + \acute{\rho}_g BD_i + u_{p,i} R_p \tag{3.10}$$

where $\tau_{stn,ij}$ is the shear stress tensor acting on the particle due to the local rate of strain in the fluid, $f_{p,i}$ is the aerodynamics force on the particles per unit volume of mixture.

The *VF* is the void fraction which is defined as the volume occupied by the gas per unit volume of gas-particle mixture, which can be written by a relation.

$$\acute{\rho}_g = (VF)\rho_g \tag{3.11}$$

For most of pulverized coal combustion application, *VF* is close to unity, so the term $(1 - VF)\tau_{stn,ij}$ may be negligible.

The last term in gas-phase momentum equation in gas-particle mixtures, $u_{p,i}r_p$, represent momentum transfer due to mass addition. It is the summation of distribution for particle velocity, $u_{p,i}^{ps}$, associated with different particle sizes *k*, as follow:

$$u_{p,i}R_p = \sum_k u_{p,i}^{ps}R_p^{ps} \tag{3.12}$$

where R_p^{ps} is the burning rate of particles in the same size class per unit volume of mixture.

<u>*Particle (discrete) phase momentum*</u>: The particle phase continuity equation for discrete phase can be written in the form.

$$\frac{\partial(\acute{\rho}_p u_{p,i})}{\partial t} + \frac{\partial(\acute{\rho}_p u_{p,i}u_{p,j})}{\partial x_j} + \sum_k \left[\acute{\rho}_p\left(u_{p,j}^{ps}\right)_{rel}\left(u_{p,j}^{ps}\right)_{rel}\right] = -u_{p,i}R_p + f_{p,i} + \acute{\rho}_p BD_i \tag{3.13}$$

where

$$\acute{\rho}_p u_{p,i} = \sum_k \acute{\rho}_{p,i}^{ps} u_{p,i}^{ps} \tag{3.14}$$

$$\left(u_{p,j}^{ps}\right)_{rel} = u_{p,j}^{ps} - u_{p,i} \tag{3.15}$$

If all particles move uniformly, the term of summation $\sum_k \left[\acute{\rho}_p\left(u_{p,j}^{k}\right)_{rel}\left(u_{p,j}^{k}\right)_{rel}\right]$ is negligible.

<u>*Overall Continuity of gas-particle mixture*</u>: by summation of equations for gas and particle phases and neglecting the term $(1 - VF)\tau_{stn,ij}$, the equation formulation is:

$$\frac{\partial(\acute{\rho}_g u_{g,i} + \acute{\rho}_p u_{p,i})}{\partial t} + \frac{\partial(\acute{\rho}_g u_{g,i}u_{g,j} + \acute{\rho}_p u_{p,i}u_{p,j})}{\partial x_j} = -\frac{\partial p_i}{\partial x_i} + \frac{\partial(1-VF)\tau_{stn,ij}}{\partial x_j} + \frac{\partial(VF)\tau_{ij}}{\partial x_j} + \left(\acute{\rho}_g + \acute{\rho}_p\right)BD_i - \sum_k \left[\acute{\rho}_p\left(u_{p,j}^{ps}\right)_{rel}\left(u_{p,j}^{ps}\right)_{rel}\right] \tag{3.16}$$

<u>*Drag law for particle motion*</u>:

The aerodynamics force is modeled using drag law for particle motion. The drag force for velocity component *i* [Munson09], is given by:

$$Drag\ force = \left|f_{p,i}\right| = \left(\frac{1}{2}\rho_g\left|u_{g,i}\right|^2\right) C_D Area_o \tag{3.17}$$

where C_D is the drag coefficients, which is a dimensionless parameter and $Area_o$ is the projection area of object in the counter-flow direction. The Reynolds number is written as:

$$Re = \frac{\rho_g|u_{g,i}|LC_o}{\mu} \tag{3.18}$$

The LC_o is the characteristic length of object (diameter for spherical particle).

The drag coefficient for a perfect sphere is equal to 24/*Re*. However, Morsi et al. [Morsi72] provided also empirical correlations for C_D depending on *Re* from less than 0.1 to 50000 as:

$$C_D = \frac{constant1}{Re} + \frac{constant2}{Re^2} + constant3 \tag{3.19}$$

3.1.3 Energy equation

<u>*Gas-phase energy*</u>: derived from the first law of thermodynamics by applying the Reynolds transport theorem and solve for thermal energy equation instead of total energy equation which is not suitable for application yielding the thermal energy equation for gas-particle mixture.

$$\frac{\partial}{\partial t}\left[\rho_g\left(e_g + \frac{|u_{g,i}|^2}{2}\right)\right] + \frac{\partial}{\partial x_i}\left[\rho_g u_{g,i}\left(h_g + \frac{|u_{g,i}|^2}{2}\right)\right] = -\frac{\partial q_j}{\partial x_j} + q_{sr} + \tau_{ij}\frac{\partial u_{g,i}}{\partial x_j} + \rho_g BD_{g,i}u_{g,i} \tag{3.20}$$

and additional definitions for gas specie *k* and velocity component *i*:

$$\rho_g e_g = \sum_k \rho_k e_k \tag{3.21}$$

$$\rho_g h_g = \sum_k \rho_k h_k \tag{3.22}$$

$$\rho_g u_{g,i} = \sum_i \rho_i \left|u_{k,i}\right|^2 \tag{3.23}$$

$$\rho_g BD_{g,i}u_{g,i} = \sum_k \rho_k BD_{k,i} \tag{3.24}$$

$$u_{g,i} = u_{k,i} - u_{D,k,i} \tag{3.25}$$

where e_g is the specific internal energy (J/kg). The $u_{D,k,i}$ is the diffusional velocity of specie *k* and $u_{g,i}$ is the velocity of gas mixture *k* in the direction vector *i* of velocity component. The q_{sr} is specific heat radiation term (per unit volume). The $\tau_{ij}\frac{\partial u_{g,i}}{\partial x_j}$ term is the viscous dissipation or the *dissipation function*, and always positive, representing an

irreversible work due to viscous forces done on a small fluid volume. The last term represent the reversible work due to compression or expansion of fluid element.

Assuming that the diffusional transport of kinetic energy is small compared to the diffusional transport of enthalpy. q_j is the summation of the specific heat conduction term written as:

$$q_j = -K_{cond}\frac{\partial T}{\partial x_j} + \sum_k J_{m,k} h_k \tag{3.26}$$

The K_{cond} is the thermal conductivity (W/(m K)). The subscript j indicate the direction vector of heat conduction term and the $J_{m,k}$ is the mass flux (kg/(m^{2}s)) for specie *k*.

<u>*Gas-phase energy in gas-particle mixture*</u>: by separating control volume for the gas phase and particle phase, the energy equation for gas phase in the gas-particle mixture is expressed by:

$$\frac{\partial}{\partial t}\left[\acute{\rho}_g\left(e_g + \frac{|u_{g,i}|^2}{2}\right)\right] + \frac{\partial}{\partial x_i}\left[\acute{\rho}_g\left(h_g + \frac{|u_{g,i}|^2}{2}\right)u_{g,i}\right] = -\frac{\partial}{\partial x_j}\left[VFq_j + (1-VF)q_{s,j}\right] - q_{cp} + VFq_{rg} + R_p\left(\bar{h}_s + \frac{|u_{p,i}|^2}{2} + \frac{\acute{w}^2}{2}\right) - \frac{\partial}{\partial x_j}\left[(1-VF)pu_{p,i}\right] + \frac{\partial}{\partial x_j}\left[VF\tau_{ij}\frac{\partial u_{g,i}}{\partial x_j} + (1-VF)\tau_{stn,ij}\frac{\partial u_{p,i}}{\partial x_j}\right] - u_{p,i}f_{p,i} + \acute{\rho}_g BD_{g,i}u_{g,i} + \bar{p}_s s_v \tag{3.27}$$

where h_g is the mass averaged enthalpy, $q_{s,j}$ is the heat transfer through the boundary particle, q_{cp} is the heat transfer to the particles from the gas by conduction per unit volume of mixture, q_{rg} is the specific radiative heat transfer absorbed by gas, $\bar{h}_s$ is the average enthalpy of gas over the particle control surface, s_v is the particle dilatation rate per unit volume of mixture and $\bar{p}_s$ is the averaged pressure on the particle surface. $\acute{w}$ is the gas velocity at control surface of particle (m/s).

<u>*Discrete-phase energy*</u>: derived by applying Reynolds transport theorem with energy of a single particle giving the energy equation for a discrete phase particle-cloud equation.

$$\frac{\partial}{\partial t}\left[\acute{\rho}_p\left(e_p + \frac{|u_{p,i}|^2}{2}\right)\right] + \frac{\partial}{\partial x_i}\left[\acute{\rho}_p u_{p,i}\left(e_p + \frac{|u_{p,i}|^2}{2}\right)\right] = -R_p\left(\bar{h}_s + \frac{|u_{p,i}|^2}{2} + \frac{\acute{w}^2}{2}\right) + u_{p,i}f_{p,i} + \acute{\rho}_p BD_{g,i}u_{p,i} + q_{cp} + q_{rp} - \bar{p}_s s_v \tag{3.28}$$

where e_p is the internal energy of particle and q_{rp} is the specific radiative heat transfer absorbed by particle.

<u>*Overall energy of gas-particle mixture*</u>: by superposition of the energy equation for gaseous phase and particulate phase, overall energy equation becomes:

$$\frac{\partial}{\partial t}\left[\acute{\rho}_g\left(e_g+\frac{|u_{g,i}|^2}{2}\right)+\acute{\rho}_p\left(e_p+\frac{|u_{p,i}|^2}{2}\right)\right]+\frac{\partial}{\partial x_i}\left[\acute{\rho}_g\left(e_g+\frac{|u_{g,i}|^2}{2}\right)u_{g,i}+\acute{\rho}_p\left(e_p+\frac{|u_{p,i}|^2}{2}\right)u_{p,i}\right]=-\frac{\partial}{\partial x_j}\left[VFq_j+(1-VF)q_{s,j}\right]+VFq_{rg}+q_{rp}+\left[VF\tau_{ij}\frac{\partial u_{g,i}}{\partial x_j}+(1-VF)\tau_{stn,ij}\frac{\partial u_{p,i}}{\partial x_j}\right]+BD_{g,i}\left(\acute{\rho}_g u_{g,i}+\acute{\rho}_p u_{p,i}\right) \quad (3.29)$$

3.2 Turbulent dispersion of particle

The particle dispersion due to effect of turbulence in the fluid flow to particles can be described by either the particle cloud model [Baxter93] or stochastic tracking such as the discrete random walk model (DRW) [Gosman83] as discussed in the review. The stochastic tracking is applied for the CFD model in this thesis due to its simplicity. In this approach, the instantaneous fluid velocity is calculated from mean and fluctuating components of fluid velocity as:

$$u_i=\bar{u}_i+\acute{u}_i \quad (3.30)$$

In this approach, a number of representative particles (number of tries) must be sufficient to describe the particle dispersion. For small tracking particles moving in the fluid flow, the integral time can be approximated by:

$$Time_{Integration}\approx\left(C_{time\ integration}\right)\left(\frac{k}{\varepsilon}\right) \quad (3.31)$$

Using this equation, the time integration can be estimated from the ratio of turbulent kinetic energy to its dissipation rate. The integral time-scale constant ($C_{time\ integration}$) is equal to 0.15 for the k-ε turbulent model and to 0.3 for the RSM.

The characteristic lifetime of the eddy can be defined as constant and equal to double value of the time integration.

$$Eddy\ lifetime=2\,Time_{Integration} \quad (3.32)$$

In the k-ε and the k-ω model, the discrete random walk (DRW) model calculates the root mean square (RMS) for three fluctuating velocities from turbulent kinetic energy given by:

$$\sqrt{\overline{\acute{u}_x^2}+\overline{\acute{u}_y^2}+\overline{\acute{u}_z^2}}=\sqrt{\frac{2k}{3}} \quad (3.33)$$

3.3 Turbulence

In pulverized coal combustion process, the mixing rate of species is influenced by turbulent flow. A direct method to solve for the time-dependent conservation equations for turbulent flows was limited by computational efficiency. The numerical method to solve Navier-Stokes and continuity equation exactly in order to predict the details of turbulent flow behavior called 'Direct Numerical Simulation' (DNS). Unfortunately, this method requires large computer capacity and is also hardly applicable in the practical combustion

problem. At present, all methods to describe turbulent flow can be categorized into three broad categories.

1) *Reynolds-averaged Navier-Stokes equation* (RANS): focusing on the mean flow and the effects of turbulence on mean flow properties. The extra Reynolds stress term can be described by the well known k-ε turbulent model and also Reynolds stress model (RSM). Turbulent models includes in this category are the standard k-ε, RNG k-ε, Realized k-ε, SST k-ω and Reynolds stress model (RSM).
2) *Large eddy simulation* (LES): method to solve unsteady flow Navier-Stokes equations by tracking only behavior of large eddies and neglect small eddies. The effect of mean flow plus large eddies are included by sub-grid scale model. An intermediate computational cost is required.
3) *Direct numerical simulation* (DNS): compute the mean flow and all turbulent velocity fluctuations. The unsteady Navier-Stokes equations are solved within refined grids that are sufficiently fine that they can resolve the Kolmogorov length scales at which energy dissipation takes place and with time steps sufficiently small to resolve the period of the fastest fluctuations. This method consumes high computational time.

Computational expenses of described turbulent models are also presented in Fig. 3.1.

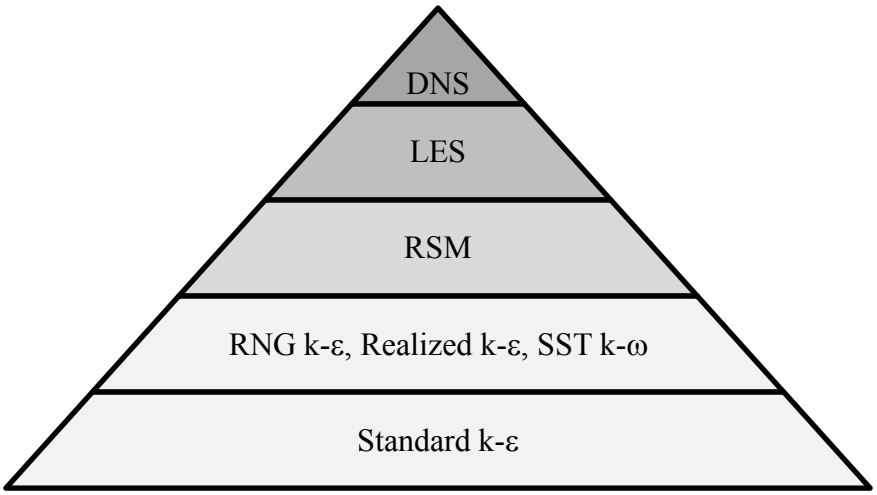

Figure 3.1: Computational costs of turbulent models.

Because coal combustion simulation is a complex problem and requires high computer capacity, only two equation models and RSM model are investigated in this thesis using experimental data from laboratory scaled 100 kW_{th} oxy-coal furnace [Toporov08a] to determine a suitable turbulent model in a preparatory step to further apply to the numerical predictions in a new pilot scaled 0.4 MW_{th} lignite oxy-fuel furnace at BTU Cottbus. Details of investigated laboratory scaled case are explained in chapter 5 and results of testing are summarized in chapter 6 of this thesis. First, the RANS equation are described, and then various RANS models will be explained emphasizing mainly on two equation models such as standard k-ε, RNG k-ε, Realized k-ε and k-ω SST including more advanced RSM models for complex flow fields.

3.3.1 Reynolds-averaged navier-stokes (RANS) equation

In combustion simulation, time mean averaged variables are sufficient to illustrate the results of combustion process. Therefore, with appropriate descriptions of the characteristics of the turbulent fluctuation and its influence to the mean flow field, computational cost can be reduced by coarser grid spacing and larger time step. This method called *Reynolds-averaged navier-stokes* (RANS), which is derived from three conservative of fluid flows.

Three dimensional motions in a viscous fluid flow in time and space can be described by continuity, momentum (Navier-Stokes equation) and energy (enthalpy) equation as following [Tannehill97].

Continuity equation: $$\frac{\partial \rho_g}{\partial t} + \frac{\partial (\rho_g u_i)}{\partial x_i} = 0 \tag{3.34}$$

Momentum equation: $$\frac{\partial (\rho_g u_i)}{\partial t} + \frac{\partial (\rho_g u_i u_j)}{\partial x_j} = -\frac{\partial p_i}{\partial x_i} + \frac{\partial \tau_{ij}}{\partial x_j} + \rho_g g_i \tag{3.35}$$

Energy equation (1st Law of Thermodynamics): in term of specific internal energy, *e*:

$$\frac{\partial (\rho_g e)}{\partial t} + \frac{\partial (\rho_g e)}{\partial x_i} = -\frac{\partial q_j}{\partial x_j} + \Phi + \frac{\partial Q}{\partial t} \tag{3.36}$$

By using the definition of enthalpy: $$h_g = e + \frac{p}{\rho_g} \tag{3.37}$$

Energy equation (1st Law of Thermodynamics): in term of specific enthalpy for gas mixture, h_g:

$$\left(\frac{\partial (\rho_g h_g)}{\partial t} - \frac{\partial p}{\partial t}\right) + \left(\frac{\partial (\rho_g u_i h_g)}{\partial x_i} - \frac{\partial (u_i p)}{\partial x_i}\right) = -\frac{\partial q_j}{\partial x_j} + \Phi + \frac{\partial Q}{\partial t} \tag{3.38}$$

The $\frac{\partial Q}{\partial t}$ is the rate of heat production per unit volume (source term of heat generation). The *dissipation function*, Φ, which represent an irreversible work done on a small fluid volume, has the form:

$$\Phi = \tau_{ij} \frac{\partial u_i}{\partial x_j} \tag{3.39}$$

In which τ_{ij} is the viscous stress tensor defined as:

$$\tau_{ij} = \mu \left[\left(\frac{\partial \bar{u}_i}{\partial x_j} + \frac{\partial \bar{u}_j}{\partial x_i}\right) - \frac{2}{3}\delta_{ij} \frac{\partial \bar{u}_k}{\partial x_k}\right] \tag{3.40}$$

g_i is body force per unit mass, $q_j = -K_{cond} \frac{\partial T}{\partial x_j}$ is the heat conduction and $K_{cond} = \Gamma_h = \frac{\mu}{\sigma_h * C_P} = \frac{\mu}{\sigma_h}$ is the heat conduction coefficient or diffusion coefficient of enthalpy and

σ_h is the Prandtl/Schmidt number. When applying energy equation, the equation of state in the context of thermodynamics should be mentioned and relation between thermodynamics variables such as pressure, density, temperature, internal energy and specific enthalpy (p, ρ, T, e, h) should be created.

In order to solve partial differential equation, the space of specific interest (control volume) is divided into a number of elements. The spacing of the division should be fine enough to solve the structure of turbulent flow and its transient variation. The time and length scales are usually very small compared to the turbulent conditions in the ones of mean gas flow. For this reason, the *steady state assumption* has been used with auxiliary relationship to separate instantaneous velocity into mean and fluctuating components. This method called "*time averaging concept"* [Tannehill97].

After inserting the mean and fluctuation components of velocity and density into three main conservative equations, maintaining above relations together with continuity equation. The *time averaging* RANS equation [Tannehill97] finally has the form:

Reynolds continuity equation:
$$\frac{\partial \overline{\rho_g}}{\partial t} + \frac{\partial}{\partial x_j}\left(\overline{\rho_g}\bar{u}_j + \overline{\acute{\rho}_g \acute{u}_j}\right) = 0 \qquad (3.41)$$

Reynolds momentum equation:

$$\frac{\partial}{\partial t}\left(\overline{\rho_g}\bar{u}_i + \overline{\acute{\rho}_g \acute{u}_\iota}\right) + \frac{\partial}{\partial x_j}\left(\overline{\rho_g}\bar{u}_i\bar{u}_j + \bar{u}_i\overline{\acute{\rho}_g \acute{u}_j}\right) = -\frac{\partial \overline{p_\iota}}{\partial x_i} + \frac{\partial}{\partial x_j}\left(\bar{\tau}_{ij} - \bar{u}_j\overline{\acute{\rho}_g \acute{u}_\iota} - \overline{\rho_g}\overline{\acute{u}_\iota \acute{u}_j} - \overline{\acute{\rho}_g \acute{u}_\iota \acute{u}_j}\right) \qquad (3.42)$$

Reynolds energy equation (Incompressible flow, Static temperature form):

$$\frac{\partial \rho_g C_P \bar{T}}{\partial t} + \frac{\partial \rho_g C_P \bar{u}_j \bar{T}}{\partial x_j} = \frac{\partial}{\partial x_j}\left[K_{cond}\frac{\partial \bar{T}}{\partial x_j} - \rho_g C_P \overline{\acute{T}\acute{u}_j}\right] + \frac{\partial \bar{p}}{\partial t} + \left[u_i \frac{\partial \bar{p}}{\partial x_i} + \overline{\acute{u}_\iota \frac{\partial \acute{p}}{\partial x_\iota}}\right] + \bar{\Phi} + \frac{\partial Q}{\partial t} \qquad (3.43)$$

where the mean dissipation function is:
$$\bar{\Phi} = \bar{\tau}_{ij}\frac{\partial \bar{u}_i}{\partial x_j} + \overline{\tau_{\iota J}\frac{\partial \acute{u}_\iota}{\partial x_J}} \qquad (3.44)$$

and mean stress tensor is defined as:
$$\bar{\tau}_{ij} = \mu\left[\left(\frac{\partial \bar{u}_i}{\partial x_j} + \frac{\partial \bar{u}_j}{\partial x_i}\right) - \frac{2}{3}\delta_{ij}\frac{\partial \bar{u}_k}{\partial x_k}\right] \qquad (3.45)$$

where δ_{ij} is the Kronecker delta. Gaseous mixture inside furnace is assumed to be *incompressible* in this thesis because pressure in combustion chamber is approximately equal to one atmospheric pressure (1 atm). Note that for *incompressible flow*, density variation is vanished from RANS equation and the parameter due to density fluctuation must be zero ($\acute{\rho} = 0$). The last Reynolds energy equation has been written by treating *T* (temperature) as an independent variable because of the fact that one of the significant numerical results is temperature profile rather than enthalpy or internal energy.

In Reynolds momentum equation, the term $\rho_g \overline{\acute{u}_\iota \acute{u}_J}$ called *Reynolds stress* caused by various turbulent fluctuations which require additional closure equations. Type of RANS turbulent models are ranging from zero-, one-, two-equation and Reynolds stress model (RSM) as reviewed in chapter 2. The historical progress of turbulent model originated

from *Boussineq hypothesis* [Boussinesq1877] in the zero-equation model. However, in this thesis, only two-equation models such as standard *k-ε*, RNG *k-ε*, Realized *k-ε*, *k-ω* SST and RSM seven-equation models are explained here. Only equation formulations for the standard *k-ε* are described in details to provide basic expressions of two equation models. Equation formulations for others two-equation models and their model constants are briefly explained after the standard *k-ε*. The details for all two-equation models including model constants are available in the standard CFD book and fundamental turbulence flow as reviewed in the literature review in chapter 2.

3.3.2 Standard k-ε model

The most widely used closure equation called the standard *k-ε* model [Launder72], which based on the formulation of transport equation for turbulent kinetic energy, *k*, and its dissipation rate, *ε*. The transport equation for turbulent kinetic energy is derived from exact equation of RANS equation, while transport equation for dissipation is obtained from empirical method.

Turbulent kinetic energy:

$$\frac{\partial \rho_g \bar{k}}{\partial t} + \frac{\partial \rho_g \bar{u}_i \bar{k}}{\partial x_i} = \frac{\partial}{\partial x_j}\left[\left(\mu + \frac{\mu_t}{\sigma_k}\right)\frac{\partial \bar{k}}{\partial x_j}\right] + G_k + G_b - \rho_g \varepsilon - Y_M + S_k \tag{3.46}$$

Dissipation rate:

$$\frac{\partial \rho_g \varepsilon}{\partial t} + \frac{\partial \rho_g \bar{u}_i \varepsilon}{\partial x_i} = \frac{\partial}{\partial x_j}\left[\left(\mu + \frac{\mu_t}{\sigma_\varepsilon}\right)\frac{\partial \varepsilon}{\partial x_j}\right] + C_{1\varepsilon}\frac{\varepsilon}{k}(G_k + C_{3\varepsilon}G_b) - \rho_g C_{2\varepsilon}\frac{\varepsilon^2}{k} + S_\varepsilon \tag{3.47}$$

Where G_k and G_b are the generation of turbulence kinetic energy due to the mean velocity gradients and buoyancy, respectively. S_k and S_ε are input source terms for the equations of kinetic energy and its dissipation. Y_M is the contribution of the fluctuating dilatation in compressible turbulence to the overall dissipation rate. σ_k and σ_ε are the turbulent Prandtl numbers.

The eddy viscosity ν_t is explained by the *Prandtl-Kolmogorov relationship* as:

$$\nu_t = \frac{\mu_t}{\rho_g} = C_\mu \frac{\bar{k}^2}{\varepsilon} \tag{3.48}$$

In the end, the turbulent production term due to kinetic energy, G_k, can be formulated with the *Boussinesq gradient-diffusion hypothesis* [Boussineq1877] for incompressible fluid:

$$G_k = -\rho_g \overline{\acute{u}_i \acute{u}_j}\frac{\partial \bar{u}_j}{\partial x_i} = \left[\mu_t\left(\frac{\partial \bar{u}_i}{\partial x_j} + \frac{\partial \bar{u}_j}{\partial x_i}\right)\right]\frac{\partial \bar{u}_i}{\partial x_j} = \mu_t S^2 \tag{3.49}$$

While *S* is the *modulus of the mean rate of strain tensor* defined as:

$$S = \sqrt{2S_{ij}S_{ij}} \tag{3.50}$$

and the *strain rate tensor*, S_{ij}, was defined by:

$$S_{ij} = \frac{1}{2}\left(\frac{\partial \bar{u}_i}{\partial x_j} + \frac{\partial \bar{u}_j}{\partial x_i}\right) \tag{3.51}$$

The parameter constants C_μ, σ_k, σ_ε, $C_{1\varepsilon}$, $C_{2\varepsilon}$ is achieved by comprehensive data fitting for a wide range of turbulent flow from literature [Launder74]. The influence of buoyancy and the degree of effect is determined by using the constant $C_{3\varepsilon}$ calculated by:

$$C_{3\varepsilon} = \tanh\left|\frac{v}{u}\right| \tag{3.52}$$

where v and u are the component of flow velocity parallel and perpendicular to the gravitational vector, respectively.

3.3.3 Overviews of other two-equation models

<u>*RNG k-ε model*</u>: [Yakhot92, Yakhot86] derived from Navier-Stokes equation with mathematical technique from Renormalization Group (RNG). With this turbulent model, several drawbacks of *standard k-ε* can be significantly improved. It can enhance accuracy by including the effect of highly swirling flow, rapidly strained and low-Reynolds number flows. The RNG *k-ε* has the form:

Turbulent kinetic energy:

$$\frac{\partial \rho_g \bar{k}}{\partial t} + \frac{\partial \rho_g \bar{u}_i \bar{k}}{\partial x_i} = \frac{\partial}{\partial x_j}\left[\alpha_k \mu_{eff} \frac{\partial \bar{k}}{\partial x_j}\right] + G_k + G_b - \rho_g \varepsilon - Y_M + S_k \tag{3.53}$$

Dissipation rate:

$$\frac{\partial \rho_g \varepsilon}{\partial t} + \frac{\partial \rho_g \bar{u}_i \varepsilon}{\partial x_i} = \frac{\partial}{\partial x_j}\left[\alpha_\varepsilon \mu_{eff} \frac{\partial \varepsilon}{\partial x_j}\right] + C_{1\varepsilon}\frac{\varepsilon}{k}(G_k + C_{3\varepsilon}G_b) - \rho_g C_{2\varepsilon}^* \frac{\varepsilon^2}{k} + S_\varepsilon \tag{3.54}$$

The main different from *standard k-ε* is only the additional term:

$$C_{2\varepsilon}^* = C_{2\varepsilon} + \frac{C_\mu \eta_{RNG}{}^3\left(1 - \eta_{RNG}/\eta_{RNG,0}\right)}{1+\beta(\eta_{RNG})^3} \tag{3.55}$$

$$\eta_{RNG} = S\frac{\bar{k}}{\varepsilon} \tag{3.56}$$

where

The inverse effective Prandtl number, α_k and α_ε are determined using the RNG theory [Yakhot92, Yakhot86]. Only the parameter β is adjustable.

<u>*Realized k-ε model*</u>: [Shih95] cooperated the new formulation of turbulent viscosity by combination between the Bousinessq relationship and the eddy viscosity μ_t. The transport equation of turbulent dissipation rate, ε is derived from exact equation of the mean-square

vorticity fluctuation. This model will generate non-physical turbulent viscosities when the computational domain composed of rotating and stationary fluid zone.

Turbulent kinetic energy:

$$\frac{\partial \rho_g \bar{k}}{\partial t} + \frac{\partial \rho_g \bar{u}_j \bar{k}}{\partial x_j} = \frac{\partial}{\partial x_j}\left[\left(\mu + \frac{\mu_t}{\sigma_k}\right)\frac{\partial \bar{k}}{\partial x_j}\right] + G_k + G_b - \rho_g \varepsilon - Y_M + S_k \tag{3.57}$$

Dissipation rate:

$$\frac{\partial \rho_g \varepsilon}{\partial t} + \frac{\partial \rho_g \bar{u}_j \varepsilon}{\partial x_j} = \frac{\partial}{\partial x_j}\left[\left(\mu + \frac{\mu_t}{\sigma_\varepsilon}\right)\frac{\partial \varepsilon}{\partial x_j}\right] + \rho C_1 S\varepsilon - \rho_g C_2 \frac{\varepsilon^2}{k+\sqrt{\mu\varepsilon}} + C_{1\varepsilon}\frac{\varepsilon}{k}C_{3\varepsilon}G_b + S_\varepsilon \tag{3.58}$$

where

$$C_1 = max\left(0.43, \frac{\eta}{\eta+5}\right) \tag{3.59}$$

$$\eta = S\frac{k}{\varepsilon} \tag{3.60}$$

$$S = \sqrt{2S_{ij}S_{ij}} \tag{3.61}$$

SST k-ω model: [Menter94] blends the robust and accurate formulation by apply the *standard k-ω model* in the near-wall region but switch to the *standard k-ε model* in the far field. This method can be achieved by modification with 'blending function' that will set to unity in the near wall area and to zero far away from surface. From this approach, the *SST k-ω* model is suitable for wide class of flow. The specific dissipation rate (ω) is defined as the ratio of kinetic dissipation rate to kinetic energy (ε/k). The transport equations are presented as:

Turbulent kinetic energy:

$$\frac{\partial \rho_g \bar{k}}{\partial t} + \frac{\partial \rho_g \bar{u}_i \bar{k}}{\partial x_i} = \frac{\partial}{\partial x_j}\left[\left(\mu + \frac{\mu_t}{\sigma_k}\right)\frac{\partial \bar{k}}{\partial x_j}\right] + \tilde{G}_k - Y_k + S_k \tag{3.62}$$

Dissipation rate:

$$\frac{\partial \rho_g \omega}{\partial t} + \frac{\partial \rho_g \bar{u}_j \omega}{\partial x_j} = \frac{\partial}{\partial x_j}\left[\left(\mu + \frac{\mu_t}{\sigma_\omega}\right)\frac{\partial \omega}{\partial x_j}\right] + G_\omega - Y_\omega + D_\omega + S_\omega \tag{3.63}$$

$\tilde{G}_k$ is the generation of turbulent kinetic energy due to mean velocity gradients, determined from previous expression of G_k in the standard k-ε model. G_ω is the generation of ω. Y_k and Y_ω represent the dissipation of k and ω due to turbulence. S_k and S_ω are source terms.

3.3.4 RSM model

The RSM model [Launder89,75, Gibson78] is the most complicated and has great potential within all RANS models. It accounts for the influence from swirling, rotational flows and also rapid changed in strain rate. The RSM closes the RANS equations by solve sev-

en additional transport equations in three dimensional problems simultaneously. However, this method consumes the most computational expense among RANS models. The RSM model closes the RANS equations by solving transport equations for the Reynolds stresses with equation for the dissipation rate. Five transport equations are required for 2D problem and seven equations for 3D problem. The transport equation is expressed as:

Transport equation for the RSM model:

$$\frac{\partial \rho_g \overline{\acute{u}_\iota \acute{u}_J}}{\partial t} + \frac{\partial \rho_g u_k \overline{\acute{u}_\iota \acute{u}_J}}{\partial x_k} = -\frac{\partial}{\partial x_k}\left[\rho_g \overline{\acute{u}_\iota \acute{u}_J \acute{u}_k} + \overline{\acute{P}\left(\delta_{lk}\acute{u}_\iota + \delta_{\iota k}\acute{u}_J\right)}\right] + \frac{\partial}{\partial x_k}\left[\mu \frac{\partial \overline{\acute{u}_\iota \acute{u}_J}}{\partial x_k}\right] - \rho\left(\overline{\acute{u}_\iota \acute{u}_k}\frac{\partial u_j}{\partial x_k} + \overline{\acute{u}_J \acute{u}_k}\frac{\partial u_i}{\partial x_k}\right) - \rho_g \beta\left(g_i \overline{\acute{u}_J VF} + g_j \overline{\acute{u}_\iota VF}\right) + \acute{P}\left(\frac{\partial \acute{u}_\iota}{\partial x_j} + \frac{\partial \acute{u}_J}{\partial x_i}\right) - 2\mu \frac{\overline{\partial \acute{u}_\iota}}{\partial x_k}\frac{\overline{\partial \acute{u}_J}}{\partial x_k} - 2\rho_g \Omega_k\left(\overline{\acute{u}_J \acute{u}_m} e_{ikm} + \overline{\acute{u}_\iota \acute{u}_m} e_{jkm}\right) + S_{user} \quad (3.64)$$

If the Reynolds stresses are defined as $R_{ij} = \rho_g \overline{\acute{u}_\iota \acute{u}_J}$, descriptions of each term in the set of RSM transport equations can be written depending on this Reynolds stresses as:

$$\begin{aligned} &Time\ derivative + Convection \\ &\quad = Turbulent\ diffusion + Molecular\ diffusion \\ &\quad + Stress\ production(SP) + Buoyancy\ production(BP) \\ &\quad + Pressure\ strain(PS) + Dissipation + Production\ due\ to\ rotation \\ &\quad + user\ defined\ source\ term \end{aligned}$$

Determination of each term and its reference is presented as following equations.

Turbulent diffusion term (*PS*) is modeled using the gradient-diffusion model presented by Daly [Daly70]. However, the turbulent diffusion can be calculated using formulation equation by Lien [Lien94] to remedy the computational instability as:

$$Turbulent\ diffusion = \frac{\partial}{\partial x_k}\left(\frac{\mu_t}{\sigma_k}\frac{\partial \overline{\acute{u}_\iota \acute{u}_J}}{\partial x_k}\right) \quad (3.65)$$

The turbulent viscosity μ_t is determined as the same as in the standard k-ε model.

The linear pressure-strain model [Gibson78, Fu87, Launder89] is applied in this thesis. In this model, the pressure-strain is determined by the sum of three terms, representing slow, rapid and wall-reflection pressure-strain terms.

$$PS = Slow\ pressure\ strain + Rapid\ pressure\ strain + Wall\ reflection\ pressure\ strain \quad (3.66)$$

$$Slow\ pressure\ strain = -C_{ps,1}\rho_g \frac{\varepsilon}{k}\left[\overline{\acute{u}_\iota \acute{u}_J} - \frac{2}{3}\delta_{ij}k\right] \quad (3.67)$$

$$Rapid\ pressure\ strain = -C_{ps,2}\left[\left(P_{PS,ij} + F_{PS,ij} + \frac{5}{6}G_{PS,ij} - C_{PS,ij}\right) - \frac{2}{3}\delta_{ij}\left(P_{PS,kk} + \frac{5}{6}G_{PS,kk} - C_{PS,kk}\right)\right] \quad (3.68)$$

$$Wall\ reflection\ pressure\ strain = \acute{C}_{ps,1}\frac{\varepsilon}{k}\left[\overline{\acute{u}_k\acute{u}_m}n_k n_m\delta_{ij} - \frac{3}{2}\overline{\acute{u}_i\acute{u}_k}n_j n_k - \right.$$
$$\left. -\frac{3}{2}\overline{\acute{u}_j\acute{u}_k}n_i n_k\right]\frac{C_l k^{\frac{3}{2}}}{\varepsilon d_{n,wall}} + \acute{C}_{ps,2}\left[PS_{km,2}n_k n_m\delta_{ij} - \frac{3}{2}PS_{ik,2}n_j n_k - \frac{3}{2}PS_{jk,2}n_i n_k\right]\frac{C_l k^{\frac{3}{2}}}{\varepsilon d_{n,wall}} \quad (3.69)$$

The parameter C_l is expressed using von Kármán constant (0.4187) as:

$$C_l = \frac{C_\mu^{\frac{3}{4}}}{0.4187} \quad (3.70)$$

where n_i, n_k, n_m is the unit component normal to wall and $d_{n,wall}$ is the normal distance to the wall.

Turbulent kinetic energy for the RSM model:

$$\frac{\partial \rho_g \bar{k}}{\partial t} + \frac{\partial \rho_g \bar{u}_i \bar{k}}{\partial x_i} = \frac{\partial}{\partial x_j}\left[\left(\mu + \frac{\mu_t}{\sigma_k}\right)\frac{\partial \bar{k}}{\partial x_j}\right] + \frac{1}{2}(SP_{ii} + BP_{ii}) - \rho_g \varepsilon(1 + 2M_t^2) + S_k \quad (3.71)$$

The SP is the stress production term and BP is the buoyancy production terms. Mt is the turbulent Mach number as in the standard k-ε equation formulations.

Dissipation rate equation for the RSM model:

$$\frac{\partial \rho_g \varepsilon}{\partial t} + \frac{\partial \rho_g \bar{u}_i \varepsilon}{\partial x_i} = \frac{\partial}{\partial x_j}\left[\left(\mu + \frac{\mu_t}{\sigma_\varepsilon}\right)\frac{\partial \varepsilon}{\partial x_j}\right] + C_{1\varepsilon}\frac{1}{2}(SP_{ii} + C_{3\varepsilon}BP_{ii}) - \rho_g C_{2\varepsilon}\frac{\varepsilon^2}{k} + S_\varepsilon \quad (3.72)$$

The parameter $C_{3\varepsilon}$ is modeled as the same as in the standard k-ε model. Advantages and disadvantages for all two equations and RSM model are compared in Table 3.1.

Table 3.1: Comparison advantages and disadvantage of turbulent flow models investigated in this thesis.

Turbulent model	Advantage	Disadvantage	Reference
Standard k-ε	for wide range of flow	Low accuracy for high swirling flow and near-wall flow	[Launder74]
RNG k-ε	overcome standard k-ε drawback	10-15% more CPU time	[Yakhot92, Yakhot86]
Realized k-ε	Superior performance in rotation, high adversed-pressure gradient and separated flow	produce non-physical velocities when apply to multi-referenced frame system	[Shih95]
SST k-ω	Blend robustness and accuracy from both standard k-ε at the far-fields and standard k-ω near wall-bounded and free-shear flow	still less accuracy than RSM when exhibit anisotropy of nor-mal stress	[Menter94]
RSM	Great potential for complex flows	most expensive CPU cost in RANS models	[Launder89,75, Gibson78]

3.4 Coal devolatilization

3.4.1 Devolatilzation process

There are two terms commonly used to describe the process of coal conversion, which are coal pyrolysis or coal devolatilization. The pyrolysis is a thermo-chemical decomposition of organic material at elevated temperatures without the participation of oxygen, while devolatilization is the same process in the presence of oxygen which is generally better explains the process in coal conversion in conventional furnace. Devolatilization of coal depends particularly on many factors; for example, peak temperature, heating rate, pressure and particle size. Coal of medium rank show thermoplastic behavior and melt when heated in contradiction to high-rank coals which exhibit less plasticity and retain their pore structure during devolatilization. First, the coal particles are distributed and injected into burners by coal-oxidant stream and then heated up by radiative and convective heat transfer. Thermal radiation is the predominant heat transfer mechanism precisely after the particle-injection into a furnace regarding almost cold air surrounds the particles in the first stage of devolatilization. When the particle temperature reaches around 650 K, thermal decomposition of coal molecules occurs and gaseous products from the devolatilization process are released to the gas phase and volatile are transported by diffusion via pore structures. This process is called "devolatilization" and the gaseous product of devolatilization called "*volatile matter*" (VM) composed of "tar" or heavy hydrocarbon ($C_aH_bO_c$), light hydrocarbon (C_aH_b) and light gases such as CO, CO_2, H_2, H_2O. Char-N, char-S and volatile-N, volatile-S further form toxic species such as NO_x and SO_x which will convert further to N_2 and S or SO_3 depending on conditions o atmospheres inside furnace. To prevent confusion in the definitions of volatile and tar, it should be noted that volatile matter is composed of "tar" in literature and previous standard text book [Serio87, Smoot93]. The emitted combustible gaseous species react homogeneously in the gas phase and forms a flame. The solid residue of thermal decomposition called "*char*" consists mainly of carbon and ash. The schematic diagram for coal devolatilization is illustrated in Fig. 3.2 Note that char-N, char-S and volatile-N, volatile-S is omitted in the diagram when coal-N, coal-S conversion is out of the scope of this thesis.

3.4.2 CPD Models for coal devolatilization

Reviews in the past have presented modeling efforts in coal devolatilization and the network model is the most accurate models as reviewed in chapter 2. The CPD network model provided good results comparing to other less complicated models [Jovanovic12]; therefore, the CPD network model was selected and used for all investigated cases in chapter 5 to estimate the rate of devolatilization for Lusatian lignite and Rhenish lignite, when no experimental data available. Advantages of the CPD model is that it is applicable for wide ranks of coal types and five parameters for the model can be directly approximated by proximate and ultimate analysis of coal properties.

In the CPD model, the percolation theory is based on the Bethe lattice, described by the coordination number $LC_{\sigma+1}$ and the fraction of intact bridges, *IB*.

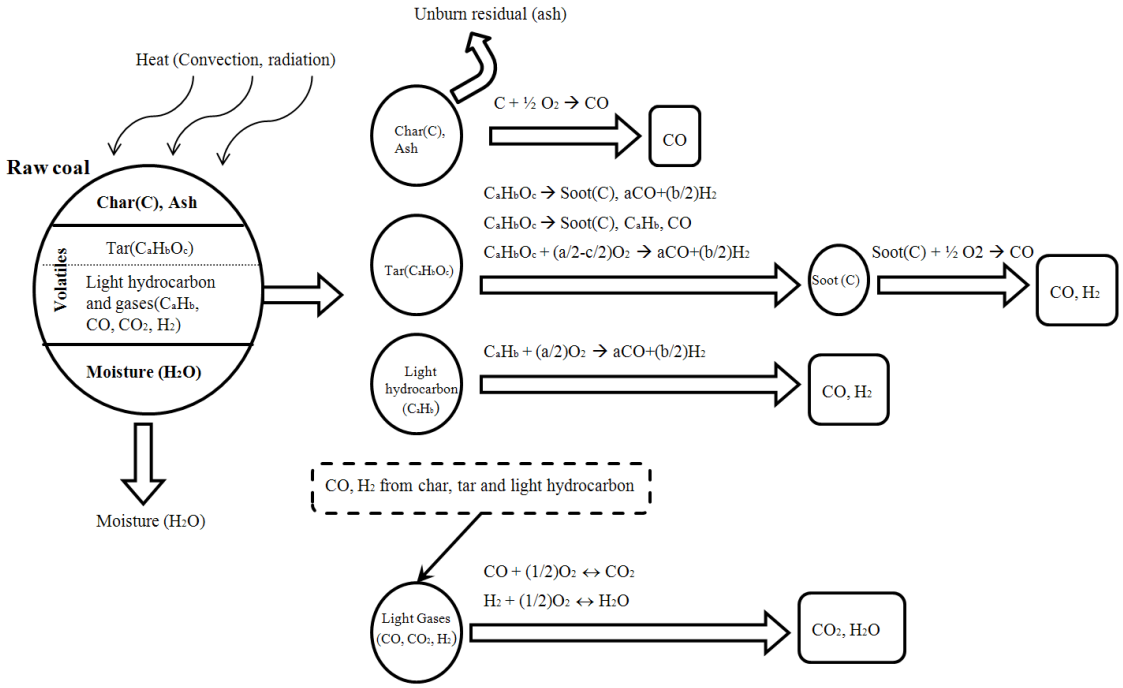

Figure 3.2: Schematic diagram for devolatilization process of coal particles.

The theory has been adapted to provide the descriptions of the yield and mass distribution of tar from the breakup of the macromolecular network and the production of light gases from bridge material. The rates of char and volatile (tar and gases) production depend on five input coal-specific parameters which are initial fraction of bridges in the coal lattice, IB_0, initial fraction of char bridges, chb_0, lattice coordination number, $LC_{\sigma+1}$, cluster molecular weight, $MW_{cluster}$ and side chain molecular weight, MW_{δ}. Coal-dependent chemical structure coefficients for the model are obtained directly from measurements of solid-state nuclear magnetic resonance (^{13}C NMR) from eight coals at Argonne National Laboratory, five coals at Sandia National Laboratory, three coals from Advanced Fuel Research (AFR) and three coals from The Advanced Combustion Engineering Research Center (ACERC) at Brigham Young University and University of Utah (19 coals in total) [Fletcher92a-92c, SmithKL94].

Coal is treated as a molecular network of aromatic ring clusters of many sizes and types in the CPD model [Grant89, Fletcher90, 92a-92c, SmithKL94], connected by a variety of chemical bridges of different bond strengths. To simplify problem, only two types of bridges are considered which are labile bridges and stable or char bridges. Reaction begins with a labile bridge, £, decomposed to form a reactive bridge intermediate, £*, which is unstable and later react by two competitive reactions. The intermediated bridge, £*, further forms side chain, δ_{sc}, that still attached to aromatic cluster. The side chains, δ_{sc}, finally undergo a cracking reaction to form light gas, LG_1. For another competitive reaction, the intermediated bridge, £*, forms a stable char bridge, chb, and light gas, LG_2. This competitive reaction scheme of the CPD reaction sequence is illustrated in Fig. 3.3.

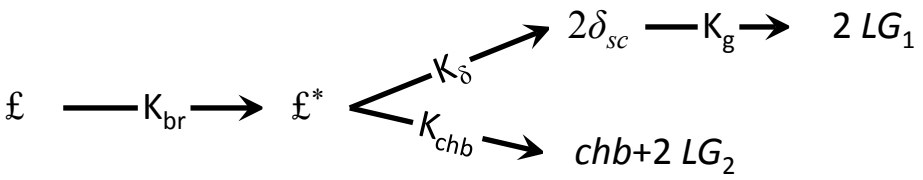

Figure 3.3: The competitive reaction of coal bridge, adapted from [SmithKL94, Fletcher92a].

Where K_{br}, K_{δ}, K_g, K_{chb} are rate constants for CPD model. All mass connected to the infinite lattice is considered to be char. Competition for the reactive intermediate, £*, is dominated by the ratio of the rate of side-chain formation to the rate of char formation. Because the competitive processes depend only on the ratio of rate constants, $RRC = K_{br}/K_{chb}$, it is enough to define a combined composite rate constant as:

$$RRC = \frac{K_{br}}{K_{chb}} = A_{RRC}\exp\left[-\frac{E_{RRC}\pm V_{RRC}}{RT}\right] \tag{3.73}$$

where $A_{RRC} = A_{br}/A_{chb}$, $E_{RRC} = E_{br} - E_{chb}$, and V_{RRC}, are the corresponding distributed activation terms. The reaction rate equations for the bridge-breaking (subscript '*br*') and gas-release steps (subscript '*g*') are given respectively in the Arrhenius form written as:

$$K_{br} = A_{br}\exp\left[-\frac{E_{br}\pm V_{br}}{RT}\right] \tag{3.74}$$

$$K_g = A_g\exp\left[-\frac{E_g\pm V_g}{RT}\right] \tag{3.75}$$

A set of coal-independent kinetic coefficients A_{br}, E_{br}, V_{br}, A_g, E_g and V_g are also reported by Grant [Grant89]. A steady-state approximation is assumed for the intermediate species, £*, which imply that $d£^*/dt \approx 0$ resulting in $£^* \approx K_{br}(K_{\delta} + K_{chb})$ and reaction rates.

$$\frac{d£}{dt} = -K_{br}£ \tag{3.76}$$

$$\frac{d(chb)}{dt} = -K_{chb}£^* \approx \frac{K_{br}K_{chb}£}{K_{chb}+K_{\delta}} = \frac{K_{br}£}{RRC+1} \tag{3.77}$$

$$\frac{d\delta_{sc}}{dt} = 2K_{\delta}£^* - K_g\delta_{sc} \approx \frac{K_{\delta}K_{br}£}{K_{chb}+K_{\delta}} - K_g\delta_{sc} = \frac{2(RRC)K_{br}£}{RRC+1} - K_g\delta_{sc} \tag{3.78}$$

$$\frac{dLG_1}{dt} = K_g\delta_{sc} \tag{3.79}$$

$$\frac{dLG_2}{dt} = 2\frac{d(chb)}{dt} \tag{3.80}$$

The dynamic variables are bridge population parameters, δ_{sc}, £ and *chb*. The number of intact bridges, *IB*, and the fraction of broken bridges, f_{bb}, is defined by:

$$IB = £ + chb \tag{3.81}$$
$$f_{bb} = 1 - IB \tag{3.82}$$

The models assumed to be imposed to conservation of mass so that the first three differential equations are solved for bridge parameters.

$$LG = LG_1 + LG_2 \tag{3.83}$$
$$LG_1 = 2f_{bb} - \delta_{sc} \tag{3.84}$$
$$LG_2 = 2(chb - chb_0) \tag{3.85}$$

Subjected to initial boundary conditions:

$$chb(t=0) = chb_0 \tag{3.86}$$
$$£(t=0) = £_0 = IB_0 - chb_0 \tag{3.87}$$
$$\delta_{sc}(t=0) = 2f_{bb,0} = 2(1 - chb_0 - £_0) \tag{3.88}$$
$$LG(t=0) = LG_1(t=0) = LG_2(t=0) \tag{3.89}$$

All initial conditions are expressed in terms of initial parameters c_0 and $£_0$. Mass fraction of light gas, tar and char are expressed as:

$$f_{gas}(t) = \frac{m_{gas}(t)}{m_{total}} = \frac{(RBC)(LG)(LC_{\sigma+1})}{4+2(RBC)(1-chb_0)(LC_{\sigma+1})} \tag{3.90}$$

$$f_{tar}(t) = \frac{m_{tar}(t)}{m_{total}} = \frac{2[\mathrm{F1}F3(IB)+r\mathrm{F2}F4(IB)]}{2+(RBC)(1-chb_0)(LC_{\sigma+1})} \tag{3.91}$$

$$f_{char}(t) = 1 - f_{gas}(t) - f_{tar}(t) \tag{3.92}$$

where $RBC = m_{lb}/m_{cite}$ is the ratio of bridge mass to site mass. The average molecular weight of a labile bridge, m_{lb}, is twice the molecular weight of a side chain, MW_δ, ($m_{lb} = 2MW_\delta$) and the average molecular weight of the aromatic part of the cluster, m_{cite}, is calculated by [Fletcher92a]:

$$m_{cite} = MW_{cluster} - MW_\delta(LC_{\sigma+1}) \tag{3.93}$$

F1, *F2*, *F3*(*IB*) and *F4*(*IB*) are determined by statistical relations depending on percolation lattice statistics by a number of n-site clusters [Grant89] given by:

$$F1 = 1 + r\left[\frac{£}{p} + \frac{(LC_{\sigma-1})\delta}{4(1-p)}\right] \tag{3.94}$$

$$F2 = \left[\frac{\delta}{2(1-IB)} + \frac{£}{p}\right] \tag{3.95}$$

$$F3(IB) = \left[\frac{1-IB}{1-IB^*}\right]^{\sigma+1} = \left(\frac{IB^*}{IB}\right)^{\frac{(LC_{\sigma+1})}{(LC_{\sigma-1})}} \tag{3.96}$$

$$F4(IB) = \left[\frac{\delta_{sc}}{2(1-IB)} + \frac{£}{IB}\right] \tag{3.97}$$

where *IB** is the root of equation:

$$IB^*(1-IB^*)^{(LC_{\sigma-1})} = IB(1-IB)^{(LC_{\sigma-1})} \quad (3.98)$$

Finally, a simple cross-linking mechanism of metaplast is described by a one-step Arrhenius expression as:

$$\frac{dm_{cross}}{dt} = -\frac{dm_{meta}}{dt} = k_{cross} m_{meta} \quad (3.99)$$

The m_{cross} is the amount of metaplast which has been reattached and m_{meta} is the mass of metaplast. K_{cross} is an Arrhenius-type rate constant given by [Fletcher92a]:

$$K_{cross} = A_{cross} \exp\left[-E_{cross}/(RT)\right] \quad (3.100)$$

3.4.3 Correlations for CPD Models

In the end of calculations, the CPD model applies nine kinetic parameters (E_{br}, A_{br}, E_{RRC}, E_g, A_g, E_{RRC}, IB, E_{cross}, A_{cross}) and requires five coal specific input-parameters (IB_0, chb_0, $LC_{\sigma+1}$, $MW_{cluster}$, MW_δ) to characterize the initial lattice configuration. Genetti et al. [Genetti99a, 99b] proposed nonlinear polynomial correlations used to calculate five input-parameters for the CPD models from proximate and ultimate analysis of coal properties. Measurements of solid-state ^{13}C NMR spectroscopy from 30 coals were used to develop the correlations. The variable IB_0, $LC_{\sigma+1}$, $MW_{cluster}$ and MW_δ are calculated by quadratic fitted curve using equation [Genetti99a]:

$$variable\ for\ CPD\ model = C1 + C2(MF_C) + C3(MF_C^2) + C4(MF_H) + C5(MF_H^2) + C6(MF_O) + C7(MF_O^2) + C8(MF_{VM}) + C9(MF_{VM}^2) \quad (3.101)$$

The nonlinear quadratic coefficients are shown in Table 3.2.

Table 3.2: Correlations for CPD devolatilization model [Genetti99a].

Coefficients	MW_δ	$MW_{cluster}$	chb_0	$LC_{\sigma+1}$
C1	4.220 E+2	1.301 E+3	4.898 E-1	-5.2105 E+1
C2	-8.647	1.639 E+1	-9.816 E-3	1.6387
C3	4.639 E-2	-1.875 E-1	1.330 E-4	-1.0755 E-2
C4	-8.473	-4.548 E+2	1.555 E-1	-1.2369
C5	1.182	5.171 E+1	-2.439 E-2	9.3194 E-2
C6	1.154	-1.007 E+1	7.052 E-3	-1.6567 E-1
C7	-4.340 E-2	7.608 E-2	2.192 E-4	4.0956 E-3
C8	5.568 E-1	1.360	-1.105 E-2	9.2610 E-3
C9	-6.546 E-3	-3.136 E-2	1.009 E-4	-8.2672 E-5

The parameters, chb_0, represent stable biaryl type linkages in low-volatile bituminous coals and early cross-linking in lignites. Because cross-linking occurs at different heating rates, this parameter, chb_0, change as a function of heating rate. The estimation of chb_0 was achieved from pyrolysis experiments conducted by Watt M. [WattM96] at Brigham Young University and and drop tube and flat flame burner pyrolysis experiments conduct-

ed by Fletcher T.H. [Fletcher92b] at Sandia National Laboratories. The correlation, chb_0 correlates well with mass fraction of carbon, MF_C, for high-rank coal, while correlates well with mass fraction of oxygen, MF_O, for low-rank coals expressed as:

$$chb_0 = \min\left[0.36, \max\left((0.118MF_C - 10.1), 0.0\right)\right] + \min\left[0.15, \max\left((0.014MF_O - 0.175), 0.0\right)\right] \quad (3.102)$$

In this equation, MF_C and MF_O are based on dry-ash-free basis (DAF).

Finally, the five coal specific input-parameters (IB_0, chb_0, $LC_{\sigma+1}$, $MW_{cluster}$, MW_δ) are estimated and used to determine the rate of volatile production in lignite oxy-fuel combustion.

3.5 Char heterogeneous reaction

3.5.1 Char reactions and combustion regime

After coal particles are devolatilized in the first step, the residual char undergoes the secondary step of heterogeneous reaction with diffusion species such as O_2, CO_2, H_2O and H_2. However, the char-H_2 reaction is smaller in comparison with reaction between residual char and other reacted species (O_2, CO_2 and H_2O) approximately three orders of magnitude, so the last reaction in negligible in this research as suggested by Walker et al. [Walker59] and reviewed by some researchers [Smoot85, Smoot79, Laurendeau78]. Using this assumption, char reacts heterogeneously and simultaneously with O_2, CO_2 and H_2O by following reactions:

$$C(s) + 1/2\ O_2 \rightarrow CO \quad (3.103)$$

$$C(s) + CO_2 \rightarrow 2CO \quad (3.104)$$

$$C(s) + H_2O \rightarrow CO + H_2 \quad (3.105)$$

It should be noted that the first reaction is based on the assumption that the product CO is transported away instead of CO_2 when this assumption provide a good calculation in experiments of low-rank coal [Field69]. At combustion temperature, the structure of coal such as pore structure, external surface area of residual char and rate of burnout play a significant role in char heterogeneous reaction and diffusion rate.

A combustion regime in the process of coal combustion is presented in Fig. 3.4.

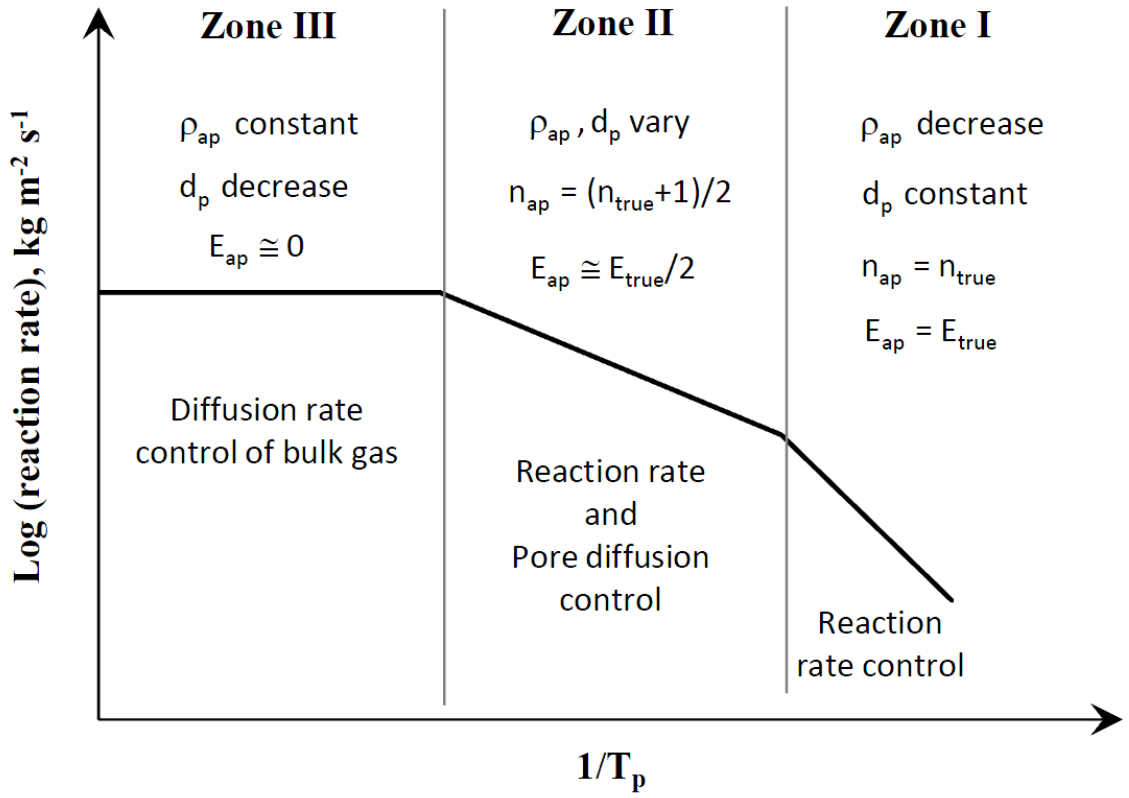

Figure 3.4: Combustion regime of coal combustion [Smoot85].

Combustion in zone I occurs at low temperatures and chemical reaction is the rate-limited control. For a higher temperature in zone II, combustion is controlled by both chemical reaction rate and diffusion through pore. For a further increasing temperature, the overall rate is limited by only diffusion rate. For changes of size and apparent density of residual char particles in zone I, the apparent density, ρ_{ap}, decrease while particle diameter, d_p, remains nearly constant. This is because diffusion gas reacts from surface toward the center through particle pores and cracks. In contrast to zone II, the fast reaction occurs in zone III at high temperature and diffusion gas (O_2, CO_2 or H_2O) react at external surface area of char. The particle size decrease while the apparent density constant which could also refer to a shrinking core model [Zygourakis88]. The apparent activation energy, E_{ap}, is approximately half of true activation energy, E_{true}, in combustion zone II. In addition, the apparent reaction order, n_{ap}, in zone II is not the same as in zone I and is found to have a relation:

$$n_{ap} = \frac{n_{true}+1}{2} \tag{3.106}$$

3.5.2 General model of char reaction

This general model of char reaction combines influences of char kinetic and diffusion limited rate by using kinetic controlled equation at low particle temperature while applying diffusion controlled equation at higher particle temperature, therefore it is sometime called the *Kinetic diffusion limited rate* (KD) model in literatures. Formulation of equations for char particle reaction rate (burning rate) were reviewed in many researches

[Field67, Laurendeau78, SmithIW82, Smoot85, SmithKL94]. Total char burning rate, $R_{t,c}$ (kg/s), is calculated by multiplying the burning rate of char per external surface area, $R_{s,c}$, to external surface area of char, A_p (= πd_p^2), assuming spherical shape of char particle as:

$$R_{t,c} = -\frac{dm_{t,c}}{dt} = A_p R_{s,c} Y_c \tag{3.107}$$

where d_p is the diameter of char particle (m). Y_c is the mass fraction of residual carbon in the char particle according to fundamental assumption of as dilution effect, while char is burned perfectly at the beginning but char burning rate is gradually reduced with residual carbon in char particle. The residual carbon mass fraction Y_c is determined from knowledge of char burnout [Murphy10] as:

$$Y_c = \frac{m_c}{m_{c,0}} = 1 - U_c \tag{3.108}$$

Where m_c is the residual carbon mass (kg) in char particle (assuming composed of carbon and ash) and $m_{c,0}$ is the initial carbon mass (kg) calculated from proximate and ultimate analysis of specific coal. U_c is the burnout which refers to a fraction of unburned carbon in char particle. From above equation, the burnout can be determined from the fraction of unburned carbon by relation:

$$U_c = 1 - \frac{m_c}{m_{c,0}} = \frac{m_{c,0} - m_c}{m_{c,0}} \tag{3.109}$$

The burning rate of char particle at the char surface, $R_{s,c}$, can be calculated by mass-balance [SmithIW82]:

$$R_{s,c} \equiv R_{diff,c} = R_{ch,c} \tag{3.110}$$

where $R_{s,c}$ is the burning rate of char per external surface area, A_p, assuming spherical shape (kg/(m^2 s)), $R_{ch,c}$ is the chemical reaction rate of reaction (kg/(m^2 s)), $R_{Kin,c}$ is the chemical kinetic rate of reaction (kg/(m^2 s)). The surface reaction rate is controlled solely by diffusion mass transfer rate of oxygen to the particle as:

$$R_{s,c} \equiv K_D\left(C_g - C_s\right) = R_{Kin,c}(C_s)^{n_{ap}} \tag{3.111}$$

where $R_{Kin,c}$ is the chemical kinetic rate of char reaction. n_{ap} is the apparent order of reaction, K_D is the mass transfer coefficient (m/s), C_s is the oxygen concentration at the outer surface of the particle and C_g is the oxygen concentration in the bulk gas (kg/m^3). By eliminating an unknown C_s, the equation of burning rate has the new form as:

$$R_{s,c} = (C_g)^{n_{ap}}\left(1 - \frac{R_{s,c}}{C_g K_D}\right)^{n_{ap}} R_{Kin,c} = \left(C_g - \frac{R_{s,c}}{K_D}\right)^{n_{ap}} R_{Kin,c} \tag{3.112}$$

The product $C_g K_D$ is the maximum possible combustion rate from the diffusion mass transfer limit to the particle assuming fast reaction. It should be noted that the combustion rate $R_{s,c}$ is never greater than the product of mass transfer limit $C_g K_D$, which also means that the ratio $R_c/(C_g K_D)$ in the parenthesis is never greater than unity. This ratio can be interpreted as the ratio of the actual burning rate to maximum possible burning rate (mass

transfer limit). In practical combustion simulation, the overall char burning rate per external surface area, $R_{s,c}$, is determined by iterative procedure in the form of Eq. (3.112).

In practical calculations, it is convenient to relate the burning rate, $R_{s,c}$, to the partial pressure of reactant gas (P_g and P_s) instead of gas concentration (C_g and C_s) and define the diffusional reaction rate coefficient, K_{diff} (kg/(m^2 s Pa$^{n_{ap}}$)), instead of K_D (m/s), presented by Field et al. [Field67] as:

$$R_{diff} = K_{diff}\left(P_g - P_s\right) \tag{3.113}$$

where R_{diff} is the mass diffusion flux of gas at the char surface. The chemical reaction rate, $R_{ch,c}$, on the right hand side of Eq. (3.110) often expressed experimentally in the form of partial pressure and the apparent order of reaction, n_{ap} given by

$$R_{ch,c} = R_{Kin,c}(P_s)^{n_{ap}} \tag{3.114}$$

while the chemical rate coefficient $R_{Kin,c}$ is defined in an Arrhenius form of equation.

$$R_{Kin,c} = A_{Kin,c}e^{\left(-\frac{E_{Kin,c}}{RT_p}\right)} \tag{3.115}$$

By replacing $R_{ch,c}$ and R_{diff} from Eqs. (3.113) and (3.114) in the Eq. (3.110) and rearranging terms as in Eq. (3.112) based on the partial pressure (P_g and P_s) and the diffusional reaction rate coefficients, K_{diff}, an another form of equation for char reaction per external surface area is re-written as:

$$R_{s,c} \equiv K_{diff}\left(P_g - P_s\right) = R_{Kin,c}(P_s)^{n_{ap}} \tag{3.116}$$

which could solved iteratively by equation:

$$R_{s,c} = (P_g)^{n_{ap}}\left(1 - \frac{R_{s,c}}{P_g K_{diff}}\right)^{n_{ap}} R_{Kin,c} = \left(P_g - \frac{R_{s,c}}{K_{diff}}\right)^{n_{ap}} R_{Kin,c} \tag{3.117}$$

when the apparent order of reaction $n_{ap} = 1$, the char reaction rate is presented as:

$$R_{s,c} = P_g\left(\frac{1}{R_{Kin,c}} + \frac{1}{K_{diff}}\right)^{-1} \tag{3.118}$$

An overall mass transfer coefficient, K_{diff}

From Fick's Law of diffusion, mass flux of reactant gas, J_s (kg/(m^2 s)), at the surface is expressed as [Laurendeau78, SmithIW82]:

$$J_s = h_D\left(C_g - C_s\right) \tag{3.119}$$

where h_D is the mass transfer coefficient (m/s). C_s is the oxygen concentration at the outer surface of the particle and C_g is the oxygen concentration in the bulk gas. The overall particle reaction rate $R_{s,c}$ is related to mass diffusion flux of gas, R_{diff}, at the char surface by [Laurendeau78]:

$$R_{s,c} \equiv R_{diff} = \Lambda J_s \tag{3.120}$$

The gravimetric stoichiometric coefficient [Laurendeau78], Λ, is defined as:

$$\Lambda = \frac{MW_c}{\upsilon_g MW_g} \tag{3.121}$$

where MW_c and MW_g are the molecular weight of carbon and reactant gas, respectively. ν_g is the stochiometric coefficient of reactant gas. If the gas is oxygen and the product of reaction is CO in reaction $C + ½O_2 \rightarrow CO$, ν_g is equal to 0.5 and $\Lambda = 12/(0.5\times32) = 0.75$. If the product of reaction is CO_2 in reaction $C + O_2 \rightarrow CO_2$, ν_g is equal to 1 and $\Lambda = 12/(1\times32) = 0.375$. For reaction with CO_2 and H_2O ($C + CO_2 \rightarrow 2CO$, $C + H_2O \rightarrow CO+H_2$), ν_g of both reaction are equal to 1; hence, Λ are 0.375.

The mass transfer coefficient h_D (unit in m/s) is determined from the correlation of Sherwood number for a spherical particle [Field67, SmithIW82, Laurendeau78] as:

$$Sh_{sphere} \equiv \frac{h_D d_p}{D_{T_m,P}} = 2\left(1 + B_{sh} Re^{1/2} Sc^{1/2}\right) \tag{3.122}$$

where *Re* and *Sc* is the Reynolds number and Schmidt number. The parameter B_{sh} is a constant varying between 0.3 and 0.35 [Field67, Mulcahy69, Laurendeau78]. The Schmidt number is about 0.7 (≈1) for oxygen diffusing through nitrogen at combustion temperatures. Pulverized coal diameter is usually less than 100 μm in practical flame, resulting in $Re<100$ and mostly not even exceed 1[Field67]. In pulverized coal flame with $d_p \leq 100$ μm, relative velocities between gas and particle are generally sufficiently small so that *Re* is approximately equal to zero ($Re \approx 0$) [Laurendeau78, SmithIW82]. With this assumption of zero Re, the Schmidt number for sphere is equal to 2 ($Sc \approx 2$) and the mass transfer coefficient is given by:

$$h_D \cong \frac{2D_{T_m,P}}{d_p} \tag{3.123}$$

where $D_{Tm,P}$ is the diffusion coefficient at mean temperature (m^2/s), T_m, and pressure *P*. T_m is the mean temperature in the boundary layer near to particle surface determined by mean value between particle temperature T_p and bulk gas T_g ($T_m = ½(T_p+T_g)$ [Field67]. To determine the diffusional reaction rate coefficient, K_{diff} [Field67], the gas concentration C_g and C_s is replaced by partial pressure using ideal gas law as:

$$C_g = P_g MW_g/(RT_m) \tag{3.124}$$

$$C_s = P_s MW_g/(RT_m) \tag{3.125}$$

An alternative form of Eq. (3.112) is achieved by applying definition of the diffusional reaction rate coefficient, K_{diff} by Field et al. [Field67] based on the difference of partial pressure of reactant gas (P_g - P_s) by inserting the mass flux of reactant J_s from Eq. (3.119) into Eq. (3.120) and gas concentration from Eqs. (3.124)-(3.125) into Eq. (3.119). The mass diffusion flux is:

$$R_{diff} \equiv K_{diff}\left(P_g - P_s\right) = \left(\frac{MW_c}{\upsilon_g MW_g}\right)\left(\frac{2D_{T_m,P}}{d_p}\right)\left(\frac{P_g MW_g}{RT_m} - \frac{P_s MW_g}{RT_m}\right) \tag{3.126}$$

From this relation, K_{diff} can be determined as:

$$K_{diff} = \frac{2MW_c D_{T_m,P}}{\upsilon_g RT_m d_p} \tag{3.127}$$

From above equation, it should be note that the ratio $(1/\nu_g)$ is defined as a mechanism factor, φ, in the calculation of Field et al. which equal to 1 when CO_2 is the product and equal to 2 when CO is the product. The mechanism factor of value 2 (CO is a product) was recommended by Field [Field69] from an experimental observation of low-rank coal between 1200 K and 2000 K for pulverized coal diameter of 82 and 105 μm. By either approaches of calculation by Field et al., Laurendeau or Smith [Field67, SmithIW82, Laurendeau78], K_{diff} is finally expressed in the form of Eq. (3.127).

The diffusion coefficient at mean temperature, $D_{Tm,P}$ is approximated by a power law based on pressure, temperature and diffusion coefficient at reference state (P_0, T_0 and $D_{T0,P0}$) as:

$$D_{T_m,P} = D_{T_0,P_0}\left(\frac{T_m}{T_0}\right)^{1.75}\left(\frac{P_0}{P}\right) \tag{3.128}$$

The reference pressure, P_0, is at 1 atmospheric pressure (1 atm) and the reference temperature, T_0, is set to be 1600 K as in the experiment low-rank coal [Field69].The last term of pressure ratio can be omitted when lignite oxy-fuel combustion in this thesis occurs at atmospheric pressure. The diffusion coefficient at reference state, $D_{T0,P0}$, for a binary gas mixture (O_2 in CO_2, CO_2 in CO_2 and H_2O in CO_2) can be determined either by directly calculation based on a theory of interaction of molecules by Hirshfelder et al. [Hirschfelder54] assuming a Lennard-Jones potential or by approximation of Fuller et al. [Fuller66] by comparing predictions with experiments. The method by Hirschfelder et al. is used in this thesis which has a prediction error less than 10%.

By replacing $D_{T_m,P}$ from Eq. (3.128) in Eq. (3.127) and inserting relevant constants (MW_c = 12, T_0 = 1600 K, $P_0 = P$ = 1 atm), the diffusional reaction rate coefficient, K_{diff}, depends only on T_m, d_p and ν_g as:

$$K_{diff} = \left(\frac{24D_{T_0,P_0}}{\upsilon_g RT_0^{1.75}}\right)\left(\frac{T_m^{0.75}}{d_p}\right) = C_{diff}\left(\frac{T_m^{0.75}}{d_p}\right) \tag{3.129}$$

The first term in parenthesis on the right hand side of equation is often presented in term of a diffusion rate constant (C_{diff}, (kg/(m s Pa $K^{0.75}$))) depending on a pair of gas mixture and stochimetric coefficient of reactant gas, ν_g. The diffusion coefficient at reference state

$D_{T0,P0}$, stochimetric coefficient of reactant gas ν_g, and a diffusion rate constant C_{diff} for a binary mixture of O_2 in CO_2, CO_2 in CO_2 and H_2O in CO_2 are calculated and listed in Table 3.3.

Table 3.3: Diffusion parameters for diffusional reaction rate coefficient, K_{diff}.

binary gases	$D_{T0,P0}$ (m^2/s)	ν_g	C_{diff} ($kg/(m\ s\ Pa\ K^{0.75})$)
O_2 in CO_2	0.000274416	0.5	3.91374E-12
CO_2 in CO_2	0.000212509	1	1.51541E-12
H_2O in CO_2	0.000340425	1	2.42759E-12

3.5.3 Intrinsic reaction rate

General form of equation for char reaction explained previously does not account for the effect of char swelling, internal diffusion of reactant gas in the porous char, intrinsic rate of chemical reaction of reactant with the internal surface of the char particle. Thus, Smith [SmithIW82] proposed a correlation between an overall burning rate of char particle per external surface area $R_{s,c}$ and intrinsic chemical reactivity coefficient $R_{i,c}$ written as:

$$R_{s,c} = \eta_{eff}\gamma_{size}\rho_{ap}A_sR_{i,c}\left[(C_g)^{n_{true}}\left(1-\frac{R_{s,c}}{C_gK_D}\right)^{n_{true}}\right] \qquad (3.130)$$

The η_{eff} is the effectiveness factor or the ratio of actual combustion rate to the rate attainable if no pore-diffusion resistance existed. γ_{size} is the characteristic size of the particle defined by the volume of char particle divided by external surface area. ρ_{ap} is the apparent density of char particle, kg/m^3 and A_s is specific internal surface area of char particle, m^2/kg. When comparing Eq. (3.130) with general model of char reaction and replacing apparent reaction order with true reaction order, the above equation can be rearranged to be:

$$R_{s,c} = \left(\eta_{eff}\gamma_{size}\rho_{ap}A_sR_{i,c}\right)\left[(P_g)^{n_{true}}\left(1-\frac{R_{s,c}}{P_gK_{diff}}\right)^{n_{true}}\right] \qquad (3.131)$$

Smith [SmithIW78] used published data to correlate the intrinsic chemical reactivity coefficient, $R_{i,c}$, for a wide range of porous carbons based on true order of reaction. Values of true reaction orders from zero to one ($0< n_{true} <1$) are found in experiments which results in apparent reaction order varying from 0.5 to 1 calculated by the knowledge of combustion regime in Fig. 3.4 and the relation in Eq. (3.106).

The characteristic size of the particle for a sphere is determined by:

$$\gamma_{size} = \frac{(4/3)\pi\left(d_p/2\right)^3}{4\pi\left(d_p/2\right)^2} = \frac{d_p}{6} \qquad (3.132)$$

The intrinsic chemical reactivity coefficient $R_{i,c}$ (in kg/(m^2 s Pa$^{n_{true}}$) is defined in an Arrhenius equation:

$$R_{i,c} = A_{i,c} e^{\left(-\frac{E_{i,c}}{RT_p}\right)} \tag{3.133}$$

Where $A_{i,c}$ and $E_{i,c}$ are the pre-exponential factor and activation energy for intrinsic kinetic rate. Smith [SmithIW78] presented a brief summary of variation of true reaction over wide ranks of porous carbon (char) and concluded that no general way of determining a universal reaction order. For experiments without reaction order, the true reaction order was set to be unity at above 1000 K and 0.5 below this temperature. A true reaction order of unity (n_{true} = 1) was found for pulverized-coal chars burned under 5-10 kPa of O_2 between 1200 and 2000 K [Field69, Field70] and therefore used in this thesis.

Smith [SmithIW78] determined the intrinsic reactivity coefficient, $R_{i,c}$, was calculated for the porous carbons from various coal samples by means of equation related to true reaction order, n_{true}, at an oxygen pressure of 1 atm (about 101 kPa) similar to Eq. (3.114) from general char reaction model as:

$$R_{s,c} = R_{i,c}(P_s)^{n_{true}} \tag{3.134}$$

Effects of pore diffusion can be accounted by progressive conversion model with constant effective diffusivity and negligible gas film resistance. Aris [Aris57] provide equation for an effectiveness factor, η_{eff}, for a spherical particle, which later applied by Dutta and Wen [Dutta77] written by eqaution:

$$\eta_{eff} = \frac{3}{\Phi_{\text{th}}}\left(\frac{1}{\tanh\Phi_{\text{th}}} - \frac{1}{\Phi_{\text{th}}}\right) \tag{3.135}$$

Alternative formulation for effectiveness factor are presented by Liu and Niksa [LiuG04] and applied for CBK8 char kinetic model in coal combustion problem by Gharebaghi et al. [Gharebaghi11b] using relation:

$$\eta_{eff} = \frac{1}{\Phi_{\text{th}}}\left(\frac{1}{\tanh\Phi_{\text{th}}} - \frac{1}{\Phi_{\text{th}}}\right) \tag{3.136}$$

Another equation formulation was also applied for CBK8 char kinetic model by Sun and Hurt [Sun00], and later in coal combustion simulation by Pallarés et al. [Pallarés07] and oxy-coal combustion by Leiser [Leiser11]. The equation has the form:

$$\eta_{eff} = \frac{1}{\Phi_{\text{th}}}\left(\frac{1}{\tanh(3\Phi_{\text{th}})} - \frac{1}{3\Phi_{\text{th}}}\right) \tag{3.137}$$

Where Φ_{th} is the Thiele modulus [Thiele39].

Mehta [Mehta71] showed that the relation between η_{eff} and Φ_{th} for any true order of reactions (n_{true}) can be estimated by using the curve for the first order of reaction (n_{true} = 1) with around 20% maximum error and resulting in the modified equation of the Thiele modulus [Mitchell07] as:

$$\Phi_{\text{mod,th}} = \Phi_{\text{th}} \left(\frac{n_{true}+1}{2}\right)^{0.5} \tag{3.138}$$

Where the original Thiele modulus is calculated by [Smoot85, SmithKL94, Laurendeau78]:

$$\Phi_{\text{th}} = \gamma_{size} \left(\frac{v_g A_s \rho_{ap} k_{i,c} C_s^{(n_{true}-1)}}{D_{eff}}\right)^{0.5} \tag{3.139}$$

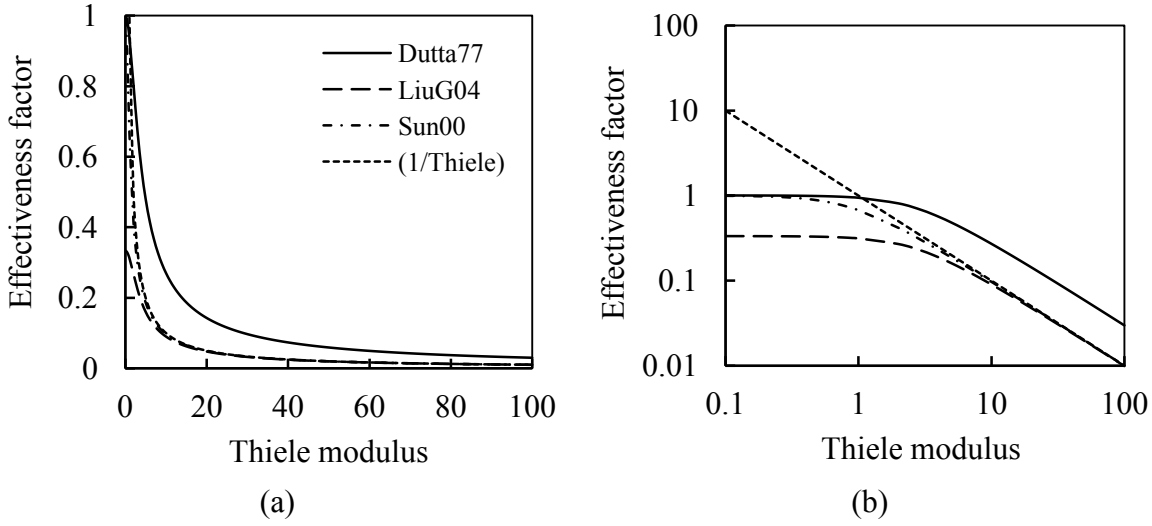

Figure 3.5: Relation between effectiveness factor (η_{eff}) and Thiele modulus (Φ_{th}) for intrinsic char reaction model (a) normal scale, (b) logarithmic scale.

Fig. 3.5 shows relation between η_{eff} and Φ_{th} calculated by equations from different references [Dutta77, LiuG04, Sun00] as reviewed in chapter 2. From Fig. 3.5, it is clear that relation of Thiele modulus (Φ_{th}) created by Sun and Hurt [Sun00] lies between the relation by Dutta and Wen [Dutta77] and Liu and Niksa [LiuG04]. The relation by Liu and Niksa [LiuG04] was developed for the Langmuir-Hinshelwood rate expression; hence, it is not suitable for the power-law rate expression implemented in this thesis.

From calculation using Eq. (3.135), the Thiele modulus (Φ_{th}) is less than 0.001 and the effectiveness factor (η_{eff}) is approximately equal to one ($\eta_{eff} \cong 1$) independent from type of bulk species surrounding char particles (O_2, CO_2 or H_2O). This is based on calculation for oxy-fuel conditions of 21-30% O_2 in bulk CO_2, particle diameter of 100 µm, ν_g of 0.5 for O_2 and of 1 for CO_2 (Table 12), internal pore surface area of 200,000 m^2/kg, apparent density of 1100 kg/m3, particle temperature of 1600 K, gas temperature of 1000 K, binary diffusion coefficient in Table 3.3, pore radius of 2.31 nm, porosity of 0.65 and kinetic rates for char-O_2 reaction by Smith [SmithIW82] or Leiser [Leiser11] and for char-CO_2 reaction by Roberts et al. [Roberts00] or Leiser. From Fig. 3.5, when the Thiele modulus (Φ_{th}) is very low, the relation by Dutta and Wen [Dutta77] or by Sun and Hurt [Sun00] result in the same value of the effectiveness factor of one. For this reason, the relation by Dutta and Wen [Dutta77] in Eq. (3.135) was used for char intrinsic model in the numerical investigations in this thesis.

The effective diffusion coefficient, D_{eff} (in m^2/s), combined influences of both bulk diffusion (K_{diff}) and Knudsen diffusion (D_{Kn}) of reactant gas through pores using expression [Satterfield91, Laurendeau78, Mitchell07]:

$$D_{eff} = 1/\left(\frac{1}{K_{diff}} + \frac{1}{D_{Kn}}\right) \tag{3.140}$$

The Knudsen diffusion [Laurendeau78, Satterfield91, Mitchell07, SmithIW82, Smoot85, SmithKL94], D_{Kn}, can be determined linearly proportional to mean pore radius by:

$$D_{Kn} = \left(\frac{\theta_{poro}}{\tau_{tor}}\right)\frac{2\bar{r}_p}{3}\sqrt{\frac{8RT_p}{\pi MW_g}} = \left(\frac{\theta_{poro}}{\tau_{tor}}\right)97\bar{r}_p\sqrt{\frac{T_p}{MW_g}} \tag{3.141}$$

where $\bar{r}_p$ is the mean pore radius of particle. Mean pore radius can be approximated by specific surface area, A_s, porosity of solid char, θ_{poro}, tortuosity factor, τ_{tor}, and char particle density [Smith82, Wheeler51] by:

$$\bar{r}_p = \frac{2(\theta_{poro})(\tau_{tor})^{0.5}}{A_s\rho_{ap}} \tag{3.142}$$

It should be emphasized that this mean value is an approximation in the case of no experimental measurement for a specific char particle existed. The mean pore radius for Lusatian lignite-char was measured at elevated temperatures between 700 and 1150 °C using N_2-BET and CO_2-BET surface area methods by Al-Makhadmeh [Al-Makhadmeh09] and had average value from all temperatures of 2.31 nm. When the mathematical models from this work is based on coal properties of lignite especially Lusatian lignite for 0.4 MW_{th} oxy-fuel furnace at BTU Cottbus, therefore this value is applied to all numerical models in this thesis. Applying constant mean pore radius also helps to simplify the problem, reduce required computational time and increase robustness of computational stability.

In general, the porosity, θ_{poro}, can be calculated by [SmithKL94, Smoot85, Wheeler51]:

$$\theta_{poro} = 1 - \frac{\rho_{ap}}{\rho_{true}} \tag{3.143}$$

where ρ_{ap} and ρ_{true} are the apparent and true density of char particle.

As mentioned in the reviews (chapter 2), Lusatian lignite-char was classified to be Cenosphere (Large internal hole at the core) or Crassisphere (Scattering internal holes). Therefore, the total porosity of Lusatian char in this thesis is averaged from values between these two groups (50%-80%) which has a value of 0.65.

The total internal surface area of particle, A_s, can varies with burnout and random pore models (RPM) can be used for estimation of the area [Gavalas80, Bhatia80, Simons82, Charpenay92]. Simons [Simons82] calculated the total internal surface area at any stage of conversion by:

$$A_s = A_{s,0}(1 - U_c)\sqrt{\frac{U_c}{\theta_{poro,0}} + (1 - U_c)} \tag{3.144}$$

where $A_{s,0}$ is the initial total internal surface area at the beginning of char reaction, U_c is the fractional burnout in Eq. (3.109) and $\theta_{poro,0}$ is the initial porosity. For low rank coals, the volumetric model is used and the internal surface area of remaining char per mass of initial char is written as [Charpenay92]:

$$A_s = A_{s,0}(1 - U_c) \tag{3.145}$$

The surface area by the RPM from Simons [Simons82] and from Charpenay et al. [Charpenay92] were implemented into the numerical CFD models in chapter 5 to clarify the effect of including pore tree models to the predictions.

Although, the random pores models can be used in the absence of experimental measurements, the total internal surface area for lignite-char in oxy-fuel conditions was recently measured by Al-makldameh [Al-Makhadmeh09]. The CO_2-BET area measured for Lusatian lignite-char [Al-Makhadmeh09] is around 37.29 m^2/g at 700 °C which is 10 times larger than N_2-BET surface area (=3.42 m^2/g) at the same temperature in contrast to the differences at higher testing temperatures (850, 1000, 1150 °C) in the same work which is less than 2 times. The internal surface area used in numerical investigation (chapter 5) is determined by averaging values of CO_2-BET surface areas from the experiments by Al-Makhadmeh [Al-Makhadmeh09] over testing temperatures (700-1150 °C), resulting in a value of 200197.5 m^2/kg (or 200 m^2/g).

In the intrinsic model, density and diameter (d_p, ρ_{ap}) of char particle are changed during char conversion. Both variables can be obtained from either the residual carbon mass fraction Y_c in Eq. (3.108) or the fraction of unburned carbon in char particle, U_c, in Eq. (3.109) written as [SmithIW82, Essenhigh94, Waters88, Mitchell89, Essenhigh89]:

$$d_p = d_{p,0}(Y_c)^{\alpha_{BM}} = d_{p,0}(1 - U_c)^{\alpha_{BM}} \tag{3.146}$$

$$\rho_{ap} = \rho_{ap,0}(Y_c)^{\beta_{BM}} = \rho_{ap,0}(1 - U_c)^{\beta_{BM}} \tag{3.147}$$

Where $d_{p,0}$ and $\rho_{ap,0}$ are the char diameter and apparent density of char particle at the initial stage of char reaction. In this equation, the parameters of burnout, α_{BM}, lies between 0 and 1 ($0 \leq \alpha_{BM} \leq 1/3$) and for a spherical particle:

$$3\alpha_{BM} + \beta_{BM} = 1 \tag{3.148}$$

Therefore, the parameter β_{BM} lies between 0 and 1 ($0 \leq \beta_{BM} \leq 1$). If char particle is burned with assumption of gradually reducing diameter but constant density as in combustion zone III for diffusion rated control, the parameter α_{BM} is equal to 1/3 while β_{BM} to 0 ($\alpha_{BM} = 1/3$, $\beta_{BM} = 0$). However, if the particle is burned with density reduction but constant diameter as in combustion zone I for chemical rated control, the parameter α is equal to 0 while β_{BM} to 1 ($\alpha_{BM} = 0$, $\beta_{BM} = 1$).

As reviewed by Smith [SmithIW82,] $\alpha_{BM} = \beta_{BM} = ¼$ for sized graded particles of pulverized semi-anthracite char [SmithIW71b], in contrast to brown coal char [Hamor73] in which $\alpha_{BM} = 1/3$ while $\beta_{BM} = 0$ (constant density). When the Lusatian lignite is utilized in this thesis which is classified to be in the group of brown coal, the latter parameters is used in this work.

Related constant parameters in the intrinsic model implemented in this thesis are listed in Table 3.4.

Table 3.4: Constant parameters for intrinsic reaction rate model.

Parameter	Value	Reference
Mean pore radius, $\bar{r}_p$	2.31 nm	[Al-Makhadmeh09]
Total internal surface area, A_s (CO_2-BET) - Constant ($A_s = A_{s,0}$) - Random pore model (RPM) - RPM, low-rank coal	 200197.5 m^2/kg Eq. (3.144) Eq. (3.145)	 [Al-Makhadmeh09] [Simons82] [Charpenay92]
Porosity, $\theta_{poro} = \theta_{poro,0}$	0.65	[Al-Makhadmeh09]
Burning mode, brown coal char	$\alpha_{BM} = 1/3$, $\beta_{BM} = 0$	[Hamor73]

3.5.4 Global reaction rate

The global kinetic reaction rate is the basic formulation to calculate the reaction rate of coal and char particle [Levenspiel99]. The total burning rate of char particle is assumed to be fully controlled by chemical kinetic as in combustion zone I, therefore the total burning rate per external surface area of char particle is equal to chemical reaction rate.

$$R_{s,c} = R_{ch,c} = R_{Kin,c}(P_s)^{n_{ap}} \tag{3.149}$$

The chemical reaction rate, $R_{ch,c}$, is calculated by relation of kinetic rate, $R_{Kin,c}$, partial pressure of O_2 at particle surface, P_s, and the apparent order of reaction, n_{ap}. The kinetic rate, $R_{Kin,c}$, is determined by Eq. (3.115) as explained in previous section of general model for char reaction. The total burning rate depends on residual mass fraction of carbon in char particle at the current time of reaction and external surface area of char particle assuming spherical shape in Eq. (3.107).

3.5.5 Kinetic parameters for lignite oxy-fuel combustion

In this thesis, three models for char reaction are applied and tested in a smaller scaled oxy-fuel furnace (100 kW_{th}) and suitable models are selected for the numerical predictions of a 0.4 MW_{th} oxy-fuel furnace at BTU Cottbus which are explained later on the following chapter in this thesis. Both general model of char reaction (Kinetic diffusion limited rate, KD) and intrinsic reaction rate model are applied to the predictions of a laboratory scaled 100 kW_{th} oxy-fuel furnace to evaluate the effect of model's selection to the numerical results. Another significant factor is the selection of kinetic parameters for char reaction either with O_2, CO_2 or H_2O which can highly influences the results of pre-

dictions. Therefore, this section described and summarized kinetic parameters used for numerical investigation in this thesis.

Kinetic parameters for Kinetic diffusion limited rate model (KD):

To start, all kinetic parameters for kinetic diffusion limited rate model including char-O_2, char-CO_2 and char-H_2O reactions are summarized in Table 3.5.

Table 3.5: Kinetic parameters for char reaction applying to kinetic diffusion limited rate model (KD).

Reference	$A_{k,c}$ kg m^{-2} s^{-1} Pa^{-1}	$E_{k,c}$ J/kmol	n_{ap}	**Particle temperature, T_p** K	
Char-O_2:					
Field69-O_2 (CFD)	0.005	7.40E+07	1	950	2000
Tappe09a-O_2 (TBK1[a], Oxy 21%)	0.00345	6.566E+07	0.588	1073	1273
	0.00345	2.899E+07	0.588	1273	1353
Tappe09b-O_2 (TBK2[a], Oxy 30%)	0.003754	4.329E+07	0.588	1073	1273
	0.003754	4.329E+07	0.588	1273	1353
Char-CO_2:					
Mayers34a-CO_2	0.000135	1.36E+08	1	1123	1223
	0.00635	1.62E+08	1	1223	1673
Char-H_2O:					
Mayers34b-H_2O	0.319	2.08E+08	1	1133	1233
	0.00192	1.47E+08	1	1273	1433

[a] TBK1, TBK2 mean dried Lusatian lignite type 1 (high moisture, low ash) and lignite type 2 (low moisture, high ash), respectively.

For char oxidation (Char-O_2 reaction), in the absence of kinetic parameters for Lusatian-lignite oxidation, the kinetic parameters for the kinetic-diffusion limited rate model proposed by Field [Field67,69] can be used for thermo-chemical predictions of char oxidation. The experiments were performed at the British Coal Utilization Research Association (BCURA) using direct measurement of the weight loss of particles carried in laminar flow reactor. The apparent order of reaction is expected to be unity (n_{ap} = 1) suggested by Field and the chemical kinetic rate depends on first order of partial pressure.

$$R_{s,c} = R_{ch,c} = R_{Kin,c}(P_s) \tag{3.150}$$

Therefore the char reaction rate per external surface area is presented by first order of partial pressure as:

$$R_{s,c} = P_g \left(\frac{1}{R_{Kin,c}} + \frac{1}{K_{diff}} \right)^{-1} \tag{3.151}$$

Chemical rate coefficients $R_{Kin,c}$ were originally presented in three styles of formulation by Field determined by fitting curves employing regression analysis which were an Arrhenius, linear and quadratic equation.

Arrhenius equation: $$R_{Kin,c} = A_{Kin,c} e^{\left(-\frac{E_{Kin,c}}{RT_p}\right)} \quad (3.152)$$

Linear equation: $$R_{Kin,c} = const1_{Kin,c} + const2_{Kin,c} T_p \quad (3.153)$$

Quadratic equation: $$R_{Kin,c} = const1_{Kin,c} + const2_{Kin,c} T_p + const3_{Kin,c} T_p^2 \quad (3.154)$$

where $A_{Kin,c}$ and $E_{Kin,c}$ are the pre-exponential factor and activation energy for Arrhenius rate. $const1_{Kin,c}$, $const2_{Kin,c}$ and $const3_{Kin,c}$ are constants for each equations and $E_{Kin,c}$ is the activation energy. These constants including related reaction order and valid particle temperature range for each equation are summarized in Table 3.6 and Table 3.7.

Table 3.6: Constant parameters of Arrhenius equation for kinetic diffusion limited rate model (KD) [Field69].

	$A_{Kin,c}$ kg m^{-2} s^{-1} Pa	$E_{Kin,c}$ J / kmol	n_{ap}	**Particle temperature, T_p** K	
Arrhenius eq.	0.859610165	1.495E+08	1	950	1650

Table 3.7: Constant parameters of linear and quadratic equations for kinetic diffusion limited rate model (KD) [Field69].

	$const1_{,Kin,c}$ kg m^{-2} s^{-1} Pa	$const2_{Kin,c}$ kg m^{-2} s^{-1} Pa	$const3_{Kin,c}$ kg m^{-2} s^{-1} Pa	n_{ap}	Particle temperature, T_p K	
Linear eq.	-4.83592E-05	3.80E-08	-	1	1400	2000
Quadratic eq.	-8.88231E-06	-1.24E-08	1.56E-11	1	1400	2000

It was recommended by author that the linear and quadratic equation fitted well to the experiments in the temperature range from 1400 to 2000 K. However, using these fitting curves exhibits negative values of kinetic rate below 1300 K and should be realized when used to estimate reaction rate of char oxidation. In contrast to Arrhenius form which fitted well to experiments in the temperature range from 950 to 1650 K. This temperature range covers prediction from low to intermediate combustion temperature. For the Arrhenius rate expression by Field, the value of activation energy of 0.005 kg m^{-2} s^{-1} Pa and activation energy of 7.4 × 10^7 J/kmol in Table 3.5 was applied for oxy-coal combustion [Toporov08a, Jovanovic12]. These kinetic parameters are compromising values and superior than other style of equation's formulation by Field because they does not results in negative kinetic rate at low temperature (T_p < 1200 K) while still provide a good accuracy at high particle temperature (1200 K < T_p < 2000 K); hence, they were usually applied to combustion problem and also used for investigated cases of numerical simulation in this thesis which is denoted as *Field69-O_2* (*CFD*). Comparison of kinetic rates using Field's formulation is shown in Fig 3.6.

From Fig. 3.6, the kinetic parameters usually applied for combustion problem are denoted as *Field69-O_2* (*CFD*) in the plot and other parameters are denoted by their formulations of equation either to be an Arrhenius, linear or quadratic equations referring to *Field69-O_2 (CFD)*.

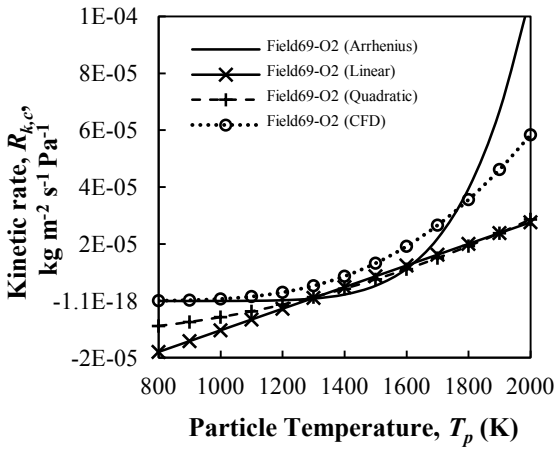

Figure 3.6: Comparison of kinetic rates using three styles of formulation by Field [Field69].

As mentioned in the literature review, some works published kinetic parameters for char oxidation under oxy-fuel conditions [Murphy06, Chui03, Khare08b] but rarely works presented kinetic parameters for lignite. For this reason, the global kinetic parameters for char oxidation in oxy-fuel conditions (21% and 30% O_2 in bulk CO_2) are determined using experimental data from the thermo-gravimetric analysis (TGA) by Tappe [Tappe09a] at the Chair of Power Plant Technology at BTU Cottbus. Two coal samples (TBK1 and TBK2) with particle diameter between 0.125-1.25 mm were used in the TGA in the temperature range of 1073-1353 K to determine kinetic parameters shown in Table 3.5. It should be noted that the kinetic parameters for oxy-fuel conditions in this thesis are taken from the experiments utilizing coal type TBK1 at 21% O_2 and TBK2 at 30% O_2. The kinetic parameters at 21% O_2 (TBK1) were later applied in the numerical case of laboratory scaled 100 kW_{th} oxy-fuel furnace because it has similar coal properties to Rhenish lignite which were utilized to operate the 100 kW_{th} oxy-fuel furnace. In the absence of experimental results at 30 % O_2 for coal type TBK1, the kinetic parameters at 30% O_2 from TBK2 were applied in numerical case of pilot scaled 0.4 MW_{th} oxy-fuel furnace.

For the Char-CO_2 and Char-H_2O reaction, it was difficult to determined kinetic data by maintaining the same experimental conditions (char type, gas temperature, pressure) for the desired reaction of interest; therefore, Smoot [Smoot79] recommended to use the kinetic parameters taken from experiments utilizing graphite particle performed by Mayer [Mayers34a, 34b] in the absence of direct measurement of experimental data. The kinetic parameters for Char-CO_2 and Char-H_2O reaction applied in the KD model in this thesis are hence taken from experiments by Mayer [Mayers34a, 34b] and already shown in Table 3.5.

In order to understand how kinetic parameters dominates final reaction rate, kinetic rates for char-O_2, char-CO_2 and char-H_2O reactions are compared and plotted in Fig. 3.7. From Fig. 3.7, it is clear that the kinetic rate of char oxidation has stronger influence on the predictions than char-CO_2 and H_2O reaction. From the plot, the kinetic rates for char oxidation of *Field69-O_2* (*CFD*), *Tappe09-O_2* (*TBK1*, *Oxy 21%*) and of *Tappe09-O_2* (*TBK2*, *Oxy 30%*) are not different.

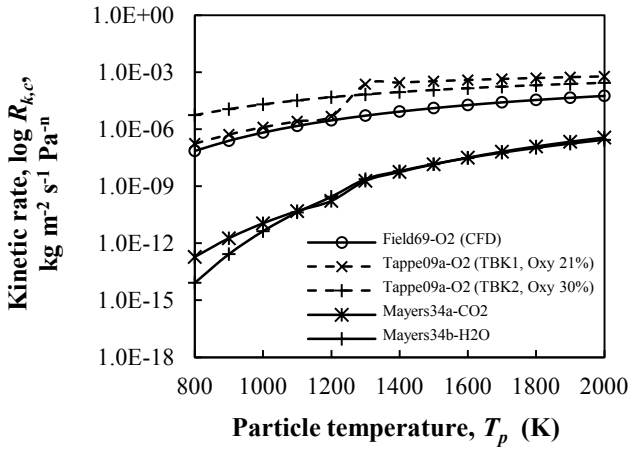

Figure 3.7: Comparison of kinetic rates of char-O_2, CO_2 and H_2O reaction.

However, all kinetic parameters for char oxidation were applied to investigated numerical cases using operating conditions, geometry and measurements for validation from 100 kW_{th} laboratory scaled oxy-fuel furnace utilizing lignite as fuel [Toporov08a] (chapter 5). It should be noted that the kinetic parameters from TBK2 at 30% of O_2 was not applied for investigated cases of 100 kW_{th} oxy-fuel furnace when this furnace operated at 21 % O_2 in bulk CO_2.

Kinetic parameters for intrinsic reaction rate model:

For the intrinsic reaction rate model, the first kinetic parameters of char oxidation (char-O_2) for numerical studies in this thesis are based on a least squares regression from a wide range of porous carbons including many chars, coke and graphite [SmithIW82, SmithIW78]. The intrinsic reaction rate coefficient, $R_{i,c}$, from regression analysis are determined at oxygen pressure of 1 atm (around 101 kPa). Additional kinetic parameters for char oxidation are from the previous work of Smith [SmithIW74] in the experiment using porous brown coal char between particle temperature from 630 – 1812 K and a true order of zero was found ($n_{true} = 0$). This parameters were included in a numerical studies when the coal structure (porosity, internal surface area) and burning mode (changes of apparent diameter and density) of Lusatian lignite is expected to be similar brown coal char than the parameters from regression fitting curve for all coal ranks proposed by Smith [SmithIW82]. The kinetic parameters from experiments using Australian Yallourn brown coal [Hamor73] are also included in the numerical studies. A true order of zero was presented for this coal.

For char reacting with CO_2, Dutta [Dutta77] published intrinsic global kinetic parameters for reactivity of coal and char in CO_2 atmosphere. However, another form of intrinsic equation was presented depending on additional parameters such as relative available pore surface area and a function of char conversion. To have the basis of comparison numerical results from different kinetic data, the same formulation of equation should be maintained. Therefore, the kinetic parameters of char-CO_2 and char-H_2O reaction in this thesis are based on the experiment to determine an intrinsic reaction rate coefficient in a pressurized thermo-gravimetric analysis (TGA) [Roberts00]. The kinetic data for high-temperature reactivity under true gasification conditions was determined from low-

temperature chemical rate data in simple bench-scale techniques. The reaction orders for both char-CO_2 and char-H_2O reaction are varied from 0.5 to 0.8 at atmospheric pressure in which the reaction order of 0.6 is assumed for both char-CO_2 and char-H_2O reaction when lignite is combusted at atmospheric pressure in oxy-fuel furnace investigated in this thesis. In addition, the kinetic parameters fitted to match experimental data of lignite oxy-fuel combustion by Leiser [Leiser11] are also included in the numerical investigation. All kinetic parameters for intrinsic reaction rate are summarized in Table 3.8.

Table 3.8: Kinetic parameters for char reaction applying to intrinsic reaction rate model.

	$A_{Kin,c}$ kg m^{-2} s^{-1} Pa^{-ntrue}	$E_{Kin,c}$ J/kmol	n_{true}	n_{ap}	Particle temperature, T_p K	
Char-O_2:						
Smith82-all coal ranks	0.03010116	1.792E+08	1	1	580	2200
Hamor73-brown coal char	93	6.783E+07	0	0.5	900	2200
Smith74-brown coal char	13.4	1.365E+08	0	0.5	630	1812
Roberts00-O_2	0.000111217	1.53E+08	0.85	0.93	1300	2000
Leiser11-O_2	0.001408507	1.46E+08	0.85	0.93	1300	2000
Char-CO_2:						
Roberts00-CO_2	0.000207356	2.09E+08	0.6	0.2	1300	2000
Leiser11-CO_2	0.000214301	2.16E+08	0.6	0.2	1300	2000
Char-H_2O:						
Roberts00-H_2O	0.001984267	2.27E+08	0.6	0.2	1300	2000
Leiser11-H_2O	0.003819713	2.24E+08	0.6	0.2	1300	2000

Although the order of reaction varies for each set of kinetic parameters from different coal rank and method used in the experiments, the intrinsic kinetic rate, $R_{i,c}$, from each char heterogeneous reactions (char-O_2, char-CO_2 and char-H_2O) can be compared using Arrhenius form of equation in Eq. (3.133) and plotted in Fig. 3.8. It is clear from the plot that char-O_2 reaction is the strongest reaction dominating final results of combustion products, heat flux and temperature of gas mixture. The kinetic parameter from Roberts [Roberts00] has low rate and close to the intrinsic kinetic rate of char-CO_2 and char-H_2O which has significant impact to the burning of char in the situation of strong Boudouard reaction ($C(s)+CO_2 \leftrightarrow 2CO$) in oxy-fuel conditions [Rathnam09, Várhegyi96]; hence, this parameters were not included in the numerical studies in this thesis. The details of selecting kinetic parameters are explained in chapter 5 for the numerical investigated cases.

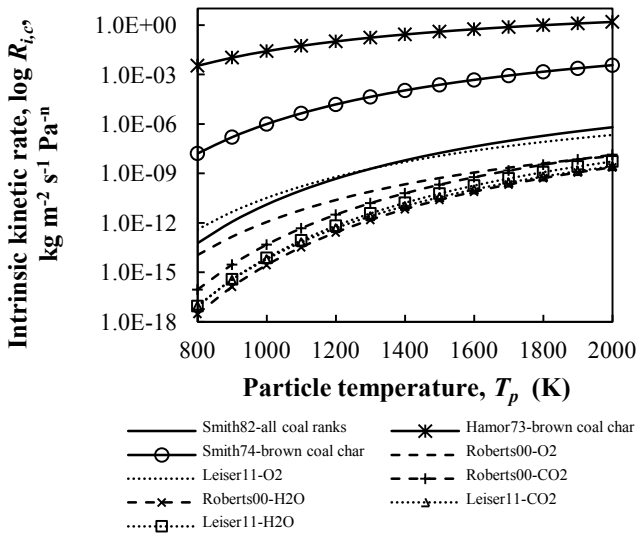

Figure 3.8: Comparison of intrinsic kinetic rates of char-O_2, CO_2 and H_2O reaction.

3.6 Volatile reactions

During coal devolatilization, volatiles, composed of hydrocarbon ($C_aH_bO_c$), light hydrocarbon (C_aH_b) and light gases (CO, CO_2, H_2, H_2O), further react with oxygen or continue their own reaction mechanisms. Volatiles can be simplified to be either hydrocarbon ($C_aH_bO_c$) or light hydrocarbon (C_aH_b) in combustion modeling, however, coal comprises with other elementary substance such as N_2 and S_2, which convert to be gas emission (NO_x, SO_x) in the end of combustion process. Hence, the volatiles are modeled to contain nitrogen and sulfur species ($C_aH_bO_cN_dS_e$). Two main aspects, further discussed in this sub-chapter, are *turbulent gaseous combustion* and *simplification of reaction mechanisms*. The *turbulent gaseous combustion* models determine the overall rate of volatile reaction from the effect of gas mixing and chemical reaction. The rate can be determined by mixing rate alone or by combination of two methods. It is not always possible to apply detailed reaction mechanism for coal combustion problem because computations will be much more expensive, therefore reducing number of reactions in consideration (*simplification of reaction mechanisms*) helps in the improvement of numerical stability (convergence) and discards unnecessary chemical reaction in a specific combustion problem. However, the required number of chemical reactions can be judged by sensitivity analysis validated with experimental results of practical combustion problem.

3.6.1 Turbulent gaseous combustion

In non-premixed turbulent hydrocarbon diffusion flames such as homogeneous gaseous reactions in coal combustion, time of turbulent mixing (t_{turb}) is either on the same order or much longer than time of chemical reaction (t_{react}) for species of interest [Smoot85, Eaton99]. In this thesis, t_{react} is assumed to have the same order of magnitude as t_{turb}.

Thus, the turbulent mixing and finite chemical reaction rates are taken into account simultaneously.

Both eddy-breakup model (EBU) [Spalding71] and finite rate eddy dissipation (FRED) [Magnussen77] are applied for numerical investigations from laboratory-scale oxy-fuel furnace (100 kW_{th}) explained in chapter 5. The FRED model was based on the eddy-breakup model (EBU) proposed by Spalding [Spalding71] and improved further by Magnussen et al. [Magnussen77]. The overall rate is assumed to be a minimum of three rates, which are the chemical reaction rate R_{chg}, the rate of dissipation of reactant eddies R_{React} and the rate of dissipation of product eddies R_{Prod}.

The chemical reaction rate R_{chg} of the k^{th} species is calculated by chemical production or depletion term as:

$$R_{chg,k} = \left(\nu_{Prod,k} - \nu_{React,k}\right) MW_k \left(k_{fw} \prod_{ir} CT_{ir}^{\alpha_{React,k}} - k_{rw} \prod_{ipd} CT_{ipd}^{\alpha_{Prod,k}}\right) \quad (3.155)$$

The $\nu_{React,k}$ and $\nu_{Prod,k}$ are the stochiometric coefficient for reactant species and product species, respectively. CT_r and CT_p are the volumetric concentration of reactants and products, related to their concentration exponents, $\alpha_{React,k}$ and $\alpha_{Prod,k}$, for reaction rates. Both chemical kinetic rates k_{fw} and k_{rw} for forward and reverse reaction of volatile and gaseous reaction are expressed by an Arrhenius equation:

$$k_{fw} = A_{g,fw} T^{TE} e^{\left(-\frac{E_{g,fw}}{RT}\right)} \quad (3.156)$$

$$k_{rw} = A_{g,rw} T^{TE} e^{\left(-\frac{E_{g,rw}}{RT}\right)} \quad (3.157)$$

where TE is the temperature exponent. The rate of dissipation of reactant eddies R_{React} of the k^{h} species is assumed to be proportional to the ratio of the turbulent kinetic dissipation $\in$ and turbulent kinetic energy K and given by:

$$R_{React,k} = \nu_{React,k} MW_k EC_1 \rho_k \frac{\varepsilon}{k} \min_r \left(\frac{MF_{ir}}{st_{ir} MW_{ir}}\right) \quad (3.158)$$

where the first empirical constant EC_1 is equal to 4.0 according to Magnussen et al. [Magnussen77]. The rate of dissipation of product eddies R_{Prod} of the k^{th} species is determined by:

$$R_{Prod,k} = \nu_{React,k} MW_k EC_1 EC_2 \rho_k \frac{\varepsilon}{k} \left(\frac{\sum_{ipd} MF_{ipd}}{\sum_{ipd} st_{ipd} MW_{ipd}}\right) \quad (3.159)$$

The second empirical constant EC_2 is equal to 0.5 recommended by Magnussen et al. [Magnussen77].

3.6.2 Simplification of reaction mechanisms

Simplification and detailed reaction mechanisms for oxy-fuel conditions have been reviewed in chapter 2 (mathematical sub-model for CFD simulation), composed of global 2-step, 3-step, 4-step and 6-step reaction mechanisms [Andersen09, Toporov08a, Kangwanpongpan12, Frassoldati09]. Only the global 2-step and 3-step reaction mechanisms were included in numerical investigations for laboratory-scale oxy-coal furnace in chapter 5 because of numerical stability previously explained in the literature reviews.

Global 2-step reaction mechanisms:

The global 2-step reaction mechanisms in this thesis are based on the reaction mechanisms presented by Peters et al. [Peters97]. The volatile-matter-bound carbon, f, for oxy-fuel conditions were not studies at present and it was set to 0.226 as found from the best results of numerical predictions in a swirling 2.4 MW_{th} pulverized coal burner, implying that carbon in volatile matter burn partially to CO and CO_2 in the first step of reactions. The CO further oxidizes to CO_2 in the second reaction. The set of reaction mechanisms are:

$$C_aH_bO_cN_dS_e + (a/2+e-c/2)O_2 \rightarrow (1-f_{vc})\, aCO + f_{vc}aCO_2 + (b/2)H_2 + (d/2)N_2 + eSO_2 \qquad (3.160)$$

$$CO + ½\, O_2 \rightarrow CO_2 \qquad (3.161)$$

The fraction f_{vc} is defined as the fraction of volatile-matter-bound carbon that reacts directly to CO_2. It is the ratio of molar fraction oxygen atom and carbon in volatile as:

$$f_{vc} = (f_O/MW_O)/(f_C/MW_C) \qquad (3.162)$$

The f_O and f_C are the mass fraction of oxygen atom and carbon in volatile, respectively. The MW_O and MW_C are the molecular weights of oxygen atom (16) and carbon (12).

In the global 2-step mechanisms, three kinetic rates for volatile oxidation in Eq. (3.160) and two kinetic rates for CO oxidation were investigated by CFD simulations. The kinetic rates for volatile oxidation in the studies were from Dryer and Glassman [Dryer73], Westbrook and Dryer [Westbrook81] and Shaw et al. [Shaw91]. The first two kinetic parameters were obtained from experiments of methane oxidation in turbulent flow reactor and from validation with detailed kinetic mechanisms from laminar flame model (HCL code [Lund78]). The last kinetic rates from Shaw et al. was included in the studies due to the assumption that volatile is defined as heavy hydrocarbon ($C_aH_bO_cN_dS_e$), which oxidizes directly to light gases (CO, CO_2, H_2), inert gas (N_2) and SO_2 in the first step of reaction, by omitting the hydrocarbon breakdown to form light hydrocarbon (C_aH_b) and soot (C_{soot}) as presented by Förtsch et al. and Leiser [Förtsch98, Förtsch03, Leiser11]. For CO oxidation, the kinetic rates from Dryer [Dryer73] was used.

In addition, modified 2-step reaction mechanisms for oxy-fuel conditions were also included in numerical investigations by maintaining kinetic rates of volatile oxidation from Shaw et al. for all tested cases. The mechanisms have the same formulation as in Eqs. (3.160)-(3.162) but the irreversible CO oxidation in Eq. (3.161) is replaced by reversible

$CO\text{-}CO_2$ reaction ($CO + ½\ O_2 \leftrightarrow CO_2$) modified to fit to oxy-fuel flame proposed by Andersen et al. [Andersen09].

Global 3-steps reaction mechanisms:

The global 3-step mechanisms in this work are similar to the simplified mechanism optimized for the perfectly stirred reactor (PSR) by Brink and Abdalla et al. [BrinkPhD98, Abdalla83]. The carbon in volatile matter ($C_aH_bO_cN_dS_e$) is assumed to burn fully to CO as mechanisms developed using experiments from turbulent flow reactor by Hautman [Hautman81]. Therefore, the combustion products from the first reactions of volatile oxidation are composed of CO, H_2, N_2 and SO_2 (without CO_2). Other subsequent reactions are the CO and H_2 oxidations to form CO_2 and H_2O. The 3-step reaction mechanisms are presented by:

$$C_aH_bO_cN_dS_e + (a/2+e-c/2)O_2 \rightarrow aCO + (b/2)H_2 + (d/2)N_2 + eSO_2 \qquad (3.163)$$

$$CO + ½\ O_2 \rightarrow CO_2 \qquad (3.164)$$

$$H_2 + ½\ O_2 \rightarrow H_2O \qquad (3.165)$$

To evaluate suitable kinetic rates (parameters) for the global 3-step mechanisms, possible kinetic parameters from previous coal combustion simulations were tested in the numerical simulations of 100 kW_{th} laboratory-scale oxy-coal furnace (chapter 5).

The kinetic rates for volatile oxidations were from Zimont and Trushin [Zimont69], Rückert et al. [Rückert03] and Shaw et at. [Shaw91]. The application of kinetic rates for volatile oxidation from Zimont and Trushin was presented in pulverized coal combustion simulation by Förtsch [Förtsch98, Förtsch03], from Shaw et al. in oxy-coal CFD simulation by Toporov et al. [Toporov08a]. Both kinetic rates for irreversible CO oxidations by Howard [Howard73] and Rückert et al. [Rückert03] were included in the numerical studies. The kinetic rates by Howard were modeled in combustion simulation by Förtsch and Brink [Förtsch98, Förtsch03, BrinkPhD98]. The kinetic rates for the H_2 oxidation for all tested cases in the global 3-step oxidation were from the studies of global reaction mechanisms by Rückert et al. [Rückert03].

The effects of including reversible $CO\text{-}CO_2$ reactions for oxy-fuel conditions were also investigated by replacing irreversible CO oxidation with the reversible reactions ($CO + ½O_2 \leftrightarrow CO_2$) modified by Andersen et al. [Andersen09].

Summary of investigated cases for volatile reactions

Investigated cases for the modeling of volatile reactions for oxy-fuel conditions are categorized into three groups of numerical studies, which are evaluation of the model for turbulent gaseous combustion (EBU, FRED), kinetic rates for volatile, CO and H_2 oxidation and influences from using reversible $CO\text{-}CO_2$ reaction. All kinetic rates (parameters) are summarized in Table 3.9 including its references. The investigated cases from three groups of evaluation are listed in Table 3.10.

Table 3.9: Kinetic rate parameters for volatile matter (VM), CO and H_2 oxidations.

Reactant	Mechanism	Reference	Reaction[a]		A_g [b]	$E_g \times 10^7$ (J/kmol)	TE[c]	Species concentration (exponent)
VM	2-step	[Dryer73]	Eq. (3.160)	f, irr	5.012E+11	2.026E+08	0	VM(0.7), O_2(0.8)
VM	2-step	[Westbrook81]	Eq. (3.160)	f, irr	2.119E+11	2.026E+08	0	VM(0.2), O_2(1.3)
VM	2,3-step	[Shaw91]	Eq.(3.160,3.163)	f, irr	1.623E+06	5.066E+07	0	VM(1), O_2(1)
VM	3-step	[Rückert03]	Eq. (3.163)	f, irr	7.280E+09	1.675E+08	0.5	VM(1), O_2(1)
VM	3-step	[Zimont69]	Eq. (3.163)	f, irr	2.330E+11	1.671E+08	0.5	VM(1), O_2(1)
CO	2-step	[Dryer73]	Eq. (3.164)	f, irr	2.239E+12	1.675E+08	0	CO(1), O_2(0.25), H_2O(0.5)
CO	2,3-step	[Andersen09]	Eq. (3.164)	f,rev	2.238E+06	4.187E+07	0	CO(1), O_2(0.25), H_2O(0.5)
CO	2,3-step	[Andersen09]	Eq. (3.164)	r,rev	1.095E+13	3.282E+08	-0.97	CO_2(1), O_2(-0.25), H_2O(0.5)
CO	3-step	[Howard73]	Eq. (3.164)	f, irr	1.300E+11	1.256E+08	0	CO(1), O_2(0.5), H_2O(0.5)
CO	3-step	[Rückert03]	Eq. (3.164)	f, irr	5.420E+09	1.256E+08	0	CO(1), O_2(0.25), H_2O(0.5)
H_2	3-step	[Rückert03]	Eq. (3.165)	f, irr	1.000E+08	8.374E+06	0	H_2(1), O_2(1)

[a] rev = reversible reaction, irr = irreversible reaction, f = forward reaction, r = reverse reaction.
[b] A_g has units in m, s, J, mol depending on product of exponential term of species concentration.
[c] TE = exponents of gas temperature.

Table 3.10: Investigated cases for volatile reactions.

Case number	Objective	Mechanisms	TGC[a] model	Kinetic rate expressions		
				VM	CO	H_2
VR1	TGC[a]	2-step	EBU	-	-	-
VR2	TGC[a]		FRED	[Dryer73]	[Dryer73]	-
VR3	kinetics		FRED	[Westbrook81]	[Dryer73]	-
VR4	kinetics		FRED	[Shaw91]	[Dryer73]	-
VR5	kinetics		FRED	[Shaw91]	[Andersen09]	-
VR6	kinetics	3-step	FRED	[Zimont69]	[Howard73]	[Rückert03]
VR7	kinetics		FRED	[Zimont69]	[Rückert03]	[Rückert03]
VR8	kinetics		FRED	[Rückert03]	[Howard73]	[Rückert03]
VR9	kinetics		FRED	[Rückert03]	[Rückert03]	[Rückert03]
VR10	kinetics		FRED	[Shaw91]	[Howard73]	[Rückert03]
VR11	kinetics		FRED	[Shaw91]	[Rückert03]	[Rückert03]
VR12	kinetics		FRED	[Shaw91]	[Andersen09]	[Rückert03]

[a] TGC = turbulent gaseous combustion.

3.7 Radiation modeling

3.7.1 Radiative transfer equation (RTE)

The radiative transfer equation (RTE) for radiative energy traveling in the $\hat{s}$ direction is determined by the sum of emission, absorption and scattering apart from and into the direction $\hat{s}$, expressed by the governing equation of quasi-steady state RTE at potions r in the direction $\hat{s}$ by [Modest03]:

$$\frac{dI_\eta(r,\hat{s})}{ds} = \kappa_\eta I_{b,\eta}(r) - \left(\kappa_\eta + \sigma_{s,\eta}\right) I_\eta(r,\hat{s}) + \frac{\sigma_{s,\eta}}{4\pi}\int_0^{4\pi} I_\eta(r,\acute{s})\Phi_{\text{ph}}(r,\hat{s},\acute{s})\, d\acute{\Omega}_{\text{s}} \quad (3.166)$$

The parameter $\left(\kappa_\eta + \sigma_{s,\eta}\right)$ often refers to the *extinction coefficient* in the standard book of radiation. The equation of transmission in any $\hat{s}$ direction is:

$$TM_\eta = \int_0^S \left(\kappa_\eta + \sigma_{s,\eta}\right) ds \quad (3.167)$$

By multiplying the RTE with exponential of transmission (e^{TM_η}), the solution for RTE is calculated by integration from location $\acute{s}$ = 0 at the wall surface to any locations inside control volume of the medium $\acute{s}$ = s, presented by:

$$I_\eta\left(TM_\eta\right) = I_\eta(0)e^{-TM_\eta} + \int_0^{4\pi} SF_\eta\left(T\acute{M}_\eta,\hat{s}\right)e^{-\left(TM_\eta - T\acute{M}_\eta\right)}\, dT\acute{M}_\eta \quad (3.168)$$

The SF_η is the source function calculated by integration over a set of direction coordinates (varying local origin), and must be integrated again over the optical coordinate for all directions. For non-scattering medium (without radiation scattering), the source function can be substituted by the local blackbody intensity:

$$SF_\eta\left(T\acute{M}_\eta,\hat{s}\right) = I_{b,\eta}\left(T\acute{M}_\eta\right) \quad (3.169)$$

The RTE is subjected to the boundary conditions for diffusely emitting and reflecting opaque surfaces, given at the position r_w on the wall surface by:

$$I(r_{wl},\hat{s}) = \epsilon(r_{wl})I_b(r_{wl}) + \frac{RF(r_{wl})}{\pi}\int_{\hat{n}\cdot\acute{s}<0}^{4\pi} I(r_{wl},\acute{s})|\hat{n}\cdot\acute{s}|\, d\acute{\Omega}_{\text{s}} \quad (3.170)$$

Where $\hat{n}$ is the normal vector outward direction from wall surface and the product of $\hat{n}\cdot\acute{s}$ is the cosine angle between two vectors. The $RF(r_{wl})$ is the reflection at wall. The integral on the right hand side of equation refers to the hemi-spherical irradiation or incoming radiative heat flux (incident radiative heat flux).

The total radiative heat flux must be integrated over all spectral band and also solid angles as:

$$q_r = \int_0^\infty q_\eta\, d\eta = \int_0^\infty \left[\int_{4\pi} I_\eta(\hat{s})\hat{s}\, d\Omega_{\text{s}}\right] d\eta \quad (3.171)$$

The radiative source term is defined as the divergence of radiative heat flux, determined from the energy balance in a volume of an infinitesimal pencil of rays by:

$$\nabla \cdot q_\eta = \kappa_\eta \left(4\pi I_{b,\eta} - \int_{4\pi} I_\eta(\hat{s})\, d\Omega_s\right) = \kappa_\eta\left(4\pi I_{b,\eta} - G_\eta\right) \tag{3.172}$$

The integral $\int_{4\pi} I_\eta(\hat{s})\, d\Omega_s$ is the *incident radiation function*, sometime refers to as G_η.

3.7.2 Solution algorithm for RTE (Discrete Ordinates Method)

The discrete ordinate method (DOM) is applied for all cases for solving the RTE. This model has advantage to takes into account the effect of the non-gray gases and the scattering particles. The number of RTE depends on the total number of gray gases N_g. The DOM applied in this research is based on the concept of angular discretization scheme, in which each octant of the angular space 4π is discretized into polar and azimuthal solid angle. The RTE is solved for different direction $\hat{s}_i$ from $i = 1$ to $i = N_d$. The integration in the RTE is interpolated using quadrature weights, $w_{DO,j}$, associated with the direction $\hat{s}_i$ expressed as:

$$\hat{s}_i \cdot \nabla \cdot I_\eta(r, \hat{s}_i) =$$
$$\kappa_\eta(r) I_{b,\eta}(r) - \left[\kappa_\eta(r) + \sigma_s(r)\right] I_\eta(r, \hat{s}_i) + \frac{\sigma_{s,\eta}(r)}{4\pi} \sum_{j=1}^{N_w} w_{DO,j}\, I_\eta\left(r, \hat{s}_j\right) \Phi_{\text{ph}}\left(r, \hat{s}_i, \hat{s}_j\right)$$

For $i = 1, 2, \ldots, N_d$ (3.173)

The set of equation for RTE by DOM is subjected to boundary conditions:

$$I(r_{wl}, \hat{s}_i) = \epsilon(r_{wl}) I_b(r_{wl}) + \frac{RF(r_{wl})}{\pi} \sum_{\hat{n}\cdot\hat{s}'<0} w_{DO,j} I_\eta\left(r_{wl}, \hat{s}_j\right) |\hat{n} \cdot \hat{s}_i| \tag{3.174}$$

when $\hat{n} \cdot \hat{s}_i > 0$.

The *incident radiation function*, G_η, is approximated by quadrature weights:

$$G_\eta = \int_{4\pi} I_\eta(\hat{s})\, d\Omega_s \cong \sum_{i=1}^{N_w} w_{DO,i}\, I_\eta(r, \hat{s}_i) \tag{3.175}$$

The *radiative heat flux inside the medium* or at a surface is determined by:

$$q_\eta(r, \hat{s}) = \int_{4\pi} I_\eta(r, \hat{s}) \hat{s}\, d\Omega_s \cong \sum_{i=1}^{N_w} w_{DO,i}\, I_\eta(r) \hat{s}_i \tag{3.176}$$

Integrating radiative heat flux over spectrum yields the *total radiative heat flux*.

$$q_r = \int_0^\infty q_\eta(r, \hat{s})\, d\eta \tag{3.177}$$

The radiative source term for spectral band η is computed from incident radiation function, estimated previously, to give:

$$\nabla \cdot q_\eta = \kappa_\eta\left(4\pi I_{b,\eta} - G_\eta\right) = \kappa_\eta\left(4\pi I_{b,\eta} - \sum_{i=1}^{N_w} w_{DO,i}\, I_\eta(r,\hat{s}_i)\right) \quad (3.178)$$

It should be note that the total radiative source term must be integrated over spectral bands. The isotropic scattering is assumed in this research, in which the phase function is equal to one ($\Phi_{\text{ph}}(r,\hat{s},\acute{s}) = 1$).

3.7.3 Weighted sume of gray gases (WSGG) model for gas radiation

Previous studies [Modest91, SmithTF82] demonstrated application feasibility of WSGG model to solve RTE by P_N approximation or DOM model. In this method, the radiative properties such as the fraction of black body radiation (weighting factor) and the absorption coefficient are spatially assumed to be constant over a number of *i* gray gases. The total emissivity can be approximated as:

$$\epsilon = \sum_{i=1}^{N_g} w_i\left[1 - \exp\left(-\kappa_i P_a L_p\right)\right] \quad (3.179)$$

$$P_a = Y_t P \quad (3.180)$$

Total molar fraction of mixture Y_t is defined as (in case of two mixtures):

$$Y_t = Y_{H_20} + Y_{CO_2} \quad (3.181)$$

To ensure that the weighting factors must sum to unity, the spectrally clear windows (with an implied $\kappa_0 = 0$) are accounted for by the weighting factor at $i = 0$ as:

$$w_{i=0} = 1 - \sum_{i=1}^{N_g} w_i \quad (3.182)$$

In the non-gray gas formulation, the radiation spectrum is divided into N_g wavelength intervals and spectral absorption coefficients κ_i are spatially constant for each gray gas. The governing equation of RTE for spectral intensity of each gray band I_i with an absorbing, emitting, and scattering medium at position *r* in the direction *s* is given by:

$$\frac{dI_i(r,\hat{s})}{ds} = \kappa_i I_{b,i}(r) - \left(\kappa_i + \sigma_{s,i}\right)I_i(r,\hat{s}) + \frac{\sigma_{s,i}(r)}{4\pi}\int_0^{4\pi} I_i(r,\acute{s})\Phi_{\text{ph}}(r,\hat{s},\acute{s})\, d\acute{\Omega}_{\text{s}} \quad (3.183)$$

In Eq. (3.183), $I_{b,i}$ is the blackbody intensity for gray gas *i* determined by the Planck function calculated from:

$$I_{b,i} = \left[FB\left(n_r,\lambda_{up,i},T\right) - FB\left(n_r,\lambda_{low,i},T\right)\right]n_r^2\frac{\sigma_{st}T^4}{\pi} \quad (3.184)$$

where $FB(n_r,\lambda_i,T)$ is the fraction of blackbody emissive power within a wavelength band from $\lambda_{low,i}$ to $\lambda_{up,i}$ [Modest03], and n_r is the refractive index. Finally, the total radiation intensity *I(r,s)* is the sum of all gray band intensities as:

$$I(r,\hat{s}) = \sum_{i=1}^{N_g}\left[I_i(r,\hat{s})\left(\lambda_{up,i} - \lambda_{low,i}\right)\right] \quad (3.185)$$

In the gray gas formulation, only one RTE of radiation intensity is solved (N_g = 1) and total absorption coefficient κ_T is calculated using equation of total emissivity:

$$\kappa_T = -\frac{\ln(1-\epsilon)}{L_P} \tag{3.186}$$

The path length L is approximated as the mean beam length L_m [Siegel08, Hottel67, Modest03] for an entire uniform isothermal medium volume, which depends on cell volume ∀ and cell surface area A_{surf} in the numerical domain of interest according to:

$$L_m = 0.9\frac{4\cdot\forall}{A_{surf}} \tag{3.187}$$

The mean beam length, L_m, for investigated cases in 100 kW_{th} oxy-fuel furnace (chapter 5) is equal to 0.344 m and in 0.4 MW_{th} oxy-fuel furnace to 0.813 m, respectively. Applying these mean beam length, the total emittances by different WSGG correlations for dry flue gas recirculation (Y_{H2O}/Y_{CO2} = 0.125) are presented in Fig. 3.9 and total absorption coefficients in Fig. 3.10.

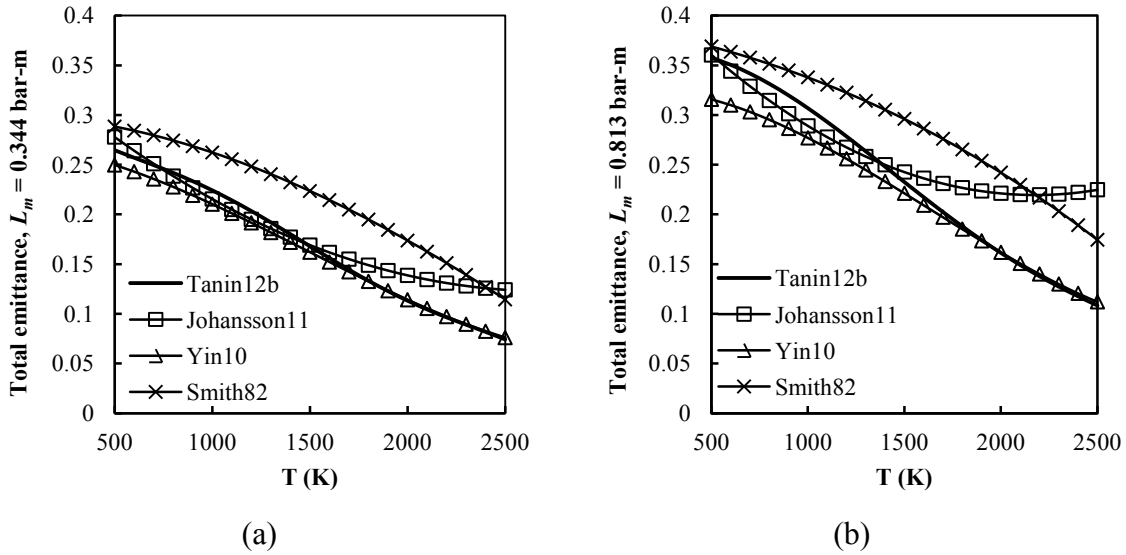

Figure 3.9: Total emittances of gas mixture calculated from different WSGG oxy-fuel correlations varying with gas temperature: (a) L_m = 0.344 m, (b) L_m = 0.813 m (Y_{H2O}/Y_{CO2} = 0.125, P = 1 bar).

If the total emittance from the new oxy-fuel correlations (fitted to HITEMP 2010 database) is used as benchmark for comparison, all predictions of total emittance follow the same trends except correlations from Smith. Total emittance calculated from correlations by Johansson highly deviated from the emittance from new oxy-fuel correlations for temperature above 2000 K. The influence is stronger for the higher path-length than the lower one.

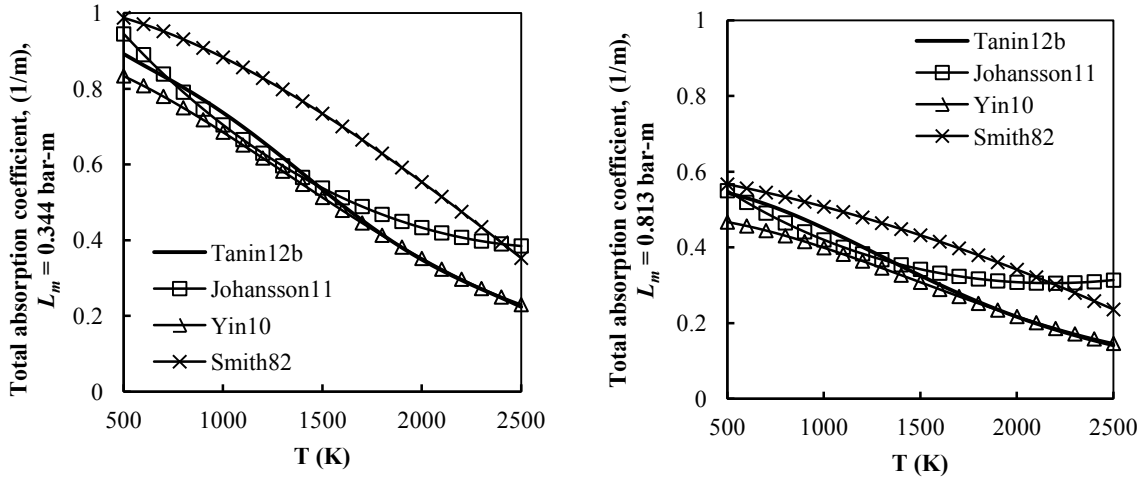

Figure 3.10: Total absorption coefficient of gas mixture calculated from different WSGG oxy-fuel correlations varying with gas temperature: (a) L_m = 0.344 m, (b) L_m = 0.813 m (Y_{H2O}/Y_{CO2} = 0.125, P = 1 bar).

3.7.4 Particles radiation (emissivity and scattering)

Particle emissivity and scattering:

Particle emissivity can be modeled as constant or varied with degree of burnout in pulverized coal flames ranging from 0.6 (carbon particle) to 1.0 (ash particle) as reviewed in chapter 2. The particle emissivity in this thesis is modeled using average value of approximately 0.85 for investigated cases in laboratory-scale oxy-fuel furnace, the same as pilot-scale oxy-fuel simulation presented by Backreedy et al. [Backreedy06]. Without experimental data, the scattering factor of particle is assumed to be equal to 0.6 m^{-1}. The constant particle emissivity and scattering factor are assumed for almost investigated case of small scale oxy-fuel burner. However, in the investigation of different correlations of gas radiation properties for the WSGG model, the particle absorption coefficient is modeled assuming that particle radiation-interaction is dominated by soot radiation.

Soot radiation:

For very small particles as soot, the scattering effect can be negligible [Modest03]. Total soot absorption coefficient (also extinction coefficient) for all optical wavelengths is calculated averaging from Planck-mean and Rosseland-mean absorption coefficient presented by Felske et al. [Felske77] written as:

$$\kappa_s \cong \kappa_{s,mean} = 3.72 f_v C_{s1} T_g C_{s2} \tag{3.188}$$

$$C_{s1} = \frac{36\pi n_s k_s}{\left(n_s^2 - k_s^2 + 2\right)^2 + 4 n_s^2 k_s^2} \tag{3.189}$$

where, κ_s is the total absorption coefficient of soot particle, f_v is the soot volume fraction and C_{s2} is the second Planck function constant (1.4388 cm K). The n_s, k_s is the index of

refraction for soot particle radiation. The averaged value of around 10^{-6} is assumed based on the experiments of turbulent oxy-fuel flame by Voigt [Voigt-MSc07]. The wavelength of important overlapping gas band of 2.7 μm is used as suggested by Felske et al. [Felske73], in the literature review.

The refraction index by Chang [Chang90] was applied for this thesis, valid for the wavelength range between 0.4 μm and 30 μm, expressed in term of wavelength as:

$$n_s = 1.811 + 0.1263 \ln \lambda + 0.027(\ln \lambda)^2 + 0.0417(\ln \lambda)^3 \quad (3.190)$$

$$k_s = 0.5821 + 0.1213 \ln \lambda + 0.2309(\ln \lambda)^2 + 0.01(\ln \lambda)^3 \quad (3.191)$$

Note that λ in these equations are in μm. After substitution all constants, the linear correlations of soot absorption coefficients is illustrated in Fig. 3.11.

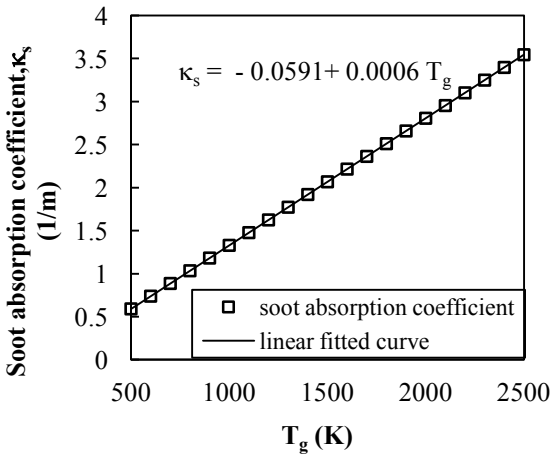

Figure 3.11: Soot absorption coefficients varying with gas temperature.

The total absorption coefficient, κ_g, is determined by rearranging equation of total emittance depending on total emittance, total pressure of gas mixture and mean beam length as:

$$\kappa_g = \frac{-\ln(1-\epsilon_g)}{PL_m} \quad (3.192)$$

Total absorption coefficients including soot radiation, $\kappa_{T,gs}$, is the sum of gas and soot absorption coefficients expressed as:

$$\kappa_{T,gs} = \kappa_g P + \kappa_s \quad (3.193)$$

Total emissivity, $\epsilon_{T,gs}$, including soot radiation is determined by:

$$\epsilon_{T,gs} = 1 - e^{-(\kappa_{T,gs})L_m} \quad (3.194)$$

Where κ_g is the total absorption coefficient of combustion gas mixture (assuming CO_2 and H_2O) calculated by the WSGG model. P is the total pressure of gas based on the unit used for fitting correlations (bar or atm) and L_m is the mean beam length of specific geometry of control volume (furnace).

If the molar fraction of H_2O to CO_2 (Y_{H2O}/Y_{CO2}) of dry recirculation is assumed (MR = Y_{H2O}/Y_{CO2} = 0.125, P = 1 bar) and mean beam length for laboratory scale 100 kW_{th} oxy-fuel furnace (0.344 m) and for pilot-scale 0.4 MW_{th} furnace are used, total absorption coefficients, $\kappa_{T,gs}$, can be determined using the new correlations for WSGG fitted to HITEMP2010 database in chapter 4 and are plotted in Fig. 3.12.

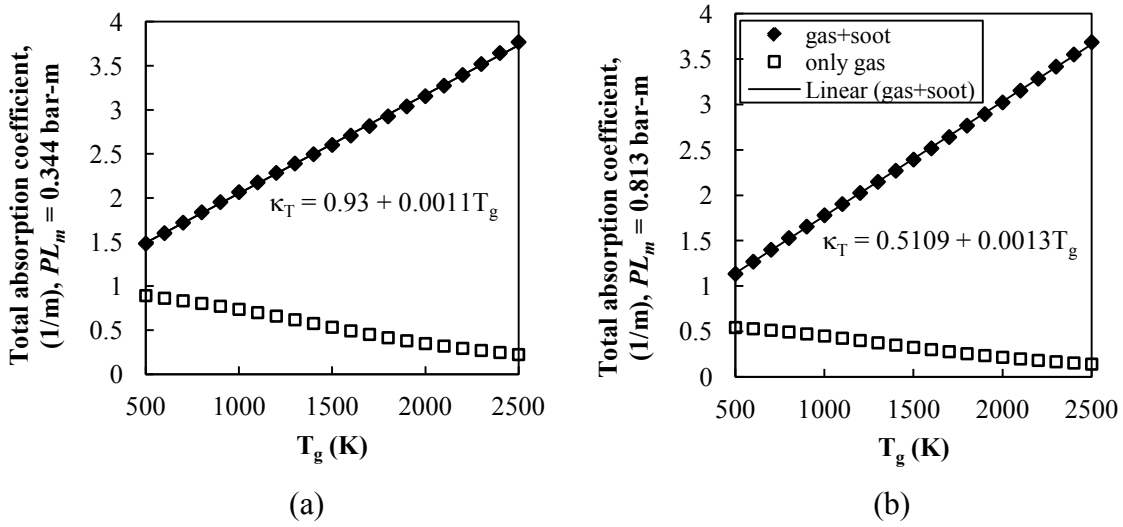

Figure 3.12: Total absorption coefficients with and without soot radiation varying with gas temperature for path-lengths: (a) L_m = 0.344 m, (b) L_m = 0.813 m (MR = Y_{H2O}/Y_{CO2} = 0.125, P = 1 bar), gas absorption coefficients calculated from new oxy-fuel correlations.

From Fig. 3.12, increasing path-length, L_m, resulted in around 50% reduction of gas absorption coefficient, and caused in slightly lower of calculated total absorption coefficients at low temperature (500 K) but merely influenced total approximation at high temperature (1500-2500 K), in which total absorption coefficients have the same trend of linear profile starting from 2.5 m^{-1} at T_g = 1500 K to 3.7 m^{-1} at T_g = 2500 K.

The related total emissivity with and without soot radiation ($\varepsilon_{T,gs}$, ε_g) are shown in Fig. 3.13. From Figs. 3.13(a) and 3.13(b), it is clear that particle radiation (soot radiation here) has highly influence on the calculation of total emissivity, especially in the high temperature-region of furnace such as center of flame core. In contrast, the total emissivity without soot radiation is declining with increasing of temperatures. This implies that particle radiation (soot radiation here) is significant and can dominate the calculation of total emissivity in hot combustion zone of pulverized coal furnace.

It can be clearly seen from Fig. 3.13 that 20-30% increasing of total emissivity is observed for the calculation using higher path-length (L_m = 0.813 m) in pilot-scale furnace. This implies the dependency of approximated total emissivity on specific value of path-

length, and the path-length must be adjusted in CFD model depending on geometry of control volume.

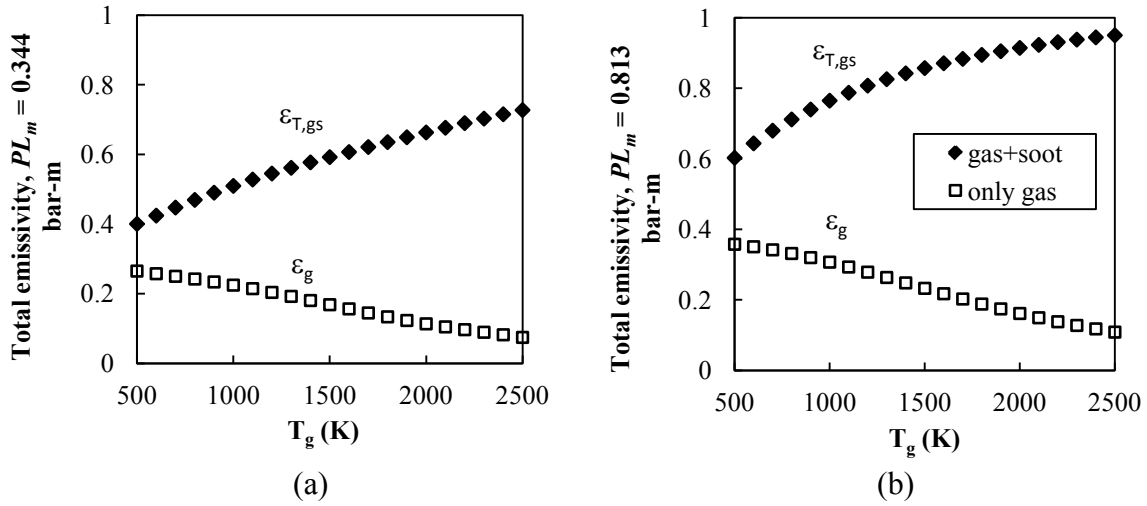

Figure 3.13: Total emissivity with and without soot radiation varying with gas temperature for path-lengths: (a) L_m = 0.344 m, (b) L_m = 0.813 m (MR = Y_{H2O}/Y_{CO2} = 0.125, P = 1 bar), gas emittances calculated from new oxy-fuel correlations.

3.8 Numerical method and solution algorithms

The steady state problem is considered to solve governing equations. For numerical algorithms, many aspects are involved such as discretization schemes, pressure-velocity coupling and iterative algorithms. All aspects are described in the following sub-topics.

3.8.1 Discretization scheme (UPWIND difference)

Various differencing schemes (UPWIND, Power-Law, Central, QUICK, Third-Order MUSCL, and hybrid schemes) have been reviewed in the literature review in chapter 2. The UPWIND scheme is applied for the CFD model in this thesis due to the advantages of numerical stability in coal combustion simulation and not extensive computational time required. The first order UPWIND is used in the first stage of numerical iteration for the calculation of solution. After that, the second order UPWIND is further applied to improve quality of results (better accuracy but higher computational expense) as explained in the review.

The UPWIND scheme is first proposed by Courant [Courant52] and further developed by Gentry et al. [Gentry66], Barakat et al. [Barakat66] and Runchal [Runchal72]. The UPWIND scheme remedies numerical instability in the central differencing scheme to indicate the flow direction [Versteeg07].

3.8.2 Pressure-velocity coupling

Although many algorithms were proposed to solve pressure-velocity coupling such as SIMPLE, SIMPLER and SIMPLEC explained in the literature review, the pressure-velocity coupling in this thesis is solved by the SIMPLE method [Versteeg07, Patankar80] due to the reason given in the review in chapter 2.

The SIMPLE stems from Semi-Implicit Method for Pressure Linked Equations, comprehensively described by Patankar [Patankar72]. The concept of SIMPLE algorithms is to solve discretized momentum equations using the guessed and correct variables for pressure and velocity on the staggered grid. In general, scalar quantities such as pressure, density and temperature are defined at the scalar grid nodes. It is clear that, if the velocities are defined at the same node of ordinary control volume, a highly non-uniform pressure field can sometimes cause in zero-pressure gradient in the momentum equation especially in 'checker-board' problem explained comprehensively by Patankar [Patankar80]. A remedy for this problem addressed is to apply the concept of staggered grid arrangement for velocity [Harlow65]. The concept is to determine scalar variables for flow properties such as density, temperature, pressure at nodal points but to calculate velocity on the staggered grids centered around the cell faces.

3.8.3 Solution algorithms

Iterative methods for discretized equations have been reviewed in the literature review. The *Gauss-Seidel* iterative method is applied in this thesis due to fast convergence, explained clearly in chapter 2. First, a system of N_{eq} equations and N_{un} unknown parameters (for flow variables, $x_{G,j}$) is introduced as:

$$\sum_{j=1}^{N_{un}}\left(a_{ij}x_{G,j}\right) = b_{G,i} \qquad \text{,for } i = 1,2,\dots,N_{eq} \qquad (3.195)$$

The subscript i is the index of equations and j is the index of unknowns. The coefficients $a_{i,j}$ is defined depending on the discretization scheme (UPWIND scheme is applied here). After rearranging set of equations to give only the dependent variable on the left hand side of equations, the iteration equation for the Gauss-Seidel iterative method with relaxation is written as:

$$x_{G,i}^{k} = \sum_{\substack{j=1 \\ j\neq i}}^{i-1}\left[\frac{-a_{ij}}{a_{ii}}x_{G,i}^{k}\right] + UR_{iter}\left(\sum_{\substack{j=1 \\ j\neq i}}^{N_{un}}\left[\frac{-a_{ij}}{a_{ii}}x_{G,i}^{(k-1)}\right] + \frac{b_{G,i}}{a_{ii}}\right)$$

For $i = 1,2,\dots,N_{eq}$ (3.196)

The parameter UR_{iter} is the relaxation parameter. In the Gauss-Seidel iterative method, each unknown is calculated from other updated unknowns, evaluated previously by initial guesses, and all unknowns are determined sequentially from the first to the final unknown. In contrast, the Jacobi method solves all unknowns simultaneously at each iterative step.

It has been explained in the literature review in chapter 2 that more refined meshes reduce the relative error of predictions. However, the convergence rate is also reduced if mesh is further refined. To solve this problem, multi-grid techniques are proposed as reviewed in chapter 2 to accelerate convergence. The details of equation formulation of multi-grid techniques are extensively explained by many authors [Versteeg07-p.229, Chung02-p.651, Brasek05-p.312, Lomax99-ch.10 p.191, Ferziger02-p.344, Tannehil98-p.165].

The algebraic multi-grid (AMG) [Hutchinson86] is applied for numerical algorithms in this thesis due to the reason that the AMG does not require re-discretization of meshes and more suitable for unstructured meshes. The AMS is applied in conjunction with implicit point iterative Gauss-Seidel iterative method to solve linear system of equations.

All investigated sub-models are summarized in Table 3.11.

Table 3.11: Summary of investigated mathematical models for oxy-coal combustion.

Fundamental process	Mathematical models	Reference
1. Formulation of equation	Euler-Lagrange approach	[Smoot79]
2. Turbulent flow	Standard k-ε	[Launder74]
	RNG k-ε	[Yakhot86]
	Realized k-ε	[Shih95]
	SST k-ω	[Menter94]
	RSM	[Launder89]
3. Devolatilization	Chemical percolation devolatilization (CPD)	[Fletcher89-92]
4. Char heterogeneous reactions	Macro-kinetic (without diffusion rate)	[Levenspiel99]
	Kinetic-diffusion limited rate (KD)	[Field76]
	Intrinsic model	[SmithIW82]
5. Volatile reaction mechanism	Global 2 step	[Westbrook81,Dryer73]
	Global 3 step	[Hautman81]
6. Turbulent gaseous reaction	Eddy dissipation model (EDM)	[Spalding71]
	Finite rate-eddy dissipation (FRED)	[Magnussen77]
7. Radiation		
-Solution for RTE	Discrete ordinate method (DOM)	[Chandrasekhar60]
-Gas radiation properties (emissivity)	Weighted sum of gray gases (WSGG) model	[Modest91,SmithTF82]
8. Numerical method		
-Discretization	1st and 2nd order UPWIND scheme	[Courant52,Barth89]
-Iterative algorithm	Implicit Gauss-Seidel	[Ralston78]
-Pressure-velocity coupling	SIMPLE	[Patankar80]

3.9 Boundary conditions for turbulence

The turbulent kinetic energy and its dissipation rate are determined from turbulence length-scale, turbulent intensity and mean flow velocity. The turbulence (characteristic) length-scale, l_{turb}, is defined as the size of the large eddies that contain the energy in turbulent flows. At the starting of the calculations, the turbulence length-scale can be estimated from characteristic length of the duct, D_{duct}, using equation similar to mixing length model as [Versteeg07-p.77]:

$$l_{turb} = 0.07\, D_{duct} \tag{3.197}$$

For fully developed turbulent flows (duct flow), the characteristic length is the hydraulic diameter ($D_{duct} = HD$). The hydraulic diameter, HD, of the simple (full) circular duct and an annulus are defined as [Munson09-p.316]:

$$HD = 4 \times \text{cross-sectional area / wetted perimeter} \tag{3.198}$$

For simple duct: $$HD = \frac{4\pi(r_{outer}^2)}{2\pi(r_{outer})} = \frac{\pi(D_{outer}^2)}{\pi(D_{outer})} = D_{outer} \tag{3.199}$$

For annulus: $$HD = \frac{4\pi(r_{outer}^2 - r_{inner}^2)}{2\pi(r_{outer}+r_{inner})} = \frac{\pi(D_{outer}^2 - D_{inner}^2)}{\pi(D_{outer}+D_{inner})} = (D_{outer} - D_{inner}) \tag{3.200}$$

The turbulence intensity is defined as the average root mean square of velocities divided by a reference mean flow velocity as:

$$I_{turb} = \frac{\sqrt{\frac{1}{3}\left(\overline{u_x'^2} + \overline{u_y'^2} + \overline{u_z'^2}\right)}}{U_m} \tag{3.201}$$

The mean kinetic energy per unit mass is written as:

$$k = \frac{1}{2}\left(\overline{u_x'^2} + \overline{u_y'^2} + \overline{u_z'^2}\right) \tag{3.202}$$

Combining two equations above, giving the relation between the turbulence intensity and kinetic energy

$$I_{turb} = \frac{\sqrt{\frac{2}{3}k}}{U_m} \tag{3.203}$$

Therefore the kinetic energy is determined by:

$$k = \frac{3}{2}(U_m I_{turb})^2 \tag{3.204}$$

The dissipation rate at the initial calculation is estimated as in the formulation of standard k-ε equation as:

$$\varepsilon = C_\mu^{3/4} \frac{k^{3/2}}{l_{turb}} \tag{3.205}$$

where $C_\mu = 0.09$ for the standard k-ε turbulent model.

The turbulent intensity at the core of fully developed duct flow is estimated from empirical correlation as:

$$I_{turb} = 0.16\left(Re_{HD}{}^{-1/8}\right) \tag{3.206}$$

The Reynolds number, Re_{HD}, is calculated based on the characteristic length (HD).

$$Re_{HD} = \frac{U_m HD}{kinematic\ viscosity} \tag{3.207}$$

3.10 Particle size distribution (Rosin-Rammler method)

At the projected face of inlet flow (primary inlet), many types of injections can be defined, for example, single, group and surface injections. Using less injections and maintaining coal feed rate results in unphysical peak temperature in the infinitesimal region. A good approach is to define injections as group or through project faces of flow boundaries. For each group injection or each injection at one projected cell-face, particle diameters can be uniform or defined by size distribution data fitted to measurement from sieve analysis. One of efficient mathematical relations to described particle distribution is proposed by Rosin and Rammler [Rosin33] and further applied to liquid droplets by Bailey et al. [Bailey83]. In the Rosin-Rammler diameter distribution method, the mass fraction of particles with diameter greater than any diameter d_p , Y_{dp}, is expressed by:

$$Y_{dp} = e^{-(d_p/\bar{d}_p)^{n_{RR}}} \tag{3.208}$$

Where $\bar{d}_p$ is the mean diameter calculated at which $Y_{dp} = e^{-1} \approx 0.368$.

The size distribution parameter, n_{RR}, is usually dependent of both Y_{dp} and d_p, determined using relation:

$$n_{RR} = \frac{\ln(-lnY_{dp})}{ln(d_p/\bar{d}_p)} \tag{3.209}$$

The Y_{dp} is the function of any diameter d_p and can be obtained from measurements by sieve analysis, which is treated as independent variables. The value of n_{RR} is approximated by averaging values from all possible n_{RR} as:

$$n_{RR} \cong \bar{n}_{RR} = average(n_{RR}) \tag{3.210}$$

4 Modeling of Radiation Properties

Radiation properties of combustion gases in oxy-fuel conditions differs from the properties in air-fired conditions due to higher amount of CO_2 and H_2O of product species as explained in the review of radiation models in chapter 2. This chapter describes the process on how to create a new set of correlations for WSGG model under variations of H_2O and CO_2 gases in oxy-fuel conditions. The new oxy-fuel correlations for WSGG models are created in the way that the emissivity calculated by WSGG models is fitted to emissivity charts generated by line-by-line (LBL) calculation from the new HITEMP 2010 database. The emissivity charts from LBL calculation are generated at different molar fraction of H_2O to CO_2 (MR = Y_{H2O}/Y_{CO2}) from MR of 0.125 to 4 and pressure path-length of absorbing gases (P_aL) between 0.001 and 60 bar-m.

The mathematical modeling including equations of emissivity of gases for WSGG model has been explained in chapter 3. In oxy-fuel conditions, only the parameters related to emissivity weighting factor w_i (or fraction of blackbody radiation) and absorption coefficients κ_i of each i gray gas are of interest. However, the ratio of molar fraction (MR) is needed to be maintained during fitting process of new correlations under oxy-fuel conditions. All calculations from the following process of obtaining correlations are based on specific molar ratios MR evaluated at a total pressure of 1 bar written in Table 4.1.

Table 4.1: Ratios of molar fraction under oxy-fuel conditions (P_t = 1 bar).

Ratio of molar fraction		Total molar fraction	Gas molar fraction		Percentage of gas	
Y_{H2O}: Y_{CO2}	MR = Y_{H2O}/Y_{CO2}	$Y_t = Y_{H2O}+Y_{CO2}$	Y_{H2O}	Y_{CO2}	% H_2O	% CO_2
1:8	0.125	1	0.11111	0.88889	11.11	88.89
1:4	0.25	1	0.2	0.8	20	80
1:2	0.5	1	0.33333	0.66667	33.33	66.67
3:4	0.75	1	0.42857	0.57143	42.86	57.14
1	1	1	0.5	0.5	50	50
2	2	1	0.66667	0.33333	66.67	33.33
4	4	1	0.8	0.2	80	20

From the table, it is noted that the molar ratio MR of 0.125 refers to the case of dry flue gas recirculation (dry-FGR), while MR of 1 refers to the case of wet flue gas recirculation (wet-FGR) in oxy-fuel conditions.

The molar ratio MR is maintained during fitting the new correlations for WSGG models. Procedure to create the new correlations for WSGG model by fitting emissivity to LBL calculation using HITEMP 2010 database are briefly written here as follow

1. Generate spectral absorption coefficients κ_η of individual gas (CO_2 or H_2O) by LBL calculation.
2. Determine spectral absorption coefficients of mixture $\kappa_{\eta,mix}$.

3. Using $\kappa_{\eta,mixture}$ from step 2 to create emissivity charts for mixture by varying molar fraction (MR) in oxy-fuel conditions as listed in Table 4.1 and path-lengths varies from 0.001 – 60 bar-m which covers range of oxy-fuel combustion.
4. Fit total emissivity from correlation ϵ_{WSGG} to total emissivity from HITEMP 2010 database ϵ_{HITEMP} by minimizing least square error and adjusting absorption coefficients κ_i and emissivity weighting factor w_i using number of gray gases N_g.

The final obtained correlations for WSGG model (κ_i, w_i) were evaluated by the benchmark of one-dimensional parallel infinite plates calculated by LBL calculation which will be explained in the last section (section 4.3) of this chapter. The spectral line-by-line absorption cross section were calculated by using supercomputer "CESUP" available at The Federal University of Rio Grande do Sul (UFRGS) at Brazil. The spectral line-by-line calculations were performed by author of this thesis under collaboration and financial support by DAAD-PROBRAL research program and supervision by Prof. Francis Henrique Ramos Franca, the head of radiation research group of the Thermal Science and Energy Research Group (GESTE) at UFRGS.

The new correlations were subsequently implemented into mathematical models of lignite oxy-fuel combustion using CFD as tool to calculate total emissivity of gaseous mixture under oxy-fuel conditions to provide the predictions of solutions (chapter 6) for radiative transfer equation (RTE) such as wall heat transfer (q_{wl}, kW/m^2) and radiative source term ($\dot{\boldsymbol{q}}$, kW/m^3) for two investigated oxy-fuel cases (described in chapter 5).

4.1 Line-by-line (LBL) calculation with HITEMP 2010 database

4.1.1 HITEMP 2010 database

HITEMP 2010 is a new molecular spectroscopic database at high-temperature (valid at temperature above 1000 K) [Rothman10] developed from previous version of HITEMP 1995 [Rothman95] and HITRAN (**HI**gh-resolution **TRAN**smission) molecular spectroscopic database [Rothman87-09]. Nowadays, the HITEMP 2010 database has been recognized as the international standard for providing the necessary fundamental spectroscopic parameters for diverse atmospheric and laboratory transmission and radiance calculations. HITEMP database resolved the drawback of HITRAN database by including many missing excited state spectral transitions called 'hot lines'. The HITEMP 2010 is a modification of HITEMP 1995 by including additional H2O spectral lines at high temperature by BT2 database [Barber06] and also CO_2 spectral lines at high temperature by CDSD-1000 database [Tashkun03,08]. The HITEMP 2010 database is based on measurements and theoretical calculations, while some spectral lines of the HITEMP 1995 database are calculated from the extrapolation for excited states without experimental basis. The HITEMP 2010 contains 111 million transitions for H_2O with a spectral coverage of 0-30,000 cm^{-1}, and of 11 million for CO_2 with a spectral coverage of 258 – 9648 cm^{-1} [Rothman10]. Number of spectral molecular transitions from the new HITEMP 2010 database and all previous versions are compared in the Table 4.2.

Table 4.2: Number of spectral molecular transitions from HITRAN and HITEMP databases.

	HITRAN				HITEMP	
Year	1992	1996	2004	2008	1995	2010
H_2O	48,523	49,444	63,196	69,201	1,174,009	111,377,777
CO_2	60,790	60,802	62,913	312,479	1,032,269	11,167,618

4.1.2 Line-by-line (LBL) calculations

Line-by-line (LBL) calculations allow precise solution of the radiation heat transfer through the integration of all absorption lines that form the spectrum. This task requires the knowledge of the spectral absorption coefficients κ_η, which can be formulated by the following equation:

$$\kappa_\eta = N_{mol} \sum_q LI_q(T) f_q(\eta) \tag{4.1}$$

where LI_q is the line intensity and $f_q(\eta)$ is a line shape function of the q^{th} transition line [Rothman98]. N_{mol} is the number density of the absorbing molecules of the participating gases (CO_2 or H_2O in this work), which can be calculated from the ideal gas state equation:

$$(P_a/1.01325)V_a = N_a k_B T \tag{4.2}$$

$$k_B = \frac{R}{A_v} \tag{4.3}$$

where R is the gas constant (= 82.05746 cm^3 atm mol^{-1} K^{-1}) and k_B is the Boltzmann constant (1.3807 × 10^{-23} J/K); P_a and V_a are the partial pressure and volume of the absorbing gases; N_a is the number of particles in the gas and A_v is the Avogadro constant, equal to 6.02214179 × 10^{23} molecules/mole. In Eq. (4.2), the number of 1.01325 is a conversion factor to change the units of P_a in bar to atm, which is the basic unit for LBL calculations in the HITEMP 2010 database. From the definition, N_{mol} is equal to N_a / V_a and, after substitution k_B from Eq. (4.3) to Eq. (4.2), one finds that:

$$N_{mol} = \left(\frac{A_v}{R}\right)\left(\frac{(P_a/1.01325)}{T}\right) = (7.3389327 \times 10^{21})\left(\frac{(P_a/1.01325)}{T}\right) \tag{4.4}$$

The line intensity LI_q at temperature T is expressed as: [Rothman98]

$$LI_q(T) = LI_q(T_0)\frac{Q(T_0)}{Q(T)}\frac{\left[1-\exp\left(-\frac{hc\eta}{k_B T}\right)\right]}{\left[1-\exp\left(-\frac{hc\eta}{k_B T_0}\right)\right]}\frac{\exp\left(-\frac{hcE_s}{k_B T}\right)}{\exp\left(-\frac{hcE_s}{k_B T}\right)} \tag{4.5}$$

where h, c are the Planck constant (6.626 × 10^{-34} J s) and the speed of light in vacuum (2.998 × 10^8 m/s), respectively. E_s is the lower state energy of the transition; T_0 is the ref-

erence temperature (T_0 = 296 K) [Rothman98]. The total internal partition sum for a specific temperature T, denoted as $Q(T)$, [Gamache90] is used in Eq. (4.5) to account for how the molecules in thermodynamic equilibrium are distributed among the various energy states. The calculation of the total internal partition sum, at each temperature under consideration, involves a summation over thousands of energy levels and can be very time consuming. For this reason, $Q(T)$ is approximated for each specific molecular specie for temperatures between 70 and 3000 K by a FORTRAN program called TIPS2008 [Fischer03] using the Lagrange 4-point interpolation to minimize the possibility of constants producing error in the final partition sums. $Q(T)$ for 38 molecular species including CO_2 and H_2O in TIPS2008 are calculated by the product of rotational and vibrational partition functions Q_{rot} and Q_{vib} as [Fischer03]:

$$Q(T) = Q_{rot}(T) \times Q_{vib}(T) \tag{4.6}$$

where the rotational and vibrational partition functions are written as:

$$Q_{rot}(T) = DF_{ind} \sum_{rota} \left[DF_{rota} \exp\left(\frac{-E_{rot}}{k_B T}\right) \right] \tag{4.7}$$

$$Q_{vib}(T) = \prod_{vib} \frac{1}{1 - \exp\left(\frac{hcE_{vib}}{k_B T}\right)} \tag{4.8}$$

in which DF_{rot} is the degeneracy of the rotational state of energy E_{rot}; DF_{ind} is the state-independent degeneracy factor; E_{vib} is the vibrational state of energy.

At higher pressure than 1.0 bar ($P \geq 1.0$ bar) and temperature lower than 2000 K, collision broadening dominates [Modest03], and the line shape profile $f_q(\eta)$ is assumed to follow a Lorentz profile as:

$$f_q(\eta) = \frac{1}{\pi} \frac{\gamma_q}{\left[{\gamma_q}^2 + (\eta - \eta_q)^2 \right]} \tag{4.9}$$

where η_q is the wavenumber at line center of transition q_{th}. For each spectral line transition q^{th}, γ_q is the pressure broadened line half-width, which is given by:

$$\gamma_q(P, P_a, T) = \left(\frac{T_0}{T}\right)^{n_{air}} \left[\gamma_{air,q}(P_0, T_0)(P - P_a) + \gamma_{self,q}(P_0, T_0) P_a \right] \tag{4.10}$$

where P_0 and T_0 are the reference pressure and temperature (P_0 = 1 atm and T_0 = 296 K) [Rothman98]; $\gamma_{air,q}$ and $\gamma_{self,q}$ are the air-broadened half-width at half maximum and the self-broadened half-width at line transition q^{th}, respectively; P_a is the partial pressure of absorbing gas and n_{air} is the coefficient of temperature dependence of the air-broadened half-width. From all previous equations, the spectral absorption coefficient κ_η of the mixture expressed in Eq. (4.1) depends only on the partial pressure P_a (= $Y_a P$), the total pressure P and the gas temperature T. Neglecting the overlap between the lines, the spectral absorption coefficient of the mixture is computed by the summation of the coefficients of each gas:

$$\kappa_{\eta,mixture} = \kappa_{\eta,H_2O} + \kappa_{\eta,CO_2} \tag{4.11}$$

In oxy-fuel conditions, the molar fraction ratios of H_2O to CO_2 (MR = Y_{H2O}/Y_{CO2}) vary from less than 1.0 (for instance MR = 0.125, 0.25, 0.5 and 0.75), a condition that is referred to as dry flue gas recirculation (dry-FGR), to equal to or more than 1.0 (for instance, MR = 1.0, 2.0 and 4.0), which is known as wet flue gas recirculation (wet-FGR). Spectral absorption coefficients κ_η for each absorbing gas (H_2O and CO_2 in this paper) are calculated over the range of temperature between 400 and 2500 K, a range that covers temperatures in most of combustion applications. In this research, LBL calculations are conducted using spectral resolution of 0.067 cm^{-1} (= 0.067 cm^{-1}) for wavenumber ranging from 0.000001 to 10000 cm^{-1}. The total pressure P for all LBL calculations is set equal to 1.0 bar (P = 1.0 bar) while molar fractions Y_{H2O} and Y_{CO2} that are considered in this work are listed in Table 4.3.

Table 4.3: Molar fraction ratios (MR) for oxy-fuel conditions.

Recycle mode	MR	Y_{H2O}	Y_{CO2}
Dry	0.125 (1:8)	0.11111	0.88889
	0.25 (1:4)	0.2	0.8
	0.5 (1:2)	0.33333	0.66667
	0.75 (3:4)	0.42857	0.57143
Wet	1.0	0.5	0.5
	2.0	0.66667	0.33333
	4.0	0.8	0.2

4.2 RTE for one-dimensional infinite plates

The RTE for an emitting-absorbing and non-scattering medium is written as: [Modest03]

$$\frac{\partial I_\eta(r,\hat{s})}{\partial s} = \kappa_\eta I_{b,\eta}(r) - \kappa_\eta I_\eta(r,\hat{s}) \tag{4.12}$$

subjected to boundary conditions for diffusely emitting and reflecting opaque surfaces:

$$I_\eta(r_{wl},\hat{s}) = \varepsilon(r_{wl}) I_{b,\eta} + \frac{(1-\varepsilon(r_{wl}))}{\pi} \int_{\hat{n}\cdot\acute{s}<0} I_\eta(r_{wl},\acute{s})|\hat{n}\cdot\acute{s}|d\acute{\Omega}_s \tag{4.13}$$

where r is a vector of coordinate for location; $I_{b,\eta}$ is a blackbody intensity; $\hat{n}$ is the normal vector outward the wall surface; $\epsilon(r_{wl})$ is the emittance of the wall element at location r_{wl}; $\acute{s}$ is the incoming direction; and $\acute{\Omega}_s$ is the solid angle in the direction of $\acute{s}$. The total intensity I for a specific path-length L is given by the integration of the spectral intensity over the entire wavenumber spectrum:

$$I(L) = \int_\eta \left[I_{b,\eta}(1 - \exp(-\kappa_\eta L)\right] d\eta \tag{4.14}$$

Total emittance is defined as the ratio between the total intensity I in Eq. (4.14) and the total intensity I_b of a blackbody at the same temperature of the medium:

$$\epsilon(L) = I(L)/I_b \tag{4.15}$$

where the total blackbody intensity is well known presented by:

$$I_b = \frac{\sigma T^4}{\pi} \tag{4.16}$$

in which σ is the Stefan-Boltzmann constant (5.67×10^{-8} W/(m^2 K^4)). Spectral radiation intensity I_η is solved from RTE in Eq. (4.12) by the discrete ordinate method (DOM) [Siegel08, Hottel67] for one-dimensional infinite parallel plates. The RTE for spectral radiation intensity I_η is divided into two sets of differential equation in positive ($\mu_{DO,l} > 0$) and negative direction ($\mu_{DO,l} < 0$) as:

$$\mu_{DO,l} \frac{\partial I_\eta^+(x,\mu_{DO,l})}{\partial x} = -\kappa_\eta(x) I_\eta^+\left(x, \mu_{DO,l}\right) + \kappa_\eta(x) I_{b,\eta}(T(x)) \tag{4.17}$$

$$\mu_{DO,l} \frac{\partial I_\eta^-(x,\mu_{DO,l})}{\partial x} = -\kappa_\eta(x) I_\eta^-\left(x, \mu_{DO,l}\right) + \kappa_\eta(x) I_{b,\eta}(T(x)) \tag{4.18}$$

with discrete boundary conditions:

$$I_\eta^+\left(x_0, \mu_{DO,l}\right) = \epsilon(x_0) I_{b,\eta}(T(x_0)) + 2(1-\epsilon(x_0)) \sum_{l=1}^{N_w} \left[w_{DO,l} \mu_{DO,l} I_\eta^-\left(x_0, \mu_{DO,l}\right)\right] \tag{4.19}$$

$$I_\eta^-\left(x_L, \mu_{DO,l}\right) = \epsilon(x_L) I_{b,\eta}(T(x_L)) + 2(1-\epsilon(x_L)) \sum_{l=1}^{N_w} \left[w_{DO,l} \mu_{DO,l} I_\eta^+\left(x_L, \mu_{DO,l}\right)\right] \tag{4.20}$$

where $\mu_{DO,l}$ and $w_{DO,l}$ are the ordinates and quadrature weights; x_0 and x_L are the location of boundary walls at $x = 0$ and $x = L$ and $\epsilon(x_0)$ and $\epsilon(x_L)$ are wall emissivities at each location, respectively. The solid angle was discretized into a finite number of equidistant ordinates, composed of fifteen ordinates for positive directions and other fifteen ordinates for negative directions. Gaussian quadrature was used in which the weights were adjusted for best estimation of integral over the full range of solid angles. In this paper, both surfaces are black, $\epsilon(x_0) = \epsilon(x_L) = 1$. Therefore, the second terms on the right of Eqs. (4.19) and (4.20) are omitted and the boundary conditions are:

$$I_\eta^+\left(x_0, \mu_{DO,l}\right) = I_{b,\eta}(T(x_0)) \tag{4.21}$$

$$I_\eta^-\left(x_L, \mu_{DO,l}\right) = I_{b,\eta}(T(x_L)) \tag{4.22}$$

The one-dimensional slab is discretized into N_{mesh} computational cells with index m for any node location. Finally, solution of the positive and negative radiation intensities for each ordinate μ_l (cosine direction) and each wavenumber η are:

$$I_{\eta,l}^+\left(x_m, \mu_{DO,l}\right) = \frac{\mu_l I_{\eta,l}^+\left(x_{m-1}, \mu_{DO,l}\right) + \kappa_\eta(x_m) I_{b,\eta}(T(x_m)) \Delta x_{m-1/2}}{\mu_{DO,l} + \kappa_\eta(x_m) \Delta x_{m-1/2}} \tag{4.23}$$

$$I_{\eta,l}^-\left(x_m, \mu_{DO,l}\right) = \frac{\mu_l I_{\eta,l}^+\left(x_{m+1}, \mu_{DO,l}\right) + \kappa_\eta(x_m) I_{b,\eta}(T(x_m)) \Delta x_{m+1/2}}{\mu_{DO,l} + \kappa_\eta(x_m) \Delta x_{m+1/2}} \tag{4.24}$$

In this study, the distance between one-dimensional infinite plates is divided into 100 uniformly computational cell (N_{mesh} = 100), with thirty ordinates and quadrature weights (N_w = 30). The net radiative heat flux $q_{r,m}$ and radiative source term $\dot{q}_{m,x}$ at any node location in the numerical mesh *m* are given by [Hottel67, Chandrasekhar60]:

$$q_{r,m} = 2\pi \sum_{l=1}^{N_w} \left[w_{DO,l} \mu_{DO,l} \left(I_{\eta,l}^{+}(x_m, \mu_{DO,l}) - I_{\eta,l}^{-}(x_m, \mu_{DO,l}) \right) \right] \tag{4.25}$$

$$\dot{q}_{m,x} = 2\pi \sum_{l=1}^{N_w} \left[w_{DO,l} \left(I_{\eta,l}^{+}(x_m, \mu_{DO,l}) - I_{\eta,l}^{-}(x_m, \mu_{DO,l}) \right) \right] - 4\pi \kappa_{\eta}(x_m) I_{b,\eta}(T(x_m)) \tag{4.26}$$

4.3 New correlations for WSGG model

Emittance charts generated by LBL-HITEMP 2010 for different temperatures at three pressure path-length of 1.0, 10, 60 bar-m for MR = 0.125-4.0 are plotted in Fig. 4.1. Observing Fig. 4.1, it is clear that, for pressure path-length product of 1.0 bar-m, the effect of the molar ratios MR on the emittance calculations for lower temperature (400 to 1500 K) are more important than for higher temperatures (1500 to 2500 K). On the other hand, for higher pressure path-lengths (*PL* = 10 and 60 bar-m), in which the effect of the ratio MR at high temperature (1000 to 2500 K) are more important than for lower (400 to 1000 K).

New correlations of the WSGG model in oxy-fuel conditions were created in this work by fitting to total emissivity calculated by LBL calculation from HITEMP 2010 database. Equation's formulation for WSGG model described in chapter 3 of this thesis is used as basis for creating the new correlations.

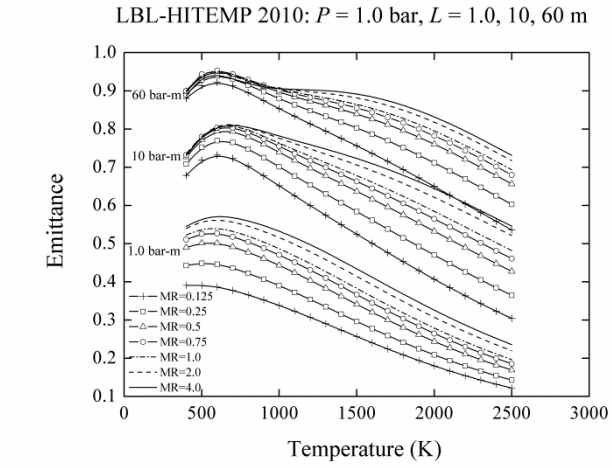

Figure 4.1: Total emittance calculated from LBL integration of HITEMP 2010 database for different MR and path-lengths of 1.0, 10 and 60 bar-m.

In general, the weighting factors w_i are assumed to be a temperature dependent polynomial function of order (N_c-1) [SmithTF82, Modest03, Hottel67]:

$$w_i = \sum_{j=1}^{N_c} b_{i,j} T^{j-1} \qquad i = 1,2,\dots,N_g \tag{4.27}$$

where $b_{i,j}$ are the coefficients of the polynomial functions.

In the determination of the correlations proposed by Smith et al. [SmithTF82], the parameters $b_{i,j}$ depends on unit of temperature and therefore were expressed in number of three-decimal digits (0.001) multiplied by a power of 10, 10^4, 10^7, 10^{11} for each j polynomial coefficient as presented in Smith et al. [SmithTF82], which is caused by operating temperature in furnace in the range of 600-2400 K. Hence, this resulted in different precision of $b_{i,j}$ for each j polynomial coefficient while it should be in the same level of accuracy. It has been suggested by some authors [Yin10, Johansson10] that the relative error of the WSGG model prediction can be minimized by normalizing the temperature with specific reference temperature, T_{ref}. With this formulation, all temperature dependent polynomial coefficients turn to be dimensionless and have the same order of magnitude and accuracy. Therefore, the weighting factors in this research are also calculated with the use of a temperature-dependent relation normalized by T_{ref} written as:

$$w_i = \sum_{j=1}^{N_c} c_{i,j} \left(\frac{T}{T_{ref}}\right)^{j-1} \qquad i = 1,2,\dots,N_g \tag{4.28}$$

where $c_{i,j}$ are the temperature dependent polynomial coefficients, which are dimensionless. The polynomial coefficients $c_{i,j}$, the absorption coefficients κ_i, the number of gray gases N_g, the number of polynomial coefficients N_c and the reference temperature T_{ref} were determined by the minimization of the relative errors between the total emittance calculated by correlations obtained in this research and by the LBL integration of the spectral lines generated from the HITEMP 2010 database.

For a specific molar ratio MR, only one set of polynomial coefficients $c_{i,j}$ and absorption coefficient κ_i is obtained. However, these coefficients could be related to MR as reported in the work of Johansson et al. [Johansson11] with another type of correlations such as:

$$c_{i,j} = C1_{i,j} + C2_{i,j} MR + C3_{i,j} MR^2 \tag{4.29}$$

$$\kappa_i = CK1_i + CK2_i MR + CK3_i MR^2 \tag{4.30}$$

The molar ratio of H_2O to CO_2 is given by:

$$MR = Y_{H_2O} / Y_{CO_2} \tag{4.31}$$

It has been observed that the molar ratio dependent polynomial coefficients in Eqs. (4.29) and (4.30) of order two provide the best fitting to both the polynomial coefficients $c_{i,j}$ and the absorption coefficient κ_i at all molar ratios MR ranging from 0.125 to 4.0. As shown in Fig. 4.2, the second order molar ratios polynomial coefficients is required to fit correlations of the total emittance from LBL calculations using HITEMP 2010 database. On the other hand, a linear equation was enough for a good fitting of the SNB model using HITRAN 1992 database according to Johansson et al. [Johansson11].

Total emittance at molar ratios of H_2O/CO_2 (MR) between 0.125-4 were generated from LBL calculations of HITEMP 2010 database for temperatures between 400-2500 K and pressure path-lengths from 0.001-60 bar-m, and used as reference to determine the new correlations for oxy-fuel conditions. To determine the correlations, a non-linear multiple regression analysis was carried out. The Levenberg-Marquardt (LM) algorithm [Levenberg94, Marquardt63] and non-linear multiple regression analysis was applied in this research. The LM algorithm is a combination of the steepest descent and the Gauss-Newton method [Nocedal06], which is similar to the steepest descent when the solution is far from the solution, and turns to be a Gauss-Newton method when the solution is close to the correct one.

The procedure to fit correlations with total emittances from LBL-HITEMP 2010 database is outlined below:

1) Emittance charts at a specific molar ratio of H_2O to CO_2 (MR) were calculated by varying temperatures from 400 to 2500 K and pressure path-length from 0.001 to 60 bar-m. Seven charts were created at MR = 0.125, 0.25, 0.5, 0.75, 1, 2, 4 and all charts were based on the pressure of 1.0 bar.

2) To approximate the absorption coefficients of all gray gases κ_i, the Levenberg-Marquardt (LM) algorithm was applied to the summation of total emittances that were generated from LBL integration of HITEMP 2010 database for all temperatures determined by Eq. (4.15) at specific MR. The number of gray gases N_g must be fixed before determining the weighting factor w_i. The summation of the total emittances are expressed applying Eq. (3.179) at specific pressure path-length of L_p as:

$$\epsilon_{ip} = \sum_{t=1}^{N_t} \epsilon_{t,ip} = \sum_{i=1}^{N_g} \left[\left(\sum_{t=1}^{N_t} w_{i,t,ip} \right) \left(1 - \exp(-\kappa_i P_a L_{ip}) \right) \right] \qquad (4.32)$$

for $ip = 1,2, \dots, N_p$

The subscript t and ip represent index of each temperature and pressure path-length. N_t and N_p are the number of temperatures and path-lengths used in the calculation. A total number of 22 temperatures (N_t = 22) were employed in this work in the range of 400 to 2500 K with an increment of 100 K. The number of path-lengths N_p depends on the number of unknowns that needs to be solved in the non-linear minimization problem. For four gray gases (N_g = 4), the problem contains eight unknowns, which are four unknowns for absorption coefficients κ_1, κ_2, κ_3 and κ_4 and other four unknowns for the summations of the weighting factors over all temperatures $\sum_{t=1}^{N_t} w_{1,t,ip}$, $\sum_{t=1}^{N_t} w_{2,t,ip}$, $\sum_{t=1}^{N_t} w_{3,t,ip}$ and $\sum_{t=1}^{N_t} w_{4,t,ip}$. It should be noted that number of pressure path-lengths in the calculations of the LM algorithm must be higher than the number of unknowns related to the number of gray gases (N_g) here. This requires at least eight equations ($N_p \geq 8$) to solve the set of non-linear equations. To ensure the best fitted correlations for all path-lengths in combustion atmospheres, twenty one path-lengths (N_p = 21) were used in this work in the range of 0.001-60 bar-m. It should be emphasized again that this step focuses only on acquiring absorption coefficients for all gray gases, κ_i.

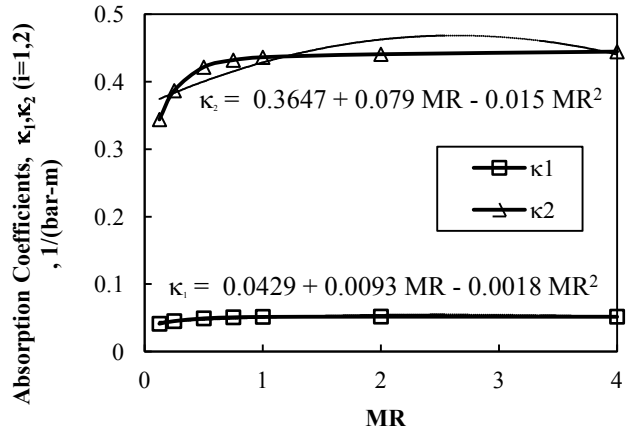

(a)

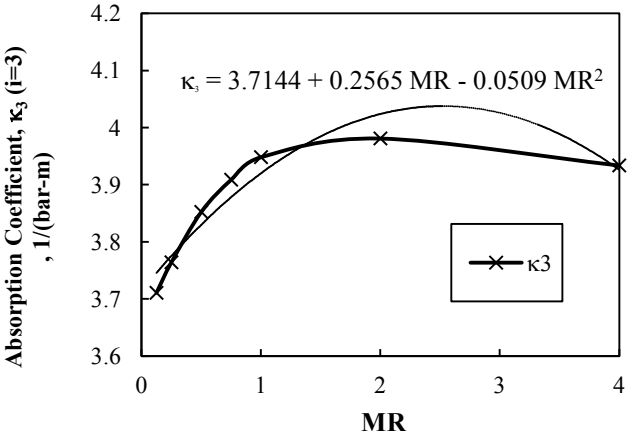

(b)

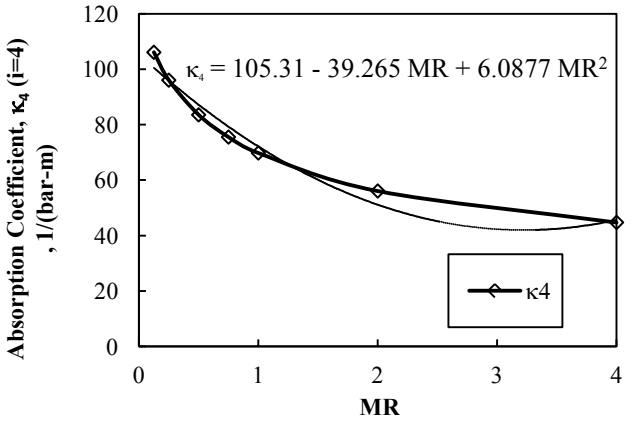

(c)

Figure 4.2: Absorption coefficients of each gray gas from the new correlations for WSGG model using the second order molar ratios dependent polynomial coefficients in Table 4.4 (dashed lines), comparing to absorption coefficients from the proposed correlations in Tables 4.5 and 4.6 (solid lines with symbols).

3) After κ_i is determined from step 2 for one specific MR, the weighting factors w_i are determined at specific temperature of index t by varying path-length of index p. The number of equations are still equal to the number of path-lengths (N_p) as:

$$\epsilon_{t,ip} = \sum_{i=1}^{N_g}\left[w_{i,t,ip}\left(1-\exp(-\kappa_i P_a L_{ip})\right)\right] \qquad ip = 1,2,\ldots,N_p \tag{4.33}$$

If $N_g = 4$, the problem contains four unknowns for the weighting factors $w_{1,t}$, $w_{2,t}$, $w_{3,t}$ and $w_{4,t}$ at each temperature and 21 equations ($N_p = 21$) to be solved. For $N_p \geq 4$, the solution of the system of equations can be achieved by the LM algorithm.

4) The temperature dependent polynomial coefficients $c_{i,j}$ were fitted to the weighting factors w_i calculated from step 3 using Eq. (4.28) and the non-linear multiple regression analysis.

5) The molar ratio dependent polynomial coefficients $C1_{i,j}$, $C2_{i,j}$, $C3_{i,j}$, $CK1_i$, $CK2_i$ and $CK3_i$ were fitted using $c_{i,j}$ and κ_i calculated from step 3 and 4 in Eqs. (4.29) and (4.30) and the non-linear multiple regression analysis.

In the procedure of fitting correlations, the number of gray gases N_g was chosen to be 3 and 4, the number of polynomial coefficients N_c was set as 4, 5 and 6, and the reference temperature T_{ref} was taken as 1000, 1200, 1450, 2000 and 2500 K. It was found that increasing the number of gray gases improved the accuracy of the correlations for all path-lengths while using more polynomial coefficients provided better curve fitting through all the range of operating temperatures T. After evaluation, $N_g = 4$, $N_c = 6$ and $T_{ref} = 2000$ K resulted in the best fitting of correlations for the total emittance that was generated from the LBL integration of the HITEMP 2010 database for all molar ratios MR.

The weighting factors $w_{1,t}$, $w_{2,t}$, $w_{3,t}$ and $w_{4,t}$ varying with temperatures from 400-2500 K for MR = 0.125 and MR = 1.0 calculated in step 3) are shown in Fig. 4.3. The weighting factors for other values of MR are also presented in Tables C.1-C.3 and Figs. C.1 and C.2 in Appendix C.

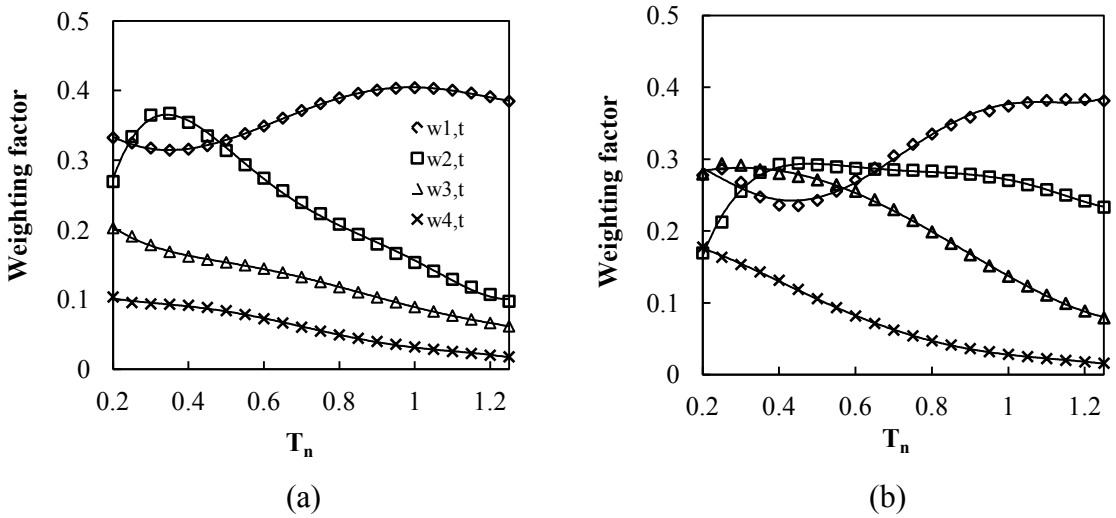

Figure 4.3: The plots of weighting factors $w_{1,t}$, $w_{2,t}$, $w_{3,t}$ and $w_{4,t}$ varying with normalized temperatures (T_n), $T_{ref} = 2000$ K (solid line = polynomial fitted curves, symbol = values evaluated for each gas temperature, T) for: (a) MR = 0.125, (b) MR = 1.0.

The temperature dependent polynomial coefficients $c_{i,j}$ and the absorption coefficients κ_i for four gray gases and the transparent window are listed in Table 4.4. The molar ratio dependent polynomial coefficients of the absorption coefficients ($CK1_i$, $CK2_i$ and $CK3_i$) and weighting factors ($C1_{i,j}$, $C2_{i,j}$ and $C3_{i,j}$) are presented in Table 4.5 and Table 4.6, respectively. T_{ref} was selected from the evaluation of the deviation of the total emittance from the LBL integration of HITEMP 2010 in Tables 4.7 and 4.8. From both tables, the deviation is minimized at T_{ref} = 2000 K. The sum of variance of the total emittance, $\sum Var$, calculated by these new correlations in Tables 21 and 22, are expressed by:

$$\sum Var = \sum_{t=1}^{N_t} \sum_{ip=1}^{N_p} \left(\frac{\epsilon_{t,ip} - \epsilon_{t,ip,HITEMP}}{\epsilon_{t,ip,HITEMP}} \right)^2 \tag{4.34}$$

Sum of the variance for total emittance (Eq. (4.34)) calculated from the new correlation ($c_{i,j}$, w_i) and polynomial coefficients based on MR deviated from LBL-HITEMP 2010 are also presented in Table 4.7 and Table 4.8. In Table 4.7, the average sum of the variances from all values of MR (MR = 0.125-4.0) are minimized and equal to 1.62% when the reference temperature has a value of either 2000 or 2500 K. However, the average sum of the variance for total emittance calculated from polynomial coefficients based on MR in Table 4.8 is minimized and has a value of 2.26 when the reference temperature is equal to 2000 K. Therefore, a minimum sum of the variance for the emittance is found when the reference temperature is set to 2000 K considering both types of coefficients in Table 4.7 and Table 4.8. Furthermore, when T_{ref} = 2000 K, the average sum of the variance increases from 1.62% to 2.26% when the molar ratios dependent correlations ($CK1_i$-$CK3_i$) are applied. Therefore, error in the prediction of the total emittance increases when the new correlations based on MR are applied.

The correlations for WSGG model in Tables 4.4-4.6 were implemented into CFD combustion model via external C-programming subroutines named user defined function (UDF-function) in ANSYS FLUENT program. In CFD numerical model of oxy-fuel furnace, the emissivity of gas at each computational cell is re-calculated depending on specific gaseous temperature T and partial pressure of gaseous mixture P_a using formulation in Eq. (3.180) and parameters in Tables 4.4-4.6.

4.4 Benchmark of one dimensional infinite plates

In order to evaluate the accuracy of the proposed oxy-fuel correlations, the radiative source terms and the net radiative heat fluxes calculated using the new correlations are compared with LBL calculations from HITEMP 2010 database for one-dimensional infinite plates. Ten different cases are investigated in this work for conditions of isothermal homogeneous, non-isothermal homogeneous and non-isothermal non-homogeneous gas mixtures. For all cases, the wall is assumed to be black (ϵ_w= 1) and maintained at the temperature of 700 K. The total pressure P is 1.0 bar, while the partial pressures P_a for each cases are calculated using Eqs. (3.180) and (3.181). All investigated cases are summarized in Table 4.9.

For both isothermal and non-isothermal cases, two molar ratios are investigated: MR = 0.125 and MR = 1.0. For the case with MR = 0.125, the total molar fraction of the mix-

ture ($Y_t = Y_{H2O} + Y_{CO2}$) is equal to 0.9 which refers to the case of isothermal and non-isothermal dry-FGR oxy-fuel conditions (case 1.1 and 2.1). For MR = 1.0, the total molar fraction Y_t is constant at 0.96 to represent the isothermal and non-isothermal wet-FGR oxy-fuel conditions (case 1.2 and 2.2) [Kangwanpongpan12]. For the non-isothermal cases, the temperature between the infinite plates for the investigated cases is similar to a cosine profile from experiments in oxy-fuel conditions [Johansson10], which is given by:

$$T = 1400\ \text{K} - (400\ \text{K}) \cos\left(\frac{2\pi x}{L}\right) \tag{4.35}$$

where x is the length coordinate along the space between the infinite slab and L is the distance between the plates. By using this temperature profile, the minimum and maximum gaseous temperatures are equal to 1000 K at the wall (boundary conditions) and 1800 K at the mid-distance between the plates ($x = 0.5\ L$). The cases using non-isothermal temperature profile in Eq. (4.35) are denoted as case 2.1 and 2.2. Additional non-isothermal cases with an opposite sign of cosine term (case 3.1 and 3.2) refer to the case of hot gas near the walls (T = 1800 K) and cold gas at the mid-distance of between the walls (T = 400 K).

From experiments of oxy-fuel conditions in wet flue gas recirculation [Kangwanpongpan12], molar fractions Y_{H2O} and Y_{CO2} are both uniform and equal to 0.48 (Y_t = 0.96), corresponding to cases 2.2 and 2.4 in Table 4.9. For the case of dry flue gas recirculation, the molar ratio Y_{CO2} is equal to 0.8; however, the molar fraction of water (Y_{H2O}) is more representative of actual conditions by the following profile:

$$Y_{H_20} = 0.12 + 0.04 \cos\left(\frac{2\pi x}{L}\right) \tag{4.36}$$

The above variation of the molar fraction Y_{H2O} is applied in the case of non-isothermal and non-homogeneous (case 4.1) in Table 4.9, which represents the case of dry-FGR oxy-fuel conditions in practical flames. Applying Y_{H2O} by Eq. (4.36) and using Y_{CO2} = 0.8 results in variation of molar ratios MR between 0.1 and 2.

To further validate the new correlations for all possible molar ratios MR (MR = 0.125-4), additional non-isothermal and non-homogeneous cases (case 4.2-4.5) are also tested. In case 4.2 and 4.3, either the molar fraction Y_{H2O} or Y_{CO2} is constant at 0.12, while the other one follows the profile below:

$$Y_{H_20\ or\ CO_2} = 0.12 + 0.09 \cos\left(\frac{2\pi x}{L}\right) \tag{4.37}$$

This molar fraction results in the range of MR from 0.57 at the wall (x = 0, L) up to 4.0 at the mid-distance of plates ($x = 0.5\ L$) when Y_{H2O} is constant at 0.12 and Y_{CO2} varies according to Eq. (4.37); otherwise, MR varies from 1.75 at the wall down to 0.25 at the mid-distance.

Table 4.4: Weighting factors coefficients $c_{i,j}$ and absorption coefficients κ_i for the WSGG model in oxy-fuel conditions at various molar ratios (MR) of H_2O to CO_2.

i	j κ_i (bar-m)$^{-1}$	1 $c_{i,1}$	2 $c_{i,2}$	3 $c_{i,3}$	4 $c_{i,4}$	5 $c_{i,5}$	6 $c_{i,6}$
MR = 0.125							
1	0.041173	0.4329	-0.7255	1.1384	0.2661	-1.1786	0.4713
2	0.343891	-0.5151	7.2071	-21.319	28.355	-17.95	4.3778
3	3.710740	0.3461	-1.1838	3.0944	-4.1157	2.5339	-0.5857
4	106.08	0.1443	-0.4216	1.5071	-2.7378	2.1386	-0.5994
MR = 0.25							
1	0.045079	0.3607	-0.1849	-1.0644	4.061	-3.9878	1.2272
2	0.386642	-0.4713	6.375	-18.102	23.534	-14.68	3.5389
3	3.764160	0.2999	-0.4354	0.8603	-1.1531	0.6442	-0.1167
4	96.0343	0.1755	-0.471	1.4103	-2.4705	1.9323	-0.5459
MR = 0.5							
1	0.049191	0.3026	0.3705	-3.3957	7.9979	-6.8847	2.0098
2	0.421502	-0.4235	5.4049	-14.682	18.707	-11.509	2.7377
3	3.852390	0.2614	0.1391	-0.5843	0.5412	-0.374	0.1325
4	83.534	0.1954	-0.3374	0.6829	-1.3044	1.1421	-0.349
MR = 0.75							
1	0.050784	0.2887	0.5335	-4.2296	9.4993	-8.0354	2.3307
2	0.431878	-0.4066	4.9951	-13.339	16.952	-10.41	2.4659
3	3.908780	0.2529	0.2466	-0.6019	0.3143	-0.1583	0.0746
4	75.5255	0.1974	-0.1456	-0.1062	-0.1181	0.3554	-0.1542
MR = 1							
1	0.051446	0.2853	0.5853	-4.5894	10.205	-8.6057	2.496
2	0.436145	-0.3976	4.7799	-12.689	16.172	-9.9506	2.3557
3	3.948270	0.2532	0.2151	-0.2515	-0.3589	0.3293	-0.0498
4	69.781	0.1941	0.0337	-0.7945	0.8954	-0.3114	0.0104
MR = 2							
1	0.051832	0.2872	0.5807	-4.9092	11.012	-9.3465	2.7294
2	0.440593	-0.3748	4.396	-11.671	15.104	-9.382	2.2263
3	3.981020	0.2655	-0.0908	1.3035	-2.9227	2.0978	-0.495
4	56.0818	0.175	0.5481	-2.6576	3.5816	-2.0627	0.4412
MR = 4							
1	0.051687	0.2911	0.505	-4.8039	11.037	-9.4886	2.7969
2	0.444449	-0.3416	4.0487	-10.799	14.158	-8.8559	2.1031
3	3.933740	0.279	-0.4828	3.0103	-5.573	3.8801	-0.9391
4	44.7501	0.1471	1.069	-4.449	6.1082	-3.6923	0.84

Table 4.5: Polynomial coefficients for the absorption coefficients based on MR as independent variable.

i	$CK1_i$	$CK2_i$	$CK3_i$
1	0.0429	0.0093	-0.0018
2	0.3647	0.079	-0.015
3	3.7144	0.2565	-0.0509
4	105.31	-39.265	6.0877

Table 4.6: Polynomial coefficients for weighting factors based on MR as independent variable.

i	j	$C1_{i,j}$	$C2_{i,j}$	$C3_{i,j}$
1	1	0.3947	-0.1214	0.0243
1	2	-0.4512	1.142	-0.2296
1	3	0.1492	-5.2222	1.0115
1	4	1.8824	9.182	-1.7493
1	5	-2.3284	-6.9298	1.3038
1	6	0.7698	1.9063	-0.3549
2	1	-0.4974	0.1092	-0.0179
2	2	6.8986	-2.3198	0.4077
2	3	-19.988	8.0021	-1.4482
2	4	26.208	-11.007	2.0311
2	5	-16.44	7.1199	-1.3278
2	6	3.9847	-1.7876	0.3349
3	1	0.3189	-0.072	0.0158
3	2	-0.7222	1.0304	-0.2478
3	3	1.5053	-1.935	0.5931
3	4	-1.8378	1.6332	-0.6619
3	5	1.0337	-0.7798	0.3857
3	6	-0.2107	0.1782	-0.0933
4	1	0.1648	0.0329	-0.0095
4	2	-0.6012	0.6942	-0.0687
4	3	2.0308	-3.096	0.3691
4	4	-3.4361	4.7494	-0.5919
4	5	2.5803	-3.1714	0.4017
4	6	-0.7069	0.7869	-0.1003

Table 4.7: Sum of the variance for the computation of the total emittance calculated from the coefficients ($c_{i,j}$, w_i) in Table 4.4 and from LBL integration of HITEMP 2010 data at different reference temperatures, $T_{ref.}$

MR	1000 K	1200 K	1450 K	2000 K	2500 K
0.125	3.21	2.42	2.28	2.32	2.31
0.25	2.10	2.26	2.20	2.13	2.12
0.5	1.83	1.84	1.79	1.80	1.81
0.75	1.58	1.59	1.55	1.55	1.55
1.0	1.51	1.33	1.40	1.36	1.37
2.0	1.25	1.07	1.10	1.06	1.06
4.0	1.15	1.13	1.18	1.10	1.09
Average	1.80	1.66	1.64	1.62	1.62

Table 4.8: Sum of the variance in the computation of the total emittance from polynomial coefficients based on MR in Tables 4.5 and 4.6 ($C1_{i,j}$, $C2_{i,j}$, $C3_{i,j}$, $CK1_i$, $CK2_i$ and $CK3_i$) and from LBL integration of the HITEMP 2010 at different reference temperatures, $T_{ref.}$

MR	1000 K	1200 K	1450 K	2000 K	2500 K
0.125	4.91	5.33	4.98	4.88	4.88
0.25	2.23	2.36	2.12	2.15	2.13
0.5	2.58	2.48	2.31	2.36	2.33
0.75	2.58	2.09	1.93	1.98	1.96
1	2.40	1.60	1.44	1.49	1.48
2	2.23	2.50	1.97	2.01	2.07
4	6.28	6.62	1.15	0.98	1.38
Average	3.32	3.28	2.27	2.26	2.32

Table 4.9: Investigated cases for the evaluation of the new correlations for WSGG models (P = 1.0 bar).

Case		$T(K)$	Y_{H2O}	Y_{CO2}	Y_t	MR
Isothermal	1.1	1200	0.1	0.8	0.9	0.125
	1.2	1200	0.48	0.48	0.96	1
Non-isothermal	2.1	Eq. (4.35)	0.1	0.8	0.9	0.125
	2.2	Eq. (4.35)	0.48	0.48	0.96	1
Non-isothermal (negative cosine term)	3.1	[a]Eq. (4.35)	0.1	0.8	0.9	0.125
	3.2	[a]Eq. (4.35)	0.48	0.48	0.96	1
Non-homogeneous, non-isothermal	4.1	Eq. (4.35)	Eq. (4.36)	0.8	Eq. (3.181)	Eq. (4.31)
Non-homogeneous, non-isothermal	4.2	Eq. (4.35)	0.12	Eq. (4.37)	Eq. (3.181)	Eq. (4.31)
	4.3	Eq. (4.35)	Eq. (4.37)	0.12	Eq. (3.181)	Eq. (4.31)
	4.4	Eq. (4.35)	0.15	Eq. (4.38)	Eq. (3.181)	Eq. (4.31)
	4.5	Eq. (4.35)	Eq. (4.38)	0.15	Eq. (3.181)	Eq. (4.31)

[a] with negative cosine term.

Another molar fraction profile is used in the case 4.4 and 4.5 for either H_2O or CO_2 to provide the same standard of testing due to the reason that not all correlations from other researcher [Johansson11] are valid up to the molar ratio MR of 4.0. This molar fraction profile is defined as:

$$Y_{H_20\ or\ CO_2} = 0.15 + 0.075\cos\left(\frac{2\pi x}{L}\right) \tag{4.38}$$

Either Y_{H2O} or Y_{CO2} is formulated by the above profile and the other one is constant at 0.15. Thus, the molar ratio MR ranges from 0.67 to 2 when Y_{H2O} is constant, and from 0.5 to 1.5 when Y_{CO2} is constant. The variations of molar ratios of non-homogeneous mixture in case 4.1-4.5 are also plotted with normalized distance (x/L) between infinite plates and summarized in Fig. 4.4.

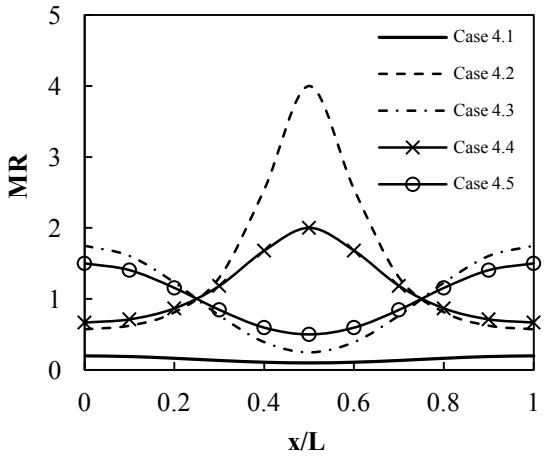

Figure 4.4: Profiles of molar ratios (MR = Y_{H2O}/Y_{CO2}) for non-homogeneous mixture (case 4.1-4.5).

5 Descriptions of Investigated CFD Cases

Although the literature review in chapter 2 provided a guide on how to select each mathematical sub-models for lignite oxy-fuel combustion, none of them shows complete evaluations of all mathematical sub-models under oxy-fuel conditions. From the review, sub-models, which mainly influences final predictions of aerodynamics quantities (velocity), thermodynamics quantities (temperature, burnout characteristics and heat flux) and chemical quantities (product species), are the models for turbulent flow, devolatilization, global volatile reaction mechanisms, turbulent gaseous combustion, char heterogeneous reactions and radiation.

In order to investigate influence of these sub-models selections to accuracy of predictions from CFD numerical simulation, numerical simulation from two lignite oxy-fuel cases are investigated in this thesis.

The first investigated numerical CFD cases from 100 kW_{th} oxy-fuel furnace [Toporov08a] is created aiming to study influences of selection of several possible sub-mathematical models to accuracy of predictions of velocity, temperature and oxygen concentration. The evaluation were done in the preparatory steps in order to determine the most suitable choices of sub-mathematical models additional to literature review in chapter 2 and due to the fact that none of velocity measurements are performed in 0.4 MW_{th} oxy-fuel test facility at BTU Cottbus leading to lack of conclusions of validation for turbulent flow's quantities such as axial and tangential velocity. The main reason is that these velocity's predictions could dominates the re-circulation's zone near to swirling burner which also results in the degree of species production rates in turbulent reacting flow.

5.1 Laboratory scaled 100 kW_{th} oxy-fuel furnace

5.1.1 Geometry and operating conditions

The geometry and operating conditions adopted in this research are based on experiments carried out by Toporov et al. [Toporov08a] utilizing a vertical laboratory-scale 100 kW_{th} oxy-fuel furnace. The combustion takes place in a cylindrical and down-fired furnace with a length of 2.1 m and an inner diameter of 0.4 m (Fig. 5.1(a)). The swirl pulverized coal burner installed on the top of the furnace consists of three oxidant mixture streams, primary (coal carrying), secondary swirling and staging stream (Fig. 5.1(b)).

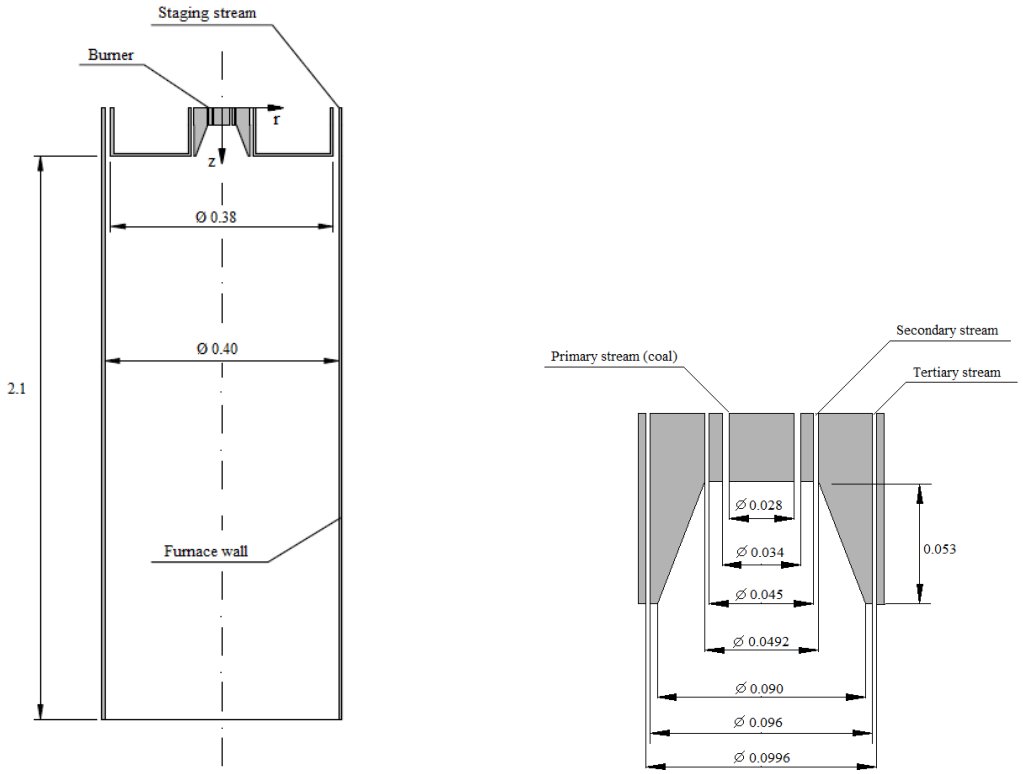

Figure 5.1: Geometry of 100 kW_{th} oxy-fuel combustion chamber (a) furnace (b) swirl burner (dimensions in meters) [Kangwanpongpan12], adapted from [Toporov08a].

Coal particles are injected into the furnace through the primary stream enclosed by a secondary swirling stream. The Rhenish lignite is used in this experiment which has a coal properties listed in Table 5.3. The tertiary stream is injected through an annulus orifice enclosing the burner quarl. An oxidant staging stream is also utilized in the furnace in order to reduce the oxygen/fuel ratio at the burner region. The operating conditions applied in this work are summarized in Table 5.1 and Table 5.2.

Table 5.1: Flow parameters for 100 kW_{th} vertical down-fired oxy-fuel furnace (quarter model), determined based on full-scale model from literature [Toporov08a, Kangwanpongpan12].

Inlet stream[a]	Mass flow rate (kg/s)	T (°C)	O_2 (% volume)	CO_2 (% volume)
Coal	0.0004514	-	-	-
PS	0.0012222	40	0.19	0.81
SS (swirl)	0.0018472	60	0.21	0.79
TS	0.0001042	60	0.21	0.79
Stag.	0.0038125	900	0.21	0.79
Outlet (average)	-	514.91	0.207	0.793

[a] PS = primary stream, SS = secondary stream, TS = tertiary stream, Stag. = staging stream.

Table 5.2: Wall parameters for 100 kW_{th} vertical down-fired oxy-fuel furnace, adapted from [Toporov08a, Kangwanpongpan12].

Wall	Type[a]	T (°C)	Emissivity
Burner quarl	adiabatic	-	1
Burner side	Const. T	300	0.2
Furnace	Const. T	1000	0.7

[a] Const. T = constant temperature.

Table 5.3: Coal properties of Rhenish lignite [Toporov08a].

Coal properties	$Rhenish_{100MWth}$ (% by mass)
Proximate analysis:	
Fixed carbon	40.9
Volatiles	46.6
Ash	4.1
Moisture	8.4
Low Heating Value (LHV)[a], MJ/kg	22.173
Ultimate analysis:	
C	67.4
H	4.24
O	14.7
N	0.86
S	0.3
Ash	4.1
Moisture	8.4

[a] [Toporov06]

5.1.2 Computational mesh

Due to the axis-symmetric geometry of combustion chamber, a quarter (1/4) scaled computational mesh was created. In order to reduce the computational effort, the quarter model was build up and improved from computational mesh of 1/6 model from the previous studies [Kangwanpongpan12]. In Fig. 5.2, the new mesh was composed of approximately 600,000 cells and especially dense at the burner area applying a periodic boundary condition in the swirling direction of flow.

Sensitivity analysis for the numerical mesh refinement was studied, starting from 100,000 300,000 and 600,000 cells, denoted as 100k, 300k and 600k cells in chapter 6, respectively. The results of studies (chapter 6) show that slightly improvements of results are found for the accuracy of predictions, if the numerical meshes are further refine from 300,000 to about 600,000 cells. Hence, the 600,000 meshing cells is selected to ensure the best predictions for small scale oxy-fuel furnace close to the measurements of velocity, temperature and O_2 concentration.

Further refinement is not appropriated for numerical studies because too much necessary computing time for numerical research. For roughly approximation, the simulation with 600,000 computational cells required around 4 days of computational time per one investigated case and 35 cases were studied in total. This needed about 5 months (140 days) not including the time required for setting up the model, which is unpractical research routine. Therefore, all numerical cases are performed with 600,000 computational cells based on this reason.

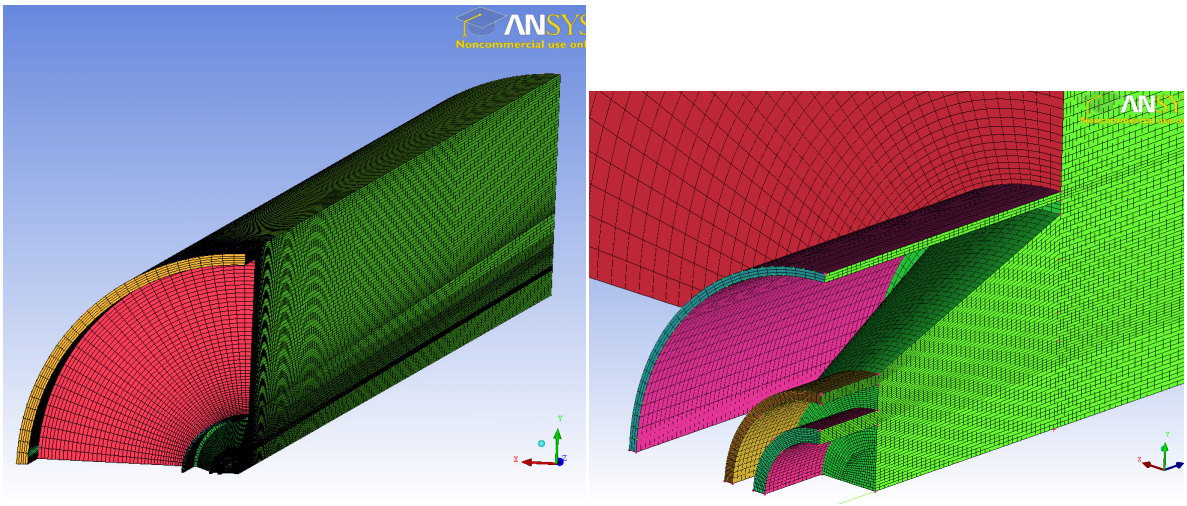

(a) (b)

Figure 5.2: Computational mesh of 600,000 cells for 100 kW_{th} oxy-fuel furnace: (a) furnace, (b) swirl burner.

5.1.3 Investigated cases

Many sub-mathematical models for the prediction of lignite oxy-fuel combustions are available from a number of literatures described in the literature review in chapter 2. As explained in chapter 3, factors effecting results of numerical predictions are selection of turbulent flow model, char reaction model and its kinetic parameters, simplified volatile reaction mechanism and its kinetic parameters, turbulent gaseous combustion model, radiation modeling of gas properties. Because the radiation properties change tremendously in oxy-fuel environments as suggest by the review of Wall [Wall07] and Tofttegarrd [Toftegaard10]; therefore, the new correlations for the weighted sum of gray gases models (WSGG) are created by fitting to an emissivity calculated by line-by-line HITEMP 2010 database in which details are already explained in chapter 4. Selection of other sub-models can influences final results of numerical prediction such as radiation modeling [Johansson10-11, Yin10, Rehfeldt11, Porter10, Ströhle11] and devolatilization models [Jovanovic12]. For this reason, the effects of sub-model's selection are investigated by performing many numerical cases. All investigated cases including their abbreviated name of each case are shown in Table 5.4. Descriptions of sub-model studies are presented in the following Table 5.5.

Table 5.4: Summary of investigated cases of laboratory-scale 100 kW_{th} oxy-fuel furnace (swirl burner) for the study of sub-model selections.

Fundamental study[a]	Case	Tested sub-models[b]	Reference for parameters[c]	Case name
Turlulence models	a1	Standard k-ε	-	Std. k-e
	a2	RNG k-ε	-	RNG k-e
	a3	Realized k-ε	-	Realized k-e
	a4	SST k-ω	-	SST k-omega
	a5	RSM	-	RSM
Char: models/kinetic	b1	KD	O_2[Field67]	KD-Field
			CO_2[Mayers34a]	
			H_2O[Mayers34b]	
	b2	Global rate	O_2[Field67]	Global-BTU
		KD	CO_2[Mayers34a]	
			H_2O[Mayers34b]	
	b3 /c1	Intrinsic	kinetic rate by Smith [SmithIW82] A_s = constant [Al-Makhadmeh09].	Intrin-Smith82 /As-Al-Makhadmeh09
Char: models/kinetic/A_s	b4	Intrinsic	kinetic rate by Leiser [Leiser11] A_s = constant [Al-Makhadmeh09].	Intrin-Leiser11
Char: internal surface area (A_s)	c2	Intrinsic	kinetic rate by Smith [SmithIW82] A_s from RPM model by Simons [Simons82].	As-Simons82
	c3	Intrinsic	kinetic rate by Smith [SmithIW82] A_s from RPM model by Charpenay et al. [Charpenay92].	As-Charpenay92
Char: w/wo CO_2 and H_2O	d1	KD	react. w. O_2[Field67]/CO_2[Mayers34a]/H_2O[Mayers34b]	KD-O2CO2H2O
	d2	KD	react. w. only O_2[Field67]	KD-O2
	d3	Intrinsic	react. w. O_2[Field67]/CO_2[Mayers34a]/H_2O[Mayers34b]	Intrin-O2CO2H2O
	d4	Intrinsic	react. w. only O_2[Field67]	Intrin-O2
Volatile: TGC model /mech.	e1	EDM/2-step	-	EDM2
Volatile: volatile rate, 2-step, kinetic	e2	FRED/2-step	volatile rate by Shaw et al. [Shaw91] CO rate by Dryer et al. [Dryer73]	FRED2 (FRED2-Shaw)
	e3	FRED/2-step	kinetic rates by Westbrook et al. [Westbrook81] CO rate by Dryer et al. [Dryer73]	FRED2-WB
	e4	FRED/2-step	volatile rate by Dryer et al. [Dryer73] CO rate by Dryer et al. [Dryer73]	FRED2-Dryer
Volatile: volatile rates, 3-step, kinetic	f1	FRED/3-step	volatile rate by Shaw et al. [Shaw91] CO rate by Rückert et al. [Rückert03] H_2 rate by Rückert et al. [Rückert03]	FRED3 (FRED3-SR)
	f2	FRED/3-step	volatile rate by Shaw et al. [Shaw91] CO rate by Howard et al. [Howard73] H_2 rate by Rückert et al. [Rückert03]	FRED3-SH
	f3	FRED/3-step	volatile rate by Rückert et al. [Rückert03] CO rate by Rückert et al. [Rückert03] H_2 rate by Rückert et al. [Rückert03]	FRED3-RR
	f4	FRED/3-step	volatile rate by Rückert et al. [Rückert03] CO rate by Howard et al. [Howard73] H_2 rate by Rückert et al. [Rückert03]	FRED3-RH
	f5	FRED/3-step	volatile rate by Zimont et al. [Zimont69, Förtsch03] CO rate by Rückert et al. [Rückert03] H_2 rate by Rückert et al. [Rückert03]	FRED3-ZR
	f6	FRED/3-step	volatile rate by Zimont et al. [Zimont69, Förtsch03]	FRED3-ZH

Fundamental study[a]	Case	Tested sub-models[b]	Reference for parameters[c]	Case name
			CO rate by Howard et al. [Howard73] H_2 rate by Rückert et al. [Rückert03]	
Volatile: volatile rate, rev. CO	g1	FRED/2-step, rev. CO	volatile rate by Shaw et al. [Shaw91] rev. CO rate by Andersen et al. [Andersen09]	FRED2r
	g2	FRED/3-step, rev. CO	volatile rate by Shaw et al. [Shaw91] rev. CO rate by Andersen et al. [Andersen09] H_2 rate by Rückert et al. [Rückert03]	FRED3r
Radiation: particle radiation	h1	constant	constant emissivity (0.85) and scattering factor (0.6 m^{-1})	Smith82-abs-const.
	h2	as soot (wo. scattering)	as soot radiation by Felske et al. [Felske77]	Smith82-abs-Felske
	h3	wo. particle radiation	without particle radiation (only gas radiation)	Smith82-wo.part.rad.
Radiation: gas emissivity	I1	WSGG model (particle radiation as soot)	correlations by Smith et al. [SmithTF82]	Smith82
	I2		new oxy-fuel correlations from HITEMP 2010 (table)	Tanin12-table
	I3		new oxy-fuel correlations from HITEMP 2010 (MR)	Tanin12-coef
	I4		oxy-fuel correlations by Johansson et al. [Johansson11]	Johansson11
	I5		oxy-fuel correlations by Yin et al. [Yin10]	Yin10

[a] Char = char heterogeneous reactions, kinetic = kinetic rate, Volatile = Volatile homogeneous reactions, volatile rate = kinetic rate for volatile oxidation, As = internal surface area, w/wo CO_2 and H_2O = with and without CO_2 and H_2O reaction, TGC = Turbulenct gaseous combustion, rev. CO = reversible CO oxidation, 2-step = global 2-step reaction mechanism, 3-step = global 3-step reaction mechanism, Radiation = Radiation properties of gas mixture.

[b] KD = Kinetic-diffusion limited rate, Global rate =Global reaction rate model, Intrinsic = Intrinsic reaction rate, EDM = Eddy dissipation model, FRED = Finite rate eddy dissipation, rev. CO = reversible CO oxidation, const. = constant value, scatt. = including particle radiation scattering, wo. = without, WSGG = Weighted-sum-of-gray-gases model.

[c] react. = reaction, w. = with, volatile rate = kinetic rate for volatile oxidation, CO rate = kinetic rate for CO oxidation, H2 rate = kinetic rate for H2 oxidation, rev. = reversible reaction, As = internal surface area of pore, RPM = random pore models, table = tabulated style, MR = molar ratio dependent.

The numerical results for prediction are compared with experimental data of velocity, temperature and O_2 concentration from 100 kW_{th} oxy-fuel furnace [Toporov08a] and evaluation of suitable sub-models are later presented in chapter 6. After assessing all sub-models, the set of final selected sub-models are applied for numerical predictions of a 0.4 MW_{th} oxy-fuel furnace operated at BTU Cottbus.

5.1.4 Numerical methods and solution strategies

The numerical methods, solution algorithms and numerical techniques to accelerate convergence have been reviewed in chapter 2 (literature review) and the selected methods are summarized in chapter 3 (mathematical modeling). The numerical model is based on the Lagrangian approach for particles (discrete phase) and Eulerian approach for gases, called Euler-Lagrange formulation. Because the complexity of coal combustion modeling to account for many sub-models, the steady-state (time independent) flow simulation is considered due to the objective of this research to investigate mathematical modeling, not for comprehensively research in oxy-fuel flame stability. The reduction of required computing time also provides more research time to focus on the effects of employing different sub-models in oxy-fuel numerical predictions.

Table 5.5: Descriptions of study for the effects of applying different sub-models and its correlations for the combustion predictions in laboratory-scale 100 kW_{th} oxy-fuel case.

Sub-model	Descriptions of study	Case
Turbulent flow	Model	a
Char reaction	Model (KD, Global, intrinsic)/kinetic	b
	Pore model for internal surface area	c
	Effect of including reaction with CO_2 and H_2O	d
Volatile reaction	Model (EDM, FRED)	e1,e2
	Kinetic rate for volatile oxidation, 2-step	e2-e4
	Kinetic rate for volatile oxidation, 3-step	f1-f6
	Global reaction mechanim (2- and 3-step)	e2,f1
	Effect of including reversible CO reaction, 2-step	e2,g1
	Effect of including reversible CO reaction, 3-step	f1,g2
	Comparing 3-step to 2-step with reversible CO reaction*	f1,g1
Particle radiation	Constatnt emissivity (scattering), non-scattering soot or without particle radiation	h1-h3
Gas radiation	Correlations for emissivity by WSGG model	I1-I5

* Comparison based on previous results of predictions

The SIMPLE algorithm is selected as referring to literature review, and applied to account for the pressure-velocity coupling in the RANS equations. The solutions are achieved by the Gauss-Seidel point-iterative method accelerated by the algebraic multi-grid (AMG) technique in CFD code previously mentioned.

To accelerate numerical convergence while maintaining numerical stability, the strategies to perform numerical CFD simulation are outlined as follow:

Step 1 – Converging simulation without reaction and radiation (cold flow simulation) using 1st order UPWIND discretization scheme. Set under-relaxation factors (URF) of 0.3 for pressure, 0.7 for density (continuity), 0.7 for momentum, 0.8 for turbulence, 0.95 for gas species, 0.95 for species (only O_2 and CO_2 in gas mixture in oxy-fuel atmosphere, the small amount of inert gases and air-in leakage are negligible) and 0.95 for energy equation. The URF for momentum equation (but reduce to 0.5-0.6 for high swirling flow) equation. For high swirling flow or high skew meshes, the URF of density, momentum and turbulence should be reduced to improve convergence, for instance, URF for density = 0.6, for momentum = 0.6 and for turbulence = 0.7.

Step 2 – In the case of high swirling secondary stream at burner, converging continuity and momentum equations using 2nd order UPWIND scheme before accounting for chemical reaction provides numerical stability for convergence.

Step 3 - To increases the stability of convergence, URF for some equations should be adjusted before initiate reaction. The URF for pressure should be increase slightly to 0.5, in contrast to momentum, which should be reduced to 0.2.

Step 4 – Starting ignition (patching) by including small high temperature region near to primary inlet where coal particles are burned. At this step, other species involving chemical reaction (volatile, CO, H_2, H_2O, N_2, SO_2) and discrete (particle) phase can be taken into account now. The non-zero values of combustion products are required to accelerate numerical convergence. The products of combustion are usually CO_2 and H_2O; however, only molar fraction of H_2O in the patching region should be set (the value of 0.01 can be used, which means 1% of H_2O is assumed to be presence in the patching region) due to the fact that CO_2 is already fed into furnace through secondary and staging stream.

Step 5 – Introducing discrete (particle) phase in the carrier stream at burner (primary stream here) and accounting for chemical reaction of coal combustion. The small value of URF for discrete phase is required to ensure the numerical convergence. From numerical experience and several tries, the URF for the discrete phase should start at 0.0001 for the large-scale CFD model and at 0.001 for smaller-scale CFD model of oxy-fuel furnace. The URF of the discrete phase is stepwise increased but not too fast, to prevent flame extinction at the burner quarl in CFD model. This can be occurred because too large step of calculations causes in the unphysical phenomena due to the nature of numerical stability. The final values for URF for the discrete phase were found to be 0.01 for both scales. Further increasing the URF for the discrete phase leads to instability of calculation. However, the adjustment of final value of the URF is dependent of number of particles including in the calculations. Particle-radiation interaction for the discrete phase should not be accounted for at this step.

Step 6 – After converging previous solution, accuracy of predictions can be improved by applying 2nd order UPWIND scheme for species, energy except radiation (requiring intensively higher computational effort), which is always calculated using the 1st order scheme.

Step 7 – Accounting for radiation calculation. The solutions for the RTE are determined by the DOM and additional set up are needed. Apply the WSGG model for gas radiation properties such as absorption coefficients and setting scattering coefficients for gas mixture (value of 0.6 assumed as presented by Backreedy et al. [Backreedy06]). The new oxy-fuel correlations for the WSGG model are implemented into CFD model through the user defined function (UDF) using external C-programming code. The non-gray gases formulation (band radiation models) is applied as explained in chapter 4, which does not require path-lengths in the calculation. Wavelength intervals for each gray gas can be assumed, which has no influence on the final solution of the RTE because the gas mixture is assumed to be gray without any specific band centers (no locations of band center). It should be emphasized that the wall emissivity must be set because the wall emissivity interacted with each gray gas (gray band) is first set to be unity at the start of radiation calculation. The wall emissivities for the laboratory-scale 100 kW_{th} oxy-fuel cases are shown in Table 5.3.

Step 8 – Accounting for particle-radiation interaction. Particle emissivity and particle scattering factor must be set. The particle emissivity for coal particles varies from 0.6 to 1.0 as reviewed in chapter 2. When there is no measurement of these values published for oxy-fuel flame, the value of 0.85 is assumed averaged between 0.6 for fly ashes and 1.0 for unburned carbon as reviewed by Barcena et al. and Chui et al. [Barcena07, Chui93] in chapter 2. The particle scattering factor is set to 0.6 from discussion in the review. It must be emphasized that either scattering coefficients for gas mixture or particle scattering fac-

tor for the effect of particles-radiation interacttion can be taken into account in the CFD model. Therefore, accounting for particle scattering will neglect the scattering coefficients for gas mixture after turning on the particle-radiation interaction.

Step 9 – After converging previous solution. Although the numerical stability is reduce, increasing the URF of species and energy close to unity (0.97-0.99) can results in better accuracy of predictions. However, these URF are sensitive to the number of coal particle including in the calculation, and must be determined for each combustion problem.

5.1.5 Pre-calculated parameters

In addition to reaction rates for char and volatile reactions, some parameters must be pre-calculated and used as inputs for CFD calculations. The parameters are hydraulic diameter and turbulence intensity, five speific parameters for the CPD model for coal devolatilization, stoichiometry of volatile reactions, discrete (particle) phase injections and size distributions of pulverized coal particles (Rosin-Rammler distribution method). All parameters are listed from Table 5.6 to Table 5.12.

The calculation of initial guess for turbulence parameters are already explained in chapter 3, in which the turbulence intensity is expressed by Eq. (3.197) and the hydraulic diameter (HD) by Eqs. (3.198)-(3.200). The turbulence parameters are presented in Table 5.6.

Because no details of blade angle for swirling flow was presented in the referenced investigated 100 kW_{th} oxy-fuel case, therefore the axial and tangential component of the swirling flow (SS) are approximated from geometry of annulus pipe (inner and outer radius) using equation of swirling number (SN) presented by Beer and Chigier [Beer72] expressed as:

$$SN = Tangential\ momentum/(Axial\ momentum * r_{outer}) \quad (5.1)$$

Table 5.6: Turbulence intensity and hydraulic diameter (HD) for inlet flow in 100 kW_{th} oxy-fuel furnace.

Inlet[a]	Flow rates* kg/s	Area* m^2	Density[b] kg/m^3	Velocity m/s	kine. viscous[c] m^2/s	HD* m	Re	I_{turb} %
PS	0.001222	7.304E-05	1.6287	10.274	1.0278E-05	0.0013	1334.9	6.51
SS	0.001847	7.768E-05	1.5211	15.632	1.1724E-05	0.0010	1324.9	6.51
TS	0.000104	1.383E-04	1.5211	0.495	1.1724E-05	0.0009	37.2	10.18
Stag	0.003813	3.063E-03	0.4309	2.889	1.1102E-04	0.0048	126.0	8.74
outlet(sum)	0.006986	3.142E-02	0.6333	0.351	5.7736E-05	0.0440	267.6	7.96

* For a quarter (1/4) model using periodic boundary conditions.
[a] PS = primary inlet stream, SS = secondary swirl inlet stream, TS = tertiary inlet stream, Stag = staging stream, outlet = outlet (exit) of furnace.
[b] Density calculated using FluidEXL library by Professor Hans-Joachim Kretzschmar from Department of Technical Thermodynamics, the University of Applied Sciences Zittau/Görlitz (FH), "http://thermodynamik.hs-zigr.de".
[c] kine. viscous. = kinematic viscosity (calculated by the same thermodynamic library as densityb).

The swirling number can be approximated using geometry of annulus pipe (inner and outer radius) as:

$$SN \cong (2/3) * \frac{(1-(r_{inner}/r_{outer})^3)}{(1-(r_{inner}/r_{outer})^2)} * tan(\theta) \quad (5.2)$$

If the swirl number is specified previously from measurement in laboratory such as in 100 kW_{th} oxy-fuel furnace [Toporov08a], the angular flow component of swirling stream, θ, can be estimated by this equation and the axial component, COS(θ), and tangential component, SIN(θ), are determined using this angle (θ).

The boundary condition for axial and tangential component of swirling flow are calculated and listed in Table 5.7.

Table 5.7: Tangential and axial component of swirling flow determined by pipe geometry and swirl number.

Inner radius of swirling pipe, r_{inner}	0.0225
Outer radius of swirling pipe, r_{outer}	0.0246
r_{inner}/r_{outer}	0.9146341
SN	1.2[a]
TAN(θ)[b]	1.2526731
blade angle (θ), in radian	0.8970972
blade angle (θ), in degree	51.399883
Tangential component, SIN(θ)	0.7815192
Axial component, COS(θ)	0.6238812

[a] Swirl number from literature of investigated case [Toporov08a].
[b] Calculated using equation in [Beer72].

The five parameters for the CPD mode is pre-calculated using the polynomial correlations by Genetti et al. [Genetti99a] described in chapter 2, and calculated values are given in Table 5.8.

Table 5.8: Five coal specific input-parameters for the CPD model (Rhenish coal).

Parameter	Definition	Value
IB_0	Initial fraction of bridge in coal lattice	0.582
chb_0	Initial fraction of char bridge	0.060
$LC_{\sigma+1}$	Lattice coordination number	5.13
$MW_{cluster}$	Cluster Molecular weight	297.7
MW_{δ}	Side chain molecular weight	36.1

Stoichiometric parameters for the global 2-step and 3-step reaction mechanism in numerical simulations of 100 kW_{th} oxy-coal furnace are listed in Table 5.9 and Table 5.10, respectively. Molecular weighted of lignite in the calculation was assumed to be 30

kg/kmol. The standard state enthalpy of volatile-species for both reaction mechanisms are the same, determining by the stoichiometric calculation and equal to -3.27 × 10^8 J/kmol.

Table 5.9: Stoichiometric parameters for global 2-step reaction mechanisms, CO as intermediate specie. The calculation is based on coal properties of Rhenish lignite.

Reactant		Product				
VM[a]	O_2	CO	CO_2	H_2O	N_2	SO_2
1	1.258	1.0994	0.321	1.354	0.0198	0.006

[a]VM refers to volatile matter in coal particle.

Table 5.10: Stoichiometric parameters for global 3-step reaction mechanisms, CO and H_2 as intermediate specie. The calculation is based on coal properties of Rhenish lignite.

Reactant		Product			
VM	O_2	CO	H_2	N_2	SO_2
1	0.4205	1.4204	1.354	0.0198	0.006

Many detailed parameters for particle tracking are needed to be pre-calculated, influent by number of face-cells at flow boundaries, number of diameters used in the Rosin-Rammler distribution method, particle tries, number of computational cells in the control volume along trajectory path, trajectory length (assumed as furnace length if particle just flows straight to the outlet) and step length factor. The step length factor is used in order to control the characteristic time step to integrate the equations of particle movement. The integrated time step is defined as the estimated transit time (time for particle to travel through the control volume of fluid phase) divided by the step length factor as:

$$\Delta_{t_{charact}} = \frac{\Delta_{t_{transit}}}{step\ length\ factor} \tag{5.3}$$

Tracking parameters for discrete phase are listed in Table 5.11.

For the Rosin-Rammler distribution, the mean diameter is determined by graphical plots in Fig. 5.3 at $Y_{dp} = e^{-1} = 0.368$. The size distribution parameter is calculated using Eq. (3.208) in chapter 3 in the Rosin-Rammler distribution method. Both parameters are listed in Table 5.12.

Table 5.11: Particle tracks for the discrete phase injections for 100 kW_{th} furnace (surface injections).

Index	Descriptions	Values
a	Total cells	640,000
b	Number of burner	1
c	Surface injection (number of face cells)	270
d	Number of diameters (Rosin Rammler distribution)	6
e	Number of particle tries (turbulence dispersion)	20
f	Total particles in the domain (=b×c×d×e)	32400
g	Total number of trajectory cells	210
h	Furnace length (m)	2.153
i	Step length factor	20
j	Number of calculating steps for 1 particle (g×i)	4200
k	Estimated length scale (g,i)	0.0005
l	Total Maximum number of steps (e×j)	84000

Table 5.12: Parameters for Rosin-Rammer distribution for coal particle (Rhenish lignite).

Parameters	Values
Mean diameter, $\bar{d}_p$	35
Size distribution parameter, n_{RR}	1.2061

The mass fraction Y_{dp} (Rhenish pulverized coal) measured by sieve analysis and approximated by Rosin-Rammler method are compared and plotted in Fig 27.

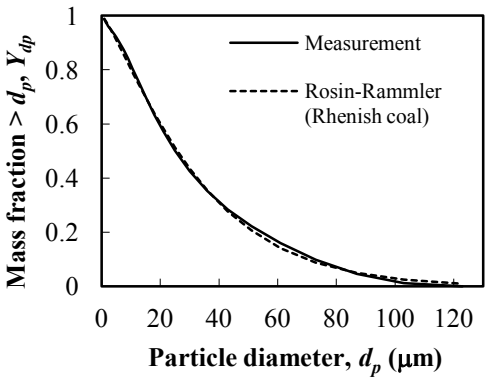

Figure 5.3: Approximated size distribution for Rhenish lignite by Rosin-Rammler distribution method (dash line) and measurement (solid line).

5.2 Pilot scaled 0.4 MW_{th} oxy-fuel test facility

5.2.1 Descriptions of test facility

Experimental measurements for numerical validation were obtained by a 0.4 MW_{th} oxy-fuel test facility available at the Chair of Power Plant Technology at BTU Cottbus commissioning since 2011. The experimental results for 0.4 MW_{th} oxy-fuel furnace were based on measurements performed by Corrêa da Silva [Corrêa da Silva12]. The facility was designed for investigations of pulverized coal combustion in oxy-fuel atmospheres, which is financially supported by Federal Ministry of Research and Technology (BMBF), Germany. The pilot-scale furnace has a thermal heat capacity of 0.4 MW_{th} and is equipped with a horizontal swirl burner and a refractory-lined and water-cooled wall-furnace. The geometries of the furnace and swirl burner are illustrated in Fig. 5.4 and Fig. 5.5.

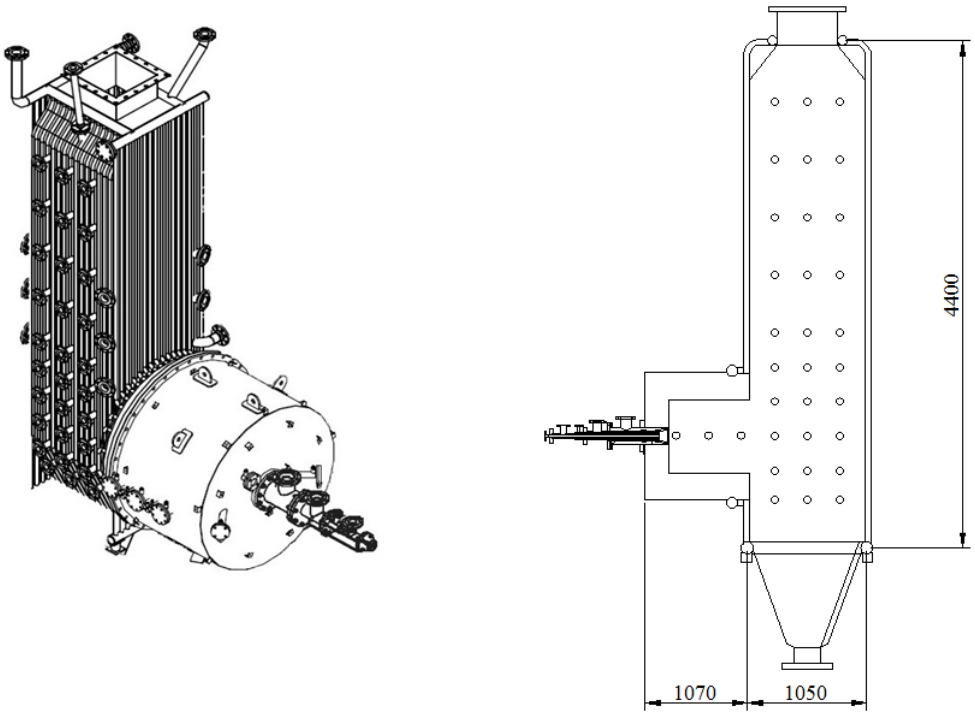

Figure 5.4: Geometry of 0.4 MW_{th} oxy-fuel furnace and dimension.

A schematic diagram for the 0.4 MW_{th} oxy-fuel test facility is illustrated in Fig. 5.6. The process in this pilot-scale plant can be divided into three major systems. These are fuel and oxidant delivery, combustion, instrumentation and control system. Other important systems are fuel grinding unit, drying and blending unit, flue gas treatment system, bulk vessels to storage oxygen and carbon dioxide, fans, electrical heaters, heat exchangers and cooling systems.

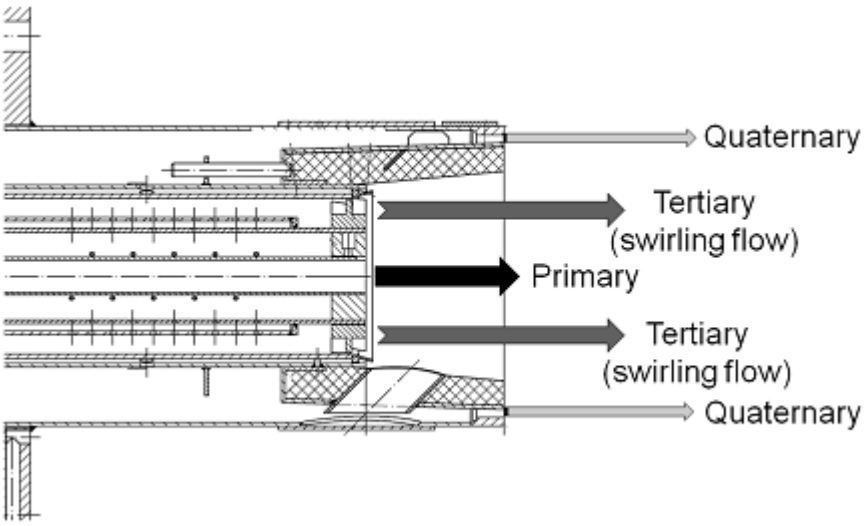

Figure 5.5: Drawing of burner and descriptions of inlet streams.

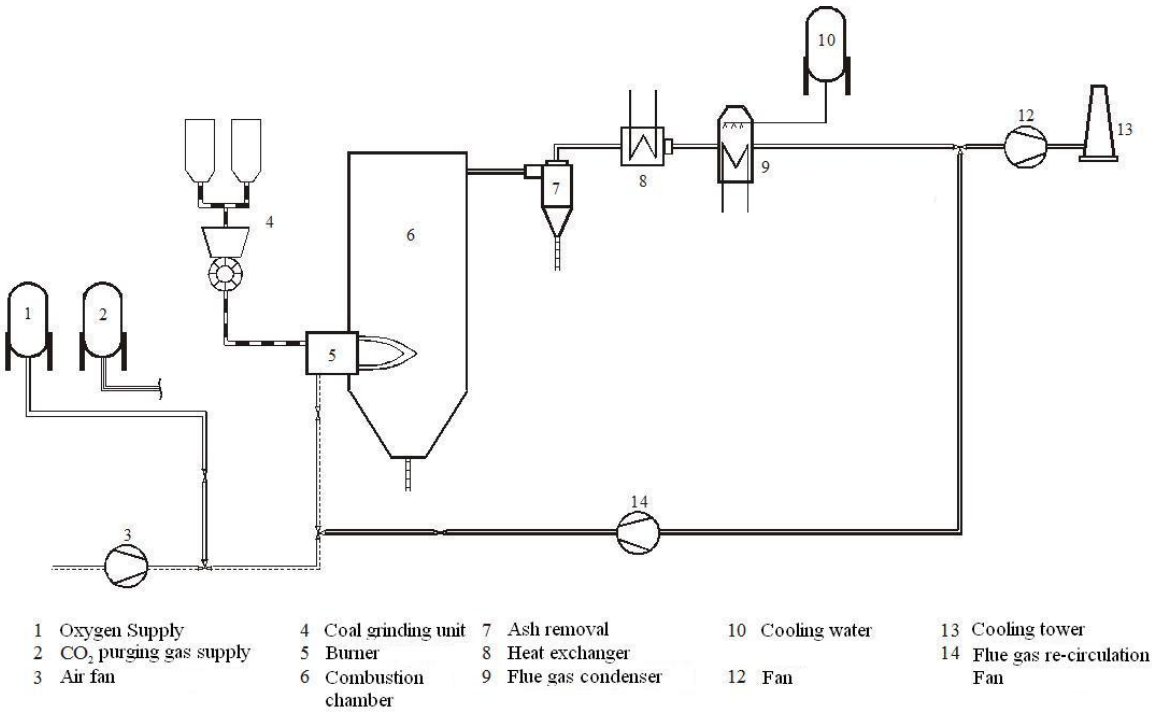

Figure 5.6: Schematic diagram of the 0.4 MW_{th} oxy-fuel test facility.

Gases are premixed and injected through three inlet streams as shown in Fig. 5.6, which are primary (coal carrier), secondary swirl and tertiary stream for staging purpose. Three degrees of swirling blades are available, 30°, 45° and 60°. It is possible to perform numerical simulations using all blades; however, only experimental results with the installation of 45° swirling blade were used as benchmark for validation of numerical CFD model, because the objective of this thesis is to investigate numerical model and validate it with experiments, not for studying oxy-fuel flame stability or the effects of changing

blade angles to aerodynamics. The flame type-0 (low swirling) can occur in oxy-fuel flame comparing to high swirling flame type-2 in air-firing when retrofitting using the same heat capacity (0.48 MW_{th}-0.8 MW_{th}) as commented by Wall et al. [2ndWorkshopOxyIEA07]. Therefore it is expected that the higher molecular weight of rich CO_2 in oxy-fuel flames can results in more inertia force, hence, the higher swirling blade is postulated to increase the recirculation of flow back into burner quarl, which can improve burning efficiency and also flame stability. For this reason, the intermediate blade angle of 45° is selected for the first experiments and expected to provide stable flame in the furnace.

5.2.2 Quantitative measurements

The hemi-spherical radiative heat flux from the medium to the furnace walls were measured by IFRF ellipsoidal radiometer [IFRF10]. It is consisted of a cavity with an aperture at one focus and a thermopile at the other as illustrated in Fig. 5.7.

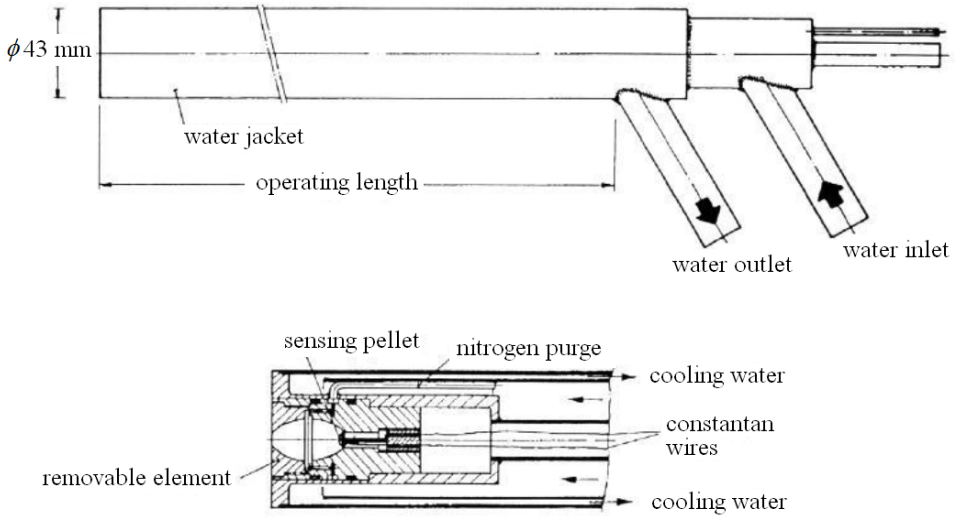

Figure 5.7: Overview of the IFRF ellipsoidal radiometer [IFRF10].

The ellipsoidal cavity has the optical property of focusing all radiation entering the orifice onto the surface of the thermopile. In order to minimize radiation loss due to absorption at the surface of the ellipsoid the latter is plated with a layer of gold. The thermopile is a heat flow plug of stainless steel with two thermocouple junctions at each end (constantan wire) which produces an electromagnetic field proportional to the energy absorbed at the pellet. A protective window is mounted in the cavity to avoid damage to the thermopile and errors due to convection. A purge flow of dry nitrogen (35-50 *litre*/*hour*) is injected on the orifice side of the window in order to prevent the entry of combustion gases. The response time of this instrument is long relative to the frequency of total radiative flux fluctuations, so that only steady state measurements are possible.

The temperature in the furnace will be measured by VDI water cooled suction pyrometer as illustrated in the Fig. 5.8. Basically, the pyrometer has a diameter of 40 mm and consists of two concentric shields, which head is fitted to the end of the water cooled probe, through which the gases are sucked by a compressed-air injector. The two outer ceramics must be fixed with special ceramic cement. A When using pyrometers at a high temperature, the cooling water must be in contact with the entire external tube. To prevent the building of bubbles the complete filling of the suction tube with cooling water is necessary. This is achieved by holding the tube in a horizontal position and directing the supply and removal of water upwards. The water supply is fixed to the rear connecting piece (the cooling water is first led to the internal and later external tubes) and filled with water. Degassing is performed by the output tube connection. Finally, the suction tube is moved up and down at its ends so that all air can escape.

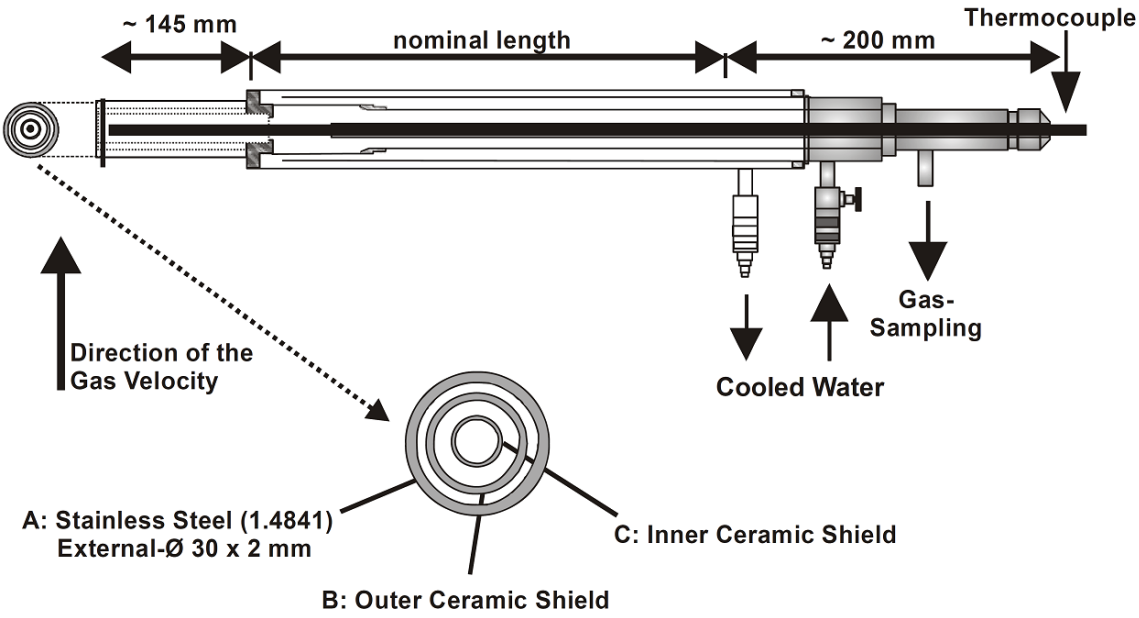

Figure 5.8: Overview of VDI water cooled suction pyrometer [VDI 1994-2011].

Both probes will be calibrated before and after measurement campaigns. The calibration process, using comparison techniques, will be performed by a blackbody furnace and a temperature calibrator. The blackbody furnace has a cylindrical radiation cavity of silicon carbide with internal dimensions consisting of a diameter of 50 mm and length of 350 mm for inserting the probe. The emissivity as a function of internal emissivity and geometry has a value of 0.9782. This furnace operates at temperature up to 1500 °C with a maximal heat flux emitted by the blackbody of 550 kW/m². The temperature calibrator consists of an electrically heated tube furnace able to operate at temperature of up to 1500 °C.

For gas analysis the sample gas collected by a hot, non-cooled suction tube is cooled and dried before directly led through an online continuous gas analyzer for O_2, CO, CO_2 measurements. The ABB Magnos 106 analyzer is used to measure O_2 concentration based on the magneto-mechanical measuring principle. This is based on the specific paramagnetic behavior of oxygen. It has an extremely sensitive paramagnetic cell which makes measurements very accurate. The smallest measuring range is 0-1 Vol% O_2, and the larg-

est measuring range is 0-100 Vol% O_2. The ABB Uras 14 will be used for CO and CO_2 measurements.

5.2.3 Summary of sub-model selection

Many sub-models are investigated using numerical simulations and validated with experimental results from a 100 kW_{th} oxy-coal furnace as described previously. Discussions for the selections of sub-models and comments are explained in details in the numerical results and validation in chapter 6 of this thesis. Finally, sub-models of numerical simulation for the 0.4 MW_{th} oxy-fuel furnace are summarized in Table 5.13.

Table 5.13: Summary of sub-model selections evaluated from investigated case of 100 kW_{th}.

Fundamental study[a]	Sub-models[b]	Reference for parameters[c]
Turbulent models	Standard k-ε	[Launder73]
Char: models/kinetic	KD	react. w. O_2[Field67]/CO_2[Mayer34a]/H_2O[Mayer34b][d]
Volatile: TGC model /mech.	FRED/3-step	volatile rate by Shaw et al. [Shaw91]
		CO rate by Rückert et al. [Rückert03]
		H_2 rate by Rückert et al. [Rückert03]
Radiation: particle	soot absorption	mean absorption coefficient by Felske et al. [Felske77]
Radiation: gas emissivity	WSGG model	new oxy-fuel correlations from HITEMP 2010 (table)

[a] Char = char heterogeneous reactions, kinetic = kinetic rate, Volatile = Volatile homogeneous reactions, TGC = turbulenct gaseous combustion, mech. = reaction mechanisms, particle = particle emissivity/absorption coefficient.

[b] KD = Kinetic-diffusion limited rate, FRED = Finite rate eddy dissipation, 3-step = global 3-step reaction mechanism, soot absorption = soot absorption coeffcient, WSGG = Weighted-sum-of-gray-gases model.

[c] react. = reaction, w. = with, volatile rate = kinetic rate for volatile oxidation, CO rate = kinetic rate for CO oxidation, H_2 rate = kinetic rate for H_2 oxidation, rev. = reversible reaction, As = internal surface area of pore, RPM = random pore models, table = tabulated style, MR = molar ratio dependent.

[d] Although accounting for char oxidation only can provide good prediction from laboratory-scale burner, the burner is still operated with dry flue gas recirculation with less amount of water. For the pilot-scale furnace, the water content is approximatedly 20% (by Vol.) refering to the condition of wet fluegas recirculation, in which the char reaction with H_2O can effect the numerical results.

5.2.4 Operating conditions

Proximate and ultimate analysis for Lusatian lignite utilizing in a 0.4 MW_{th} oxy-fuel furnace are already described in chapter 1, denoted as $TBK_{0.4MWth}$. The furnace can be operated at full or partial load. The partial load operation (around 90%) is used for investigation in this thesis, which refers to thermal load of approximately 350 kW_{th}. The burner and furnace are operated at full load by maintaining the same adiabatic temperature of combustion gas as in air-fired condition with the same thermal capacity (400 kW_{th}). The overall ratio of oxygen/fuel ratio is kept at 1.163 (0.0993, 0.7092 and 0.3545 at primary, secondary and staging stream, respectively shown in Table 5.14) and the mass flow for secondary flow (swirling) to tertiary flow is around 2 to produce the high swirling flame. The swirl number can be estimated using equation present by Beer and Chigier [Beer72] depending on tangential momentum and axial momentum of massflow and has approxi-

mated value of 2 for the installed blade of 45°, implying the flow with intermediate swirl. Flow parameters and wall parameters (operating conditions) for the 0.4 MW_{th} oxy-fuel furnace are presented in Table 5.14 and Table 5.15.

Table 5.14: Flow parameters for 0.4 MW_{th} pilot-scale oxy-fuel furnace for partial load operation (87.5% or 350 kW_{th})**.**

Inlet stream[a]	Mass flow rate (kg/h)	T (°C)	O_2 (% Vol.)	CO_2 (% Vol.)	O_2/fuel ratio
Coal	56.34	-	-	-	-
PS	65.8	17.3	0.19	0.81	0.1051
SS (swirl)	212	153.1	0.33	0.444	0.7112
TS (Stag.)	106	153.1	0.33	0.444	0.3556
Outlet (average)	-	129.82	0.306	0.507	-
				Total	1.172

[a] PS = primary stream, SS = secondary stream, TS = tertiary stream, Stag. = staging stream.

Table 5.15: Wall parameters for 0.4 MW_{th} pilot-scale oxy-fuel furnace.

Wall	Type	T (°C)	Emissivity
Burner quarl	Adiabatic	-	1
Cylindrical muffle: burner side	Const. T	874	0.7
Cylindrical muffle: outer annulus	Const. T	874	0.7
Furnace box: lower part	Const. T	750	0.6
Furnace box: upper part	Const. T	500	0.2
Furnace box: bottom	Const. T	750	0.6
Furnace box: outlet (average)	Const. T	129.82	0.2

[a] Const. T = constant temperature.

5.2.5 Computational mesh

For boiler meshing, the axis-symmetric boundary condition is not valid because the swirling flame is axis-symmetric in the rotational direction of the muffle of burner (cylindrical part) but not inside furnace (rectangular box-part). The vane for secondary flow produces swirling flow in the clockwise direction (Fig. 5.9), influencing flow inside the furnace to flow slightly upward on the left hand side and downward on the right hand side. Therefore the assumption of axis-symmetry cannot be applied inside the furnace's box, even the symmetric boundary condition is also not valid. For this reason, complete mesh of 0.4 MW_{th} oxy-fuel furnace is required to provide physical results of oxy-fuel predictions. The computational mesh for 0.4 MW_{th} oxy-fuel furnace including close-up figure of burner's mesh is presented in Fig. 5.9.

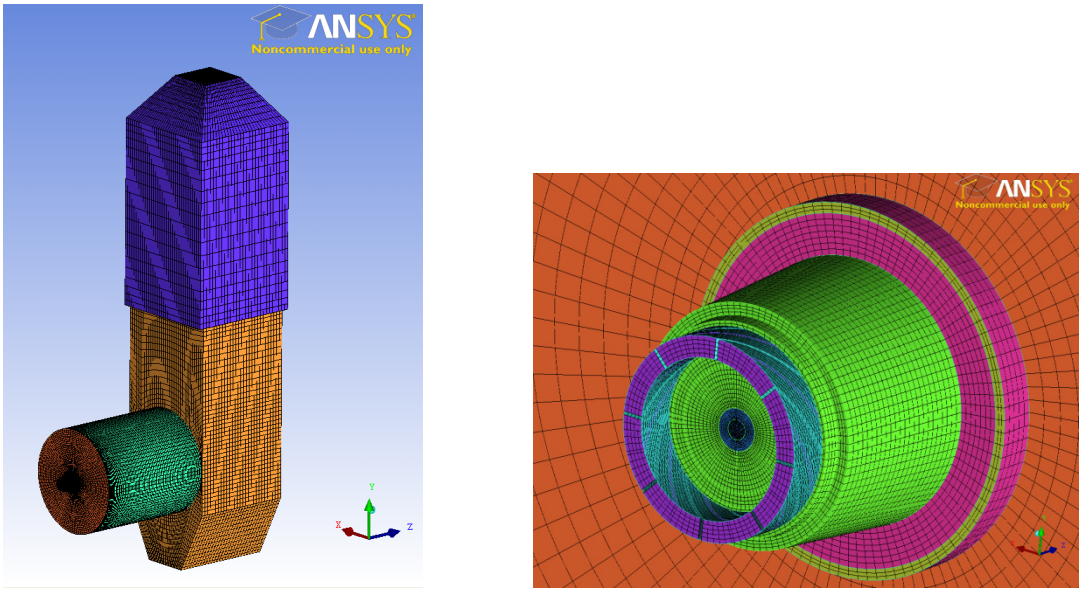

(a) (b)

Figure 5.9: Computational mesh of 1 Million cells for 0.4 MW_{th} oxy-fuel furnace: (a) furnace, (b) swirl burner.

Four sizes of overall computational meshes are tested for mesh dependency of the boiler simulation. There are 500,000, 700,000, 1 Million and 1.6 Million cells created for 45° blade of swirling blades. The abbreviations for numerical results applying each mesh size are 500k, 700k, 1Mio and 1.6Mio, consequently. Suitable number of meshing cells is concluded in the first numerical test and maintained to provide all numerical results in chapter 6 for validation with measurements from experiments.

5.2.6 Pre-calculated parameters

Some parameters must be pre-determined as the same as the smaller scale model (100 kW_{th} CFD case). The required pre-calculated parameters are the turbulence parameters, correlation for the CPD model, stoichiometry of volatile reaction, discrete phase injections and size distributions. There are listed from Table 5.16 to Table 5.20.

Table 5.16: Turbulence intensity and hydraulic diameter (HD) for inlet flow in 0.4 MW_{th} oxy-fuel furnace.

Inlet[a]	Flow rates (kg/s)	Area (m^2)	Density[b] (kg/m^3)	Velocity (m/s)	kine. viscous[c] (m^2/s)	HD (m)	Re	I_{turb} (%)
PS	0.018278	0.0004524	1.734	23.294	9.0021E-06	0.024	62104.24	4.03
SS	0.058889	0.0038453	0.974	15.722	2.2325E-05	0.024	16902.02	4.74
TS (stag.)	0.029444	0.0037888	0.974	7.978	2.2325E-05	0.012	4288.57	5.62
outlet (sum)	0.106611	0.1689210	1.040	0.607	1.9924E-05	0.411	12523.62	4.92

[a] PS = primary inlet stream, SS = secondary swirl inlet stream, TS = tertiary inlet stream, Stag = staging stream, outlet = outlet (exit) of furnace.
[b] Density calculated using FluidEXL library by Professor Hans-Joachim Kretzschmar from Department of Technical Thermodynamics, the University of Applied Sciences Zittau/Görlitz (FH), "http://thermodynamik.hs-zigr.de".
[c] kine. viscous. = kinematic viscosity (calculated by the same thermodynamic library as densityb).

Table 5.17: Five coal specific input-parameters for the CPD model (Lusatian lignite, $TBK_{0.4MWth}$).

Parameter	Definition	Value
IB_0	Initial fraction of bridge in coal lattice	0.644
chb_0	Initial fraction of char bridge	0.150
$LC_{\sigma+1}$	Lattice coordination number	4.459
$MW_{cluster}$	Cluster Molecular weight	332.083
MW_{δ}	Side chain molecular weight	47.630

Table 5.18: Stoichiometric parameters for global 3-step reaction mechanisms, CO and H_2 as intermediate specie. The calculation is based on coal properties of Lusatian lignite ($TBK_{0.4MWth}$).

Reactant		Product			
VM	O_2	CO	H_2	N_2	SO_2
1	0.0812	1.0156	1.3082	0.0165	0.0165

Table 5.19: Particle tracks for the discrete phase injections in 0.4 MW_{th} furnace (surface injections) pre-calculated based on applying 1 Million computational cells.

Index	Descriptions	Values
a	Total cells	1 Million
b	Number of burner	1
c	Number of injections (surface injections)	1150
d	Number of diameters (Rosin Rammler distribution)	5
e	Number of particle tries (turbulence dispersion)	8
f	Total particles in the domain (=b×c×d×e)	46000
g	Total number of trajectory cells	323
h	Furnace length (m)	6.528
i	Step length factor	20
j	Number of calculating steps for 1 particle (g×i)	6460
k	Estimated length scale (g,i)	0.0010
l	Total Maximum number of steps (e×j)	51680

The number of computational cells at the primary inlet at burner of 0.4 MW_{th} furnace is about 1150 cells. This value is sixth time higher than 270 cells at primary stream of the 100 kW_{th} model. Furthermore, the total computational meshes in 0.4 MW_{th} model is around 1 Million, which is double in the number of cells than the smaller scale furnace. Another consideration is the mesh quality. The meshing in the 0.4 MW_{th} model is more complicated than the 100 kW_{th} model because of containing both cylindrical and rectangular control volume requiring more mesh refinement for the CFD model and implying the longer calculating time. Therefore, surface injection-type is not suitable for the bigger scale model and group injection is more appropriated. Pulverized coal particles are injected with surface injections applying meshing cells-dependent parameters for the discrete phase models listed in Table 5.19. Particle distribution for Lusatian coal is determined applying parameters for Rosin-Rammler particle distribution (Table 5.20 based on sieve

analysis from coal container utilized for operation of 0.4 MW_{th} oxy-fuel furnace. Plot of approximation and measurement for coal particle distribution are shown in Fig. 5.10.

Table 5.20: Parameters for Rosin-Rammer distribution for coal particles (Lusatian lignite, $TBK_{0.4MWth}$).

Parameters	Values
Mean diameter, $\bar{d}_p$	60
Size distribution parameter, n_{RR}	0.8957

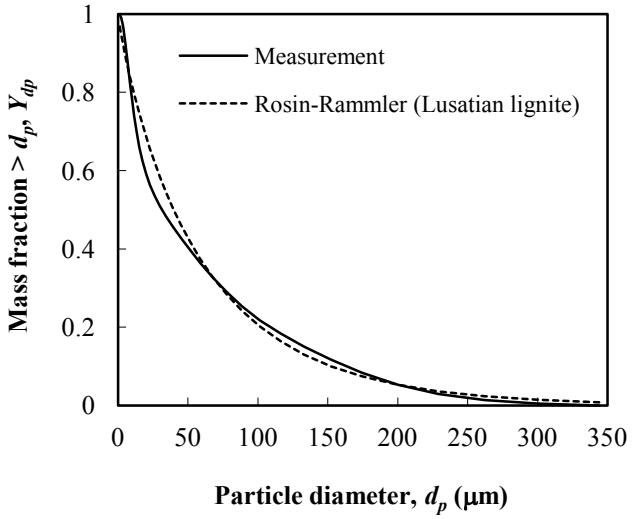

Figure 5.10: Approximated size distribution for Lusatian lignite ($TBK_{0.4MWth}$) by Rosin-Rammler distribution method (dash line) and measurement (solid line).

5.2.7 Positions of measurement

Temperature measurements are performed by inserting water cooled VDI suction pyrometer at different locations starting from the side walls of furnace. Seven horizontal locations are prepared for the measurements and later used for numerical validation. The location of measurements are shown in Fig. 5.11. The horizontal location along the plotting line in CFD control volume is listed in Table 5.21, indicating by the starting and ending point of the plotting line. Distances from port A, B, C from burner quarl are listed in Table 5.22, and additional locations are shown in Table 5.23. Radiation quantity (surface incident radiation) for hemi-spherical radiation intensity is measured by ports listed in Table 5.24. Gas concentrations and hemi-spherical radiation intensity are measured at the same location as temperature measurements using gas suction cooled probe and IFRF ellipsoidal radiometer, consequently.

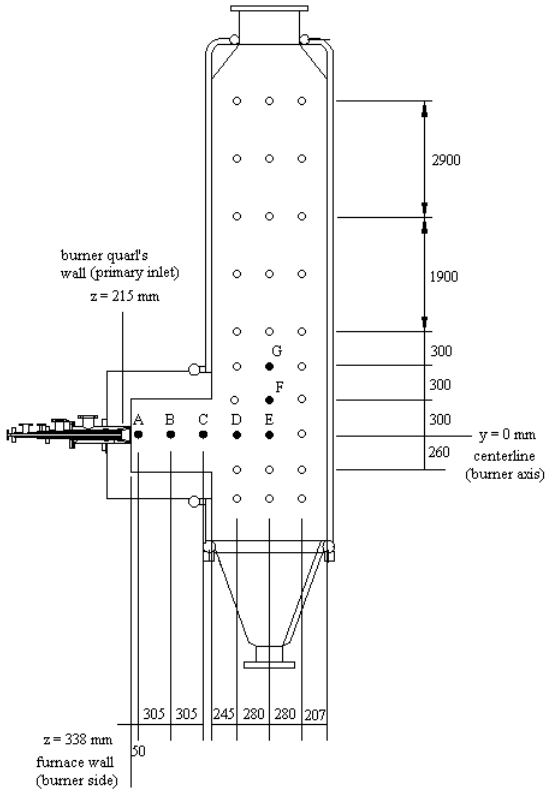

Figure 5.11: Locations of measurement (black dots) or starting and ending point for line plotting along x-direction in CFD control volume.

Table 5.21: Locations of measurements, specifying by line name defined by the starting and ending point for line plotting along x-direction in CFD control volume.

Line name	Starting side wall's position (left)			Ending side wall's position (right)		
	x0(m)	y0(m)	z0(m)	x1(m)	y1(m)	z1(m)
A	-0.475	0	0.388	0.475	0	0.388
B	-0.475	0	0.693	0.475	0	0.693
C	-0.475	0	0.998	0.475	0	0.998
D	-0.456	0	1.607	0.456	0	1.607
E	-0.456	0	1.887	0.456	0	1.887
F	-0.456	0.3	1.887	0.456	0.3	1.887
G	-0.456	0.6	1.887	0.456	0.6	1.887

Table 5.22: Distance from burner quarl (primary inlet).

Line	Δz (m) [a]
A	0.173
B	0.478
C	0.783

[a] distances based on reference location of 0.215 m at position between quarl and cylindrical part.

Table 5.23: Additional investigated plotting lines inside 0.4 MW_{th} furnace.

Line descriptions	Starting side wall's position (left)			Ending side wall's position (right)		
	x0(m)	y0(m)	z0(m)	x1(m)	y1(m)	z1(m)
Centerline from burner (horizontal)	0	0	0.215	0	0	2.321
Vertical line from hopper (furnace box)	0	-0.962	1.887	0	3.438	1.887

Table 5.24: Positions of measurement for surface incident radiation (hemi-spherical intensity) located parallel to burner's centerline on surface of cylindrical wall of furnace (z-direction).

Line name	Starting side wall's position (left)			Ending side wall's position (right)		
	x0(m)	y0(m)	z0(m)	x1(m)	y1(m)	z1(m)
ABC	-0.475	0	0.388	-0.475	0	0.998
DE	-0.456	0	1.607	-0.456	0	1.887

6 Numerical Results, Validation and Discussion

Numerical results in this chapter are explained separately due to different purposes of studies. The case of one-dimensional parallel infinite plates in chapter 4 is used for validation of radiation model for gas properties of various mixtures in oxy-fuel conditions from ratios of molar fraction MR from 0.125 to 4, which guarantees an accuracy of prediction of radiation properties of gaseous mixtures.

The first investigated numerical CFD case of 100 kW_{th} oxy-fuel furnace in chapter 5 is created aiming to study influences of selection of several possible sub-mathematical models to accuracy of predictions of velocity, temperature and oxygen concentration. After evaluation influence of selection of sub-mathematical models validated with experimental measurements in 100 kW_{th} oxy-fuel furnace from publication, the numerical CFD model for lignite oxy-fuel combustion is established and applies to the numerical predictions of the new 0.4 MW_{th} oxy-fuel test facility at BTU Cottbus using Lusatian lignite as resource of burning. The numerical results of temperature, gaseous concentrations (O_2, CO_2, H_2O) and hemi-spherical radiation intensity were compared and validated with experimental values obtained from the test facility.

6.1 One-dimensional infinite plates

As explained in chapter 4, the proposed oxy-fuel correlations can be evaluated by the radiative source terms and the net radiative heat fluxes calculated using the new correlations compared with LBL calculations from HITEMP 2010 database for one-dimensional infinite plates. Ten cases are investigated for conditions of isothermal homogeneous, non-isothermal homogeneous and non-isothermal non-homogeneous gas mixture, already summarized in Table 4.9 (chapter 4).

For abbreviated name of testes cases, the results using the set of correlations proposed by Smith et al. [SmithTF82] with three gray gases are denoted as Smith82, by Johansson et al. [Johansson11] with four gray-one clear gases as WSGG4-Johansson11, and by Yin et al. [Yin10] with four gray-one clear gases as WSGG4-Yin10. For the results using correlations from the present work, two approaches were tested. If radiation quantities were calculated using new oxy-fuel correlations for absorption coefficient κ_i and emittance weighting factor w_i from Table 4.4, this case is referred as WSGG4table-Tanin12. Otherwise, if molar ratio dependent polynomial coefficients ($C1_{i,j}$, $C2_{i,j}$, $C3_{i,j}$, $CK1_i$, $CK2_i$ and $CK3_i$) from Table 4.5 and Table 4.6 are applied, it is denoted as WSGG4coef-Tanin12.

Relative errors of the net radiative heat flux at the walls and the radiative source term from the new correlations with respect to LBL integration of HITEMP 2010 database are compared in Table 6.1 for path-lengths of 1.0, 10 and 60 m for conditions of isothermal homogeneous, non-isothermal homogeneous and non-isothermal non-homogeneous gas mixture using the test cases which were discussed in Table 4.9 (chapter 4) of this thesis.

6.1.1 Total emissivity

Total emittances from the new correlations for WSGG model at MR = 0.125-4.0 are presented in Appendix D. The total emittance at MR = 0.125 (dry-FGR) and MR = 1.0 (wet-FGR) for temperatures varying from 400 to 2500 K and pressure path-lengths ranging from 0.001 to 60 bar-m are plotted with the ones generated by LBL calculations from HITEMP 2010 database in Fig. 6.1 for MR = 0.125 (Fig. 6.1(a)) and MR = 1.0 (Fig. 6.1(b)).

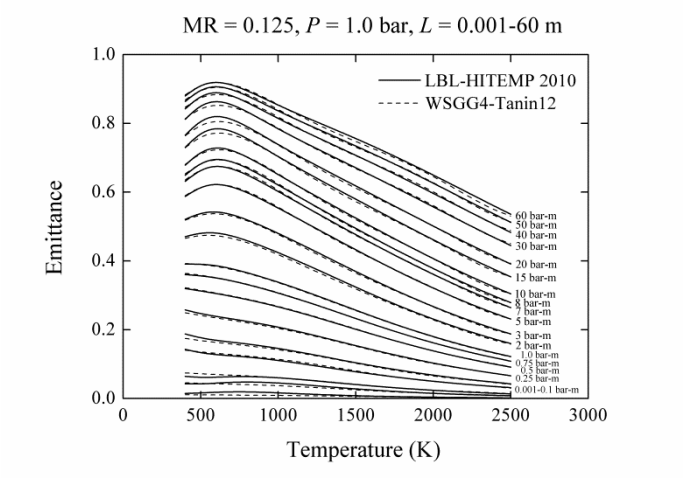

(a)

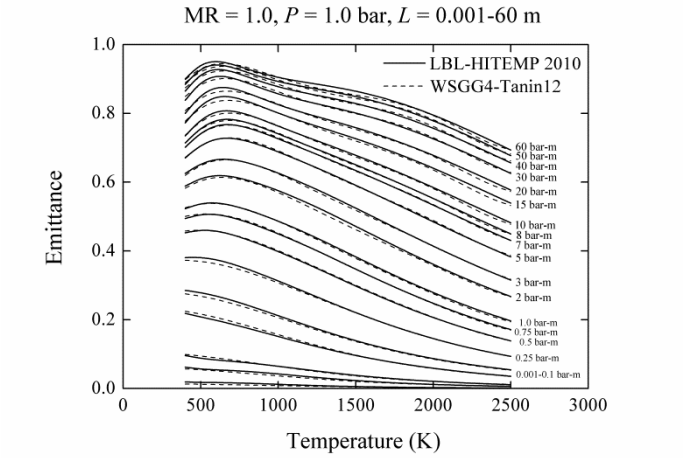

(b)

Figure 6.1: Total emittance dependence with temperatures calculated from LBL integration of HITEMP 2010 database (solid lines) and from the proposed correlations of the WSGG model (dashed lines): (a) MR = 0.125, (b) MR = 1.0.

In order to evaluate the influence of the path-length and temperature in the calculation of total emittance, Fig. 6.2 shows the total emittance for MR = 0.125 (Fig. 6.2(a)) and for MR = 1.0 (Fig. 6.2(b)) varying with path-lengths up to 60 m at three temperatures: 500, 1500 and 2000 K. A stepwise of 0.1 m is used for an increment of path-length in the calculation. In both Figs. 6.2(a) and 6.2(b), the emittance decreases when the temperature of the combustion gas increases from 500 K to 2000 K. It is also shown in Fig. 6.2(a) and

6.2(b) that this effect is more important for MR = 0.125 (isothermal dry-FGR) than for MR = 1.0 (isothermal wet-FGR).

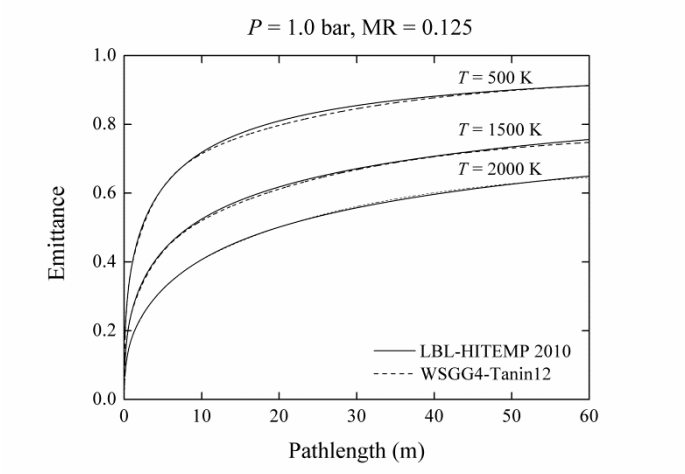

(a)

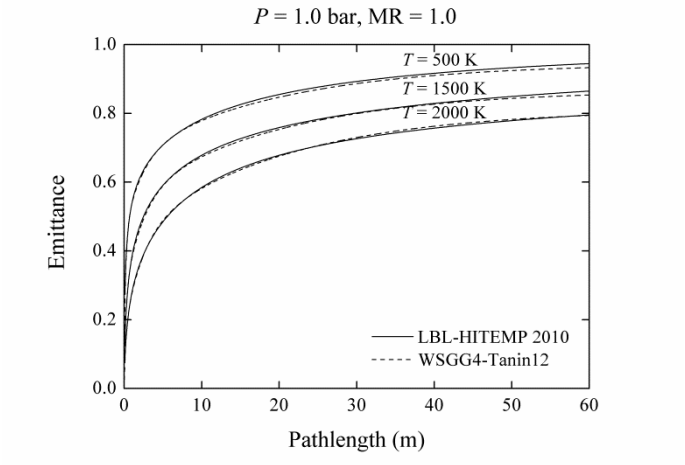

(b)

Figure 6.2: Total emittance dependence with path-lengths at 500, 1500 and 2000 K calculated from LBL integration of HITEMP 2010 database (solid lines) and from the proposed correlations for WSGG model (dashed lines): (a) MR = 0.125, (b) MR = 1.0.

For an influence of the molar ratios MR and path-length using the new correlation compared with the benchmark LBL-HITEMP 2010 solution, the total emittances are plotted varying the path-lengths for MR = 0.125 and 1.0 in Figs. 6.3(a)-6.3(c), at temperatures of 500, 1500 and 2000 K, consequently. As seen in the figures, applying these new correlations provide more accurate predictions of emittance at temperatures close to flame temperature (1500 and 2000 K) than in the lower temperature zones (500 K), such as in gaseous regions at the exit of furnace near super-heater or at the hopper area. It is clear from these figures that changing the molar ratio MR in combustion atmosphere affects the calculation of the emittance at higher temperatures (2000 K) more importantly than at lower temperatures (500 and 1000 K).

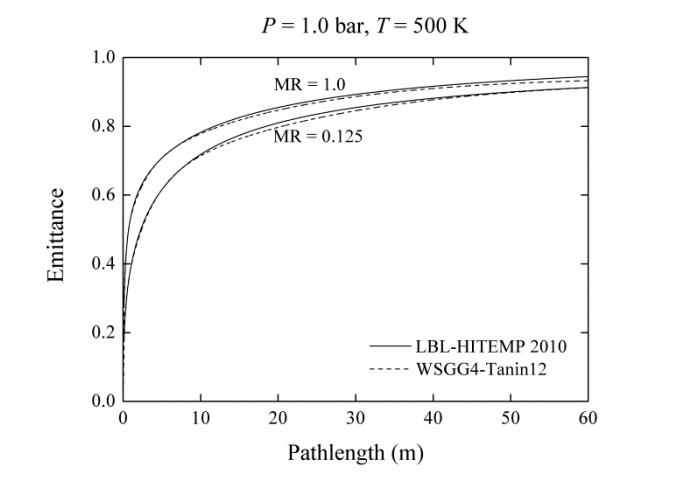

(a)

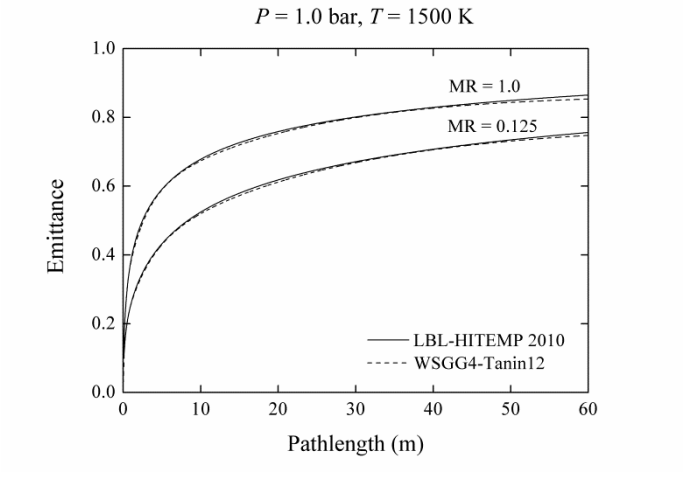

(b)

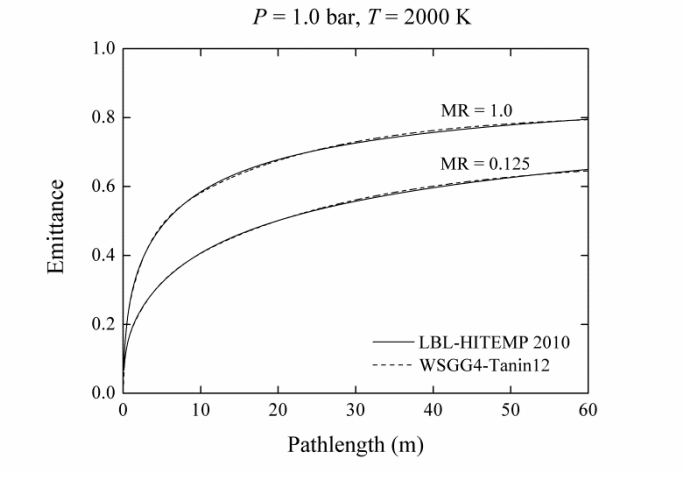

(c)

Figure 6.3: Total emittance dependence with path-lengths at MR = 0.125 and 1.0 calculated from the LBL integration of HITEMP 2010 database (solid lines) and from the proposed correlations of the WSGG model (dashed lines): (a) T = 500 K, (b) T = 1500 K, (c) T = 2000 K.

When applying different correlations from this study and from other papers, total emittances varying with temperatures for path-lengths of 1.0,10 and 60 m are compared with the benchmark LBL-HITEMP 2010 solution in Fig. 6.4(a) for MR = 0.125 (isothermal dry-FGR) and in Fig. 6.4(b) for MR = 1.0 (isothermal wet-FGR), consequently. It is clear from the figure that the path-length have more influence than the temperature on the calculation of the total emittances from different correlations. The total emittances by correlations from other works are more importantly deviated from the LBL-HITEMP 2010 solution for higher path-lengths than at for lower values.

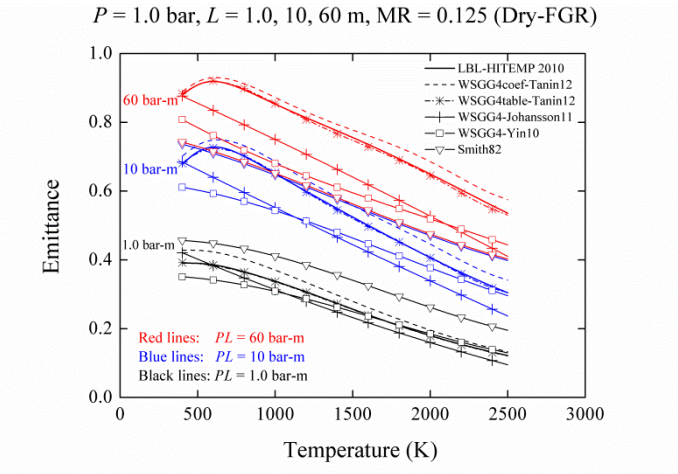

(a)

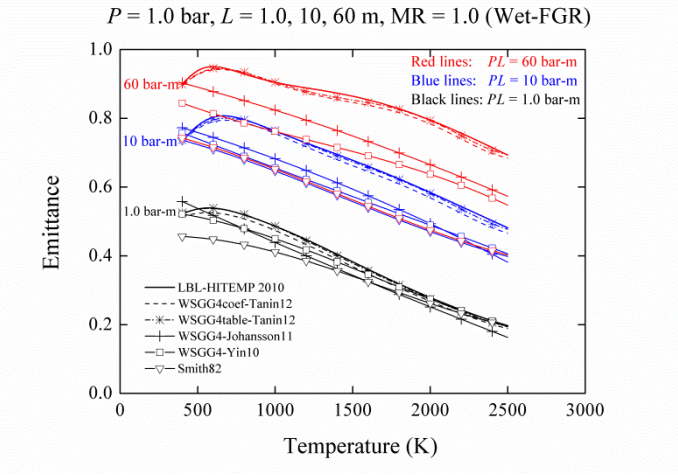

(b)

Figure 6.4: Total emittance dependence with temperatures applying different correlations of the WSGG model for: (a) MR = 0.125, (b) MR = 1.0.

Figs. 6.5(a) and 6.5(b) show total emittances calculated from different correlations with path-lengths varying up to 60 m for MR = 0.125 and 1.0, respectively. As seen, the correlations from this study provided the best accuracy in comparison to the LBL-HITEMP 2010 solution for all path-lengths. Applying correlations from Johansson et al. (WSGG4-Johansson11) resulted in the second best results, and followed by correlations from Yin et al. (WSGG4-Yin10). Correlations from Smith et al. (Smith82) resulted in predictions with the lowest accuracy among all correlations. Errors from the calculation of emittance from

correlations from the other authors increased for path-lengths larger than 5.0 bar-m (PL > 5.0 bar-m). The emittance calculated from the correlations of Smith et al. (Smith82) are not included in Fig. 6.5 because only the correlation for MR = 1.0 were available in the paper.

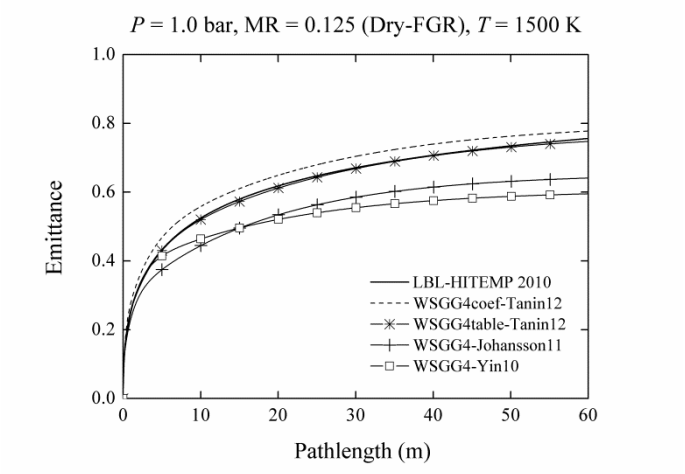

(a)

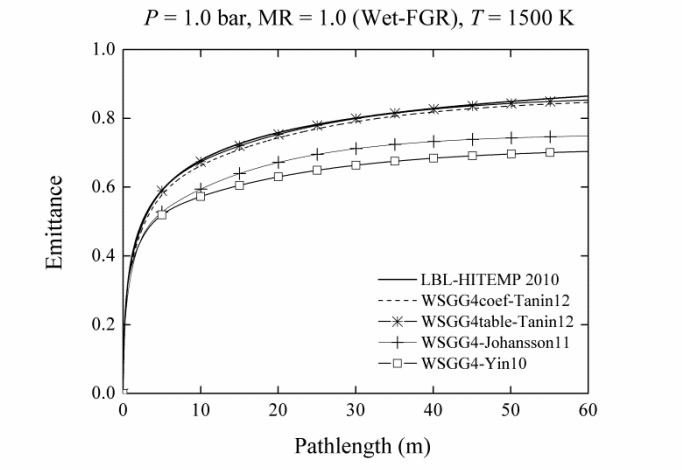

(b)

Figure 6.5: Total emittance dependence with path-lengths applying different correlations of the WSGG model for: (a) MR = 0.125, (b) MR = 1.0.

6.1.2 Radiative source term and heat flux

To evaluate the relative errors for the new oxy-fuel correlations, radiative source terms and net radiative heat fluxes at the walls computed by the LBL integration of HITEMP 2010 database is used as a benchmark for comparison with results obtained by applying the proposed correlations of the WSGG model. The results applying correlations from other works are also included and shown in Table 6.1.

Errors of the radiative heat flux at the wall, $err(q_w)$, the radiative source term at the mid-distance between plates ($x = 0.5L$), $err(\nabla q_{half})$, and the radiative source term over the do-

main ($0 < x < L$), $err(\nabla q_{avg})$ are evaluated by varying path-lengths from 0.5-60 m with a stepwise of 0.5 m. The relative errors are expressed by:

$$err(q_w) = \frac{|q_{w,HITEMP} - q_{w,WSGG}|}{|q_{w,HITEMP}|} \times 100 \quad (6.1)$$

$$err(\nabla q_{half}) = \frac{|\dot{q}_{half,HITEMP} - \dot{q}_{half,WSGG}|}{|\dot{q}_{half,HITEMP}|} \times 100 \quad (6.2)$$

$$err(\nabla q_{avg}) = \frac{\int_{x=0}^{x=L} |(\dot{q}_{HITEMP} - \dot{q}_{WSGG})|}{\int_{x=0}^{x=L} |(\dot{q}_{HITEMP})|} \times 100 \quad (6.3)$$

where $\dot{q}_{HITEMP}$ is the radiative source term from LBL integration of HITEMP 2010 database and $\dot{q}_{WSGG}$ is the radiative source terms calculated by different correlations for WSGG model from this and the other works; $q_{w,HITEMP}$ and $q_{w,WSGG}$ are the radiative heat flux at the wall from LBL-HITEMP 2010 and from different correlation for WSGG model, respectively.

The relative errors of the radiative source terms and heat flux applying the new oxy-fuel correlations proposed in this study are presented for the case of homogeneous mixture in Fig. 6.6 (uniform distribution of MR) and of non-isothermal and non-homogeneous mixture in Fig. 6.7. For isothermal medium in Fig. 6.6, the maximum relative errors of heat flux, $err(q_w)$, increased from 7.0% for case 1.1 in Fig. 6.6(a) (MR = 0.125, $Y_t = 0.9$) to 10% for case 1.2 in Fig. 6.6(b) (MR = 1.0, $Y_t = 0.96$). For non-isothermal cases, the errors increased from 15% for case 2.1 in Fig. 6.6(c) to 30% for case 2.2 in Fig. 6.6(d). The errors reduced to less than 10% for non-isothermal cases 3.1 and 3.2 in Figs. 6.6(e) and 6.6(f) with a negative cosine term.

The relative error of radiative heat flux was less than 15% for the non-homogeneous medium, cases 4.1, 4.3 and 4.5 in Figs. 6.7(a), 6.7(c) and 6.7(e), except cases 4.2 and 4.4 in which errors were less than 26 %. Cases 4.2 and 4.4 imply oxy-fuel conditions with high maximum MR of 2 and 4, respectively.

The relative errors of radiative heat flux are within 30% for all cases and increasing MR results in more errors except the case of negative cosine term of temperature profile (case 3.1 and 3.2), especially at higher path-length (L = 60 m). This implies that more H_2O contents in oxy-fuel conditions induce additional errors in the heat flux calculation. The relative errors of the heat flux tend to increase with path-lengths for almost all cases excluding case 4.3.

In Fig. 6.6, Average radiative source term errors, $err(\nabla q_{avg})$, for isothermal and non-isothermal cases (cases 1-3) were lower than 12 %, while for non-homogeneous cases (cases 4.1-4.5) the error were less than 20 % except for extreme conditions of MR variation (0.125-4) in cases 4.2 and 4.3, which were lower than 30 %. For isothermal and non-isothermal cases (cases 1-3), when MR changed from 0.125 to 1.0, the average radiative source term errors for all path-lengths tended to increase slightly, except for case 3.2 with a negative cosine term in the temperature profile.

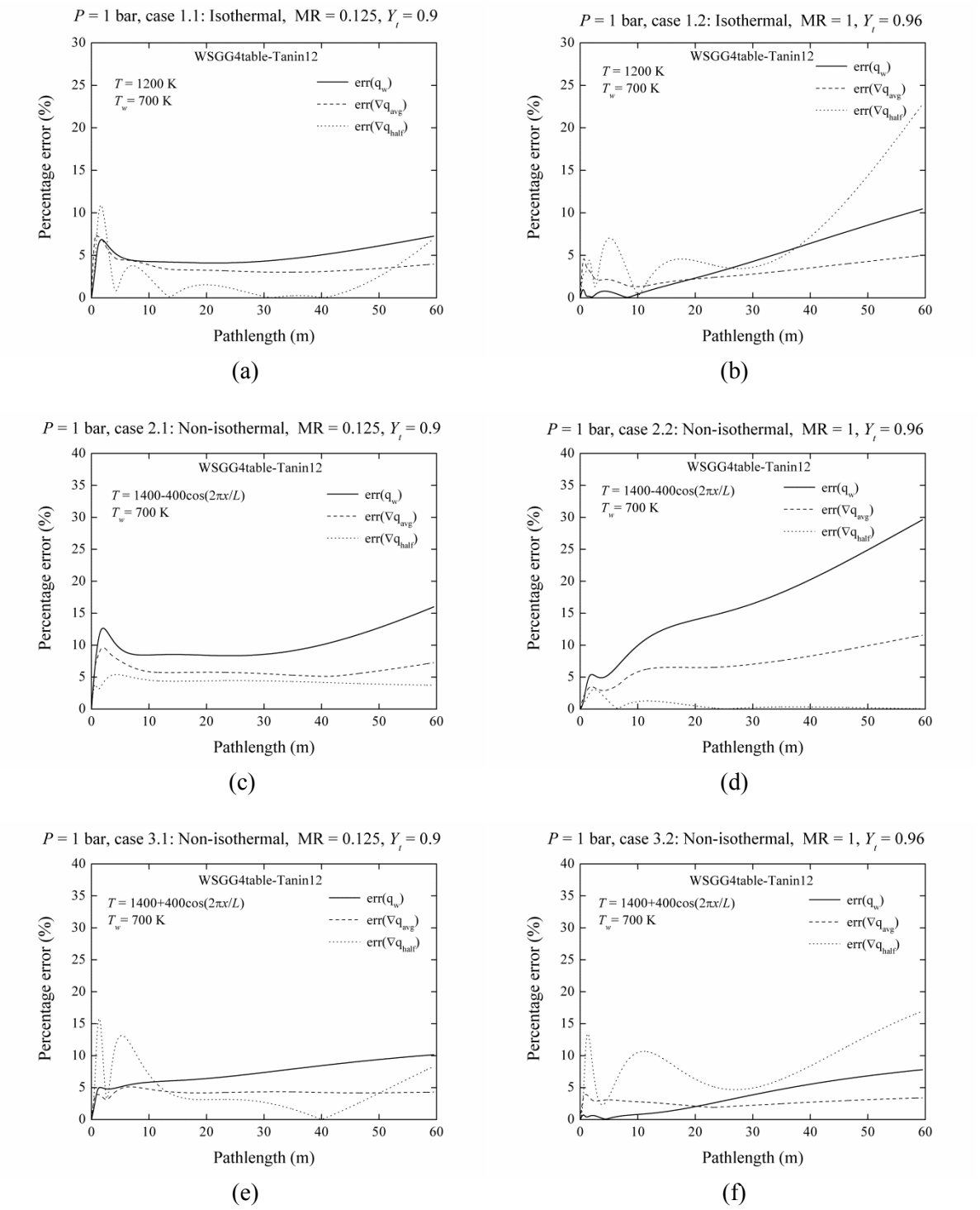

Figure 6.6: Relative errors of radiative heat flux and source term ($err(q_w)$, $err(\nabla q_{avg})$ and $err(\nabla q_{half})$) applying the new oxy-fuel correlations for isothermal and non-isothermal homogeneous cases (case 1-3).

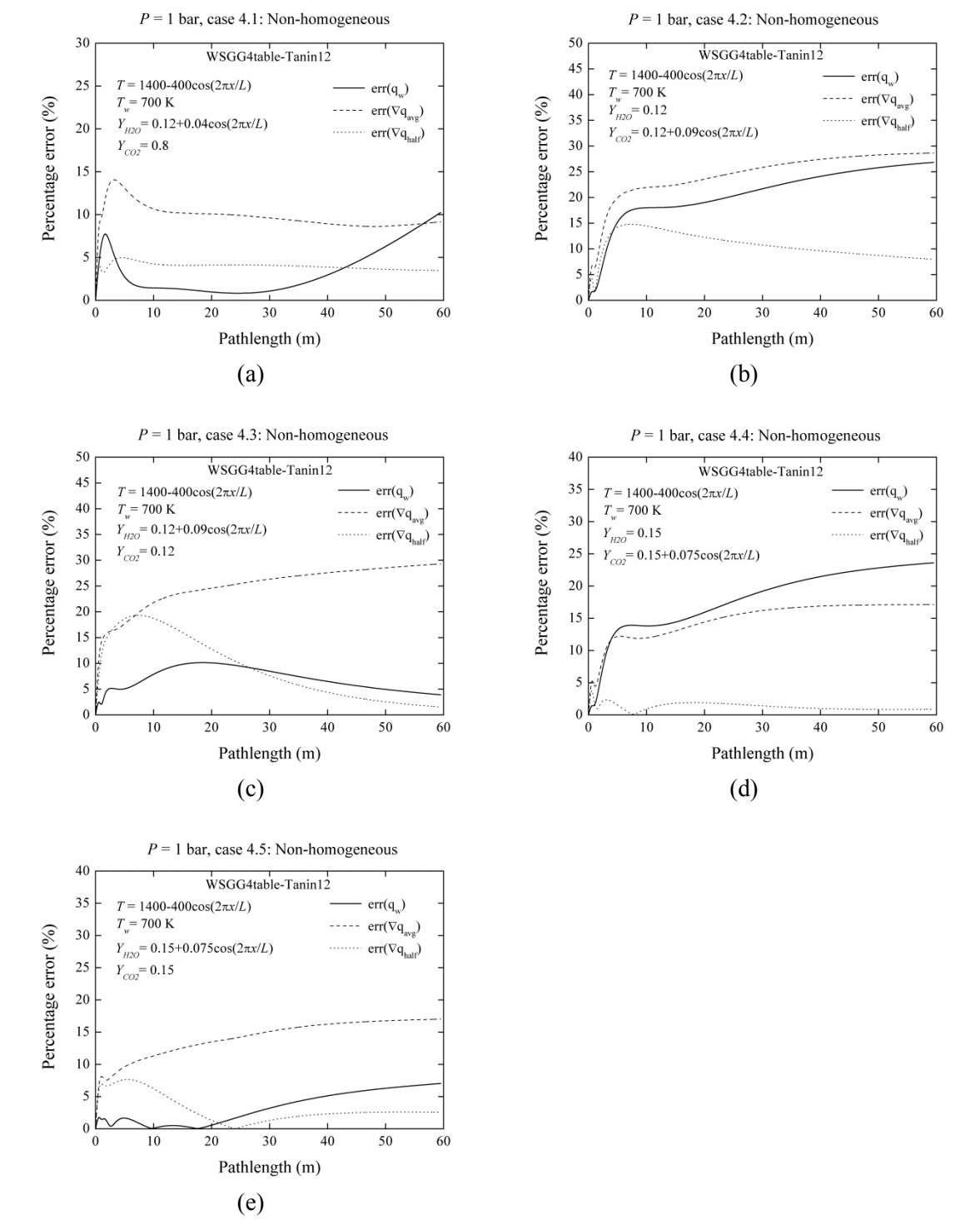

Figure 6.7: Relative errors of radiative heat flux and source term ($err(q_w)$, $err(\nabla q_{avg})$ and $err(\nabla q_{half})$) applying the new oxy-fuel correlations for non-isothermal non-homogeneous cases (case 4).

For the non-homogeneous cases (cases 4.1-4.5), the errors were within 15 % in case 4.1, 17 % in cases 4.4-4.5 (MR = 0.125-2) and 30 % in cases 4.2-4.3 (MR = 0.125-4). Additional errors in cases 4.2-4.3 was due to the limitation of the number of gray gases in the WSGG model to cope with oxy-fuel conditions with stronger fluctuations of MR from 0.125 to 4.0.

Errors for the radiative source term at the mid-distance between one-dimensional infinite plates, $err(\nabla q_{half})$, were less than 23 % for all cases in Fig. 6.6 and Fig. 6.7. However, it should be noted that this error did not increase with path-lengths. Uncertainties when applying the new oxy-fuel correlations for all investigated cases (cases 1-4) to the calculation of radiative properties were within 30 % for radiative heat flux errors and 15 % for average radiative source term errors.

In oxy-fuel conditions, gaseous mixture between hot black walls ($\varepsilon_w = 1$, $T = 700$ K) in case 4.1 represents dry flue gas recirculation (dry-FGR) with temperature profile of gas from oxy-fuel experiment given by Eq. (4.35). Case 4.1 better represents dry-FGR in oxy-fuel conditions than either case 1.1 (isothermal) or case 2.1 (non-isothermal) because of the variation of H_2O in oxy-fuel furnace, as demonstrated in experiments of oxy-propane firing flame [Andersson08b], while case 2.2 is a reasonable representation of wet-FGR case with MR = 1.0.

For these oxy-fuel cases, relative errors for the radiative heat flux, $err(q_w)$, the average source term $err(\nabla q_{avg})$, and the source term at the mid-distance between the plates, $err(\nabla q_{half})$, were evaluated for different correlations for WSGG model considering different path-lengths in Fig. 6.8. For the predictions of the radiative heat flux for case 4.1 (dry-FGR) and 2.2 (wet-FGR), errors of up to 85 % were found when applying correlations of Smith82. When applying correlations of WSGG4-Johansson11 and WSGG4-Yin10, the maximum heat flux errors increased from approximately 20 % in the case of dry-FGR (case 4.1) to 50 % of wet-FGR (case 2.2). The heat flux errors using either correlations of WSGG4coef-Tanin12 or WSGG4table-Tanin12 were only 5 % in the case of dry-FGR and increased to 10 % in the case of wet-FGR. This indicates that errors less than 10 % for the radiative heat flux errors are expected for dry-FGR and wet-FGR.

For a better sense of the radiative quantities, the radiative source terms, $\dot{q}$, and the radiative heat fluxes, q_w, along the length coordinate x applying different correlations for WSGG model for case 4.1 (dry-FGR) and 2.2 (wet-FGR) are plotted in Fig. 6.9 and Fig. 6.10 for path-lengths of 1.0, 10 and 60 m. The radiative source terms and the radiative heat fluxes for all cases (case 1-4) are also presented in Appendix E. Additional plots for radiative heat fluxes (incident wall flux) varying with path-lengths from 0.5 to 60 m (P = 1 bar), applying various oxy-fuel correlations, are also presented in Appendix F.

To evaluate the accuracy of the solutions, Table 6.1 also shows the relative errors of the radiative source terms and heat flux ($err(q_w)$, $err(\nabla q_{avg})$ and $err(\nabla q_{half})$) in comparison with the LBL integration of the HITEMP 2010 database using different correlations for the WSGG model. The relative errors for path-lengths from 0.5-60 m (case 1-4) applying all correlations are also illustrated in Appendix G.

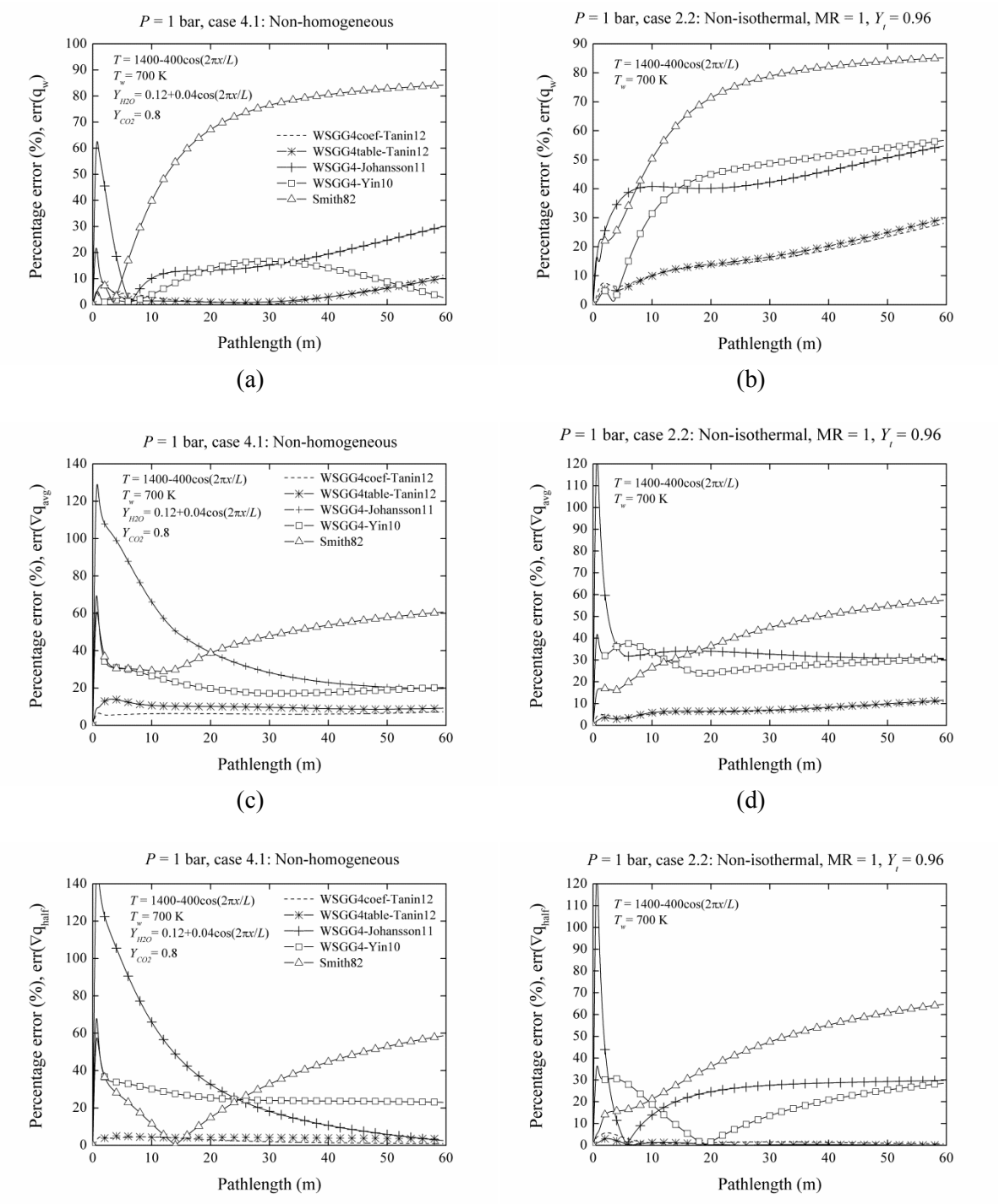

Figure 6.8: Comparison of relative errors of radiative heat flux and source term ($err(q_w)$, $err(\nabla q_{avg})$ and $err(\nabla q_{half})$) applying different correlations for WSGG model varying with path-lengths (left hand side: (a),(c),(e) = case 4.1 (dry-FGR), right hand side: (b),(c),(d) = case 2.2 (wet-FGR)).

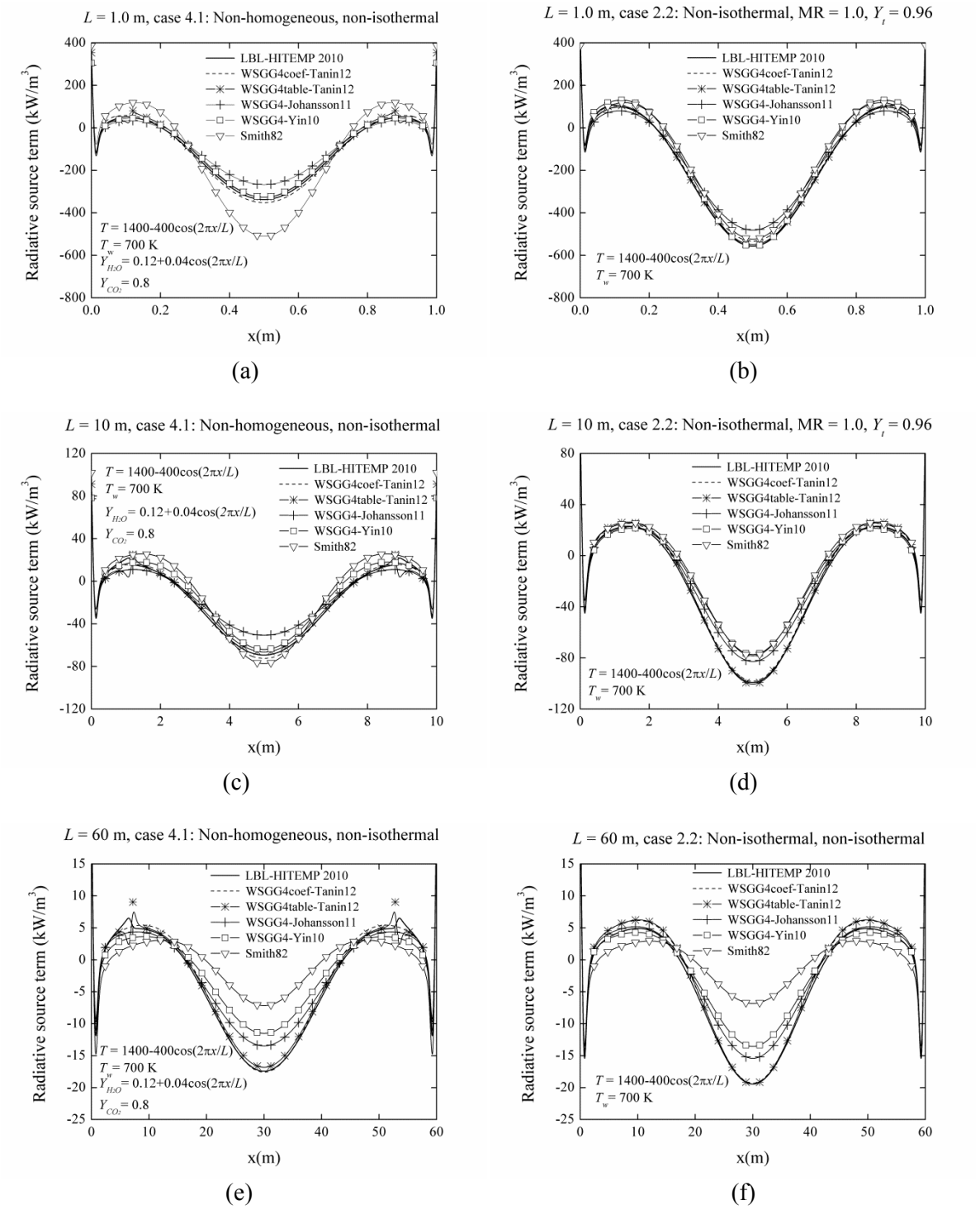

Figure 6.9: Radiative source terms ($\dot{q}$) computed with different correlations of the WSGG model along length coordinates for dry-FGR (left hand side) in case 4.1 and wet-FGR (right hand side) in case 2.2: (a) and (b) L = 1.0 m, (c) and (d) L = 10 m, (e) and (f) L = 60 m. For all cases, total pressure equal to P = 1.0 bar.

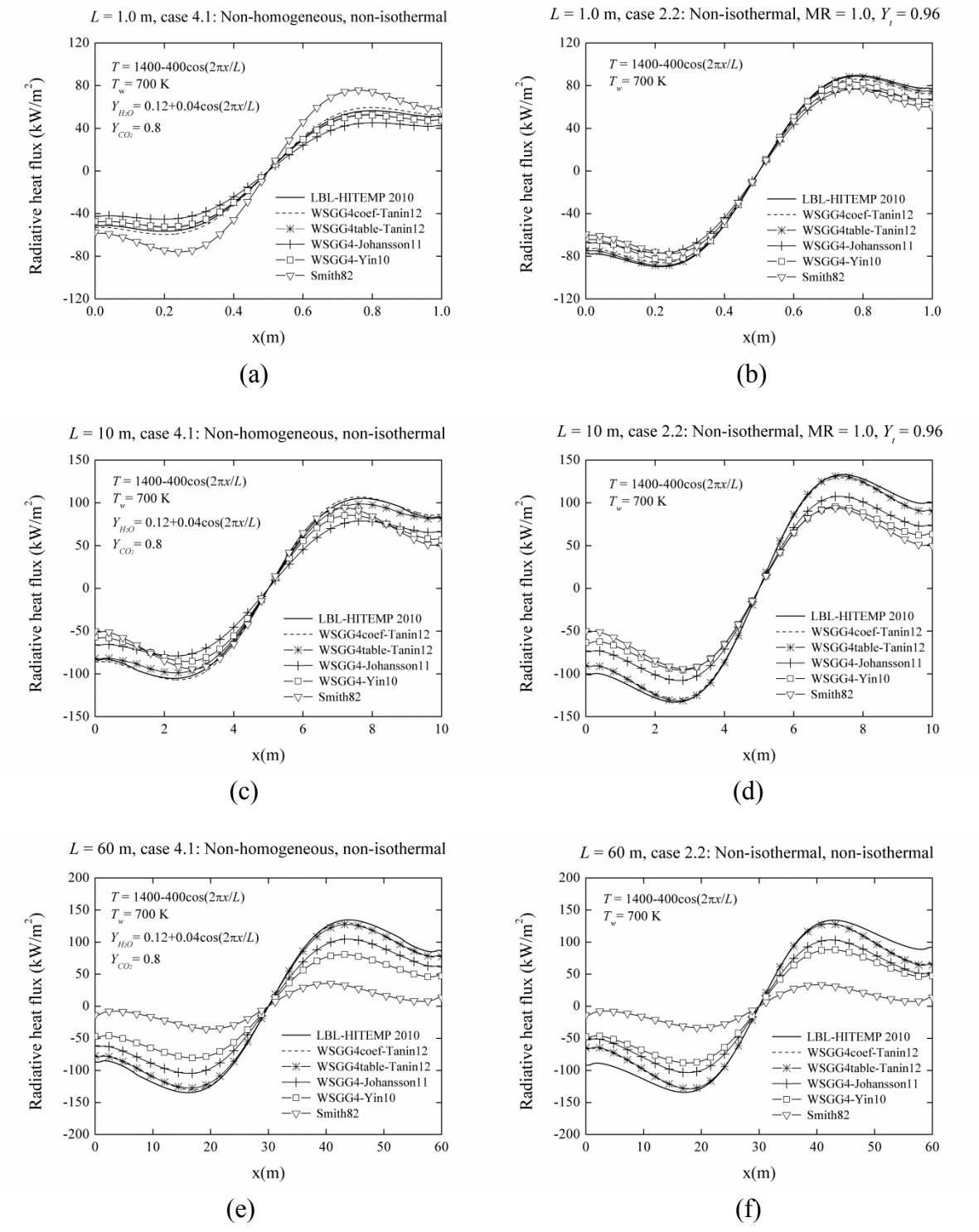

Figure 6.10: Radiative heat fluxes (q_w) computed with different correlations of the WSGG model along length coordinates for dry-FGR (left hand side) in case 4.1 and wet-FGR (right hand side) in case 2.2 for: (a) and (b) L = 1.0 m, (c) and (d) L = 10 m, (e) and (f) L = 60 m. For all cases, total pressure equal to P = 1.0 bar.

Table 6.1: Deviation in the computation of the radiative heat fluxes and heat sources using different correlations and the LBL integration of HITEMP 2010 data for path-lengths of 1, 10 and 60 m (L = 1.0, 10.0, 60.0 m), in percentage (%).

Case	WSGG4table-Tanin12			WSGG4coef-Tanin12			WSGG4-Johansson11			WSGG4-Yin10			Smith82		
	q_w	∇q_{half}	∇q_{avg}	q_w	∇q_{half}	∇q_{avg}	q_w	∇q_{half}	∇q_{avg}	q_w	∇q_{half}	∇q_{avg}	q_w	∇q_{half}	∇q_{avg}
L = 1.0 m															
1.1	6.0	8.7	7.1	3.9	0.4	5.1	48.6	25.9	54.8	5.6	23.9	39.5	17.8	11.1	17.7
1.2	0.0	2.5	3.5	2.5	4.1	4.6	22.3	35.2	59.7	1.1	2.1	52.7	14.6	27.1	15.6
2.1	10.0	2.9	7.9	0.8	7.1	9.7	53.2	147.8	127.5	7.4	50.1	54.2	10.8	50.2	55.3
2.2	3.5	1.3	2.7	6.0	4.2	4.5	11.8	93.8	101.3	2.2	31.7	35.7	22.7	6.0	16.8
3.1	4.9	15.5	3.8	4.6	28.0	8.4	113.6	93.7	168.1	41.2	22.7	110.1	40.0	113.5	52.9
3.2	0.3	14.0	3.9	2.5	9.6	5.0	93.7	97.8	168.1	31.8	2.2	107.5	4.0	9.8	12.0
4.1	6.7	3.1	9.2	3.4	4.5	6.7	58.7	140.8	120.8	5.1	51.9	52.9	12.9	51.3	54.3
4.2	1.4	0.1	5.4	0.6	1.6	12.8	11.0	315.8	180.3	15.6	69.3	113.1	7.7	10.1	23.6
4.3	1.3	12.1	14.4	0.0	10.5	17.8	83.5	146.8	155.7	0.5	150.7	155.9	9.7	42.7	36.4
4.4	1.1	1.6	3.9	0.1	4.9	8.3	27.0	190.3	186.2	13.1	34.7	95.8	10.7	13.4	25.4
4.5	1.2	7.0	8.4	1.0	12.1	15.5	65.7	175.8	159.4	28.3	76.9	123.5	1.5	28.1	32.0
Average	3.3	6.3	6.4	2.3	7.9	8.9	53.6	133.1	134.7	13.8	46.9	85.5	13.9	33.0	31.1
L = 10 m															
1.1	4.3	2.4	3.9	0.2	0.0	4.6	9.2	25.3	42.6	6.6	5.2	22.2	18.4	55.4	27.5
1.2	0.4	0.2	1.3	1.1	2.0	2.8	15.8	30.3	54.5	7.0	28.7	32.9	25.6	51.6	18.9
2.1	8.5	4.5	5.8	4.5	6.1	8.8	16.0	60.8	69.2	4.1	29.2	30.5	43.3	10.6	35.5
2.2	10.0	1.2	5.8	10.1	1.1	5.1	40.8	13.9	33.0	31.3	18.8	33.4	50.3	21.2	26.5
3.1	5.8	7.0	4.8	2.4	8.6	6.9	52.0	1.6	85.4	11.4	3.2	56.3	2.9	42.8	33.9
3.2	0.8	10.5	2.8	2.8	7.7	4.4	1.6	28.4	85.4	6.6	33.7	62.1	21.8	5.4	11.4
4.1	1.4	4.3	10.7	2.9	4.5	6.2	10.1	65.9	66.1	3.9	30.1	26.4	39.8	11.5	29.3
4.2	18.0	14.5	21.9	15.8	0.6	27.6	24.1	495.7	237.8	10.6	11.7	41.2	34.1	13.1	23.5
4.3	7.9	18.7	21.8	5.9	15.5	16.5	3.8	69.6	81.4	25.3	46.0	50.7	2.7	30.8	30.8
4.4	13.8	0.9	12.0	11.7	11.9	14.9	42.2	12.4	36.4	3.1	11.0	54.5	31.7	17.1	23.8
4.5	0.1	6.2	11.3	2.6	14.8	12.3	16.8	51.0	65.5	24.2	18.9	60.1	16.1	1.5	11.4
Average	6.5	6.4	9.3	5.5	6.6	10.0	21.1	77.7	77.9	12.2	21.5	42.8	26.1	23.7	24.8
L = 60 m															
1.1	7.3	7.0	4.0	7.7	14.8	6.9	11.2	28.9	40.1	1.2	18.3	17.8	53.2	100.0	38.8
1.2	10.5	22.8	5.0	9.6	19.4	4.8	33.1	46.1	45.3	22.4	52.7	28.1	51.3	100.0	26.1
2.1	16.0	3.7	7.3	18.4	1.5	9.4	34.9	0.2	21.5	6.2	22.7	24.1	85.6	59.5	61.6
2.2	29.6	0.0	11.6	28.1	0.6	10.9	54.7	29.8	30.7	56.7	28.4	30.4	85.1	64.7	57.4
3.1	10.1	8.3	4.3	5.3	12.1	7.3	3.9	34.2	67.1	5.1	31.2	39.3	37.3	65.9	41.7
3.2	7.8	17.0	3.4	8.6	17.3	3.4	34.2	14.2	67.1	17.9	26.7	48.2	46.1	65.9	28.5
4.1	10.3	3.5	9.2	11.3	0.9	7.2	30.0	2.5	19.7	2.8	23.0	20.3	84.1	58.6	60.6
4.2	26.8	8.0	28.6	25.3	15.7	26.1	22.4	443.1	270.0	15.1	4.7	28.9	69.0	28.2	35.7
4.3	3.9	1.5	29.3	2.2	4.1	9.5	27.0	73.1	63.2	20.4	57.4	54.7	55.2	8.5	31.2
4.4	23.6	0.9	17.1	21.7	11.8	15.9	41.6	38.4	41.1	8.3	6.2	44.1	72.8	35.1	39.4
4.5	7.0	2.6	17.0	8.8	7.2	8.1	35.9	15.1	33.2	9.4	29.4	61.6	67.4	19.5	29.9
Average	13.9	6.8	12.4	13.4	9.6	10.0	29.9	66.0	63.5	15.0	27.3	36.1	64.3	55.1	41.0

As seen in Table 6.1, errors of only 5 % for the radiative source term at the mid-distance were found for both case of dry and wet flue gas recirculation (case 4.1 and 2.2). The relative average errors for these oxy-fuel cases were still within 15 % for source term and 30 % for the radiative heat flux at walls. Maximum error for oxy-fuel cases of 30 % occurred in the case of wet-FGR (isothermal case 2.2).

According to results in Table 6.1, applying Smith82 correlations resulted in high relative errors of both the radiative source term and heat flux at high path-length (L = 60 m). In turn, the radiative source term and heat flux from WSGG4-Johansson11 highly deviated from LBL-HITEMP 2010 at low and middle path-length (L = 1 and 10 m). At middle path-length (L =10 m), average errors of heat flux was 26 % for Smith82, while the maximum source term error was found to be 78 % for WSGG4-Johansson11.

6.2 Laboratory scaled 100 kW_{th} oxy-fuel furnace

All investigated cases for each fundamental sub-model using laboratory-scale oxy-fuel furnace are presented in Table 5.4 in chapter 5. The aspects are ranging from turbulent flows, char heterogeneous reactions, reaction mechanisms for volatile reaction, turbulent gaseous combustion and radiation properties of combustion products. Results of predictions from numerical investigations are explained and deeply discussed in for each sub-model. The selection of the model for devolatilization process is not included in the studies of sub-models because the comparison of models has already discussed and concluded in the numerical studies by Jovanovic et al. [Jovanovic12] and the CPD model is applied for all investigated case according to the reasons explained and reviewed in chapter 2. First, the mesh dependency is tested to decide the suitable number of computational cells to represent furnace control volume. The other fundamental sub-models are then investigated using the considered number of cells.

6.2.1 Computational mesh dependency

The predictions of velocity profile from three different numbers of computational cells are presented in Fig. 6.11 and Fig. 6.12. It was clear that the results from 300k meshing size significantly change from the results using 100 k cells. The axial velocity using the 100k mesh results in better predictions in overall, in contrast to the general opinion that the more refined mesh give results more close to experiments, despite slightly over-predicting peak axial velocity at 0.2 m axial distance from burner (Fig. 6.11(b)). The tangential velocity using 300k and 600k meshing cells provide better predictions of peak tangential velocity (Fig. 6.12), in contrast to the results at far radial distance of higher than 0.13 m at axial distant of 0.2 m from burner.

For temperature predictions in Fig. 6.13, the predictions using the 100k cells shows worse prediction at the axial distance of 0.2 m from burner. The temperature at the burner outlet from 100k cells is higher than from 300k and 600k cells about 100 °C and also at the far radial distance starting from 0.13 m from centerline at the axial distance of 0.2 m from burner. The predictions of O_2 concentrations using different meshes are showed in Fig. 6.14. At the axial distance of 0.05 m from burner in Fig. 6.14(a), the results from 100k cells slightly over-predict O_2 species at the short radial distance of less than 0.05 m from centerline, although under-predicting O_2 species after this radial positions. The big error is found for the O_2 prediction at the far radial distance and the axial position of 0.2 m from burner, in which up to 100 % deviation is investigated comparing to experiments. The more refined meshes (300k and 600k cells) provide O_2 prediction nearly matching with experiments at the same locations.

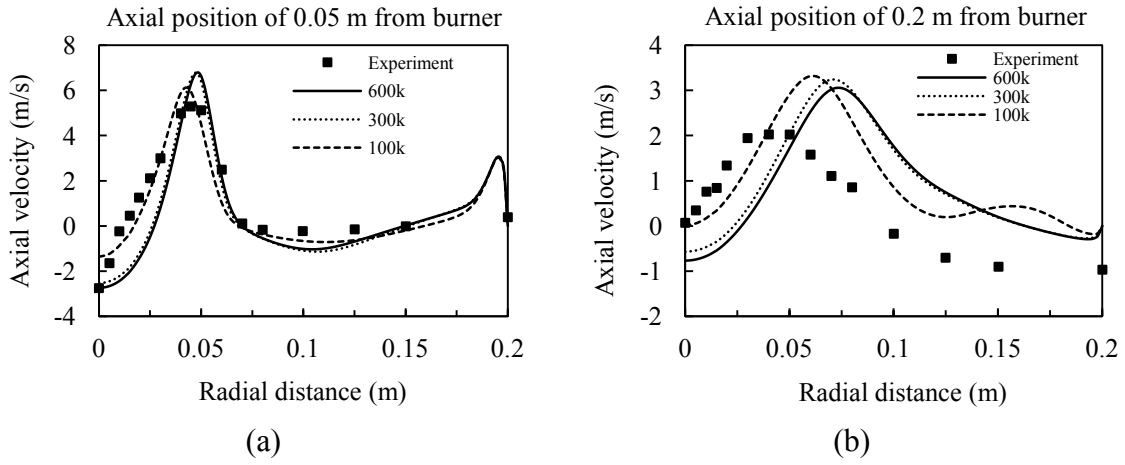

Figure 6.11: Comparison of axial velocity at two axial positions applying different computational mesh sizes: (a) 0.05 m, (b) 0.2 m.

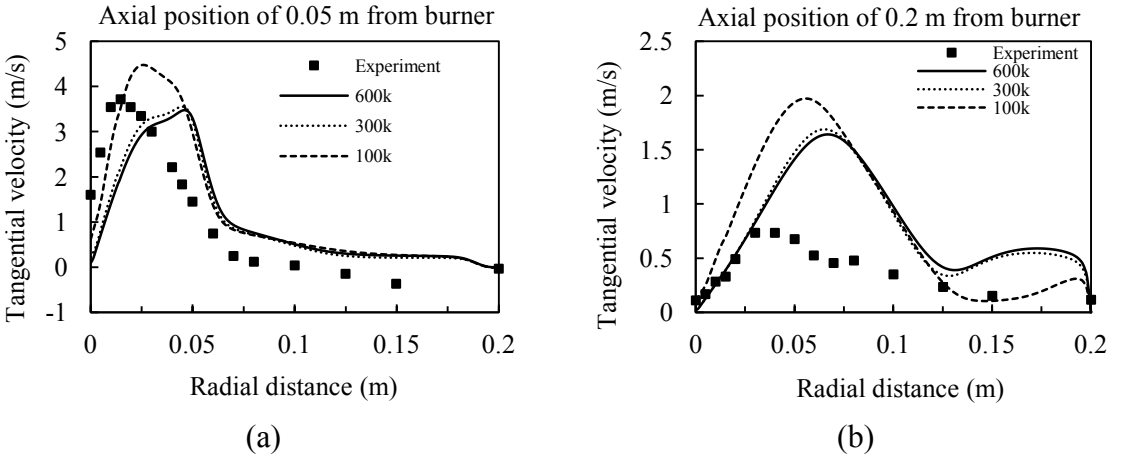

Figure 6.12: Comparison of tangential velocity at two axial positions applying different computational mesh sizes: (a) 0.05 m, (b) 0.2 m.

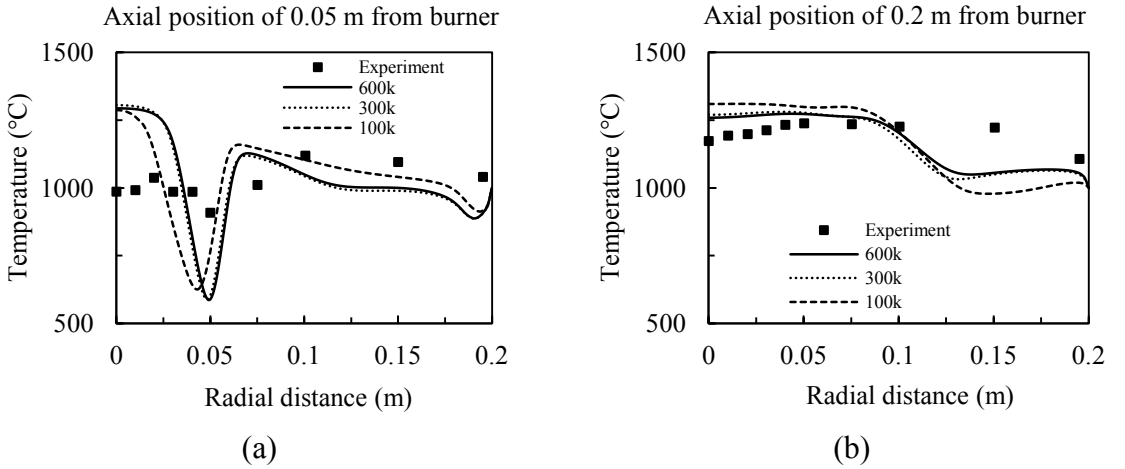

Figure 6.13: Comparison of temperatures at two axial positions applying different computational mesh sizes: (a) 0.05 m, (b) 0.2 m.

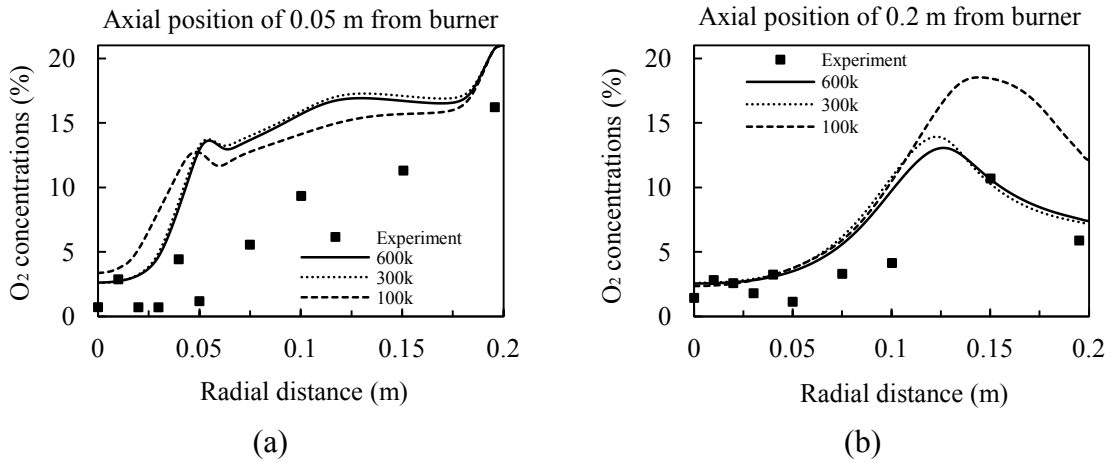

Figure 6.14: Comparison of O_2 concentrations at two axial positions applying different computational mesh sizes: (a) 0.05 m, (b) 0.2 m.

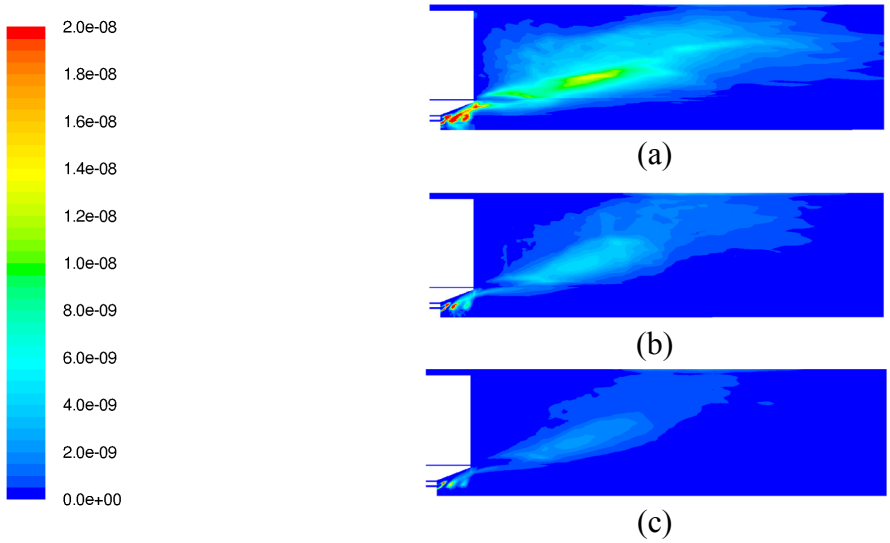

Figure 6.15: Comparison of particle burning rates from computational meshes of: (a) 100k, (b) 300k, (c) 600k.

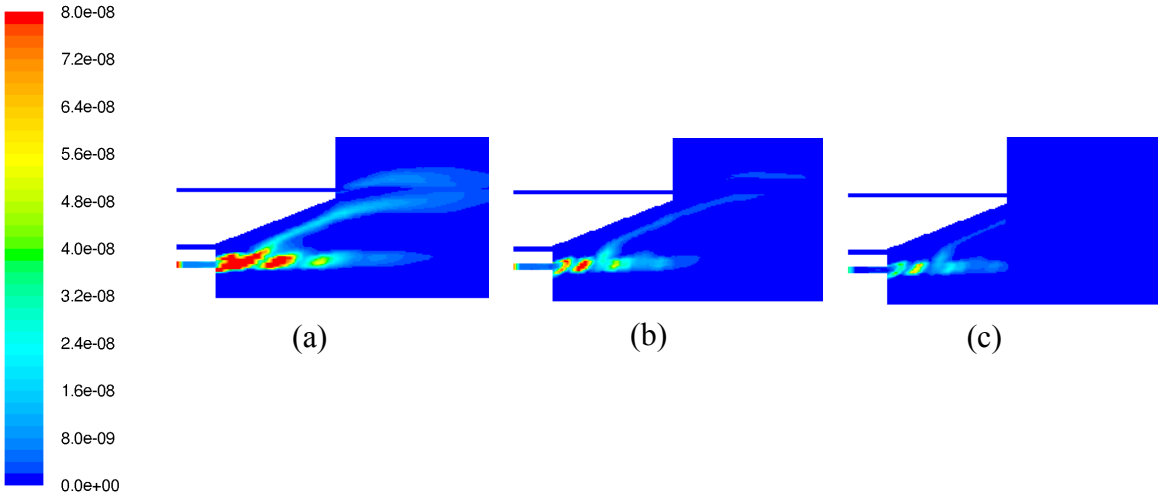

Figure 6.16: Comparison particle devolatilized rates from computational meshes of: (a) 100k, (b) 300k, (c) 600k.

From the comparison of burning rate of pulverized coal particles, char burnout occurs intensely inside burner's quarl region for the case using 100k cells, showing by the intensive red-color area in Fig. 6.15. This implies that coal particles may burn outside the burner's quarl if the mesh is not enough refined expressed by the green yellow area in Fig. 6.15(a). At the outlet of primary stream, pulverized coal particles strongly devolatilze in the case of low-resolution mesh (100k). Further mesh refinement results in smaller region of devolatilization and also less peak devolatilzed rate.

The results of particle burning rate in Fig. 6.15 and devolatilized rate in Fig. 6.16 provide more understanding of how number of computational cells effect the magnitude rate of particle undergoing chemical reaction. Using higher meshing cells may not improved overall combustion calculations; however, showing much more important influence for the prediction of the particle burning and devolalized rate in macroscopic level.

6.2.2 Turbulent models

According to the reason commented in the literature review, the DNS and LES turbulent model are not the focus of this thesis and only RANS models are investigated here. Many researches recommended the RSM for the predictions of turbulent behaviors in the high swirling flow fields. However, this conclusion still depends on type of combustion application and other factors such as how strong of the swirling stream in the feeding gases to produce recirculation zone of flame core, flame-types, size and dimension of furnace, positions of investigations inside control volume (furnace), investigation under reacting or non-reacting flow calculations, outer diameter of confined cylindrical furnace, gas mass flow rate or velocity flow rate and the presence of particulate phase (coal particles).

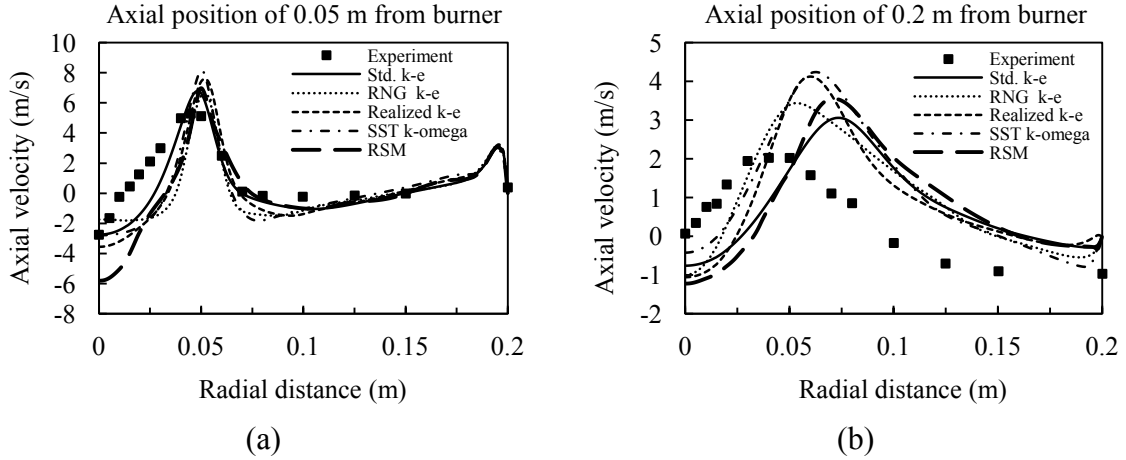

Figure 6.17: Comparison of axial velocity applying different turbulent models: (a) at axial position of 0.05 m, (b) 0.2 m, distant from burner.

From the plots of axial velocity at 0.05 m distant from burner, the predictions from all turbulent models provided similar results (Fig. 6.17), except that the RSM resulted in three times lower in magnitude of backward velocity at the center of furnace (zero distance). This finding contrasts to the previous recommendation in the reviews (chapter 2)

that the RSM can provided more accurate velocity predictions and also common believe that the higher order turbulent models always has higher accuracy. Approximately 1 m/s higher peak axial velocity is observed when applying the SST k-ω and the Realized k-ε models.

At the distance of 0.2 m from the burner (Fig. 6.17(b)), all turbulent models provided good trends of axial velocity predictions. The same as axial position of 0.05 m (Fig. 6.17(a)), the higher peak axial velocity predictions are found when applying the SST k-ω and the Realized k-ε models, following by the RSM and the RNG k-ε models. The most close peak velocity prediction is from the standard k-ε model, which still deviated from experiments around 1 m/s (50% deviation based on experimental value of 2 m/s). However, all models except the standard k-ε model and the RSM resulted in slightly better estimations at radial distance lower than 0.028 m from centerline.

Different turbulent models give various trends of line-plots for the tangential velocity as illustrated in Fig. 6.18 at two axial distances from burners. For axial position of 0.2 m from burner, minimum peak tangential velocity close to experiments is observed applying either the RSM or standard k-ε model. Other turbulent models over-predict maximum tangential velocity at location of 0.2 m distant from burner in Fig. 6.18(b). The predicted tangential velocity from all models at 0.2 m axial distance from burner follow the same trend after the radial distance of 0.07 m from centerline.

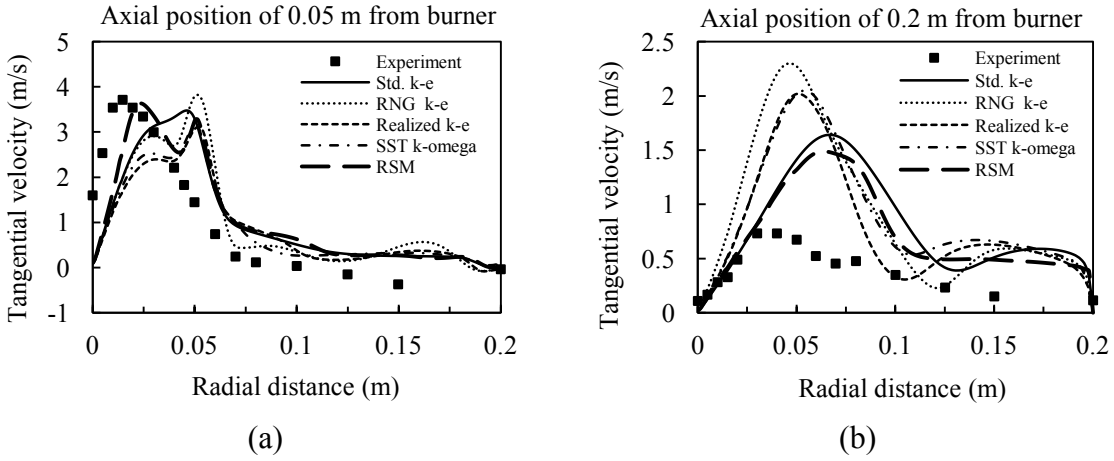

Figure 6.18: Comparison of tangential velocity applying different turbulent models: (a) at axial position of 0.05 m, (b) 0.2 m, distant from burner.

From plots of temperature profile at axial distance of 0.05 m close to burner, the RSM model results in the maximum deviation from experiments at the radial distance lower than 0.05 m. In Fig. 6.19(a), the standard k-ε model has the best estimation among other turbulent models. For the axial distance of 0.2 m far from burner's quarl, the RSM model shows superior quality of prediction than other models both short radial distance close to centerline and far radial distance, although the small deviations from measurements are found when comparing results from all turbulent models.

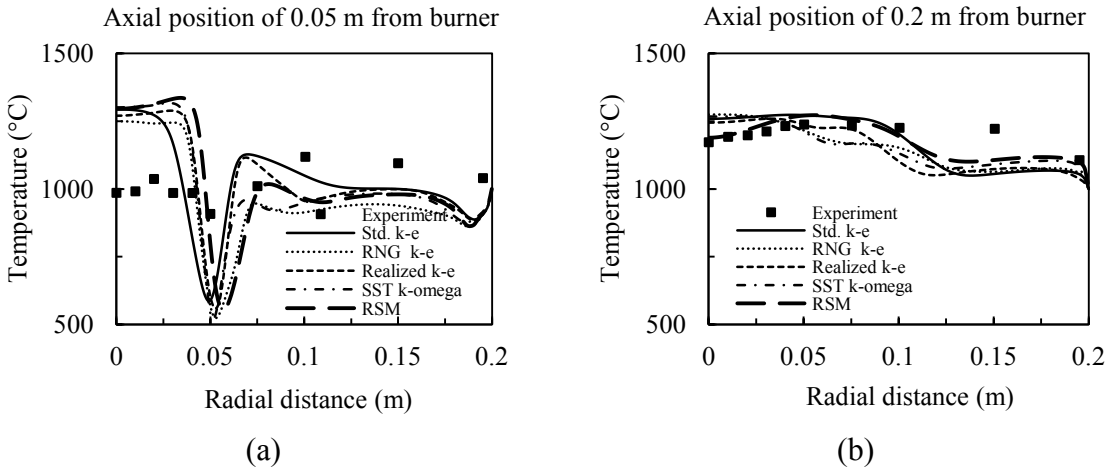

Figure 6.19: Comparison of temperature profile applying different turbulent models: (a) at axial position of 0.05 m, (b) 0.2 m, distant from burner.

At axial position of 0.05 m in Fig. 6.20(a), the predictions of O_2 concentration by the standard k-ε and Realized k-ε model are the most accurate at radial distance higher than 0.05 m. However, the standard k-ε model slightly over-predicted temperature than the Realized k-ε model at the radial distance lower than 0.05 m.

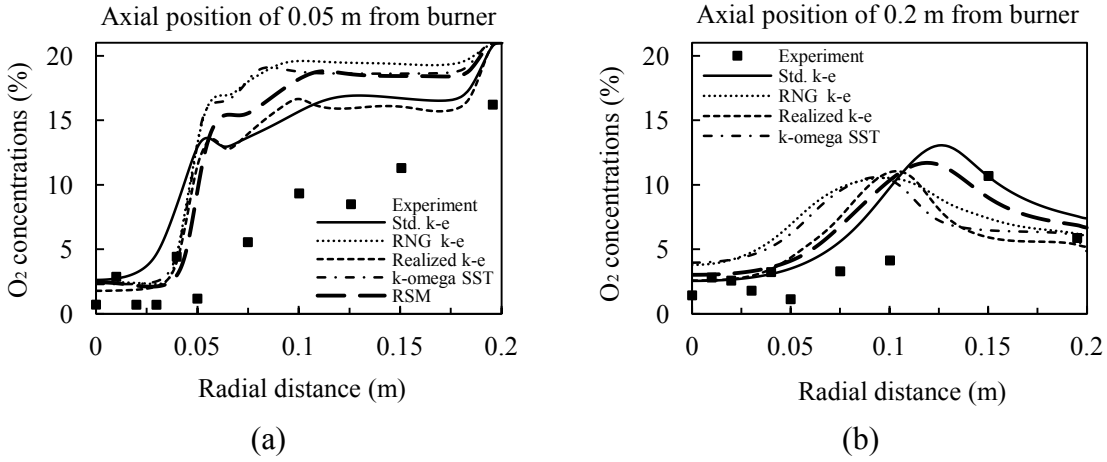

Figure 6.20: Comparison of O_2 concentrations (% by volume) applying different turbulent models: (a) at axial position of 0.05 m, (b) 0.2 m, distant from burner.

Considering overall trends of predictions at far axial distance from burner in Fig. 6.20(b), the standard k-ε gives the best trend of estimation, although slightly over-predicting temperature near furnace wall (radial distance of 0.2 m).

From the contour plots of temperature profile applying various turbulent models, the RNG k-ε model results in the small area of intensive hot flame as clearly seen in Fig. 6.21(b). The same effect of hot flame zone also occur when applying the RSM and SST k-ω model, but with small regions. Considering the length of flame core, the RNG k-ε and SST k-ω model provided the longest flame core-length, following by the standard

k-ε, the Realized k-ε model and the RSM, consequently. The flame has the most wideness in the case of using the standard k-ε model.

The back flow velocity is strongest when applying the RSM indicated by the wide dark-blue area in the contour plot in Fig. 6.22(e). The region of highest magnitude of back flow velocity shift downstream for the RNG k-ε model. Weak recirculation-zones (brighter blue area) inside oxy-fuel furnace are similar from all models.

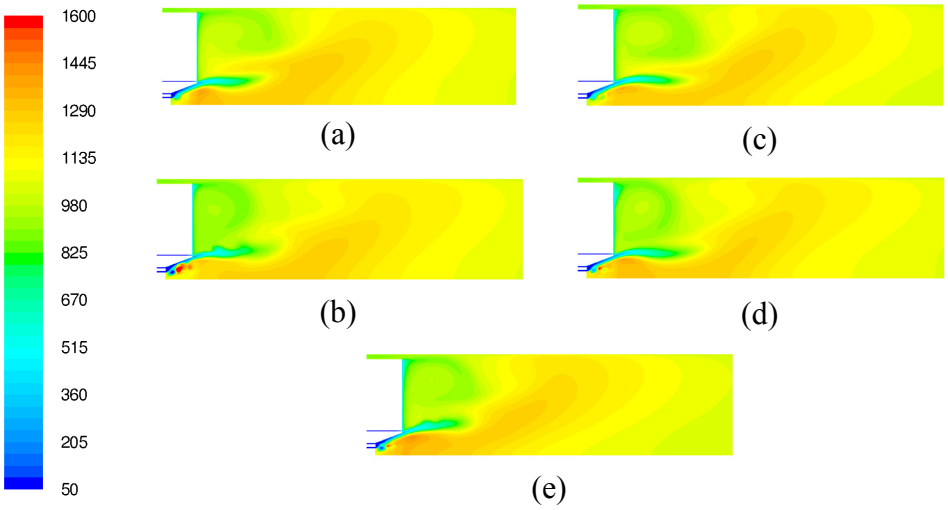

Figure 6.21: Comparison of temperature profiles applying different turbulent models: (a) standard k-ε, (b) RNG k-ε, (c) Realized k-ε, (d) SST k-ω, (e) RSM.

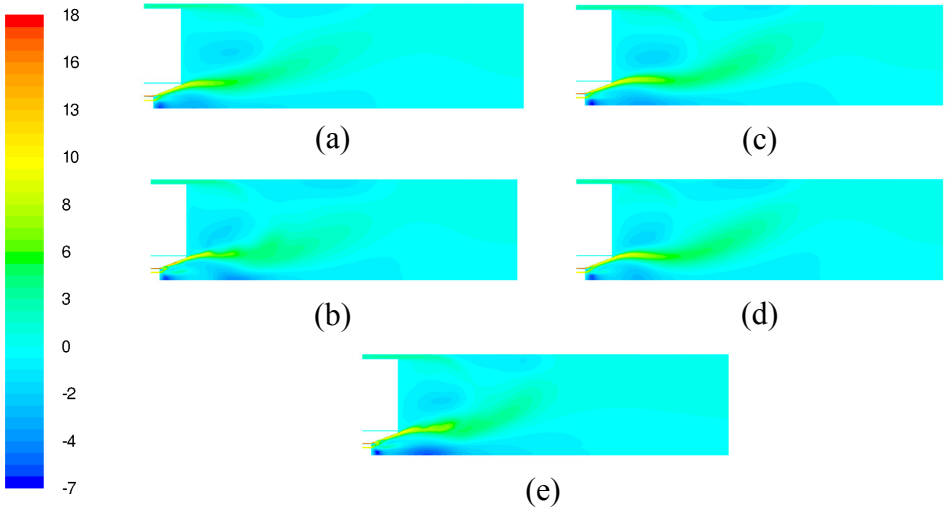

Figure 6.22: Comparison of axial velocity profiles applying different turbulent models: (a) standard k-ε, (b) RNG k-ε, (c) Realized k-ε, (d) SST k-ω, (e) RSM.

6.2.3 Char reaction models

The char reaction models play an important role in the estimation of chemical-thermodynamic quantities (temperature and O_2 specie in Fig. 6.25 and Fig. 6.26) but not in the aerodynamic quantities (velocity in Fig. 6.23 and Fig. 6.24).

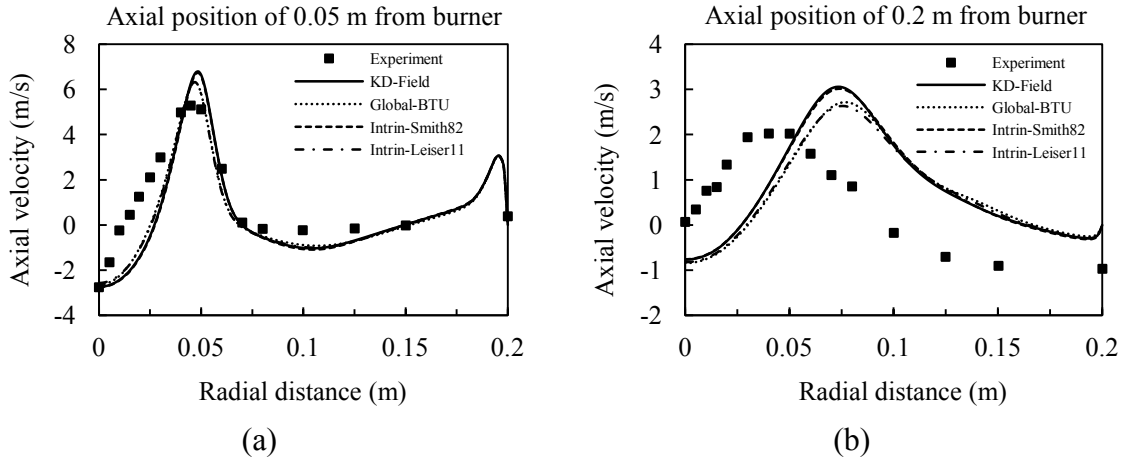

Figure 6.23: Comparison of axial velocity applying different char reaction models: (a) at axial position of 0.05 m, (b) 0.2 m, distant from burner.

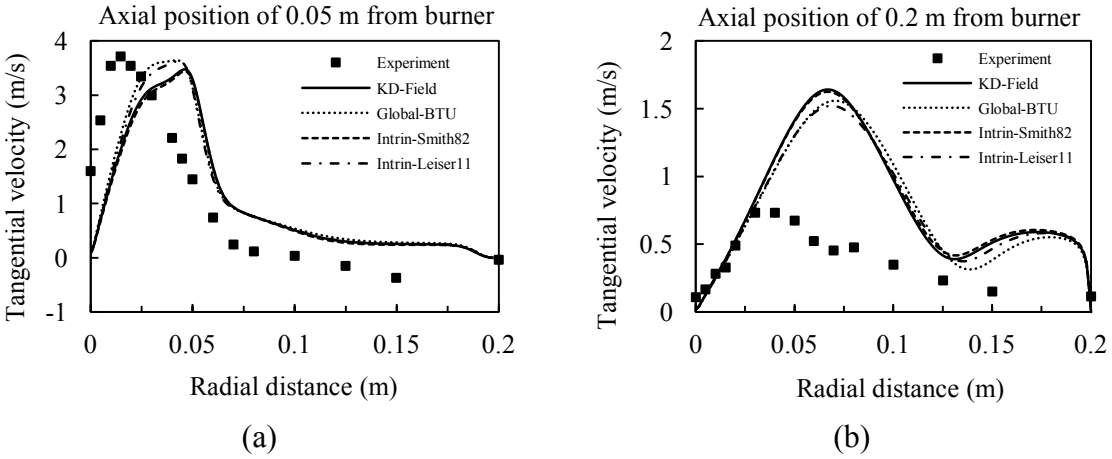

Figure 6.24: Comparison of tangential velocity applying different char reaction models: (a) at axial position of 0.05 m, (b) 0.2 m, distant from burner.

The temperature predictions follow the same trend at both axial positions from burner. At axial location of 0.05 m from burner in Fig. 6.25(a), temperature predictions is more close to experiments at the zero radial distance (flame center) using the intrinsic rate model with kinetic rate by Leiser11 and global reaction rate model with kinetic rate for char reaction from TGA for 21% O_2/79% CO_2. Only temperature prediction from Intrin-Leiser11 deviates from other results at axial position of 0.2 m, in which slightly lower prediction of around 100 K is investigated (Fig. 6.25(b)).

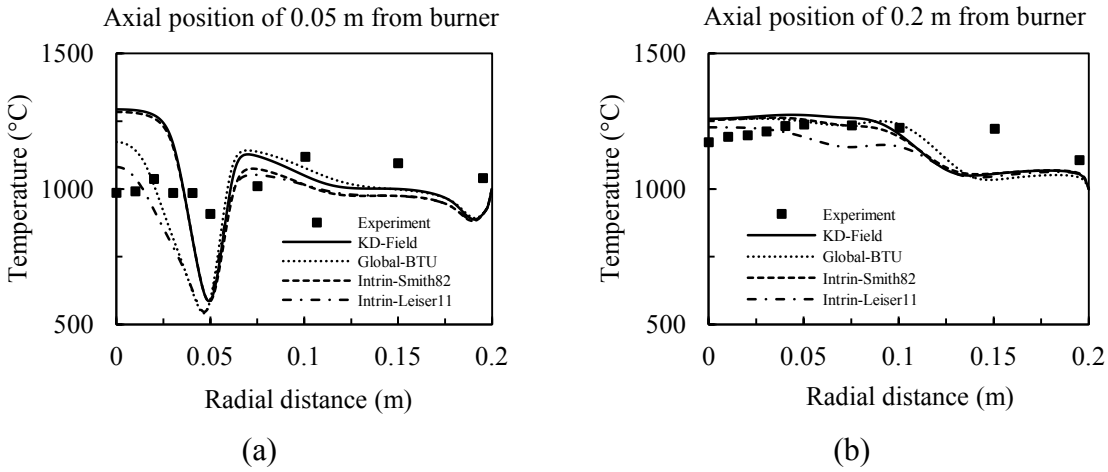

Figure 6.25: Comparison of temperature profile applying different char reaction models: (a) at axial position of 0.05 m, (b) 0.2 m, distant from burner.

Although good predictions of temperature applying intrinsic model with kinetic rate from Leiser11 or global reaction rate model with kinetic rate from TGA, O_2 species are more over-estimated than applying other char reaction models and kinetic rates at the radial distance of less than 0.05 m at location 0.05 m downstream from burner (Fig. 6.26(a)). Better prediction for O_2 concentration is obvious between the radial distances of 0.05 and 0.18 m from flame center-axis. At axial position of 0.2 m from burner, the Intrin-Leiser11 and Global-BTU result in slightly higher magnitude of temperature at radial distance outside 0.13 m toward furnace wall (Fig. 6.26(b)). In overall, applying kinetic diffusion limited rate with kinetic rate by Field (KD-Field) is still be a good approach for O_2 prediction.

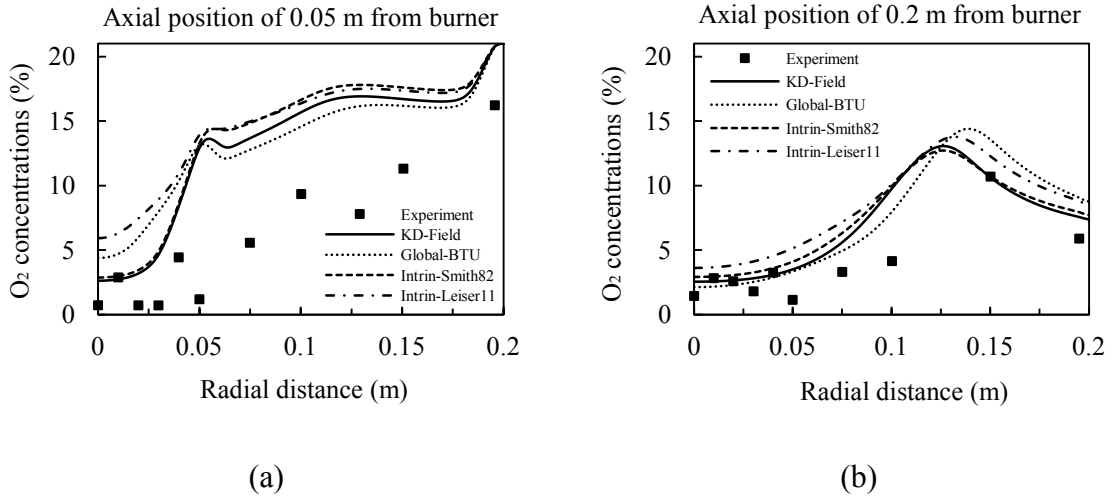

Figure 6.26: Comparison of O_2 concentrations (% by volume) applying different char reaction models: (a) at axial position of 0.05 m, (b) 0.2 m, distant from burner.

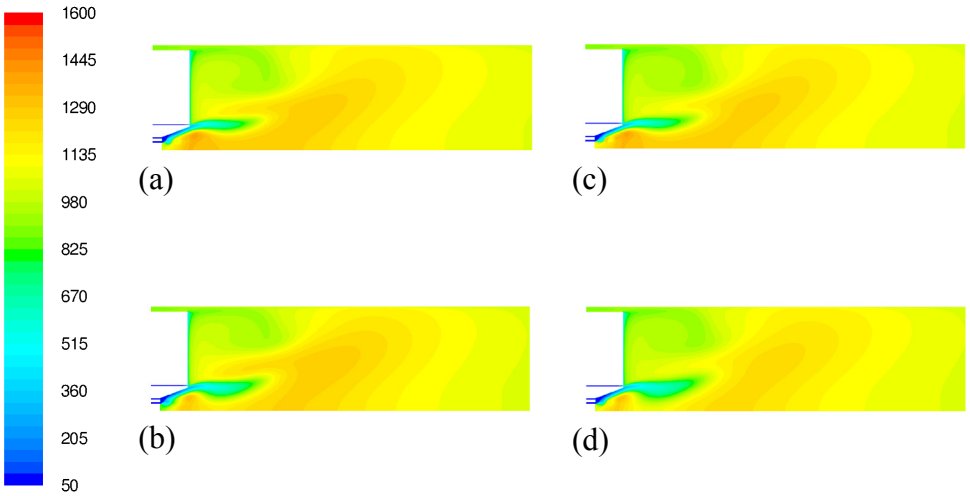

Figure 6.27: Comparison of temperatures from different char reaction rate models applying global 3-step reaction mechanisms for volatile reactions: (a) KD-Field, (b) Global-BTU, (c) Intrin-Smith82, (d) Intrin-Leiser11.

For temperature profiles applying different char reaction models, more intensive hot flames inside burner quarl's region are observed applying the kinetic diffusion limited rate by Field (KD-Field) in Fig. 6.27(a) and the intrinsic model with kinetic rate by Smith82 in Fig. 6.27(b). The Intrin-Leiser11 result in unphysical narrow flame core as clearly seen in Fig. 6.27(d) due to slower char reaction rates discussed later in char heterogeneous reactions. The KD-Field approach gives the most physical flame shape comparing with others.

Char reaction with O_2 specie takes place outside quarl area for the KD-Field and Global-BTU approach (Fig 6.28(a) and 6.28(b)). Intrinsic models (Fig 6.28(c) and 6.28(d)) result in less active char-O2 reaction, especially the Intrin-Leiser11 approach that has the lowest magnitude of char oxidation rate among approaches. Char oxidation rate is maximized for the KD-Field and Global-BTU model following by Intrin-Smith82 and Intrin-Leiser11 models, respectively.

Reaction rates of both Boudouard reaction (char-CO_2 reaction) and char-H_2O reaction is strong (red area in figures) when applying the KD-Field model obviously investigated in Fig. 6.29(a) and Fig. 6.29(b), following by the Global-BTU. The char-CO_2 reaction rate is higher than char-H_2O reaction rate applying the Intrin-Smith82 model, although opposite outcome is found using the Intrin-Leiser11 model.

For overall burning rate from different char reaction models, the rates are stronger applying the KD-Field and Intrin-Smith82 models, showed by red area in Fig. 6.31(a) and 6.31(c).

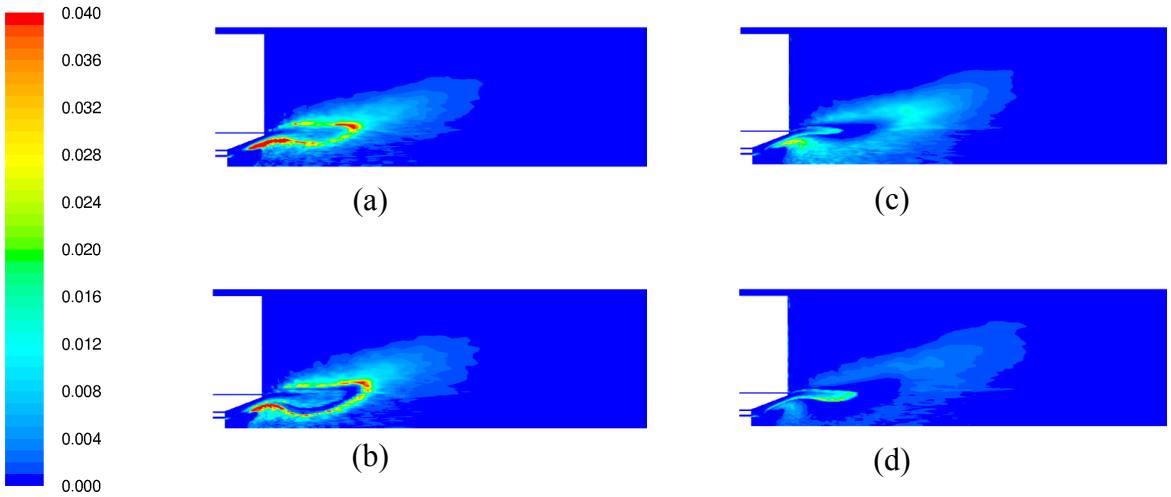

Figure 6.28: Comparison of reaction rates of char heterogeneous reaction with O_2 from different char reaction rate models applying global 3-step reaction mechanisms for volatile reactions: (a) KD-Field, (b) Global-BTU, (c) Intrin-Smith82, (d) Intrin-Leiser11.

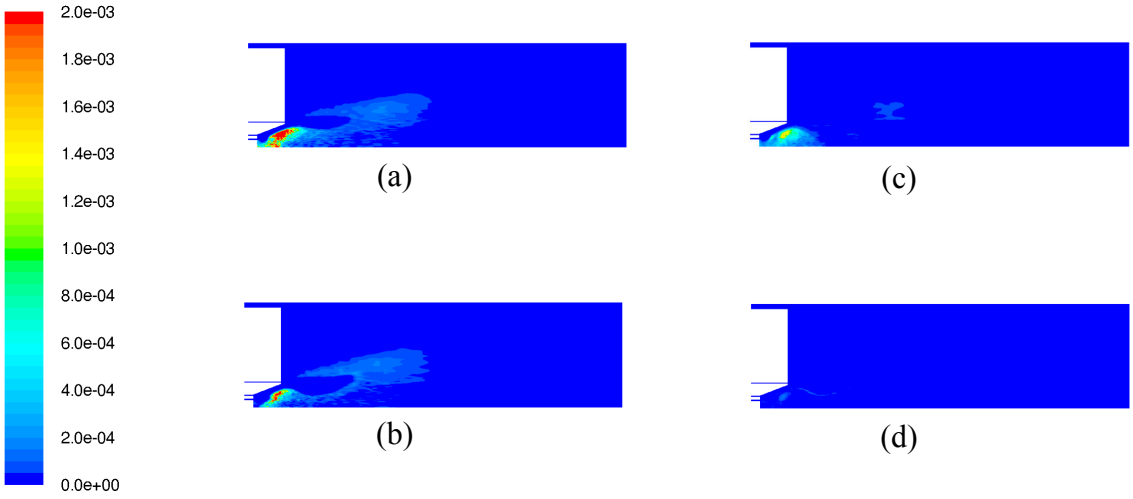

Figure 6.29: Comparison of reaction rates of char heterogeneous reaction with CO_2 from different char reaction rate models applying global 3-step reaction mechanisms for volatile reactions: (a) KD-Field, (b) Global-BTU, (c) Intrin-Smith82, (d) Intrin-Leiser11.

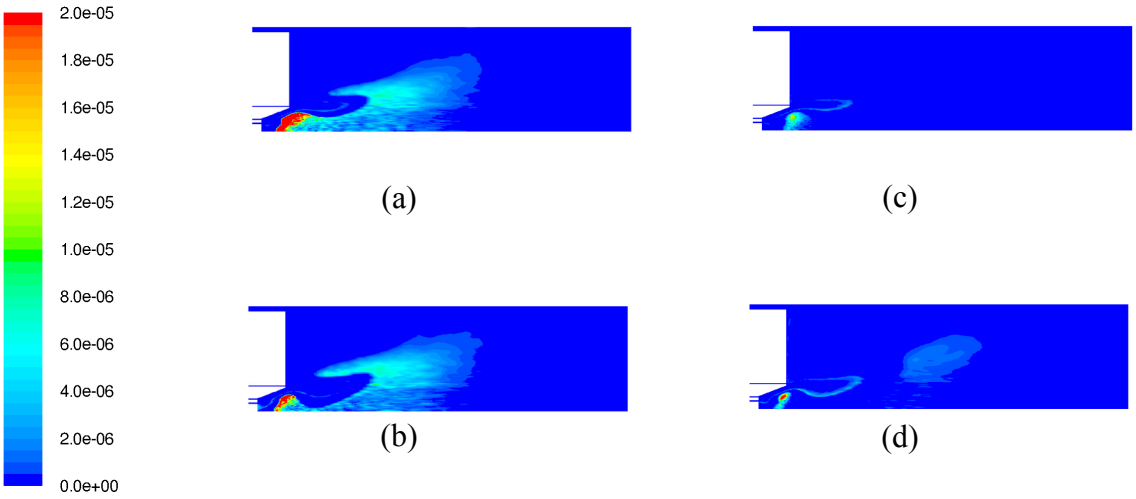

Figure 6.30: Comparison of reaction rates of char heterogeneous reaction with H_2O from different char reaction rate models applying global 3-step reaction mechanisms for volatile reactions: (a) KD-Field, (b) Global-BTU, (c) Intrin-Smith82, (d) Intrin-Leiser11.

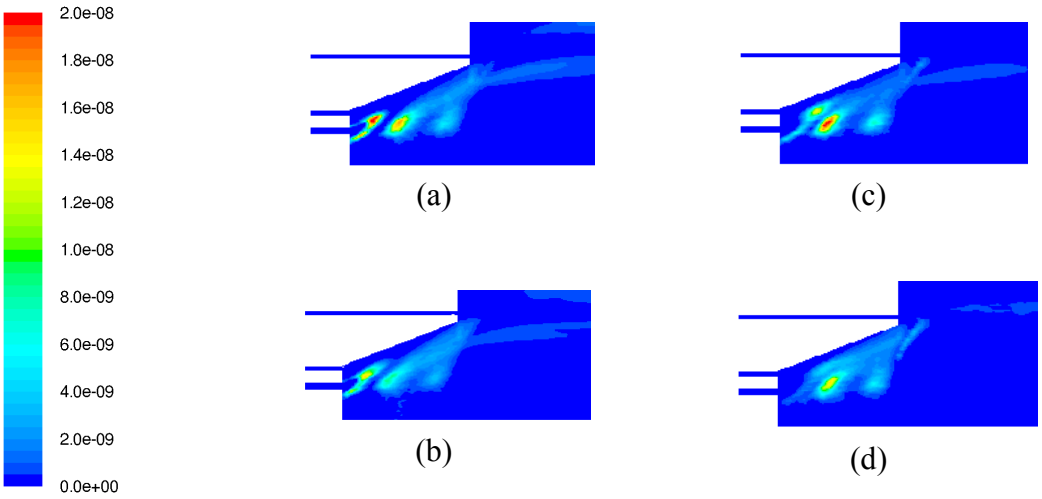

Figure 6.31: Comparison of particle burning rate from different char reaction rate models applying global 3-step reaction mechanisms for volatile reactions: (a) KD-Field, (b) Global-BTU, (c) Intrin-Smith82, (d) Intrin-Leiser11.

6.2.4 Pore models for char internal surface area

Various pore models for the estimation of internal specific area of char particles are tested in this thesis either modeling as set of constant values (specific internal area and mean pore radius) as burnout dependent models (Simons82), and also for low-rank coal (Charpenay92) explained in the literature reviews in chapter 2 and mathematical models in chapter 3.

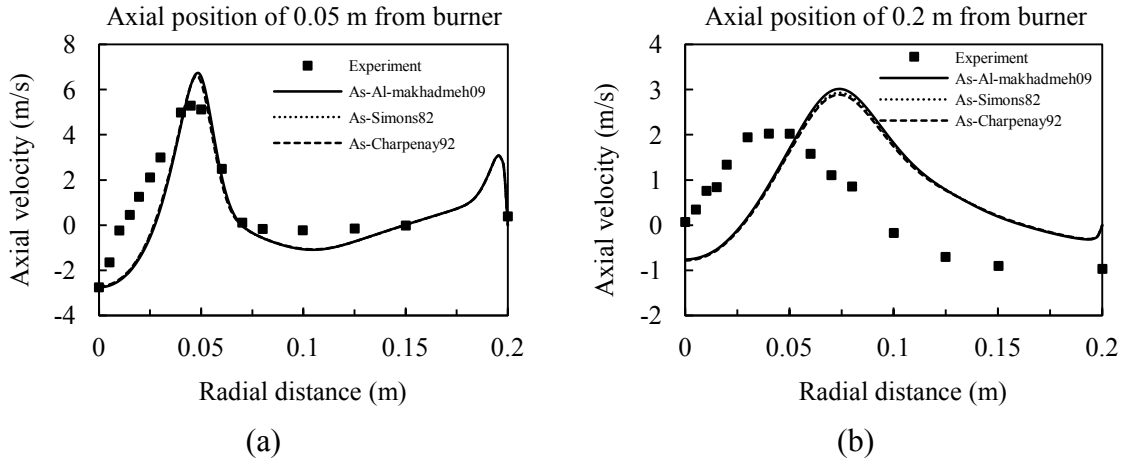

Figure 6.32: Comparison of axial velocity applying different pore models for internal surface area in the intrinsic model: (a) at axial position of 0.05 m, (b) 0.2 m, distant from burner.

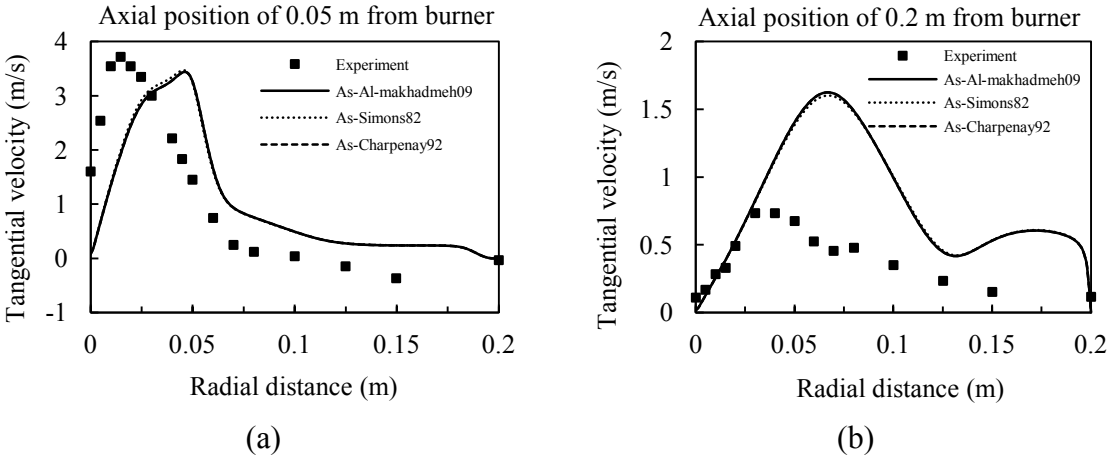

Figure 6.33: Comparison of tangential velocity applying pore models for internal surface area in the intrinsic model: (a) at axial position of 0.05 m, (b) 0.2 m, distant from burner.

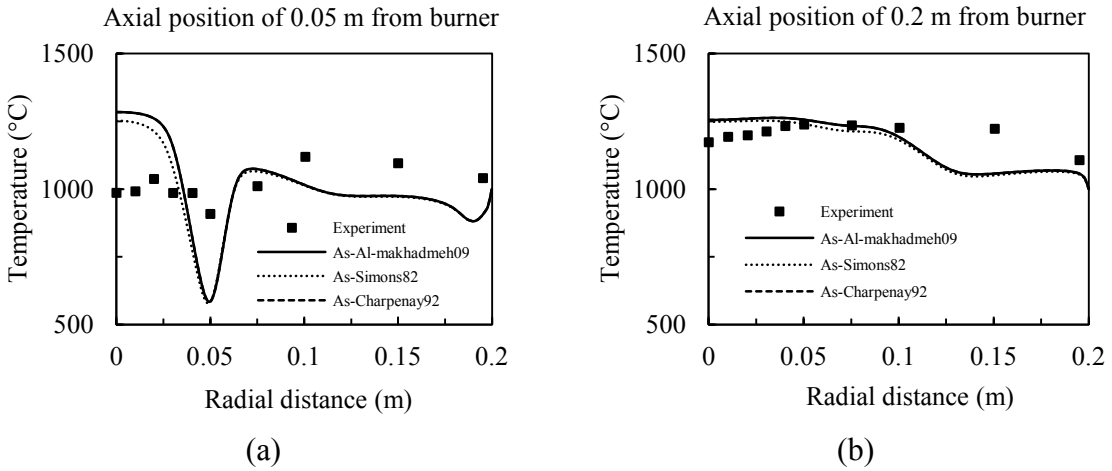

Figure 6.34: Comparison of temperature profile applying pore models for internal surface area in the intrinsic model: (a) at axial position of 0.05 m, (b) 0.2 m, distant from burner.

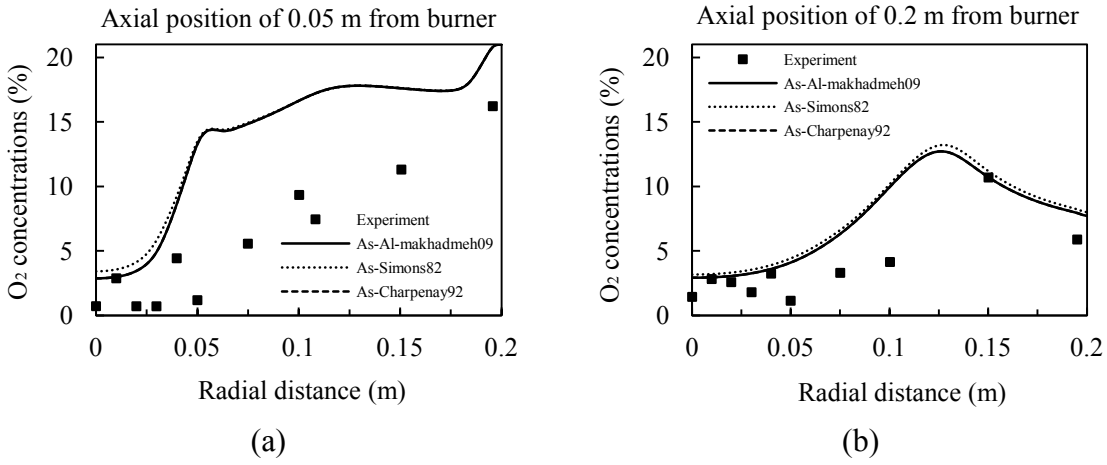

Figure 6.35: Comparison of O_2 concentrations (% by volume) applying pore models for internal surface area in the intrinsic model: (a) at axial position of 0.05 m, (b) 0.2 m, distant from burner.

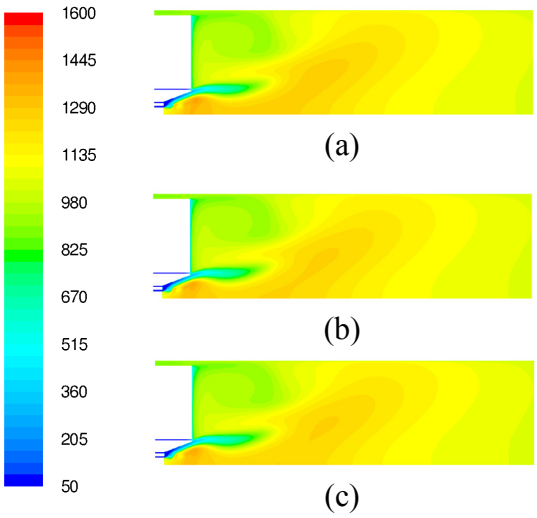

Figure 6.36: Comparison of temperatures from different pore models for intrinsic reaction rate applying global 3-step reaction mechanisms for volatile reactions: (a) Ag-Al-makhadmeh09 (constant from measurements [Al-makhadmeh09]), (b) Ag-Simons82 (varied with burnout), (c) Ag-Charpenay92 (low-rank coal).

Applying different pore models do not effects final predictions of velocity (Fig. 6.32 and Fig 6.33), temperature (Fig. 6.34) and O_2 concentration (Fig. 6.35). Nevertheless, hot temperature zones at flame core are still different as shown by orange-color area in Fig. 6.36(a)-(c). Modeling specific internal surface char area as constant using data from Al-makhadmeh09 results in continuous hot flame zone starting from inside flame core toward swirling directions.

6.2.5 Char reaction with CO_2 and H_2O

The effects of including and excluding char-CO_2 and char-H_2O reactions are investigated and the results of velocity, temperatures and O_2 concentrations are compared with experiments. Including char-CO_2 and char-H_2O reactions resulted in only slightly deviations from the other results for temperature and O_2 concentrations and nearly unchanged results for velocity profiles (hence, omitting here), for both applying the kinetic diffusion limited rate model (KD) and the intrinsic model (Intrin). The results support the idea expected previously due to the fact that the char-H_2O reaction has less influence inside oxy-fuel furnace with dry flue gas recirculation (less amount of H_2O). Including char-CO_2 and char-H_2O reactions does not improved accuracy of results but causes in longer computing time unnecessarily.

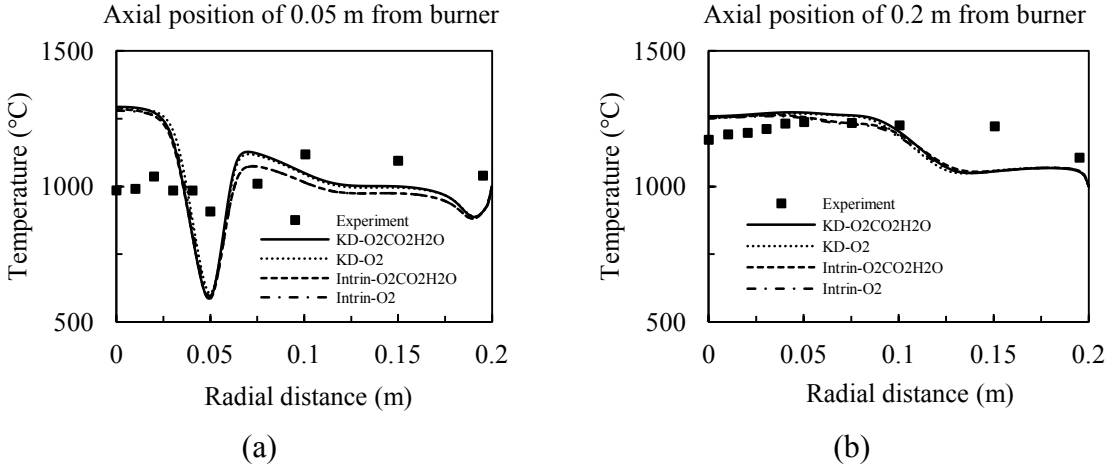

Figure 6.37: Comparison of temperature profile by including and excluding char reactions with CO_2 and H_2O: (a) at axial position of 0.05 m, (b) 0.2 m, distant from burner.

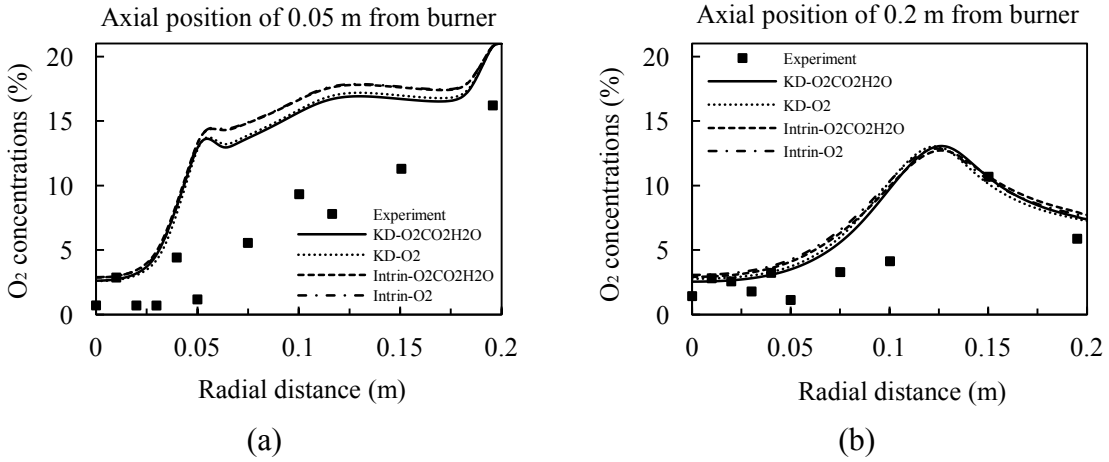

Figure 6.38: Comparison of O_2 concentrations (% by volume) by including and excluding char reactions with CO_2 and H_2O: (a) at axial position of 0.05 m, (b) 0.2 m, distant from burner.

The reaction rates of char oxidation including and excluding reaction with CO_2 and H_2O are similar, clear seen by comparing Fig. 6.39(a) to Fig. 6.39(b) applying the kinetic diffusion limited rate model (KD) and Fig. 6.39(c) to Fig. 6.39(d) for the intrinsic model.

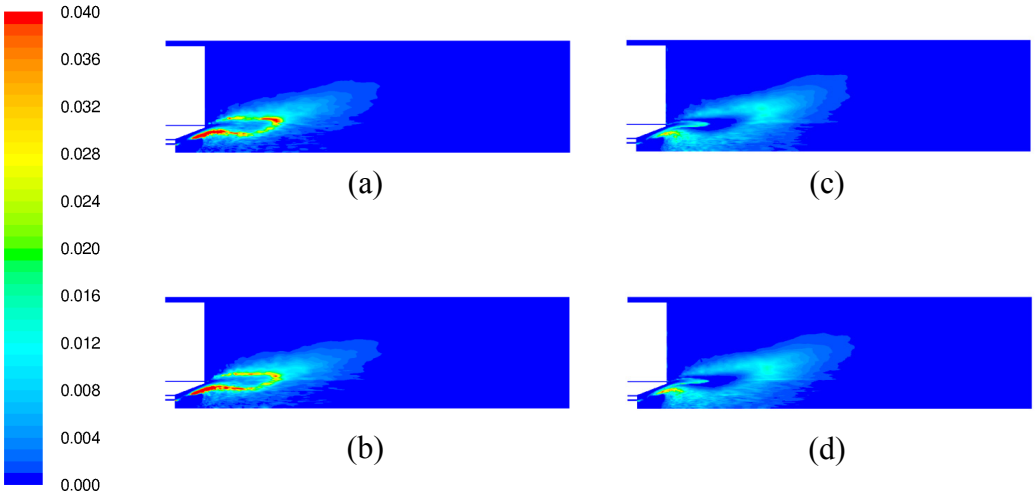

Figure 6.39: Comparison of reaction rates of char heterogeneous reaction with O_2 with and without reaction with CO_2 and H_2O applying kinetic diffusion-limited rate and intrinsic models: (a) KD-O2CO2H2O, (b) KD-O2, (c) Intrin-O2CO2H2O, (d) Intrin-O2.

6.2.6 Models for turbulent gaseous reaction

Selection for turbulent gaseous combustion models effects strongly both aerodynamic and thermo-chemical results (velocity, temperature and O_2 concentration). Considering all predictions, the eddy dissipation model (EDM) with global 2-step reaction mechanism yields numerical results deviated from experiments as shown in Fig. 6.40-6.43.

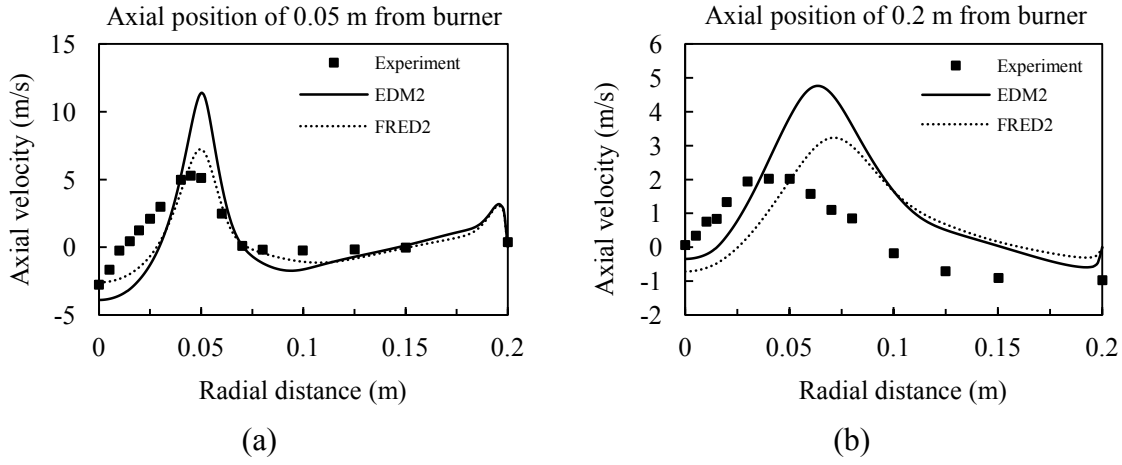

Figure 6.40: Comparison of axial velocity applying different models for turbulent gaseous reaction: (a) at axial position of 0.05 m, (b) 0.2 m, distant from burner.

For axial velocity, the EDM over-estimates value of peak velocity approximately double at radial distance of around 0.05 m from centerline in both axial positions (Fig. 6.41(a-b)). Three times less value of predicted tangential velocity by the EDM than the finite rate eddy dissipation model (FRED) is presented in Fig. 6.41(a) at short radial distance between 0-0.05 m before the peak value. The maximum difference of predicted tangential velocity is nearly 100 % at the radial distance of 0.125 m and 0.2 m axial distant from burner illustrated in Fig. 6.41(b).

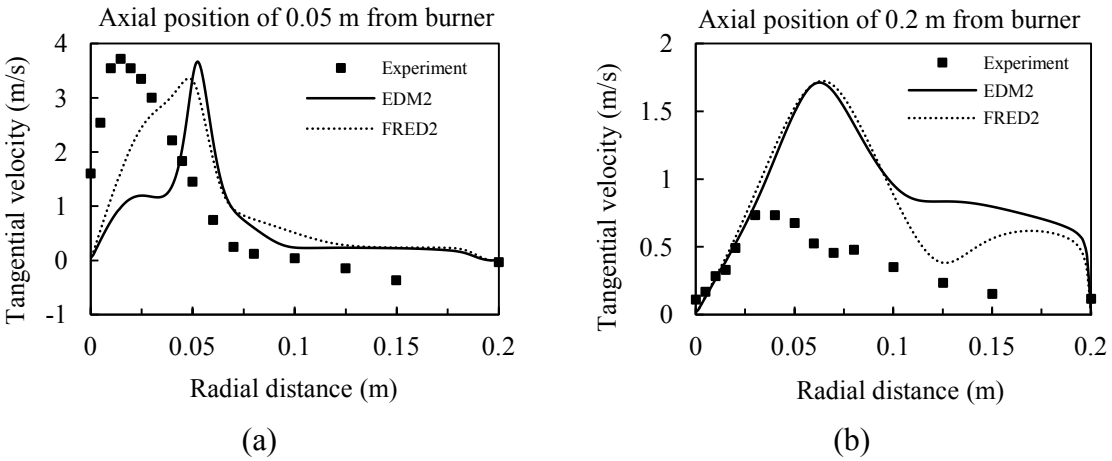

Figure 6.41: Comparison of tangential velocity applying different models for turbulent gaseous reaction: (a) at axial position of 0.05 m, (b) 0.2 m, distant from burner.

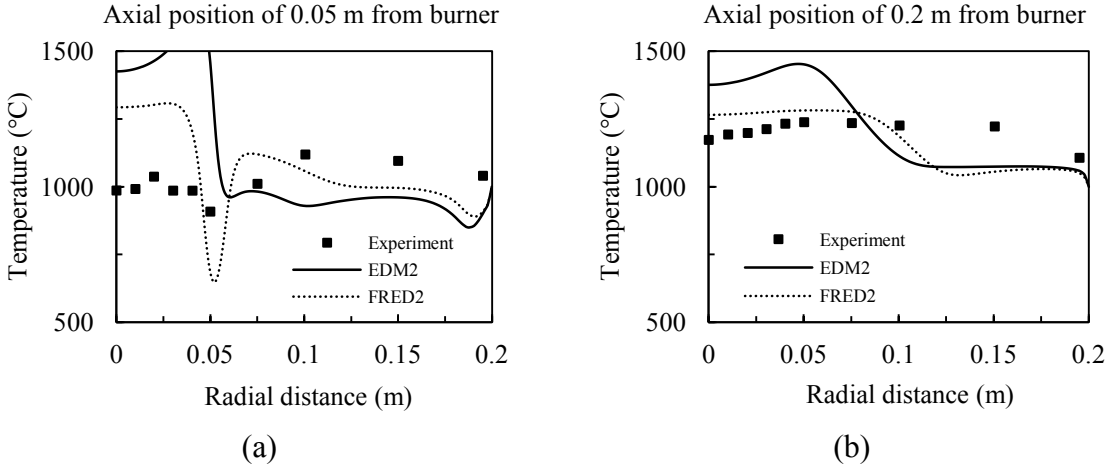

Figure 6.42: Comparison of temperature profile applying different models for turbulent gaseous reaction: (a) at axial position of 0.05 m, (b) 0.2 m, distant from burner.

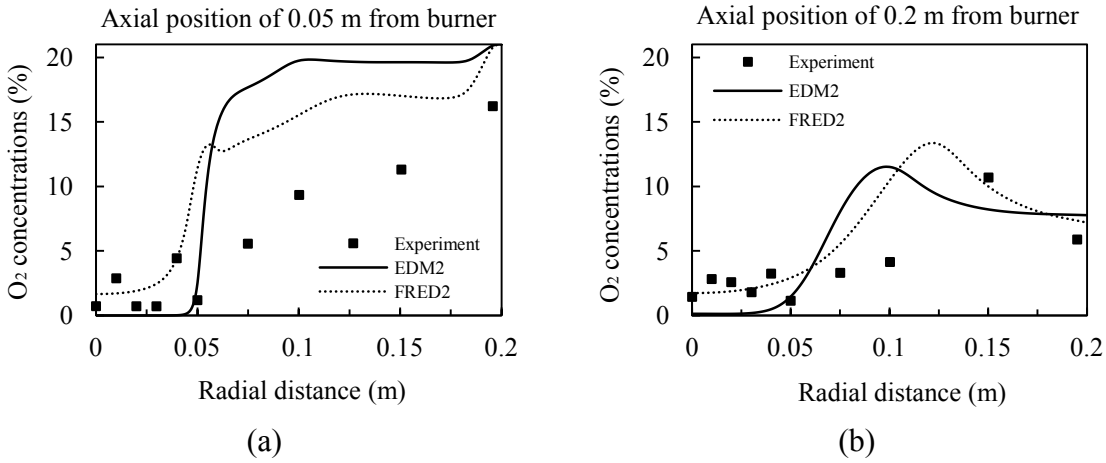

Figure 6.43: Comparison of O_2 concentrations (% by volume) applying different models for turbulent gaseous reaction: (a) at axial position of 0.05 m, (b) 0.2 m, distant from burner.

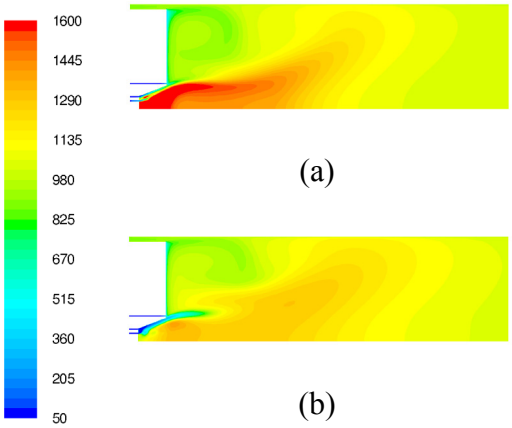

Figure 6.44: Comparison of temperatures from different turbulent gaseous reaction models: (a) EDM 2-step, (b) FRED 2-step.

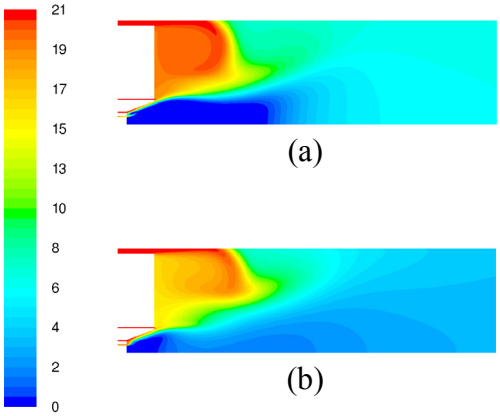

Figure 6.45: Comparison of O_2 concentrations from different turbulent gaseous reaction models: (a) EDM 2-step, (b) FRED 2-step.

The deviation of predicted temperature from measurement at 0.05 m from burner (Fig. 6.42(a)) and at zero radial distance (flame center) from the EDM is around 45%, while equal to 26% for the FRED model. Moreover, the EDM also slightly under predicted temperature at radial distance higher than 0.05 m toward furnace wall in the same plot. For temperature at 0.2 axial distant from burner (Fig. 6.42(b)), temperature at flame center is higher than experiments approximately 50 °C for the FRED model and 150 °C for the EDM. For O_2 concentrations, the maximum difference of prediction is around 4% at both axial positions in Fig. 6.43(a) and 6.43(b), and the FRED provides the better trends of estimation. The EDM results in too fast O_2 consumption at the flame center of swirling flame as clearly expressed at both axial distances. Obviously strong O_2 consumption is also presented by dark-blue color in Fig. 6.45(a), this also causes in too much intensive hot flame region represented by red color area in Fig. 6.44(a).

6.2.7 Reaction mechanisms for volatiles and gas reaction

From the previous testing of models for turbulent gaseous reaction, the FRED model result in more realistic O_2 consumption and not too much peak temperature of hot flame zone, therefore was selected for the next testing of number of steps for global reaction mechanisms (2- and 3-steps). The results show that only slightly different of predictions using 2- and 3-step reaction mechanisms are found for velocity at both axial positions (Fig. 6.46 and Fig 6.47).

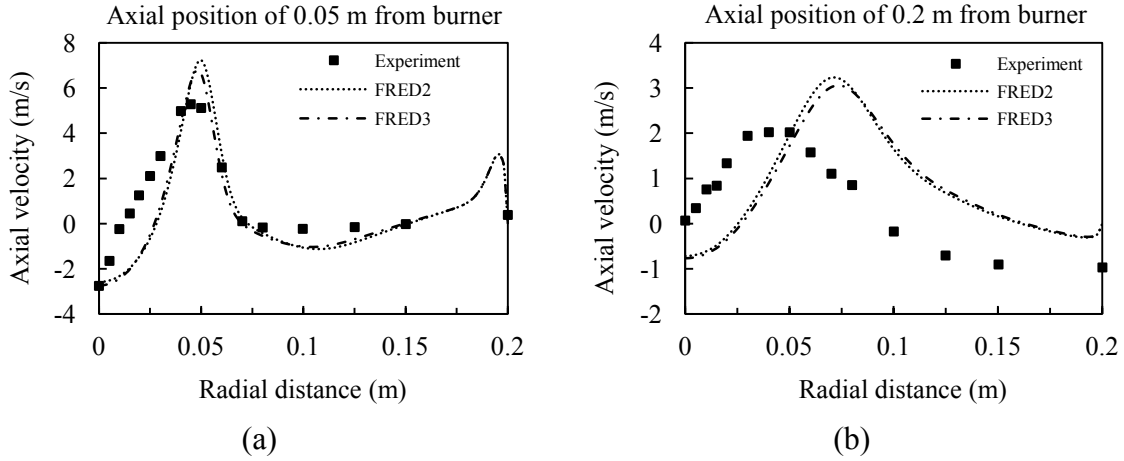

Figure 6.46: Comparison of axial velocity applying 2-step and 3-step reaction mechanisms: (a) at axial position of 0.05 m, (b) 0.2 m, distant from burner.

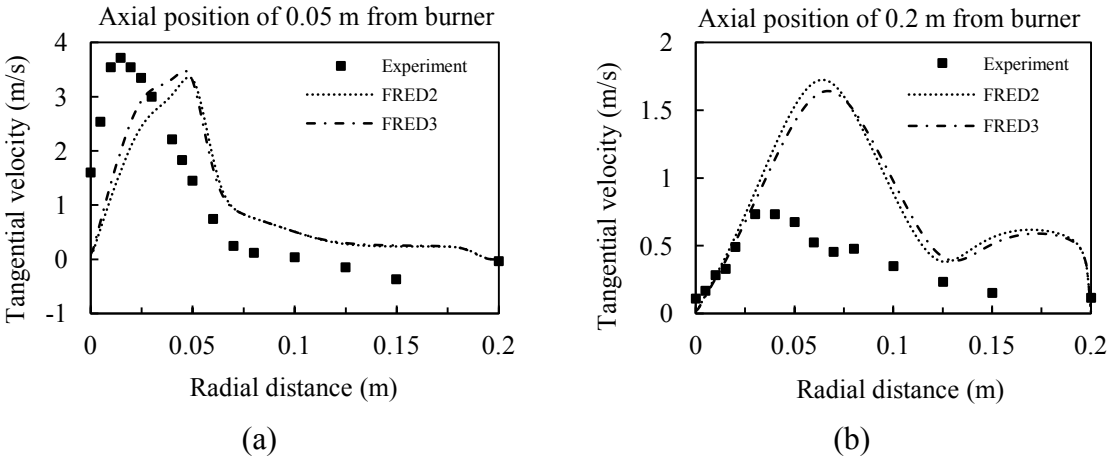

Figure 6.47: Comparison of tangential velocity applying 2-step and 3-step reaction mechanisms: (a) at axial position of 0.05 m, (b) 0.2 m, distant from burner.

Temperature and O_2 specie predictions at axial position of 0.2 m are nearly the same (Fig. 6.48 and Fig 6.49). However, main difference between applying 2- or 3-step reaction mechanisms is observed at the short radial distance of less than 0.05 m (inside flame core). There is no difference between using two approaches at radial distance after 0.05 m.

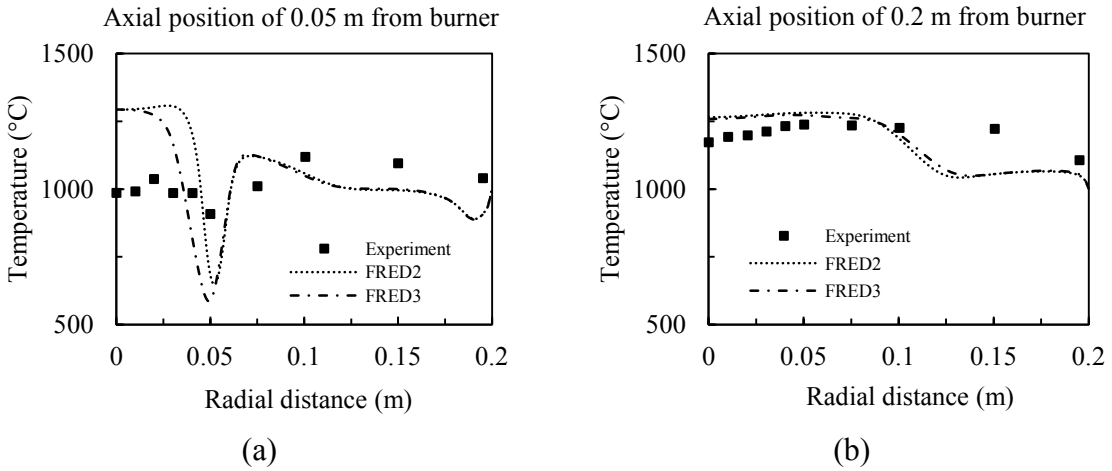

Figure 6.48: Comparison of temperature profile applying 2-step and 3-step reaction mechanisms: (a) at axial position of 0.05 m (b) 0.2 m, distant from burner.

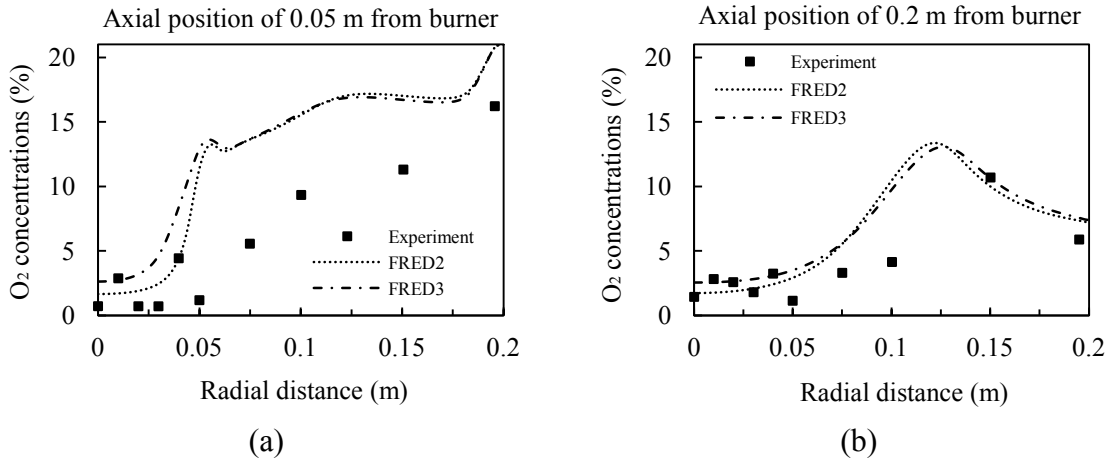

Figure 6.49: Comparison of O_2 concentrations (% by volume) applying 2-step and 3-step reaction mechanisms: (a) at axial position of 0.05 m (b) 0.2 m, distant from burner.

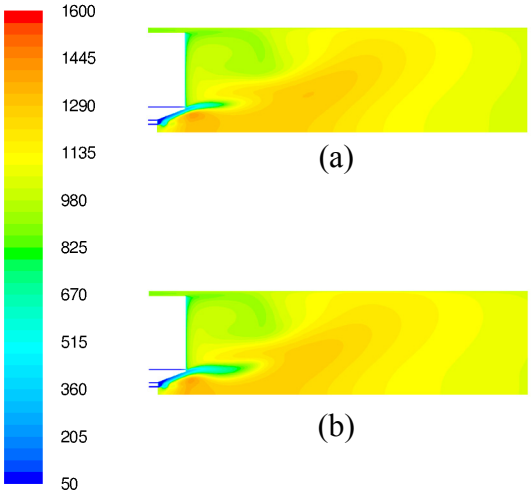

Figure 6.50: Comparison of temperatures from global 2-step and 3-step volatile reaction mechanisms applying finite rate-eddy dissipation model (FRED): (a) FRED 2-step, (b) FRED 3-step.

Both reaction mechanisms result in the similar flame shapes represented by dark-orange color shown in the contour plots of temperature profiles in Fig. 6.50(a) and 6.50(b), although the width of swirling flame is more extended tangentially when using 2-step mechanisms.

The 2- and 3-step mechanisms calculate different product from hydrogen-element (H) from volatile content of coal particle. The 2-step mechanisms defines the water (H_2O) as the product specie from combustion process, while defines H_2 as the product for 3-step mechanisms. This brings changes of chemical reactions such as heat release from reactions and also temperature prediction from the style of reaction mechanisms at post-flame, already discussed in the literature reviews in chapter 2.

6.2.8 Kinetic rates for volatile oxidation (2-step mechanisms)

Although some literatures presented accomplishments of applying kinetic rates for oxy-fuel flame predictions for both natural gas and for coal combustion (Appendix B). None of them presented the influences of kinetic rates for volatile reactions to the final predictions. For this reason, some widely applied kinetic rates of volatiles oxidation are selected and tested in this thesis. One rate of volatile oxidation is taken from the successful implementation into CFD prediction for coal combustion (Shaw et al. [Shaw91]) and additional two rates are from the studies of modeling for hydrocarbon oxidation from classical paper by Westbrook et al. [Westbrook81] and Dryer et al. [Dryer73]. Changing kinetic rates has only small influence on velocity prediction as shown in Fig. 6.51 and Fig 6.52.

Kinetic rates for volatile oxidation influence the temperature and O_2 predictions shown in Fig. 6.53 and Fig. 6.54, consequently. The kinetic rate for volatile oxidation by Shaw results in more accurate numerical results for temperature at both axial positions and O_2 concentration at the axial position of 0.2 m, especially at the radial distance of 0.05 m from centerline for temperature predictions.

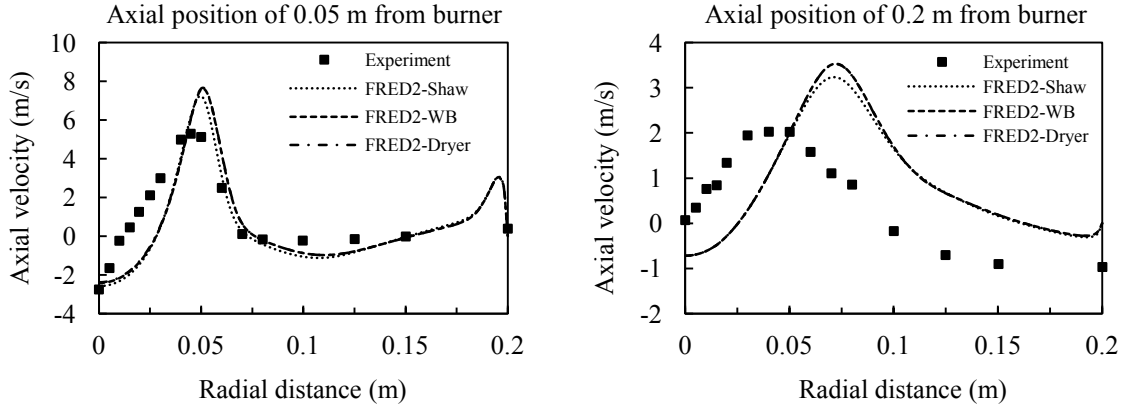

(a) (b)

Figure 6.51: Comparison of axial velocity applying different kinetic rates for volatile oxidation in 2-step reaction mechanisms: (a) at axial position of 0.05 m, (b) 0.2 m, distant from burner.

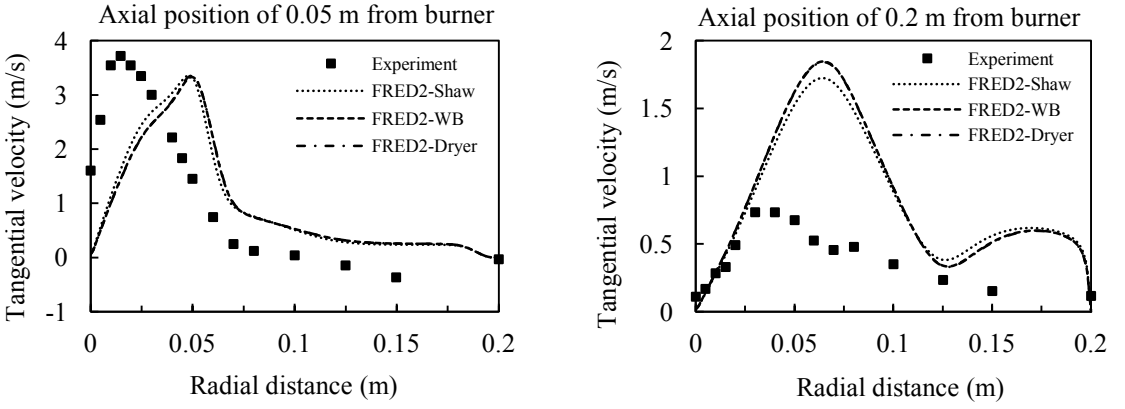

(a) (b)

Figure 6.52: Comparison of tangential velocity applying different kinetic rates for volatile oxidation in 2-step reaction mechanisms: (a) at axial position of 0.05 m, (b) 0.2 m, distant from burner.

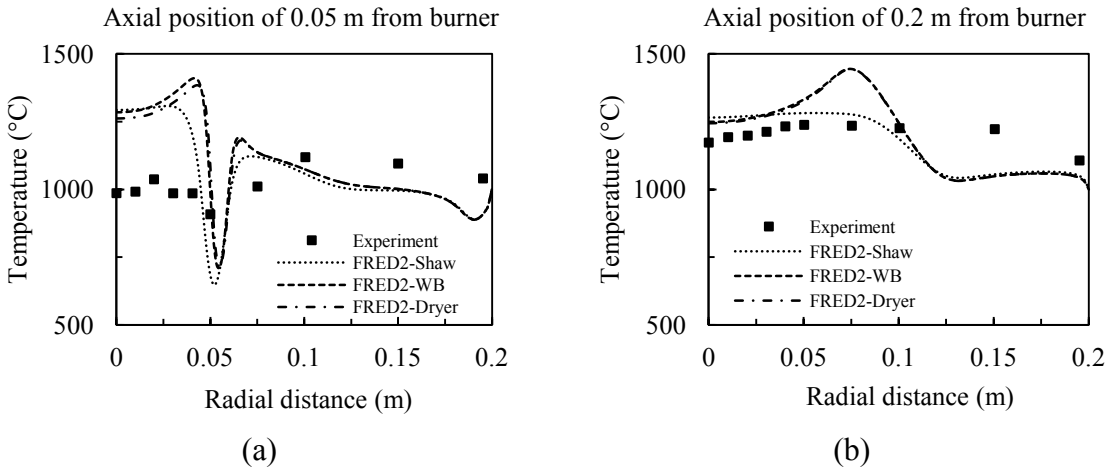

Figure 6.53: Comparison of temperature profile applying different kinetic rates for volatile oxidation in 2-step reaction mechanisms (a) at axial position of 0.05 m (b) 0.2 m, distant from burner.

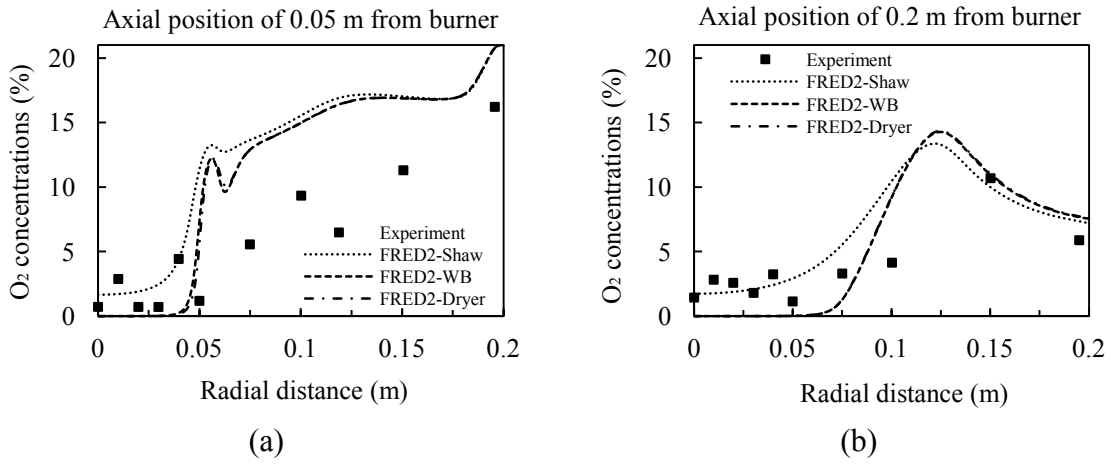

Figure 6.54: Comparison of O_2 concentrations (% by volume) applying different kinetic rates for volatile oxidation in 2-step reaction mechanisms (a) at axial position of 0.05 m (b) 0.2 m, distant from burner.

Although the Shaw's kinetic rate slightly over-predicting O_2 content at short radial distance for both axial positions in Fig. 6.54, overall trends from all kinetic rates are still similar and deviated from other results for less than 2% (by volume).

Contour plots of temperature profiles at the mid-plane of furnace provide an insight into the location of hot flame where the maximum heat released from hydrocarbon fuel (coal) (Fig. 6.55). The combustion takes place inside burner quarl area applying the Shaw's kinetic parameters. The peak temperatures are outside the qual region applying kinetic rate for volatile oxidation by Dryer and Westbrook. This is somehow implying flame instability when applying kinetic rates from Dryer and Westbrook.

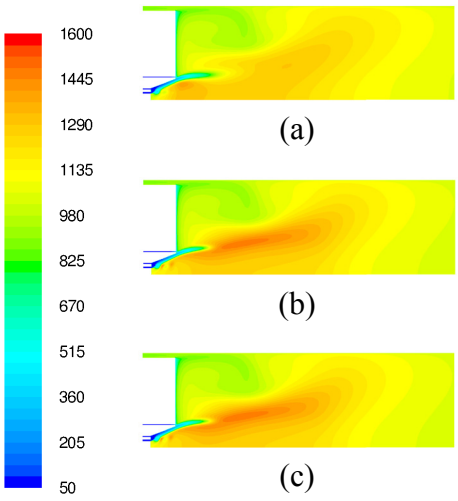

Figure 6.55: Comparison of temperatures from different volatile kinetic rates applying global 2-step reaction mechanisms: (a) VM-Shaw/CO-Dryer, (b) VM-Dryer/CO- Dryer, (c) VM-Westbrook/CO- Dryer.

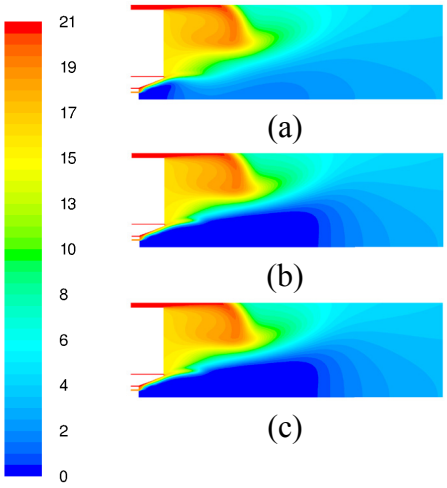

Figure 6.56: Comparison of O_2 concentrations from different volatile kinetic rates applying global 2-step reaction mechanisms: (a) VM-Shaw/CO-Dryer, (b) VM-Dryer/CO- Dryer, (c) VM-Westbrook/CO- Dryer.

The results of O_2 predictions indicate that regions of complete O_2 consumption (zero of $\%O_2$ specie) are presented applying kinetic rate for volatile oxidation by Dryer and Westbrook, represented by the wide strong-blue color area in Fig. 6.56.

The volatile kinetic rate by Dryer and Westbrook lead to higher volatile reaction rate presented in Fig. 6.57. This is in agreement with the wide area of zero O_2 species (complete O_2 consumption) using the two kinetic rates shown in Fig. 6.56.

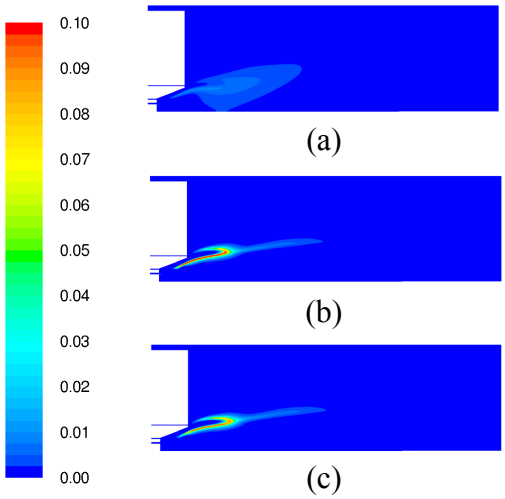

Figure 6.57: Comparison of reaction rate of volatile matter (VM) from different volatile kinetic rates applying global 2-step reaction mechanisms: (a) VM-Shaw/CO-Dryer, (b) VM-Dryer/CO-Dryer, (c) VM-Westbrook/CO- Dryer.

6.2.9 Kinetic rates for volatile/CO oxidation (3-step mechanisms)

Numerical results for axial and tangential velocity applying various kinetic rates for volatile and CO oxidation are plotted in Fig. 6.58 and Fig. 6.59. Using these different kinetic rates has only small influence on the predictions of velocity. This is in an agreement with the numerical investigations applying global 3-step reaction mechanism in the previous sub-section.

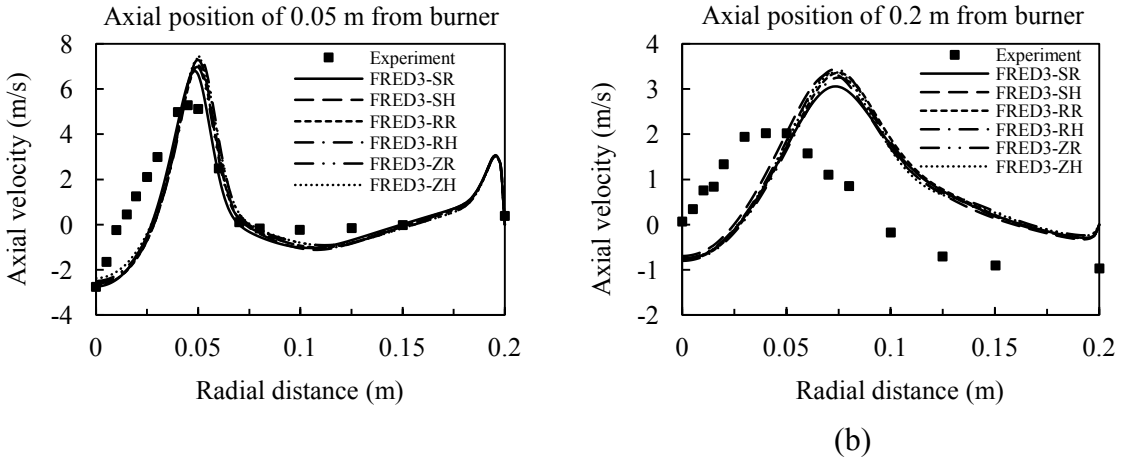

Figure 6.58: Comparison of axial velocity applying different kinetic rates for volatile oxidation in 3-step reaction mechanisms (a) at axial position of 0.05 m (b) 0.2 m, distant from burner.

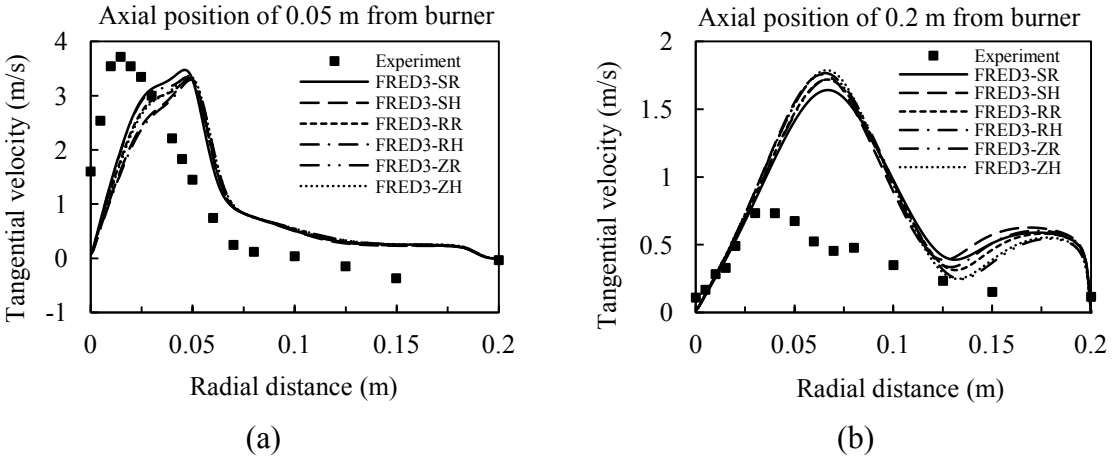

Figure 6.59: Comparison of tangential velocity applying different kinetic rates for volatile oxidation in 3-step reaction mechanisms (a) at axial position of 0.05 m (b) 0.2 m, distant from burner.

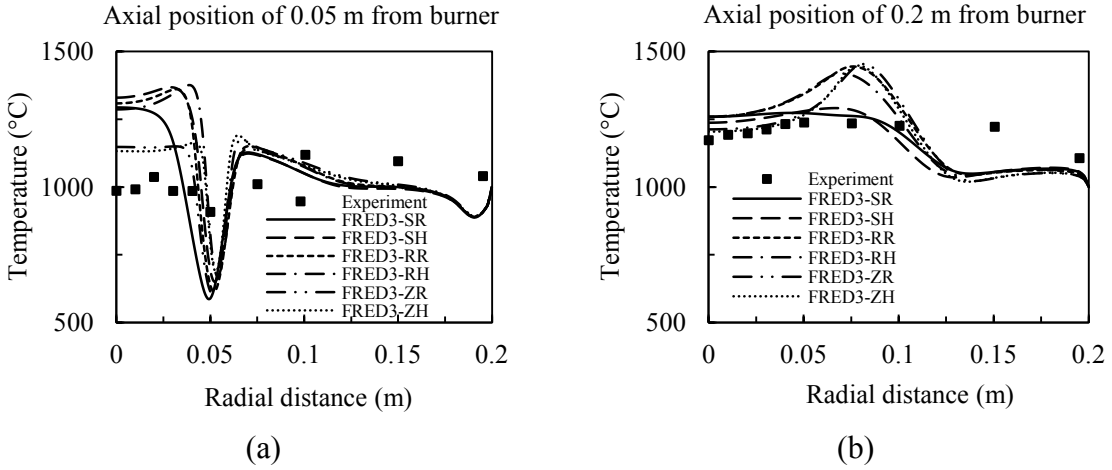

Figure 6.60: Comparison of temperature profile applying different kinetic rates for volatile oxidation in 3-step reaction mechanisms (a) at axial position of 0.05 m (b) 0.2 m, distant from burner.

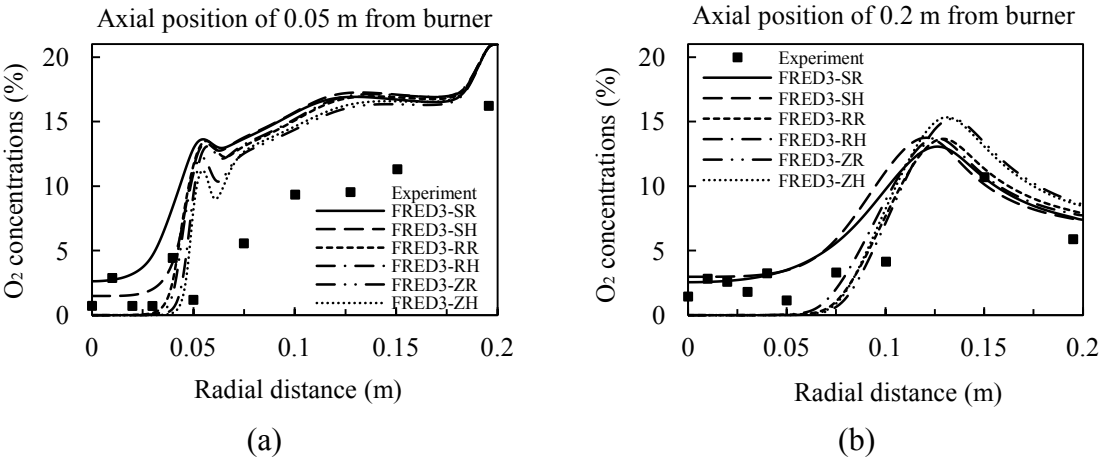

Figure 6.61: Comparison of O_2 concentrations (% by volume) applying different kinetic rates for volatile oxidation in 3-step reaction mechanisms (a) at axial position of 0.05 m (b) 0.2 m, distant from burner.

It is clearly seen from temperature predictions in Fig. 6.60 and O_2 predictions in Fig. 6.61 that kinetic rates has high influence on the final numerical solutions. The kinetic rates for volatile by Zimont gives better temperature predictions near flame centerline at the radial distance of less than 0.05 in both axial positions; however, applying the rates results in over-predictions of peak temperature at the radial distance of 0.75 m and axial distance of 0.2 m (Fig. 6.60(b)) and merely dependent of kinetic rates for CO oxidation (either by Rückert or Howard). In contrast to temperature predictions using the kinetic rate of volatile oxidation by Shaw, overestimations of temperature are found at the short radial distance of less than 0.05 m at the axial distance close to burner quarl (Fig. 6.60(a)). In addition, the kinetic rates for CO oxidation has higher influence on temperature and O_2 predictions when the volatile kinetic rate by Shaw is applied, especially at close axial distance to burner (Fig. 6.60(a) and Fig. 6.61(a)) and short radial distance of less than 0.05 m. Applying the Zimont's kinetic rates, good predictions for O_2 concentrations are observed at axial distance of 0.05 m but under-predictions of O_2 concentrations at the axial position of 0.2 m are presented in Fig. 6.61(b), indicating too much O_2 consumption using the rates.

In some situations, comparing predictions for velocity, temperature and O_2 concentrations to measurements at specific locations is not enough to see the flame aerodynamics, implying flame stability caused by the selection of sub-models in the CFD predictions. Contour plots of temperature at the mid-plane of furnace geometry applying different volatile and CO kinetic rates are illustrated in Fig. 6.62. Applying the kinetic rates by Rückert and Zimont results in maximum temperature occurring outside the burner quarl zone, which is caused by the stronger rate of volatile reactions.

The O_2 predictions using kinetic rates for volatile oxidation by Shaw and different kinetic rates for CO oxidation are shown in Fig. 6.63(a) and Fig. 6.63(b), applying CO oxidation rate by Rückert leads to slightly lower O_2 concentrations at the post flame region of around 2% (by volume). The wider of area of zero O_2 concentrations (strong blue color) are observed applying the volatile oxidation rates by Rückert and Zimont, implying the area of the highest O_2 consumption. These are caused by the higher rate of reaction of volatile reaction comparing to Shaw's kinetic rate.

Reaction rates for volatile oxidations applying three kinetic rate (Shaw, Rückert and Zimont) are presented in Fig. 6.64. It is obvious that the highest volatile reaction rate is shown in the figure when the rate by Zimont is applied, following by Rückert and minimum by Shaw, respectively. The rate of volatile oxidation induces final solutions of temperature and O_2 predictions as discussed previously.

The rate of CO oxidation influences the location of hot flame region because the enthalpy of formation for CO oxidation is negative and equal to -283.3 kJ/mole of CO, implying heat releasing from reaction. The reaction rates of CO oxidation applying different kinetic rates for volatile and CO oxidation are expressed in Fig. 6.65. The reaction for CO oxidation take place outside the burner quarl area applying volatile reaction rates by Rückert and Zimont.

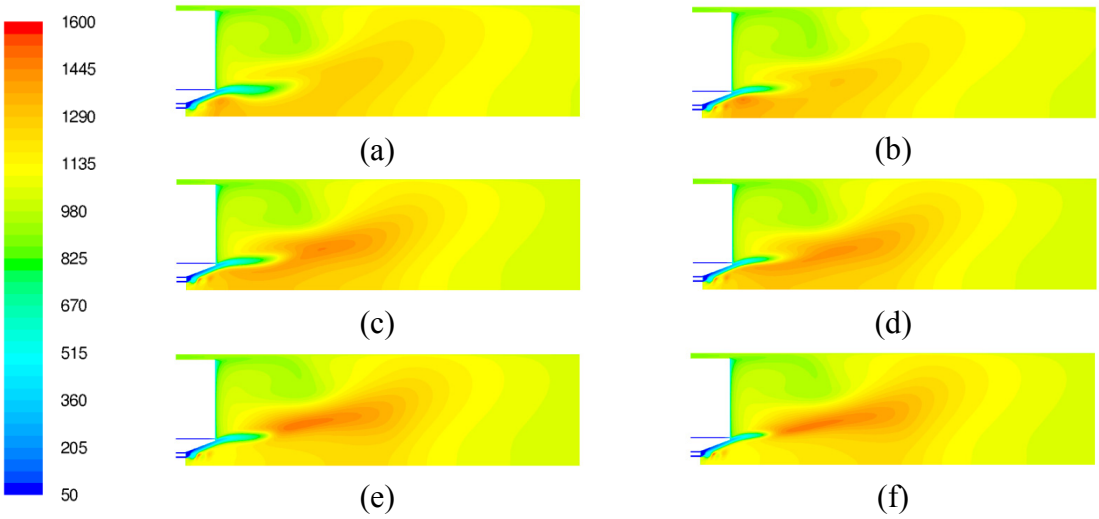

Figure 6.62: Comparison of temperatures from different volatile kinetic rates applying global 3-step reaction mechanisms: (a) VM-Shaw/CO-Rückert, (b) VM-Shaw/CO-Howard, (c) VM-Rückert /CO-Rückert, (d) VM- Rückert /CO-Howard, (e) VM-Zimont/CO-Rückert, (f) VM-Zimont /CO-Howard.

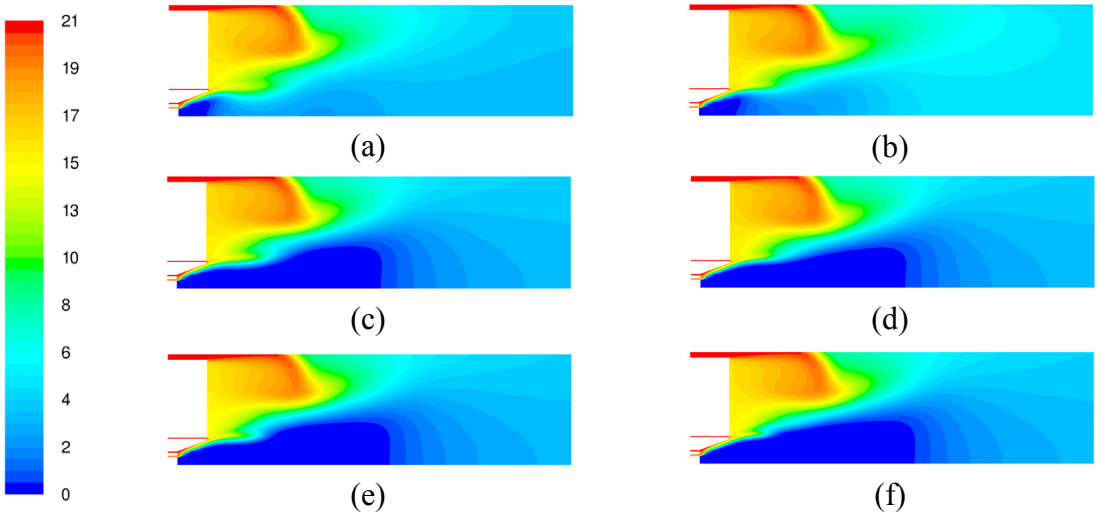

Figure 6.63: Comparison of O_2 concentrations from different volatile kinetic rates applying global 3-step reaction mechanisms: (a) VM-Shaw/CO-Rückert, (b) VM-Shaw/CO-Howard, (c) VM-Rückert /CO-Rückert, (d) VM- Rückert /CO-Howard, (e) VM-Zimont/CO-Rückert, (f) VM-Zimont /CO-Howard.

Shorter CO consumption regions are observed when the CO oxidation rate by Howard is applied, implying faster CO reaction rate at a short axial distance from burner. The maximum CO oxidation rate occurs inside the burner quarl applying the Shaw's kinetic rate. This results in maximum temperature inside the quarl area as discussed already because the CO oxidation is the key reaction that causes hot flame temperature region in the flame, in contrast to results by other kinetic rates for volatile oxidation (Fig. 6.65(c)-6.65(d)).

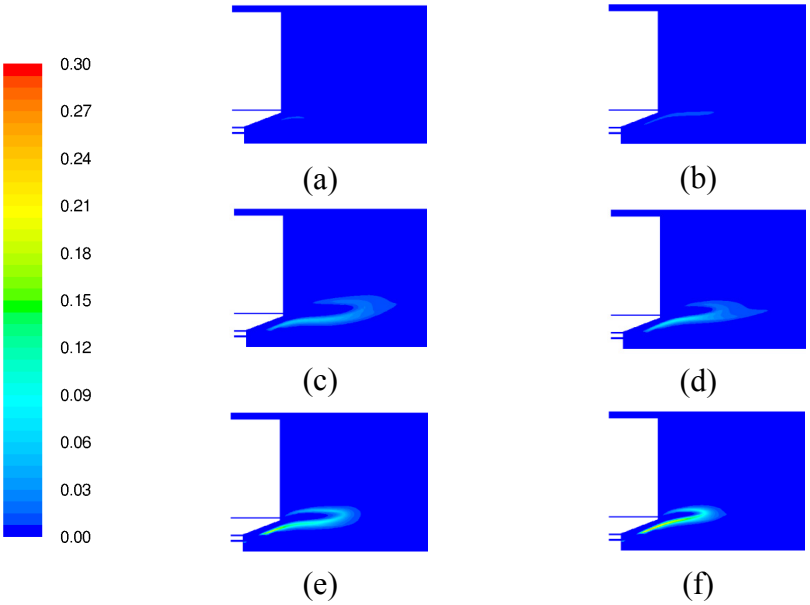

Figure 6.64: Comparison of reaction rate of volatile matter (VM) from different volatile kinetic rates applying global 3-step reaction mechanisms: (a) VM-Shaw/CO-Rückert, (b) VM-Shaw/CO-Howard, (c) VM- Rückert /CO-Rückert, (d) VM- Rückert /CO-Howard, (e) VM-Zimont/CO-Rückert, (f) VM- Zimont /CO-Howard.

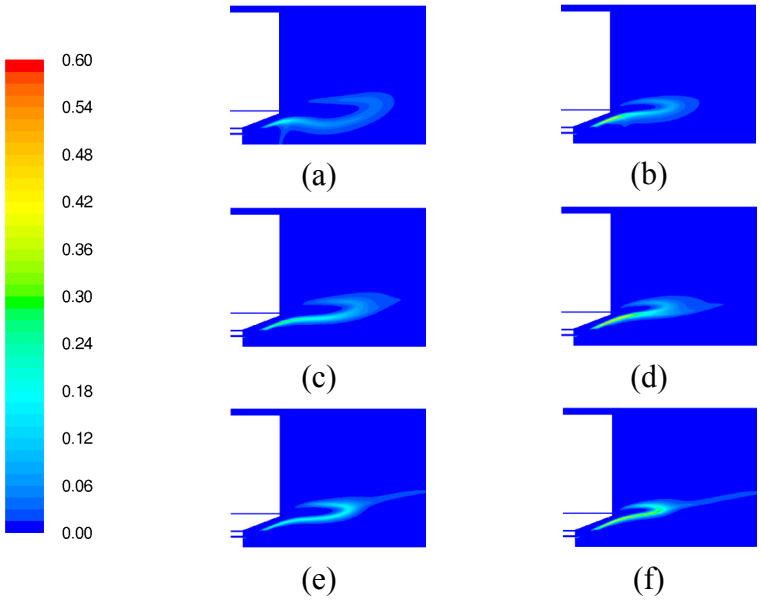

Figure 6.65: Comparison of reaction rate of CO oxidation from different volatile kinetic rates applying global 3-step reaction mechanisms: (a) VM-Shaw/CO-Rückert, (b) VM-Shaw/CO-Howard, (c) VM- Rückert /CO-Rückert, (d) VM- Rückert /CO-Howard, (e) VM-Zimont/CO-Rückert, (f) VM- Zimont /CO-Howard.

H_2 oxidation rate is one of the key reactions leading to the region of hot flame temperature inside flame. The enthalpy of formation for H_2 oxidation is negative and equal to -241.8 kJ/mole of H_2 implying heat releasing from reaction. Comparing with the enthalpy of formation for CO oxidation (-283.3 kJ/mole of CO), the heat release from CO oxida-

tion is slightly higher. Another factor is the carbon contents (C) in coal particle, which is generally higher than hydrogen contents (H), clearly seen in the ultimate analysis for Lusatian coal in chapter 1 (12 times higher). This implies that CO oxidation influences temperature predictions (results from heat releasing from fuel) than H_2 oxidation in the coal combustion. The reaction rate of H_2 reaction is the highest when volatile oxidation rate by Zimont is applied, following by the rates by Rückert and finally by Shaw as shown in Fig. 6.66.

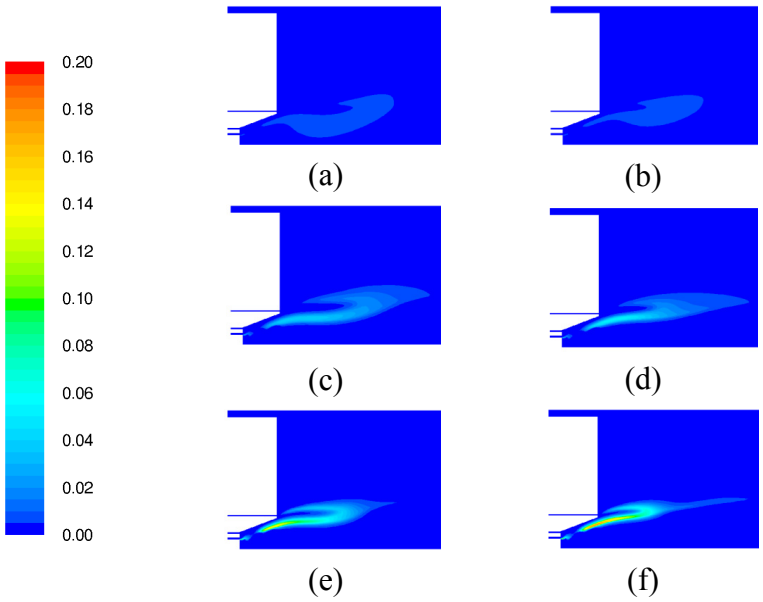

Figure 6.66: Comparison of reaction rate of H_2 oxidation from different volatile kinetic rates applying global 3-step reaction mechanisms: (a) VM-Shaw/CO-Rückert, (b) VM-Shaw/CO-Howard, (c) VM- Rückert /CO-Rückert, (d) VM- Rückert /CO-Howard, (e) VM-Zimont/CO-Rückert, (f) VM- Zimont /CO-Howard.

6.2.10 Reversible CO oxidation in 2-step mechanisms

By taking into account CO reversible oxidation applying kinetic rate by Andersen [Andersen09], only slightly changes for predicted velocity, temperature and O_2 concentrations are observed in the following Fig. 6.67-6.70. The maximum change is the numerical results for temperature at axial position of 0.05 m, the maximum flame temperature (1300 °C) in the flame core drops faster in the radial direction when including CO reversible oxidation using the global 2-step reaction mechanisms. This implies the narrower flame core clearly illustrated in the contour plot of flame temperature in Fig. 6.71.

At the axial position of 0.05 m in Fig. 6.70(a), slightly improvement of O_2 prediction is investigated at the radial distance of less than 0.05 m. The lower calculated O_2 concentration is presented for axial distance of 0.2 m in Fig. 6.70(b) at the radial distance of higher than 0.125 m.

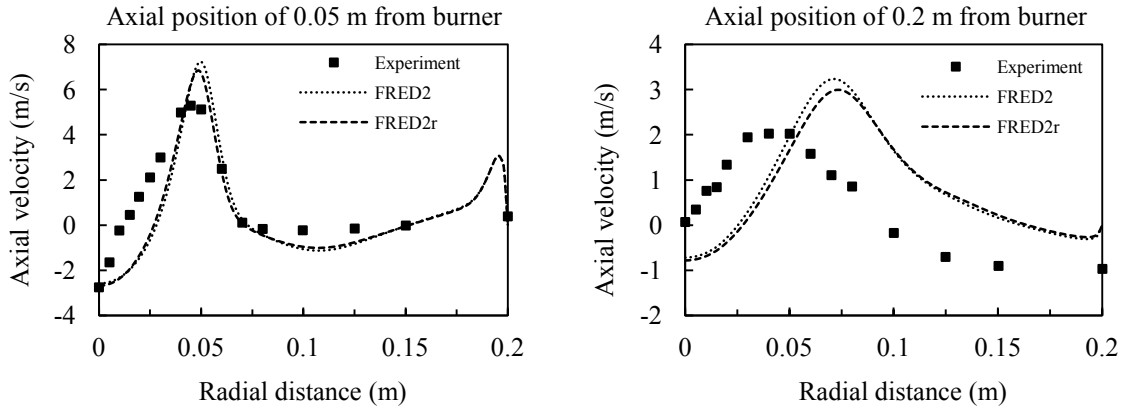

Figure 6.67: Comparison of axial velocity by including reversible CO oxidation in 2-step reaction mechanisms: (a) at axial position of 0.05 m, (b) 0.2 m, distant from burner.

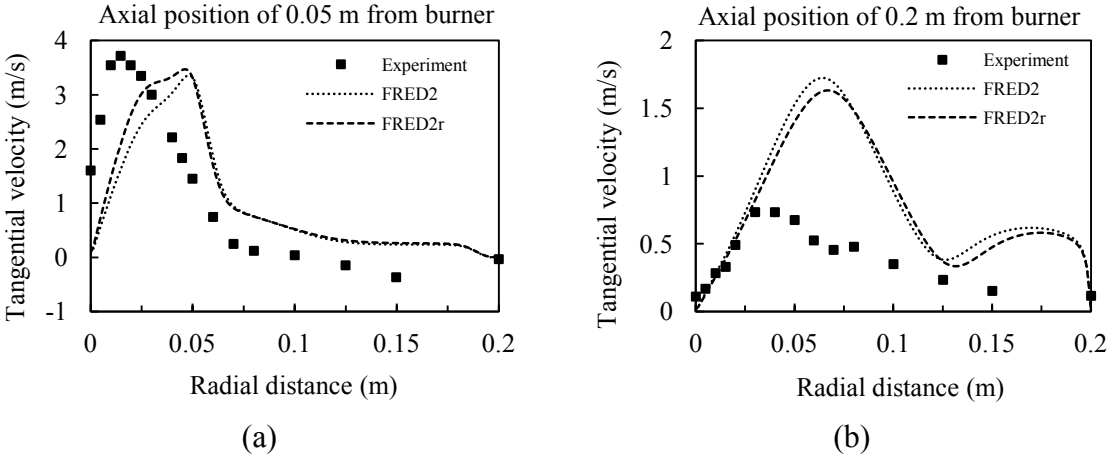

Figure 6.68: Comparison of tangential velocity including reversible CO oxidation in 2-step reaction mechanisms: (a) at axial position of 0.05 m, (b) 0.2 m, distant from burner.

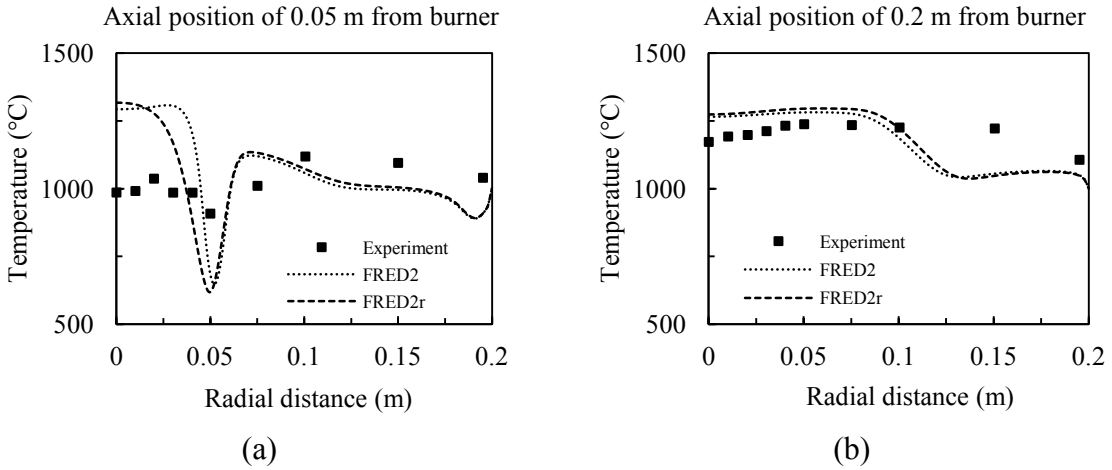

Figure 6.69: Comparison of temperature profile including reversible CO oxidation in 2-step reaction mechanisms: (a) at axial position of 0.05 m, (b) 0.2 m, distant from burner.

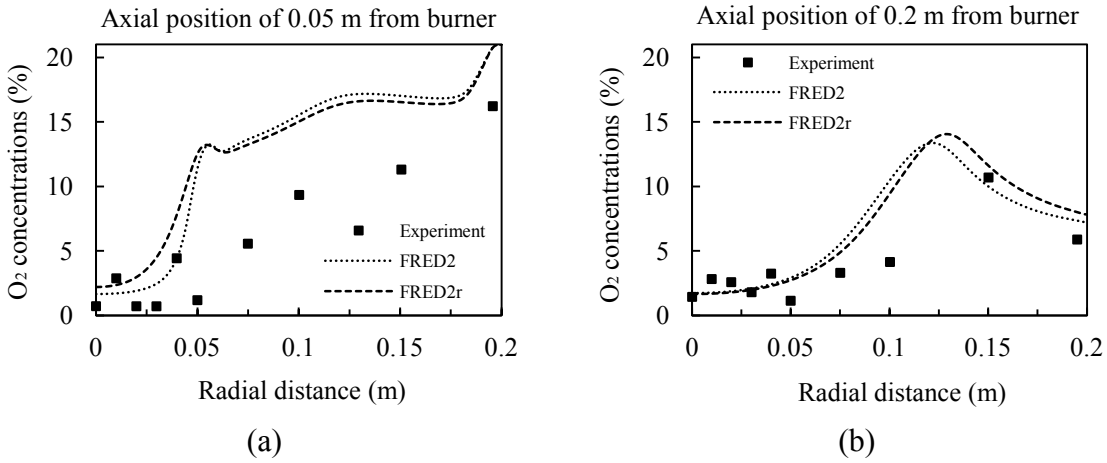

Figure 6.70: Comparison of O_2 concentrations (% by volume) including reversible CO oxidation in 2-step reaction mechanisms: (a) at axial position of 0.05 m, (b) 0.2 m, distant from burner.

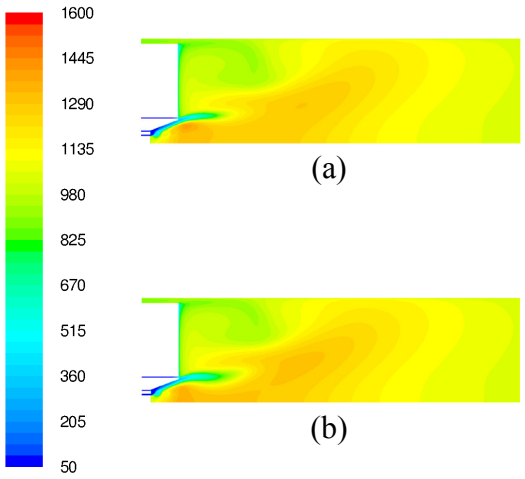

Figure 6.71: Comparison of temperature profiles applying global 2-step volatile reaction mechanisms with and without reversible CO oxidation: (a) FRED 2-step, (b) FRED 2-step with reversible CO oxidation.

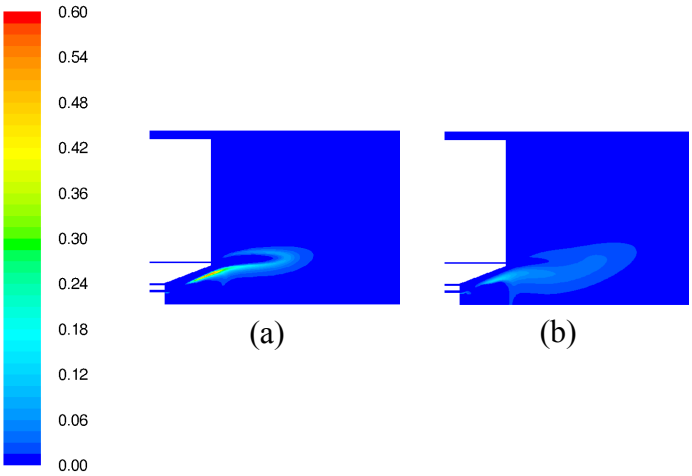

Figure 6.72: Comparison of reaction rate of CO oxidation applying global 2-step volatile reaction mechanisms with and without reversible CO oxidation: (a) FRED 2-step, (b) FRED 2-step with reversible CO oxidation.

The wider hot flame zone at the flame center is evidently observed applying CO irreversible oxidation in Fig. 6.71(a). Including CO reversible oxidation with the global 2-step mechanisms also results in the detached hot flame region as shown in Fig. 6.71(b). The CO oxidation rate applying irreversible kinetic rate is also higher in the flame boundary clearly seen in Fig. 6.72(a), comparing to weaker CO oxidation rate in Fig. 6.72(b).

6.2.11 Reversible CO oxidation in 3-step mechanisms

From these numerical investigations, including the CO reversible oxidation does not yield better predictions when applying the global 3-step reaction mechanisms (plots are omitted here), in contrast to slight improvements of the results observed applying the global 2-step reaction mechanisms previously explained.

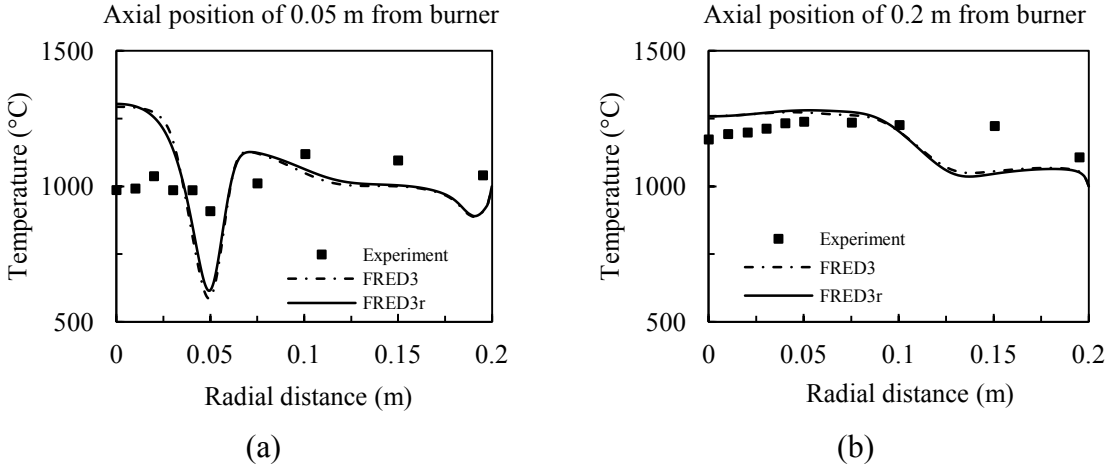

Figure 6.73: Comparison of temperature profile including reversible CO oxidation in 3-step reaction mechanisms: (a) at axial position of 0.05 m, (b) 0.2 m, distant from burner.

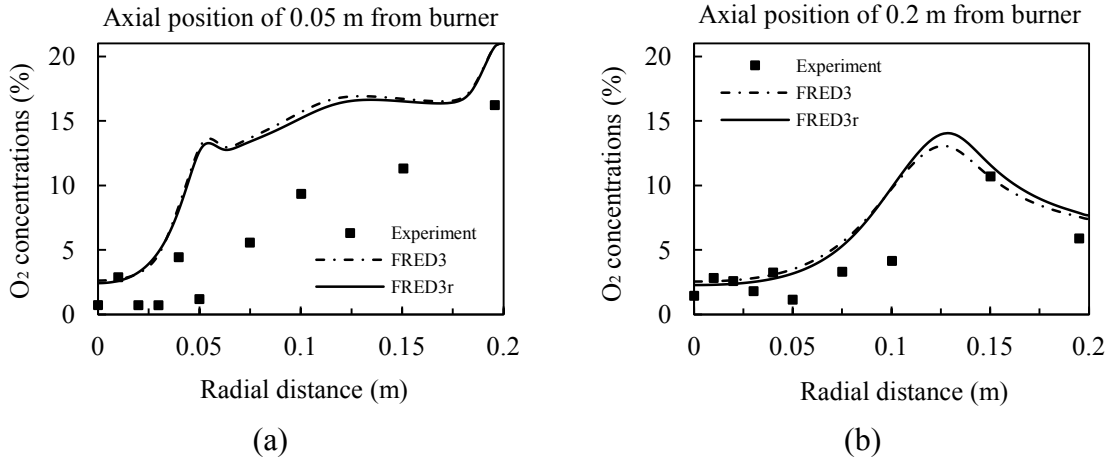

Figure 6.74: Comparison of O_2 concentrations (% by volume) including reversible CO oxidation in 3-step reaction mechanisms: (a) at axial position of 0.05 m, (b) 0.2 m, distant from burner.

6.2.12 Particle radiation modeling

Applying different approaches for particle radiation models does not effects velocity predictions; hence, only numerical results for temperature, O_2 concentration, radiative heat flux and radiative source term are discussed here. Because there are no experimental results for radiation quantities published in the referenced work as temperature and O_2 concentration, therefore only changes of numerical results are discussed without validation.

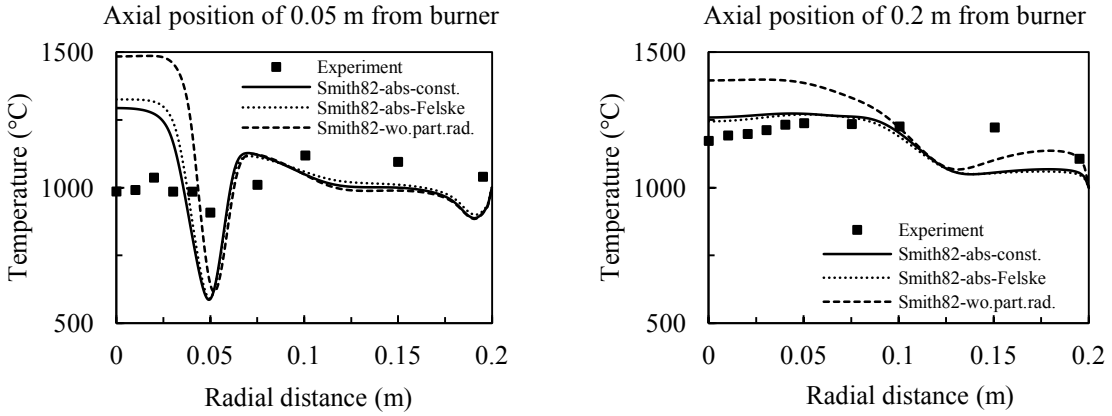

(a) (b)

Figure 6.75: Comparison of temperatures applying Smith's correlations for WSGG model with and without particle radiation (constant particle emissivity or as soot radiation [Felske77]).

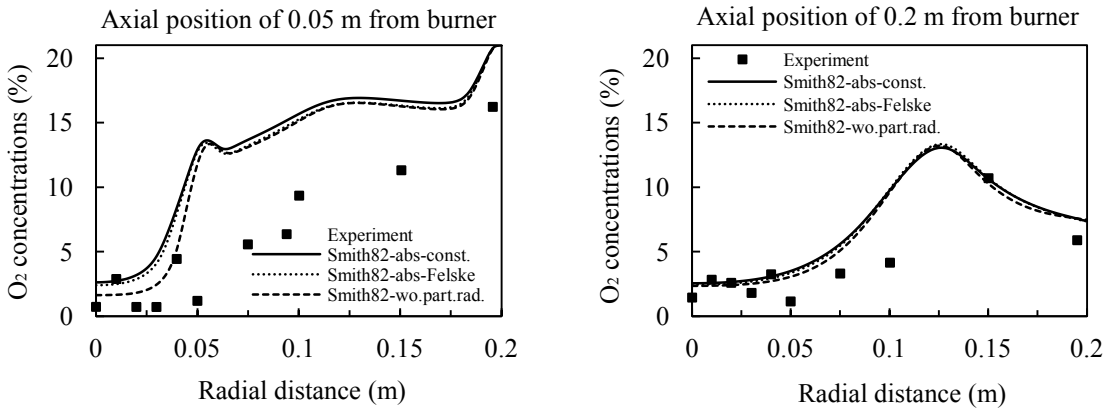

(a) (b)

Figure 6.76: Comparison of O_2 concentrations applying Smith's correlations for WSGG model with and without particle radiation (constant particle emissivity or as soot radiation [Felske77]).

Comparing predictions of temperatures, modeling particle radiation as constant emissivity (Smith82-abs-const) or as soot dominated radiation (Smith82-abs-Felske) yield much lower temperature at the flame center around 200-250 °C than without particle radiation

(Smith-wo.part.rad.) at axial position of 0.05 from burner in Fig. 6.75(a). At axial position of 0.2 m from burner, excluding the particle radiation in the CFD models results in over-estimation of temperature at the flame core (center) of approximately 200 °C deviated from experimental result and around 100 °C higher than predictions from other approaches. For this reason, it is clear that accounting for particle radiation is important to provide a good predictions temperature at the flame center near the region of coal particle injections, in which the particle radiation has more influence than other regions inside the furnace. Slightly lower O_2 concentration is investigated for the whole radial distances at the axial position of 0.05 m from burner. Nevertheless this change of O_2 prediction is not evidently observed at the axial position of 0.2 m from burner in Fig. 6.76(b).

Comparison of predicted radiation quantities applying different approaches for particle radiation models are shown in Fig. 6.77. The quantities are radiative heat flux, radiative source term, total emissivity and total absorption coefficient along the centerline distant from burner quarl. Neglecting the calculation of particle radiation effects significantly radiation quantities as presented in all predictions in Fig. 6.77(a)-6.77(d). However, the final solution of thermodynamic quantities (temperature and species concentrations) still highly depends on the dimension and geometric shape of the considered furnace, implying the influence of path-lengths to the calculation of total radiation quantities such as total emissivity and total absorption coefficient. Five time lower minimum radiative source term (-2500 kW/m^3) is investigated along axial distance at the furnace centerline from burner applying soot dominated particle radiation (Fig. 6.77(a)). This implies the higher influence of heat sink in the computational volume near the flame center and also effecting change of radiative heat flux at the furnace wall presented in Fig. 6.77(b).

In Fig. 6.77(b), the higher heat absorption is found at the first radial distance of less than 0.6 m from burner, indicating by the higher minimum negative radiative heat flux (-25 kW/m^2) considering particle radiation as soot dominated radiation, comparing to minimum value of -15 kW/m^2 omitting the particle radiation. This higher of heat absorption in the short axial distance from burner along the furnace wall results in the lower flame temperature at the control volume close to the burner due to the fact that some heat is transferred through the furnace wall. Heat absorption is slightly lower around 2 kW/m^2 when applying soot particle radiation at the axial distance of higher than 0.6 m from burner.

The results of radiative source term along centerline and radiative heat flux along wall surface of the oxy-fuel furnace are the results from radiative transfer calculations by calculated total emissivity and absorption coefficients in Fig. 6.77(c) and Fig. 6.77(d), respectively. Including particle radiation as soot radiation (Smith82-abs-Felske) yields higher both total absorption coefficients and also total emissivity.

In Fig. 6.77(c), the total emissivity is approximately constant at 0.5 including soot radiation, while equal to around 0.1 neglecting particle radiation (five times higher). The total absorption coefficient is four times higher when taking into account soot radiation and equal to around 1.7 comparing to 0.4 for excluding particle radiation (Fig. 6.77(d)).

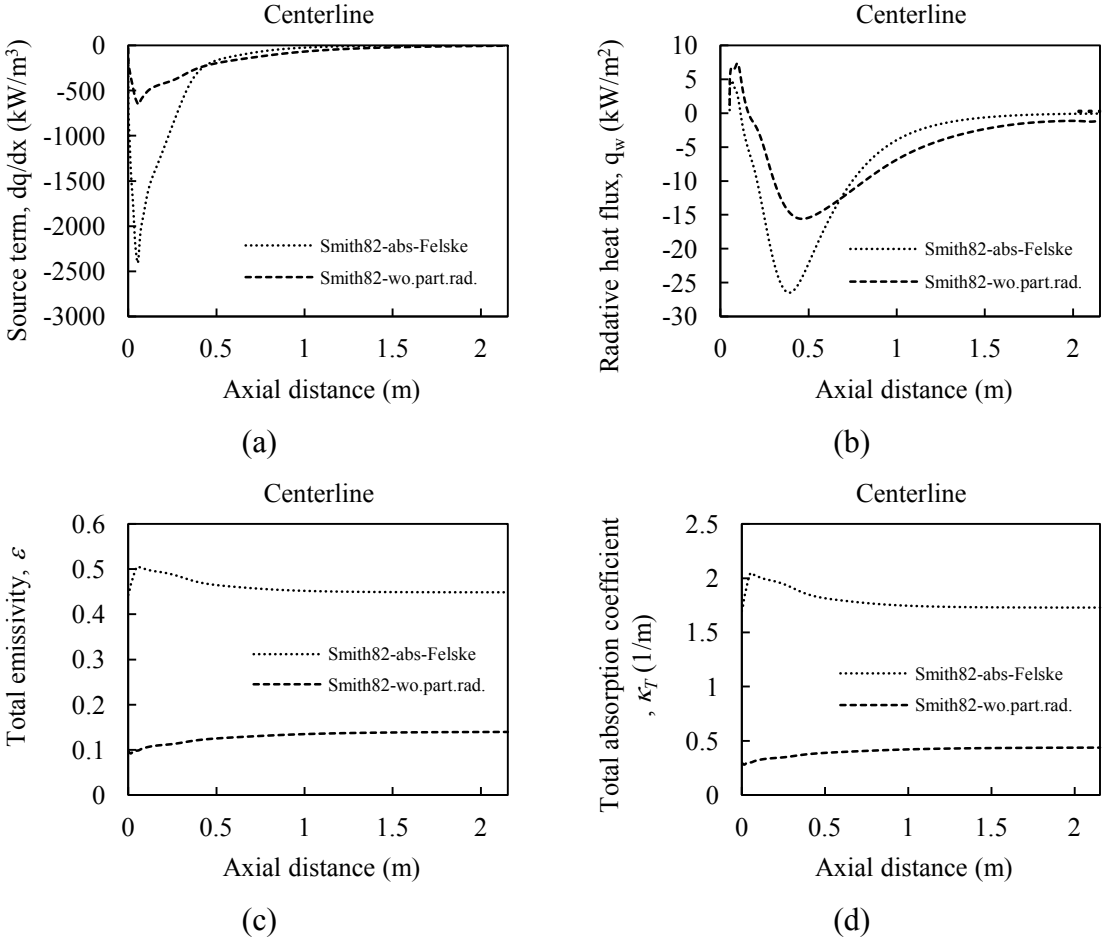

Figure 6.77: Comparison of radiation quantities along centerline of furnace distant from burner, applying Smith's correlations for WSGG model with and without particle radiation (as soot radiation [Felske77]): (a) radiative source term (kW/m^3), (b) radiative heat flux (kW/m^2), (c) total emissivity, (d) total absorption coefficients (1/m).

Contour profiles for temperature and O_2 predictions are shown in Fig. 6.78 and Fig. 6.79. Omitting particle radiation modeling, flame temperature is hotter comparing to the results by modeling particle radiation as soot radiation, evidently seen by wide area of red and strong orange color in Fig. 6.78(a). This leads to the wide area of the lowest O_2 concentrations in the furnace presented in Fig. 6.79(a) due to the higher reaction rate from hotter flame.

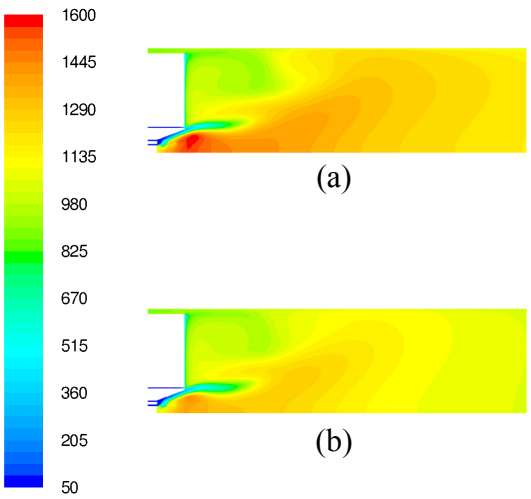

Figure 6.78: Comparison of temperatures applying Smith's correlations for WSGG model with and without particle radiation: (a) only gas radiation, (b) with particle radiation (as soot radiation [Felske77]).

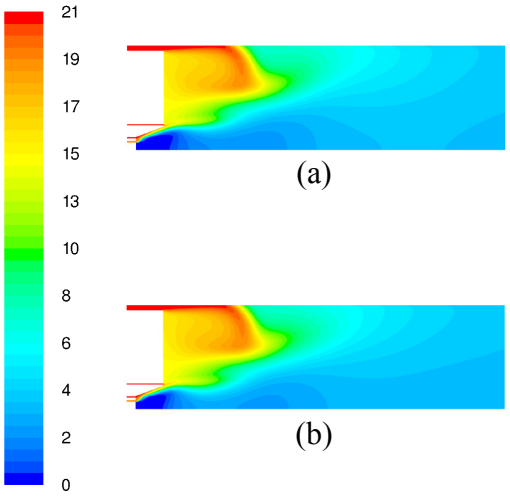

Figure 6.79: Comparison of O_2 concentration applying Smith's correlations for WSGG model with and without particle radiation: (a) only gas radiation, (b) with particle radiation (as soot radiation [Felske77]).

Minimum radiative source term in the furnace applying soot dominated particle radiation is around -3000 kW/m^3 (1000 kW/m^3 lower than without particle radiation), presented by the dark-blue area in Fig. 6.80(b). The lower radiative source term accounting for soot radiation implies the higher radiative heat absorption into combustion gas, finally resulting in the lower flame temperature illustrated before in Fig. 6.78(b).

Taking soot dominated particle radiation into account, total predicted emissivity and absorption coefficient is both 5 times higher than without particle radiation modeling (Fig. 6.77(c) and Fig. 6.77(d)). This effect is strong inside the burner quarl region and gradually expanding over the entire furnace to the exit, illustrated in Fig. 6.82-6.83.

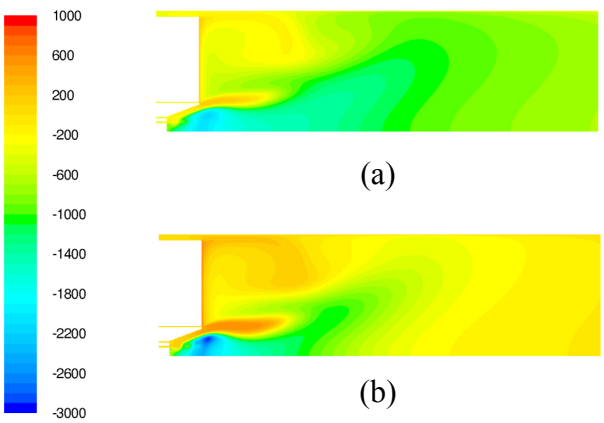

Figure 6.80: Comparison of radiative source terms (kW/m^3) applying Smith's correlations for WSGG model with and without particle radiation: (a) only gas radiation, (b) with particle radiation (as soot radiation [Felske77]).

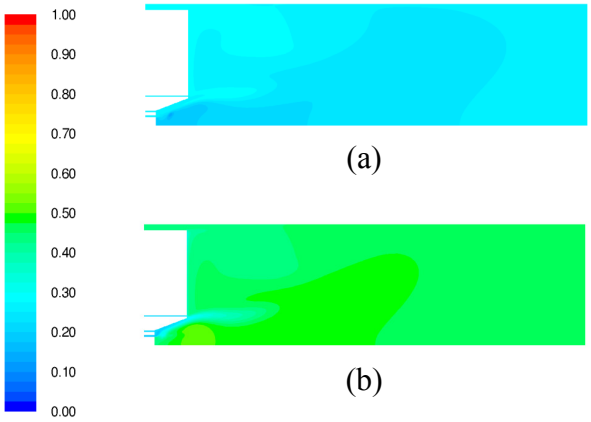

Figure 6.81: Comparison of total emissivity applying Smith's correlations for WSGG model with and without particle radiation: (a) only gas radiation, (b) with particle radiation (as soot radiation [Felske77]).

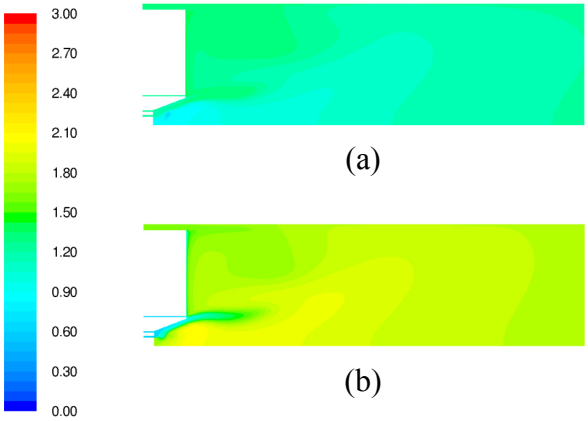

Figure 6.82: Comparison of total absorption coefficients applying Smith's correlations for WSGG model with and without particle radiation: (a) only gas radiation, (b) with particle radiation (as soot radiation [Felske77]).

6.2.13 Correlations for gas radiation

Predictions for radiative properties (source term, heat flux, total emissivity and total absorption coefficients) are plotted in Fig. 6.83 with the soot dominated particle radiation and in Fig. 6.84 with only gas radiation. Comparing two figures, including particle radiation influences significantly all radiative quantities. Variations of the profiles for radiative source term, total emissivity and total absorption coefficients are obviously investigated when only gas radiation is considered. This is because the particle radiation dominates overall radiative heat transfer calculations and has more effect to the final solution than gas radiation, refereeing to the pre-calculations for soot radiation explained in chapter 2. In addition from both figures, the magnitudes of values for all radiative quantities also change tremendously. For instance, peak minimum radiative source term decrease from about -1000 kW/m^3 without particle radiation in Fig. 6.84(a), to -2500 kW/m^3 with soot dominated particle radiation in Fig. 6.83(a). The magnitudes of minimum value for radiative heat flux reduce from about -20 kW/m^2 in Fig. 6.84(b) to -30 kW/m^2 in Fig. 6.83(b). This increment of -5 kW/m^2 effects the heat transfer calculations in the way that heat transfer rate through furnace wall is slightly higher when including particle radiation, due to the lower flame temperature inside oxy-fuel furnace illustrated previously.

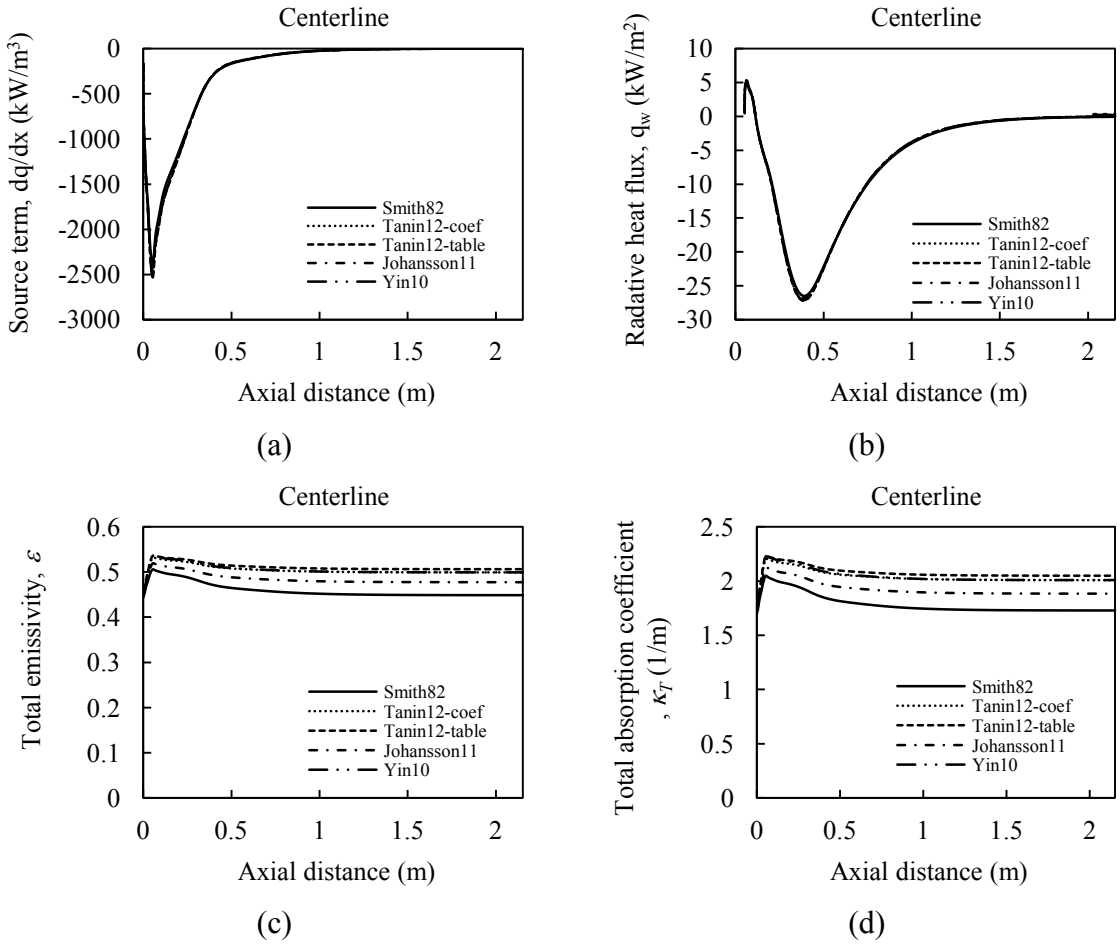

Figure 6.83: Predictions for radiative properties along centerline of furnace distant from burner, applying different correlations for WSGG model, with particle radiation (as soot radiation [Felske77]): (a) radiative source term (kW/m^3), (b) radiative heat flux (kW/m^2), (c) total emissivity, (d) total absorption coefficients (1/m).

Contour plots for total absorption coefficients are presented in Fig. 6.85. It is clear that total absorption coefficient by Smith's correlations in Fig. 6.85(a) is the lowest comparing to applying other WSGG's correlations. The total absorption coefficients is the highest applying the new oxy-fuel correlations fitted to HITEMP database presented in Fig. 6.85(b).

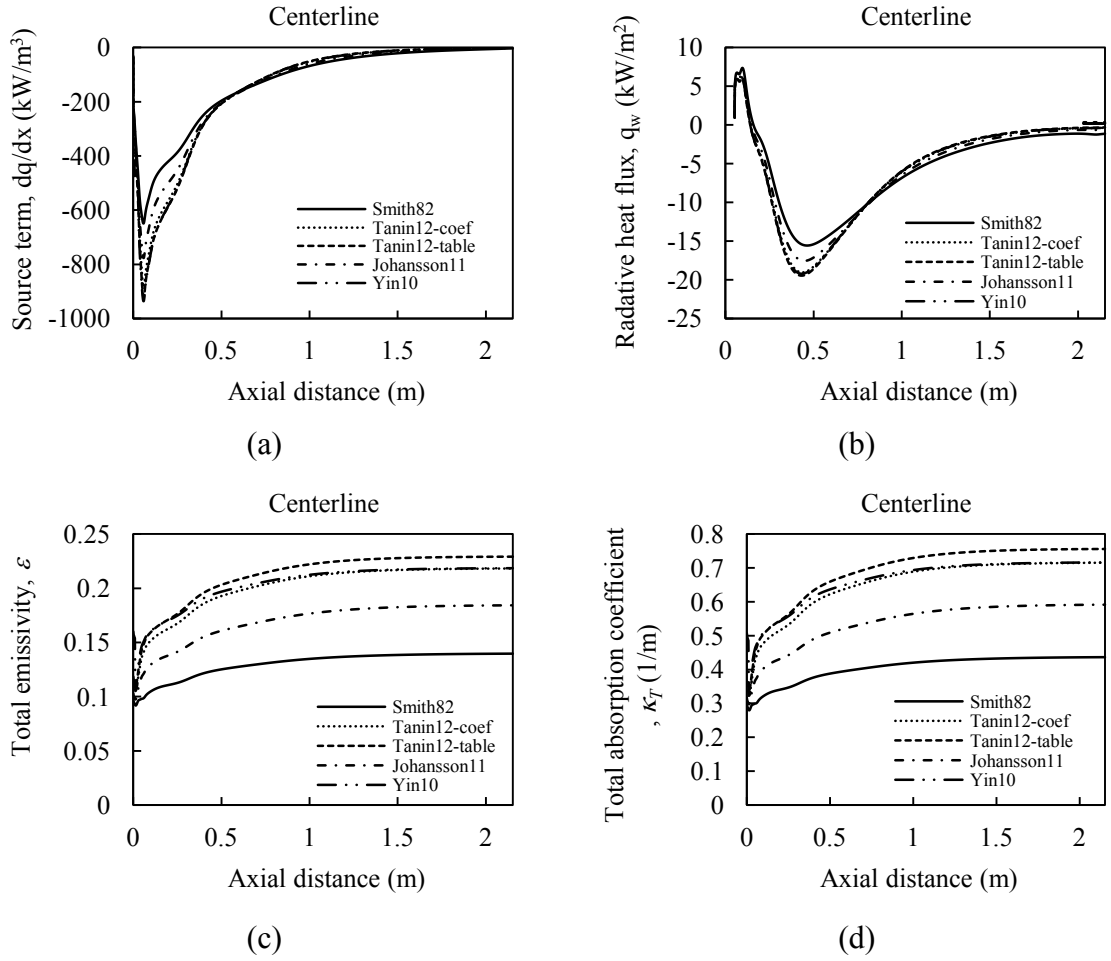

Figure 6.84: Predictions for radiative properties along centerline of furnace distant from burner, applying different correlations for WSGG model, without particle radiation (only gas radiation): (a) radiative source term (kW/m^3), (b) radiative heat flux (kW/m^2), (c) total emissivity, (d) total absorption coefficients (1/m).

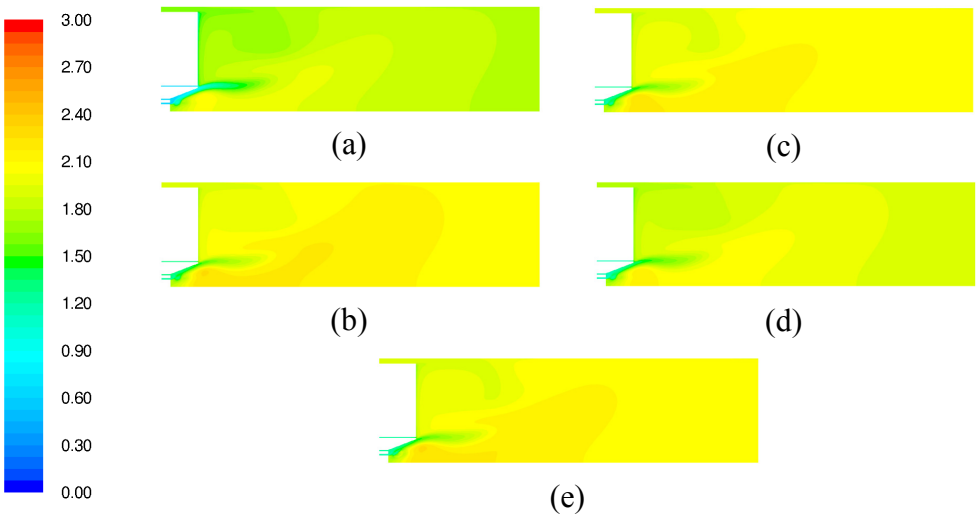

Figure 6.85: Comparison of total absorption coefficients (gas and soot) applying different correlations for WSGG model with particle radiation (as soot radiation [Felske77]): (a) Smith, (b) new oxy-fuel correlations-tables, (c) new oxy-fuel correlations-coefficients, (d) Johansson, (e) Yin.

6.3 New pilot scaled 0.4 MW_{th} oxy-fuel test facility

The results from numerical investigations of sub-models in a laboratory 100 kW_{th} oxy-fuel furnace are used for applying to the pilot scaled 0.4 MW_{th} oxy-fuel furnace. There were already summarized in chapter 5. The measurements of experimental results for 0.4 MW_{th} oxy-fuel furnace were based on experiments by Corrêa da Silva [Corrêa da Silva12] explained in chapter 5 including equipments for measurements and related locations of measurements. First the mesh independency of the CFD model is tested to find a suitable number of computational cells. The results of aerodynamic, thermo-chemical and radiation quantities are further discussed as follow.

6.3.1 Mesh dependency

Number of computational cells in the numerical investigations starts from 500,000 to 1.6 million, denoted as 500k, 700k, 1Mio and 1.6 Mio, respectively. The difference between temperature predictions along the radial distances, applying different mesh size (Fig. 6.86(a)-(c)), is found at the port location A, B and C.

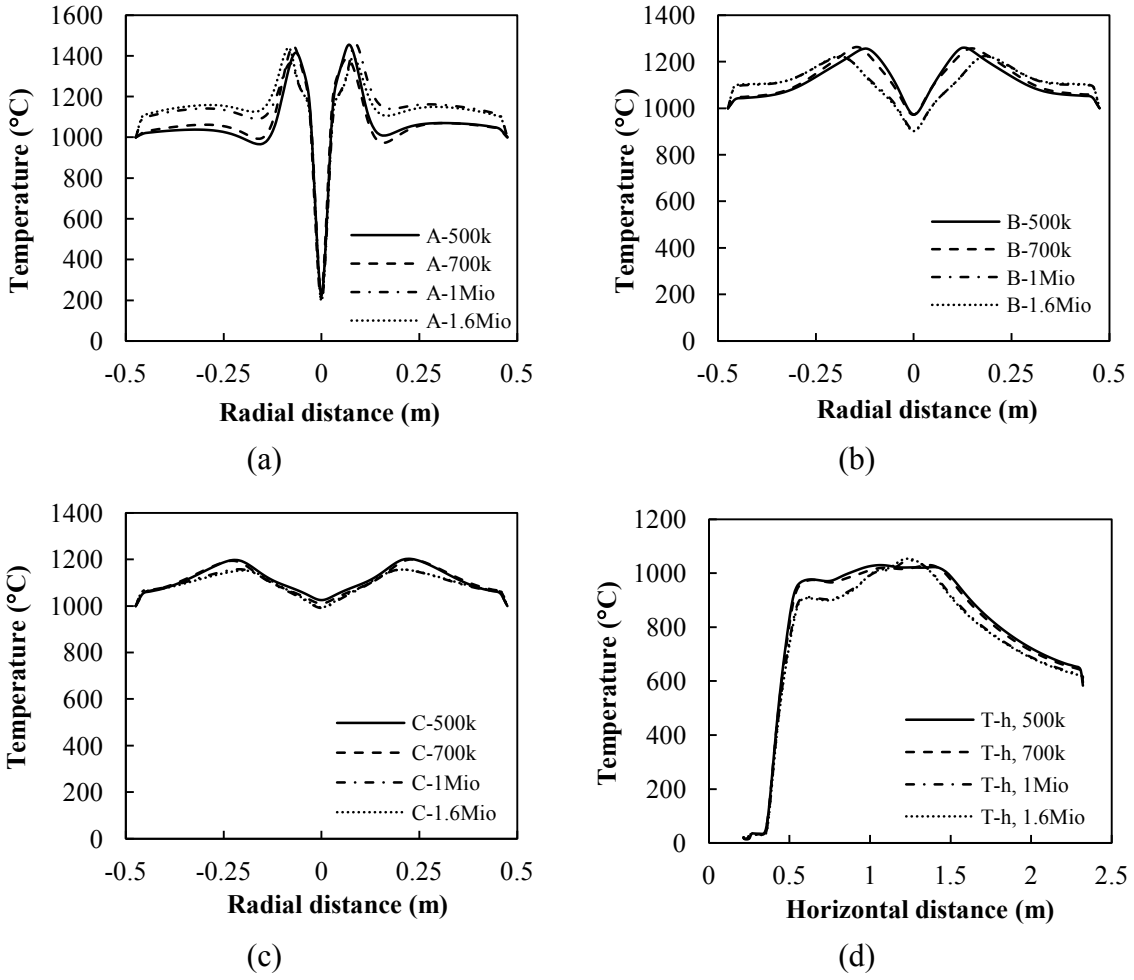

Figure 6.86: Comparison of temperatures applying different computational mesh sizes at location of measurement: (a) port A, (b) port B, (c) port C, (d) horizontal distance from burner.

The temperature predictions are nearly unchanged if mesh is refined to above 1 million cells, implying suitable number of meshing cells. This influence is more evident at the port location close to burner (port A in Fig. 6.86(a)). At the port location B and C away from the burner (Fig. 6.86(b)-(c)), the results still follow the same trend but with less deviations. Temperature predictions along horizontal distance from burner in Fig. 6.86(d) yield the same results as the plots along radial distances (port A, B and C), in that the temperature predictions along horizontal distance is nearly unchanged for mesh of higher than 1 million cells.

The O_2 predictions along radial distance at the port location A, B and C are shown in Fig. 6.87(a)-(c). It is clear that the results applying 500k and 700k mesh is not sufficient and deviated from the results applying more refined mesh of 1 and 1.6 million cells (1Mio and 1.6Mio in figures). The same trend is found also for O_2 predictions along horizontal distance away from burner in Fig. 6.87(d) but at distance of higher than 1 m from burner (inside furnace box).

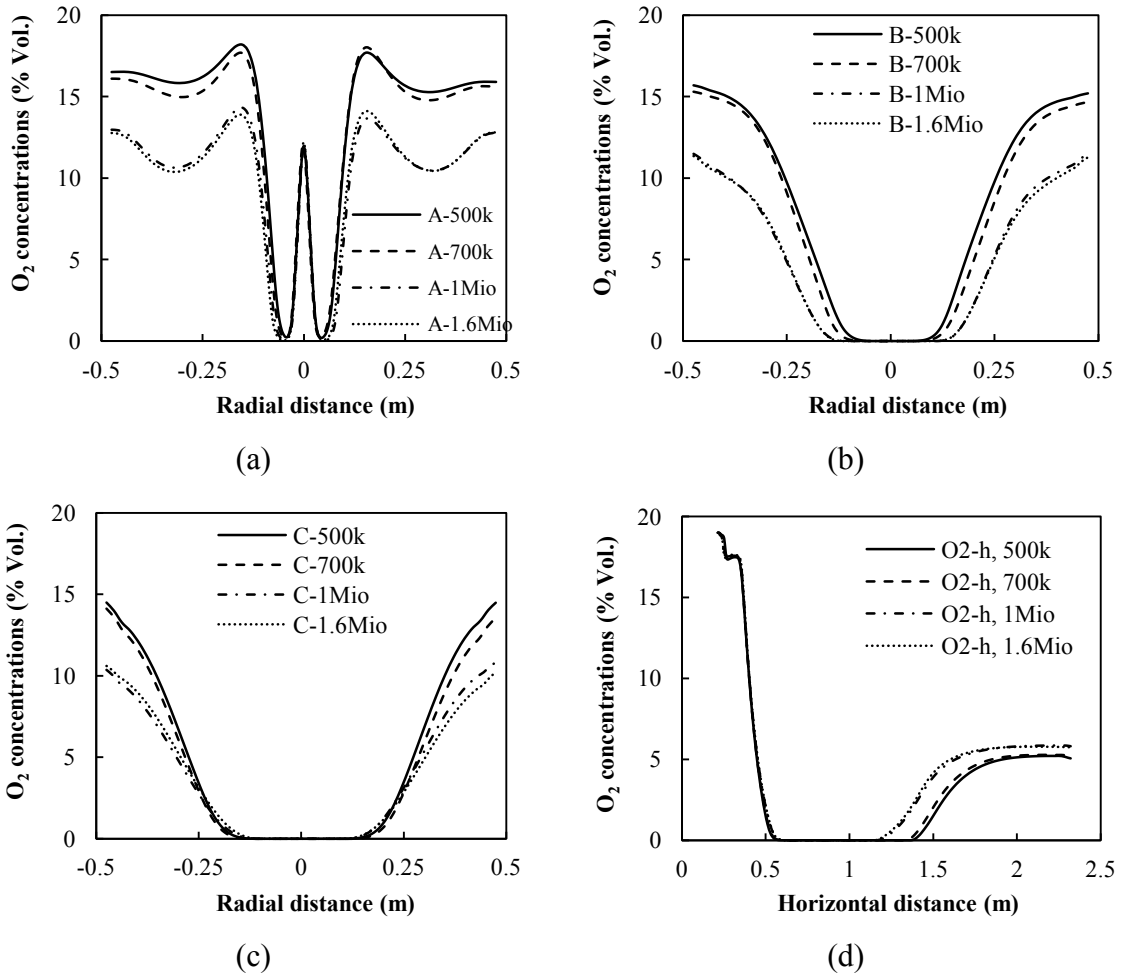

Figure 6.87: Comparison of O_2 concentrations (% by volume) applying different computational mesh sizes at location of measurement: (a) port A, (b) port B, (c) port C, (d) horizontal distance from burner.

6.3.2 Aerodynamic quantities

According to mesh dependency test explained in the previous sub-chapter, the computational mesh of around 1 million is suitable for further numerical simulation to provide aerodynamic, thermo-chemical and radiation predictions. The prediction of axial velocity applying 1 million numerical cells is presented in Fig. 6.88.

It shoud be emphasized that there was no equipments for measuring aerodynamic quantities such as axial and tangential velocity. However, contour plot of axial velocity is illustrated in the figure to show the flame aerodynamics. The region, where intensive swirling flow takes place, was shown by strong dark-blue color near the burner quarl zone. This strong back recirculated flow is significant in the swirling flame because the trajectories of both hot fluid flow and coal particles increase. This helps in mixing between fuel and oxidants in the reaction zone and hence also flame stability.

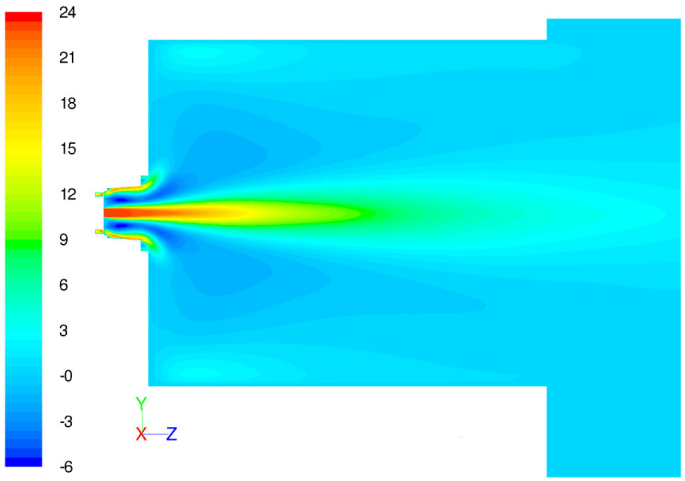

Figure 6.88: Axial velocity (m/s) profiles (1 Million computational cells).

6.3.3 Thermo-chemical quantities

Temperature predictions for 0.4 MW_{th} oxy-fuel furnace are plotted and compared with experiments along radial direction from centerline of cylindrical part in Fig. 6.89 and along axial direction along centerline in Fig. 6.90. The percentage deviations from experiments are also listed in Tables 6.2-6.4, dependent of plotting direction.

In Fig. 6.89(a), temperature predictions followed experimental trends for port A-C, except inside the flame's core region due to high momentum mass flow both from coal particle injections and also complex phenomena of gas expansion from coal reaction. The maximum average percentage deviations from temperature predictions for port A-C are less than around 33 % as shown in Table 6.2.

In Fig. 6.89(b), underestimations of temperature predictions were investigated. The magnitudes of difference are between 200-300 °C and the maximum average percentage deviations was less than 6% (data for port B in Table 6.2). Temperature predictions along horizontal distance (centerline of burner's axis) are in agreements with experiments from port B to E in Fig. 6.90(a) with maximum percentage deviation from experiment of 6% at port B. From Fig. 6.90(a), percentage deviation of temperature prediction at port A is high, caused by longer ignition time from numerical calculations and coal particles are burned at distance from burner as shown at horizontal distance of around 0.5 m distant from burner at port B's . Therefore it is reasonable to evaluate percentage deviations after the port B's location. The maximum average percentage deviations of temperature predictions from experiments for port B-E are within around 18 %. The temperature predictions along vertical direction along vertical direction of furnace box's centerline are compared with values from experiments in Fig. 6.90(b). The relative errors (percentage deviations) are less than 22 % at the centerline of furnace box for both port F and G as listed in Table 6.4.

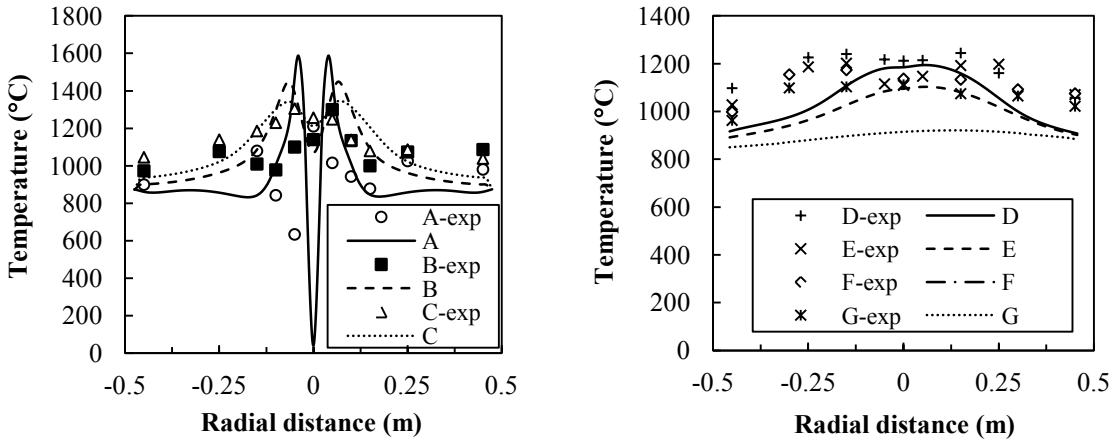

(a) (b)

Figure 6.89: Comparison of temperatures along radial distances at all measurement locations with experimental results: (a) port A-C, (b) port D-G.

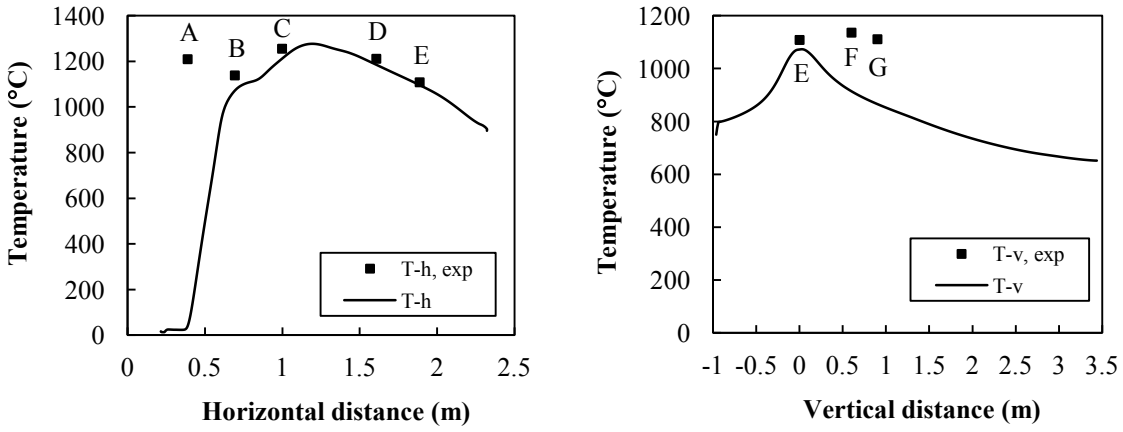

(a) (b)

Figure 6.90: Comparison of temperature profiles distant from burner quarl with experimental results along: (a) horizontal distance, (b) vertical distance.

Table 6.2: Percentage deviations from measurements at port A-G for temperatures (°C) along radial direction.

Port	Average deviation (%)	Maximum	Minimum
A	33.0	122.1	3.8
B	13.8	32.3	6.0
C	7.3	15.1	0.1
D	9.2	18.3	1.7
E	10.5	19.0	1.2
F	14.4	20.6	11.3
G	15.9	20.7	11.7

Table 6.3: Percentage deviations from measurements at port A-E for temperatures (°C) along centerline of burner's axis.

Port	Deviation (%)
A	-
B	6.0
C	3.5
D	2.2
E	1.2
Average	**3.2**
Maximum	**6.0**
Minimum	**1.2**

Table 6.4: Percentage deviations from measurements at port F and G for tempertures (°C) along centerline of furnace's box.

Port	Deviation (%)
F	12.46
G	17.86
Average	**15.2**
Maximum	**17.9**
Minimum	**12.5**

The results of predicted O_2 concentration (% dry by volume) are plotted against radial distance from port A-G in Fig. 6.91, horizontal distance along centerline of cylindrical part of furnace in Fig. 6.92(a) and vertical distance along centerline of furnace box in Fig. 6.92(b).

All O_2 predictions in Fig. 6.91(a) follow the trends of experiments except inside flame core's region. The much more delayed O_2 consumption was found, which can be observed by difference of O_2 predictions, especially at port A from experimental measurements. This can be caused by influence of applying reaction and kinetic rates from developed CFD model, too fast reaction rate from either char or gaseous reaction after volatile matter is releasing from coal particles, investigated in the O_2 predictions for port A in Fig. 6.91(a). Another reason is the using of reduced step of reaction mechanisms for volatile and gaseous combustion, which cannot perfectly describe combustion behaviors and also cause in too much overall rate of reaction due to lack of radical species's predictions from more complicated or details reaction mechanisms. From Table 6.5, the maximum average deviations from port A is around 120 %, caused by magnitude of predictions near to the flame core's region at radial distance of ±0.05 m from centerline according to the reason that have been explained previously. From Table 6.6, the maximum deviation is up to 100%. The reason is that the O_2 concentrations is expected to be zero at the post-flame region due to complete burning from simplified assumption of global reaction mechanism of gaseous reactions. The same phenomena is found and expressed by around 48% percentage deviations at port F and G in Table 6.7.

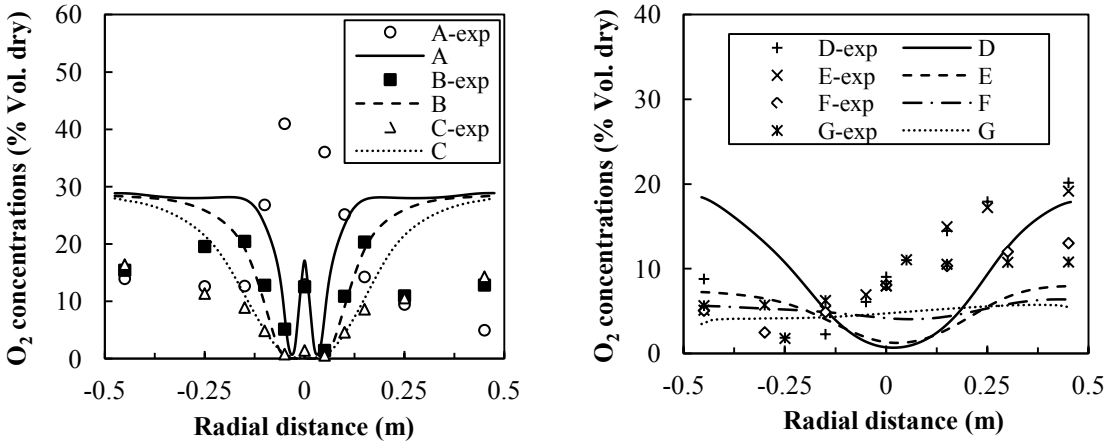

(a) (b)

Figure 6.91: Comparison of O_2 concentrations (%Vol. dry) along radial distances at all measurement locations with experimental results: (a) port A-C, (b) port D-G.

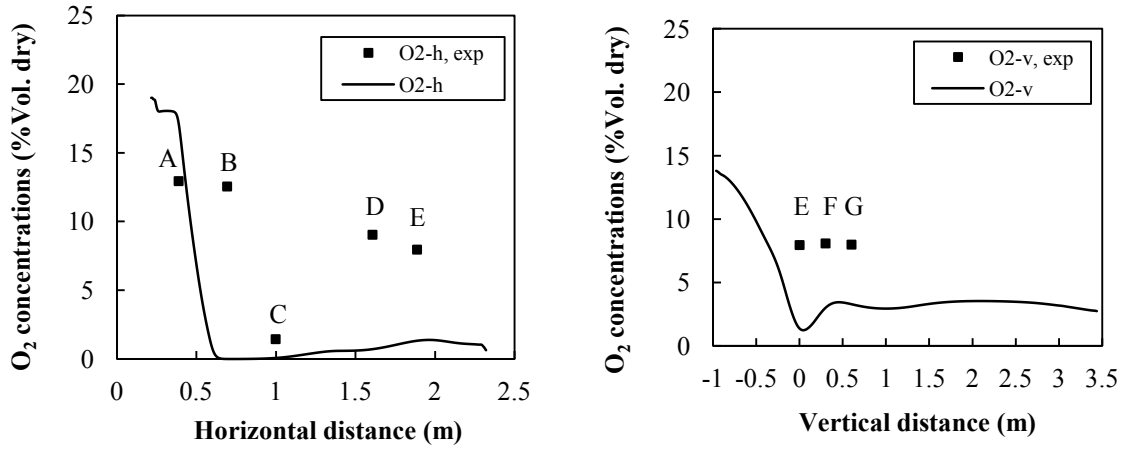

(a) (b)

Figure 6.92: Comparison of O_2 concentrations (%Vol. dry) with experimental results: (a) horizontal distance from burner quarl, (b) vertical distance along furnace's box.

Table 6.5: Percentage deviations from measurements at port A-G for O_2 concentration (%Vol. dry) along radial direction.

Port	Average deviation (%)	Maximum	Minimum
A	123.3	480.7	7.3
B	61.8	480.7	2.4
C	49.5	106.9	3.2
D	121.5	464.3	11.7
E	83.6	241.9	18.6
F	47.7	114.0	0.8
G	40.8	49.9	27.6

Table 6.6: Percentage deviations from measurements at port A-E for O_2 concentration (%Vol. dry) along centerline of burner's axis.

Port	Deviation (%)
A	32.12
B	99.98
C	94.71
D	92.06
E	83.31
Average	**80.4**
Maximum	**100.0**
Minimum	**32.1**

Table 6.7: Percentage deviations from measurements at port F and G for O_2 concentration (%Vol. dry) along centerline of furnace's box.

Port	Deviation (%)
F	47.78
G	41.60
Average	**44.7**
Maximum	**47.8**
Minimum	**41.6**

The O_2 predictions are plotted along centerline distant from burner in Fig. 6.92(a). As shown in Table 6.6, the average deviation is maximized at port B at the horizontal distance of around 1.5 m from burner quarl. The average value from Port A to E is approximatedly 80%. The O_2 predictions are underestimated at port F and G shown in Fig. 6.92(b) at the post-flame region and have percentage deviation of less than 48% (Table 6.7).

Results of numerical predictions of CO_2 concentration (%Vol. dry) for all ports of measurements are illustrated in Fig. 6.93 and 6.94 and the percentage deviations from measurements are listed in Tables 6.8-6.10. The CO_2 predictions follow the trends of experiments for all ports except inside the region of flame core as observed in O_2 predictions for port A. The maximum average percentage deviations for CO_2 predictions for port A-G is less than 21% as shown in Table 6.8. The unsymmetric of CO_2 experimental profiles in Fig. 6.93(b) were influenced by the high swirling flow velocity from swirling burner in the clockwise direction of burner's axis (positive inward direction into furnace volume of cylindrical part). The CO_2 prediction is plotted along horizontal distance at centerline of burner's axis in Fig. 6.94(a). It is clear from the figure that good trends of predictions are found, expecially at the post flame region (port D and E). The maximimum percentage deviations is found at port B and has value of approximately 9%, comparing to much lower value of around 6% for port A and C and less than 1% for port D and E (Table 6.9). For vertical direction along centerline of furnace box in Fig. 6.94(b), percentage deviations are within 2.5% for both port F and G.

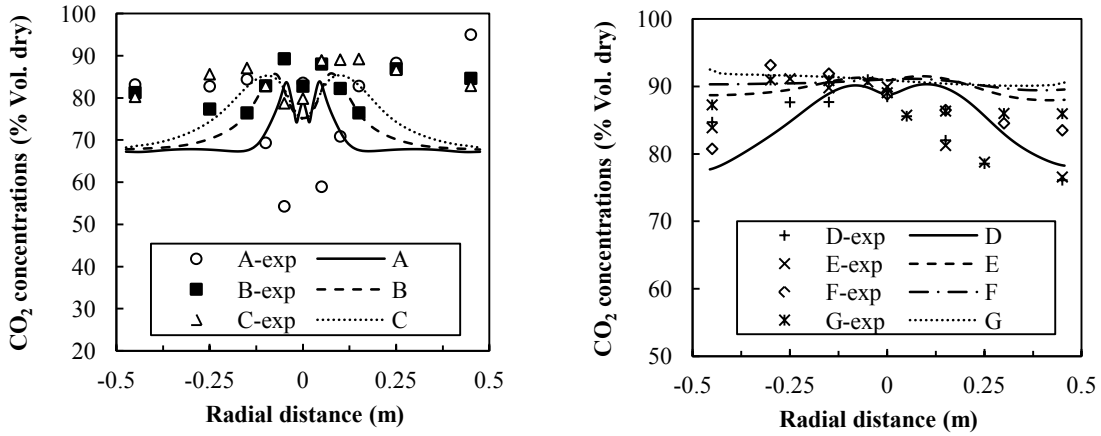

(a) (b)

Figure 6.93: Comparison of CO_2 concentrations (%Vol. dry) along radial distances at all measurement locations with experimental results: (a) port A-C, (b) port D-G.

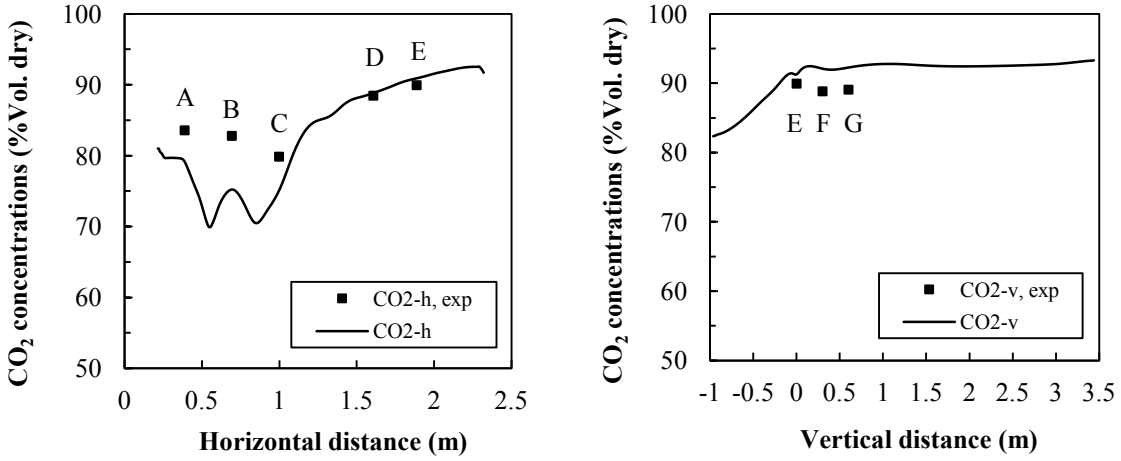

(a) (b)

Figure 6.94: Comparison of CO_2 concentrations (%Vol. dry) with experimental results: (a) horizontal distance from burner quarl, (b) vertical distance along furnace's box.

Table 6.8: Percentage deviations from measurements at port A-G for CO_2 concentration (%Vol. dry) along radial direction.

Port	Average deviation (%)	Maximum	Minimum
A	20.9	51.5	1.5
B	8.6	19.8	0.7
C	8.9	17.2	2.8
D	4.5	9.4	0.4
E	6.4	14.9	0.6
F	5.3	11.8	1.4
G	3.5	6.0	0.6

Table 6.9: Percentage deviations from measurements at port A-E for CO_2 concentration (%Vol. dry) along centerline of burner's axis.

Port	Deviation (%)
A	5.28
B	9.16
C	5.99
D	0.41
E	1.08
Average	**4.4**
Maximum	**9.2**
Minimum	**0.4**

Table 6.10: Percentage deviations from measurements at port F and G for CO_2 concentration (%Vol. dry) along centerline of furnace's box.

Port	Deviation (%)
F	2.47
G	2.16
Average	**2.3**
Maximum	**2.5**
Minimum	**2.2**

The CO predictions are illustrated in Fig. 6.95 and Fig. 6.96. The CO predictions can follow the trends of measurements for port A-C in the significant region of reaction zone. The CO predictions for port D-G have symmetric profiles, in contrast to experimental results that are scattering (Fig. 6.95(b)). Because CO is near to zero for many locations in Fig. 6.95(a) and at port D, E and G in 6.95(b), the percentage deviations for such locations are not available due to avoiding deviding zero value of referenced experimental data. The CO predictions along horizontal direction at centerline of burner's axis are shown in Fig. 6.96(a) and along vertical direction at centerline of furnace box in Fig. 6.96(b). From Table 6.11, percentage deviation for CO prediction is maximized at port A and has value of around 105%.

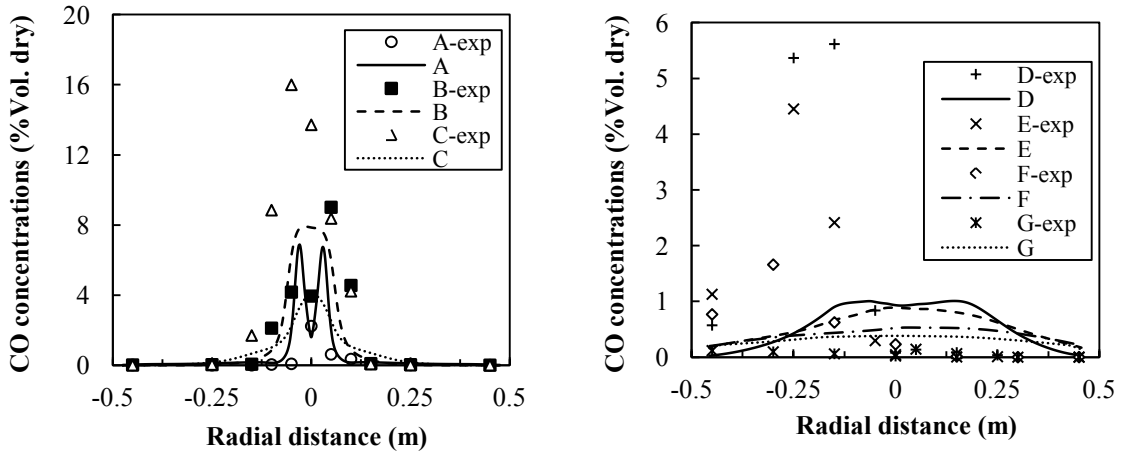

Figure 6.95: Comparison of CO concentrations (%Vol. dry) along radial distances at all measurement locations with experimental results: (a) port A-C, (b) port D-G.

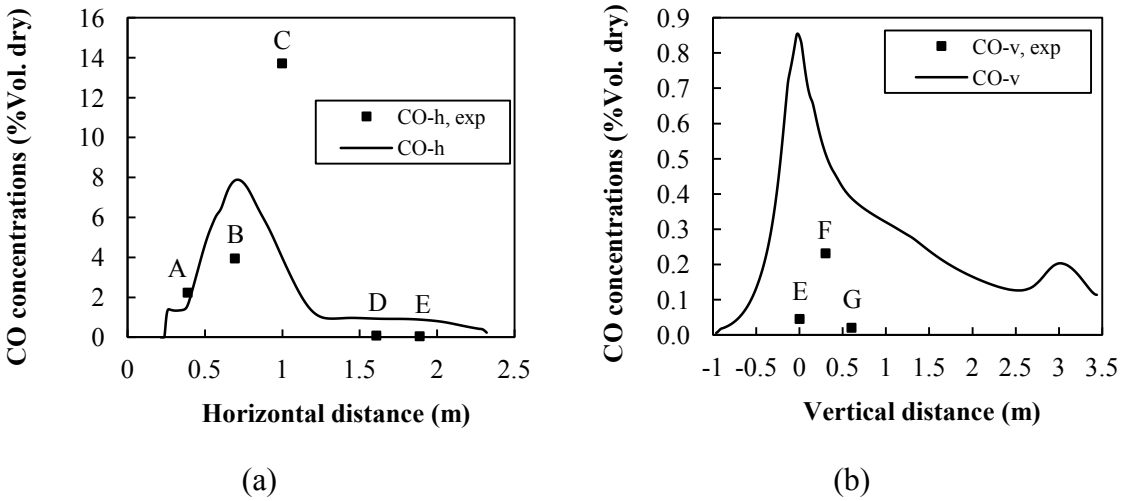

Figure 6.96: Comparison of CO concentrations (%Vol. dry) with experimental results: (a) horizontal distance from burner quarl, (b) vertical distance along furnace's box.

Table 6.11: Percentage deviations from measurements at port A-F for CO concentration (%Vol. dry) along centerline of burner's axis.

Port	Average deviation (%)	Maximum	Minimum
A	104.5	267.2	28.0
B	83.6	100.0	36.9
C	86.6	100.0	61.3
D	-	-	-
E	-	-	-
F	86.4	121.5	30.8
G	-	-	-

Table 6.12: Percentage deviations from measurements at port A-E for CO concentration (%Vol. dry) along centerline of burner's axis.

Port	Deviation (%)
A	27.96
B	99.04
C	70.72
D	-
E	-
Average	**65.9**
Maximum	**99.0**
Minimum	**28.0**

Table 6.13: Percentage deviations from measurements at port F and G for CO concentration (%Vol. dry) along centerline of furnace's box.

Port	Deviation (%)
F	121.47

The CO predictions follow the trends of experiments shown in Fig. 95(a) for radial distance, in Fig. 96(a) for horizontal distance from burner and in Fig. 96(b) for vertical distance inside furnace's box. The maximum percentage deviation is around 100% for all ports expressed in Tables 6.11-6.13.

The contour plots of temperatures, O_2, CO_2 and CO concentration (%Vol. dry) are illustrated in Fig. 6.97. The flame is highly swirl that can be observed in Fig. 6.97(a) in the red-orange color area, representing flame shape. The area of complete O_2 consumption is shown in the dark-blue color area in Fig. 6.97(b), which is in agreement with the presence of CO specie in the same region as shown in Fig. 6.97(d). The final CO_2 concentration is around 90% at the post flame region showing by orange color-area in Fig. 6.97(c).

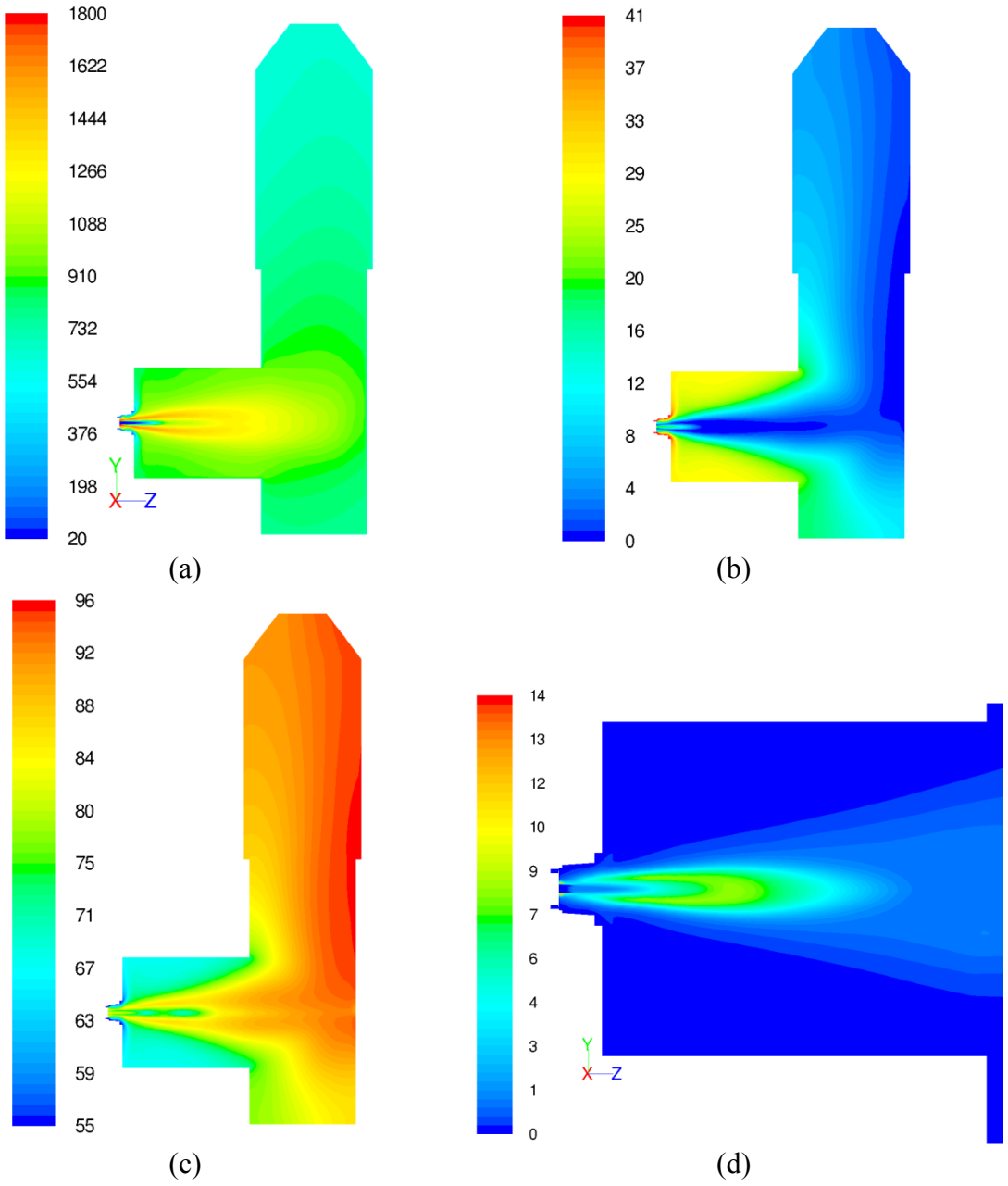

Figure 6.97: Contour plots of numerical predictions at the mid-plane of furnace for: (a) temperature (°C), (b) O_2 concentration (%Vol. dry), (c) CO_2 concentration (%Vol. dry), (d) CO concentration (%Vol. dry).

6.3.4 Radiation quantity

Predictions for hemi-spherical radiation intensity are compared with measurements utilizing IFRF ellipsoidal radiometer illustrated in Fig. 135, plotting along horizontal distance. The hemi-spherical radiation intensities for port A-C (Fig. 6.98(a)) are slightly underestimated, Underestimated predictions were found also at port D and E in Fig. 6.98(b). The percentage deviations for predictions of hemi-spherical radiation intensities are less than 17% for port A-C shown in Table 6.14.

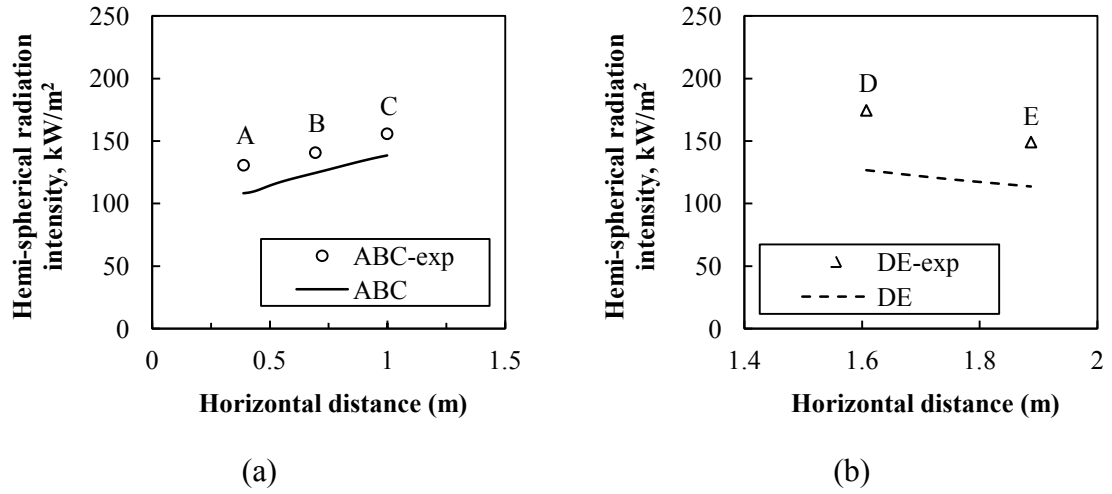

Figure 6.98: Comparison of hemi-spherical radiation intensity (or surface incident radiation, in kW/m^2) with experimental results along wall surface of furnace from: (a) port A to C (cylindrical part), (b) port D to E (furnace's box).

Table 6.14: Percentage deviations from measurements for hemi-spherical radiation intensity (port A-E).

Port	Deviation (%)	Port	Deviation (%)
A	17.1	D	27.4
B	11.3	E	23.7
C	11.2		
Average	**13.2**	Average	**25.6**

The deviations are maximized at around 28% at port D at the post-flame region shown in Table 6.14. This is mainly caused by underpredictions of flame temperature at the post flame region from estimation of uniform wall radiation emissivity for boundary conditions in CFD calculation. Furthermore, to avoid the highly skew meshing elements (low quality mesh) in the control volume of CFD model, some geometric simplification had been applied that caused in the slightly shift of locations of the furnace's side walls in the furnace's box. This caused in the expected higher deviations of predictions of hemi-spherical radiation intensity at side wall of furnace for port D, E, F and G.

7 Conclusions and Recommendations

7.1 Conclusions

For radiation model of gaseous properties under oxy-fuel conditions, the new correlations for WSGG model fitted to emissivity from LBL calculations using an up to date HITEMP 2010 database are proposed in this research. The correlations are valid for gaseous temperature between 400-2500 K and pressure path-lengths of 0.001-60 bar-m which can covers most of oxy-fuel conditions. The relative errors of average radiative source terms over length coordinate, radiative source terms at the mid-distance between plates and radiative heat fluxes are evaluated by comparing with the benchmark from LBL calculation using HITEMP 2010 database. Uncertainties for predictions of radiative quantities for all investigated cases (including oxy-fuel case 4.1 and 2.2) are within 30 % for radiative heat flux and 15 % for radiative source terms. It should be emphasized again that using molar ratio dependent correlation in Table 4.5 and Table 4.6 induced more errors of the calculation of emissivity; therefore, temperature dependent correlations of weighting factors and absorption coefficients in Table 4.4 should be applied to provide better accurate solutions for RTE. Relative errors of radiative source term and radiative heat flux at wall deviated from LBL HITEMP 2010 database are also evaluated in this research. For all cases, the new oxy-fuel correlations provided the best agreement with the radiative source terms and heat flux at wall from LBL HITEMP 2010. In addition, this research also show deficiencies of radiative source term and heat flux's predictions using existing correlations for oxy-fuel conditions from other papers fitted to either EWB model or SNB model with HITRAN 1992 database.

From the investigated oxy-fuel cases validated with experimental results from a laboratory scaled 100 kW_{th} oxy-coal furnace, mesh dependency of the problem and all submodels for oxy-fuel combustion of pulverized lignite have been tested. From the mesh dependency, the computational mesh of 300k cells is enough to provide a good velocity, temperature and O_2 predictions. However, slightly difference can still be found when the mesh is further refined to be 600k cells. Therefore, the number of cells in all testing is maintained at 600k to ensure the accuracy of the predictions.

Varying turbulent models has slightly influence on accuracy of predictions. All results still follow the same trends and it is not clear that which model is better than other in the overall predictions. The RSM only predicted the correct temperature at the center of flame core (zero radial distance and axial position of 0.2 m from burner) but resulted in underestimation of axial velocities at the same location comparing to experiments and results from other turbulent models. Furthermore, the RSM and SST k-ω model yield overestimation of O_2 concentration at the radial distance between 0.05 m and 0.2 m (axial position of 0.05 m). The hot temperature zone of predictions near to burner quarl was observed for the results applying the RNG k-ε and SST k-ω model. This was caused by the different method to calculated turbulent quantities (turbulent kinetic energy and its dissipation), used for determining the homogeneous reaction rate of volatiles and gases. In conclusion, when not much deviations were found, the standard k-ε model is still a good approach and applied for all investigated cases because of the minimum required computational time among all turbulent models.

For char reaction models, a good predictions of temperature were observed applying intrinsic model with kinetic rate from Leiser [Leiser11] or global reaction rate model with kinetic rate from TGA from BTU. However, the mentioned two approaches results in the overpredictions of O_2 concentration near to flame center (near zero radial distance) at axial position of 0.05 m from burner. In addition, using different random pore models nearly has no influence on the predictions. After evaluating accuracy from all results, the kinetic diffusion limited rate (KD) applying kinetic parameters by Field [Field69] are still the best approach and selected for the predictions for the case of 0.4 MW_{th} oxy-coal furnace.

Including char reaction with CO_2 and H_2O resulted in slightly changes of predictions. However, it should be emphasized that fuel is burned under the conditions of dry flue gas recirculation with less amount of water in the combustion products. Therefore excluding char-CO_2 and char-H_2O reaction may cause in considerably changes in the oxy-fuel boiler with wet flue gas recirculation, such as 0.4 MW_{th} oxy-fuel furnace at BTU Cottbus. For this reason, these two heterogeneous reactions are still included in the CFD model applying for 0.4 MW_{th} oxy-fuel furnace case.

Turbulent gaseous combustion model is crucial to the qualities of final predictions. As explained in the reviews, to account for turbulent combustion in the infinitesimal scale by the eddy dissipation concepts can exhibit flame instability for oxy-coal flame, in which hot gas temperature can only be maintained outside quarl area. In contrast to the eddy dissipation (EDM) and finite rate eddy dissipation model (FRED), these models can provide stable oxy-fuel flame inside burner quarl, in which the latter model (FRED) can remedy an overestimation of temperature when applying the EDM by incorperating the kinetic rates into the turbulent combustion model.

From investigated 100 kW_{th} oxy-fuel cases, by applying 2-step reaction mechanisms, the EDM overpredicted axial velocity at both axial position from burner and also at the far radial distance from centerline at the axial position of 0.2 m from burner. Besides, the EDM resulted in too much peak temperature predictions close to burner area in the center of flame core (zero radial distance) and also overestimated O_2 concentration at the axial position of 0.05 m from burner. Neglecting kinetic rate in the EDM caused in too hot flame temperature prediction and also too fast O_2 consumption rate inside the quarl area, as presented in temperature and O_2 profile at the mid-plane of oxy-coal furnace. Based on this investigation, the FRED is the best model for the application to oxy-coal combustion problem.

After testing 2- and 3-step reaction mechanisms, it is found that increasing step of reaction mechanisms from 2-step to 3-step has small influence on the velocity predictions but effected more the temperature and O_2 prediction at the short radial distance and axial position of 0.05 m from burner. Although nearly no difference between two results were observed, the conclusion can be changed if amount of water contents change in oxy-fuel furnace utilizing wet flue gas recycled system as in the bigger scaled 0.4 MW_{th} oxy-coal furnace, in which char reaction with H_2O has higher contribution to the overall char reaction rate. For this reason, the global 3-step mechanism is suitable for general predictions of oxy-fuel combustion.

The pre-exponential factor and activation energy for kinetic rate of volatile oxidation has significantly influence on the oxy-coal predictions, as shown in the results in chapter 6. Using different kinetic parameters for volatile oxidation resulted in various peak flame location inside the oxy-coal furnace. The kinetic parameters by Shaw et al. [Shaw91] provided stable oxy-fuel flame inside burner quarl for both 2-step and 3-step reaction mechanisms. Applying kinetic parameters by Dryer [Dryer73] and Westbrook [Westbrook81] caused in the presence of peak flame temperature outside quarl region, implying instability of flame in the quarl. Strong O_2 consumption rates were found applying these two parameters, showing by the dark blue area in the O_2 profiles at the mid-plane of furnace. For 3-step reaction mechanisms, all velocity predictions were the same. Applying kinetic parameters for volatile oxidation by Zimont [Zimont69] yielded better temperature prediction at the center of flame core (axial position of 0.05 m) but also overpredicted peak temperature prediction at axial position of 0.2 m from burner. Considering all results, the kinetic rates by Shaw et al. were selected to incorporate to CFD model for oxy-coal predictions.

Including reversible CO oxidation rates by Andersen et al. [Andersen09] can slightly change to the final predictions. Comparing numerical results with experiments, accounting for the reversible CO oxidation rate did not significantly improve the accuracy of predictions. Therefore, irreversible CO oxidation was applied further to the numerical simulation in the 0.4 MW_{th} oxy-fuel furnace.

Particle radiation is important to the thermodynamic quantities but not for aerodynamic predictions. Including particle radiation models, either as constant particle emissivity or as soot dominated radiation can remedy an overestimation of temperature at near to the flame center for both axial position from burner (0.05 and 0.2 m) around 250 °C. This was caused by different calculation of solution for RTE, to yield the predictions of total absorption coefficients, emissivity, radiative source term and heat flux through furnace walls, illustrating in the radiation plots in chapter 6. Another finding outcome from the investigations is that omitting particle radiation in the numerical model resulted in overestimation of flame temperature.

The results from applying various correlations for gas radiation applying WSGG model were investigated under the conditions with and without particle radiation (modeled as soot domination). Because the particle radiation has higher influence on the calculation of radiation heat transfer, the predictions of radiation quantities applying various correlations for gas radiation were slightly different than other when particle radiation was included, implying change in the conclusion of results when applying solely gas radiation for oxy-fuel flames as in natural gas firing. Another aspect is that dry flue gas recycled (dry-FGR) was used in the laboratory scaled oxy-fuel furnace in the investigated cases, therefore if the content of water is higher such as in the wet flue gas recirculation (wet-FGR), the molar ratios will be changed, hence the amount of combustion species. This brings some change in spectral radiation absorption and emission and also radiation transfer calculations. Therefore, conclusion of the tests can be changed for the condition of wet-FGR oxy-fuel flame. This aspect can be further investigated in the future research.

After investigating influences of mathematical sub-models to the predictions of 100 kW_{th} oxy-fuel furnace, the results of developed sub-models was applied to 0.4 MW_{th} oxy-fuel furnace at Brandenburg University of Technology Cottbus. For this specific type of oxy-

fuel furnace installed with single swirling burner and operating at 85% load capacity, the computational mesh of 1 million cells is found to be appropriate for this specific combustion problem by comparing numerical predictions of temperature and O_2 predictions in the preparatory step. Results of numerical predictions for temperature, O_2, CO_2, CO concentration and hemi-spherical radiation intensity were discussed in chapter 6.3. The maximum average percentage deviations from temperature predictions for all ports are less than 33% for all port's locations. The high magnitude of percentage deviations for temperature and O_2 concentrations were found especially in the flame core's region. The percentage deviation for O_2 predictions is maximized at around 120% at port A due to high fluctuation of flame aerodynamics inside the flame core and drop to the value of less than 40% at port G. Percentage deviation for CO_2 concentrations are less than 21% for all port's locations and magnitude of CO_2 concentration at the post-flame region inside the furnace's box is around 90%, in agreements with the conditions of high CO_2 concentrations in oxy-fuel furnace. CO predictions follow the same trends as oxy-fuel flame from experiments along radial distance in the combustion zone for port A-C, along horizontal direction at centerline distant from burner qual for port A-E and along vertical direction at centerline of furnace box for port E-G.

The numerical CFD model provided suitable trends of hemi-spherical radiation intensity along cylindrical wall of oxy-fuel furnace for port A-E. Good agreements with radiation measurements by IFRF ellipsoidal radiometer were found for port A-C, having the percentage deviation of less than 17%. The percentage deviations is increasing to around 28% for port D and E because the reason explained in the numerical results (chapter 6.3) that percentage deviations for hemi-spherical radiation intensity is expected to be higher at the furnace wall inside furnace box (port D and E) according to simplification of furnace geometry to avoid low quality of meshing elements. In conclusion, the developed mathematical sub-models for CFD simulation has been successfully applied to the scale-up oxy-fuel furnace.

7.2 Recommendations

Although sensitivity analysis and influence of sub-models in the predictions of oxy-coal combustion has been investigated applying both laboratory scaled furnace (100 kW_{th}) and pilot scaled furnace (0.4 MW_{th}), an insight into the coal combustion modeling in the oxy-fuel conditions can be extended by further applying more complex approaches for each sub-model. This can be done depending on available computational resources and research time.

Nowadays, the LES model had been applied to coal combustion problem including oxy-coal combustion as explained in the literature reviews. The models required an appropriate number of computer clusters, which also effecting time of research. Based on rough estimation, numerical simulation with RANS model (standard k-ε) required 4 days to converge solution for CFD model of oxy-coal furnace case, which has computational cells around 1 million. The LES model can significantly increase research time; nevertheless, yield realistic flame fluctuation in the post flame region.

It is evident, especially in pressurized oxy-fuel environments, that Langmuir-Hinshelwood (L-H) kinetic rate can better estimate the burning behavior of char reaction. One approach to apply the L-H kinetic rates into numerical model is to use CBK model. The L-H kinetic rate is superior than the n-order power law Arrhenius rate in the way that the order of reaction can be varied in the L-H model, but not for n-order power law model. This is in agreement with the observation reviewed in chapter 2 that the order of reaction is usually varied during burnout.

Even though the global reaction mechanisms can provide a good prediction for velocity, temperature, radiation quantities and combustion species in the oxy-fuel conditions utilizing lignite as fuel, the detailed mechanisms can be used and testing trying to improve accuracy of predictions. The examples of detailed mechanisms are CHEMKIN code and GRI-Mech from University of California at Berkeley.

For the new correlations for WSGG model applying to oxy-fuel conditions, valid molar ratios (MR) of H_2O to CO_2 for the application of the correlations are from 0.125-4.0. Although, this range of MR can cover most of oxy-fuel combustion conditions, the range can be extended further for a specific research purpose for MR of less than 0.125 or higher than 4.0. In addition, if the new spectroscopic radiation database is going to be improved and available in the future, the new correlations can be optimized again to fit to the emissivity charts generated by the LBL-calculation from the new database.

In this thesis, particle radiation is modeled as constant particle emissivity and as soot dominated particle radiation. For the future work, the value of particle emissivity can be calculated based on parameters measured by radiation instruments in oxy-fuel condition. New equation formulation of particle radiation varying with burnout can also be created, using the model presented by Chui et al. [Chui93] for pulverized coal combustion in air-fired conditions as a guidance. If particle radiation is modeled by soot domination, soot volume fraction can be measured in the experiments of coal burning for specific oxy-fuel conditions (varying percentages of O_2/CO_2) and also for specific fuel-types.

8 References

OCC1-09 1st Oxyfuel Combustion Conference (OCC1), IEA GHG International Oxy-Combustion Network, Cottbus, Germany, 8th-10th September 2009, Available at: http://www.ieaghg.org/index.php?/conferences.html [Accessed online on October 2011].

OCC2-11 2nd Oxyfuel Combustion Conference (OCC2), IEA GHG International Oxy-Combustion Network, Queensland, Australia, 12th-16th September 2011, Available at: http://www.ieaghg.org/index.php?/conferences.html [Accessed online on October 2011].

2ndWSOxyIEA07 2nd Workshop of the Oxy-Fuel Combustion Network, IEA GHG International Oxy-Combustion Network, Windsor, USA, 25th – 26th January 2007.

Abdalla83 Abdalla A.Y., Bradely D., Chin S.B., Lam C., Global reaction schemes for hydrocarbon oxidation, Oxidation Communications 4(1-4) (1983) 113-130.

Akimoto10 Akimoto K., Sano F., Homma T., Oda J., Nagashima M., Kii M., Estimates of GHG emission reduction potential by country, sector, and cost, Energy Policy 38(7) (2010) 3384-3393.

Al-Abbas12 Al-Abbas A.H., Naser J., Dodds D., CFD modelling of air-fired and oxy-fuel combustion in a large-scale furnace at Loy Yang A brown coal power station, Fuel 102 (2012) 646–665.

Al-Abbas11 Al-Abbas A.H., Naser J., Dodds D., CFD modelling of air-fired and oxy-fuel combustion of lignite in a 100 KW furnace, Fuel 90(5) (2011) 1778-1795.

Allam09 Allam R.J., Improved oxygen production technologies, Energy Procedia 1(1) (2009) 461–470.

Allam92 Allam R.J., Spilsbury C.G., A study of the extraction of CO2 from the flue gas of a 500 MW pulverised coal fired boiler, Energy Conversion and Management 33(5–8) (1992) 373–378.

Al-Makhadmeh09 Al-Makhadmeh L., Coal Pyrolysis and Char Combustion under Oxy-Fuel Conditions, Doctoral thesis, University of Stuttgart, Germany, 2009.

Alphen10 Alphen K., Noothout P.M., Hekkert M.P., Turkenburg W.C., Evaluating the development of carbon capture and storage technologies in the United States, Renewable and Sustainable Energy Reviews 14(3) (2010) 971-986.

ÁlvarezL12 Álvarez L., Gharebaghi M., Jones J.M., Pourkashanian M., Williams A., Riaza J., Pevida C., Pis J.J., Rubiera F., Numerical investigation of NO emissions from an entrained flow reactor under oxy-coal conditions, Fuel Processing Technology 93(1) (2012) 53-64.

ÁlvarezL11 Álvarez L., Gharebaghi M., Pourkashanian M., Williams A., Riaza J., Pevida C., Pis J.J., Rubiera F., CFD modelling of oxy-coal combustion in an entrained flow reactor, Fuel Processing Technology 92(8) (2011) 1489-1497.

Andersen09 Andersen J., Rasmussen C.L., Giselsson T., Glarborg P., Global combustion mechanisms for use in CFD modelling under oxy-fuel conditions, Energy & Fuels 23 (2009) 1379-1389.

Anderson95 Anderson J.D., Computational Fluid Dynamics: The Basics with Applications, McGraw-Hill, Inc., USA, 1995.

Andersson07 Andersson K., Characterization of oxy-fuel flames – their composition, temperature and radiation, Chalmers University of Technology, PhD Thesis, Göteborg, 2007.

Andersson08a Andersson K., Johansson R., Hjartstäm S., Johnsson F., Leckner B., Radiation intensity of lignite-fired oxy-fuel flames, Experimental Thermal and Fluid Science 33 (2008a) 67-76.

Andersson08b Andersson K., Johansson R., Johnsson F., Leckner B., Radiation intensity of propane-fred oxy-fuel flames: Implications for soot formation Energy & Fuels 22(3) (2008b) 1535-1541.

Andersson11a Andersson K., Johansson R., Johnsson F., Thermal radiation in oxy-fuel flames, International Journal of Greenhouse Gas Control 5S (2011a) S58-S65.

Andersson11b Andersson K., Johansson R., Johnsson F., Modelling of particle radiation in oxy-fuel flames, 2nd Oxyfuel Combustion Conference, IEA GHG International Oxy-Combustion Network, Queensland, Australia, 12th-16th September, 2011b.

Andersson07 Andersson K., Johnsson F., Flame and radiation characteristics of gas-fired O2/CO2 combustion, Fuel 86 (2007) 656-668.

Andersson06 Andersson K., Johnsson F., Process evaluation of an 865 MWe lignite fired O2/CO2 power plant, Energy Conversion and Management 47 (2006) 3487–3498

Anheden05 Anheden M., YanJ. , Smedt G.D., Denitrogenation (or oxy-fuel concepts), Oil Gas Sci. Technol., 60(3) (2005) 485–495.

ANSYS12 ANSYS FLUENT 12.0 User's Guide, April 2009.

Anthony76 Anthony D.B., Howard I.B., Coal devolatilization and hydrogasification, AIChE J. 22 (1976) 625-656.

Aris57 Aris R., On shape factors for irregular particles-I. The steady-state problem. Diffusion and reaction, Chem. Eng. Sci. 6 (1957) 262-268.

Aroussi00 Aroussi A., Kucukgokoglan S., Menacer M., Pickering S.J., Numerical simulation of a single burner flow, 9th International Symposium on Flow Visualization, 2000.

Ashworth10 Ashworth P., Boughen N., Mayhew M., Millar F., From research to action: Now we have to move on CCS communication, International Journal of Greenhouse Gas Control 4(2) (2010) 426-433.

Aspelund07 Aspelund A., Jordal K., Gas conditioning - the interface between CO2 capture and transport, Int. J. Greenhouse Gas Control 1(3) (2007) 343–354.

ASTM04 ASTM. 2004. Annual Book of ASTM Standards, Vol. 05.06. American Society for Testing and Materials, West Conshohocken, PA. Specifically: ASTM D-388. Standard Classification of Coals by Rank.

Backreedy06 Backreedy R.I., Fletcher L.M., Ma L., Pourkashanian M., Williams A., Modelling pulverised coal combustion using a detailed coal combustion model, Combustion Science and Technology 178 (2006) 763-787.

Badzioch70 Badzioch S., Hawksley P.G.W., Kinetics of thermal decomposition of pulverized coal particles, Ind. Eng. Chem. Process Des. Develop. 9 (1970) 521-530.

Bailey83 Bailey A.G., Balachandran W., Williams T.J., The Rosin-Rammler size distribution for liquid droplet ensembles, J. Aerosol Sci. 14 (1983) 39-46.

Bailey90 Bailey J.G., Tate A., Diessel C.F.K., Wall T.F., A char morphology system with applications to coal combustion, Fuel 69 (1990) 225-239.

Barakat66 Barakat H.Z., Clark J.A., Analytical and experimental study of transient laminar natural convection flows in partially filled containers, Proceedings of 3rd International Heat Transfer Conference, Chicago, Vol. II, paper 57, page 152, 1966.

Barber06 Barber R.J., Tennyson J., Harris G.J., Tolchenov R.N., A high-accuracy computed water line list, Monthly Notices of the Royal Astronomical Society 368 (2006) 1087–1094.

Barcena07 Barcena S.R., Saari R., Mani R., Batroukh S.E., Thomson M.J., Real time, non-intrusive measurement of particle emissivity and gas temperature in coal-fired power plants, Measurement Science and Technology 18 (2007) 3479–3488.

Barth89 Barth T.J., Jespersen D.C., The design and application of upwind schemes on unstructured meshes, AIAA Paper 89-0366, 1989.

Baum71 Baum M.M., Street P.J., Predicting the combustion behavior of coal particles, Combust. Sci. Technol. 5 (1971) 231-243.

Baxter93 Baxter L.L., Smith P.J., Turbulent dispersion of particles: The STP model, Energy & Fuels 7 (1993) 852–859.

Becher11-PartA Becher V., Clausen S., Fateev A., Spliethoff H., Validation of spectral gas radiation models under oxyfuel conditions. Part A: Gas cell experiments, International Journal of Greenhouse Gas Control 5S (2011) S76-S99.

Becher07 Becher V., Goanta A., Gleis S., Spliethoff H., Controlled staging with non-stoichiometric burners for oxyfuel processes, The 32nd international technical conference on coal utilization and fuel systems, the power of coal, Clearwater, Florida, 10th-15th June 2007.

Beer72 Beer J.M., Chigier N.A., Combustion Aerodynamics, Fuel and energy science series, Elsevier Science Ltd.,1972.

Beér07 Beér J.M., High efficiency electric power generation: the environmental role, Prog Energy Combust Sci, 33 (2) (2007) 107-134.

Benelli07 Benelli G., Brunetti J., Carrai L., Sigali S., RANS simulation of a gas turbine combustor: a study on aerodynamics, mixing and heat transfer in combustive conditions, 3rd European Combustion Meeting (ECM), 2007.

Benfell00 Benfell K.E., Liu G., Roberts D.G., Harris D.J., Lucas J.A., Bailey J.G., Wall T.F., Modeling char combustion: The influence of parent coal petrography and pyrolysis pressure on the structure and intrinsic reactivity of its char, Proceedings of the Combustion Institute 28 (2000) 2233-2241.

Beysel09 Beysel G., Enhanced cryogenic air separation – a proven process applied to oxyfuel, 1st Oxyfuel Combustion Conference, IEA GHG International Oxy-Combustion Network, Cottbus, Germany, 8th-10th September 2009.

Bhatia80 Bhatia S.K., Perlmutter D.D., A random pore model for fluid-solid reactions. I: Isothermal, kinetic control, AIChE J. 26 (1980) 379-384.

Blazek05 Blazek J., Computational Fluid Dynamics: Principles and Applications, 2nd edition, Elsevier Ltd., 2005.

Blesl-10 Blesl M., Kober T., Bruchof D., Kuder R., Effects of climate and energy policy related measures and targets on the future structure of the European energy system in 2020 and beyond, Energy Policy 38(10) (2010) 6278-6292.

Borrego07a Borrego A.G., Alvarez D., Comparison of chars obtained under oxy-fuel and conventional pulverized coal combustion atmospheres, Energy & Fuels 21 (2007a) 3171–3179.

Boussinesq1877 Boussinesq J., Théorie de l'Écoulement Tourbillant, Mem. Présentés par Divers Savants Acad. Sci. Inst. Fr. 23 (1877), 46-50.

BP-review11 BP Statistical Review of World Energy, June 2011. Available at: http:// bp.com/statisticalreview [Accessed online on March 2012].

Brandt79 Brandt A., Multi-level adaptive computations in fluid dynamics, Technical Report AIAA-79-1455, AIAA, Williamsburg, VA, 1979.

Brandt72	Brandt A., Multilevel adaptive technique (MLAT) for fast numerical solutions to boundary value problems, Lecture Notes in Physics 18, Springer-Verlag, Berlin, 1972, page 82-89.
Brink00a	Brink A., Hupa M., Breussin F., Lallemant N., Weber R., Modeling of oxy-natural gas combustion chemistry, Journal of Propulsion and Power 16 (2000a) 609-614.
Brink00b	Brink A., Mueller C., Kilpinen P., Hupa M., Possibilities and limitations of the eddy break-up model, Combustion and Flame123 (2000b) 275-279.
Brink99	Brink A., Kilpinen P., Hupa M., Kjäldman L., Study of alternative descriptions of methane oxidation for CFD modeling of turbulent combustors, Combustion Science and Technology 141 (1999) 59-81.
BrinkPhD98	Brink A., Eddy Break-Up Based Models For Industrial Diffusion Flames with Complex Gas Phase Chemistry, PhD thesis, Department of Chemical Engineering, Åbo Akademi University, Finland, 1998.
Buhre05	Buhre B.J.P., Elliott L.K., Sheng C.D., Gupta R.P., Wall T.F., Oxy-fuel combustion technology for coal-fired power generation, Progress in Energy and Combustion Science 31 (2005) 283-307.
Burdyny10	Burdyny T., Struchtrup H., Hybrid membrane/cryogenic separation of oxygen from air for use in the oxy-fuel process, Energy 35 (2010) 1884-1897.
Carvalho98	Carvalho M.G., Farias T., Modelling of heat transfer in radiating and combusting systems. Trans. IChemE. 76(Part A) (1998) 175-184.
Castillo11	Castillo R., Thermodynamic analysis of a hard coal oxyfuel power plant with high temperature three-end membrane for air separation, Applied Energy 88 (2011) 1480–1493.
Chae09	Chae T., Yu T., Bang B.R., Kim S.C., Yang W., A numerical study on characteristics of oxy-pulverized coal combustion in a corner-firing boiler of 125 MWth scale, The 34th International Technical Conference on Clean Coal & Fuel Systems, Clearwater, Florida, USA, 31th May-4th June, 2009.
Chandrasekhar60	Chandrasekhar S., Radiative Transfer, Dover Publications, 1960.
Chang90	Chang H., Charalampopoulos T.T., Determination of the wavelength dependence of refractive indices of flame soot, Proceedings of the Royal Society (London) A 430, 1990, page 577-591.
Charpenay92	Charpenay S., Serio M.A., Solomon P.R, The prediction of coal char reactivity under combustion conditions, Symposium (International) on Combustion 24 (1992) 1189-1197.
CHEMKIN	CHEMKIN, Reaction Design, Inc., Available at: http://www.reactiondesign.com/ or http://www.sandia.gov/chemkin/ [accessed online on 2 April 2012].
ChenL10	Chen L., Gazzino M., Ghoniem A.F., Characteristics of pressurized oxy-coal combustion under increasing swirl number, The 35th International Technical Conference on Clean Coal & Fuel Systems, Clearwater, Florida, USA, 6th-10th June, 2010.
ChenL12	Chen L., Yong S.Z., Ghoniem A.F., Oxy-fuel combustion of pulverized coal: Characterization, fundamentals, stabilization and CFD modeling, Progress in Energy and Combustion Science 38(2) (2012) 156-214.
Choi12	Choi D.G., Thomas V.M., An electricity generation planning model incorporating demand response, Energy Policy 42 (2012) 429-441.
ChuH11	Chu H., Liu F., Zhou H., Calculations of gas thermal radiation transfer in one-dimensional planar enclosure using LBL and SNB models, International Journal of Heat and Mass Transfer 54 (2011) 4736-4745.
Chui93	Chui E.H., Hughes PM.J., Raithby G.D., Implementation of the finite volume method for calculating radiative transfer in a pulverized fuel flame, Combustion Science and Technology 92 (1993) 225-242.
Chui03	Chui E.H., Douglas M.A., Tan Y., Modeling of oxy-fuel combustion for a western Canadian sub-bituminous coal, Fuel 82 (2003) 1201-1210.
Chung02	Chung T.J., Computational Fluid Dynamics, Cambridge University Press, 2002.
ChungTS11	Chung T.S., Patiño-Echeverri D., Johnson T.L., Expert assessments of retrofitting coal-fired power plants with carbon dioxide capture technologies, Energy Policy 39(9) (2011) 5609-5620.
CO2Emiss-IEA11	CO_2 Emissions from Fuel Combustion - 2011 Highlight, IEA Statistics, International Energy Agency (IEA), 2011.
Coelho98	Coelho P.J., GonÇalves J.M., Carvalho M.G., Trivic D.N., Modelling of radiative heat transfer in enclosures with obstacles, International Journal of Heat and Mass Transfer 41(4–5) (1998) 745-756.
Corrêa da Silva12	Corrêa da Silva R., Investigation of Pulverized, Pre-Dried Lignite Combustion under Oxy-Fired Conditions in a Large-Scale Laboratory Furnace, Doctoral Thesis, BTU Cottbus, 2012.
CostCO2-IEA11	Cost and Performance of Carbon Dioxide Capture from Power Generation, International Energy Agency, 2011. Available at: www.iea.org [Accessed online on March 2012].
Costa07	Costa M. and Azevedo J.L.T., Experimental Characterization of an Industrial Pulverized Coal-Fired Furnace under Deep Staging Conditions, Combustion Science and Technology 179(9) (2007) 1923-1935.
Courant52	Courant R., Isaacson E., Rees M., On the solution of nonlinear hyperbolic differential equations by finite differences,Communication on Pure and Applied Mathematics, Vol. V (1952) 243-255.
Croiset00	Croiset E., Thambimuthu K., Palmer A., Coal combustion in O2/CO2 mixtures compared with air, Canadian Journal of Chemical Engineering 78(2) (2000) 402-407.
Croiset01	Croiset E., Thambimuthu K.V., NOx and SO2 emissions from O2/CO2 recycle coal combustion, Fuel 80(14) (2001) 2117-2121.

Crowe77 Crowe C.T., Sharma M.P., Stock D.E., The Particle-Source-in-Cell (PSI-CELL) for gas droplet flows. J. Fluids Engr. 99(2) (1977), 325-331.

Cuoci10 Cuoci A., Frassoldati A., Faravelli T., Ranzi E., Candusso C., Tolazzi D., CFD simulation of a turbulent oxy-fuel flame, Processes and technologies for sustainable energy, The Italian Section of the Combustion Institute, Ischia, Italy, 27th-30th Jun, 2010.

Dally10 Dally B.B., Szego G.G., Christo F., Medwell P.R., Investigation of the mixing patterns inside a MILD combustion furnace, Proceedings of the 8th international symposium on high temperature air combustion and gasification (HiTACG-8), Poland, 5-7 July 2010, page 1-7.

Daly70 Daly B.J., Harlow F.H., Transport equations in turbulence, Phys. Fluids. 13 (1970) 2634–2649.

Dalzell69 Dalzell W.H., Sarofim A.F., Optical constants of soot and their application to heat-flux calculations, ASME Journal of Heat Transfer 91 (1969) 100-104.

Damen06 Damen K., Troost M., Faaij A., Turkenburg W., A comparison of electricity and hydrogen production systems with CO2 capture and storage. Part A: Review and selection of promising conversion and capture technologies, Progress in Energy and Combustion Science 32 (2006) 215–246.

Darde09 Darde A., Prabhakar R., Tranier J.-P., Perrin N., Air separation and flue gas compression and purification units for oxy-coal combustion systems, Energy Procedia 1 (2009) 527–534.

Davison07 Davison J., Performance and costs of power plants with capture and storage of CO2, Energy 32(7) (2007) 1163-1176.

Demuren84 Demuren A.O. and Rodi W., Calculation of turbulence-driven secondary motion in non-circular ducts, J. Fluid Mech. 140 (1984) 189–222.

Denison93 Denison M.K., Webb B.W., An absorption-line blackbody distribution function for efficient calculation of total gas radiative transfer, Journal of Quantitative Spectroscopy and Radiative Transfer 50 (1993) 499-510.

Denison95a Denison M.K., Webb B.W., Development and application of an absorption line blackbody distribution function for CO2, International Journal of Heat and Mass Transfer 38 (1995a) 1813-1821.

Denison95b Denison M.K., Webb B.W., The spectralline-based weightedsum-of-gray-gasesmodel for H2O/CO2 mixtures, ASME Journal of Heat Transfer 117 (1995b) 788–792.

Dillon04 Dillon D.J., Panesar R.S., Wall R.A., Allam R.J., White V., Gibbins J., et al. Oxy-combustion processes for CO2 capture from advanced supercritical PF and NGCC power plant, 7th international conference on greenhouse gas control technologies, Vancouver, Canada, September 2004.

Dillon05 Dillon D.J., White V., Allam R.J., Wall R.A., Gibbins J., Oxy-Combustion Processes for CO2 capture from power plant, report 2005/9, IEA Greenhouse Gas Research and Development Programme (IEA GHG), June 2005.

Doukelis09 Doukelis A., Vorrias I., Grammelis P., Kakaras E., Whitehouse M., Riley G., Partial O2-fired coal power plant with post-combustion CO2 capture: A retrofitting option for CO2 capture ready plants, Fuel 88 (2009) 2428–2436.

Dryer73 Dryer F.L., Glassman I., High-temperature oxidation of CO and CH4, Symposium (International) on Combustion 14 (1973) 987–1003.

Durbin11 Durbin P.A., Pettersson Reif B.A., Statistical Theory and Modeling for Turbulent Flows, 2nd edition, John Wiley & Sons, Ltd., 2011.

Dutta77 Dutta S., Wen C.Y., Belt R.J., Reactivity of coal and char. 1. In carbon dioxide atmosphere, Ind. Eng. Chem. Process Des. Dev., 16 (1977) 20–30.

Eaton99 Eaton A.M., Smoot L.D., Hill S.C., Eatough C.N., Components, formulations, solutions, evaluation, and application of comprehensive combustion models, Progress in Energy and Combustion Science 25 (1999) 387–436.

EcoGlobalCCS11 Economic Assessment of Carbon Capture and Storage Technologies: 2011 Update, Global CCS Institute, Canberra, Australia. Available at: www.globalccsinstitute.com [Accessed online on March 2012].

Edelman69 Edelman R.B., Fortune O.F., A quasi-global chemical kinetic model for the finite rate combustion of hydrocarbon fuels with application to turbulent burning and mixing in hypersonic engines and nozzles, The AIAA 7th Aerospace Sciences Meeting, AIAA Paper No. 69-86, 1969.

Edge12 Edge P.J., Heggs P.J.,Pourkashanian M., Stephenson P.L., Williams A., A reduced order full plant model for oxyfuel combustion, Fuel 101 (2012) 234-243.

Edge11a Edge P., Gharebaghi M., Irons R., Porter R., Porter R.TJ., Pourkashanian M., Smith D., Stephenson P., Williams A., Combustion modelling opportunities and challenges for oxy-coal carbon capture technology, chemical engineering research and design 89 (2011a) 1470–1493.

Edge11b Edge P.J., Heggs P.J.,Pourkashanian M., Williams A., An integrated computational fluid dynamics–process model of natural circulation steam generation in a coal-fired power plant, Computers & Chemical Engineering 35(12) (2011b) 2618-2631.

Edge11c Edge P., Gubba S.R., Ma L., Porter R., Pourkashanian M., Williams A., LES modelling of air and oxy-fuel pulverised coal combustion - impact on flame properties, Proceedings of the Combustion Institute 33 (2011c) 2709–2716.

Edwards76 Edwards D.K., Molecular gas band radiation, Adv. Heat Transfer 12 (1976) 115-193.

ETP-IEA08/10 Energy Technology Perspectives (ETP-IEA) 2008/2010 - Scenarios & Strategies to 2050, International Energy Agency (IEA).

Erfurth12 Erfurth J., Radiative Heat Transfer in Coal-Fired Furnaces and Oxycoal Retrofit Considerations, PhD Thesis, RWTH Aachen, Shaker Verlag, 2012.

Erfurth09a Erfurth J., Toporov D., Förster M., Kneer R., Numerical Simulation of a 1200 MW pulverised fuel oxy-firing furnace, 4th International Conference on Clean Coal Technologies (CCT2009), Dresden, Germany, 18th-21th May 2009a.

Erfurth09b Erfurth J., Toporov D., Förster M., Kneer R., Simulation of radiative Heat Transfer in a large-scale Oxycoal Furnace, 24th German Flame Day - Combustion and Furnaces, Ruhr-Universität Bochum, 16th - 17th September 2009b.

Eskeland12 Eskeland G.S., Rive N.A., Mideksa T.K., Europe's climate goals and the electricity sector, Energy Policy 41 (2012) 200-211.

Essenhigh89 Essenhigh R.H., An integration path for the carbon-oxygen reaction with internal reaction, Symposium (International) on Combustion 22 (1989) 89–96.

Essenhigh94 Essenhigh R.H., Influence of initial particle density on the reaction mode of porous carbon particles, Combustion and Flame 99 (1994) 269–279.

CostCO2-IEA06 Estimating future trends in the cost of CO2 capture technologies, IEA Greenhouse Gas R&D Programme (IEA GHG), 2006/5, January 2006.

Fan01 Fan J., Qian L., Ma Y., Sun P., Cen K., Computational modeling of pulverized coal combustion processes in tangentially fired furnaces, Chemical Engineering Journal 81(1–3 (2001) 261–269.

Felske84 Felske J.D., Charalampopoulos T.T., Hura H.S., Determination of refractive indices of soot particles from the reflectivities of compressed soot particles, Combustion Science and Technology 37 (1984) 263-284.

Felske73 Felske J.D., Tien C.L., Calculation of the emissivity of luminous flames, Combustion Science and Technology (1973) 25-31.

Felske77 Felske J.D., Tien C.L., The use of the Milne-Eddington absorption coefficient for radiative heat transfer in combustion systems, ASME Journal of Heat Transfer 99(3) (1977) 458-465.

Ferziger02 Ferziger J.H., Peric M., Computational Methods for Fluid Dynamics, 3rd edition, Springer, 2002.

Field67 Field M.A., Gill D.W., Morgan B.B., Wawksley P.G.W., Combustion of Pulverised Coal, The British Coal Utilisation Research Association (BCURA), Leatherhead, Surrey, England, 1967.

Field70 Field M.A., Measurements of the effect of rank on combustion rates of pulverized coal, Combustion and Flame 14 (1970) 237-248.

Field69 Field M.A., Rate of combustion of size-graded fractions of char from a low-rank coal between 1200 K and 2000 K, Combustion and Flame 13 (1969) 237–252.

Filkoski06 Filkoski, R. V., Petrovski, I. J., and Karas, P., Optimisation of Pulverised Coal Combustion by means of CFD/CTA Modelling, J. of Thermal Sci. 10(3) (2006) 161-179.

Fischer03 Fischer J., Gamache R.R., Goldman A., Rothman L.S., Perrin A., Total internal partition sums for molecular species in the 2000 edition of the HITRAN database, J. Quant. Spectrosc. Radiat. Transfer 82 (2003) 401-412.

Fiveland84 Fiveland W.A., Discrete ordinates solutions of the radiative transport equation for rectangular enclosures, ASME Journal of Heat Transfer 106 (1984) 699-706.

Fiveland87 Fiveland W.A., Discrete ordinate methods for radiative heat transfer in isotropically and anisotropically scattering media, ASME Journal of Heat Transfer 109 (1987) 809-812.

Fiveland88 Fiveland W.A., Three-dimensional radiative heat-transfer solutions by the discrete-ordinates method, Journal ofThermophysics and Heat Transfer 2(4) (1988) 309-316.

Fletcher92a Fletcher T.H, Kerstein A.R., Pugmire R.J., Solum M.S., Grant D.M, Chemical percolation model for devolatilisation. 3. Direct use of carbon-13 NMR data to predict effects of coal type, Energy & Fuels 6 (1992a) 414–431.

Fletcher92b Fletcher T.H., Hardesty D.R., Compilation of Sandia coal devolatilization data: milestone report, for DOE/PETC FWP 0709, Sandia Report SAND92-8209, available NTIS, 1992b.

Fletcher92c Fletcher T.H., Kerstein A.R., Pugmire R.J., Solum M.S., Grant D.M., A Chemical percolation model for devolatilization, Sandia National Laboratories, New Mexico, 1992c [Report No.: SAND928207].

Fletcher90 Fletcher T.H., Kerstein A.R., Pugmire R.J., Grant D.M., Chemical percolation model for devolatilization. 2. Temperature and heating rate effects on product yields, Energy & Fuels 4 (1990) 54-60.

Förtsch03 Förtsch D., A kinetic model of pulverised coal combustion for computational fluid dynamics, Doctoral Thesis, University of Stuttgart, 2003.

Förtsch98 Förtsch D., Kluger F., Schnell U., Spliethoff H., Hein K.R.G., A kinetic model for the prediction of NO emissions from staged combustion of pulverized coal, Symposium (International) on Combustion 27 (1998) 3037–3044.

Fox03 Fox R.O., Computational Models for Turbulent Reacting Flows, Cambridge University Press, Cambridge, UK, 2003.

Frassoldati09 Frassoldati A., Cuoci A., Faravelli T., Ranzi E., Candusso C., Tolazzi D., Simplified kinetic schemes for oxy-fuel combustion, 1st International Conference on Sustainable Fossil Fuels for Future energy (S4FE2009), Rome, Italy, 6-10 July 2009.

Fu87 Fu S., Launder B.E., Leschziner M.A., Modeling strongly swirling recirculating jet flow with Reynolds-stress transport closures". The 6th Symposium on Turbulent Shear Flows, Toulouse, France, 1987.

Fuller66 Fuller E.N., Schettler P.D., Giddings J.C., A New Method for Prediction of Binary Gas-Phase Diffusion Coefficients, Industrial and Engineering Chemistry 18, Vol. 58, No. 5, May 1966.

Galarça08 Galarça M.M., Maurente A., Vielmo H.A., França F.H.R., Correlations for the weighted-sum-of-gray-gases model using data generated from the absorption-line blackbody distribution function, Proceedings of the 12th Brazilian Congress of Thermal Engineering and Sciences, 10-14th November 2008, Belo Horizonte, Minas Gerais, Brazil.

Galletti11 Galletti C., Coraggio G., Tognotti L., Validation of oxy-fuel combustion modelling via pilot and semi-industrial furnace tests, 25th German Flame Day-Combustion and Furnaces, Karlsruhe Institute of Technology, Karlsruhe, Germany, 14th-15th Sep, 2011.

Galletti10 Galletti C., Modesti A., Pelagallo S., Brunetti I., Rossi N., Tognotti L., Validation of oxy-combustion modelling via semi-industrial furnace tests, Processes and technologies for sustainable energy, The Italian Section of the Combustion Institute, Ischia, Italy, 27th-30th Jun, 2010.

Gamache90 Gamache R.R., Total internal partition sums in the temperature range 70-3000 K: atmospheric linear molecules, J. Quant. Spectrosc. Radiat. Transfer 142 (1990) 205-219.

Gampe06 Gampe U., Hellfritsch S., Gonschorek S., Oxyfuel Technology for Fossil Fuel-fired Power Plants with Carbon Sequestration - Technical and Economic Feasibility, ENERDAY Workshop on Energy Economics and Technology, 21 April 2006, Dresden.

Gavalas80 Gavalas G.R., A random capillary model with application to char gasification at chemically controlled rates, AIChE J. 26 (1980) 577-585.

Gavalas81a Gavalas G.R., Cheong P.H., Jain R., Model of coal pyrolysis. 1: Qualitative development, Ind. Eng. Chem. Fundam. 20 (1981a) 113-122.

Gavalas81b Gavalas G.R., Jain R., Cheong P.H., Model of coal pyrolysis. 2: Qualitative formulation and results, Ind. Eng. Chem. Fundam. 20 (1981b) 122-132.

Geier12 Geier M., Shaddix C.R., Davis K.A., Shim H.-S., On the use of single-film models to describe the oxy-fuel combustion of pulverized coal char, Applied Energy 93 (2012) 675-679.

Geier10 Geier M., Shaddix C.R., Haynes B.S., Oxy-combustion of pulverized coal: modeling of char-combustion kinetics, 27th Annual International Pittsburgh Coal Conference, Istanbul, Turkey, 11th-14th October 2010.

Genetti99a Genetti D., Fletcher T.H., Development and application of a correlation of 13CNMR chemical structural analyses of coal based on elemental composition and volatile matter content, Energy & Fuels 13 (1999a) 60-68.

Genetti99b Genetti D.B., An Advanced Model of Coal Devolatilization Based on Chemical Structure, Master Thesis, Department of Chemical Engineering, Brigham Young University, 1999b.

Gentry66 Gentry R.A., Martin R.E., Daly B.J., An Eulerian differencing method for unsteady compressible flow problems, Journal of Computational Physic 1 (1966) 87-118.

Gharebaghi11a Gharebaghi M., Irons R.M.A., Ma L., Pourkashanian M., Pranzitelli A., Large eddy simulation of oxy-coal combustion in an industrial combustion test facility, International Journal of Greenhouse Gas Control 5(1) (2011a) S100-S110.

Gharebaghi11b Gharebaghi M., Irons R.M., Pourkashanian M., Williams A., An investigation into a carbon burnout kinetic model for oxy–coal combustion, Fuel Processing Technology 92 (2011b) 2455-2464.

Ghoniem11 Ghoniem A.F., Needs, resources and climate change: Clean and efficient conversion technologies, Progress in Energy and Combustion Science 37(1) (2011) 15-51.

Gibbins08 Gibbins J., Chalmers H., Carbon capture and storage, Energy Policy 36 (2008) 4317–4322.

Gibson78 Gibson M.M., Launder B.E., Ground effects on pressure fluctuations in the atmospheric boundary layer, J. Fluid Mech. 86 (1978) 491–511.

Glarborg03 Glarborg P., Jensen A.D., Johnsson J.E., Fuel nitrogen conversion in solid fuel fired systems, Progress in Energy and Combustion Science 29 (2003) 89-93.

Glassman08 Glassman I., Yetter R.A., Combustion, 4th edition, Academic Press, 2008.

Goanta08 Goanta A., Becher V., Bohn J.P., Gleis S., Spliethoff H., Controlled staging with non-stoichiometric burners for oxy-fuel processes - numerical validation, The 33rd International Technical Conference on Coal Utilization & Fuel Systems, Clearwater, Florida, USA, 1st-5th June 2008.

Goody52 Goody R.M., A statistical model for water-vapour absorption, Quarterly Journal of the Royal Meteorological Society 78(336) (1952) 165-169.

Görres95 Görres J., Schnell U., Hein K.R.G., Trajectories of burning coal particles in highly swirling reactive flows, International Journal of Heat and Fluid Flow 16 (1995) 440–450.

Gosman83 Gosman A.D., Ioannides E., Aspects of computer simulation of liquid-fuelled combustors, J. Energy. 7(6) (1983) 482-490.

GranIR96 Gran I.R., Magnussen B.F., A numerical study of a bluff-body stabilized diffusion flame. Part 1. Influence of turbulence modeling and boundary conditions, Combustion Science and Technology 119 (1996) 171-190.

Grant89 Grant D.M., Pugmire R.J., Fletcher T.H., Kerstein A.R., Chemical model of coal devolatilization using percolation lattice statistics, Energy & Fuels 3 (1989) 175-186.

Griebe01 Griebe S., Krautz H.J., Development of a cycloid firing system for lignite and co-combustion of sewages sludge and biomass with high efficiency and low emission, 18th International Pittsburgh Coal Conference, Newcastle, New South Wales, Australia, December 2001.

GRI-Mech3.0 GRI-Mech 3.0, The University of California at Berkeley, Stanford University, SRI (Stanford Research Institute) International and sponsored by the Gas Research Institute. Available at: http://www.me.berkeley.edu/gri-mech/ [accessed online on 2 April 2012].

GuM11 Gu M., Dong H., Liu X., Li J., Study on Pulverized Coal Combustion in O2/CO2 Atmosphere, Asia-Pacific Power and Energy Engineering Conference, Wuhan, Chaina, 25th-28th March 2011.

Guo03 Guo Y.C., Chan C.K., Lau K.S., Numerical studies of pulverized coal combustion in a tubular coal combustor with slanted oxygen jet, Fuel 82(8) (2003) 893-907.

Habermehl12 Habermehl M., Erfurth J., Toporov D., Förster M., Kneer R., Experimental and numerical investigations on a swirl oxycoal flame, Applied Thermal Engineering 49 (2012) 161-169.

Habib12 Habib M.A., Ben-Mansour R., Badr H.M., Ahmed S.F., Ghoniem A.F., Computational fluid dynamic simulation of oxyfuel combustion in gas-fired water tube boilers, Computers & Fluids 56 (2012) 152-165.

Hadjipaschalis09 Hadjipaschalis I., Kourtis G., Poullikkas A., Assessment of oxyfuel power generation technologies, Renewable and Sustainable Energy Reviews 13 (2009) 2637–2644.

Ha-Duong11 Ha-Duong M., Loisel R., Actuarial risk assessment of expected fatalities attributable to carbon capture and storage in 2050, International Journal of Greenhouse Gas Control 5(5) (2011) 1346-1358.

Hammond11 Hammond G.P., Ondo Akwe S.S., Williams S., Techno-economic appraisal of fossil-fuelled power generation systems with carbon dioxide capture and storage, Energy 36 (2011) 975-984.

Hamor73 Hamor R.J., Smith I.W., Tyler R.J., Kinetics of combustion of a pulverized brown coal char between 630 and 2200 °K, Combustion and Flame 21 (1973) 153-162.

Harlow65 Harlow F.H., Welch J.E., Numerical calculation of time-dependent viscoud incompressible flow of fluid with free surface, Phys. Fluids 8 (1965) 2182-2189.

Harten83 Harten A., High resolution schemes for hyperbolic conservation laws, J. Computational Physics 49 (1983) 357-393.

Haryanto11 Haryanto A., Hong K.S., Modeling and simulation of an oxy-fuel combustion boiler system with flue gas recirculation, Computers and Chemical Engineering 35 (2011) 25-40.

Hashim11 Hashim S.S., Mohamed A.R., Bhatia S., Oxygen separation from air using ceramic-based membrane technology for sustainable fuel production and power generation, Renewable and Sustainable Energy Reviews 15 (2011) 1284–1293.

Hautman81 Hautman D.J., Dryer F.L., Schug K.P., Glassman I., A multiple-step overall kinetic mechanism for the oxidation of hydrocarbons, Combustion Science and Technology 25 (1981) 219-235.

Haynes99 Haynes B.S., Chemical kinetic computations of vaporization of mineral constituents during coal combustion, a report on SKIPPY, University of Sydney, Sydney, Australia, August 1999.

Hecht11 Hecht E.S., Shaddix C.R., Molina A., Haynes B.S., Effect of CO2 gasification reaction on oxy-combustion of pulverized coal char, Proceedings of the Combustion Institute 33 (2011) 1699–1706.

Heil11 Heil P., Toporov D., Förster M., Kneer R., Experimental investigation on the effect of O2 and CO2 on burning rates during oxyfuel combustion of methane, Proceedings of the Combustion Institute 33 (2011) 3407–3413.

Hendrickson75 Hendrickson T.A.(ed.), Synthetic Fuel Data Handbook, Cameron Engineers, Inc., Denver, CO, 1975.

Herzog12 Herzog H., CCS project database. Available at: http://sequestration.mit.edu/tools/projects/index.html [Accessed online on March 2012].

Higginbotham11 Higginbotham P., White V., Fogash K., Guvelioglu G., Oxygensupply for oxyfuel CO2capture, International Journal of Greenhouse Gas Control 5(1) (2011) S194–S203.

Hirschfelder54 Hirschfelder J.O., Curtiss C.F., Bird R.B., Molecular Theory of Gases and Liquids, John Wiley & Sons, Inc., 1954.

Hjärtstam12 Hjärtstam S., Johansson R., Andersson K., Johnsson F., Computational fluid dynamics modeling of oxy-fuel flames: The role of soot and gas radiation, Energy & Fuels 26 (2012) 2786-2797.

Hohenwarter07 Hohenwarter U., Griendl L., Design of a novel oxycoal burner for controlled staged combustion, The 32nd International Technical Conference on Coal Utilization & Fuel Systems, Clearwater, Florida, USA, 10th-15th July 2007.

Hong09 Hong J., Chaudhry G., Brisson J.G., Field R., Gazzino M., Ghoniem A.F., Analysis of oxy-fuel combustion power cycle utilizing a pressurized coal combustor, Energy 34 (2009) 1332–1340.

Hong10 Hong J., Field R., Gazzino M., Ghoniem A.F., Operating pressure dependence of the pressurized oxy-fuel combustion power cycle, Energy 35 (2010) 5391-5399.

Hottel07 Hottel H.C., Noble J.J., Sarofim A.F., in: D.W. Green, R.H. Perry (Eds.), Heat and Mass Transfer, Chapter 5, in Perry's Chemical Engineers' Handbook, 8th ed., McGraw-Hill, New York, 2007.

Hottel67 Hottel H.C., Sarofim A.F., Radiative Transfer, McGraw-Hill, New York, 1967.

Howard73 Howard J.B., Williams G.C., Fine D.H., Kinetics of carbon monoxide oxidation in postflame gases, Symposium (International) on Combustion 14 (1973) 975–986.

Howarth66 Howarth C.R., Foster P.J., Thring M.W., The effect of temperature on the extinction of radiation by soot particles, Proceedings of the Thitd International Heat Transfer Conference 5, Hemisphere, Washington D.C.,1966, page 122-128.

Hsiao03 Hsiao G., Mongia H., Swirl cup modeling part III: Grid independent solution with different turbulence models, AIAA-2003-1349, 41st Aerospace Sciences Meeting and Exhibit, Reno, Nevada, Jan. 6-9, 2003.

Hu12 Hu Y., Yan J., Characterization of flue gas in oxy-coal combustion processes for CO2 capture, Applied Energy 90 (2012) 113–121.

Huang12 Huang Y., Wang M., Stephenson P., Rezvani S., McIlveen-Wright D., Minchener A., Hewitt N., Dave A., Fleche A., Hybrid coal-fired power plants with CO2 capture: A technical and economic evaluation based on computational simulations, Fuel 101 (2012) 244-253.

Hurt98 Hurt R., Sun J., Lunden M., A kinetic model of carbon burnout in pulverized coal combustion, Combustion and Flame 113 (1998) 181-197.

Hurt01 Hurt R.H., Calo J.M., Semi-global intrinsic kinetics for char combustion modeling, Combustion and Flame 125 (2001) 1138–1149.

Hurt05 Hurt R.H., Haynes B.S., On the origin of power-law kinetics in carbon oxidation, Proceedings of the Combustion Institute 30 (2005) 2161–2168.

Hutchinson86 Hutchinson B.R. Raithby G.D., A multigrid method based on the additive correction strategy, Numerical Heat Transfer 9 (1986) 511–537.

IFRF10 International Flame Research Foundation (IFRF), Measurement Equipment Ellipsoidal Radiometer, Doc. No. C76/y/1/3b, April 2010.

IPCC07 IPCC Fourth Assessment Report (AR4): Climate Change 2007, Synthesis Report, Contribution of Working Groups I, II, Intergovernmental Panel on Climate Change (IPCC), Pachauri, R.K. and Reisinger, A. (eds.), Geneva, Switzerland, 2007. Available at: http://www.ipcc.ch/publications_and_data/ar4/syr/en/spms3.html [Accessed online on March 2012].

IPCC05 IPCC, 2005: IPCC Special Report on Carbon Dioxide Capture and Storage. Prepared by Working Group III of the Intergovernmental Panel on Climate Change [Metz, B., O. Davidson, H. C. de Coninck, M. Loos, and L. A. Meyer (eds.)]. Cambridge University Press, Cambridge, United Kingdom and New York, NY, USA.

Irfan11 Irfan M.F., Usman M.R., Kusakabe K., Coal gasification in CO2 atmosphere and its kinetics since 1948: A brief review, Energy 36 (2011) 12-40.

Johansson11b Johansson R., Andersson K., Johnsson F., The influence of particle and gaseous radiation in oxy-fuel combustion, The 36th International Technical Conference on Clean Coal & Fuel Systems, Clearwater, Florida, USA, 5th-9th June 2011b.

Johansson10 Johansson R., Andersson K., Leckner B., Thunman H., Models for gaseous radiative heat transfer applied to oxy-fuel conditions in boilers, International Journal of Heat and Mass Transfer 53 (2010) 220–230.

Johansson11 Johansson R., Leckner B., Andersson K., Johnsson F., Account for variations in the H2O to CO2 molar ratio when modelling gaseous radiative heat transfer with the weighted-sum-of-grey-gases model, Combust. Flame 158 (2011) 893-901.

Jones88 Jones W.P., Lindstedt R.P., Global reaction schemes for hydrocarbon combustion, Combustion and Flame 73(3) (1988) 233-249.

Jovanovic12 Jovanovic R., Milewska A., Swiatkowski B., Goanta A., Spliethoff H., Sensitivity analysis of different devolatilisation models on predicting ignition point position during pulverized coal combustion in O2/N2 and O2/CO2 atmospheres, Fuel 101 (2012) 23-37.

Kakaras07a Kakaras E., Doukelis A., Giannakopoulos D., Koumanakos A., Economic implications of oxyfuel application in a lignite-fired power plant, Fuel 86 (2007a) 2151–2158.

Kakaras07b Kakaras E., Koumanakos A., Doukelis A., Giannakopoulos D., Vorrias I., Oxyfuel boiler design in a lignite-fired power plant, Fuel 86 (2007b) 2144–2150.

Kakaras07c Kakaras E., Koumanakos A., Doukelis A., Giannakopoulos D., Vorrias I., Simulation of a Greenfield oxyfuel lignite-fired power plant, Energy Conversion and Management 48 (2007c) 2879–2887.

Kangwanpongpan12 Kangwanpongpan T., Corrêa da Silva R., Krautz H.J., Prediction of oxy-coal combustion through an optimized weighted sum of gray gases model, Energy 41 (2012a) 244-251.

Kangwanpongpan10a Kangwanpongpan T., Corrêa da Silva R., Tappe S., Klatt M., Krautz H.J., Numerical comparison of spectral non-gray gases modeling in a swirling Oxyfuel burner, The 35th International Technical Conference on Coal Utilization & Fuel Systems, Clearwater, Florida, USA, 6th -10th June 2010a.

Kangwanpongpan10b Kangwanpongpan T., Corrêa da Silva R., Krautz H.J., Prediction of oxy-coal combustion through an optimized weighted sum of gray gases model, 23th International Conference on Efficiency Cost Optimization Simulation and Environmental Impact of Energy Systems, Lusanne, Switzerland, 14th - 17th June 2010b.

Kangwanpongpan09 Kangwanpongpan T., Krautz H.J., Numerical simulation of lignite combustion in O2/CO2 environment by Eddy-Dissipation Model, 1st International Oxyfuel Combustion Conference, Cottbus, Germany, 7th -11th September 2009.

Kanniche10 Kanniche M., Gros-Bonnivard R., Jaud P., Valle-Marcos J., Amann J.-M., Bouallou C., Pre-combustion, post-combustion and oxy-combustion in thermal power plant for CO2 capture, Applied Thermal Engineering, 30 (2010), pp. 53–62

Karlström11 Karlström O., Brink A., Hupa M., Tognotti L., Multivariable optimization of reaction order and kinetic parameters for high temperature oxidation of 10 bituminous coal chars, Combustion and Flame 158 (2011) 2056–2063.

Kaß09 Kaß H., Tappe S., Krautz H.J., The combustion of dry lignite under Oxy-fuel process conditions in a 0.5 MWth test plant, Energy Procedia 1 (2009) 423-430.

Kather06 Kather A., Klostermann M., Hermsdorf C., Mieske K., Eggers R., Köpke D., Konzept für ein 600 MWel Steinkohlekraftwerk mit CO2-Abtrennung auf Basis des Oxyfuel-Prozesses, Kraftwerksbetrieb unter künftigen Rahmenbedingungen, 38. Kraftwerkstechnisches Kolloquium, Dresden, Germany, October 24-25, 2006.

Kee80 Kee R.J., Miller J.A., Jefferson T.H., CHEMKIN: A general-purpose, problem-independent, transportable, fortran chemical kinetics code package, Sandia National Laboratories, report SAND80-8003, 1980.

Kee89 Kee R.J., Rupley F.M., Miller J.A., Chemkin-II: A fortran chemical kinetics package for the analysis of gas-phase chemical kinetics, Sandia National Laboratories, report SAND89-8009, 1989.

Kee96 Kee R.J., Rupley F.M., Meeks E., CHEMKIN-III: A fortran chemical kinetics package for the analysis of gasphase chemical and plasma kinetics, Sandia National Laboratories, report SAND96-8216, 1996.

Khare08a Khare S., Heat Transfer in Oxyfuel Combustion, Doctoral Thesis, The University of Newcastle, Australia, 2008.

Khare08b Khare S.P., Wall T.F., Farida A.Z., Liu Y., Moghtaderi B., Gupta R.P., Factors influencing the ignition of flames from air-fired swirl pf burners retrofitted to oxy-fuel, Fuel 87 (2008) 1042–1049.

KimG09 Kim G., Kim Y. and Joo Y.J., Conditional Moment Closure for Modeling Combustion Processes and Structure of Oxy-Natural Gas Flame, Energy Fuels 23 (9) (2009) 4370–4377.

KimHS10 Kim H.S., Shin M.S., Jang D.S., Lee D.K., In-depth numerical analysis on the determination of amount of CO2 recirculation in LNG/O2/CO2 combustion, Applied Thermal Engineering 30 (2010) 616–662.

KimJP08 Kim J.P., Schnell U., Scheffknecht G., Comparison of different global reaction mechanisms for MILD combustion of natural gas, Combustion Science and Technology, 180 (2008) 565–592.

Knaus97 Knaus H., Schneider R., Han X., Ströhle J., Schnell U., Hein K.R.G., Comparison of different radiative heat transfer models and their applicability to coal-fired utility boiler simulations, 4th Internatational Conference on Technologies and Combustion for a Clean Environment, Lisbon, Portugal, 7-10 July 1997.

Knaus01 Knaus H., Schnell U., Hein K.R.G., On the modelling of coal combustion in a 550 MWel coal-fired utility boiler, Progress in Computational Fluid Dynamics, An International Journal 1(4) (2001) 194-207.

Kneer10 Kneer R., Toporov D., Förster M., Christ D., Broeckmann C., Pfaff E., Zwick M., Engels S., Modigell M., OXYCOAL-AC: Towards an integrated coal-fired power plant process with ion transport membrane-based oxygen supply, Energy Environ. Sci. 3 (2010) 198-207.

Kobayashi77 Kobayashi H., Howard J.B., Sarofim A.F., Coal devolatilization at high temperatures, Symposium (International) on Combustion 16(1) (1977) 411-425.

Krishnamoorthy10a Krishnamoorthy G., A new weighted-sum-of-gray-gases model for CO2-H2O mixtures, International Communications in Heat and Mass Transfer 37 (2010) 1182-1186.

Krishnamoorthy10b Krishnamoorthy G., A comparison of gray and non-gray modeling approaches to radiative transfer in pool fire simulations, Journal of Hazardous Materials 182 (2010) 570–580.

Krishnamoorthy10c Krishnamoorthy G., Sami M., Orsino S., Perera A., Shahnam M., Huckaby E.D., Radiation modelling in oxy-fuel combustion scenarios, International Journal of Computational Fluid Dynamics 24(3-4) (2010) 69-82.

Krishnamurthy09 Krishnamurthy N., Paul P.J. Blasiak W., Studies on low-intensity oxy-fuel burner, Proceedings of the Combustion Institute 32(2) (2009c) 3139-3146.

Krzywanski11 Krzywanski J., Czakiert T., Muskala W., Nowak W., Modelling of CO2, CO, SO2, O2 and NOx emissions from the oxy-fuel combustion in a circulating fluidized bed, Fuel Processing Technology 92(3) (2011) 590-596.

Krzywanski10a Krzywanski J., Czakiert T., Muskala W., Sekret R., Nowak W., Modeling of solid fuels combustion in oxygen-enriched atmosphere in circulating fluidized bed boiler: Part 1. The mathematical model of fuel combustion in oxygen-enriched CFB environment, Fuel Processing Technology 91(3) (2010a) 290-295.

Krzywanski10b — Krzywanski J., Czakiert T., Muskala W., Sekret R., Nowak W., Modeling of solid fuel combustion in oxygen-enriched atmosphere in circulating fluidized bed boiler: Part 2. Numerical simulations of heat transfer and gaseous pollutant emissions associated with coal combustion in O2/CO2 and O2/N2 atmospheres enriched with oxygen under circulating fluidized bed conditions, Fuel Processing Technology, Volume 91, Issue 3, March 2010b, Pages 364-368.

Kucukgokoglan01 — Kucukgokoglan S., Aroussi A., Pickering S.J., CFD simulations of two co-rotating burner flows, The 6th Asian Symposium on Visualization, 2001.

Kuhr10 — Kuhr C., Ehmann M., Bergins C., Rehfeldt S, Modeling of char combustion in CO2/H2O and N2/O2 atmospheres, The 35th International Technical Conference on Clean Coal & Fuel Systems, Clearwater, Florida, USA, 6th-10th June, 2010.

Kuo05 — Kuo K.K., Principle of Combusion, 2nd edition, John Wiley & Sons, Inc., Hoboken, New Jersey, 2005.

Kuramochi12 — Kuramochi T., Ramírez A., Turkenburg W., Faaij A., Comparative assessment of CO2 capture technologies for carbon-intensive industrial processes, Progress in Energy and Combustion Science 38(1) (2012) 87-112.

Lallemant00 — Lallemant N., Breussin F., Weber R., Ekman T., Dugue T., Samaniego J.M., Charon O., Van Den Hoogen A.J., Van Der Bemt J., Fufisaki W., Imanari T., Nakamura T., Iino K. Heat Transfer and Pollutant Emissions Characteristics of Oxy-Natural Gas Flames in the 0.7-1 MW Thermal Input Range. J. Inst. Energy 73 (2000) 169–182.

Lalleman97 — Lallemant N., Dugue J., Weber R., Analysis of The Experimental Data Collected during The OXYFLAM-1 and OXYFLAM-2 Experiments, IFRF Doc. No. F85/y/4, 1997.

Lalleman96 — Lallemant N., Sayre A., Weber R., Evaluation of emissivity correlations for H2O-CO2-N2/air mixtures and coupling with solution methods of the radiative transfer equation, Progress in Energy and Combustion Science 22 (1996) 543-574.

Launder72 — Launder B., Spalding D., Lectures in Mathematical Models of Turbulence, Academic Press, London, England, 1972.

Launder75 — Launder B.E., Reece G.J., Rodi W., Progress in the development of a Reynolds-stress turbulence closure, J. Fluid Mech. 68(3) (1975) 537–566.

Launder89 — Launder B.E., Second-moment closure: Present... and future?, Inter. J. Heat Fluid Flow 10(4) (1989) 282–300.

Launder74 — Launder B.E., Spalding B., The numerical computation of turbulent flows, Comput. Methods Appl. Mech. Eng. 3 (1974) 269-289.

Laurendeau78 — Laurendeau N.M., Heterogeneous kinetics of coal char gasification and combustion, Progr. Energy Combust. Sci. 4 (1978) 221-270

Leckner72 — Leckner B., Spectral and total emissivity of water vapor and carbon dioxide, Combustion and Flame 19 (1972) 33-48.

Lee80 — Lee S.C, Tien C.L., Optical constants of soot in hydrocarbon flames, 18th Symposium (International) on Combustion, The Combustion Institute, 1980, page 1159-1166.

Leiser11 — Leiser S., Numerical simulation of oxy-fuel combustion, Doctoral Thesis, University of Stuttgart, 2010, in: Shaker Verlag Aachen 2011.

Leonard90 — Leonard B.P., Mokhtari S., ULTRA-SHARP nonoscillatory convection schemes for high-speed steady multidimensional flow, Report No. NASA TM-102568 (ICOMP-90-12), NASA Lewis Research Center, 1990.

Levenberg94 — Levenberg K., A method for the solution of certain non-linear problems in least squares, Quarterly of Applied Mathematics 2 (1994) 164-168.

Levenspiel99 — Levenspiel O., Chemical Reaction Engineering, 3rd edition, John Wiley & Sons, Inc., 1999.

Libby94 — Libby P.A., Williams F.A., Turbulent Reacting Flows, Academic Press, San Diego, CA, 1994.

Liebetruth01 — Liebetruth M., Görner K., Wolfgang M., Modelling the combustion of predryed lignite, 13th IFRF Member's Conference, 17 May 2001.

Lien94 — Lien F.S., Leschziner M.A., Assessment of turbulent transport models including non-linear RNG eddy-viscosity formulation and second-moment closure, Computers and Fluids 23(8) (1994) 983–1004.

LiuG04 — Liu G., Niksa S., Coal conversion submodels for design applications at elevated pressures. Part II. Char gasification, Progress in Energy and Combustion Science 30 (2004) 679–717.

LiuH00 — Liu H., Katagiri S., Kaneko U., Okazaki K., Sulfation behavior of limestone under high CO2 concentration in O2/CO2 coal combustion, Fuel 79(8) (2000) 945-953.

LiuH01 — Liu H., Katagiri S., Okazaki K., Drastic SOx removal and influences of various factors in O2/CO2 pulverized coal combustion system, Energy & Fuels 15(2) (2001) 403-412.

LiuH11 — Liu H., Liang X., Strategy for promoting low-carbon technology transfer to developing countries: The case of CCS, Energy Policy 39(6) (2011) 3106-3116.

LiuJ12 — Liu J., Chen S., Liu Z., Peng K., Zhou N., Huang X., Zhang T., and Zheng C., Mathematical Modeling of Air– and Oxy–Coal Confined Swirling Flames on Two Extended Eddy-Dissipation Models, Ind. Eng. Chem. Res. 51(2) (2012) 691–703.

Lockwood81 Lockwood F.C., Shah N.G., A new radiation solution method for incorporation in general combustion prediction procedures. Symp. (Int) Combust. 18 (1981) 1405-1414.

Lohwasser11 Lohwasser R., Madlener R., Economics of CCS for coal plants: Impact of investment costs and efficiency on market diffusion in Europe, Energy Economics 34 (2012) 850-863.

Lomax99 Lomax H., Pulliam T.H., Zingg D.W., Fundamentals of Computational Fluid Dynamics, 26 August 1999.

Lou07 Lou C., Zhou H., Yu P., Ziang Z., Measurements of the flame emissivity and radiative properties of particulate medium in pulverized-coal-fired boiler furnaces by image processing of visible radiation, Proceedings of the Combustion Institute 31 (2007) 2771–2778.

Lund78 Lund C.M., HCT-A general computer program for calculating time-dependent phenomena involving one-dimensional hydrodynamics, transport, and detailed chemical kinetics, University of California, Lawrence Livermore National Laboratory, report UCRL-52504, 1978.

Lupant07 Lupant D., Pesenti B., Evrard P., Lybaert P., Numerical and experimental characterization of a self-regenerative flameless oxidation burner operation in a pilot-scale furnace, Combust. Sci. Technol. 179 (2007) 437–453.

Lutz90 Lutz A.E., Kee R.J., Miller J.A., Senkin: A fortran program for predicting homogeneous gas phase chemical kinetics with sensitivity analysis, Sandia National Laboratories, report SAND87-8248, 1990.

MaL09 Ma L., Mitchell R., Modeling char oxidation behavior under Zone II burning conditions at elevated pressures, Combustion and Flame 156 (2009) 37–50.

Magel95 Magel H.C., Schneider R., Risio B., Numerical simulation of utility boilers with advanced combustion technologies, The 8th Symposium on Transport Phenomena in Combustion (ISTP-8), San Francisco, USA, 16-20 July 1995.

Magel96a Magel H.C., Schnell U., Hein K.R.G., Modelling of hydrocarbon and nitrogen chemistry in turbulent combustor flows using detailed reaction mechanisms, 3rd Workshop on Modelling of Chemical Reaction Systems, Heidelberg, 24-26 July 1996a.

Magel96b Magel H.C., Schnell U., Hein K.R.G., Simulation of detailed chemistry in a turbulent combustor flow, Symposium (International) on Combustion 26 (1996b) 67-74.

Magnussen77 Magnussen B.F., Hjertager B.H., On mathematical modeling of turbulent combustion with special emphasis on soot formation and combustion, Symposium (International) on Combustion 16 (1977) 719-729.

Magnussen81 Magnussen B.F., On the structure of turbulence and a generalized eddy dissipation concept for chemical reaction in turbulent flow, 19th AIAA Meeting, St. Louis, Missouri, USA, 12-15 January 1981.

Mancini11a Mancini N.D., Mitsos A., Ion transport membrane reactors for oxy-combustion - Part I: intermediatefidelity modeling, Energy 36 (2011a) 4701-4720

Mancini11b Mancini N.D., Mitsos A., Ion transport membrane reactors for oxy-combustion - Part II: Analysis and comparison of alternatives, Energy 36 (2011b) 4721-4739.

Manickam09 Manickam B., Dinkelacker F., Lobe T., Tertychnyy M., Enriched Oxygen Combustion Simulation for Rotary Kiln Application, 4th European Combustion Meeting (ECM), Vienna University of Technology, Vienna, Austria, 14th - 17th April 2009.

Marinov96 Marinov N.M., Westbrook C.K., Pitz W.J., Detailed and global chemical kinetics model for hydrogen, In: Chan S.H. (editor), Transport phenomena in combustion, Washington DC, Taylor & Francis, 1996.

Marquardt63 Marquardt D.W., An algorithm for the least-squares estimation of nonlinear parameters, SIAM Journal of Applied Mathematics 11 (1963) 431-441.

Mayers34a Mayers A.M., The rate of reduction of carbon dioxide by graphite, Journal of the American Chemical Society 56 (1934a) 70-76.

Mayers34b Mayers A.M., The rate of reduction of graphite by steam. Journal of the American Chemical Society 56 (1934b) 1879-1881.

McAdams54-ch.4 McAdams W.H., Heat Transmission, 3rd ed., McGraw-Hill, New York, 1954, in: Chap. 4, Hottel H.C., radiant-heat transmission.

McJeon11 McJeon H.C., Clarke L., Kyle P., Wise M., Hackbarth A., Bryant B.P., Lempert R.J., Technology interactions among low-carbon energy technologies: What can we learn from a large number of scenarios?, Energy Economics 33(4) (2011) 619-631.

Mehta71 Mehta B.N., Aris R., Communications on the theory of diffusion and reaction - VII The isothermal pth order reaction, Chem. Eng. Sci. 26 (1971) 1699-1712.

Menter94 Menter F.R., Two-equation eddy-viscosity turbulence models for engineering applications, AIAA Journal, 32 (1994) 1598-1605.

Mitchell07 Mitchell R.E., Ma L., Kim B.J., On the burning behavior of pulverized coal chars, Combustion and Flame 151 (2007) 426–436.

Mitchell89 Mitchell R.E., On the products of the heterogeneous oxidation reaction at the surfaces of burning coal char particles, Symposium (International) on Combustion 22 (1989) 69–78.

Modest03 Modest M.F., Radiative Heat Transfer, 2nd ed., Academic Press, Amsterdam, 2003.

Modest02 Modest M.F., Zhang H., The full-spectrum corrrelated-k distribution for thermal radiation from molecular gas-particulate mixtures, ASME Journal of Heat Transfer 124(1) (2002) 30-38.

Modest91 Modest MF., The weight-sum-of-gray-gases model for arbitrary solution methods in radiative transfer, Journal of Heat Transfer 113 (1991) 650-656.

Morsi72 Morsi S.A. Alexander A.J., An investigation of particle trajectories in two-phase flow systems, J. Fluid Mech. 55(2) (1972), 193–208.

Moullec12 Moullec Y.L., Assessment of carbon capture thermodynamic limitation on coal-fired power plant efficiency, International Journal of Greenhouse Gas Control 7 (2012) 192-201.

Mulcahy69 Mulcahy M.F.R., Smith I.W., Kinetics of combustion of pulverized fuels: a review of theory and experiment, Rev. Pure Appl. Chem. 19 (1969) 81–108.

MüllerM10 Müller M., Lemp O., Leiser S., Schnell U., Grathwohl S., Maier J., Scheffknecht G., Kluger F., Mönckert P., Advanced modeling of pulverized coal combustion under oxy-fuel conditions, The 35th International Technical Conference on Clean Coal & Fuel Systems, Clearwater, Florida, USA, 6th-10th June, 2010.

Munson09 Munson B.R., Young D.F., Okiishi T.H., Huebsch W.W., Fundamentals of Fluid Mechanics, 6th edition, John Wiley & Sons, Inc., 2009.

Murphy06 Murphy J.J., Shaddix C.R., Combustion kinetics of coal chars in oxygen-enriched environments, Combust Flame, 144(4) (2006) 710–729.

Murphy10 Murphy J.J., Shaddix C.R., Effect of reactivity loss on apparent reaction order of burning char particles, Combustion and Flame 157 (2010) 535–539.

Nagl-11 Nagl S., Fürsch M., Paulus M., Richter J., Trüby J., Lindenberger D., Energy policy scenarios to reach challenging climate protection targets in the German electricity sector until 2050, Utilities Policy 19(3) (2011) 185-192.

Nakayama92 Nakayama S., Noguchi Y., Kiga T., Miyamae S., Maeda U., Kawai M., et al., Pulverized coal combustion in O2/CO2 mixtures on a power plant for CO2 recovery, Energy Conversion and Management 33 (5–8) (1992) 379–386.

Nikolopoulos11 Nikolopoulos N., Nikolopoulos A., Karampinis E., Grammelis P., Kakaras E., Numerical investigation of the oxy-fuel combustion in large scale boilers adopting the ECO-Scrub technology, Fuel 90 (2011) 198–214.

NiksaS96 Niksa S., Coal combustion modelling, report, IEAPER/31, IEA Clean Coal Center, 1996, ISBN: 92-9029-279-2.

Niksa91 Niksa S., Kerstein A.R., Flashchain theory for rapid coal devolatilization kinetics. 1: Formulation, Energy & Fuels 5 (1991) 647-665.

Niksa03 Niksa S., Liu G., Hurt R.H., Coal conversion submodels for design applications at elevated pressures. Part I. devolatilization and char oxidation, Progress in Energy and Combustion Science 29 (2003) 425–477.

Nocedal06 Nocedal J., Wright S.J., Numerical Optimization, 2nd ed., Springer Verlag, 2006.

Normann09 Normann F., Andersson K., Leckner B., Johnsson F., Emission control of nitrogen oxides in the oxy-fuel process, Progress in Energy and Combustion Science 35 (2009) 385-397.

NozakiT97 Nozaki T., Takano S., Kiga T., Omata K., Kimura N., Analysis of the flame formed during oxidation of pulverized coal by an O2–CO2 mixture, Energy 22 (1997) 199–205.

Ochs09 Ochs T., Oryshchyn D., Woodside R., Summers C., Patrick B., Gross D., et al., Results of initial operation of the Jupiter Oxygen Corporation oxyfuel 15 MWth burner test facility, Energy Procedia 1 (2009) 511–518.

Odenberger10 Odenberger M., Johnsson F., Pathways for the European electricity supply system to 2050—The role of CCS to meet stringent CO2 reduction targets, International Journal of Greenhouse Gas Control 4(2) (2010) 327-340.

Olajire10 Olajire A.A., CO2 capture and separation technologies for end-of-pipe applications – A review, Energy 35(6) (2010) 2610-2628.

Orfanoudakis07 Orfanoudakis N., Hatziapostolou A., Krallis K., Sardi K., Vlachakis N., Experimental and numerical investigations in the near-burner region of a versatile multi-fuel burner, Journal of Computational Methods in Sciences and Engineering 7 (2007) 3–19.

Owczarek00 Owczarek C., Krautz H.J., Griebe S., Cycloid combustion - a new concept for industrial combustion with low-calorific fuels, 5th European Conference on Industrial Furnaces and Boilers, Porto, Portugal, April 2000.

Pallarés07 Pallarés J., Arauzo I., Williams A., Integration of CFD codes and advanced combustion models for quantitative burnout determination, Fuel 86 (2007) 2283–2290.

Patankar80 Patankar S.V., Numerical Heat Transfer and Fluid Flow, Hemisphere Publishing Corporation, USA, 1980.

Payne89 Payne R., Chen S.L., Wolsky A.M., Richter W.F., CO2 recovery via coal combustion in mixtures of oxygen and recycled flue gas, Combustion Science and Technology 67 (1989) 1-16.

Pehnt09 Pehnt M., Henkel J., Life cycle assessment of carbon dioxide capture and storage from lignite power plants, Int. J. Greenhouse Gas Control 3(1) (2009) 49–66.

Penner59 Penner S.S., Quantitative molecular spectroscopy and gas emissivities, Addison Wesley, Reading, MA, 1959.

Peters97 Peters A.F., Weber R., Mathematical Modeling of a 2.4 MW Swirling Pulverized Coal Flame, Combustion Science and Technology 122 (1997) 131-182.

Pfeiler10 Pfeiler C., Raupenstrauch H., Application of different turbulence models to study the effect of local anisotropy for a non-premixed piloted methane flame, Computer Aided Chemical Engineering 28 (2010) 49–54.

Pires11 Pires J.C.M., Martins F.G., Alvim-Ferraz M.C.M., Simões M., Recent developments on carbon capture and storage: An overview, Chemical Engineering Research and Design 89(9) (2011) 1446-1460.

Pollak11 Pollak M., Phillips S.J., Vajjhala S., Carbon capture and storage policy in the United States: A new coalition endeavors to change existing policy, Global Environmental Change 21 (2) (2011) 313-323.

PopeCornellU Pope S.B., Turbulence and Combustion Group, Cornell University, College of Engineering. Available at: http://tcg.mae.cornell.edu/pubs.html [Accessed online on March 2012].

Pope00 Pope S.B., Turbulent Flows, Cambridge University Press, 2000.

Porter10 Porter R., Liu F., Pourkashanian M., Williams A., Smith D., Evaluation of solution methods for radiative heat transfer in gaseous oxy-fuel combustion environments, Journal of Quantitative Spectroscopy and Radiative Transfer 111 (2010) 2084-2094.

Praetorius09 Praetorius B., Schumacher K., Greenhouse gas mitigation in a carbon constrained world: The role of carbon capture and storage, Energy Policy 37(12) (2009) 5081–5093.

Radoux98 Radoux F., Maalman T., Lallemant N., Narrow angle radiometer probe, IFRF Doc. C 73/y/10, IFRF, Ijmuiden, The Netherlands, 1998.

Ralston78 Ralston A., Rabinowitz P., A First Course in Numerical Analysis, 2nd edition, International Student Edition, McGraw-Hill, Tokyo, 1978.

Rathnam09 Rathnam R.K., Elliott L.K., Wall T.F., Liu Y., Moghtaderi B., Differences in reactivity of pulverised coal in air (O2/N2) and oxy-fuel (O2/CO2) conditions, Fuel Processing Technology 90 (2009) 797-802.

Rayleigh71 Rayleigh L., On the light from the sky, its polarization and colour, Philos. Mag. 41 (1871) 107-120,274-279 (reprinted in Scientific Papers by Lord Rayleigh, Vol. I: 1869-1881, no. 8, Dover, New York, 1964).

Rehfeldt11 Rehfeldt S., Kuhr C., Ehmann M., Bergins C., Modeling of radiative properties of an oxyfuel atmosphere with a weighted sum of gray gases for variable carbon dioxide and water vapor concentrations, Energy Procedia 4 (2011) 980-987.

Rehfeldt09 Rehfeldt S., Kuhr C., Ehmann M., Bergins C., Scheffknecht G., Maier J., et al. Basic experiments and CFD calculations of air and oxyfuel firing of lignite and bituminous coals in 0.5 and 1 MW scale combustion test facilities, The 34th International Technical Conference on Clean Coal & Fuel Systems, Clearwater, Florida, USA, 31th May-4th June 2009.

Riviere95 Riviere P.H., Soufiani A., Taine J., Correlated-k fictitious gas model for H2O infrared radiation in the voigt regime, J. Quant. Spectrosc. Radiat. Transfer 53 (1995) 335-346.

Roberts00 Roberts D.G., Harris D.J., Char gasification with O2, CO2, and H2O: Effects of pressure on intrinsic reaction kinetics, Energy & Fuels 14 (2000) 483-489.

Rogge10 Rogge K.S., Hoffmann V.H., The impact of the EU ETS on the sectoral innovation system for power generation technologies - Findings for Germany, Energy Policy 38(12) (2010) 7639-7652.

Rogge11 Rogge K.S., Schneider M., Hoffmann V.H., The innovation impact of the EU Emission Trading System - Findings of company case studies in the German power sector, Ecological Economics 70(3) (2011) 513-523.

Román11 Román M., Carbon capture and storage in developing countries: A comparison of Brazil, South Africa and India, Global Environmental Change 21(2) (2011) 391-401.

Romano10 Romano M.C., Lozza G.G., Long-term coal gasification-based power with near-zero emissions. Part B: Zecomag and oxy-fuel IGCC cycles, International Journal of Greenhouse Gas Control 4 (2010) 469–477.

Rosen11 Rosen L., Degenstein N., Shah M., Wilson J., Kelly S., Peck J., Christie M., Development of oxygen transport membranes for coal-based power generation, Energy Procedia 4 (2011) 750–755.

Rosin33 Rosin P., Rammler E., The laws governing the fineness of powdered coal, J. Inst. Fuel 7 (1933) 29–36.

Rothman87 Rothman L.S., Gamache R.R., Goldman A., Brown L.R., Toth R.A., Pickett H.M., et al., The HITRAN database - 1986 edition, Appl. Opt. 26 (1987) 4058–4097.

Rothman92 Rothman L.S., Gamache R.R., Tipping R.H., Rinsland C.P., Smith M.A.H., Benner D.C., et al., The HITRAN molecular database - editions of 1991 and1992, J. Quant. Spectrosc. Radiat. Transfer 48 (1992) 469–507.

Rothman98 Rothman L.S. , Rinsland C.P. , Goldman A., Massie S.T., Edwards D.P., Flaud J.M., Perrin A., Camy-Peyret C., Dana V., Mandin J.Y., Schroeder J., Maccann A., Gamache R.R.,. Wattson R.B, Yoshino K., Chance K.V., Jucks K.W., Brown L.R., Nemtchinov V., Varanasi P., The HITRAN molecular spectroscopic database and HAWKS (HITRAN atmospheric workstation): 1996 edition, J. Quant. Spectrosc. Radiat. Transfer 60 (1998) 665-670.

Rothman05 Rothman L.S., Jacquemart D., Barbe A., ChrisBenner D., Birk M., Brown L.R., et al., The HITRAN 2004 molecular spectroscopic database, J. Quant. Spectrosc. Radiat. Transfer 96 (2005) 139–204.

Rothman09 Rothman L.S., Gordon I.E., Barbe A., Benner D.C., Bernath P.F., Birk M., et al., The HITRAN 2008 molecular spectroscopic database, J. Quant. Spectrosc. Radiat. Transfer 110 (2009) 533–572.

Rothman95 Rothman L.S., Wattson R.B., Gamache R.R., Schroeder J., McCann A., HITRAN, HAWKS and HITEMP high-temperature molecular data-base, Proc. Soc. Photo-Opt. Instrum. Eng. 2471 (1995) 105–111.

Rothman10 Rothman L.S., Gordon I.E., Barber R.J., Dothe H., Gamache R.R., Goldman A., Perevalov V.I., Tashkun S.A., Tennyson J., HITEMP, the high-temperature molecular spectroscopic database, J. Quant. Spectrosc. Radiat. Transfer 111 (2010) 2139-2150.

Rotta51a Rotta J., Statistiche theorie nichthomogener turbulenz, Zeitschrift für Physik A Hadrons and Nuclei 129 (1951a) 547-573.

Rotta51b Rotta J., Statistische theorie nichthomogener turbulenz, Zeitschrift für Physik A Hadrons and Nuclei 131 (1951b) 51-77.

Rubin07 Rubin E.S., Yeh S., Antes M., Berkenpas M., Davison J., Use of experience curves to estimate the future cost of power plants with CO2 capture, International Journal of Greenhouse Gas Control 1 (2007) 188-197.

Rückert03 Rückert F.U., Sabel T., Schnell U., Hein K.R.G., Risio B., Comparison of different global reaction mechanisms for coal-fired utility boilers, Progress in Computational Fluid Dynamics, An International Journal (PCFD) 2003, Volume 3, Issue 2/3/4, pp.130-139.

Runchal72 Runchal A.K., Convergence and accuracy of three finite difference schemes for a two-dimensional conduction and convection problem, International Journal of Numerical Methods in Engineering 4 (1972) 541-550.

Saario05 Saario A., Rebola A., Coelho P.J., Costa M., Oksanen A., Heavy fuel oil combustion in a cylindrical laboratory furnace: measurements and modeling, Fuel 84 (2005) 359–369.

Satterfield91 Satterfield C.N., Heterogeneous Catalysis in Industrial Practice, 2nd edition, McGraw-Hill, Inc., New York, 1991.

Schaffel09 Schaffel N., Mancini M., Szlek A., Weber R., Mathematical modeling of MILD combustion of pulverized coal, Combustion and Flame 156 (2009) 1771–1784.

Scheffknecht11 Scheffknecht G., Al-Makhadmeh L., Schnell U., Maier J., Oxy-fuel coal combustion - A review of the current state-of-the-art, International Journal of Greenhouse Gas Control 5(1) (2011) S16–S35.

Scholes10 Scholes C.A., Smith K.H., Kentish S.E., Stevens G.W., CO2 capture from pre-combustion processes - Strategies for membrane gas separation, International Journal of Greenhouse Gas Control 4 (2010) 739-755.

Schreiber10 Schreiber A., Zapp P., Markewitz P., Vögele S., Environmental analysis of a German strategy for carbon capture and storage of coal power plants, Energy Policy 38(12) (2010) 7873-7883.

Scutaru94 Scutaru D., Rosenmann L., Taine J., Approximate intensities of CO2 hot bands at 2.7, 4.3 and 12μm for high temperature and medium resolution applications, J. Quant. Spectrosc. Radiat. Transfer 52 (1994) 765-781.

Serio87 Serio M.A., Solomon P.R., Suuberg E.M., Variations in char reactivity with coal type and pyrolysis conditions, Int. Conf. Coal Science, Elsevier, Amsterdam, 1987.

Shackley09 Shackley S., Reiner D., Upham P., Coninck H., Sigurthorsson G., Anderson J., The acceptability of CO2 capture and storage (CCS) in Europe: An assessment of the key determining factors: Part 2. The social acceptability of CCS and the wider impacts and repercussions of its implementation, International Journal of Greenhouse Gas Control 3(3) (2009) 344-356.

Shaw91 Shaw D.W., Zhu X., Misra M.K., Essenhigh R.H., Determination of global kinetics of coal volatiles combustion, Symposium (International) on Combustion 23 (1991) 1155-1162.

Shih95 Shih T.H. Liou W.W., Shabbir A., Yang Z., Zhu J., a new k-e eddy-viscosity model for high Reynolds number turbulent flows - model development and validation, Computers Fluids. 24(3) (1995) 227–238.

Siegel08 Siegel R., Howell J.R., Thermal radiation heat transfer, 4th ed., Taylor & Francis, 2008.

Simons82 Simons G.A., The pore tree structure of porous char, Symposium (International) on Combustion 19 (1982) 1067-1076.

SinghB11 Singh B., Strømman A.H., Hertwich E.G., Comparative life cycle environmental assessment of CCS technologies, International Journal of Greenhouse Gas Control 5(4) (2011) 911-921.

SinghD03 Singh D., Croiset E., Douglas P.L., Douglas M.A., Techno-economic study of CO2 capture from an existing coal-fired power plant: MEA scrubbing vs. O2/CO2 recycle combustion, Energy Conversion and Management 44 (19) (2003) 3073–3091.

Smart10a Smart J.P., O'Nions P., Riley G.S., Radiation and convective heat transfer, and burnout in oxy-coal combustion, Fuel 89 (2010a) 2468-2476.

Smart09 Smart J.P., O'Nions P., Riley G.S., Jamieson E., Radiation and convection heat transfer in oxyfuel combustion, 1st Oxyfuel Combustion Conference, IEA GHG International Oxy-Combustion Network, Cottbus, Germany, 8th-10th September 2009.

SmithIW82 Smith I.W., The combustion rates of coal chars: a review, Symposium (International) on Combustion 19(1) (1982) 1045–1065.

SmithIW78 Smith I.W., The intrinsic reactivity of carbons to oxygen, Fuel 57 (1978) 409-414.

SmithIW74 Smith I.W., Tyler R.J., The Reactivity of a Porous Brown Coal Char to Oxygen between 630 and 1812 °K, Combustion Science and Technology 9 (1974) 87-94.

SmithIW71a Smith I.W., Kinetics of combustion of size-graded pulverized fuels in the temperature range 1200-2270 °K, Combustion and Flame 17 (1971a) 303-314.

SmithIW71b Smith I.W., The kinetics of combustion of pulverized semi-anthracite in the temperature range 1400-2200°K, Combustion and Flame 17 (1971b) 421-428.

SmithKL94 Smith K.L., Smoot L.D., Fletcher T.H., Pugmire R.J., The Structure and Reaction Processes of Coal, The Plenum Chemical Engineering Series, Plenum Press, New York, 1994.

SmithTF82 Smith T.F., Shen Z.F., Friedman J.N., Evaluation of coefficients for the weighted sum of gray gases model, ASME J. Heat Transfer 104 (1982) 602-608.

Smoot93 Smoot L.D., Fundamentals of Coal Combustion: for Clean and Efficient Use, Coal Science and Technology 20, Elsevier, Amsterdam, 1993.

Smoot79 Smoot L.D., Pratt D.T., Pulverized-Coal Combustion and Gasification: Theory and Applications for Continuous Flow Processes, Plenum Press, New York and London, 1979.

Smoot85 Smoot L.D., Smith P.J. Coal Combustion and Gasification, Plenum Press, New York, 1985.

Solomon88 Solomon P.R., Hamblen D.G., Carangelo R.M., Serio M.A., Deshpande G.V., General model of coal devolatilization, Energy & Fuels 2 (1988) 405-422.

Spalding71 Spalding D.B., Mixing and chemical reaction in steady confined turbulent flames, Symposium (International) on Combustion 13 (1971) 649–657.

Speight05 Speight J.G., Handbookd of Coal Analysis, John Wiley & Sons, Inc., New Jersey and Canada, 2005.

Speziale91 Speziale C.G.,Sarkar S., Gatski T.B., Modelling the pressure-strain correlation of turbulence: An invariant dynamical systems approach, J. Fluid Mech. 227 (1991) 245–272.

Stadler11 Stadler H., Beggel F., Habermehl M., Persigehl B., Kneer R., Modigell M., Jeschke P., Oxyfuel coal combustion by efficient integration of oxygen transport membranes, International Journal of Greenhouse Gas Control 5 (2011) 7–1

Stadler09 Stadler H., Toporov D., Förster M., Kneer R., On the influence of the char gasification reactions on NO formation in flameless coal combustion, Combustion and Flame 156 (2009) 1755–1763.

Stanger11 Stanger R., Wall T., Sulphur impacts during pulverised coal combustion in oxy-fuel technology for carbon capture and storage, Progress in Energy and Combustion Science 37(1) (2011) 69-88.

Stechow11 Stechow C., Watson J., Praetorius B., Policy incentives for carbon capture and storage technologies in Europe: A qualitative multi-criteria analysis, Global Environmental Change 21(2) (2011) 346-357.

Steeneveldt06 Steeneveldt R., Berger B., Torp T.A., CO2 Capture and Storage: Closing the Knowing–Doing Gap, Chemical Engineering Research and Design 84(9) (2006) 739-763.

Stefanidis06 Stefanidis G.D., Merci B., Heynderickx G.J., Marin G.B., CFD simulations of steam cracking furnaces using detailed combustion mechanisms, Computers and Chemical Engineering 30 (2006) 635–649.

Stigson12 Stigson P., Hansson A., Mårten Lind M., Obstacles for CCS deployment: an analysis of discrepancies of perceptions, Mitigation and Adaptation Strategies for Global Change 17 (2012) 601-619.

Stockwell01 Stockwell N., Zhang C., Ishii T., Hino Y., Numerical simulations of turbulent non-premixed combustion in a regenerative furnace, ISIJ International 41(10) (2001) 1272-1281.

Ströhle11 Ströhle J., Wide band correlated-k approaches for non-grey radiation modelling in oxy-fuel combustion with dry recycling, Fuel 90 (2011) 3007–3013.

Strömberg09 Strömberg L., Lindgren G., Jacoby H., Giering R., Anheden M., Burchhardt U., et al., Update on Vattenfall's 30 MWth oxyfuel pilot plant in Schwarze Pumpe, Energy Procedia 1 (1) (2009) 581–589.

Strube11 Strube R., Manfrida G., CO2 capture in coal-fired powerplants - Impact on plant performance, International Journal of Greenhouse Gas Control 5(4) (2011) 710–726.

Stull60 Stull V.R., Plass G.N., Emissivity of dispersed carbon particles, Journal of the Optical Society of America 50 (1960) 121-129.

Sun00 Sun J., Hurt R.H., Mechanisms of extinction and near-extinction in pulverized solid fuel combustion, Proceedings of the Combustion Institute 28 (2000) 2205–2213.

Taniguchi11a Taniguchi M., Yamamoto K., Okazaki T., Rehfeldt S., Kuhr C., Application of lean flammability limit study and large eddy simulation to burner development for an oxy-fuel combustion system, International Journal of Greenhouse Gas Control 5(1) (2011a) S111-S119.

Taniguchi11b Taniguchi M., Shibata T., Yamamoto K., Kuhr C., Ito O., Lean flammability limit for oxy-fuel fired pulverized coal combustion systems, Energy Procedia 4 (2011b) 892-899.

Tannehill97 Tannehill J.C., Anderson D.A., Pletcher R.H., Computational Fluid Mechanics and Heat Transfer, 2nd edition, Taylor & Francis, 1997.

Tappe09a Tappe S., Krautz H.J., Experimental Investigations of Combustion Behaviour in Various O2/CO2-Atmospheres, 4th International Conference on Clean Coal Technologies (CCT2009), Dresden, Germany, 18th-21th May 2009a.

Tappe09b Tappe, S., Krautz, H.J., ALVA 20: A 20 kWth Atmospheric Laboratory Test Facility to Investigate the Combustion Behaviour under „Close-to-Reality“ Conditions, European Combustion Meeting 2009, Vienna, Austria, April 2009b.

Tappe09c	Tappe, S., Krautz, H.J., Influence of various O2/CO2-concentrations on the burning behavior of different coal, The 34th International Technical Conference on Clean Coal & Fuel Systems, Clearwater, Florida, USA, 31th May-4th June 2009c.
Tappe09d	Tappe, S., Krautz, H.J., An experimental approch to the kinetics of the combustion in O2/CO2-atmospheres, 1st International Oxyfuel Combustion Conference, Cottbus, September 2009d.
Tashkun08	Tashkun S.A., Perevalov V.I., CDSD (carbon dioxide spectroscopic databank): updated and enlarged version for atmospheric applications, 10th HITRAN Database Conference, Cambridge MA, USA (2008). Available onlie at: ftp://ftp.iao.ru/pub/CDSD-2008/.
Tashkun03	Tashkun S.A., Perevalov V.I., Teffo J.L., Bykov A.D., Lavrentieva N.N., CDSD-1000, the high-temperature carbon dioxide spectroscopic databank, J. Quant. Spectrosc. Radiat. Transfer 82 (2003) 165–196. Available onlie at: ftp://ftp.iao.ru/pub/CDSD-1000/.
Taylor21	Taylor G.I., Diffusion by continuous movements, Proc. Lond. Math. Soc. 20 (1921) 196–212.
RoadmapIEA11	Technology Roadmap Carbon Capture and Storage in Industrial Applications, IEA, 2011.
RoadmapIEA09	Technology Roadmap Carbon Capture and Storage, IEA, 2009.
Tennekes72	Tennekes H., Lumley J.L., A First Course in Turbulence, The MIT Press, Cambridge, Massachusetts, and Londong, England, 1972.
MIT07	The future of coal: options for a carbon-constrained world, MIT, 2007.
COP15-09	The United Nations Climate Change Conference (COP15), Copenhagen Summit, UNFCCC, Copenhagen, Denmark; 2009. Available at: unfccc.int/ [Accessed online on October 2011].
Thiele39	Thiele E.W., Relation between catalvtic activity and size of particle, Industrial and Engineering Chemistry 31(7) (1939) 916-920.
Thomas49	Thomas L.H., Elliptic problems in linear differential equations over a network, Watson Sci. Comput. Lab Report, Columbia University, New York, USA, 1949.
Tian09	Tian Z.F., Witt P.J., Schwarz M.P. Yang W., Numerical modelling of brown coal combustion in a tangentially-fired furnace, Seventh International Conference on CFD in the Minerals and Process Industries, CSIRO, Melbourne, Australia, 9-11 December 2009.
Tien69	Tien C.L., Thermal Radiation Properties of Gases, Advances in Heat Transfer 5 (1969) 253-324.
Toftegaard10	Toftegaard M.B., Brix J., Jensen P.A., Glarborg P., Jensen A.D., Oxy-fuel combustion of solid fuels, Progress in Energy and Combustion Science 36(5) (2010) 581-625.
Toporov08a	Toporov D., Bocian P., Heil P., Kellermann A., Stadler H., Tschunko S., Förster M., Kneer R., Detailed investigation of a pulverized fuel swirl flame in CO2/O2 atmosphere, Combustion and Flame 155 (2008a) 605-618.
Toporov06	Toporov D., Tschunko S., Erfurth J., Kneer R., Modelling of oxycoal combustion in a small scale test facility, 7th European Conference on Industrial Furnaces and Boilers, Porto, Portugal, 18th-21th April 2006.
Torvanger11	Torvanger A., Meadowcroft J., The political economy of technology support: Making decisions about carbon capture and storage and low carbon energy technologies, Global Environmental Change 21(2) (2011) 303-312.
Tranier09	Tranier J.-P., Dubettier R., Perrin N., Air separation unit for oxy-coal combustion systems, 1st Oxyfuel Combustion Conference, IEA GHG International Oxy-Combustion Network, Cottbus, Germany, 8th-10th September 2009.
Truelove87	Truelove J.S., Discrete-ordinate solutions of the radiation transport equation, ASME Journal of Heat Transfer 109(4) (1987) 1048-1051.
Truelove88	Truelove J.S., Three-dimensional radiation in absorbing-emitting-scattering media using the discrete-ordinates approximation, Journal of Quantitative Spectroscopy and Radiative Transfer 39(1) (1988) 27-31.
Tsao99	Tsao J.M., Lin C.A., Reynolds stress modelling of jet and swirl interaction inside a gas turbine combustor, International Journal for Numerical Methods in Fluids 29 (1999) 451–464.
Turn00	Turn S., An Introduction to Combustion: Concepts and Applications, 2nd edition, International Editions, McGraw-Hill series in mechanical engineering, The McGraw-Hill Companies, Inc., 2000.
Tzimas10	Tzimas E., Georgakaki A., A long-term view of fossil-fuelled power generation in Europe, Energy Policy 38(8) (2010) 4252-4264.
Ubhayakar77	Ubhayakar S.K., Stickler D.B.,Von Rosenberg Jr. C.W., Gannon R.E., Rapid devolatilization of pulverized coal in hot combustion gases, Symposium (International) on Combustion 16(1) (1977) 427-436.
Upham11	Upham P., Roberts T., Public perceptions of CCS: Emergent themes in pan-European focus groups and implications for communications, International Journal of Greenhouse Gas Control 5(5) (2011) 1359-1367.
Van Doormal84	Van Doormaal J.P., Raithby G.D., Enhancements of the SIMPLE method for predicting incompressible fluid flows, Numer. Heat Transfer 7 (1984) 147–163.
Van Leer79	Van Leer B., Towards the ultimate conservative difference scheme. IV. A second order sequel to Godunov's method, Journal of Computational Physics 32 (1979) 101–136.

Varagani05 Varagani R.K., Châtel-Pélage F., Pranda P., Rostam-Abadi M., Lu Y., Bose A.C., Performance simulation and cost assessment of oxy-combustion process for CO2 capture from coal-fired power plants, The fourth annual conference on carbon sequestration, Alexandria, VA, USA, May 2–5, 2005.

Várhegyi96 Várhegyi G., Szabó P., Jakab E., Till F., Richard J.R., Mathematical modeling of char reactivity in Ar-O2 and CO2-O2 mixtures, Energy & Fuels 10 (1996) 1208-1214.

Vascellari12 Vascellari M., Cau G., Influence of turbulence–chemical interaction on CFD pulverized coal MILD combustion modeling, Fuel 101 (2012) 90-101.

Vascellari09 Vascellari M., Cau G., Numerical simulation of pulverized coal oxy-combustion with exhaust gas recirculation, 4th International Conference on Clean Coal Technologies (CCT2009), Dresden, Germany, 18th-21th May 2009.

VDI 1994-2011 VDI water cooled suction pyrometer, Standard of VDI/VDE 3511, part 5, Temperature measurement in industry - Installation of thermometers, 1994-2011, www.vdi.eu.

Vergragt11 Vergragt P.J., Markusson N., Karlsson H., Carbon capture and storage, bio-energy with carbon capture and storage, and the escape from the fossil-fuel lock-in, Global Environmental Change 21(2) (2011) 282-292.

Versteeg07 Versteeg H.K., Malalasekera W., An Introduction to Computational Fluid Dynamics: The Finite Volume Method, 2nd edition, Pearson Education Limited, 2007.

Viebahn12 Viebahn P., Daniel V., Samuel H., Integrated assessment of carbon capture and storage (CCS) in the German power sector and comparison with the deployment of renewable energies, Applied Energy 97 (2012) 238-248.

Viskanta08 Viskanta R., Computation of radiative transfer in combustion systems, International Journal of Numerical Methods for Heat Fluid Flow 18(3/4) (2008) 415-442.

Viskanta87 Viskanta R., Mengüç M.P., Radiation heat transfer in combustion systems, Progress in Energy and Combustion Science 13(2) (1987) 97–160.

Voigt-MSc07 Voigt S., Soot formation in oxyfuel combustion, MSc thesis, Cranfield University, 2007.

Vuthaluru06 Vuthaluru R., Vuthaluru H.B., Modelling of a wall fired furnace for different operating conditions using FLUENT, Fuel Processing Technology 87 (2006) 633–639.

Walker59 Walker P.L., Rusinko F., Austin L.G., Gas Reactions of Carbon, Advances in Catalysis 11 (1959) 133-221.

Wall09a Wall T., Liu Y., Spero C., Elliott L., Khare S., Rathnam R., et al., An overview on oxyfuel coal combustion – State of the art research and technology development, Chemical Engineering Research and Design 87 (2009) 1003-1016.

Wall11a Wall T., Stanger R., Santos S., Demonstrations of coal-fired oxy-fuel technology for carbon capture and storage and issues with commercial deployment, International Journal of Greenhouse Gas Control 5(1) (2011a) S5-S15.

Wall11b Wall T., Stanger R., Liu Y., Gas cleaning challenges for coal-fired oxy-fuel technology with carbon capture and storage, Fuel (2011b), doi:10.1016/j.fuel.2011.03.037.

Wall09b Wall T., Yu J., Coal-fired oxyfuel technology status and progress to deployment, The 34th international technical conference on clean coal & fuel systems, Clearwater, Florida, USA, 2009.

Wall07 Wall T.F., Combustion processes for carbon capture, Proceedings of the Combustion Institute 31 (2007) 31–47.

Wall73 Wall T.F., Stewart I.McC., The measurement and prediction of solids- and sootabsorption coefficients in a flame region of an industrial p.f. chamber, Proc. Combust. Inst. 14 (1973) 689–697.

WangCS88 Wang C.S., Berry G.F., Chang K.C., Wolsky A.M., Combustion of pulverized coal using waste carbon dioxide and oxygen, Combustion and Flame 72 (1988) 301-310.

WangM11 Wang M., Lawal A., Stephenson P., Sidders J., Ramshaw C., Post-combustion CO2 capture with chemical absorption: A state-of-the-art review, Chemical Engineering Research and Design 89 (2011) 1609-1624.

Warnatz06 Warnatz J., Mass U., Dibble R.W., Combustion, Physical and Chemical Fundamentals, Modeling and Simulation, Experiments, Pollutant Formation, 4th edition, Springer-Verlag Berlin Heidelberg, 2006.

Waters88 Waters B., Squires R.G., Laurendeau N.M., Mitchell R.E., Evidence for formation of CO2 in the vicinity of burning pulverized carbon particles, Combustion and Flame 74 (1988) 91-106.

WattM96 Watt M., The Chemical Structure of Coal Tar and Char During Devolatilization, M.S. Thesis, Chemical Engineering Department, Brigham Young University, 1996.

Weber90 Weber R., Visser B.M., Boysan F., Assessment of turbulence modeling for engineering prediction of swirling vortices in the near burner zone, Int. J. Heat and Fluid Flow 11(3) (1990) 225-235.

Werle10 Werle S., Wilk R.K., Ignition of methane and propane in high-temperature oxidizers with various oxygen concentrations, Fuel 89 (2010) 1833–1839.

Wesseling92 Wesseling P., An Introduction to Multigrid Methods, John Wiley & Sons, New York, 1992.

Westbrook81 Westbrook C.K., Dryer F.L., Simplified reaction mechanisms for the oxidation of hydrocarbon fuels in flames, Combustion Science and Technology 27 (1981) 31–43.

Wheeler51 Wheeler A. Reaction rates and selectivity in catalyst pores, Advances in Catalysis 3 (1951) 249-327.

Wilcox98 Wilcox D.C., Turbulence Modeling for CFD, 2nd edition, DCW Industries, Inc., La Canada, California, 1998.

Wilcox93 Wilcox D.C., Turbulence Modeling for CFD. Published by DCW Industries, Inc., La Cañada, California, USA, 1993.

Williams00 Williams A., Pourkashanian M., Jones J.M., The combustion of coal and some other solid fuels, Proceedings of the Combustion Institute 28 (2000) 2141–2162.

Williams02 Williams A., Backreedy R., Habib R., Jones J.M., Pourkashanian M., Modelling coal combustion: the current position, Fuel 81 (2002) 605-618.

Williams01 Williams A., Pourkashanian M., Jones J.M., Combustion of pulverized coal and biomass, Progress in Energy and Combustion Science 27 (2001) 587-610.

WEO10 World Energy Outlook (WEO) 2010, International Energy Agency (IEA), 2010.

WEO11 World Energy Outlook (WEO) 2011: Are We Entering a Golden Age of Gas, special report, International Energy Agency (IEA), 2011.

Woycenko95 Woycenko D.M., Van de Kamp W.L., Roberts P.A., Combustion of pulverised coal in a mixture of oxygen and recycled flue gas, Summary of the APG research program, IFRF Doc. F98/Y/4 International Flame Research Foundation (IFRF), Ijmuiden, The Netherlands, October 1995.

Yakhot86 Yakhot V., Orszag S.A., Renormalization group analysis of turbulence. I. Basic theory, J. Sci. Comput. 1 (1986) 3-51.

Yakhot92 Yakhot V., Smith L.M., The renormalization group, the ε-expansion and derivation of turbulence models, Journal of Scientific Computing 7(1) (1992) 35-61.

Yan11 Yan J., Anheden M., Faber R., Starfelt F., Preusche R., Ecke H., Padban N., Kosel D., Jentsch N., Lindgren G., Flue gas cleaning for CO2 capture from coal-fired oxyfuel combustion power generation, Energy Procedia 4 (2011) 900–907.

YangW06 Yang W., Blasiak W., CFD as applied to high temperature air combustion in industrial furnaces, IFRF Combustion Journal, Article Number 200603, November 2006.

YangW05 Yang W., Blasiak W., Numerical study of fuel temperature influence on single gas jet combustion in highly preheated and oxygen deficient air, Energy 30 (2005) 385–398.

Yin10 Yin C., Johansen L.C.R., Rosendahl L.A., Kær S.K., New weighted sum of gray gases model applicable to computational fluid dynamics (CFD) modeling of oxy-fuel combustion: derivation , validation, and implementation, Energy & Fuels 24(12) (2010) 6275–6282.

Yin11 Yin C., Rosendahl L.A., Kær S.K., Chemistry and radiation in oxy-fuel combustion: A computational fluid dynamics modeling study, Fuel 90(7) (2011) 2519-2529.

Young89 Young B.C., Smith I.W., The combustion of Loy Yang brown coal char, Combustion and Flame 76 (1989) 29-35.

Zanganeh07 Zanganeh K.E.,Shafeen A., A novel process integration, optimization and design approach for large-scale implementation of oxy-fired coal power plants with CO2 capture, International Journal of Greenhouse Gas Control 1 (2007) 47-54.

ZhouWei10 Zhou W., Moyeda D., Process evaluation of oxy-fuel combustion with flue gas recycle in a conventional utility boiler, Energy & Fuels 24(3) (2010) 2162–2169.

ZhouWu11 Zhou W., Zhao C., Duan L., Liu D., Chen X., CFD modeling of oxy-coal combustion in circulating fluidized bed, International Journal of Greenhouse Gas Control 5(6) (2011) 1489-1497.

ZhouWu10 Zhou W., Zhao C., Duan L., Liu D., Chen X., Simulation study of oxy-fuel combustion in a circulating fluidized bed, The 35th International Technical Conference on Clean Coal & Fuel Systems, Clearwater, Florida, USA, June 6-10, 2010.

Zimont69 Zimont V.L., Trushin Y.M., Total combustion kinetics of hydrocarbon fuels, Combustion Explosion and Shock waves 5 (1969) 391-394.

Zygourakis88 Zygourakis K., Sandmann C.W.Jr., Discrete structural models and their application to gas-solid reacting systems, AIChE J. 34 (1988) 2030-2040.

Appendix A: Demonstrations of oxy-fuel technology

Table A.1. Demonstrations of oxy-fuel projects (revised from [Herzog12, ChenL12, Wall09-11, EcoGlobalCCS11, CostCO2-IEA11, Ochs09]).

Project	Companies, technology providers[a]	Capacity		Plant type[b]	Fuel[c]	Start-up	Location[d]
		MWe	MWth				
Youngdong	KEPCO,KOSEP	100	300	PC	bit.	2016-2018	S. Korea
FutureGen 2.0	Ameren Energy Resources, B&W, Air Liquide, FutureGen Alliance	210	-	PC	Coal	2015-2016	USA
Black Hills Power	Black Hills Corporation, B&W	100	-	PC	sub-bit.	2016	USA
Compostilla (OXY-CFB-300) Phase II	ENDESA, CIUDEN, Foster Wheeler	320	-	CFB	anth.,bit., sub-bit., petcoke	2015	Spain
Daqing	Alstom & Datang	350,1000	-	PC	Coal	2015	China
Jänschwalde	Vattenfall, Alstom, Linde	250	-	PC	lignite	2015 (Cancel)	Germany
HBPA-Michigan/Praxair(Holland)	Praxair, State of Michigan	75	-	CFB	bit.	2014	USA
Jamestown	Jamestown BPU, Praxair Plant	50	150	CFB	bit.	2013	USA
Callide A	CS Energy, IHI, Air Liquide	30	-	PC	bit.	2012	Australia
ENEL HP Oxyfuel	ENEL	-	48	PC	Coal	2012	Italy
Compostilla (OXY-CFB-300) Phase I	ENDESA, CIUDEN, Foster Wheeler	17	-	CFB	anth.,bit.,sub-bit., petcoke	2011-2012	Spain
CIUDEN	ENDESA, Foster Wheeler (CFB), Praxir (O2 supply), Air Liquide (CPU), Leni Gas&Oil (storage)	6.7	20	PC	anth.,bit.,sub-bit., petcoke	2011	Spain
CIUDEN	ENDESA, Foster Wheeler (CFB), Praxir (O2 supply), Air Liquide (CPU), Leni Gas&Oil (storage)	10	30	CFB	anth.,bit.,sub-bit., petcoke	2011	Spain
Callide	CS Energy, IHI, Air Liquide	30	90	PC	bit.	2010	Australia
OxyCoal & OxyCoal 2, UK	Doosan Babcock, Air Products	13.3,30	40,90	PC	semi-anth.,hv bit.,NG	2009-2010	UK
Total, Lacq	TOTAL, Alstom, Air Liquide	10	30	Ind. boiler	NG	2009	France
Jupiter Pearl Plant	Jupiter	22	66	PC	NG,bit.	2009	USA
Alstom (Windsor Facility)	Alstom	5	15	PC(T-firing)	bit.,sub-bit.	2009	USA
Schwarze Pumpe	Vattenfall, Alstom, Linde	10	30	PC	lignite	2008	Germany
B&W	B&W, Air Liquide	10	30	PC	bit.,sub-bit.,lignite	2007	USA
JOC: Phase VI	JOC,NETL	-	15	PC	Coal (high sulfur), NG	2007	USA
JOC: Phase IV	JOC,NETL	400	-	PC	Coal	2003	USA
JOC: Phase III	JOC	-	1.5	PC	Coal,NG	2002	USA

[a] B&W = The Babcock & Wilcox Company, IHI = Ishikawajima-Harima Heavy Industries, JOC = Jupiter Oxygen Corporation, NETL = National Energy Technology Laboratory (Department of Energy, DOE, USA).
[b] PC = Pulverized coal plants, CFB = Circulating fluidized bed, Ind. boiler = Industrial boiler, T-firing = Tangential firing.
[c] anth. = anthracite, semi-anth. = semi-anthracite, bit. = bituminous coal, hv = high-volatile, mv = medium-volatile, lv bit. = low-volatile, sub-bit. = subbituminous coal, petcoke = petroleum coke, NG = Natural Gas.
[d] S. Korea = South Korea
N/A = Not available

Appendix B: CFD oxy-fuel simulations and sub-models

Reference	Simulated facility[a]	Fuel[b]	Code[c]	Turbulence[d]	Devolatilization[e]
[Al-Abbas12]	T-fired 550MWe boilers	Victorian brown coal	AVL Fire 2008	Std. k-ε	Single
[ChenL12]	100 kW_{th} test facility (U. RWTH Aachen)	Rhenish lign.	ANSYS® FLUENT 12	Std. k-ε, RNG k-ε, SST k-w, LES	Single
[Hjärtstam12]	Lab-scale 100 kW firing lignite unit (Chalmer U.)	Propane	ANSYS® FLUENT 12	Real. k-ε	-
[Andersson11a]	Lab-scale 100 kW firing lignite unit (Chalmer U.)	Propane, Lusatian lign.	N/A	N/A	-
[Habib12]	208 MW boiler (2 burners)	NG	FLUENT 6.2	RNG k–ε	-
[LiuJ12]	Pilot-scale IFRF furnace no.1 [Woycenko95]	Göttelborn hv bit. (hvBp)	N/A	RSM	CPD
[Habermehl12,Erfurth12]	70 MW_{th} burner, 1210 MW_{th} furnace (NRW power plant)	Kleinkopje hard coal	FLUENT 6.2	Std. k-ε	CPD
[Taniguchi11a-b]	DS®T-burner (Hitachi Power Europe, 30 MW_{th} Vattenfall's pilot plant)	35 coals (lign., sub-bit., bit., anth.) and one bio-mass.	FLUENT,OpenFOAM	Std. k-ε, LES	N/A
[ÁlvarezL12]	Entrained flow reactor (EFR)	anth., semi-anth., 2 hv. bit.	ANSYS® FLUENT 12	RNG k–ε	Single (FG-DVC)
[ÁlvarezL11]	Entrained flow reactor (EFR)	Semi-anth., 2 hv. bit.	ANSYS® FLUENT 12	RNG k–ε	Single (FG-DVC)
[Edge12,11b]	500 MWe sub-critical UK power station	Coal	ANSYS® FLUENT 12	RNG k–ε	CPD
[Edge11c]	0.5 MW_{th} Air- and oxy-fired combustion test facility with Doosan Babcock triple-staged low NOx burner and IFRF Aerodynamically air-staged burner	bit.	ANSYS® FLUENT 12	RNG k-ε and LES	Single
[Gharebaghi11a]	1 MW_{th} Combustion test facility (E.ON) with swirl-staged low NOx burner	bit.(Thoresby(UK), ElCerrejon (S. America), Cutacre(UK))	ANSYS® FLUENT 12.1	Std. k-ε, LES	Single (FG-DVC)
[Gharebaghi11b]	1 MW_{th} Combustion test facility (E.ON) with swirl-staged low NOx burner	bit.(Thoresby,UK)	ANSYS® FLUENT 12.1	Std. k-ε	CPD
[Al-Abbas11]	Lab-scale 100 kW firing lignite unit (Chalmer U.)	Lusatian lign.	AVL Fire 2008	Std. k-ε	Single

Reference	Simulated facility[a]	Fuel[b]	Code[c]	Turbulence[d]	Devolatilization[e]
[Kangwanpongpan10-12]	100 kW_{th} test facility (U. RWTH Aachen)	Rhenish lign.	ANSYS® FLUENT 12	RSM	CPD
[Kangwanpongpan09]	100 kW_{th} test facility (U. RWTH Aachen)	Rhenish lign.	FLUENT 6.3.26	RNG k–ε	CPD
[Jovanovic12]	Vertical DTR	Russian bit.	FLUENT 6.3.26	Std. k-ε, RNG k-ε, Std. k-ω, SST k-ω	Single
[Nikolopoulos11]	330 MW_e tangentially fired PC boiler (Meliti power plant, Greece), 8 burner sets (consisting of 3 burners/set)	lign. (Achlada mine)	ANSYS® FLUENT 12	Std. k-ε	Single
[ZhouWu11,10]	50 kW CFB (Southeast U., China)	Xuzhou bit.	FLUENT	Std. k-ε (fluid) / KTGF (solid)	Single
[GuM11]	Oxy-fuel furnace (Coal flow rate of 35kg/h)	pulv.	FLUENT 6.3	RNG k–ε	Two compet.
[Krzywanski11]	0.1 MW_{th} oxy-fuel CFB test rig	bit.	In-house code	N/A	Single
[Krzywanski10a-b]	670t/h CFB boiler (Turow Power Station, Poland)	Polish brown coal	In-house code	N/A	Single
[Yin10-11]	Lab-scale IFRF 0.8 MW oxy-natural gas flame furnace and 609 MW utility boiler assumed to be operated under oxy-fuel conditions (dry-FGR)	NG (mainly CH4)	ANSYS® FLUENT 12	Std. k-ε	-
[Galletti11,10]	Low NOx burner (TEA-C) installed in the 3 MW_{th} Fo.Sper furnace (ENEL, Liverno, Italy)	NG	FLUENT 6.3	SST k-ω	-
[Cuoci10]	0.78-1 MW semi-industrial furnace [Lallemant97]	NG	FLUENT 6.3.2	Std. k-ε (modified)	-
[Kuhr10]	20 kW cylindrical once-through furnace (IFK)	Lusatian lign.	FLUENT	Std. k-ε	N/A
[MüllerM10]	0.5 MW_{th} pilot scale test facility (IFK, U. Stuttgart)	Lusatian lign.	AIOLOS	Std. k-ε	FG-DVC
[ChenL10]	5 MW_{th} pressurized pilot scale coal-water slurry (CWS) oxy-fuel combustor	bit.	ANSYS® FLUENT 12	Real. k-ε, k-ω	CPD
[Krishnamoorthy10c]	Laboratory scale horizontal, cylindrical combustor [WangCS88]/300 MW frontwall- fired pulverized coal utility boiler [Costa07]	Coal	FLUENT 6.3	Std. k-ε	Constant
[ZhouWei10]	820 MW_e coal-fired boiler	bit.	FLUENT	Std. k-ε	N/A
[KimHS10]	Swirl burner (5,000 kcal/h)	LNG (CH_4)	In-house code	Std. k-ε	-
[Vascellari09]	2.4 MW_{th} IFRF furnace no.1	Göttelborn hv bit. (hvBp)	FLUENT 6.3	Std. k-ε	CPD
[Rehfeldt09]	1 MW_{th} horizontal firing facility (E.On, UK) and 500 kW_{th} down firing facility (IVD, U. Stuttgart)	Tselentis bit. and Lusatian lign.	FLUENT	Std. k-ε	Two compet.

Reference	Simulated facility[a]	Fuel[b]	Code[c]	Turbulence[d]	Devolatilization[e]
[Andersen09]	100 kW down-fired furnace (Chalmer U.)	Propane	FLUENT	Real. k-ε	-
[Krishnamoorthy09a]	300 MW frontwall- fired pulverized coal utility boiler [Costa07]	pulv.	FLUENT 6.3	Std. k-ε	Constant
[Krishnamoorthy09b]	120 MW PC tangentially fired boiler [Filkoski06]	Oslomej lign.	FLUENT 6.3	Std. k-ε	N/A
[Krishnamurthy09]	200 kW oxy-fuel burner	propane	CFX-11	Std. k-ε	N/A
[KimG09]	0.78 MW nonswirling IFRF furnace no.2 [Lallemant00]	NG	N/A	Std. k-ε (modified)	-
[Manickam09]	3 MW rotary kiln	bit.	FLUENT	Std. k-ε, RNG k-ε, Real. k-ε	Two compet.
[Chae09]	125 MW_{th} T-firing boiler (Young dong)	bit.	FLUENT 6.3	Real. k-ε	Single
[Erfurth09a-b]	1210 MW_{th} industrial boilers	bit.(Kleinkopje)	FLUENT 6.3	Real. k-ε	N/A
[Toporov08a]	100 kW_{th} test facility (U. RWTH Aachen)	Rhenish lign.	FLUENT 6.2	Std. k-ε	CPD
[Khare08b,Cao10]	IHI 1.2 MW_{th} vertical pilot scale test facility	Australian coal	FLUENT 6.2	Std. k-ε	Single
[Goanta08]	3 x 100 kW_{th} natural gas burners (TU München).	NG (mainly CH4)	ANSYS® CFX	Std. k-ε	-
[Becher07]	3 x 100 kW_{th} natural gas burners (TU München).	NG (mainly CH4)	ANSYS® CFX	Std. k-ω	-
[Hohenwarter07]	3 MW_{th} high recirculation-burner for oxy-coal (ENEL-TU Graz).	Hard coal	FLUENT 6.2.16	Std. k-ε	Single
[Toporov06]	80 kW pulverised fuel swirl burner.	pre-dried Rhenish lign.	FLUENT 6.2	Std. k-ε	CPD
[Chui04]	CANMET 0.3 MW_{th} Vertical Combustor Research Facility (VCRF)	Western Canadian sub-bit.	CFX-TASCflow	Std. k-ε	Single
[Chui03]	CANMET 0.3 MW_{th} Vertical Combustor Research Facility (VCRF)	Western Canadian sub-bit.	CFX-TASCflow	Std. k-ε	Single
[Guo03]	Oxygen–coal tubular combustor	bit.	In-house code	k–ε(fluid)–k_k (particle)	Two compet.
[Brink00a]	1MW_{th} IFRF furnace 2	NG	FLUENT	Std. k-ε	-
[NozakiT97]	IHI 1.2 MW_{th} horizontal combustion test facility	lv bit., mv bit.	VEGA-3	Std. k-ε	N/A
[WangCS88]	BCL Subscale horizontal, cylindrical combustor	sub-bit.(Wage coal,Colorado)	1-DICOG (BYU)	-	Two compet.
[Payne89]	117 kW_{th} bench scale, 3 MW_{th} pilot scale and 50 MW_e tangential fired boiler	sub bit.(Black Thunder), lignite (Beulah)	In-house code	N/A	Single

Reference	Radiation		Volatiles reactions		Char reactions	
	RTE[f]	Gas emittance[g]	Homogeneous reactions (intermediate species)[h]	Chemistry-Turbulence[i]	Reactants	Rate model/ kinetic model[j]
[Al-Abbas12]	DTM	WSGG (gray)	1-step	EBU	O_2, CO_2, H_2O	KD/Power-law
[ChenL12]	DOM (3 × 3)	WSGG (gray)	3-step (CO, H_2)	EDM	O_2, CO_2, H_2O	KD/Power-law
[Hjärtstam12]	DOM	WSGG (gray/non-gray, soot/wo. soot)	4-step	EDC	-	-
[Andersson11a]	DOM (S6 ordinates)	SNB (particle/soot radiation and wo.)	-	EDC	-	-
[Habib12]	DOM	-	1-step	EDM	-	-
[LiuJ12]	DOM	N/A	3-step (rev. water)	EDM, FRED, EDC	O_2, CO_2, H_2O	KD/CBK (O_2), Power-law (CO2,H2O)
[Habermehl12,Erfurth12]	DOM	WSGG (gray)	3-step (CO, H_2)	FRED	O_2, CO_2, H_2O	KD/Power-law
[Taniguchi11a-b]	N/A	N/A	N/A	-	N/A	N/A
[ÁlvarezL12]	DOM	WSGG (gray, domain based)	PDF tables	MF/PDF	O_2	KD/Intrinsic
[ÁlvarezL11]	DOM	WSGG (Gray, domain based)	PDF tables	MF/PDF	O_2	Intrinsic
[Edge12,11b]	DOM (3 × 3)	WSGG (Gray, domain based)	2-step (CO)	EDM	O_2	KD/Power-law
[Edge11c]	DOM	WSGG (gray)/FSK	2-step (CO)	EDM	O_2	KD/Intrinsic
[Gharebaghi11a]	DOM (3 × 3)	WSGG (gray)	2-step (CO)	EDM	O_2	KD/Intrinsic
[Gharebaghi11b]	DOM (3 × 3)	WSGG (gray)	2-step (CO)	EDC	O_2	KD/Intrinsic
[Al-Abbas11]	DTM	Uniform value of 0.24 m-1	1-step	EBU	O_2	KD/Power-law
[Kangwanpongpan10-12]	DOM (3 × 3)	WSGG (air), WSGG (oxyfuel 3-4 gray gases)	3-step (CO, H_2), rev. (CO-CO_2)	FRED	O_2, CO_2, H_2O	KD/Power-law

Reference	Radiation		Volatiles reactions		Char reactions	
	RTE[f]	Gas emittance[g]	Homogeneous reactions (intermediate species)[h]	Chemistry-Turbulence[i]	Reactants	Rate model/ kinetic model[j]
[Kangwanpongpan09]	P-1	WSGG (air)	3-step (CO, H_2)	FRED	O_2, CO_2, H_2O	KD/Power-law
[Jovanovic12]	DOM	WSGG (gray)	1-step	N/A	O_2	KD/Power-law
[Nikolopoulos11]	DOM	EWB	2-step (CO)	FRED	O_2, CO_2	KD/Power-law
[ZhouWu11,10]	N/A	N/A	3-step (CO, H_2)	N/A	O_2, CO_2, H_2O	KD/ Power-law (O_2), LH (CO_2,H_2O)
[GuM11]	DOM	N/A	N/A	N/A	O_2	KD/Power-law
[Krzywanski11]	N/A	N/A	3-step (CO, H_2)	Arrhenius	O_2, CO_2, H_2O	Arrhenius/Power-law
[Krzywanski10a-b]	Heat transf.	N/A	3-step (CO, H_2)	Arrhenius	O_2, CO_2, H_2O	Arrhenius/Power-law
[Yin10-11]	DOM (2 × 2)	WSGG (air), WSGG (oxyfuel 4 gray gases)	2-step (CO)	EDM	-	-
[Galletti11,10]	DOM, P1	WSGG (gray)	2-step, Modified 2-step	EDM, EDC	-	-
[Cuoci10]	DOM	N/A	Semi-detailed mech.(for CH_4)	EDC	-	-
[Kuhr10]	DOM	WSGG (gray)	2-step (CO)	EDM	O_2, CO_2	KD/Intrinsic
[MüllerM10]	DOM	Leckner	4-step	EDC	O_2, CO_2, H_2O	KD/Power-law
[ChenL10]	DOM	WSGG (gray)	Modified 4-step	FRED	O_2, CO_2, H_2O	KD/Power-law
[Krishnamoorthy10c]	DOM (3 × 3)	WSGG (gray), Perry, EWB, Patch mean absorption coefficient, SNB (RADCAL)	N/A	EDM	O_2	KD/Power-law
[ZhouWei10]	DOM	WSGG (gray, cell based)	2-step (CO)	EDM	N/A	N/A
[KimHS10]	FV energy loss rate	Planck mean absorption coefficient of H2O, CO2 and CO gases.	-	EBU	-	-
[Vascellari09]	P-1	N/A	Modified 4-step irrev.	EDC	O_2, CO_2, H_2O	KD/Intrinsic
[Rehfeldt09]	DOM	N/A	N/A	N/A	O_2, CO_2	N/A
[Andersen09]	P-1	-	2-step, Modified 2-step, 4-step and Modified 4-step	EDC	-	-

Reference	Radiation		Volatiles reactions		Char reactions	
	RTE[f]	Gas emittance[g]	Homogeneous reactions (intermediate species)[h]	Chemistry-Turbulence[i]	Reactants	Rate model/ kinetic model[j]
[Krishnamoorthy09a]	DOM (3 × 3)	WSGG (Gray), Perry, EWB	N/A	EDM	O_2	KD/Power-law
[Krishnamoorthy09b]	DOM	WSGG (Gray), Perry, EWB	N/A	EDM	N/A	N/A
[Krishnamurthy09]	P1	Gray model	N/A	EDC	N/A	N/A
[KimG09]	N/A	EWB	Detailed mech. (GRI Mech 2.11)	CMC	-	-
[Manickam09]	DOM, P1	N/A	PDF tables	MF/PDF	O_2	KD/Power-law
[Chae09]	P-1	WSGG (Gray)	N/A	FRED	N/A	KD/Power-law
[Erfurth09a-b]	DOM	EWB(oxy-fuel)	3 step	EDM	O_2, CO_2, H_2O	KD/Power-law
[Toporov08a]	DOM	WSGG (Gray)	3 step	FRED	O_2, CO_2, H_2O	KD/Power-law
[Khare08b,Cao10]	P-1	WSGG (Gray)	PDF tables	MF/PDF	O_2	KD/Power-law
[Goanta08]	P1, Monte Carlo	Absorption coefficient of 0.3, WSGG (Gray, domain based)	2-step (CO)	EDM, PDF Laminar. (GRI-Mech 3.0)	-	-
[Becher07]	DTM	N/A	2 multi-step react. (rev. water)	EDM	-	-
[Hohenwarter07]	P1	WSGG (Gray, cell based)	PDF tables	MF/PDF	O_2	KD/Power-law
[Toporov06]	DOM	WSGG (Gray, domain based)	3-step (CO, H_2)	EDC	O_2, CO_2, H_2O	KD/Power-law
[Chui04]	N/A	N/A	N/A	EBU	O_2	KD/Power-law
[Chui03]	N/A	N/A	N/A	EBU	O_2	KD/Power-law
[Guo03]	Four flux	-	2-step (CO)	EBU	O_2, CO_2	KD/Power-law
[Brink00a]	DTM	Absorption coefficient of 0.3	1-step, 2-step (CO), 3-step (CO, H_2)	presumed PDF, EDC	-	-
[NozakiT97]	Multi-flux	Three-gray-gas model	Volatiles comb.	EBU	O_2, CO_2, H_2O	N/A
[WangCS88]	Zone Method	Transparent gas	N/A	Chem. Equi.	O_2, CO_2, H_2O	Arrhenius/Power-law
[Payne89]	Monte Carlo	WSGG (4,7 gray gases)	N/A	N/A	N/A	KD/Power-law

Reference	Geometry		Boundary conditions		Numerical methods			Aim of research
	Dimension[k]	Mesh (cells)[l]	Inlet streams	Swirling inlets[m]	Approach	Discretization[n]	Pressure-velocity[o]	
[Al-Abbas12]	3D	293k/559k/1 Mio.	2	-	Euler-Lagrange	1st UPWIND (continuity), 2nd UPWIND (others)	SIMPLE	CFD modeling, retrofitting
[ChenL12]	2D (axisym.)/3D quarter	24k quad./590.8k hexa.	3	2nd	-	2nd UPWIND	SIMPLE	CFD modeling, turbulent models
[Hjärtstam12]	3D, quarter	375k	3	3rd	-	2nd UPWIND	SIMPLE	Soot and gas radiation
[Andersson11a]	2D (axisym.)	N/A	N/A	3rd	-	N/A	N/A	Particle/soot and gas radiation
[Habib12]	3D	1 Mio.	2	N/A	-	N/A	N/A	Compare air/oxy-firing
[LiuJ12]	2D (axisym.)	39,445	2	2nd	Euler-Lagrange	N/A	SIMPLE	Compare air/oxy-firing
[Habermehl12,Erfurth12]	3D	1,24 Mio. hexa.	3	2nd	Euler-Lagrange	N/A	SIMPLEC	CFD modeling
[Taniguchi11a-b]	N/A	N/A	-	N/A	N/A	N/A	N/A	Flameability limit
[ÁlvarezL12]	3D quarter	75k	3	N/A	Euler-Lagrange	N/A	N/A	NO_x emission
[ÁlvarezL11]	3D quarter	75k	2	N/A	Euler-Lagrange	N/A	N/A	CFD modeling
[Edge12,11b]	3D	3.2 Mio., mostly hexa. (1.8 Mio. within burners)	3	2nd, 3rd	Euler-Lagrange	N/A	N/A	Heat transfer
[Edge11c]	3D	1.6 Mio. hexa.	3	2nd, 3rd	Euler-Lagrange	N/A	N/A	Compare turbulence models
[Gharebaghi11a]	3D	3 Mio. mostly hexa.	3	1st,2nd,3rd	Euler-Lagrange	2nd UPWIND	SIMPLE	CFD with LES turbulence model
[Gharebaghi11b]	3D	350k	3	1st,2nd,3rd	Euler-Lagrange	N/A	SIMPLE	Validate modified CBK model
[Al-Abbas11]	3D	136k/224k/480k	2	2nd	Euler-Lagrange	1st UPWIND (continuity), 2nd UPWIND (others)	SIMPLE	Burner design

Reference	Geometry		Boundary conditions		Numerical methods			Aim of research
	Dimension[k]	Mesh (cells)[l]	Inlet streams	Swirling inlets[m]	Approach	Discretization[n]	Pressure-velocity[o]	
[Kangwanpongpan10-12]	3D 1/6 model (axisym.)	100k hexa.	3	2nd	Euler-Lagrange	2nd UPWIND	SIMPLE	CFD modeling
[Kangwanpongpan09]	3D 1/6 model (axisym.)	100k hexa.	3	2nd	Euler-Lagrange	2nd UPWIND	SIMPLE	CFD modeling
[Jovanovic12]	2D (axisym.)/3D	113k quad./1,216k hexa.	2	-	Euler-Lagrange	2nd UPWIND	SIMPLE	CFD modeling
[Nikolopoulos11]	3D	1,064k tet.	2/burner	2nd	Euler-Lagrange	N/A	SIMPLE	CFD modeling
[ZhouWu11,10]	2D	50,000 quad.	2	-	Euler-Euler	N/A	N/A	Combustion charcteristics
[GuM11]	3D quarter	141,899	2	2nd	Euler-Lagrange	N/A	N/A	Combustion charcteristics
[Krzywanski11]	1D, 3D	N/A	N/A	N/A	N/A	N/A	N/A	CFB simulation
[Krzywanski10a-b]	1D, 3D	N/A	N/A	N/A	N/A	N/A	N/A	CFB simulation
[Yin10-11]	3D full / quarter (fine mesh)	608k / 7,074k hexa.	2	N/A	-	N/A	N/A	Radiation modeling (new WSGG model)
[Galletti11,10]	3D quarter	3.4-4.5 Million	3	N/A	N/A	2nd UPWIND	N/A	Compare air/oxy-firing
[Cuoci10]	2D (axisym.)	50k-400k	2	-	N/A	2nd UPWIND	SIMPLE	NO_x emission
[Kuhr10]	2D (axisym.)	160k-220k quad.	2	N/A	Euler-Lagrange		N/A	CFD modeling, Boudouard reaction
[MüllerM10]	3D	2.2 Mio.	4	4rd	Euler-Lagrange		SIMPLE	Compare air/oxy-firing
[ChenL10]	2D (axisym.)	19,300	2	2nd	Euler-Lagrange		SIMPLE	Combustion characteristics of Pressurized oxy-fuel
[Krishnamoorthy10c]	2D (axisym.)/3D	916.9k (3D)	2	N/A	Euler-Lagrange	N/A	N/A	Radiation modeling (new WSGG model)
[ZhouWei10]	3D	N/A	3	N/A	Euler-Lagrange	N/A	N/A	Combustion characteristics
[KimHS10]	2D (axisym.)	2500 quad.	2	2nd	-	Power-law	SIMPLEC	Retrofitting
[Vascellari09]	2D (axisym.)	18,000	2	2nd	Euler-Lagrange	2nd UPWIND	SIMPLE	Performance and FGR

Reference	Geometry		Boundary conditions		Numerical methods			Aim of research
	Dimension[k]	Mesh (cells)[l]	Inlet streams	Swirling inlets[m]	Approach	Discretization[n]	Pressure-velocity[o]	
[Rehfeldt09]	3D (E.On) / 3D axisym. (IVD)	1.5 Mio.(E.On)/ 125k(IVD)	2 (E.On), 3 (IVD)	3rd (E.On), 2nd (IVD)	Euler-Lagrange	N/A	N/A	Compare air/oxy-firing
[Andersen09]	2D (axisym.)	30k	2	2nd	-	2nd UPWIND	N/A	Homogeneous reaction mechanism
[Krishnamoorthy09a]	3D	916,934	2	N/A	Euler-Lagrange	N/A	N/A	Compare radiation models
[Krishnamoorthy09b]	3D	N/A	2	-	Euler-Lagrange	N/A	N/A	Compare radiation models
[Krishnamurthy09]	3D 1/12 model (flame mode) / half model (flameless mode)	0.7 Mio. nodes (flame mode) / 2.4 Mio. (flame-less mode)	Vary (pipes injection)	N/A	-	N/A	N/A	Flame/Flameless
[KimG09]	2D (axisym.)	10,080 tri.	2	-	N/A	cell-center	N/A	Turbulence-chemistry
[Manickam09]	2D (axisym.)/3D	33k/400k	2	-	Euler-Lagrange	N/A	SIMPLEC	CFD modeling
[Chae09]	3D	600k	N/A	N/A	Euler-Lagrange	N/A	N/A	Boiler design
[Erfurth09a-b]	3D	1.24 Mio.	N/A	N/A	Euler-Lagrange	N/A	SIMPLE	CFD modeling, Boiler design
[Toporov08a]	3D 1/6 model (axisym.)	590.8k	4	2nd	Euler-Lagrange	N/A	SIMPLEC	CFD modeling
[Khare08b,Cao10]	2D (axisym.)	50k	2	2nd	Euler-Lagrange	N/A	N/A	Momentum flux ratio, NO_x emission
[Goanta08]	3D	N/A	4	N/A	-	N/A	N/A	Stochiometry/FGR
[Becher07]	3D	N/A	4	N/A	-	N/A	N/A	Stochiometry/FGR
[Hohenwarter07]	3D	N/A	3	N/A	Euler-Lagrange	2nd UPWIND	SIMPLE	Burner design
[Toporov06]	3D	N/A	4	2nd	Euler-Lagrange		SIMPLEC	CFD modeling
[Chui04]	3D	425k	4,5	Vary	Euler-Lagrange	N/A	N/A	Burner design
[Chui03]	3D	460k	4,5	Vary	Euler-Lagrange	N/A	N/A	Burner design
[Guo03]	2D (axisym.)	N/A	3	N/A	Euler-Euler	UPWIND	SIMPLE	Combustor design
[Brink00a]	2D (axisym.)	20k	1	1	-	N/A	N/A	Turbulence-chemistry
[NozakiT97]	3D (axisym.)	N/A	2	2nd	Euler-Lagrange	N/A	N/A	Improve combustibility
[WangCS88]	1D	N/A	2	-	N/A	N/A	N/A	Confirm operation
[Payne89]	2D	N/A	2	-	N/A	N/A	N/A	FGR, heat trasnsfer

[a] IVD = Institut für Verfahrenstechnik und Dampfkesselwesen, IFK = Institut für Feuerungs- und Kraftwerkstechnik (Institute of Combustion and Power Plant Technology), TU = Technische Universität (University of Technology), U. = University, NRW = North Rhine-Westphalia, DTR = drop tube reactor.

[b] pulv. = pulverized coal, anth. = anthracite, semi-anth. = semi-anthracite, bit. = bituminous coal, lv = low-volatile, mv = medium-volatile, hv = high-volatile, lign. = lignite, NG = natural gas, LNG = liquid natural gas.

[c] BYU = Brigham Young University.

[d] Std. k-ε = Standard k-ε, Std. k-ω = Standard k-ω, Real. k-ε = Realizable k-ε, KTGF = Kinetic Theory of Granular Flow.

[e] Single = Single step first-order reaction model [Badzioch70], two compet. = two competing rate model [Kobayashi77], CPD = Chemical percolation devolatilization model [Fletcher92], FG = Functional Group devolatilization model, FG-DVC = Funtional group-depolymerization, vaporization, and cross-linking model [Solomon88], Constant = Constant devolatilization rate model [Baum71].

[f] RTE = Radiative transfer equation, DOM = Discrete ordinate method [Chandrasekahr60], 3×3 = 3×3 ordinate directions, 2×2 = 2×2 ordinate directions, Heat transf. = Heat transfer calculations, DTM = Discrete transfer method [Lockwood81], FV = Finite-volume.

[g] WSGG = Weighted-sum-of-gray-gases model, SNB = statistical narrow band model, EWB = exponential wide band model [Edward76], FSK = full spectrum k-distribution, Leckner = Leckner's model [Leckner72], Perry = Perry's model [Hottel07].

[h] KD = Kinetic-diffusion limited rate model for char reaction rate model [Field69], Power-law = Global power-law for kinetic rate model, Intrinsic = Intrinsic model for kinetic rate [SmithIW82], CBK = Carbon burnout kinetic model [Hurt98], LH = Langmuir-Hinshellwood kinetic rate model, Arrhenius = Arrhenius-type equation.

[i] 1-step = Global 1-step reaction mechanism, 2-step = Global 2-step reaction mechanism, 3-step = Global 3-step reaction mechanism, 4-step = Global 4-step reaction mechanism, react. = reaction, mech. = mechanisms, irr. = irreversible reaction, rev. = reversible reaction, water = water gas shift reaction, comb. = combustion.

[j] EBU = Eddy break-up model [Spalding71], EDM = Eddy dissipation model [Magnussen77], FRED = Finite rate eddy dissipation model [Magnussen77], EDC = Eddy dissipation concept [Magnussen81], MF/PDF = Mixture fraction/Probability density function (chemical equialibrium model) [Pope00], Arrhenius = Arrhenius-type equation, CMC = Conditional moment closure, Laminar. = Laminar flamelets, Chem. Equi. = Chemical equilibrium.

[k] 1D = one dimension, 2D = two dimension, 3D = three dimension, axisym. = axisymmetry, quarter = quarter (1/4) model, full = full scale model

[l] Mio. = Million, quad. = quadrilateral, hexa. = hexahedral, tet. = tetrahedral, tri. = traiangular, k = 1,000 cells

[m] 1st = Primary stream, 2nd = Secondary stream

[n] 1st UPWIND = first order upwind-difference scheme, 2nd UPWIND = second order upwind-difference scheme, power-law = power-law scheme, cell-center = cell-centered collocated scheme

[o] SIMPLE = Semi-Implicit Method for Pressure-Linked Equations, SIMPLER = SIMPLE Revised, SIMPLEC = SIMPLE-Consistent.

N/A = Data Not Available

Appendix C: Oxy-fuel correlations for radiation properties

Table C.1. The weighting factors $w_{1,t}$, $w_{2,t}$, $w_{3,t}$ and $w_{4,t}$ varying with temperatures from 400-2500 K for MR = 0.125-0.5.

T	$T_n = T/T_{ref}$	MR = 0.125				MR = 0.25				MR = 0.5			
		κ_1	κ_2	κ_3	κ_4	κ_1	κ_2	κ_3	κ_4	κ_1	κ_2	κ_3	κ_4
		0.0411731	0.343891	3.71074	106.08	0.0450792	0.386642	3.76416	96.0343	0.0491914	0.421502	3.85239	83.534
		$w_{1,t}$	$w_{2,t}$	$w_{3,t}$	$w_{4,t}$	$w_{1,t}$	$w_{2,t}$	$w_{3,t}$	$w_{4,t}$	$w_{1,t}$	$w_{2,t}$	$w_{3,t}$	$w_{4,t}$
400	0.2	0.3322695	0.2693620	0.2026480	0.1036743	0.3042753	0.2442467	0.2362442	0.1229820	0.2878123	0.2041953	0.2654539	0.1485752
500	0.25	0.3247233	0.3338374	0.1907305	0.0955769	0.3010829	0.3045620	0.2329753	0.1116939	0.2917284	0.2552741	0.2724917	0.1348279
600	0.3	0.3174482	0.3646855	0.1783652	0.0936545	0.2925285	0.3404834	0.2226614	0.1069835	0.2788405	0.2956687	0.2656986	0.1272191
700	0.35	0.3143197	0.3673320	0.1684976	0.0932009	0.2859854	0.3522007	0.2115146	0.1039331	0.2653589	0.3165821	0.2553339	0.1207842
800	0.4	0.3157986	0.3543028	0.1618051	0.0917528	0.2846100	0.3484733	0.2024796	0.1001050	0.2588417	0.3219852	0.2463811	0.1134602
900	0.45	0.3207644	0.3348618	0.1571993	0.0886307	0.2885563	0.3370571	0.1953764	0.0948738	0.2602775	0.3184594	0.2390984	0.1049505
1000	0.5	0.3284360	0.3138692	0.1533296	0.0840396	0.2970411	0.3227114	0.1890140	0.0884893	0.2682196	0.3111217	0.2321188	0.0957079
1100	0.55	0.3381352	0.2933983	0.1492409	0.0784725	0.3089753	0.3077927	0.1823969	0.0814551	0.2807792	0.3027974	0.2242877	0.0863083
1200	0.6	0.3490425	0.2741612	0.1444313	0.0724232	0.3231218	0.2932960	0.1749730	0.0742489	0.2961646	0.2947074	0.2150344	0.0772203
1300	0.65	0.3603141	0.2562296	0.1387655	0.0662749	0.3382426	0.2795224	0.1665847	0.0672258	0.3128078	0.2872039	0.2042699	0.0687552
1400	0.7	0.3712708	0.2392672	0.1322184	0.0602766	0.3533854	0.2663101	0.1571728	0.0605875	0.3296264	0.2801174	0.1920091	0.0610346
1500	0.75	0.3811233	0.2232679	0.1251690	0.0545850	0.3675226	0.2536229	0.1472536	0.0544656	0.3455270	0.2732072	0.1789747	0.0541601
1600	0.8	0.3894272	0.2081093	0.1178602	0.0492697	0.3800638	0.2413421	0.1371511	0.0488861	0.3598899	0.2662353	0.1656480	0.0480937
1700	0.85	0.3959480	0.1935705	0.1104475	0.0443558	0.3907291	0.2292403	0.1270530	0.0438288	0.3724526	0.2589096	0.1523065	0.0427458
1800	0.9	0.4005478	0.1795807	0.1031231	0.0398376	0.3993396	0.2172242	0.1172048	0.0392550	0.3830265	0.2510781	0.1392902	0.0380299
1900	0.95	0.4032032	0.1661212	0.0960334	0.0357052	0.4058416	0.2052680	0.1077893	0.0351284	0.3915367	0.2426896	0.1268499	0.0338697
2000	1	0.4039792	0.1531930	0.0892763	0.0319363	0.4102736	0.1933879	0.0989236	0.0314058	0.3979931	0.2337667	0.1151475	0.0301905
2100	1.05	0.4029939	0.1408187	0.0829097	0.0285090	0.4127284	0.1816375	0.0906707	0.0280498	0.4024570	0.2243893	0.1042728	0.0269299
2200	1.1	0.4003980	0.1290304	0.0769602	0.0254003	0.4133330	0.1700913	0.0830533	0.0250265	0.4050241	0.2146727	0.0942614	0.0240348
2300	1.15	0.3963563	0.1178585	0.0714320	0.0225883	0.4122333	0.1588276	0.0760638	0.0223057	0.4058138	0.2047426	0.0851077	0.0214611
2400	1.2	0.3910374	0.1073280	0.0663142	0.0200508	0.4095859	0.1479192	0.0696766	0.0198600	0.4049629	0.1947222	0.0767813	0.0191706
2500	1.25	0.3846074	0.0974556	0.0615866	0.0177663	0.4055500	0.1374300	0.0638543	0.0176641	0.4026173	0.1847250	0.0692358	0.0171304

Table C.2. The weighting factors $w_{1,t}$, $w_{2,t}$, $w_{3,t}$ and $w_{4,t}$ varying with temperatures from 400-2500 K for MR = 0.75-2.0.

T	$T_n = T/T_{ref}$	MR = 0.75				MR = 1				MR = 2			
		κ_1	κ_2	κ_3	κ_4	κ_1	κ_2	κ_3	κ_4	κ_1	κ_2	κ_3	κ_4
		0.0507841	0.431878	3.90878	75.5255	0.051446	0.436145	3.94827	69.781	0.0518318	0.440593	3.98102	56.0818
		$w_{1,t}$	$w_{2,t}$	$w_{3,t}$	$w_{4,t}$	$w_{1,t}$	$w_{2,t}$	$w_{3,t}$	$w_{4,t}$	$w_{1,t}$	$w_{2,t}$	$w_{3,t}$	$w_{4,t}$
400	0.2	0.2813968	0.1820798	0.2758534	0.1654346	0.2774876	0.1693287	0.2791567	0.1774781	0.2686255	0.1494699	0.2749160	0.2050150
500	0.25	0.2885238	0.2280949	0.2877668	0.1511452	0.2863498	0.2123082	0.2936129	0.1632740	0.2804387	0.1865164	0.2928579	0.1923378
600	0.3	0.2722260	0.2702653	0.2836261	0.1420139	0.2677479	0.2551349	0.2914893	0.1532155	0.2577054	0.2289626	0.2955357	0.1806824
700	0.35	0.2544748	0.2949655	0.2752755	0.1333293	0.2472857	0.2815840	0.2851498	0.1429208	0.2323618	0.2571078	0.2949261	0.1668262
800	0.4	0.2449863	0.3041647	0.2681091	0.1235241	0.2359599	0.2926443	0.2799042	0.1312804	0.2178722	0.2705057	0.2953704	0.1509512
900	0.45	0.2450032	0.3040460	0.2623157	0.1126315	0.2351628	0.2942874	0.2757777	0.1186026	0.2159204	0.2746980	0.2963039	0.1340812
1000	0.5	0.2525635	0.2999974	0.2563237	0.1012828	0.2425582	0.2920629	0.2710349	0.1056614	0.2234092	0.2753666	0.2956438	0.1173347
1100	0.55	0.2651963	0.2951233	0.2488632	0.0901212	0.2552466	0.2892503	0.2643212	0.0931563	0.2364954	0.2760958	0.2918349	0.1015613
1200	0.6	0.2807740	0.2906979	0.2393876	0.0796114	0.2708774	0.2871255	0.2551193	0.0815509	0.2523261	0.2781510	0.2844105	0.0872381
1300	0.65	0.2976016	0.2869964	0.2278965	0.0700335	0.2876925	0.2858771	0.2435039	0.0711026	0.2690191	0.2815112	0.2736168	0.0745779
1400	0.7	0.3145826	0.2837663	0.2144925	0.0614523	0.3045954	0.2851802	0.2296486	0.0618348	0.2854957	0.2856862	0.2597962	0.0635115
1500	0.75	0.3306434	0.2806057	0.2000219	0.0539560	0.3205385	0.2845224	0.2144765	0.0538306	0.3008007	0.2899419	0.2440109	0.0541254
1600	0.8	0.3451810	0.2771781	0.1850726	0.0474660	0.3349383	0.2834993	0.1986478	0.0469840	0.3144252	0.2937318	0.2270691	0.0462592
1700	0.85	0.3579561	0.2731408	0.1699925	0.0418450	0.3475771	0.2817318	0.1825621	0.0411233	0.3262231	0.2965993	0.2094880	0.0396637
1800	0.9	0.3687906	0.2682946	0.1551896	0.0369739	0.3582940	0.2789849	0.1666772	0.0361057	0.3361005	0.2982236	0.1918353	0.0341457
1900	0.95	0.3776132	0.2625597	0.1409691	0.0327482	0.3670304	0.2751524	0.1513403	0.0318059	0.3440520	0.2984294	0.1745563	0.0295327
2000	1	0.3844318	0.2559472	0.1275345	0.0290695	0.3738022	0.2702305	0.1367890	0.0281075	0.3501327	0.2971633	0.1579727	0.0256670
2100	1.05	0.3893030	0.2485375	0.1150063	0.0258562	0.3786707	0.2642917	0.1231708	0.0249140	0.3544313	0.2944652	0.1423007	0.0224170
2200	1.1	0.3923152	0.2404552	0.1034411	0.0230403	0.3817260	0.2574601	0.1105624	0.0221454	0.3570554	0.2904415	0.1276722	0.0196738
2300	1.15	0.3935817	0.2318419	0.0928467	0.0205655	0.3830819	0.2498818	0.0989859	0.0197360	0.3581303	0.2852341	0.1141497	0.0173483
2400	1.2	0.3932332	0.2228410	0.0831993	0.0183847	0.3828685	0.2417090	0.0884260	0.0176316	0.3577924	0.2790026	0.1017475	0.0153674
2500	1.25	0.3914115	0.2135885	0.0744548	0.0164586	0.3812272	0.2330891	0.0788441	0.0157870	0.3561846	0.2719105	0.0904458	0.0136718

Table C.3. The weighting factors $w_{1,t}$, $w_{2,t}$, $w_{3,t}$ and $w_{4,t}$ varying with temperatures from 400-2500 K for MR = 4.0.

T	$T_n = T/T_{ref}$	MR = 4			
		κ_1	κ_2	κ_3	κ_4
		0.0516866	0.444449	3.93374	44.7501
		$w_{1,t}$	$w_{2,t}$	$w_{3,t}$	$w_{4,t}$
400	0.2	0.2601295	0.1418874	0.2603035	0.2268827
500	0.25	0.2739487	0.1738988	0.2796223	0.2167806
600	0.3	0.2494379	0.2143141	0.2863219	0.2044080
700	0.35	0.2216108	0.2423248	0.2910629	0.1878293
800	0.4	0.2057050	0.2565126	0.2969604	0.1685107
900	0.45	0.2035991	0.2619503	0.3028501	0.1481461
1000	0.5	0.2117316	0.2640976	0.3064415	0.1281423
1100	0.55	0.2255732	0.2666668	0.3060214	0.1094895
1200	0.6	0.2418062	0.2710405	0.3010760	0.0927114
1300	0.65	0.2584492	0.2771078	0.2919496	0.0780007
1400	0.7	0.2744927	0.2842552	0.2791292	0.0652131
1500	0.75	0.2891124	0.2915896	0.2637673	0.0544517
1600	0.8	0.3018991	0.2984570	0.2467831	0.0455197
1700	0.85	0.3127821	0.3043452	0.2287867	0.0381084
1800	0.9	0.3217315	0.3088713	0.2104259	0.0319888
1900	0.95	0.3287909	0.3118073	0.1922180	0.0269551
2000	1	0.3340537	0.3130571	0.1745506	0.0228177
2100	1.05	0.3376367	0.3126275	0.1576980	0.0194162
2200	1.1	0.3396679	0.3106029	0.1418403	0.0166165
2300	1.15	0.3402864	0.3071132	0.1270797	0.0143076
2400	1.2	0.3396360	0.3023159	0.1134603	0.0123983
2500	1.25	0.3378623	0.2963799	0.1009857	0.0108138

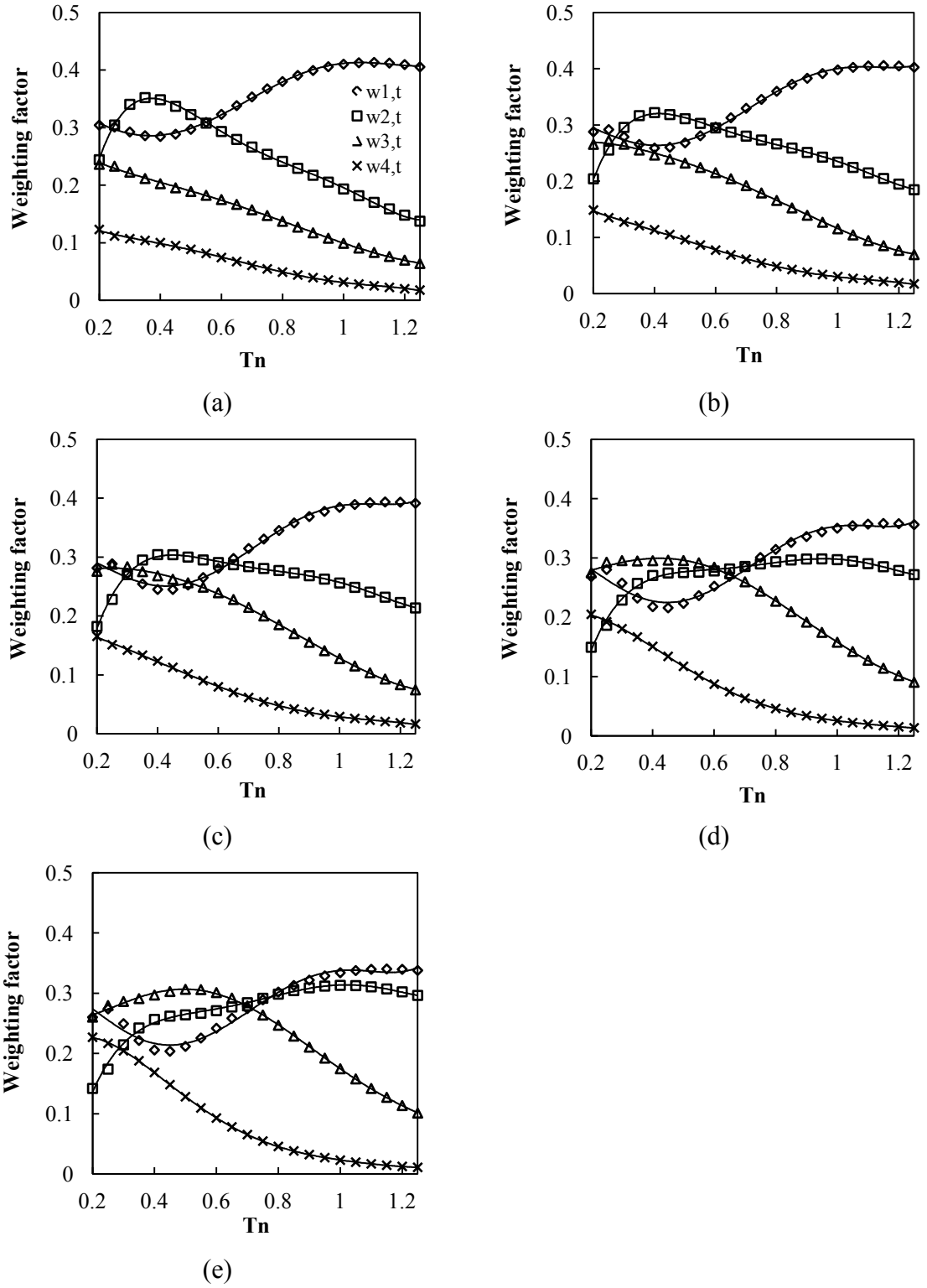

Figure C.1. The plots of weighting factors $w_{1,t}$, $w_{2,t}$, $w_{3,t}$ and $w_{4,t}$ varying with normalized temperatures (T_n), T_{ref} = 2000 K (solid line = polynomial fitted curves, symbol = values evaluated for each gas temperature, T) for: (a) MR = 0.25, (b) MR = 0.5, (c) MR = 0.75, (d) MR = 2.0, (e) MR = 4.0.

Appendix D: Total emittance charts from LBL integration of HITEMP 2010 database and from new oxy-fuel correlations

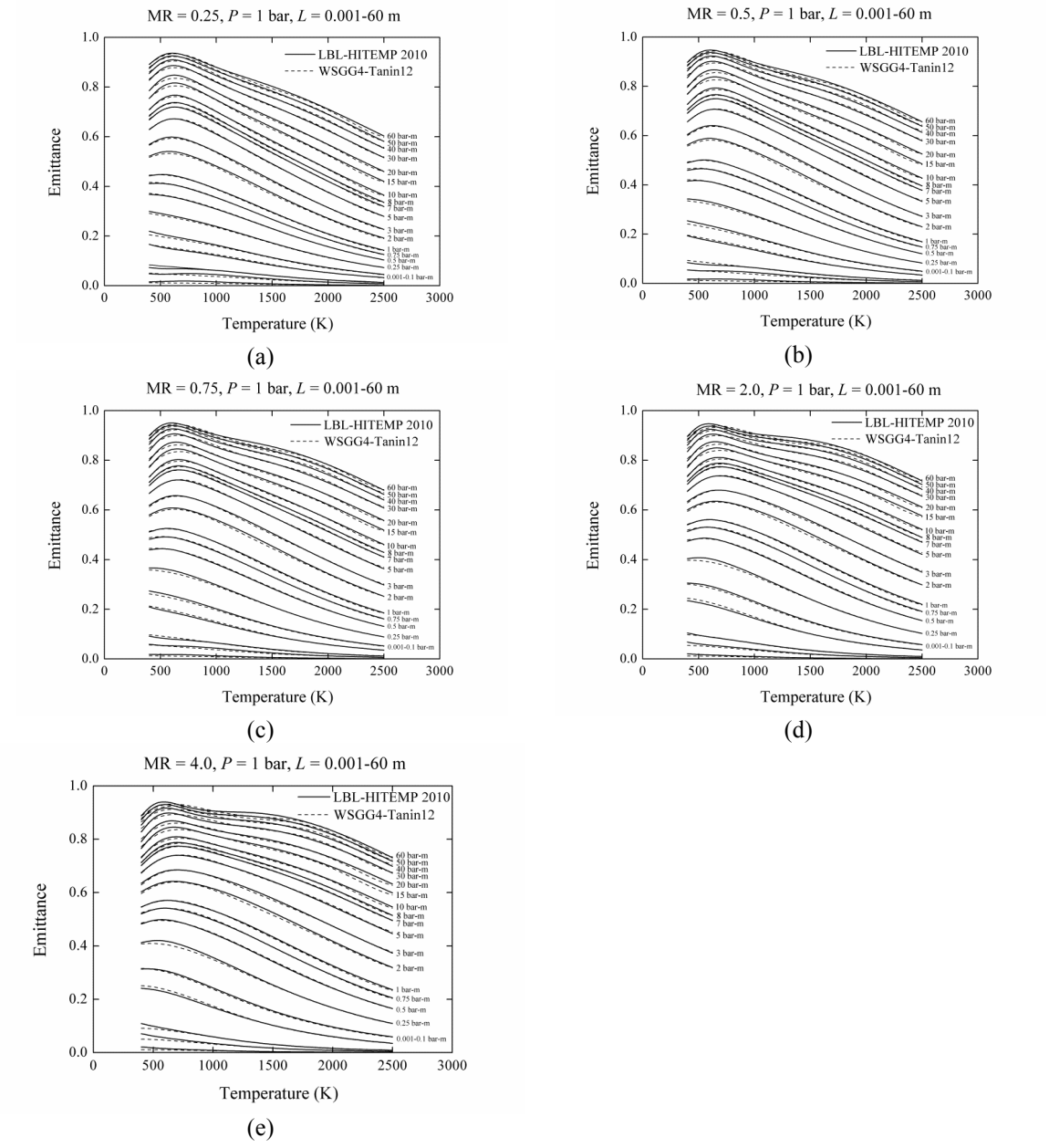

Figure D.1. Total emittance dependence with temperatures calculated from LBL integration of HITEMP 2010 database (solid lines) and from the proposed correlations of the WSGG model (dashed lines) for: (a) MR = 0.25, (b) MR = 0.5, (c) MR = 0.75, (d) MR = 2.0, (e) MR = 4.0.

Appendix E: Radiative source terms and heat fluxes for path-lengths of 1, 10 and 60 m (P = 1 bar)

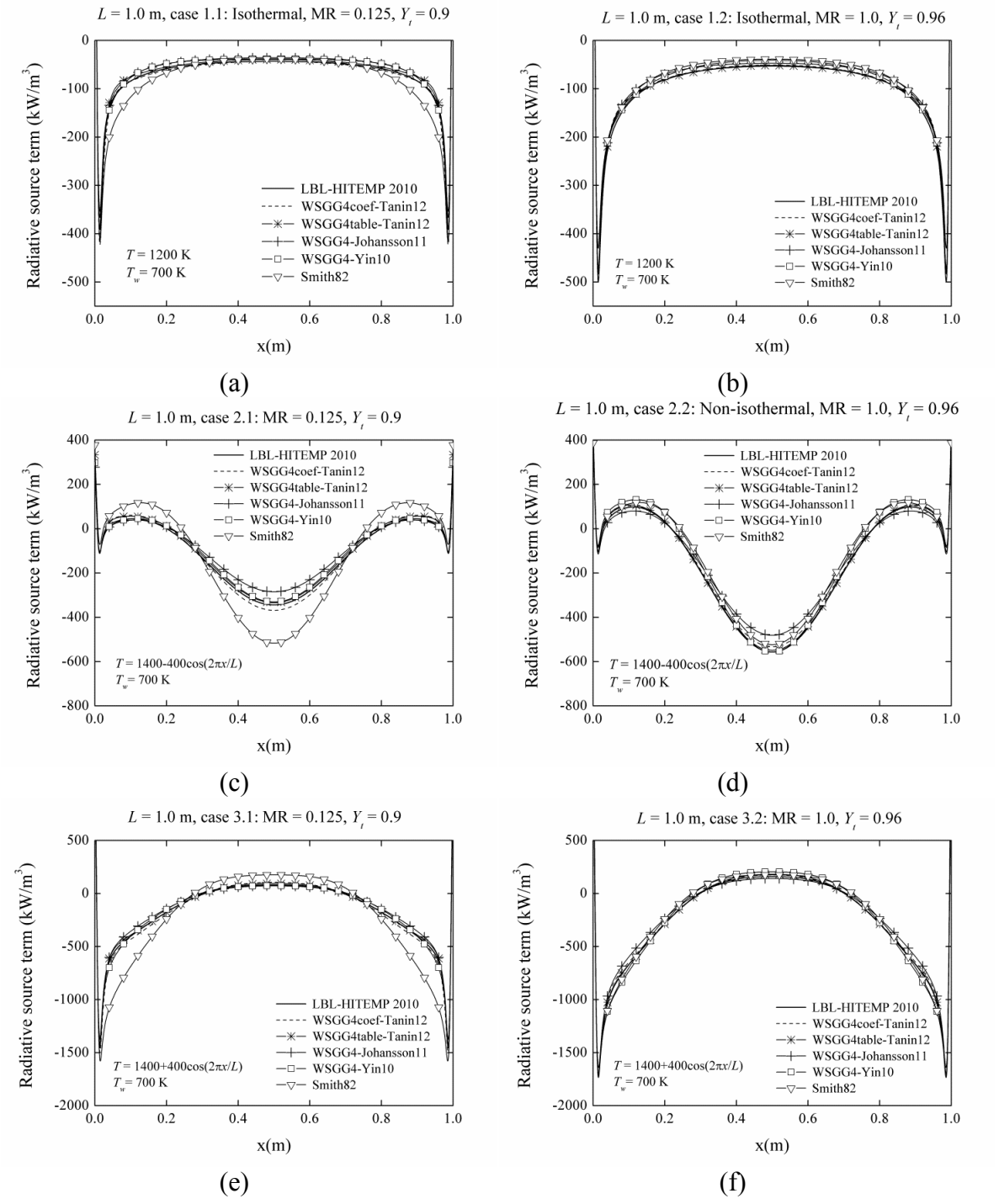

Figure E.1. Radiative source terms ($\dot{q}$) computed with different correlations of the WSGG model along length coordinates for path-lengths of 1.0 m: isothermal and non-isothermal homogeneous cases (case 1-3).

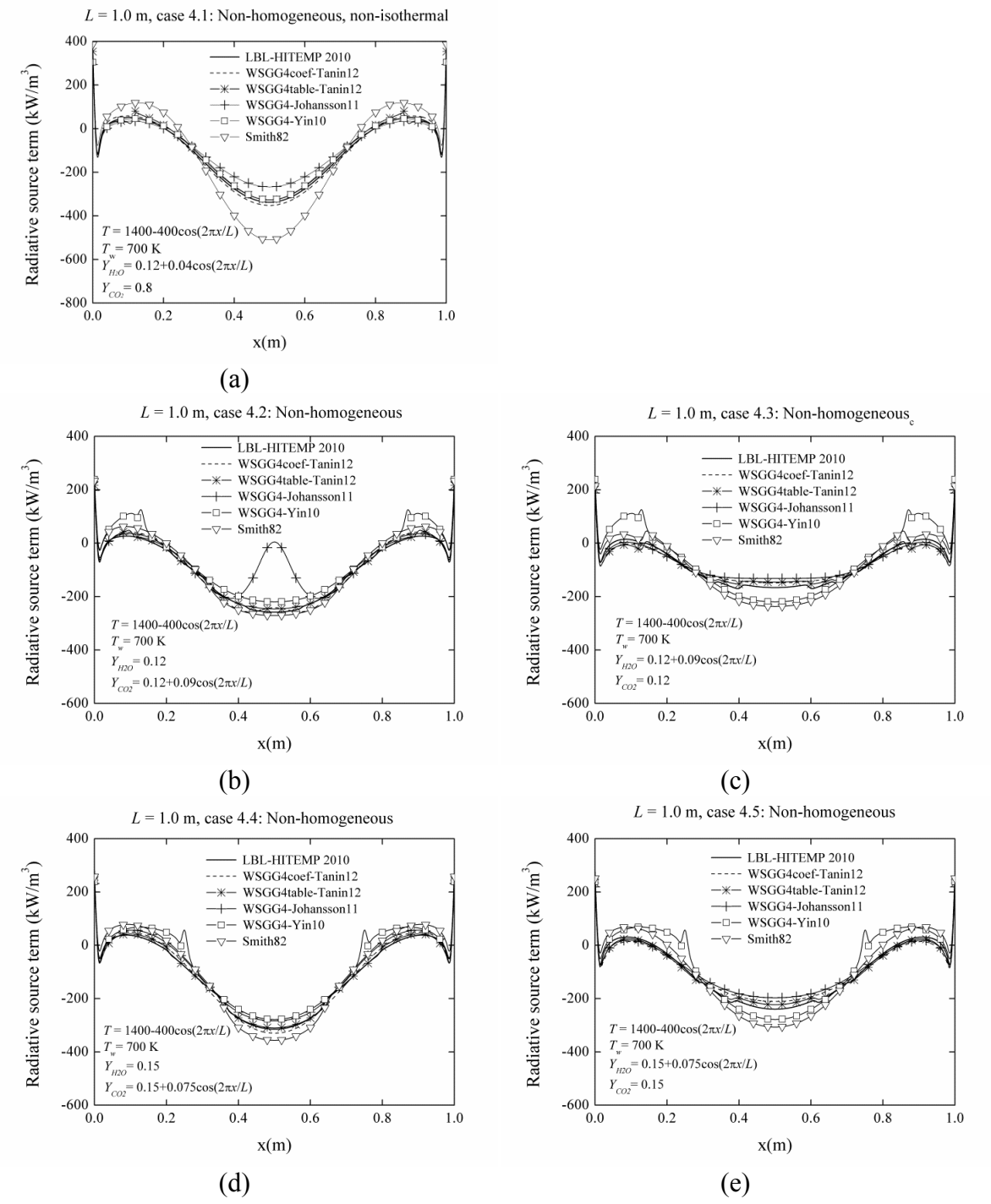

Figure E.2. Radiative source terms ($\dot{q}$) computed with different correlations of the WSGG model along length coordinates for path-lengths of 1.0 m: non-isothermal non-homogeneous cases (case 4).

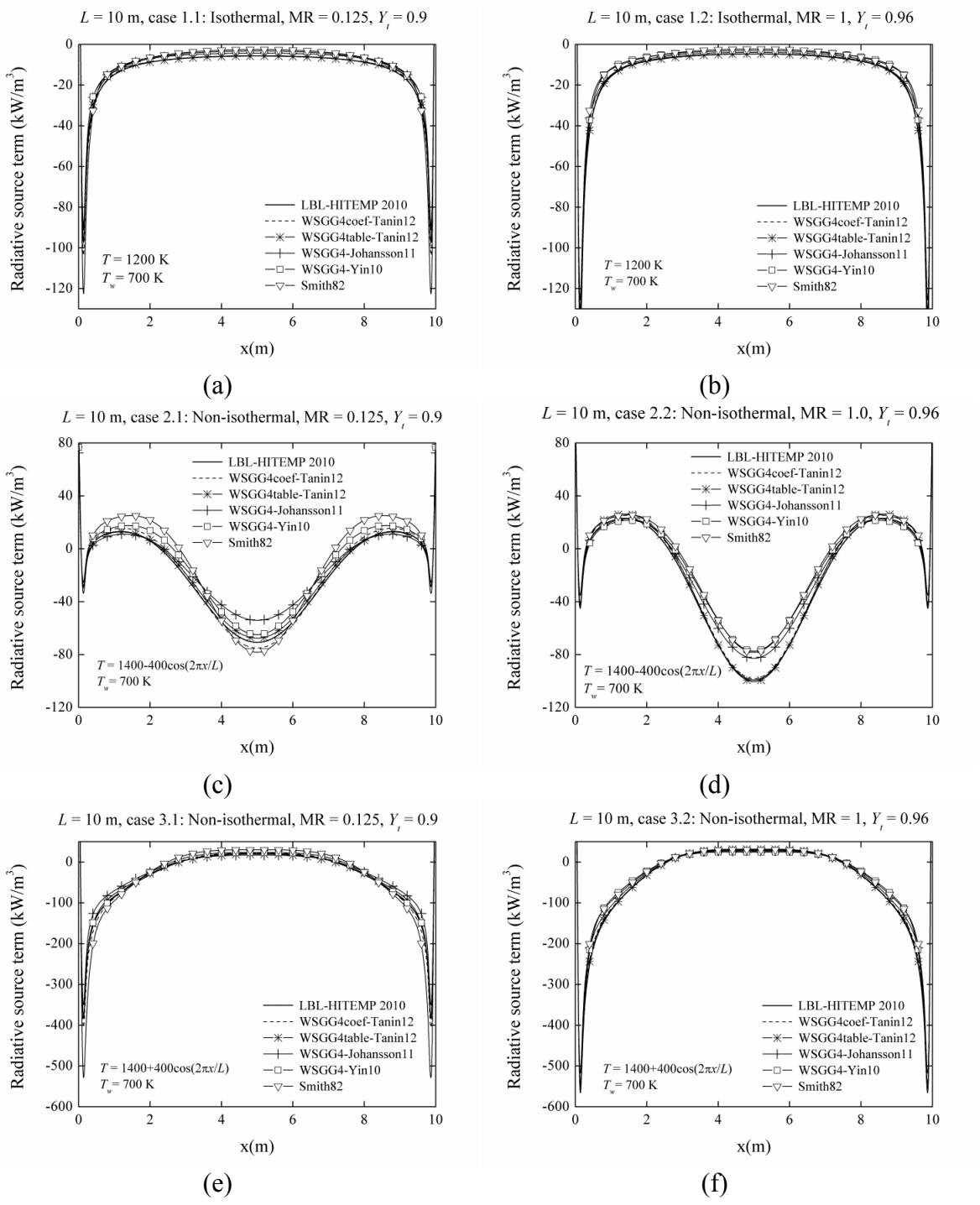

Figure E.3. Radiative source terms ($\dot{q}$) computed with different correlations of the WSGG model along length coordinates for path-lengths of 10 m: isothermal and non-isothermal homogeneous cases (case 1-3).

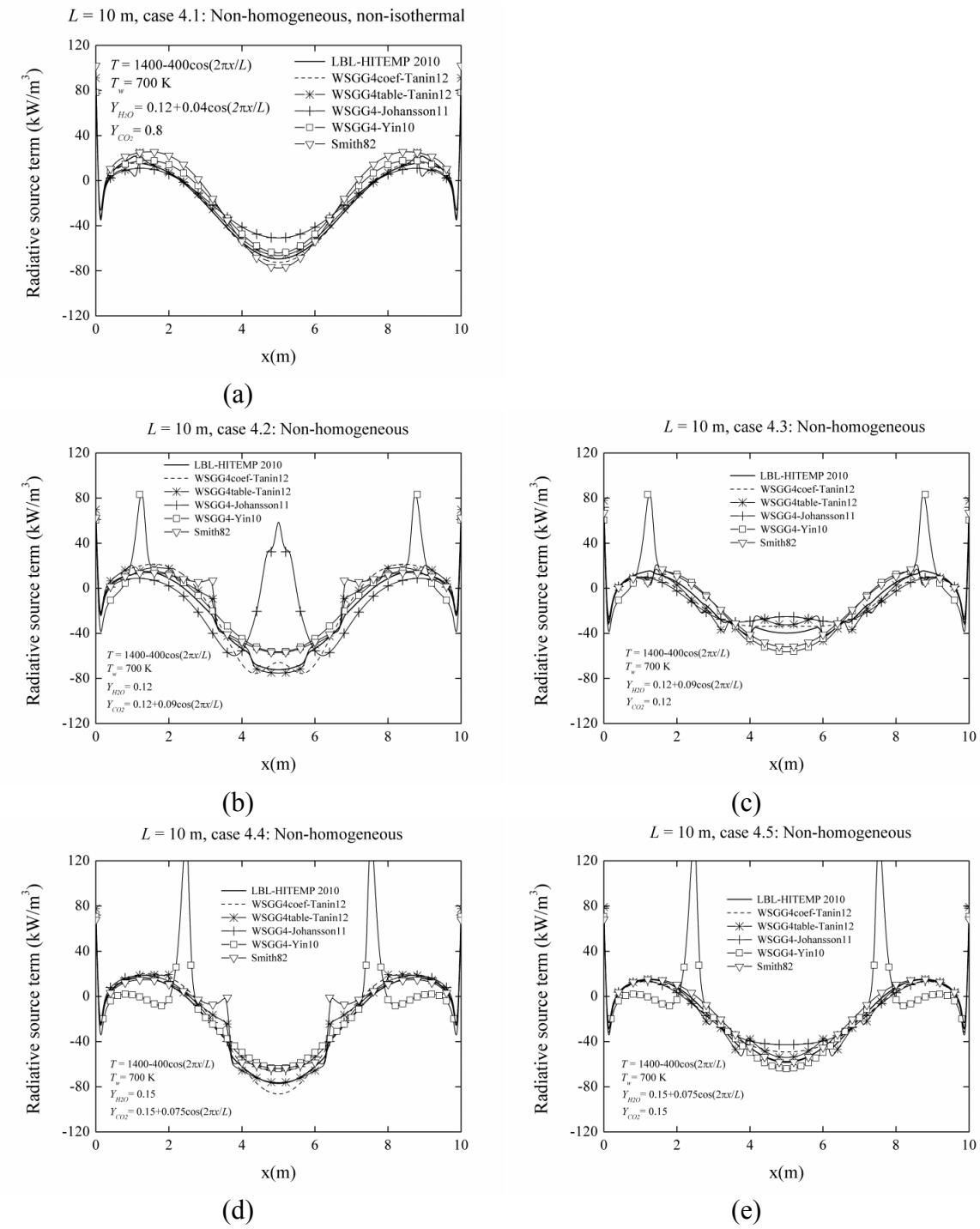

Figure E.4. Radiative source terms ($\dot{q}$) computed with different correlations of the WSGG model along length coordinates for path-lengths of 10 m: non-isothermal non-homogeneous cases (case 4).

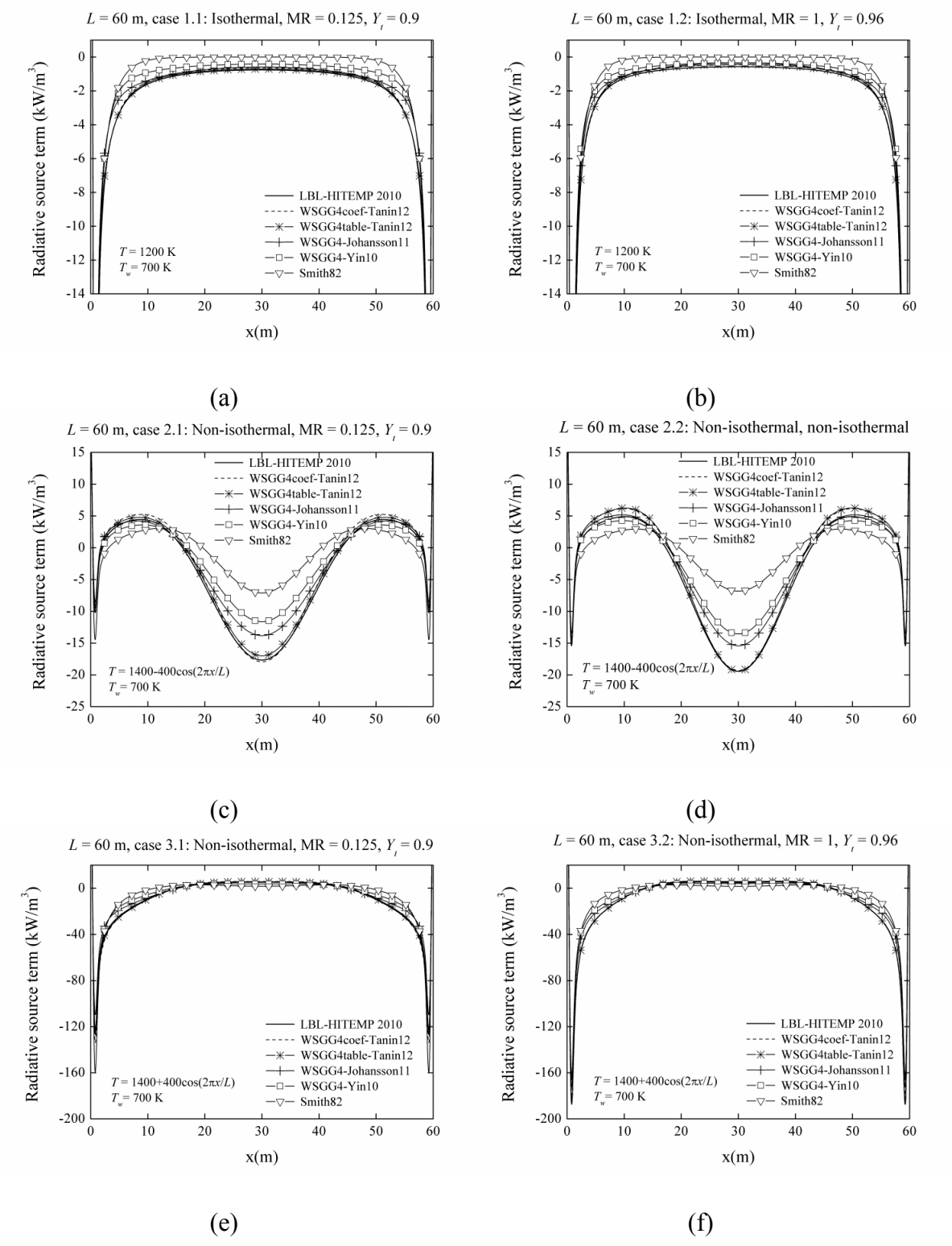

Figure E.5. Radiative source terms ($\dot{q}$) computed with different correlations of the WSGG model along length coordinates for path-lengths of 60 m: isothermal and non-isothermal homogeneous cases (case 1-3).

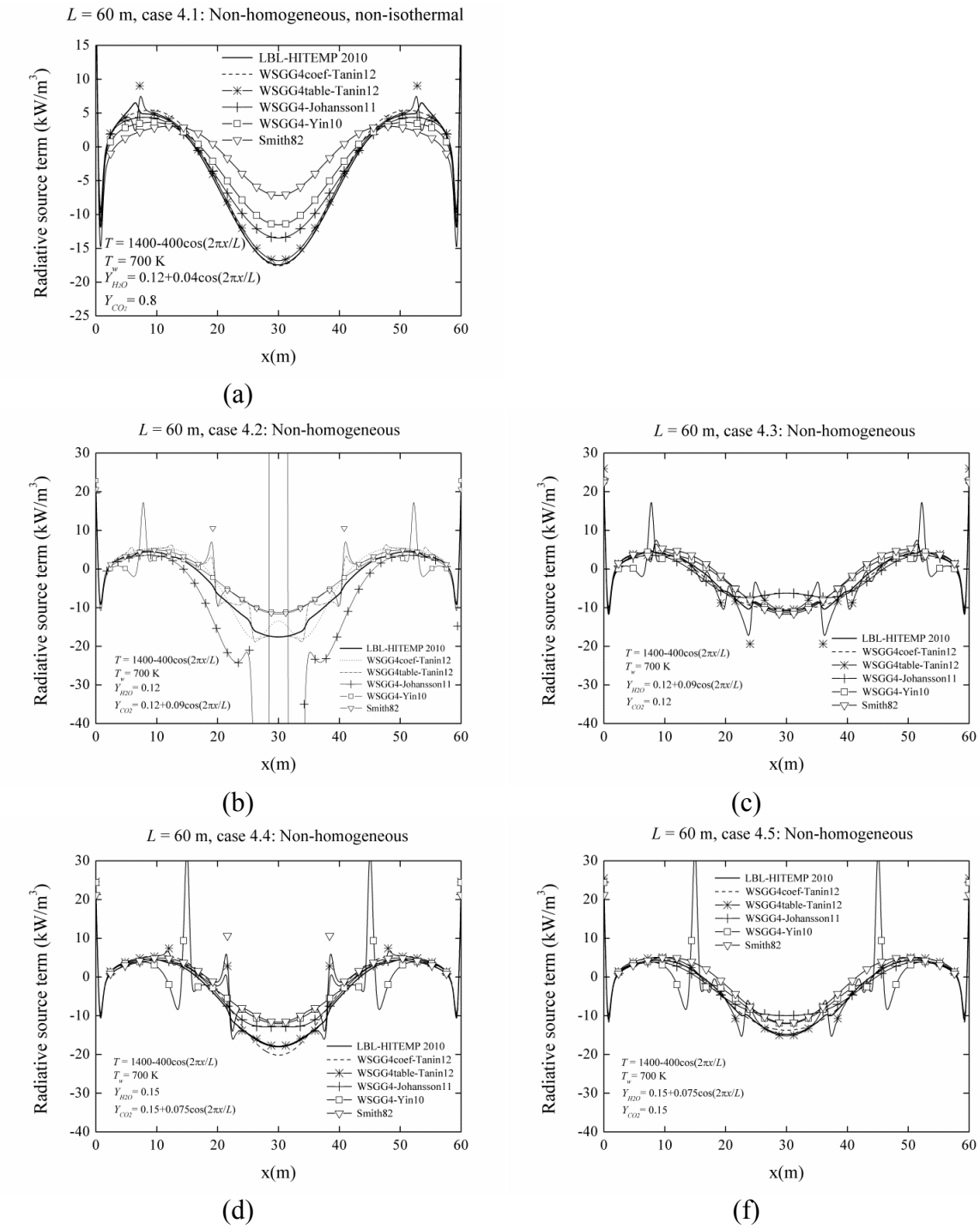

Figure E.6. Radiative source terms ($\dot{q}$) computed with different correlations of the WSGG model along length coordinates for path-lengths of 60 m: non-isothermal non-homogeneous cases (case 4).

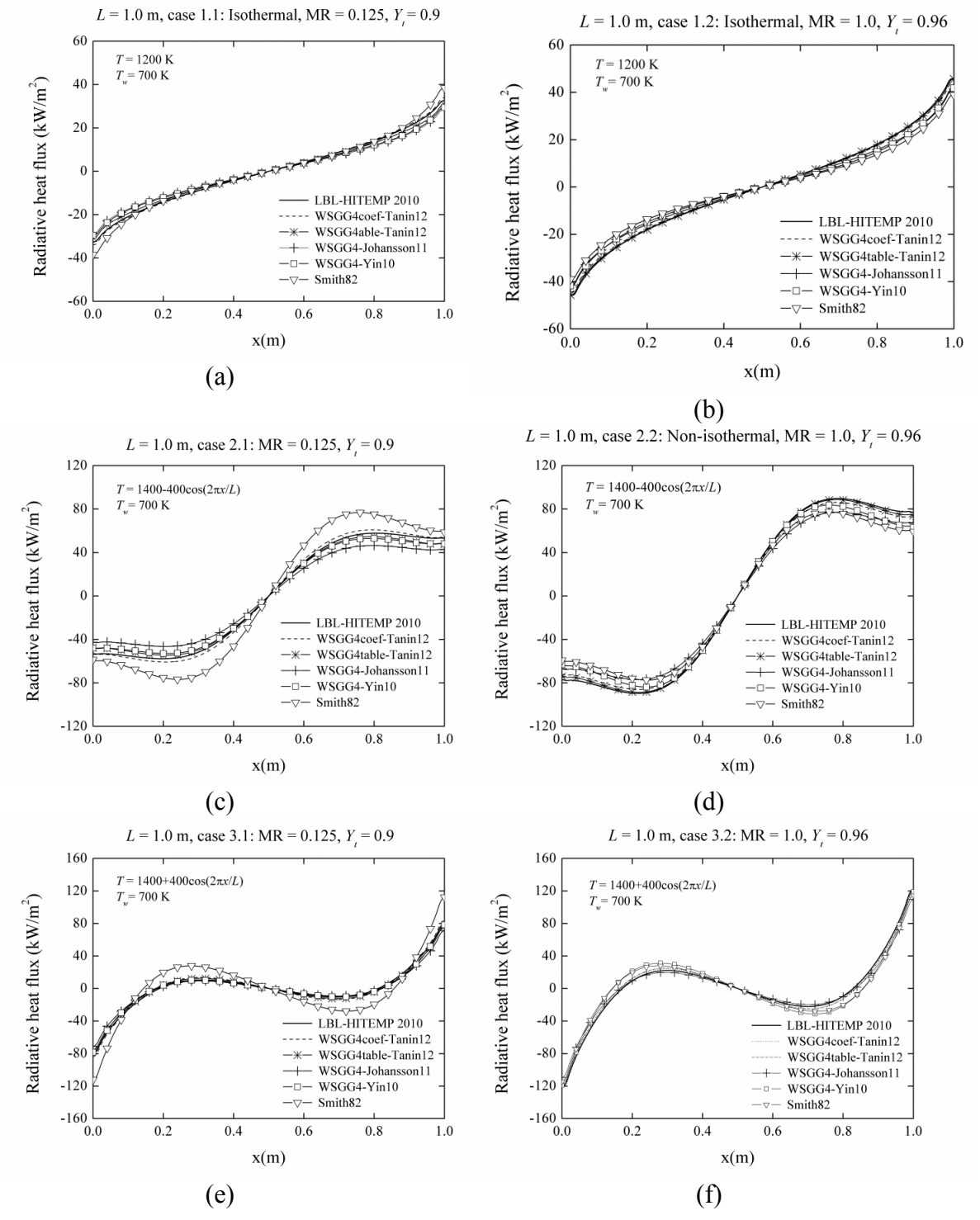

Figure E.7. Radiative heat fluxes (q_w) computed with different correlations of the WSGG model along length coordinates for path-lengths of 1.0 m: isothermal and non-isothermal homogeneous cases (case 1-3).

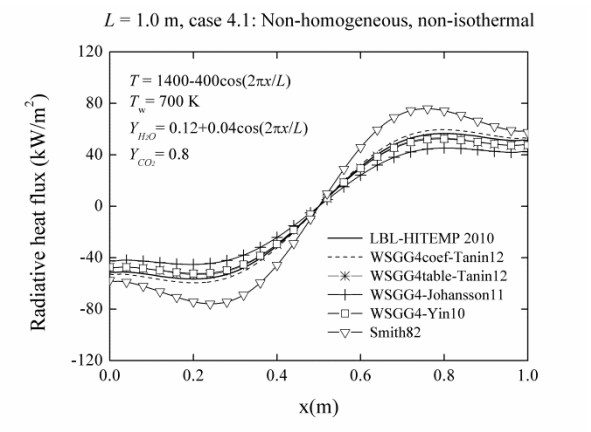

(a)

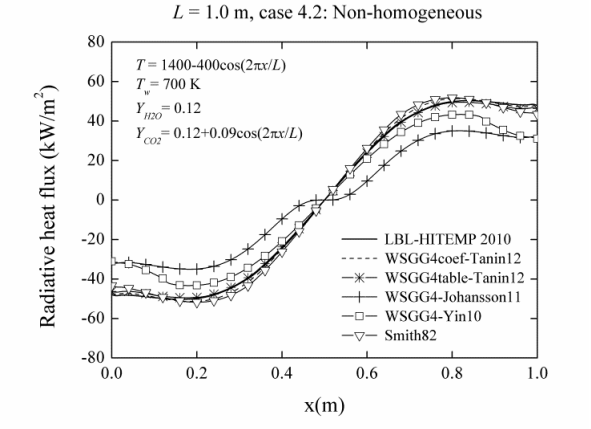

(b)

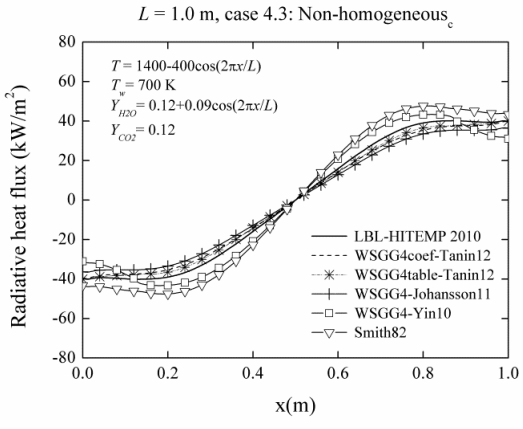

(b)

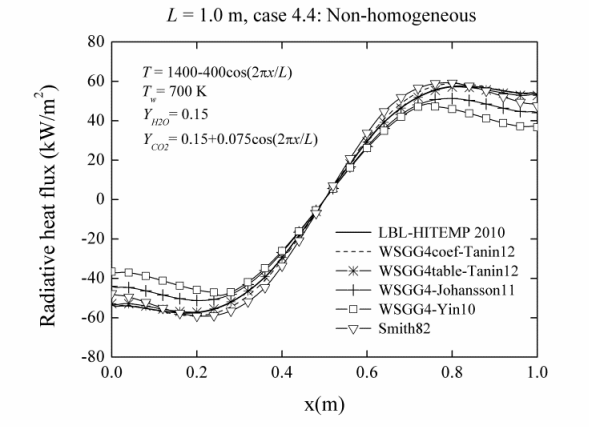

(c)

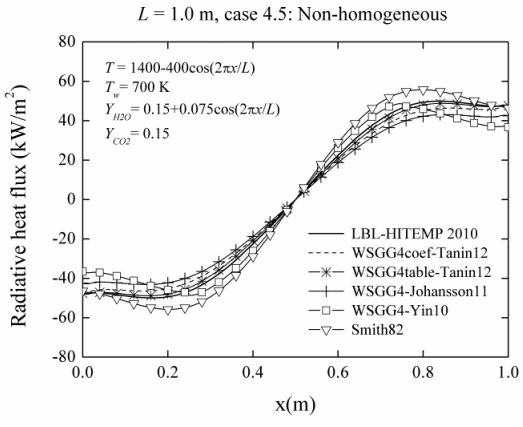

(d)

Figure E.8. Radiative heat fluxes (q_w) computed with different correlations of the WSGG model along length coordinates for path-lengths of 1.0 m: non-isothermal non-homogeneous cases (case 4).

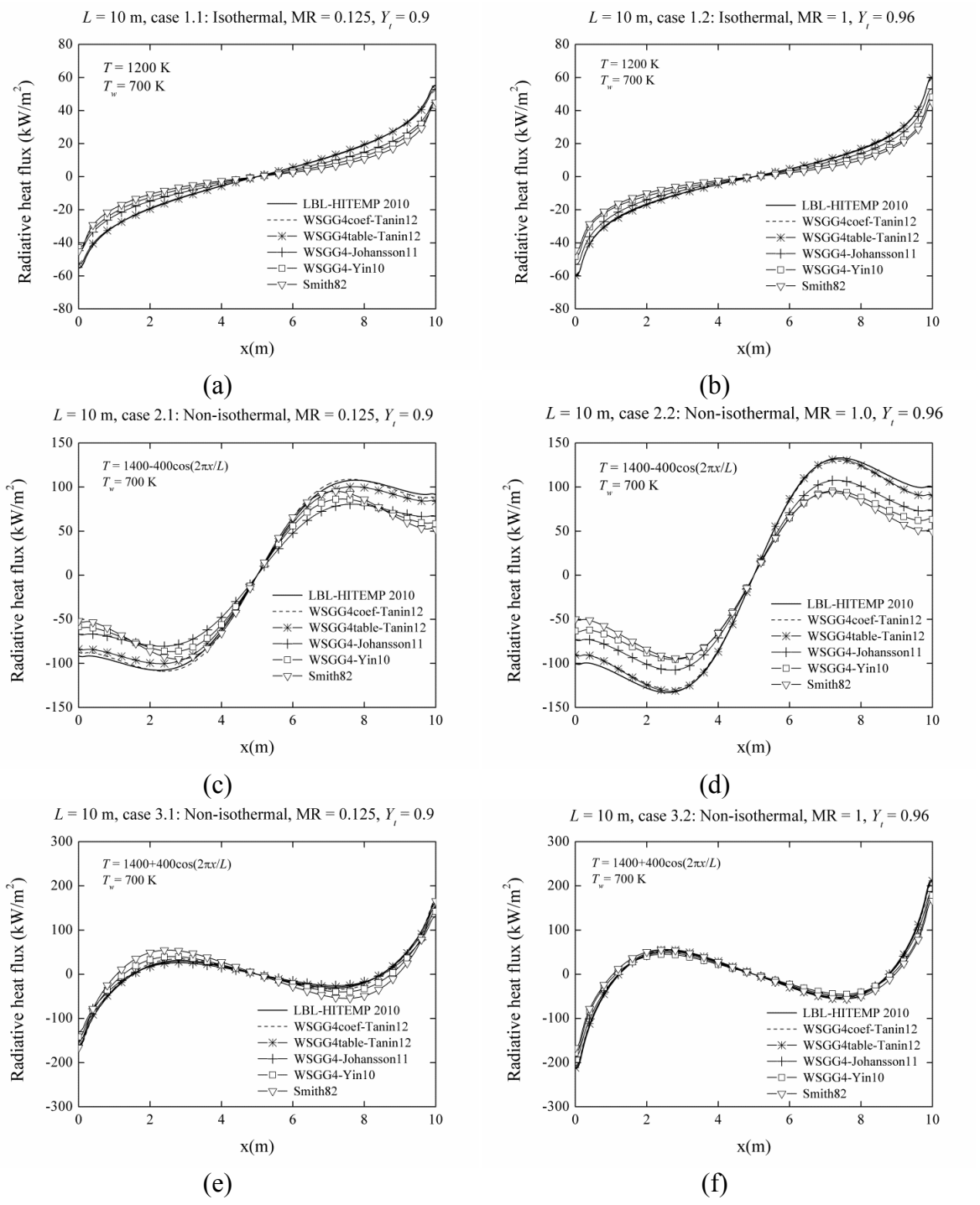

Figure E.9. Radiative heat fluxes (q_w) computed with different correlations of the WSGG model along length coordinates for path-lengths of 10 m: isothermal and non-isothermal homogeneous cases (case 1-3).

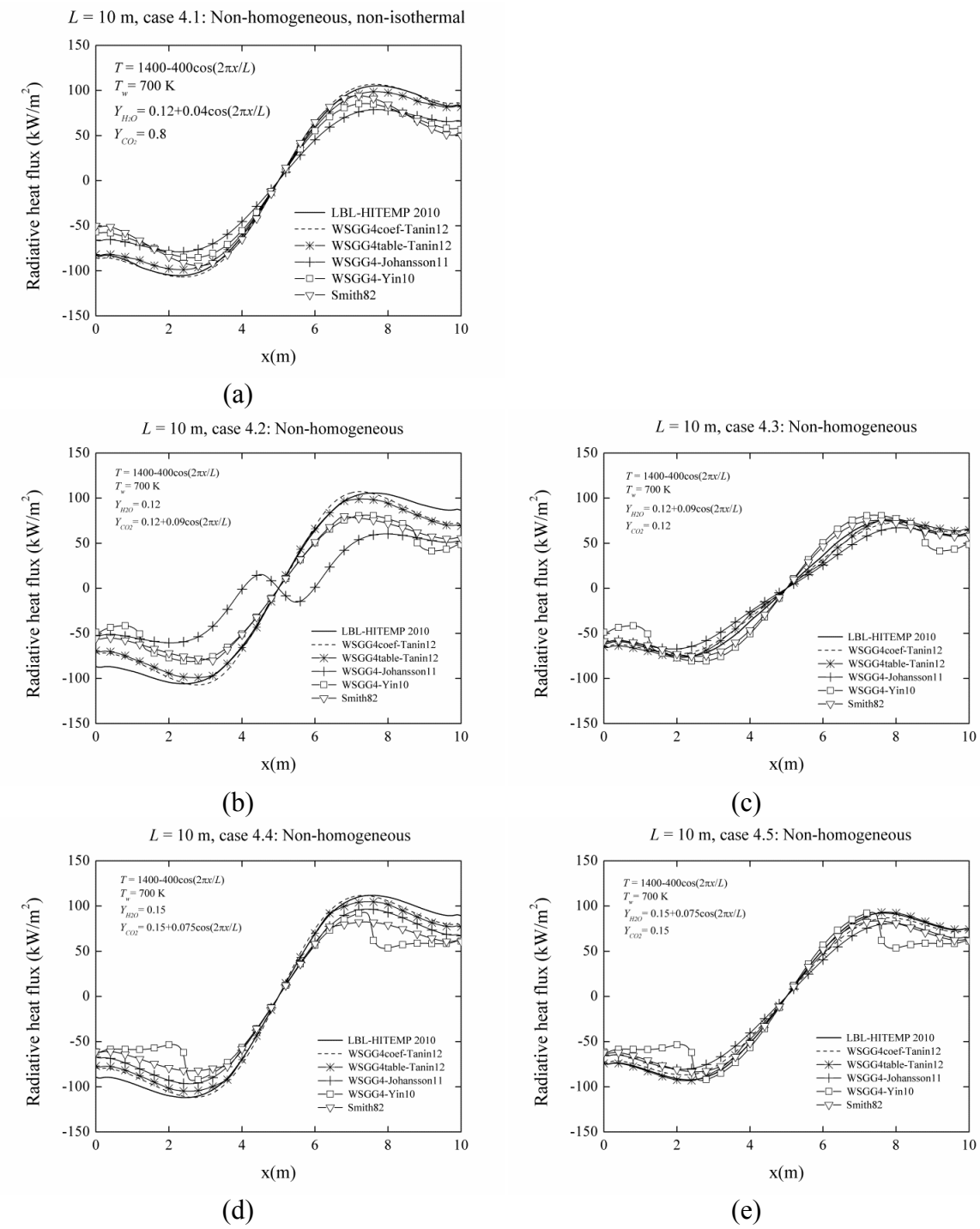

Figure E.10. Radiative heat fluxes (q_w) computed with different correlations of the WSGG model along length coordinates for path-lengths of 10 m: non-isothermal non-homogeneous cases (case 4).

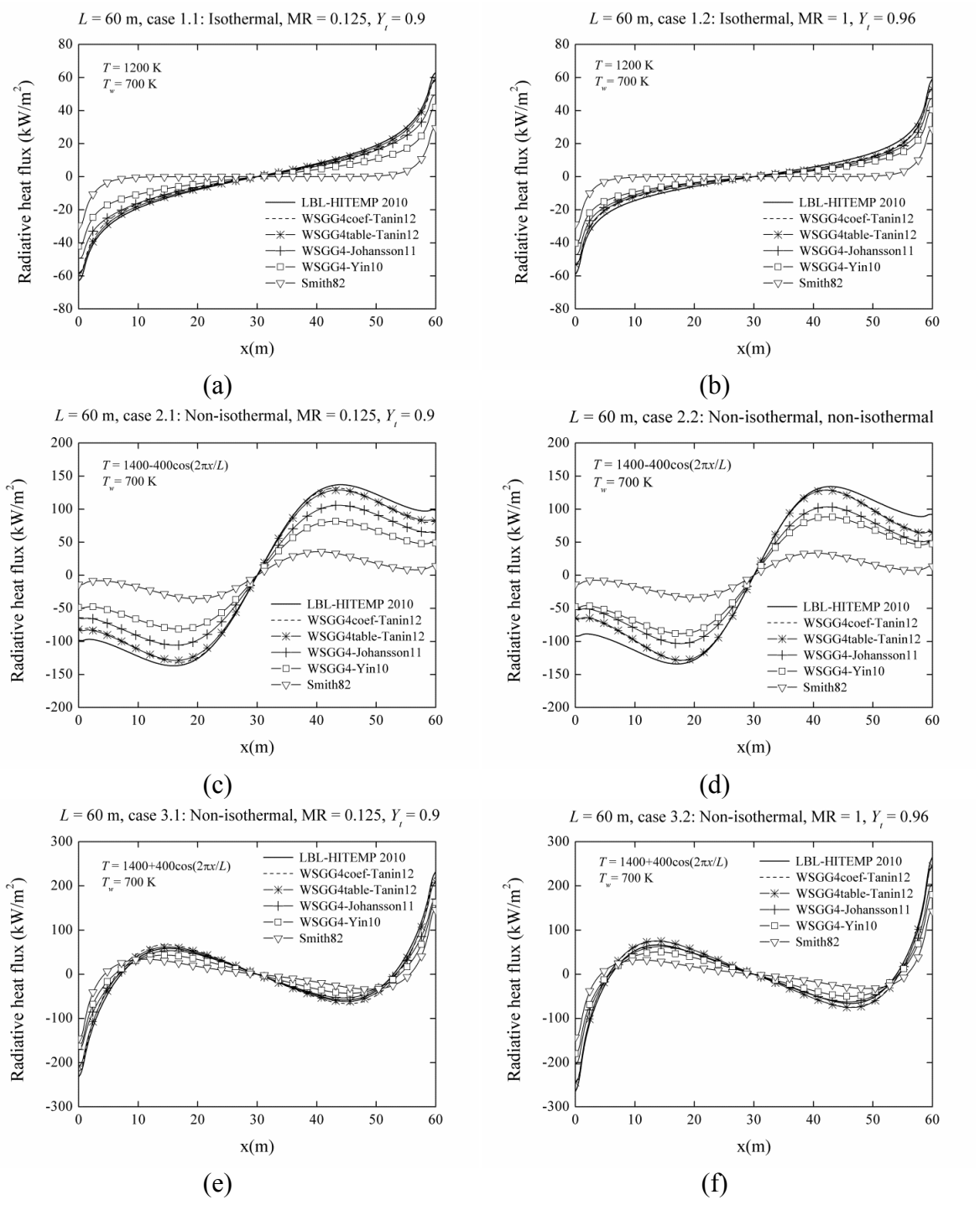

Figure E.11. Radiative heat fluxes (q_w) computed with different correlations of the WSGG model along length coordinates for path-lengths of 60 m: isothermal and non-isothermal homogeneous cases (case 1-3).

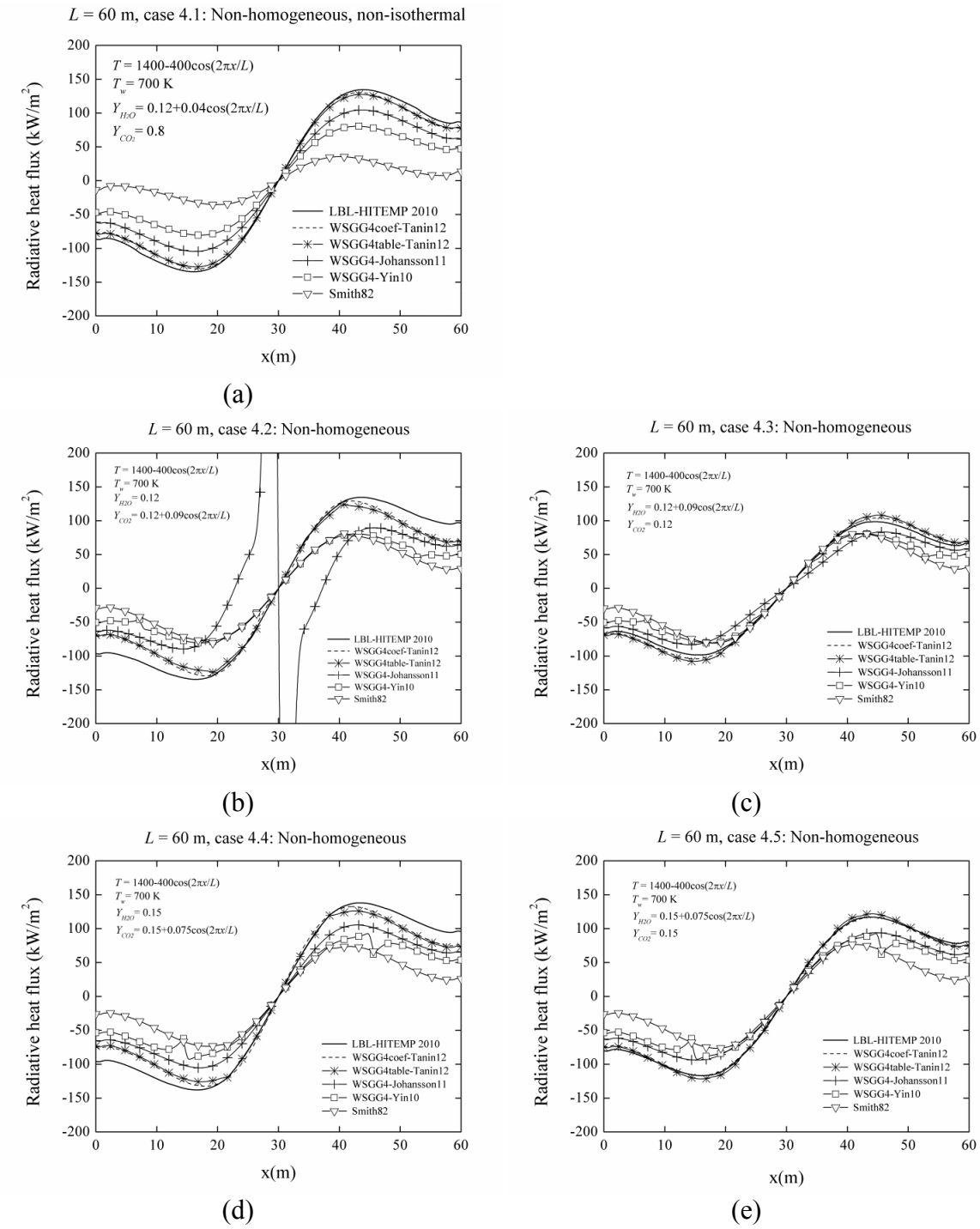

Figure E.12. Radiative heat fluxes (q_w) computed with different correlations of the WSGG model along length coordinates for path-lengths of 60 m: non-isothermal non-homogeneous cases (case 4).

Appendix F: Radiative heat fluxes (incident wall flux) varying with path-lengths from 0.5- 60 m (P = 1 bar)

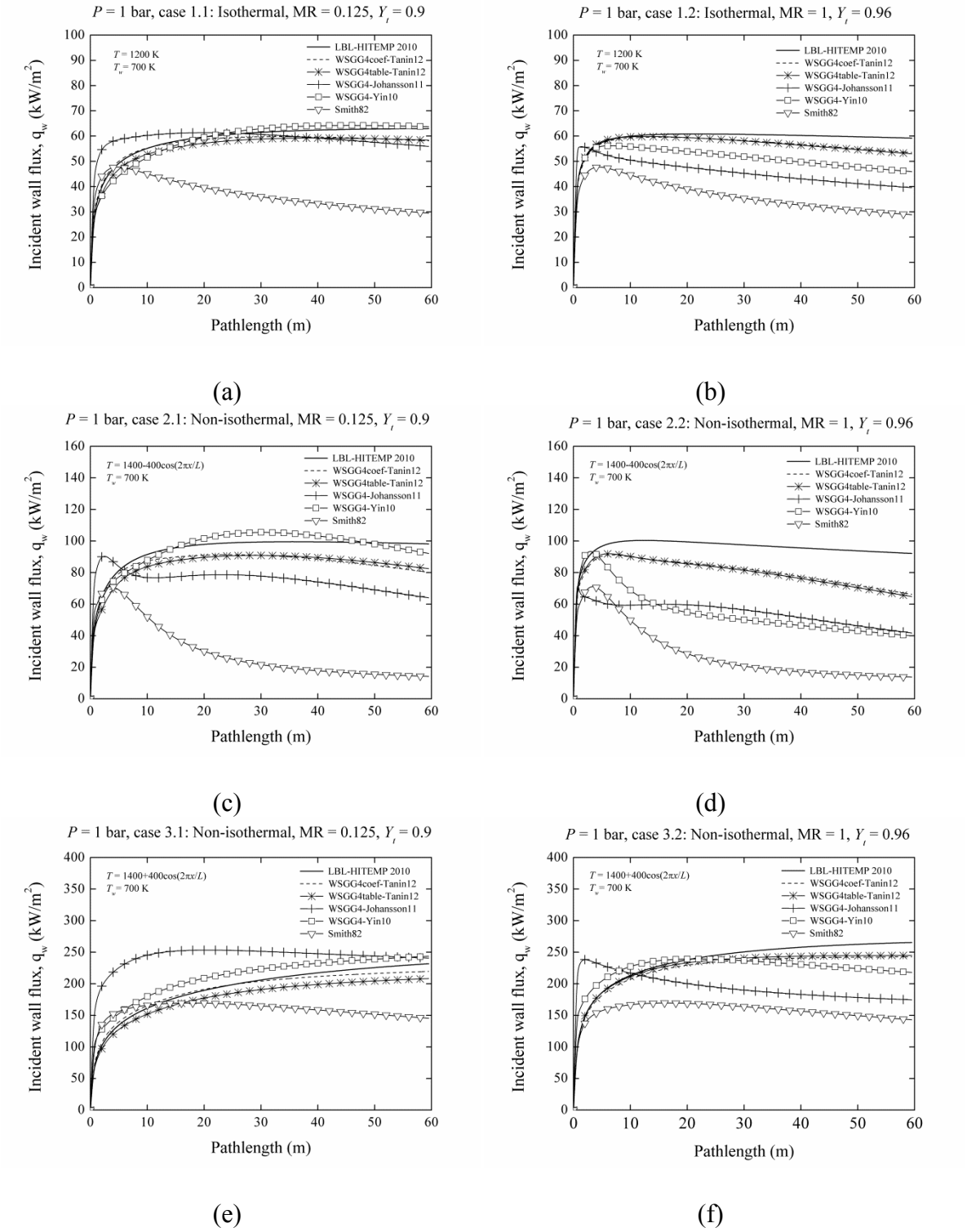

Figure F.1. Comparison of the radiative heat flux, q_w, applying different correlations for WSGG model varying with path-lengths up to 60 m: isothermal and non-isothermal homogeneous cases (case 1-3).

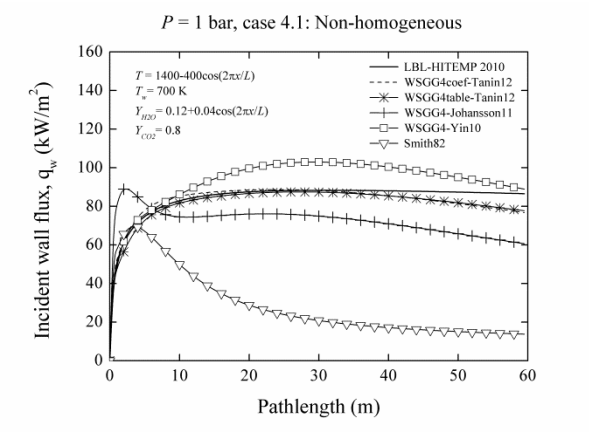

(a)

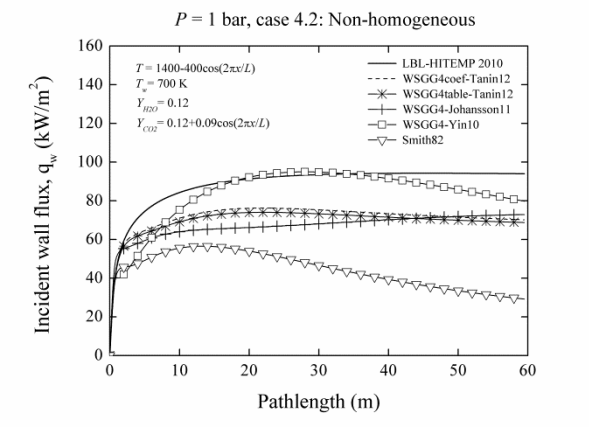

(b)

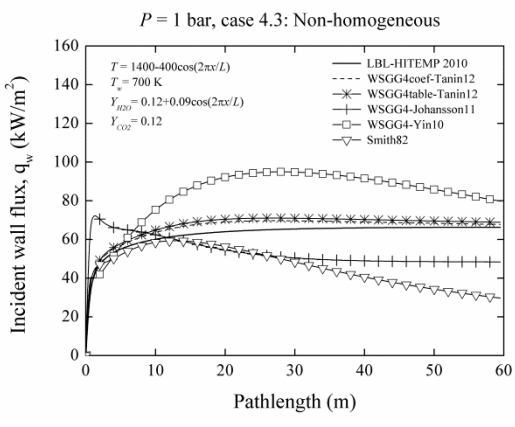

(c)

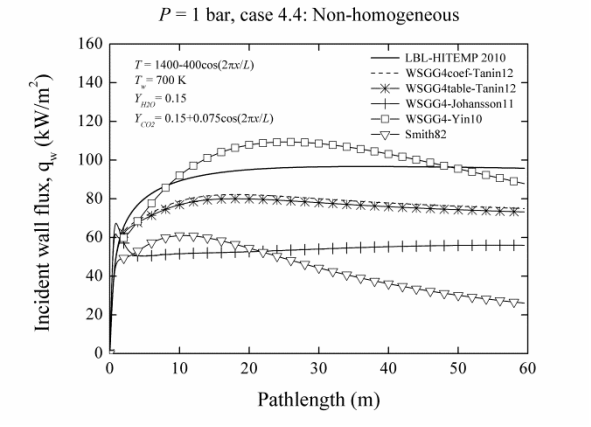

(d)

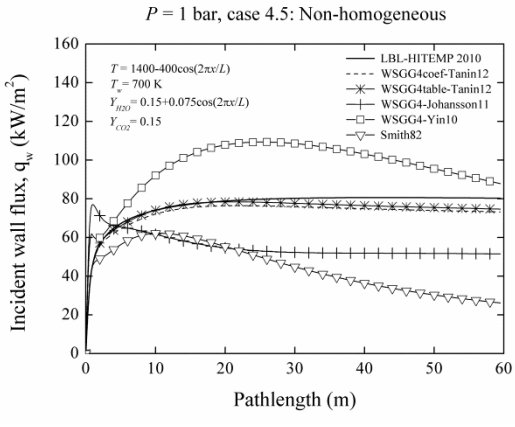

(e)

Figure F.2. Comparison of the radiative heat flux, q_w, applying different correlations for WSGG model varying with path-lengths up to 60 m: non-isothermal non-homogeneous cases (case 4).

Appendix G: Relative errors of radiative source terms and heat fluxes varying with path-lengths from 0.5- 60 m (P = 1 bar)

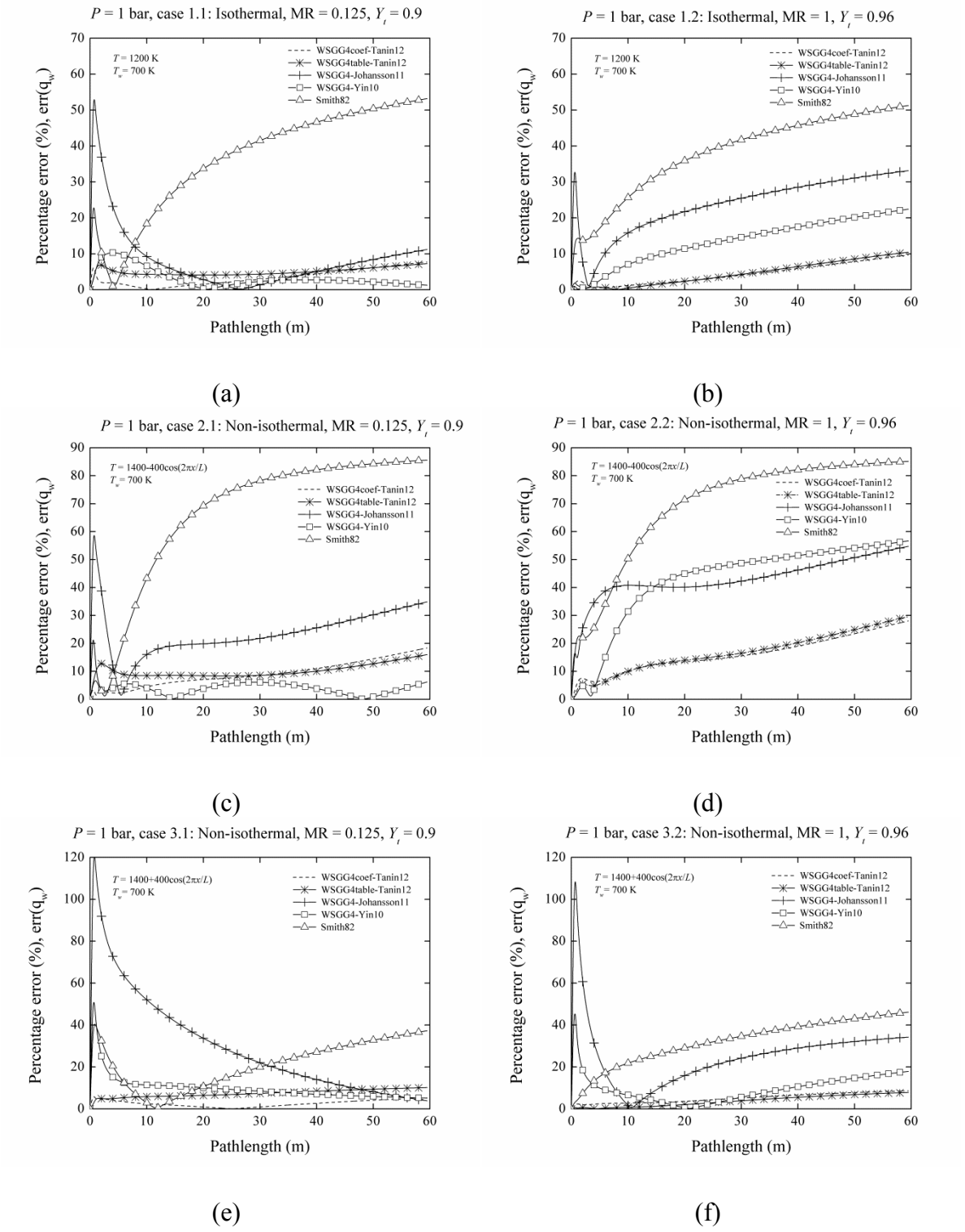

Figure G.1. Comparison of relative errors of the radiative heat flux, $err(q_w)$, applying different correlations for WSGG model varying with path-lengths up to 60 m: isothermal and non-isothermal homogeneous cases (case 1-3).

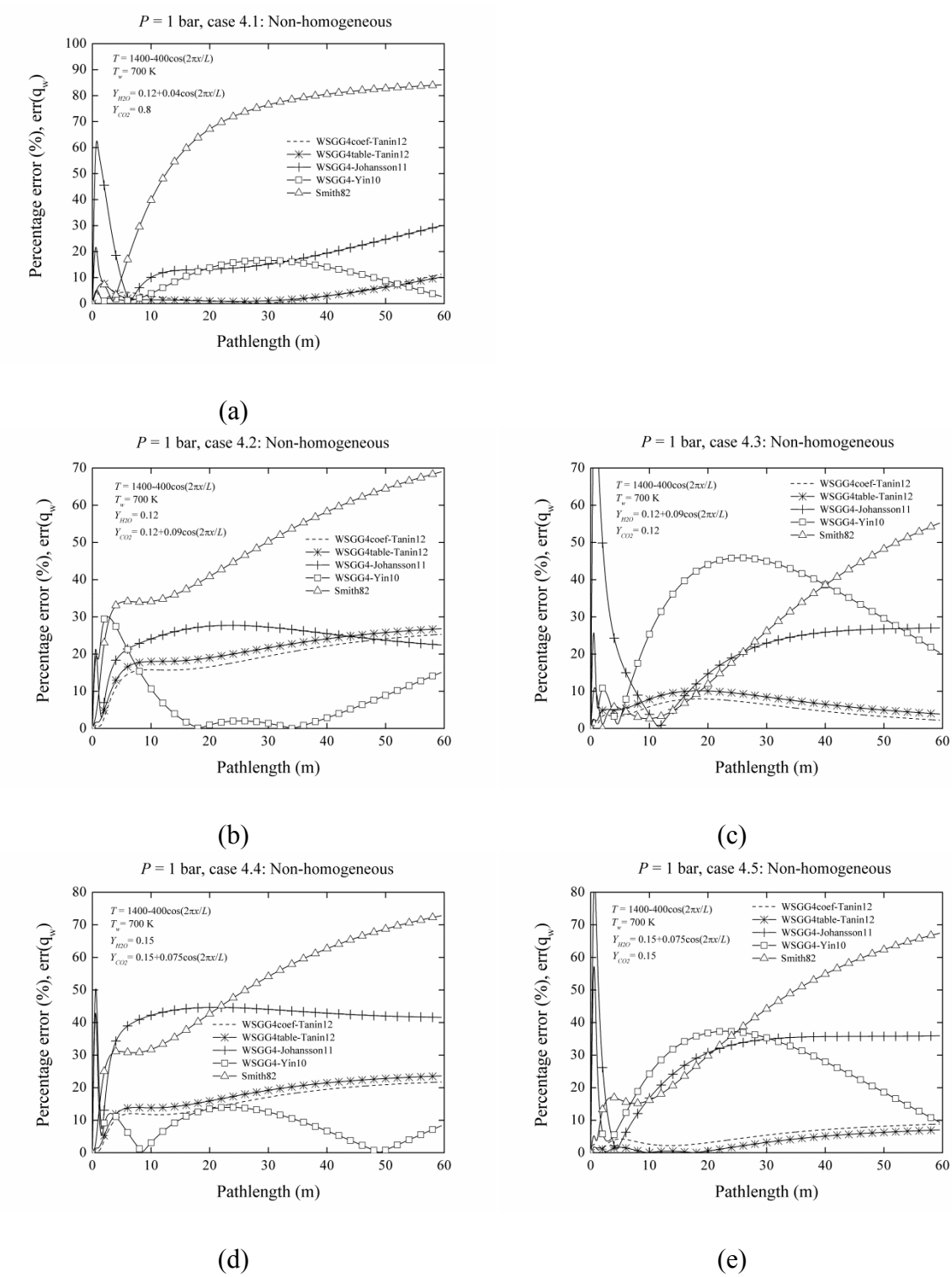

Figure G.2. Comparison of relative errors of the radiative heat flux, $err(q_w)$, applying different correlations for WSGG model varying with path-lengths up to 60 m: non-isothermal non-homogeneous cases (case 4).

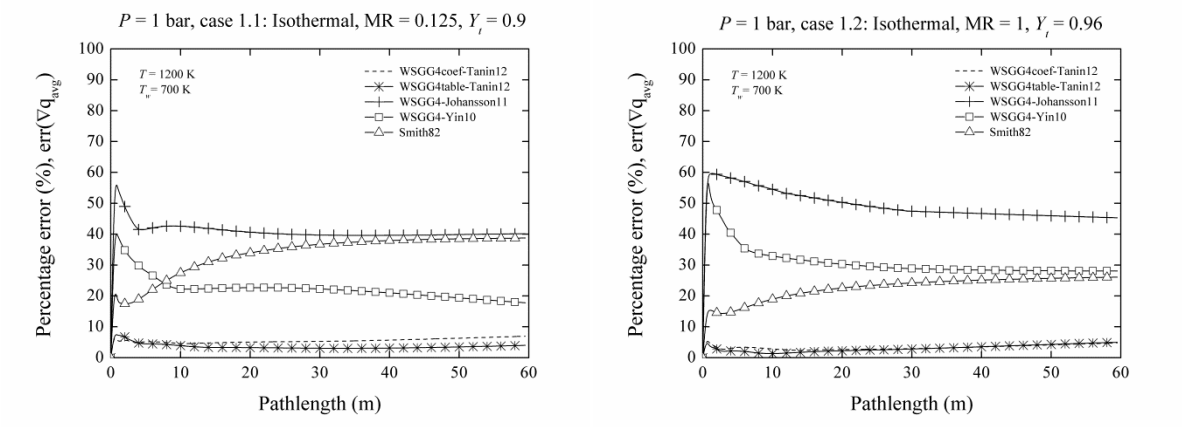

(a) (b)

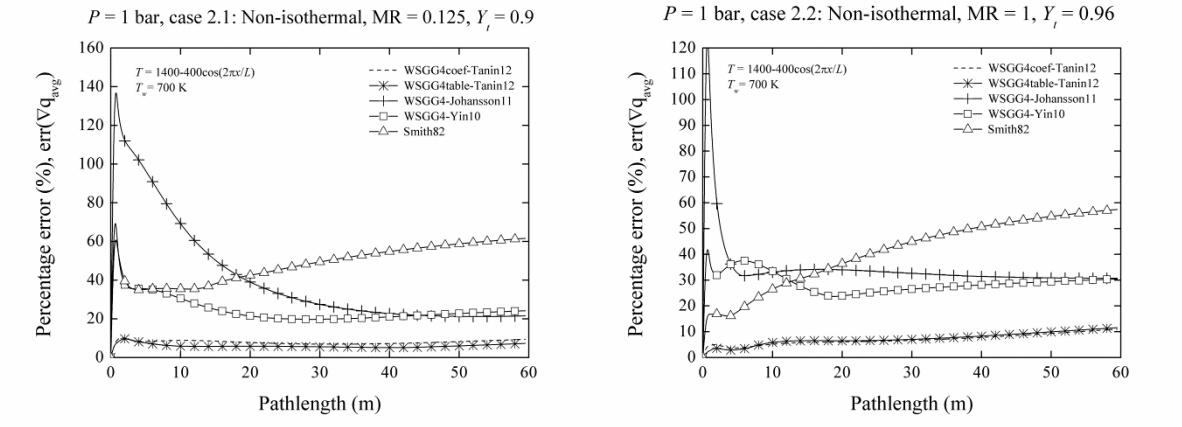

(c) (d)

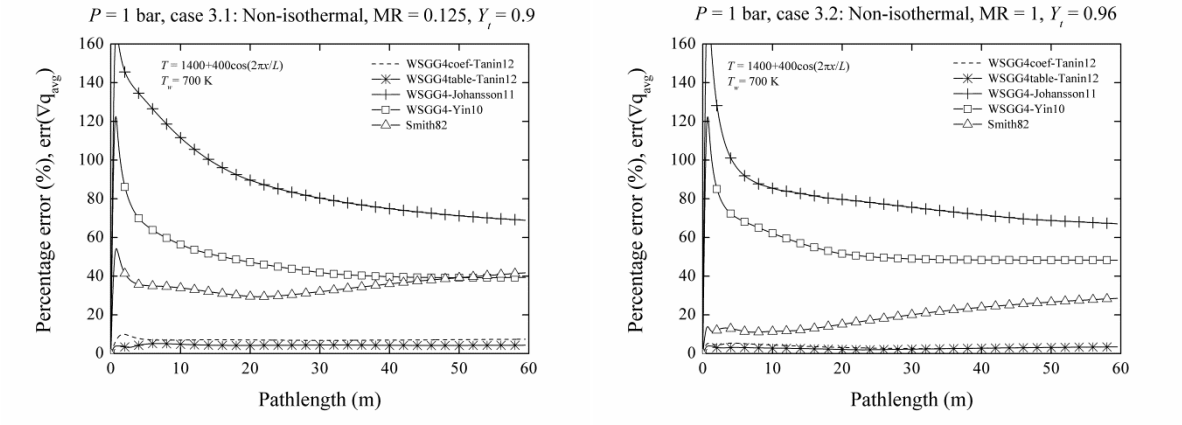

(e) (f)

Figure G.3. Comparison of relative errors of the average source term *err*(∇q_{avg}), applying different correlations for WSGG model varying with path-lengths up to 60 m: isothermal and non-isothermal homogeneous cases (case 1-3).

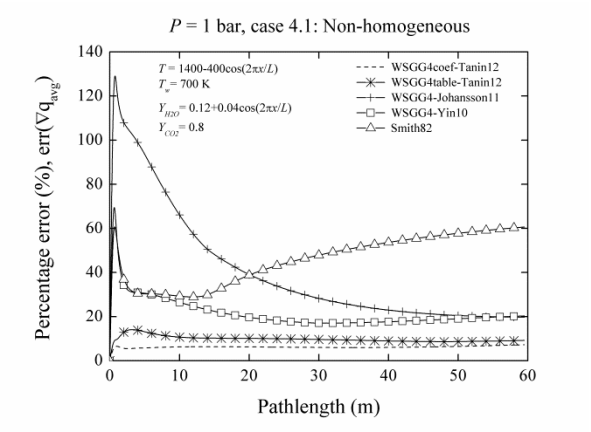

(a)

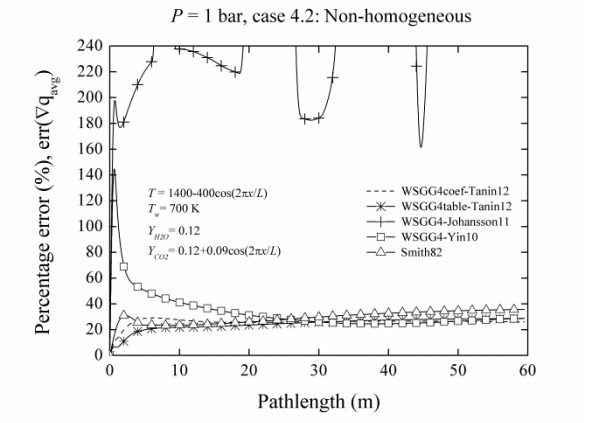

(b)

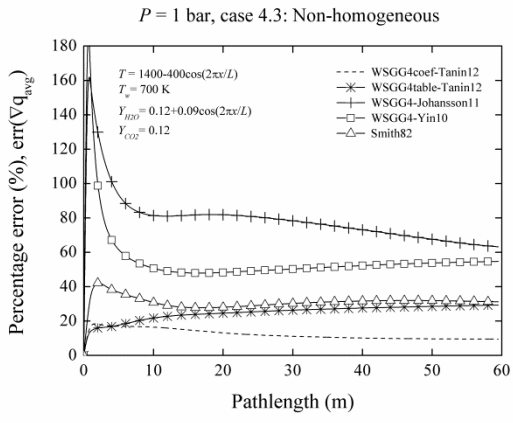

(c)

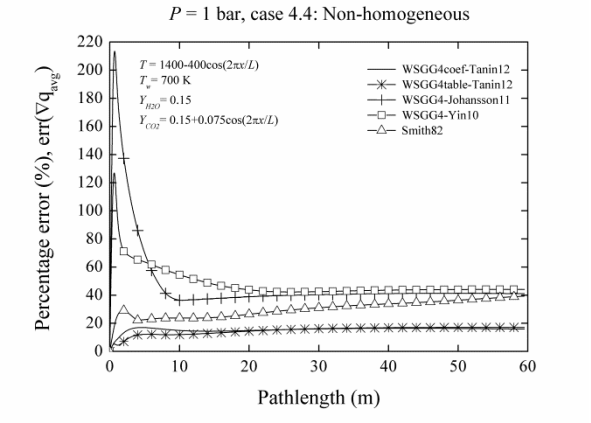

(d)

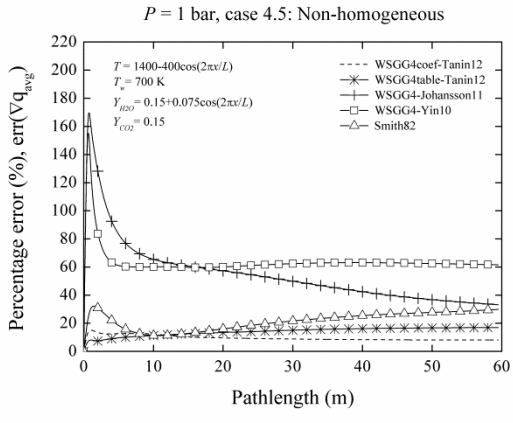

(e)

Figure G.4. Comparison of relative errors of the average source term *err(∇q_{avg})*, applying different correlations for WSGG model varying with path-lengths up to 60 m: non-isothermal non-homogeneous cases (case 4).

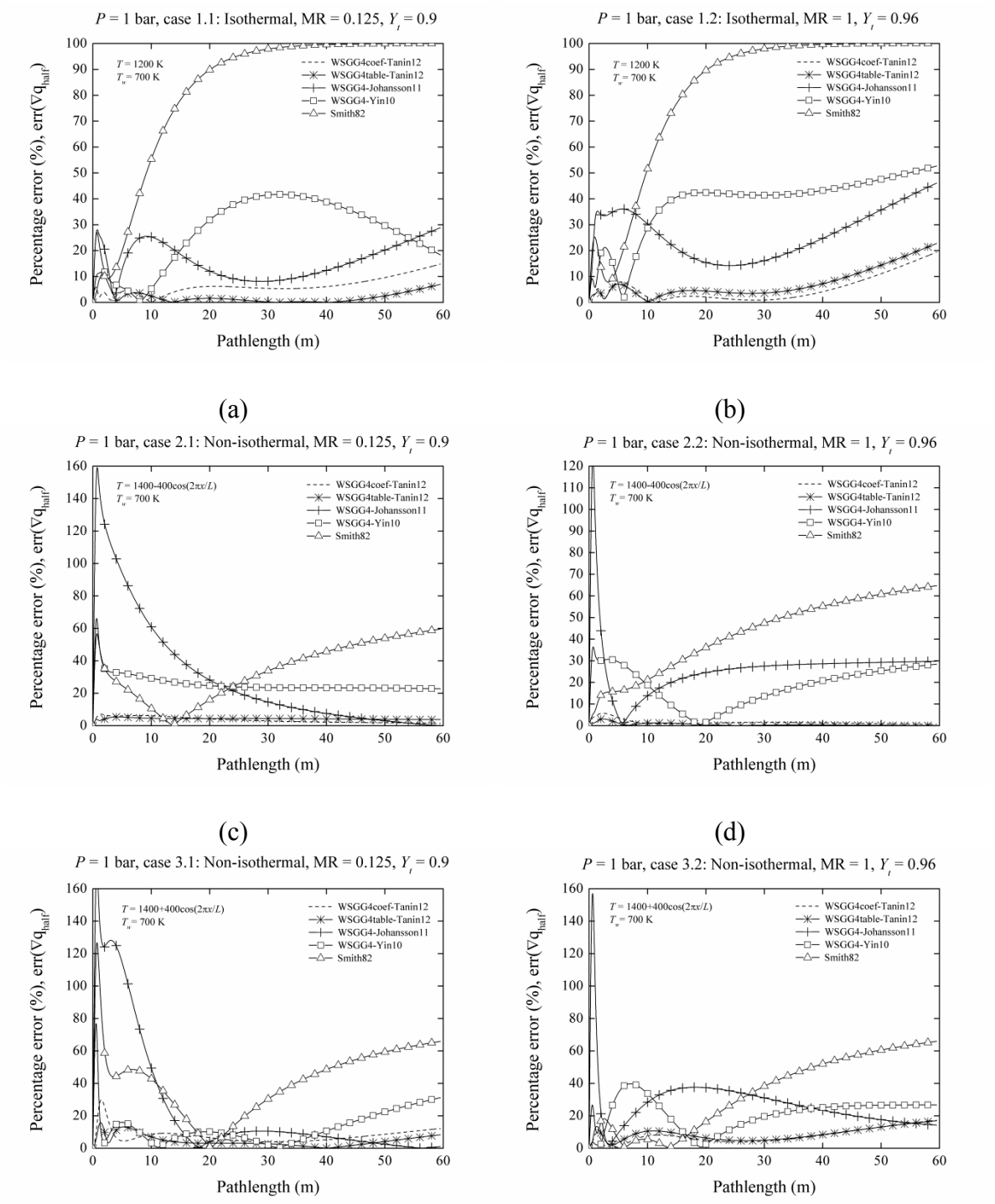

Figure G.5. Comparison of relative errors of the source term at the mid-distance between the plates, e*rr*(∇q_{half}), applying different correlations for WSGG model varying with path-lengths up to 60 m: isothermal and non-isothermal homogeneous cases (case 1-3).

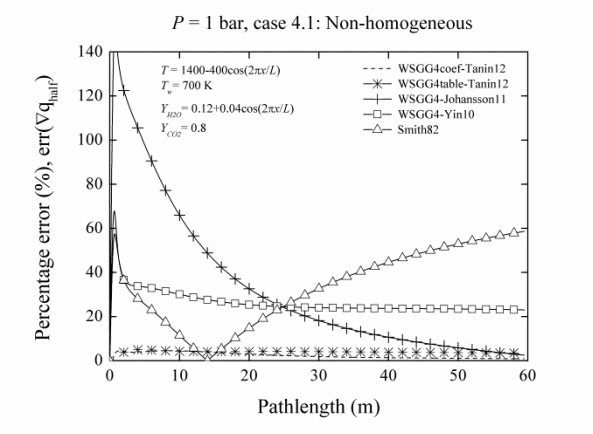

(a)

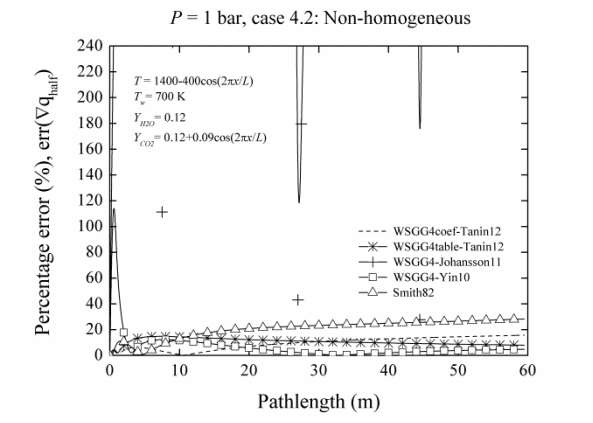

(b)

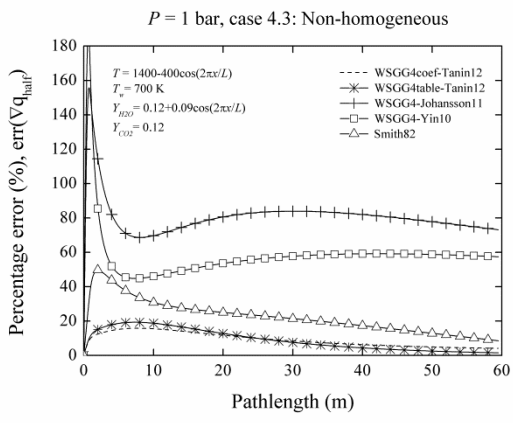

(c)

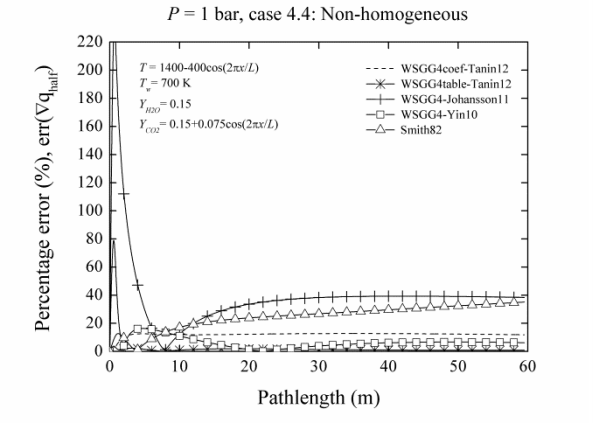

(d)

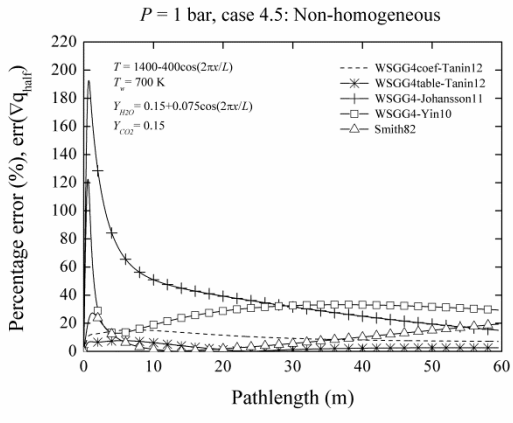

(e)

Figure G.6. Comparison of relative errors of the source term at the mid-distance between the plates, *e*rr(∇q_{half}), applying different correlations for WSGG model varying with path-lengths up to 60 m: non-isothermal non-homogeneous cases (case 4).

Appendix H: Nomenclature

A_{br} pre-exponential factor for bridge-breaking process in CPD model

$A_{Kin,c}$ pre-exponential factor of char reaction

$A_{i,c}$ pre-exponential factor of intrinsic kinetic rate model for char reaction

A_{cross} pre-exponential factor for cross-linking mechanism in CPD model

A_g pre-exponential factor of volatiles and gaseous reaction

A_s specific internal surface area of char particle, m^2/kg

A_{surf} cell surface area of control volume, m^2

$A_{s,0}$ initial specific internal surface area of char particle, m^2/kg

A_{RRC} the corresponding pre-exponential factor for CPD model

$Area_o$ projection area of object in the counter-flow direction

A_p external surface area of char particle, m^2

A_i Area vector for control surface in the *i* direction, m^2

A_v Avogadro constant, molecules/mole

a flow quantities defined in UPWIND discretized scheme

$a_{G,ij}$ flow quantities defined in UPWIND discretized scheme

BD_i body force per unit mass of species *i*

B_{sh} constant for correlation of Sherwood number for a spherical particle

$b_{i,j}$ temperature dependent polynomial coefficients for emittance

$b_{G,i}$ constant number in the linear equations of Gauss-Seidel iteration

C_P specific heats of a gas at a constant-pressure, J/(kg K)

C_v specific heats of a gas at a constant-volume, J/(kg K)

C_{diff} diffusion rate constant , kg/(m s Pa $K^{0.75}$)

C molar concentration of any species, $kmol/m^3$

C_{React} molar concentration of the reactant species, $kmol/m^3$

C_{Prod} molar concentration of the product species, $kmol/m^3$

C_g oxygen concentration in the bulk gas, kg/m^3

C_s oxygen concentration at the outer surface of the particle, kg/m^3

C_D drag coefficients

C_l parameter for RSM turbulent model

C_μ parameter constants for turbulent models

$C_{1\varepsilon}$, $C_{2\varepsilon}$, $C_{3\varepsilon}$ parameter constants for turbulent models

$C_{ps,1}$, $C_{ps,2}$ parameter constants for RSM turbulent model

$\acute{C}_{ps,1}$, $\acute{C}_{ps,2}$ parameter constants for RSM turbulent model

CT_r volumetric concentration of reactants

CT_p volumetric concentration of products

C_{s2} second Planck function constant, cm K

C(s)	char particle
CA	cell face area for UPWIND scheme
c	speed of light in vacuum, m/s
$c_{i,j}$	normalized temperature dependent polynomial coefficients for emittance
chb	fraction of char bridges for CPD model,
chb_0	initial fraction of char bridges for CPD model
$const1_{Kin,c}$	correlation of linear or quadratic equation for char reaction model
$const2_{Kin,c}$	correlation of linear or quadratic equation for char reaction model
$const3_{Kin,c}$	correlation of linear or quadratic equation for char reaction model
D_{eff}	effective diffusion coefficient of reactant gas into pores, m^2/s
D_{Kn}	Knudsen diffusion coefficient, m^2/s
$D_{Tm,P}$	diffusion coefficient at mean temperature, m^2/s
$D_{T0,P0}$	diffusion coefficient at reference state, m^2/s
DF	degeneracy factor
DF_{ind}	state-independent degeneracy factor
DF_{rot}	degeneracy factor of the rotational state of energy E_{rot}
DF_{vib}	degeneracy factor of the rotational state of energy E_{vib}
D_e, D_w	diffusion conductance at the cell faces for UPWIND scheme
D_{duct},	characteristic length of the duct for the calculation of hydraulic diameter, m
D_{outer}	outer diameter of duct in the calculation of hydraulic diameter, m
D_{inner}	inner diameter of duct in the calculation of hydraulic diameter, m
$d_{n,wall}$	normal distance to the wall for RSM turbulent model
d_p	particle diameter, m
$d_{p,0}$	char diameter at the initial stage of char reaction, m
$\bar{d}_p$	mean diameter for Rosin-Rammler particle distribution, m
E_s	state energy of the transition, cm^{-1}
E_{rot}	rotational state of energy, cm^{-1}
E_{vib}	vibrational state of energy, cm^{-1}
E_{br}	activation energy for bridge-breaking process in CPD model
E_{cross}	activation energy for cross-linking mechanism in CPD model
E_g	activation energy of volatiles and gaseous reaction, J/kmol
$E_{Kin,c}$	activation energy of char reaction, J/kmol
$E_{i,c}$	activation energy of intrinsic kinetic rate model for char reaction, J/kmol
E_{RRC}	the corresponding activation energy for CPD model
EC_1	first empirical constant for turbulent-chemistry interaction
EC_2	second empirical constant for turbulent-chemistry interaction
e	specific internal energy, J/kg
e_g	specific internal energy of gas mixture, J/kg
e_k	specific internal energy of specie k, J/kg

FB	fraction of blackbody emissive power
$F1$	statistical relations depending on percolation lattice statistics
$F2$	statistical relations depending on percolation lattice statistics
$F3(IB)$	statistical relations depending on percolation lattice statistics
$F4(IB)$	statistical relations depending on percolation lattice statistics
F_e, F_w	convective mass flux per unit area of flow for UPWIND scheme
$f_{p,i}$	aerodynamics force on the particles per volume of mixture in i direction, N/m^3
f_{bb}	fraction of broken bridges for CPD model
f_q	line shape function of q^{th} transition line
f_v	soot volume fraction
G_η	incident radiation function, W/m^3
G_k, $\tilde{G}_k$	generation of turbulent kinetic energy due to mean velocity gradients
G_b	generation of turbulence kinetic energy due to buoyancy
G_ω	generation of ω for SST k-ω model
g_i, g_j	component of the gravitational vectors in the i or j direction in turbulent equations
h	Planck constant, J·s
h_D	mass transfer coefficient, m/s
h_k	specific enthalpy of specie k, J/kg
h_g	specific enthalpy of gas mixture, J/kg
$\bar{h}_s$	average enthalpy of gas over the particle control surface
I	total radiation intensity, W/(m^2·sr)
I_η	spectral radiation intensity, W/(m^2·sr)
I_b	total blackbody radiation intensity, W/(m^2·sr)
$I_{b,\eta}$	spectral blackbody radiation intensity, W/(m^2·sr)
I_{turb}	turbulence intensity
IB_0	initial fraction of bridges in the coal lattice for CPD model,
J	total number of polynomial order
$J_{m,k}$	mass flux for specie k, kg/(m^2 s)
J_s	mass flux of reactant gas at the surface of char, kg/(m^2 s)
K_{diff}	diffusional reaction rate coefficient, kg/(m^2 s Pa)
K_{cond}	thermal conductivity, W/(m K)
K_D	mass transfer coefficient, m/s
K_b	Arrhenius rate constant for CPD model
K_δ,	Arrhenius rate constant for CPD model
K_g	Arrhenius rate constant for CPD model
K_{chb}	Arrhenius rate constant for CPD model
k	turbulent kinetic energy
$\bar{k}$	mean turbulent kinetic energy

k_{fw}	kinetic rate of forward reaction for volatiles and gaseous reaction
k_{rw}	kinetic rate of reverse reaction for volatiles and gaseous reaction
k_{c}	kinetic rate of char heterogeneous reaction
k_s	index of refraction for soot particle radiation
k_B	Boltzmann constant, J/K
L	path length or distance between one dimensional parallel infinite, m
L_m	mean beam length, m
L_p	path length related to partial pressure p of a specific gas, m
LC_o	characteristic length of object, m
$LC_{\sigma+1}$	lattice coordination number for CPD model
LG	total content of light gases for CPD model
LG_1	content of first light gas for CPD model
LG_2	content of second light gas for CPD model
LI_q	line intensity of the q^{th} transition line
l_{turb},	size of the large eddies that contain the energy in turbulent flows, m
MF	mass fraction
MW_c	molecular weight of carbon in char particle
MW_g	molecular weight of reactant gas
MF_k	mass fraction of k^{th} species
MF_r	mass fraction of a particular reactant
MF_p	mass fraction of any product species
MW_k	molecular weight of k^{th} species
MW_r	molecular weight of particular reactant
MW_p	molecular weight of any product species
$MW_{cluster}$	cluster molecular weight
MW_{δ}.	side chain molecular weight
m	mass of fluid and gaseous species, kg
m_c	residual carbon mass, kg
$m_{c,}$	initial carbon mass, kg
m_{lb}	average molecular weight of a labile bridge for CPD model, kg
m_{cross}	amount of reattached metaplast for cross-linking mechanism in CPD model
m_{meta}	amount of metaplast for cross-linking mechanism in CPD model
N_g	total number of gray gases
N_d	total number of directions for solution of RTE in DOM
N_a	number of particles in the gas, molecules
N_c	number of polynomial coefficients for the weighting factors
N_g	total number of gray gases
N_p	total number of path-lengths for procedure of fitting correlations
N_t	total number of temperatures for procedure of fitting correlations

N_{mesh}	number of computational cells
N_{mol}	number density of the absorbing molecules, molecules/cm^3
N_w	number of ordinates and quadrature weights for DOM
N_{eq}	number of equations in the linear equations of Gauss-Seidel iteration
N_{un}	number of unknowns in the linear equations of Gauss-Seidel iteration
n_i, n_k, n_m	unit component normal to wall for RSM turbulent model
n_c	order of reaction for char particle
n_{ap}	apparent order of reaction for char particle
n_{true}	true order of reaction for char particle
$\hat{n}$	normal vector outward direction from wall surface
n_r	refractive index for medium
n_{air}	coefficient of temperature dependence of the air-broadened half-width
n_s	index of refraction for soot particle radiation
$\hat{n}$	normal vector outward a surface element
n_{RR}	size distribution parameter for Rosin-Rammler particle distribution
P, p	pressure, Pa
P_a	sum of partial pressure of absorbing gases, bar
P_T	total pressure of gases, Pa
P_g	partial pressure of reactant gas in the bulk gas, Pa
P_s	partial pressure of reactant gas at the outer surface of the particle, Pa
P_0	pressure at reference state, K
p_i	pressure stress tensor, Pa
$\bar{p}_S$	averaged pressure on the particle surface, Pa
Q	heat production per unit volume (source term of heat generation), W/m^3
q	heat flux, kW/m^2
q_r	radiative heat flux, kW/m^2
q_η	radiative heat flux for spectral wavenumber η, kW/m^2
q_{sr}	specific heat radiation term (per unit volume), W/m^3
q_{cp}	specific heat transfer to the particles from the gas by conduction, W/m^3
q_{rg}	specific radiative heat transfer absorbed by gas, W/m^3
q_{rp}	specific radiative heat transfer absorbed by particle, W/m^3
$q_{s,j}$	heat transfer through the boundary particle, W/m^2
R	universal gas constant, J/(kmol K)
Re	Reynolds number
Re_{HD}	Reynolds number based on characteristic hydraulic diameter
$RF(r_w)$	is the reflection at wall
$R_{ch,c}$	chemical kinetic rate of reaction (kg/(m^2 s))
$R_{Kin,c}$	chemical kinetic rate of char reaction, kg/(m^2 s Pa^{nap})

R_{diff} mass diffusion flux of gas at the char surface, kg/(m^2 s)

R_k chemical reaction rate, kg/(m^2 s)

R_p rate of gas mass added per unit volume of mixture from particle, kg/(m^3 s)

$R_{R,s}$ rate of dissipation of reactant eddies of the s^{th} species

$R_{P,s}$ rate of dissipation of product eddies of the s^{th} species

$R_{t,c}$ total char burning rate, kg/s

$R_{s,c}$ the burning rate of char per external surface area, kg/(s m^2)

$R_{i,c}$ intrinsic chemical reactivity coefficient, kg/(m^2 s Pa^{ntrue})

r position vector for RTE

$\bar{r}_p$ mean pore radius of particle, m

r_{outer} outer radius of duct in the calculation of hydraulic diameter, m

r_{inner} inner radius of duct in the calculation of hydraulic diameter, m

S modulus of the mean rate of strain tensor for turbulent models

S_{ij} strain rate tensor for turbulent models

Sc Schmidt number

SF_η source function integrated over a set of direction coordinates

$\bar{S}\Delta\forall_u$, $\bar{S}\Delta\forall_v$ momentum source terms for UPWIND scheme

SV volumetric source terms for UPWIND scheme

S_k, S_ε input source terms for kinetic energy and its dissipation

S_ω source terms for SST k-ω model

s direction vector for RTE

s' scattering direction vector for RTE

s_v particle dilatation rate per unit volume of mixture, s^{-1}

$\hat{s}$ traveling direction for radiative energy in RTE

T_m mean temperature in the boundary layer near to particle surface

T gas temperature, K

T_p temperature at surface of char particle, K

T_g temperature of bulk gas at surface of char particle, K

T_0 temperature at reference state, K

TE temperature exponent of kinetic reaction rate for volatile and reactant gases

TM transmission of radiative energy in any direction

t time, s

U_c burnout of char particle

U_m reference mean flow velocity for calculation of turbulence intensity, m/s

u velocity or velocity in the horizontal direction, m/s

u_i velocity vector in the *i* direction, m/s

u_j velocity vector in the *j* direction, m/s

$\bar{u}_i$ *mean* velocity, m/s

$\acute{u}_i$	fluctuating velocity, m/s
$u_{g,i}$	mass-averaged gas velocity, m/s
$u_{p,i}$	mass-averaged particle velocity, m/s
$u_{D,k,i}$	diffusional velocity of specie *k*, m/s
u'_x, u'_y, u'_z	fluctuating velocity in x,y and z direction, m/s
V	volume of computational cells, m^3
VF	void fraction of the volume occupied by the gas per volume of mixture
V_{RRC}	the corresponding distributed activation term for CPD model
v	velocity in the vertical direction, m/s
w_i	weighting factor of gray gas *i*
$\acute{w}$	gas velocity at control surface of particle, m/s
x	length coordinate along the space between the infinite slab, m
x_i	length of control volume in the *i* direction, m
$x_{G,i}$	flow variables in the linear equations of Gauss-Seidel iteration
Y	molar fraction of gas
Y_c	residual carbon mass fraction
Y_{dp}	mass fraction of particles with diameter greater than any diameter d_p
Y_M	contribution of the fluctuating dilatation in compressible turbulence to the overall dissipation rate
Y_k, Y_ω	dissipation of k and ω due to turbulence

Greek letters

α_k, α_ε	inverse effective Prandtl number determined using RNG theory
α_{BM}	exponent parameters of burnout for char diameter
$\alpha_{React,k}$	rate exponents of the k^{th} species as a reactant
$\alpha_{Prod,k}$	rate exponents of the k^{th} species as a product
β_{BM}	exponent parameters of burnout for char density
β_f	property of the fluid per unit mass
γ_{size}	characteristic size of the particle for intrinsic model
δ_{ij}	Kronecker delta
δ_{sc}	side chain for CPD devolatization model
ε	dissipation rate for turbulent kinetic energy
ϵ	total emissivity
ϵ_g	total emissivity of gas mixture
$\epsilon_{T,gs}$	total emissivity of gas-soot mixture
η_{RNG}	parameter for RNG turbulent model
η	wavenumber, 1/cm

η_{eff}	effectiveness factor for intrinsic model
θ	swirling blade angle
θ_{poro}	porosity of solid char
$\theta_{poro,0}$	initial porosity of solid char
κ	absorption coefficient, 1/(Pa-m)
κ_i	absorption coefficient of gray gas *i*, 1/(Pa-m)
κ_T	total absorption coefficient of gray gas, 1/(Pa-m)
$\kappa_{T,gs}$	total absorption coefficient of gas-soot mixture, 1/m
κ_s	total absorption coefficient of soot particle, 1/m
κ_g	total absorption coefficient of gas mixture, 1/m
λ	wavelength, m
$\lambda_{up,i}$	upper wavelength band limit of each gray gas, m
$\lambda_{low,i}$	lower wavelength band limit of each gray gas, m
μ	dynamic viscosity, kg/(s m)
μ_t	turbulent viscosity, kg/(s m)
μ_{eff}	effective turbulent viscosity, kg/(s m)
ν_t	eddy viscosity
ν_g	stochiometric coefficient of reactant gas
$\nu_{React,k}$	stoichiometric coefficients for k^{th} species as a reactant
$\nu_{Prod,k}$	stoichiometric coefficients for k^{th} species as a product
ρ	mass density of gas or solid phase, kg/m^3
ρ_{ap}	apparent density of residual char particles at the initial stage, kg/m^3
$\rho_{ap,0}$	char apparent density at the initial stage of char reaction, kg/m^3
ρ_{true}	true density of residual char particles, kg/m^3
ρ_g	gas density, kg/m^3
ρ_p	particle density, kg/m^3
$\acute{\rho}_g$	mass of the gas per unit volume of gas-particle mixture, kg/m^3
$\acute{\rho}_p$	mass of the gas per unit volume of gas-particle mixture, kg/m^3
ρ_k	local time-mean species concentration for k^{th} species, kg/m^3
σ	Stefan-Boltzmann constant, W/(m^2 K^4)
σ_s	scattering coefficient, 1/(Pa-m)
σ_h	Prandtl/Schmidt number
σ_k, σ_ε	turbulent Prandtl numbers
τ_{ij}	shear stress tensor
τ_{tor}	tortuosity factor for intrinsic reaction rate model
$\tau_{stn,ij}$	shear stress tensor acting on the particle due to the local rate of strain in the fluid

ω_k	angular velocity, rad/s
$\overline{\Omega_{ij}}$	mean rate of rotation tensor for Realized k-ε model
$\acute{\Omega}_s$	solid angle for the solution of RTE in $\acute{s}$ direction
Ω_s	solid angle for the solution of RTE in $\hat{s}$ direction
$\forall$	volume of fluid or computational cell, m^3
$£^*$	reactive bridge intermediate for CPD devolatilization model
$£$	labile bridge for CPD devolatilization model
Λ	gravimetric stoichiometric coefficient
Φ_{th}	Thiele modulus of intrinsic kinetic rate model for char reaction
Φ_{ph}	scattering phase function, sr^{-1}
Φ	dissipation function for turbulent equations
Γ_w, Γ_e	diffusion coefficients on the west and east cell face for UPWIND scheme
Γ_h	heat conduction coefficient or diffusion coefficient of enthalpy
Δx_u	width of u-cells control volume
$\Delta\forall_u$	volume of u-cells control volume
Δx_v	width of v-cells control volume
$\Delta\forall_v$	volume of v-cells control volume

Subscripts:

b	blackbody value
br	bridge-breaking step for devolatilization process
C	carbon content
c	char particle
chg	chemical reaction rate for volatile and gaseous species
ch,c	chemical reaction rate for char particle
E	eastern nodes for UPWIND scheme
e	eastern cell faces for UPWIND scheme
fw	forward reaction
g	gaseous species
H	hydrogen content
I, i	randomly index of gray gases for WSGG model, direction vector for governing, turbulent equations, RTE and numerical methods.
ip	index of path-lengths
ipd	index of product species
ir	index of reactant species
J, j	randomly index of temperature dependent polynomial order of weighting factor for WSGG model, direction vector for governing, turbulent equations, RTE and numerical methods.

Kin	chemical kinetic reaction
k	index of species
l	index of Reynolds stress transport equation
low	lower wavelength band limit
m	index of Reynolds stress transport equation
O	oxygen content
P	center nodes for UPWIND scheme
Prod	product of reaction
p	particle
React	reactant of reaction
rel	relative velocity
r	index of reactant species
rot	rotational state
rw	reverse reaction
s	index of species
up	upper wavelength band limit
u	u-cells control volume
VM	volatile matter content
vib	vibrational state
v	v-cells control volume
W	western nodes for UPWIND scheme
wl	wall surface
w	western cell faces for UPWIND scheme
w,r	radiative heat flux at wall

Superscripts:

ps	index of particle sizes
´	fluctuating component

Abbreviations:

BET	Brunauer-Emmett-Teller method of measuring surface area of particle
BP	Buoyancy production for RSM
CCS	carbon capture and storage
CFD	computational fluid dynamics
CPD	chemical percolation devolatilization
CS	control surface

CV	control volume
DNS	Direct Numerical Simulation
DOM	discrete ordinate method
EWB	exponential wide band
HD	hydraulic diameter, m
HITEMP	high-temperature spectroscopic absorption database
HITRAN	high-resolution transmission molecular absorption database
KD	kinetic diffusion limited rate model
LBL	line-by-line
LES	Large eddy simulation
LM	Levenberg-Marquardt algorithm
MR	molar ratio of H_2O to CO_2
MUCSL	Monotone Upstream-Centered Schemes for Conservation Laws
PISO	Pressure Implicit with Splitting of Operators
PS	Pressure strain for RSM
QUICK	Quadratic Upwind Interpolation for Convective Kinematics
RANS	Reynolds-averaged Navier-Stokes equation
RBC	the ratio of bridge mass to site mass
RPM	random pore model
RRC	the ratio of rate constants for CPD model
RSM	Reynolds stress model
RTE	radiative transfer equation
SIMPLE	Semi-Implicit Method for Pressure-Linked Equations
SNB	statistical narrow band
SP	Stress production for RSM
TDMA	tri-diagonal matrix algorithm
TGC	turbulent gaseous combustion
TVD	total variation diminishing
UPWIND	upwind-difference
UR, URF	under-relaxation factor
VM	volatile matter content
WSGG	weighted-sum-of-gray-gases

Appendix I: List of Figures

Figure G.2: Comparison of relative errors of the radiative heat flux, $err(q_w)$, applying different correlations for WSGG model varying with path-lengths up to 60 m: non-isothermal non-homogeneous cases (case 4).

Figure G.3: Comparison of relative errors of the average source term $err(\nabla q_{avg})$, applying different correlations for WSGG model varying with path-lengths up to 60 m: isothermal and non-isothermal homogeneous cases (case 1-3).

Figure G.4: Comparison of relative errors of the average source term $err(\nabla q_{avg})$, applying different correlations for WSGG model varying with path-lengths up to 60 m: non-isothermal non-homogeneous cases (case 4).

Figure G.5: Comparison of relative errors of the source term at the mid-distance between the plates, $err(\nabla q_{half})$, applying different correlations for WSGG model varying with path-lengths up to 60 m: isothermal and non-isothermal homogeneous cases (case 1-3).

Figure G.6: Comparison of relative errors of the source term at the mid-distance between the plates, $err(\nabla q_{half})$, applying different correlations for WSGG model varying with path-lengths up to 60 m: non-isothermal non-homogeneous cases (case 4).

Appendix J: List of Tables